Binary Black Hole Mergers and Novel Approaches to Gravitational Wave Extraction in Numerical Relativity

Der Fakultät für Mathematik und Physik
der Gottfried Wilhelm Leibniz Universität Hannover

zur Erlangung des Grades

Doktor der Naturwissenschaften
Dr. rer. nat.

genehmigte Dissertation
von

Dipl.-Phys. **Christian Reisswig**
geboren am 26.01.1981 in Hannover

2010

Referent: Bernard F. Schutz
Korreferent: Nigel T. Bishop
Tag der Promotion: 04.02.2010

Binary Black Hole Mergers and Novel Approaches to Gravitational Wave Extraction in Numerical Relativity

Christian Reisswig

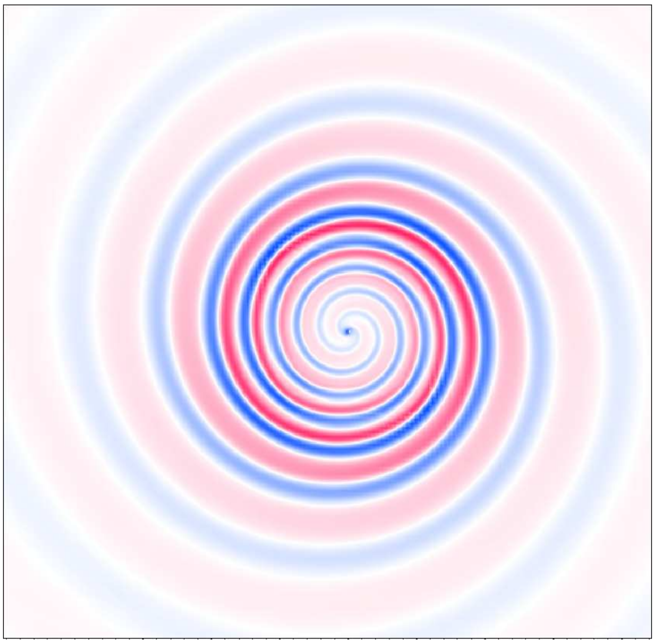

Dissertation

Gottfried Wilhelm Leibniz Universität Hannover
and
Max-Planck-Institut für Gravitationsphysik
Albert-Einstein-Institut
Potsdam / Golm

Cover figure: Gravitational radiation emitted in the orbital plane during a binary black hole merger encoded in the Weyl scalar Ψ_4. Plotted here is $r \cdot \Psi_4$ to compensate for the $1/r$ falloff that Ψ_4 obeys. One can see that the amount of radiation is particularly strong during a certain time - the time of the merger - and becomes weaker in the ring-down phase where the final black hole settles to a stationary state.

Abstract

Keywords: Black holes, Gravitational waves, Numerical Relativity.

Binary black hole mergers are supposed to be the strongest source of gravitational radiation in the Universe. These systems can radiate up to $\sim 10\%$ of their total mass leading to the colossal liberation of $\sim 10^{60}$ergs in gravitational waves as for a supermassive black hole merger with a mass of 10^7 solar-masses $M_\odot$. Hence, these systems are the first candidates to be detected in gravitational-wave interferometers like (advanced/enhanced) LIGO, (advanced) Virgo and LISA.

In this thesis, we study various aspects of binary black hole mergers with the tools of numerical relativity. By applying fully 3D simulation codes to realistic binary black hole initial data, mostly restricted to the 2D parameter subspace of equal-mass spin-aligned binaries, we determine various properties of the binary systems.

We compute the signal-to-noise ratio for the various configurations in the parameter subspace considered and can show that spin-aligned binaries will be generally "three times as loud" as spin anti-aligned binaries, hence leading to a probability of detection which will be ~ 30 times larger than for the latter binaries. In addition, we derive a phenomenological expression for the radiated energy and show that between $\sim 3.6\%$ and $\sim 10\%$ of the total mass of the binary will be emitted in gravitational waves. Furthermore, we show that binaries with spin $a_1 = -a_2$ cannot be distinguished within the given numerical accuracy, whereas configurations with spin $a_1 = a_2$ are clearly different. This indicates that gravitational-wave template banks can be modeled in terms of a single scalar spin parameter a, at least at lowest order. Even simple waveforms, such as those relative to non-spinning binaries, will be effective enough to provide a detection for most configurations of equal-mass and aligned/anti-aligned binaries.

Several properties of the merger remnant are of particular interest. Among these is the recoil velocity that the remnant can acquire due to asymmetric emission of gravitational radiation. In the 2D parameter subspace of equal-mass and spin-aligned binaries, we quantify this effect and conclude that the maximal emerging recoil of $|v_{\rm recoil}| = 441.94 \pm 1.56$km/s will not be sufficient to kick the remnant out of its host environment.

Furthermore, we consider the final spin of the merger remnant and find that the remnant is typically spun-up by the merger. We determine the conditions under which the angular momentum of the spacetime "flips sign" and under what conditions a Schwarzschild black hole is produced.

For both properties of the remnant, recoil and spin, we present simple phenomenological expressions in terms of the parameters of the initial black holes that can be used in N-body simulations of galaxy mergers and star-cluster dynamics, where it is impractical to include the full non-linear interactions of binary black hole systems.

A major achievement in this thesis is the first unambiguous determination of binary black hole merger waveforms at future null infinity $\mathscr{J}^+$. Through the application of Cauchy characteristic extraction, we are able to determine the full non-linear dynamics of the complete spacetime out to $\mathscr{J}^+$. We show that the obtained waveforms are free of any gauge effects and contain only numerical error. This also allows to assess the systematic finite-radius error inherent in all current wave-extraction measurements, and we show that current numerical relativity waveforms are valid, but corrections have to be taken into account for advanced detectors, especially for parameter estimation.

Furthermore, we develop a multiblock infrastructure coupled to an adaptive mesh-refinement driver, and use topologically adapted grids to accurately and efficiently represent the gravitational wave-zone out to large radii. This allows to causally disconnect the artificial outer boundary of the computational domain during Cauchy evolution such that the extraction world-tubes are located within the future Cauchy horizon of the compact subset of the initial Cauchy hypersurface. As a result, we are able to show that the higher harmonic modes of the wave-signal can be accurately resolved, and we demonstrate convergence of modes up to $(\ell, m) = (6, 6)$.

Zusammenfassung

Schlagworte: Schwarze Löcher, Gravitationswellen, Numerische Relativitätstheorie.

Binärsysteme zweier verschmelzender schwarzer Löcher werden als Quellen stärkster gravitativer Strahlung im Universum angesehen. Diese Systeme können bis zu $\sim 10\%$ ihrer Gesamtmasse abstrahlen, was der kolossalen Energiemenge von 10^{60}ergs gleichkommt, die bei verschmelzenden supermassiven schwarzen Löchern mit einer Masse von 10^7 Sonnenmassen $M_\odot$ in Gravitationswellen freigesetzt wird. Diese Systeme sind deshalb die ersten Anwärter, die in Gravitationswelleninterferometern wie (advanced/enhanced) LIGO, (advanced) Virgo und LISA nachgewiesen werden.

In der vorliegenden Dissertation studieren wir verschiedene Aspekte binärer schwarzer Löcher mit Hilfe der numerischen Relativitätstheorie. Durch Anwendung von dreidimensionalen Simulationscodes auf realistische Anfangsdaten binärer schwarzer Löcher, meist beschränkt auf den zweidimensionalen (2D) Parameterunterraum gleichmassiger und spin-ausgerichteter Binärsysteme, bestimmen wir verschiedene Eigenschaften der Schwarzlochsysteme. Wir berechnen das Signal-zu-Rausch-Verhältnis für unterschiedliche Konfigurationen in dem betrachteten Parameterunterraum und können zeigen, dass spin-ausgerichtete Binärsysteme generell “dreimal lauter” als spin-antiausgerichtete Systeme sind, und deshalb zu einer 30 mal höheren Detektionswahrscheinlichkeit führen als letztere Systeme. Darüber hinaus leiten wir einen phänomenologischen Ausdruck für die abgestrahlte Energie ab, und zeigen, dass zwischen $\sim 3.6\%$ und $\sim 10\%$ der Gesamtmasse der Binärsysteme in Gravitationswellen emittiert werden. Desweiteren zeigen wir, dass Binärsysteme mit Spin $a_1 = -a_2$ innerhalb der numerischen Genauigkeit nicht unterschieden werden können, jedoch sind Systeme mit Spin $a_1 = a_2$ eindeutig unterscheidbar. Dies indiziert, das Schablonenbänke für Gravitationswellen in Termen eines einzigen skalaren Spinparameters a modeliert werden können, zumindest bei niedrigster Ordnung. Es stellt sich heraus, dass sogar einfachste Wellenformen effektiv genug sind, um die meisten spin-ausgericheten Konfigurationen aufzuspühren.

Weiterhin ermitteln wir den durch asymmetrische Strahlung verursachten gravitativen Rückstoß. Wir quantifizieren diesen Effekt im betrachteten 2D Parameterunterraum und schließen auf eine maximal mögliche Rückstoßgeschwindigkeit von $|v_{\mathrm{recoil}}| = 441.94 \pm 1.56$km/s, die nicht ausreicht, um das verschmolzene schwarze Loch aus seiner Umgebung herauszuschleudern.

In einer verwandten Arbeit betrachten wir den Spin des verschmolzenen schwarzen Loches und finden, dass der Verschmelzungsprozess typischerweise zu einer Zunahme des Spins führt.

Für beide Eigenschaften, Spin und Rückstoß, präsentieren wir einfache phänomenologische Ausdrücke, die in N-Körpersimulationen von Galaxienverschmelzungen und Sternenclustern verwendet werden können.

Eine große Errungenschaft dieser Arbeit stellt die erste eindeutige Bestimmung von Gravitationswellen binärer schwarzer Löcher bei lichtartig Zukunftsunendlich $\mathscr{J}^+$ dar. Durch die Anwendung von Cauchy-charakteristischer Extraktion sind wir in der Lage, die volle nicht-lineare Dynamik der kompletten Raumzeit einschließlich $\mathscr{J}^+$ zu bestimmen. Wir zeigen, dass die errechneten Wellenformen frei von Eicheffekten sind, und ausschließlich numerische Fehler enthalten. Dies ermöglicht, den systematischen Fehler abzuschätzen, der jeder bisherigen Wellenextraktion anhaftet. Wir zeigen, dass bisherige Wellenformen gültig sind, jedoch müssen Korrekturen für die erweiterten Detektoren einbezogen werden, insbesondere wenn Parameterbestimmung entscheidend ist.

Desweiteren entwickeln wir eine Multiblock-Infrastruktur, die an einen adaptiven Netzverfeinerungstreiber gekoppelt ist, und benutzen topologisch angepasste Gitter, um die gravitative Wellenzone genau und effizient bis zu großen Radien darzustellen. Dies ermöglicht, den künstlichen äußeren Rand der Berechnungsdomäne kausal abzuschneiden, sodass die Extraktionsweltröhren innerhalb des zukünftigen Cauchy-Horizontes der kompakten Untermenge der initialen Cauchy-Hyperfläche lokalisiert sind. Demzufolge sind wir in der Lage zu zeigen, dass die höheren harmonischen Moden des Wellensignals präzise aufgelöst werden können, und wir demonstrieren Konvergenz der Moden bis zu $(\ell, m) = (6, 6)$.

Contents

Preface ix
Why binary black hole mergers? ix
Why numerical simulations? x
The challenge xi
The goal and new results obtained in this thesis xii
Organization of this thesis xv
Notations and conventions xvi

I Foundations and Mathematical Theory 1

1 Vacuum binary black hole spacetimes 3
1.1 The Einstein equations 4
1.2 Black holes 5
Black hole parameters;
Black hole properties;
1.3 Asymptotics 8
Conformal representation and structure;
Asymptotic simplicity;
The Weyl tensor;
The Newman-Penrose formalism;
The Petrov classification and the Sachs peeling property;
Asymptotic mass and momentum;
1.4 Gravitational waves 15
Gravitational waves in linearized gravity;
Energy, linear and angular momentum of gravitational waves;
Gravitational waves in the full non-linear theory;
Interaction of gravitational waves with a detector;
1.5 Binary black hole systems 21
The three stages of binary black hole coalescence;
Parameter space and properties of the remnant;

2 The Cauchy evolution system 27
2.1 The ADM formalism 28
3+1 decomposition;
Extrinsic curvature;
The ADM equations;
2.2 The BSSNOK formulation 31
Conformal-traceless 3+1 representation;
Constraint treatment;
2.3 Choosing the right gauge 35
Geodesic slicing;
Maximal slicing;
Hyperbolic slicing;
Hyperbolic $\tilde{\Gamma}$*-driver condition;*
2.4 Initial data 39
Conformal transverse-traceless initial data construction;
Bowen-York extrinsic curvature;
The puncture method;
Quasi-circular orbits and the effective potential method;
Initial parameters from post-Newtonian inspiral;
2.5 Dealing with spacetime singularities 48
Puncture evolution;

3 The characteristic evolution system 51

3.1 The Bondi-Sachs metric 51
3.2 The Einstein equations in a characteristic formulation 52
  Formulation in terms of spin-weighted scalars;
  Angular coordinate basis;
  Radial compactification;
  The evolution system;
  The constraint equations;

4 Horizons **61**
4.1 Event horizons 62
4.2 Apparent horizons 63
  Expansion;
  Trapped surfaces;
  Properties;
4.3 Isolated and dynamical horizons 65
  Isolated horizons;
  Dynamical horizons;
  Mass and spin;

5 Gravitational wave extraction: Theory **69**
5.1 Extraction I: Complex Weyl scalars 69
5.2 Extraction II: Gauge-invariant perturbations of Schwarzschild 70
  Multipolar expansion;
  Odd (axial) perturbations;
  Even (polar) perturbations;
  Obtaining the master functions from numerical spacetimes;
5.3 Extraction III: Cauchy-characteristic extraction 74
  Outline of the procedure;
  Coordinate parametrization of the world-tube;
  4D geometry around the world-tube;
  Coordinate transformation;
  Null metric;
  Metric in Bondi coordinates;
  Bondi variables for starting up the null code at the world-tube;
  Obtaining the Bondi news and Ψ_4*;*
5.4 The gravitational-wave strain 87
  The strain from the Weyl component Ψ_4*;*
  The strain from gauge invariant master-functions;
5.5 Radiated energy 88
  The radiated energy from the Weyl component Ψ_4*;*
  The radiated energy from gauge-invariant master-functions;
5.6 Radiated linear momentum 89
  The radiated linear momentum from the Weyl component Ψ_4*;*
  The radiated linear momentum from gauge-invariant master-functions;
5.7 Radiated angular momentum 91
  The radiated angular momentum from the Weyl component Ψ_4*;*
  The radiated angular momentum from gauge-invariant master-functions;

II Numerics and Implementation **95**

6 Discretization of hyperbolic PDEs **97**
6.1 Finite differences 97
  Difference operators;
  Dissipation operators;
6.2 Method of lines 99
  Runge-Kutta time integration;
6.3 Stability and well-posedness 100
  Well-posedness;
  Stability;
  Von Neumann stability analysis;
  The Courant-Friedrichs-Lewy condition;
6.4 Hyperbolicity 104
6.5 Convergence and consistency 105

Testing for convergence;

7 Computational infrastructure 109

7.1 The Cactus computational toolkit . . . 110
Structure;
Modularity;
Scheduling mechanism and control inversion;
Memory management, multi-processor distribution and message passing;

7.2 Adaptive mesh refinement . . . 113
Carpet: The Cactus AMR driver;
Mesh refinement method;
Time evolution scheme;

7.3 Multiblock schemes . . . 116
Multiple grid patches, local and global coordinates;
Interpatch interpolation;
Global derivatives;
The wave-zone: six-patch "inflated cube" system;
Adding AMR: Seven-patch system;
The Llama-code;

7.4 Spherical slices . . . 127
Variable registration;
Parallelization;
Interface;
Surface integration;
Harmonic decomposition;

8 Discretization of the evolution systems 133

8.1 The Cauchy system . . . 133
Structure of the numerical grid;
Discretization of the equations;
The CCATIE code;
The Llama code;
Calculation of puncture initial data;
Puncture tracking;
Apparent horizon finding;

8.2 The characteristic system . . . 141
Structure of the numerical grid;
Numerical implementation of the quasi-spherical approximation;
The full non-linear discretization;

9 Gravitational wave extraction: Implementation 149

9.1 Cauchy characteristic extraction . . . 149
World-tube boundary data;
Reconstruction from harmonic modes;
Interpolation to constant Bondi time and mode decomposition;
Linearized conformal factor;

9.2 Psiclops . . . 153

9.3 WaveExtract . . . 154

9.4 Psi4Lab . . . 154

10 Visualization of simulation data 157

10.1 A Visit database plugin for Carpet AMR and curvi-linear meshes . . . 157
Construction of metadata;
Construction of meshes;
Reading of data;
Examples;

III Simulations and Physics 161

11 Binary black hole merger simulations 163

11.1 Spin-aligned binaries . . . 164
Spin-kick configurations;
Configurations with larger initial separation;

Equal-mass non-spinning reference configuration;
11.2 Convergence and accuracy tests 170
Convergence of the CCATIE code;
Convergence and accuracy of the Llama code;
Convergence of the characteristic code;
Conservation of mass and angular momentum;
A comparison of wave-extraction methods and test for peeling;
The influence of upwinded advection stencils;
High order finite differencing;
Choice of conformal variable;
11.3 Ring-down and quasi-normal modes 194
11.4 Comparing different simulation codes 195

12 Gravitational recoil of binary black hole mergers 201
12.1 Systematic studies on a restricted set of spin-aligned binaries 202
Initial transients in the waveforms;
Recoil velocities;
Mode contributions to the recoil velocity;
On the influence of orbital eccentricity;
Conclusions;
12.2 Parameter space of equal-mass spin-aligned binaries 214
Spin diagrams and fits;

13 Final spin of the merger remnant 217
13.1 Spin of equal-mass spin-aligned binaries 218
Fitting formula;
13.2 Extension to unequal-mass spin-aligned binaries 220
Methods and Results;
13.3 Extension to generic mass-ratios and spins 224
Assumptions;
Analytic expression;
Results;

14 Gravitational-wave detectability of black-hole binaries 233
14.1 Introduction 233
14.2 Gravitational-wave observables 234
Numerical relativity waveforms;
Matching PN and NR waveform amplitudes;
Radiated energy;
SNR, horizon distances and event rates;
14.3 Results 240
Horizon distances and SNRs;
Influence of higher ℓ-modes;
Match between different models;
Accuracy of NR waveform amplitudes;
14.4 Fitting formulas 249
SNR;
Radiated energy;
14.5 Conclusions 254

15 Gravitational wave extraction: Results 257
15.1 The asymptotic fall-off of local waveform measurements 257
Taking advantage of multiblock schemes;
Extrapolation to infinity;
Peeling properties;
Discussion;
15.2 Unambiguous determination of gravitational waveforms 262
Cauchy evolution;
Cauchy characteristic extraction;
Test with a Schwarzschild black hole and gauge invariance;
Binary black hole merger waveform;
Observational significance;
Invariance with respect to world-tube location;
Notes on characteristic code settings;

16 Summary and outlook **271**

A Reference formulae **277**
A.1 Geometrized units . . . 277
A.2 Sensitivity curves . . . 279
A.3 Finite difference and dissipation operators . . . 280
A.4 Six-patch local coordinates and Jacobians . . . 283
A.5 Spin-weighted spheroidal harmonics . . . 285

Acknowledgments **287**

Curriculum vitae **289**

List of related publications **290**

Bibliography **291**

List of abbreviations

ADM	Arnowitt-Deser-Misner
AH	Apparent Horizon
AMR	Adapative-Mesh Refinement
API	Application Programming Interface
BBH	Binary Black Holes
BH	Black Hole
BICGSTAB	Biconjugate Gradient Stabilized
BKL	Buannano-Kidder-Lehner
BSSNOK	Baumgarte-Shapiro-Shibata-Nakamura-Oohara-Kojima
CCE	Cauchy-Characteristic Extraction
CCM	Cauchy-Characteristic Matching
CFL	Courant-Friedrichs-Lewy
DH	Dynamical Horzion
EH	Event Horizon
EMRL	Extreme Mass Ratio Limit
EOB	Effective-One-Body
GR	General Relativity
NR	Numerical Relativity
IMBH	Intermediate Mass Black Hole
I/O	Input/Output
ISCO	Innermost Stable Circular Orbit
LHS	Left-Hand Side
MoL	Method of Lines
MPI	Message Passing Interface
NEH	Non-Expanding Horizon
ODE	Ordinary Differential Equation
PDE	Partial Differential Equation
PN	Post-Newtonian
QNM	Quasi-Normal Mode
QSO	Quasi-Stellar Object
RHS	Right-Hand Side
RK	Runge-Kutta
SAT	Simultaneous Approximation Term
SBH	Stellar mass Black Hole
SMBH	Supermassive Black Hole
SNR	Signal-to-Noise Ratio
TT	Transverse Traceless
(W)ENO	(Weighted) Essentially Non-Oscillatory
(W)IH	(Weakly) Isolated Horizon

Preface

Why binary black hole mergers?

Any two gravitationally bound black holes (BHs) represent a binary black hole (BBH) system. These systems continuously loose energy and angular momentum through the emission of gravitational radiation and hence move closer to each other as they orbit. If not disrupted by external forces, the ultimate fate of any such system is the final merger to a single BH.

These merging binaries are of prominent interest to gravitational-wave analysis because they are supposed to produce the most powerful gravitational-wave signals and hence, are perfect candidates for gravitational-wave detection. For example, a 100 solar mass binary will release a total amount of about 10^{55} ergs corresponding to about 6% of its total mass, $\sim 80\%$ of which is liberated in the very last seconds during the merger itself.

The detection of gravitational waves is an outstanding experimental evidence that has to be adduced in order to confirm general relativity (GR) on an experimental level. Moreover, the ability to measure gravitational waves will open up a whole new class of astronomical observations since scientists will not be limited to the electromagnetic spectrum anymore, but it will enable them to explore the Universe in its dominant interaction at cosmological scales. Since BBH systems are expected to be the most powerful source of gravitational radiation, these binaries will probably be the first to be detected, and they will probably also be the first objects to be studied observationally with gravitational-wave detectors. Furthermore, BBHs represent the two-body problem of vacuum GR, and observing them via gravitational-wave emission may give clues on how our theories of gravitation have to be modified to eventually construct a unified theory of particle interactions. Although this is beyond the current scope of today's research, it still justifies the fundamental importance of BBH systems.

Apart from pure detection of BH merger events, various astrophysical aspects of the merger remnant are of great interest. Among these is the recoil (or "kick") velocity of the merged object. A recoil can occur if gravitational radiation is emitted asymetrically during the evolution of the binary. Since gravitational waves carry energy, angular and linear momentum, there might be a prominent direction in which linear momentum is beamed, thus resulting in a non-zero net linear momentum or "kick". In the case of supermassive BHs, which are expected to be harboured in the centers of massive galaxies, after the system has merged, the final object may have received a kick which is sufficient to overcome the binding energy of the host object so that the merger remnant is ejected from it. Clearly, the absence of a central compact object has dramatic impact on the further evolution of the host. For example, it is nowadays believed and in some cases observationally verified that at least each major galaxy contains a massive BH [1–3], as well as our own Galaxy [4, 5], and also active galactic nuclei [6, 7]. The merger of any two galaxies then implies the merger of the central BHs [8–10], and in case of (super)massive BHs, which have masses with more than 10^5 solar masses up to $M_{SMBH} \backsim 10^9 M_\odot$, the hierarchical merger during the early stages of our Universe in the epoch of structure formation might even clarify the role of supermassive BHs during the process of galaxy formation [11–22]. The successive merger of supermassive BHs might lead to the ejection of the remnant from the surrounding dark matter halo which is then no longer involved in the process of galaxy formation.

In the case of stellar BHs, *i.e.* BHs which carry a mass of up to a hundred solar masses, the most common hosts are globular clusters [23]. The ejected object is then traveling within the galactic medium and the abundance of such events leads to a galactic BH distribution [14, 24–26].

Another interesting property is the spin and mass of the final merged BH. The former can give indication on the spin distribution of astrophysical BHs [16, 27, 28] such as BHs produced at the end of the evolution of a binary system of massive stars, or the supermassive remnants produced in galaxy mergers. In addition, the *a priori* knowledge of the final spin of a binary system that has not yet merged can help in the detection of the ring-down in gravitational-wave data analysis. The final mass, or equivalently, the radiated amount of energy during binary evolution, can have impact on the dynamics of the circumbinary disc accreting onto the binary [29, 30].

BBH mergers can therefore contribute to the understanding on how today's visible Universe has formed and may someday be crucial for probing gravity experimentally in its most extreme regimes with the help of gravitational-wave analysis.

Why numerical simulations?

Current gravitational-wave detectors suffer from the heavy influence of various sources of noise in the recorded detector data stream and finding a signal within the large amounts of noise can become very delicate. Fortunately, there exist a number of techniques of greatly enhancing the chances for detecting an event. One of these techniques is the "matched-filtering" procedure in which the detector data stream is matched against a known wave-signal. In addition, and apart from data-analysis techniques of finding a signal in the recorded data, more advanced detectors such as LISA will measure gravitational waves very accurately, and it will become possible to analyze the parameters of the gravitational source with high accuracy. However, nobody knows a priori how a gravitational wave depends on the parameters of its source. Thus, in order to make sense of observed gravitational-waves, it is necessary to calculate the radiation of given gravitating sources based on theoretical models. Today's most established theory that allows for gravitational waves is known as Einstein's GR, and the determination of a source's wave signature involves solving Einstein's field equations.

Unfortunately, these equations are rather complicated, and analytical solutions are only possible for spacetimes that possess high degrees of symmetry. For example, there are solutions such as the Schwarzschild and Kerr spacetimes that model single spherically (static) or axially symmetric (stationary) BHs. However, more generic spacetimes such as BBH spacetimes do not possess such high degrees of symmetry and no solutions have been found for this problem yet.

Hence, approximate methods have to be applied and there exist a variety of different perturbative approaches. These methods suffer from the fact that they are only valid in certain regimes, *e.g.* post-Newtonian methods are only valid in regimes with non-relativistic (internal) speeds and weak gravitational fields inside the source. For BBH systems, these conditions can only be achieved if the two bodies are well separated and hence, post-Newtonian methods can only be applied as long as the BHs are still on widely separated orbits around each other and move at non-relativistic speeds. If the two bodies get close enough, the system becomes unstable and plunges together at ultra-relativistic speeds. At this point, post-Newtonian methods break down completely and can not produce reliable results.

Black hole perturbation theory as another approximate approach is based on small deviations from spherical or axial symmetry and can therefore only handle spacetimes that are not subject to large distortions away from this symmetry. Hence, this method is only valid for BBH systems that have already merged to a single BH. This BH is usually highly excited, but can be modeled according to BH perturbation theory.

Unfortunately, both perturbative methods break down at the highly non-linear merger phase, and although it is possible to combine different perturbative methods in order to cover a larger regime (*e.g.* [31]), it is still necessary to assess the accuracy of such approximations which in most cases is hard to estimate. Numerical simulations on the other hand do not rely on any perturbative assumptions in some expansion parameters. Although still an approximative approach, too, it is a necessary condition of the solution to converge to the analytical solution in the limit of infinite resolution. Therefore in principle, higher accuracy in the solution is only a question of computational power.

Hence, numerical simulations are a perfect tool for the analysis of BBH spacetimes and the computation of the associated gravitational radiation content. Especially for the construction of gravitational-wave template banks [32–35], where it is necessary to know the full waveform including the highly non-linear merger phase, numerical simulations are currently the only possible way of attaining such a solution.

The challenge

The first attempt to model BHs on a computer was done by Hahn and Lindquist in the 1960s. In their paper from 1964 [36], they tried to evolve wormhole initial data, and at that time, the term "black hole" was not even coined. Despite arising difficulties of carrying the simulation sufficiently far so that conclusive dynamical behavior from the wormhole data could be drawn, they were nevertheless able to show the gravitational collapse of the two "mouths" accompanied with "an interaction between them". The first attempts to model head-on collisions of BHs was done by Smarr in the 1970s [37–42] where he paved the way for many follow-up studies on that topic. Some of these were accomplished in the 1990s [43–46] when the computational power first permitted larger simulations.

However, it turned out that it was not so simple to just take Einstein's equations and discretize them. Despite the problems that arise when the system is under-resolved due to the lack of computational power, it turned out that the standard 3+1 split of the field equations, the Arnowitt-Deser-Misner (ADM) formalism, was numerically not stable because the equations are cast into a form that is only weakly hyperbolic. The discrete system is therefore not necessarily stable and exponentially growing modes can blow up the entire system within a finite amount of time basically causing the simulation to crash. Furthermore, Einstein's equations are an over-determined system. This means that there are more equations than unknowns, particularly there are four additional constraint equations to the six evolution equations for the six unknowns that need to be satisfied. Mathematically, if these constraints are satisfied initially, they will always be satisfied during evolution. However, due to the truncation error in numerical simulations, the constraints will never be satisfied exactly. Unfortunately, this leads to exponentially growing constraint violations and if not causing the simulation to crash, they at least render the calculation useless since the solution does not belong to the class of solutions to the full Einstein equations anymore.

Another delicate issue arises due to the gauge invariance of GR which means that physically, no coordinate system is preferable over any other. However, in numerical simulations, one has to choose a coordinate basis in order to evaluate the equations. It turned out that picking a gauge which is non-pathologic and keeps the distortions of the numerical grid reasonably small, is highly non-trivial. This is closely related to the question of how the BH singularities can be treated numerically. If singularities are to occur, they have to be avoided by all means, for infinite quantities can not be represented on computers.

Furthermore, because of finite computer resources, the spacetime that is calculated needs to be finite. This means that boundary conditions have to be imposed on the domain boundaries. However, no boundary conditions for the Einstein equations are known that model an outgoing radiation condition similar to the Sommerfeld condition that at the same time are constraint preserving. Hence constraint violating modes will travel inside the simulation domain causing the simulation to crash or at least making it highly inaccurate.

Finally, the computation of gravitational radiation is unambiguously defined only at future null infinity thus practically requiring the computation of an infinitely sized spacetime. Again, this is problematic as there are only finite computational resources.

It was not until 2005 when the first successful orbiting BBH coalescence was accomplished by Frans Pretorius [47] using a generalized harmonic formulation of the field equations with compactified outer boundaries, constraint damping terms and excision of the interior domain of the BH in order to remove the singularity from the numerical grid. At the same time, codes that were using a different formulation of the field equations, the Baumgarte-Shapiro-Shibata-Nakamura-Oohara-Kojima (BSSNOK) system with the so-called puncture technique, underwent a revolution with the discovery of "moving punctures" [48, 49] which led to superior stability and robustness. Since then the whole field of numerical relativity (NR) entered a gold-rush which still holds on. Shortly after the first full merger simulations from inspiral to merger and ring-down phase were accomplished, the field started to apply their codes to study the astrophysics of BBH mergers in a detail that has never been possible beforehands. Publications were released on a daily basis leading to a number of exciting discoveries, *e.g.* the magnitude of recoil velocities in BBH mergers and the surprising fact that non-zero initial spins of the initial BHs produce a much larger kick than unequal-mass binaries. But despite the numerous discoveries that became possible, there are still issues that need to be tackled in order to gain more accuracy and predictive power, especially for the construction of gravitational-wave templates.

One of these issues is buried in the gravitational-wave extraction methods which rely on simplified coordinate and fall-off assumptions at the extraction radius. Another pressing issue is the ability of evolving BBHs for a larger number of orbits prior to merger so as to construct effective and faithful hybrid waveforms [32–35]. Such hybrid waveforms are constructed from post-Newtonian evolutions for the first hundreds and thousands of orbits, and which are then matched to numerical relativity waveforms which encompass the last couple of orbits including merger and ring-down. In order to be able to achieve a high-quality matching, it is necessary to push the matching region more towards the early inspiral, as well as computing the gravitational wave itself as accurately as possible.

Some of these issues are addressed in this thesis and overviewed in more detail in the next section.

The goal and new results obtained in this thesis

This thesis deals with numerical BBH merger simulations with new and improved gravitational-wave extraction methods as its main result, but also considers various important physical aspects such as gravitational-wave detectability, recoil velocities and final spin of the merger remnant.

The new results obtained in this thesis are partly reported in [50–60] and constitute the author's genuine contribution to the field of numerical relativity, gravitational-wave analysis and binary black hole physics. In addition, the author has contributed to results achieved in [61–65].

We acknowledge close collaboration with Nigel T. Bishop[1], Peter Diener[2], Nils Dorband[3], Sascha Husa[4], Michael Koppitz[5], Denis Pollney[6], Luciano Rezzolla[7], Erik Schnetter[8], Bela Szilagyi[9] and Jonathan Thornburg[10].

Gravitational-wave detectability of equal-mass spin-aligned binary black hole mergers

An important result [51] in this thesis is concerned with various aspects of gravitational-wave analysis. The question that we try to address here is how well BBH merger configurations in the 2D parameter subspace of equal-mass spin-aligned/anti-aligned binaries can be seen by the various gravitational-wave detectors (see Chapter 14). With the help of numerical simulations, we find that spin-aligned binaries are more than "three times as loud" as the corresponding binaries with anti-aligned spins, thus corresponding to event rates up to 30 times larger. In addition, we consider the waveform mismatch between different spinning configurations and find that within numerical accuracy, binaries with opposite spins cannot be distinguished whereas binaries with equal spin have clearly distinct gravitational-wave emissions. This has important consequences for the construction of gravitational-wave template banks and puts high demands on parameter estimation.

---

[1] Department of Mathematical Sciences, University of South Africa, Unisa 0003, South Africa.

[2] Department of Physics & Astronomy, Louisiana State University, Baton Rouge, LA, USA, and Center for Computation & Technology, Louisiana State University, Baton Rouge, LA, USA.

[3] Max-Planck-Institut für Gravitationsphysik, Albert-Einstein-Institut, Potsdam-Golm, Germany.

[4] Departament de Física, Universitat de les Illes Balears, Palma de Mallorca, Spain.

[5] Max-Planck-Institut für Gravitationsphysik, Albert-Einstein-Institut, Potsdam-Golm, Germany.

[6] Max-Planck-Institut für Gravitationsphysik, Albert-Einstein-Institut, Potsdam-Golm, Germany.

[7] Max-Planck-Institut für Gravitationsphysik, Albert-Einstein-Institut, Potsdam-Golm, Germany, and Department of Physics and Astronomy, Louisiana State University, Baton Rouge, LA, USA.

[8] Center for Computation & Technology, Louisiana State University, Baton Rouge, LA, USA, and Department of Physics & Astronomy, Louisiana State University, Baton Rouge, LA, USA.

[9] Theoretical Astrophysics, California Institute of Technology, Pasadena, CA 91125, USA.

[10] Department of Astronomy, Indiana University, Bloomington, Indiana, USA.

Furthermore, we present a simple analytical expression for the radiated amounts of energy due to gravitational waves and find that the radiated amount of mass is between 3.6% and 10%.

We also consider higher harmonic modes and how they influence the analysis above.

Recoil velocities

One of the top astrophysical aspects of BBH mergers is the gravitational recoil of the merger remnant. We present results [55–57] based on a momentum flux analysis code on the dependence of the recoil velocity in terms of the parameters of the initial BHs in the 2D parameter subspace of equal-mass spin-aligned binaries.

In this subspace, a recoil occurs for those binaries only, whose spins are either non-equal or equal but opposite (see Chapter 12). It turns out that within the error bars, the recoil has a quadratic dependence along the direction $a_1 = -a_2$ in the 2D spin diagram, which represents a correction to the linear post-Newtonian predictions. Given a set of numerical simulations, we derive a simple analytical phenomenological expression for the recoil and extrapolate to a maximum recoil of $|v_{\text{recoil}}| = 441.94 \pm 1.56\text{km/s}$ in that parameter subspace, which is unlikely to be sufficient for ejecting the remnant from its host object.

In finding the proper functional dependence, it is crucial to consider the recoil integration constant, which arises due to radiation that would have been emitted before the simulation was started (see Section 12.1).

Final spin

Another important finding is the relation of the spin of the merger remnant to the initial spins and mass-ratio of the initial BHs. Through a large set of performed simulations, we have found a phenomenological expression for the final spin [57–59]. In the parameter subspace of equal-mass spin-aligned binaries, we construct a simple quadratic fitting formula, revealing that the final spin depends only on the total initial spins of the binary (see Section 13.1). By extending the analysis also to unequal-mass binaries, we are able to show that the remnant is typically spun-up by the merger. In addition, it is possible to produce remnants that encounter a global spin flip, *i.e.* the total angular momentum is positive, but the spin of the remnant is negative. Accordingly, it is possible to produce a final Schwarzschild BH (see Section 13.2).

With a minimal set of assumptions and without additional fits, it is possible to extend this work to generic mass-ratios and spins (see Section 13.3).

Highly accurate and efficient binary black hole merger evolutions

A major achievement in this thesis is the implementation of a multiblock scheme coupled to an adaptive mesh-refinement driver together with high-order spacetime evolutions [54]. The multiblock scheme allows for the application of topologically adapted grids so that computational resources are not lavished. For example, the gravitational wave-zone of a radiating source has spherical topology, which is not captured by the commonly used Cartesian grids. This results in a severe drawback. If the computational domain is enlarged, the computational effort scales with the number of points as N^3. Spherical grids on the other hand, simply scale as N, since the angular resolution remains constant. To maintain regularity and a nearly homogeneous distribution of angular points throughout the entire domain, a “cubed-sphere” six-patch coordinatization of S^2 is employed, and the use of a global Cartesian coordinate frame allows for a common global tensor basis, so that tedious tensor transformations between local coordinate maps can be avoided (see Section 7.3).

At the same time, it is desirable to treat the strong-field region with established mesh-refinement methods. In the case of BBHs, a hierarchy of nested grids surrounds each BH to allow for the placement of resolution where necessary.

The coupling of both schemes together with high-order finite difference operators results in superior accuracy and resolution, particularly in the wave-zone, and the presented code can deliver comparable accuracy to spectral evolution schemes. For example, in Section 11.3, we demonstrate that the merger remnant of an equal-mass non-spinning reference BBH configuration is ringing with frequencies that have a residual of less than 0.01% to the prograde quasi-normal modes of a Kerr BH for all modes up to $(\ell, m) = (6, 6)$. Convergence tests with different resolutions reveal that the wave-modes up to $(\ell, m) = (6, 6)$ converge at the given theoretical order of accuracy (see Section 11.2).

Furthermore, the artificial outer boundary of the computational domain can be sufficiently removed so that it is causally disconnected from the wave-extraction world-tubes. Thus, the interior spacetime evolution is not contaminated by any boundary effects, and gravitational waves can be extracted at a radius $r = 1000M$ and larger. In contrast, other studies have carried out extraction at $r = 350M$ at most, but are usually limited to $r < 100M$. The possibility of extracting waves with high accuracy and at large distances to the source enable a detailed analysis of the asymptotic fall-off behavior of the complex Weyl scalars and help to assess the accuracy of traditional finite-radius wave-extraction [53] (see Section 15.1). It is shown that below an extraction radius of $r = 220M$, the error in the extrapolation increases by one order of magnitude.

Finally, the scalability of the new code is outstanding, thus making it ready for computations at the peta scale with 10,000 cores and more.

Unambiguous determination of gravitational waveforms from binary black hole mergers

The second main result of this thesis is the successful determination of BBH merger waveforms where they are unambiguously defined, that is, at future null infinity. Due to the necessarily finite computational domain, previous studies of BBH merger waveforms were always limited to finite-radius wave-extraction. This, however, introduced an unknown systematic error since the mathematical identification of certain curvature components with outgoing gravitational radiation can only be unambiguously accomplished at future null infinity. By stopping the computation at a finite radius, the non-linear dynamics of the wave-zone out to future null infinity is completely neglected, and the resulting systematic error is hard, if not impossible to assess. In previous studies, it was common to extrapolate the finite-radius waveforms to infinity, but still, the result is contaminated with finite-radius effects.

We have removed this problem by the successful application of Cauchy characteristic extraction, thus evolving the entire spacetime of generic BBH mergers out to future null infinity [50, 52]. We are able to show that current finite-radius extrapolated extraction techniques are valid to a precision of about 0.01%, but corrections have to be taken into account for the advanced gravitational-wave detectors, and when parameter estimation is crucial (see Section 15.2).

The implemented code is general purpose, and can straight-forwardly be applied to other astrophysical problems such as core-collapse supernovae simulations or binary neutron star mergers.

Analysis and visualization

We have implemented a number of easy to use analysis tools for analyzing the properties of the gravitational wave-signal. Among these is a collection of Python classes, which can extract quantities like radiated energies or angular momentum, and which can be used to perform convergence tests and other post-processing analysis (see Section 9.4).

Furthermore, we have implemented a database plugin for the state-of-the-art visualization toolkit VisIt, which enables it to read the Cactus/Carpet file-format. This plugin provides full support for adaptive mesh-refinement grids and arbitrary curvi-linear meshes, so that the Cactus community, and especially numerical relativists, are able to take full advantage of sophisticated visualization and 3D data inspection (see Section 10). This plugin is freely available [66].

Finally, we have implemented a C++ template class driver for 2D data representations on topologically spherical grids for Cactus (see Section 7.4). This driver can manage parallely distributed surface data across multiple processors and offers easy-to-use functions such as surface integration and harmonic decomposition. In addition, by using multiple coordinate maps, regular derivatives can be obtained everywhere, which can be used to remove certain complications in the isolated horizon computational implementation.

In this way, other scientists can benefit from an existing infrastructure, and a great amount of code redundancy is avoided.

Organization of this thesis

This thesis is organized in three parts. In the first part, we introduce the reader to the underlying mathematical theory and concepts of numerical relativity and gravitational-wave extraction, as well as BBH mergers. In the second part, we continue with the numerics and computational implementation of the BBH and gravitational-wave extraction problem. The third part of this thesis is fully devoted to new physics results obtained with the (partially new) methods and codes described in the previous parts.

First part

In the first chapter of the first part, we repeat the fundamental properties of BHs, introduce important aspects of the assumed asymptotic structure of spacetimes for analyzing gravitational radiation and recall key concepts in gravitational wave theory. The first chapter concludes with an introduction to BBH mergers and their parameter space.

The second chapter is fully devoted to the Cauchy problem of vacuum GR, *i.e.* the question of how to reformulate the Einstein equations such that the equations are in a form that can be used for time-evolutions on a computer. Here, key points are the evolution equations themselves, gauge conditions for fixing the remaining gauge freedom, construction of BBH initial data and the handling of spacetime singularities that may occur. All of these ingredients form the basics for the BBH evolution codes used in this thesis.

The third chapter introduces a different evolution system: the characteristic problem of GR. This evolution system is important for the implementation of a new gravitational-wave extraction method applied for the first time to BBH spacetimes, and the characteristic evolution code makes use of the equations and techniques stated therein.

The fourth chapter gives a brief overview on BH horizons, especially apparent horizons. In terms of the described isolated and dynamical horizon framework, it is possible to define the mass and spin of a BH. This is of key importance for new results obtained regarding the behavior of the final mass and spin of the BBH merger remnant in terms of the initial BH parameters.

The final chapter of part I introduces the underlying theoretical methods in gravitational-wave extraction. We describe three methods that all find applications in this thesis. Of particular interest is the third method, which couples characteristic evolutions to Cauchy evolutions and yields gravitational waveforms that are determined at future null infinity. This theoretical framework is then for the first time successfully applied to BBH spacetimes in a later chapter.

Second part

The first chapter of the second part repeats some basics from numerical analysis, such as numerical stability, hyperbolicity and convergence. This is important for the understanding whether the numerical approximation to the continuum problem is a valid and accurate one, and guides us in the design of a numerical scheme. In this chapter, we also introduce the discretization method employed for the evolution equations, such as finite differences, the method of lines and Runge-Kutta time-integration.

The next chapter is devoted to the computational infrastructure that has been used and implemented. We give a brief overview on the computational framework Cactus and describe the adaptive mesh-refinement scheme that is applied. We proceed with the description of the newly implemented multiblock simulation code as well as a newly developed driver for 2-surfaces that facilitates our wave-extraction modules and can be used in the future to *e.g.* improve the isolated and apparent horizon computational implementations.

The third chapter of the second part, describes the discretization scheme of the Cauchy and characteristic evolution equations, as well as the numerical construction of initial data, puncture tracking and apparent horizon finding.

The fourth chapter mainly explains the computational details of the newly implemented Cauchy characteristic extraction code. However, we also give brief descriptions of the existing numerical implementations of the other two extraction methods that have been extensively used in this thesis. The chapter concludes with the description of a gravitational-wave analysis script to be able to extract information on the radiation-related quantities, such as energy, linear and angular momentum.

The final chapter of part II gives an overview of a visualization database plugin for the visualization toolkit VisIt. This plugin teaches VisIt how to read the Cactus/Carpet file-format for adaptive mesh-refinement and curvi-linear grids, and is freely available to the Cactus community, especially numerical relativists, that need to inspect huge amounts of data efficiently and in parallel.

Third part

The first chapter of the third part introduces the parameter subspace that is mainly considered in this thesis, describes the simulations that have been performed, and states results on the convergence of all codes that are used in this thesis. Further tests on the accuracy and consistency of the simulations strongly support the validity of the numerical results that are obtained with these codes.

The next chapter deals with the gravitational recoil that the merger remnant can acquire due to the asymmetric emission of gravitational radiation. We present a detailed study on spin-aligned binaries that is later extended to the whole 2D subspace of such binaries. A phenomenological expression for the recoil velocity in terms of the spins of the initial BHs is derived.

The third chapter of part three deals with the final spin of the remnant. Again, we derive phenomenological expressions for the spin in terms of the initial BHs. An initial study is restricted to the 2D subspace of spin-aligned binaries. Subsequent studies extend the spin to the entire 7D BBH parameter space.

The fourth chapter pursuits the question, how well spin-aligned binaries can be seen in gravitational-wave detectors. We compute the maximal horizon distances of these binaries and compare the relative chances of detecting certain spin configurations. We analyze the influence of higher wave-modes on the detector and consider, how well different spin configurations can be distinguished from each other. The chapter concludes with fitted expressions for the radiated energies and signal-to-noise ratio in terms of the spins of the initial BHs.

The last chapter considers current wave-extraction techniques and analyzes the problem of finite-radius extraction. By employing the two newly developed codes during this thesis, *i.e.* the adaptive mesh-refinement multiblock code, as well as the Cauchy-characteristic extraction code, we are able to assess the accuracy of finite-radius computations. First, by taking advantage of the multiblock code, we are able to accurately resolve the fall-off behavior of the Weyl scalars at large distances to the BBH system. Second, we present the first unambiguous BBH merger waveform computed at future null infinity and compare the result to extrapolations from finite-radius extractions.

This thesis is concluded with a summary and outlook. In a subsequent appendix, we state formulas and expressions that, for the sake of readability, have been post-poned to the end of this thesis.

Notation and conventions

In the following, we give some overview of the notation and conventions that are used here.

The notation and formalism are based on Misner, Thorne and Wheeler [67]. A tensor is written in the form

$$T^{\mu\nu}, \qquad S_{ij}, \qquad h_{AB}\,, \tag{0.0.1}$$

where greek indices range from 1 to 4, Latin indices range from 1 to 3, *i.e.* $i, j, k, ..., n$ denote spatial indices that run over components $1, 2, 3$ or x, y, z whereas greek indices denote 4-indices that run over all components $0, 1, 2, 3$ or t, x, y, z. Upper-case Latin indices label components confined to the submanifold S^2, *i.e.* they refer to coordinates on the sphere and range from 2 to 3.

We use a spacelike metric signature $(-, +, +, +)$.

The complex conjugate of a quantity A is denoted by $\bar{A}$.

∂_μ means the partial derivative $\partial/\partial x^\mu$ and $\dot{A}$ denotes the partial time-derivative of quantity A.

Sums over spherical harmonic modes are usually abbreviated as

$$\sum_{\ell,m} \equiv \sum_{\ell=2}^{\infty} \sum_{m=-\ell}^{\ell} . \tag{0.0.2}$$

The spherical harmonics themselves are used in the form as described in Section 7.4.

A tilde denotes a conformally rescaled tensor, *i.e.* $S^{ij} = \psi^n \tilde{S}^{ij}$ with n being the conformal weight.

ϵ^{ijk} is the Levi-Cevita symbol.

Round brackets denote symmetrization procedure while square denote antisymmetrizing indices.

Whenever it applies from the context, f_{ijk} denotes the discrete function on points $f_{ijk} = f(x_i, y_j, z_k)$.

We usually write Δt and Δx (or just Δ) to denote time and spatial discretization step-size but sometimes also use k and h, respectively.

We use geometrized units (see Appendix A.1), so that time and space have the dimension of mass. Consequently, the simulation parameters and output are in units of the total mass M of the spacetime.

Part I

Foundations and Mathematical Theory

Chapter 1

Vacuum binary black hole spacetimes

Black holes arise as a solution to the Einstein equations in GR either with or without external matter-energy fields. The "two-body" problem of GR is then defined by gravitationally bound BHs, *i.e.* binary black hole (BBH) systems. In vacuum[1] the dynamics of BBH systems are fully determined by the gravitational interaction of the spacetime alone, *i.e.* without any matter sources, and are hence not influenced by external matter induced forces.

Although it is astrophysically very unlikely to find a pure vacuum binary black hole system that is not surrounded by any form of accretion disk or dust[2], it is nevertheless important to understand the dynamics and properties of such systems in the absence of matter as this relativistic two-body problem represents a fundamental dynamical problem of GR. Especially for the late inspiral and merger phase, the force governing the dynamics of the system is the gravitational interaction alone. Another more profound reason to start with vacuum binary black holes is that they are simpler and hence easier to handle when using analytical or numerical models.

BBH mergers are probably common systems in the Universe. For example, it is believed that almost all galaxies contain a central supermassive black hole (SMBH) [1–3, 7, 70], and the merger of two colliding galaxies [71] practically leads to the merger of the central SMBHs [8, 9, 72].

Stellar black holes ($10 - 10^2 M_\odot$) on the other hand are the result of, *e.g.* gravitationally collapsed stars and they are hosted in *e.g.* globular clusters (see [23, 68, 69] for formation mechanisms of astrophysical BHs). Globular clusters are relatively old, dense clusters of star systems and as such, they potentially contain many collapsed and degenerate objects such as BHs that, due to the dense population, may experience close dynamical interaction and hence may also produce BBH mergers.

As BBH systems represent accelerated mass, they radiate away energy through gravitational waves, similar to accelerated charge radiating electromagnetic waves. In fact, BBH systems are the strongest sources of gravitational radiation in the Universe, and hence are the first expected candidates for gravitational-wave detection. It is therefore of primary interest to the gravitational wave astronomy community to understand the anatomy of BBH merger waveforms as these can be used as templates for searches in gravitational-wave detectors.

In this chapter, we will first briefly introduce the Einstein field equations as well as the very basic properties and parameters of BHs. We will continue with some assumptions and requirements on the associated asymptotic structure of spacetimes containing BHs and gravitational radiation. The asymptotic structure of a spacetime is important for defining gravitational waves in a suitable manner, and as we will see in Sections 1.3 and 1.4, gravitational waves are unambiguously defined only at *future null infinity*, which represents a surface in spacetime where all null rays terminate, *i.e.* it is a boundary of spacetime. In order to be able to define gravitational radiation at all, it is necessary to assume that spacetime becomes *asymptotically flat* far away from the source, *i.e.* spacetime will asymptote to Minkowski spacetime at large distances. A subsequent section will introduce the notion of gravitational waves as well as their basic properties.

Finally, we will describe the basic stages of a BBH merger system, as well as the parameters describing such a system and the properties of the merger remnant.

---

[1] We are only concerned with vacuum throughout this thesis.

[2] BHs are usually formed and located inside galaxies or globular clusters [23, 68, 69] and are therefore naturally within a gas-rich environment, or at least an environment that is not completely exhausted of matter.

1.1 The Einstein equations

The underlying theory that describes the dynamics of interacting black holes is Einstein's theory of GR[3]. This theory puts space and time together into an overarching concept of spacetime where time has no preferred meaning anymore, and it describes the fundamental interaction of gravitation as a result of spacetime being curved by matter and energy. The spacetime itself is defined as a pair (M, g), where M is a connected 4D Hausdorff C^∞ manifold and g is the pseudo-Riemannian (or Lorentzian) metric tensor. The metric tensor defines the notion of proper distances in our spacetime, and a non-constant, non-trivial metric tensor[4] implies that the spacetime is curved in some sense, *e.g.* stretched, squeezed or bend in all kinds of possible ways. The notion of a manifold on the other hand, corresponds naturally to our intuitive ideas of the continuity of space and time[5].

The Einstein field equations are a set of ten coupled partial differential equations (PDEs) for the components of the spacetime metric tensor coupled to a stress-energy tensor containing the matter source terms. In tensorial form, the equations read

$$G_{\mu\nu} = 8\pi T_{\mu\nu}\,, \tag{1.1.1}$$

where $T_{\mu\nu}$ is the stress-energy tensor of all matter fields, and $G_{\mu\nu}$ is the Einstein tensor. The Einstein tensor reads

$$G_{\mu\nu} \equiv R_{\mu\nu} - \frac{1}{2} R g_{\mu\nu}\,, \tag{1.1.2}$$

where $R_{\mu\nu}$ is the Ricci tensor and R is the Ricci scalar. The Ricci tensor and Ricci scalar represent certain contractions of the Riemann tensor $R_{\mu\nu\lambda\rho}$ which is defined as

$$R^{\mu}{}_{\nu\lambda\rho} = 2\Gamma^{\mu}{}_{\nu[\lambda,\rho]} - 2\Gamma^{\mu}{}_{\alpha[\lambda}\Gamma^{\alpha}{}_{|\nu|\rho]}\,, \tag{1.1.3}$$

where the vertical lines around the index ν mean that it should be exempted from the antisymmetrization operation, and where the Γ are the Christoffel symbols of the metric defined by

$$\Gamma^{\rho}{}_{\mu\nu} = \frac{1}{2} g^{\rho\sigma} \left(g_{\nu\sigma,\mu} + g_{\mu\sigma,\nu} - g_{\mu\nu,\sigma} \right)\,. \tag{1.1.4}$$

The following contractions of the Riemann tensor define the Ricci tensor and scalar

$$R_{\mu\nu} = R^{\alpha}{}_{\mu\alpha\nu}\,, \qquad R = R^{\mu}{}_{\mu}\,. \tag{1.1.5}$$

Since we are interested in pure vacuum, we can set the stress-energy tensor to zero. This, however, simplifies the field equations to

$$R_{\mu\nu} = 0\,. \tag{1.1.6}$$

In other words, the Einstein tensor in (1.1.1) contains second derivatives of the metric tensor so that the Einstein equations form a coupled set of ten[6] non-linear hyperbolic PDEs of second-order. The non-linearity arises from quadratic terms of the metric tensor in the Riemann tensor and is one of the aspects of the Einstein field equations that makes it hard to implement a numerically stable evolution scheme (see Section 6.3 for some basics on stability).

We can consider (1.1.6) as the starting point for doing numerical simulations of vacuum spacetimes, but unfortunately these equations are not yet in a form suitable for numerical integration. In numerical simulations, one would like to specify initial data on some initial time instance and then numerically evolve these initial data in time, *i.e.* we would like to specify metric data on an initial spatial 3D hypersurface that is evolved along a timelike vector field so that the full 4D geometry is constructed from a succession of 3D metric data on spatial hypersurfaces. The Einstein field equations in the form of (1.1.6), on the other hand, represent a set of equations for *all* of 4D spacetime, *i.e.* the field variable is the full 4D metric tensor. We therefore have to transform the field equations to a form that is suitable for numerical simulations[7]. The foliation of spacetime in terms of spatial 3D hypersurfaces results in the Cauchy evolution problem of GR and is described in Chapter 2. However, it is also possible to foliate spacetime in terms of null hypersurfaces. This results in the characteristic evolution problem and is described in Chapter 3.

---

[3] Of course black holes can also be described in terms of modified theories of gravity. However, very little is known about how to numerically evolve BHs in other theories than GR.

[4] Actually, this depends on the coordinate system used. A metric tensor can look highly non-trivial in some funny looking coordinate system and yet simply represent flat Minkowski spacetime. For a proper analysis of the curvature content one has to consider the Riemann tensor defined in (1.1.3).

[5] At very small scales of the order of the Planck length, some theories, *e.g.* loop quantum gravity [73] predict that spacetime itself is discrete. However, for distances down to $10^{-15} cm$ the continuity of spacetime could be shown experimentally on this length scale [74].

[6] As a consequence of the Bianchi identities, the Ricci tensor of a Riemannian manifold is symmetric. This means that only 10 of the 16 total components of (1.1.6) are independent.

Having formulated the equations in terms of a Cauchy problem, hyperbolicity (see Section 6.4) arises from the fact that the principle part of the equations contains only real eigenvalues and hence finite speeds of propagation. This property is very important. No information can travel faster than the speed of light, and a proper causal (*globally hyperbolic*) structure of spacetime is induced by this aspect (see for example [75]). However, there are different "flavors" of hyperbolicity (see Section 6.4) and not all hyperbolic forms of a given system lead to a successful numerical scheme in the sense that the numerical solution may grow unboundedly in time eventually terminating the simulation before the interesting physics have been extracted. One of these flavors, strong hyperbolicity, offers the desired properties of a well-behaved discrete evolution system. We present the Einstein equations written in strongly hyperbolic form in Chapter 2 and discuss aspects of their discretization in Chapter 6.

It should be noted that GR as formulated by Einstein is not the only possible way of describing gravity and BHs[8]. Higher-order corrections to GR or other theories of gravitation can be, and should be, considered as well for evolving BBHs since GR loses its predictive power at the BH singularity and physics breaks down at that point. It is obvious, also with respect to a unified theory, that GR is not the final answer to the nature of gravity and it is expected that the higher-order dynamics of BBHs will be altered by other theories of gravitation, even far from the the purely quantum scales of the Planck length or the Planck energy [76]. Hence the gravitational radiation is different at least at higher order. Future gravitational-wave detectors might be able to measure these corrections to GR and rule out different candidates for a theory of gravitation.

1.2 Black holes

A BH is a collapsing region of spacetime, *e.g.* a gravitationally collapsing star, inevitably leading to a spacetime-singularity where the curvature tensor $R_{\mu\nu\lambda\rho}$ becomes infinite[9], and where GR completely looses any predictability at the singularity. Consequently, if spacetimes are assumed to be globally hyperbolic, and hence are assumed to contain no *naked* singularities, there must be a region in spacetime surrounding this singularity where the lightcones at each point are tilted inwards so that no light ray can escape from within that region. In other words, in an asymptotically flat spacetime, no future-pointing null geodesic from this region can escape to future null infinity and therefore, this region is causally disconnected from the rest of spacetime. This also means that all singularities that a spacetime may contain are invisible from future null infinity. If this was not the case, then any new information leaking out of the singularity could contaminate the remaining part of spacetime and hence render the complete theory useless. The fact that any singularity shall be causally disconnected from the rest of spacetime is also known as the *cosmic censorship conjecture* [78]. The outer boundary of events that are connected to future null infinity (see Section 1.3) and that of those which are not is the *event horizon* (see Chapter 4). One may then define a BH as the region of spacetime inside this horizon. However, it is debatable whether this definition may be too demanding (see *e.g.* [79]), as it has certain drawbacks. For example, as we will explain in Chapter 4, the event horizon is a global property of a spacetime and hence we may define a BH only *after* the entire spacetime is known. As such, it would be impossible to locate a BH during a numerical simulation, as the full spacetime is not yet known.

---

[7] The Einstein equations can be brought to a form that is preferable for numerical simulations (see Section 2.2) since it obeys a preferable form of hyperbolicity.

[8] In some theories, BHs do not even exist.

[9] A more rigorous definition of a spacetime-singularity is given in [77].

The simplest BH solution is at the same time the first non-trivial solution that was found for the Einstein equations: the Schwarzschild solution [80]. This solution describes a spherically symmetric spacetime which becomes singular at the origin and is given by the Schwarzschild line element

$$ds^2 = -(1 - 2M/r)dt^2 + \frac{dr^2}{1 - 2M/r} + r^2(d\theta^2 + \sin^2\theta\, d\phi^2)\,, \tag{1.2.1}$$

where (r, θ, ϕ) denote the standard spherical polar coordinates and r in this metric form is intrinsically defined by the requirement that $4\pi r^2$ is the area of spacelike two surfaces S^2. As one moves away from the singularity at $r = 0$ towards $r \to \infty$, we notice that spacetime becomes *asymptotically flat*, *i.e.* it approaches Minkowski. In Section 1.3, we will discuss the important topic of asymptotic properties of spacetimes. For example, comparing with Newtonian theory reveals that M in (1.2.1) should be regarded as the gravitational mass, as measured from infinity, of the BH producing the field.

The Schwarzschild solution (1.2.1) is *static*, *i.e.* there is a timelike Killing vector which is a gradient, and is spherically symmetric, *i.e.* is invariant under the group of isometries $SO(3)$ operating on the spacelike two-spheres S^2. The event horizon of this solution is located at $r = 2M$. It can be shown [81, 82] that the Schwarzschild solution is a unique solution for static BHs, *i.e.* any solution of the vacuum field equations that is spherically symmetric, is locally isometric to the Schwarzschild solution.

A *stationary* axisymmetric rotating and unique [82, 83] solution was found by Kerr [84] and later generalized by Newman *et al.* [85] to also contain electric charge. The Kerr-Newman line-element in Boyer-Lindquist coordinates (r, θ, ϕ, t) reads

$$\begin{aligned} ds^2 &= -\frac{\Delta}{\rho^2}[dt - \alpha \sin^2\theta\, d\phi]^2 + \frac{\sin^2\theta}{\rho^2}[(r^2 + \alpha^2)d\phi - \alpha dt]^2 \\ &+ \frac{\rho^2}{\Delta}dr^2 + \rho^2 d\theta^2\,, \end{aligned} \tag{1.2.2}$$

where

$$\Delta \equiv r^2 - 2Mr + \alpha^2 + Q^2 \tag{1.2.3}$$

$$\rho^2 \equiv r^2 + \alpha^2 \cos^2\theta \tag{1.2.4}$$

$$\alpha \equiv S/M\,. \tag{1.2.5}$$

Here, α represents the angular momentum S per unit mass M as measured from infinity, and Q represents the electric charge. It is useful to also introduce the *dimensionless spin parameter* $a = \alpha/M = S/M^2$. If the cosmic censorship conjecture [78] is true, then each singularity must be covered by an event horizon (there are no *naked* singularities[10]), which imposes a condition on the parameters α, Q and M

$$M^2 \geq Q^2 + \alpha^2\,. \tag{1.2.6}$$

In cases where the charge Q vanishes, the spin parameter is bounded between $-M \leq \alpha \leq M$. In terms of the dimensionless spin-parameter a, this inequality becomes $-1 \leq a \leq 1$. This condition on the spin a is a generic condition for axisymmetric spacetimes and $|a| = 1$ can only be achieved if a slice of that spacetime is a slice of the Kerr solution [86]. This fact will become important when constructing initial data for BBH simulations (see Section 2.4). As we will see, the current method for obtaining initial data for spinning BHs involves the construction of spacetime slices that are *not* Kerr, and hence does not admit maximally spinning BHs.

---

[10] If this conjecture were not true then the region of spacetime at the singularity, where physics breaks down, would have causal influence on the rest of spacetime and hence the theory would not be globally hyperbolic.

Black hole parameters

As one could already guess from these two solutions to the Einstein field equations, it turns out that there are only 3 parameters describing a classical stationary BH: the mass M, the dimensionless spin a, and the charge Q. It can be shown that this is true for *all* stationary and axisymmetric BHs in (electro-)vacuum and has been established by the "no-hair" theorem [82, 87, 88]. However, it appears to be very unlikely that an astrophysical BH carries any charge. As astrophysical BHs are usually surrounded by disks of gas, the BH will be immediately discharged by the surrounding matter and hence neutralized. It is therefore not of major interest to consider BHs, and especially BBHs with charge. As we are also only considering the vacuum Einstein equations[11], we will completely drop the charge parameter Q.

Astrophysically, it furthermore turns out that BHs may only be found in certain mass ranges, and there is a common classification that has nowadays been established. Stellar mass black holes (SBHs) are usually formed by the gravitational collapse of a star with at least $1.5 M_\odot$ and have been categorized by masses of order $10 M_\odot \leq M \leq 100 M_\odot$. Such BHs are usually hosted in globular clusters [23, 68, 69] which are old clusters of stars and therefore contain many collapsed and degenerate objects. The next class are intermediate mass black holes (IMBHs) with masses $100 M_\odot \leq M \leq 10^5 M_\odot$ which may also be hosted in stellar clusters (see *e.g.* [89, 90] and references therein). However, these BHs are possibly very rare as there are only very little observational evidences for the existence of that mass range, but they nevertheless constitute efficient sources of gravitational radiation for current ground-based detectors [91–94] (also compare Chapter 14). The final class of BHs are supermassive black holes (SMBHs) with masses $10^5 M_\odot \leq M \leq 10^9 M_\odot$ and they are probably hosted by each larger galaxy in the Universe such as our own Milky Way [1–5, 7, 70]. There is currently no known mechanism that allows BHs to have a size that is larger than those of SMBHs. The current models suggest that SMBHs are the outcome of the hierarchical mergers of galaxies which are accompanied by the merger of their central BHs, so that the mass of the remnant is bounded by the number of hierarchical galaxy merger events within the Hubble time [11–22].

This fixes the parameters and their possible ranges when doing numerical simulations. The only free parameters for vacuum BHs are the spin a and the mass M. The dimensionless spin a is fixed by the cosmic censorship conjecture which results in condition (1.2.6) so that $-1 \leq a \leq 1$. The mass M is bound by the minimum mass necessary for a star to end up as a BH due to gravitational collapse, and the maximum mass is constrained by the possible number of hierarchical galaxy mergers within Hubble time so that $1.5 M_\odot \leq M \leq 10^9 M_\odot$ (the largest BH found has a mass of $6.4 \times 10^9 M_\odot$ [95]).

Black hole properties

Although a general (dynamical) BH can become complex in its geometry and behavior, there are some general statements and properties that can be proven mathematically about BHs. The most important aspects are the following.

Any BH that underwent dynamical interaction with matter or another BH will return to stationarity, provided that it is not disturbed by any further interaction. It could be shown that BHs are stable against perturbations [96]. An excited BH, *i.e.* a BH that is *nearly* spherical will experience a *ring-down*. During ring-down, the BH looses all perturbations away from spherical or axial symmetry due to gravitational radiation, the *quasi-normal modes*, and converges to stationarity, so that a stationary spinning BH is left behind[12]. By means of BH uniqueness, the only possible stationary and axisymmetric solution in vacuum must be the Kerr solution [82, 83]. Thus, the only information that a vacuum BH carries is its spin and mass. This is known as the "no-hair" theorem and represents a fundamental classical[13] BH property in the sense that "all that can be radiated away is radiated away" [87, 99–101]. The only possible deformations of a stationary vacuum BH are due to a change in mass M and spin a. The quasi-normal modes represent spin-weighted *spheroidal* harmonic modes of the gravitational radiation and form a discrete set of unique frequencies and damping times depending on the mass and the spin of the BH. Given gravitational radiation (or a single gravitational-wave mode), this allows one to uniquely determine the mass and spin of a BH simply from its quasi-normal mode ringing alone (see *e.g.* [102]). The quasi-normal modes of an excited Schwarzschild BH have been analyzed in [103–108] and later for spinning BHs in [109–111]. It turns out that there are *prograte* and *retrograde*, *i.e.* clockwise and counterclockwise rotating modes for each set of harmonic ℓ, m-modes and each overtone N, and that the quasi-normal mode frequencies and damping times will increase and decrease, respectively, the higher the harmonic mode.

---

[11] The Kerr-Newman line-element represents a solution to the Einstein-Maxwell system, *i.e.* the Einstein equations with non-vanishing stress-energy tensor.

[12] But only after a infinite amount of time!

[13] In candidate theories of quantum gravity, BHs can have "hair" [97, 98].

BHs therefore behave like bells: if you "hit" them with something, they will start to ring with a given harmony and return to silence afterwards.

A general BH in a dynamic environment can become pretty complex. For example, it can be proven that cross-sections of the event horizon in asymptotically flat spacetimes obeying the dominant energy condition are topologically S^2 only in stationary spacetimes [75, 86], and defining the mass and spin of such a BH can be highly non-trivial. Usually, quasi-local definitions on the BH's event or *apparent horizon* (see Chapter 4) have to be introduced. It can be shown [112] that at least the outer apparent horizon of a BH always has spherical topology, even in non-stationary cases.

1.3 Asymptotics

Many of the assumptions made for analyzing gravitational radiation and the definition of global properties such as the mass of the spacetime require a certain asymptotic behavior of spacetime: it has to become *asymptotically flat* at spatial infinity, *i.e.* it has to asymptote to Minkowski spacetime at large distances from the source. This goes back to work done by Newman and Penrose [113–115] and is based on the idealization of an *isolated self-gravitating system.* In essence, Penrose proposed to characterize far fields of *isolated systems*, *i.e.* systems for which spacetime becomes more like Minkowski as one moves away from the source, in terms of their conformal structure.

The reasons for introducing such concepts are due to the non-locality of GR. It is impossible to define global integral conservation laws for general spacetimes without Killing symmetries. Usually, integral conservation laws are expressed as the vanishing of the divergence of some flux tensor. For example, energy-momentum conservation would be expressed locally in terms of the stress energy tensor $\nabla_\mu T^{\mu\nu} = 0$. Here, deriving an integral conservation law is generally impossible, because this equation is vector-valued, and as adding vectors at different points in Riemannian spacetime calculus is not defined, it is impossible to define an infinitesimal sum for an integral.

However, if spacetime possesses symmetries then one can use the associated Killing vector field to formulate an integral conservation law by contracting the vector-valued divergence equation along the Killing vector field. The resulting scalar divergence equation can be straight-forwardly integrated.

This makes it desirable for spacetimes to have symmetries. As this is generally not the case, one could try to impose conditions on spacetime so that at least asymptotically, it possesses some of the desired symmetries. Given such asymptotic symmetries, one could then define global conservation laws at least for *all* of spacetime, but not for local parts of spacetime such as the spin or mass of a BH that is orbiting another BH (some of these aspects are discussed in Chapter 4).

This leads to Penrose's condition of isolated sources. Each spacetime containing dynamical sources such as BBHs should become asymptotically flat, *i.e.* asymptote to Minkowski for large distances to the source. One could then hope to acquire the necessary Killing symmetries that allow one to define proper integral conservation laws.

Another important aspect is gravitational radiation. As we shall see in Section 1.4, gravitational radiation is usually defined as a perturbation around a flat background spacetime. For this reason, in order to be able to identify gravitational waves from the rest of spacetime, one can only define them properly in an asymptotic regime when spacetime has become sufficiently flat.

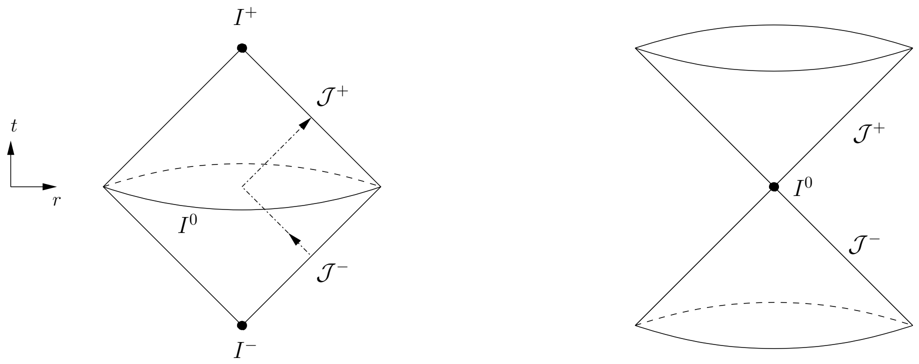

Figure 1.1: This figure shows the Penrose diagram indicating the conformal structure of spacetime. The left panel shows spacetime enclosed by the boundaries $\mathscr{J}^+$ and $\mathscr{J}^-$ with the points I^+, I^- and I^0 and with the arrows indicating ingoing and outgoing null geodesics. Because I^0 is really a point, the left figure can be misleading. In that case, it is more convenient to illustrate it according to the right figure.

As already mentioned, in order to tackle the problems above, Penrose used a conformal representation of spacetime. We will briefly review these aspects in the next subsection. Afterwards, we will give a mathematical definition of asymptotic flatness and discuss the resulting peeling property of the Weyl tensor which turns out to be important for identifying gravitational radiation. Finally, we will repeat expressions from the literature for the total mass and momentum from asymptotically flat spacetimes.

Conformal representation and structure

It is possible to make use of conformal rescalings to place "infinity" at a finite scaled distance. The *physical* metric, denoted by $\tilde{\boldsymbol{g}}$, is transformed to the *unphysical* metric $\boldsymbol{g}$ by

$$\tilde{g}_{\mu\nu} \rightarrow g_{\mu\nu} = \Omega^2 \tilde{g}_{\mu\nu} \,, \tag{1.3.1}$$

where $\Omega \geq 0$ is a smooth function which tends to zero far from the source. This represents a conformal transformation since angles are preserved by this transformation. Importantly, the null cone structure is also preserved because null vectors are mapped into null vectors by conformal transformations. We now want to choose Ω such that infinity of the physical metric is placed at a finite distance to the source in the unphysical metric so that all points of the physical metric at infinity can be represented as a hypersurface, *i.e.* the boundary of the physical spacetime, in the unphysical metric.

For a general spacetime, after an appropriate choice of the conformal factor, the outcome can be summarized in a conformal diagram as given by Figure 1.1.

We notice that there are three points, I^+, I^- and I^0. These points represent *future timelike infinity*, *past timelike infinity* and *spacelike infinity*, respectively. Future timelike infinity I^+ ($t \rightarrow \infty$, r finite) is the point which all future-pointing timelike geodesics reach. Similarly, past timelike infinity I^- ($t \rightarrow -\infty$, r finite) represents the point that all past-directed timelike geodesics approach. Finally, all spacelike geodesics will reach spacelike infinity I^0 ($r \rightarrow \infty$, t finite).

Additionally, there are two hypersurfaces, $\mathscr{J}^+$ and $\mathscr{J}^-$. These hypersurfaces represent *future null infinity* and *past null infinity*, respectively. Future null infinity $\mathscr{J}^+$ ($t + r \rightarrow \infty$, $t - r$ finite) is the boundary of spacetime that all[14] radially outgoing null geodesics reach. Radially ingoing null geodesics originate all on past null infinity $\mathscr{J}^-$ ($t - r \rightarrow \infty$, $t + r$ finite). The region bounded between these two hypersurfaces is the original spacetime. Especially $\mathscr{J}^+$ is of great importance when analyzing gravitational radiation. As we will see in Section 1.4, gravitational radiation travels along null geodesics, and knowing the asymptotic behavior of the spacetime metric in a neighborhood of $\mathscr{I}^+$ helps in understanding the properties of the radiation field. In fact, it turns out that gravitational radiation is unambiguously defined only at $\mathscr{I}^+$. A major achievement in this thesis is the numerical calculation of gravitational radiation at $\mathscr{I}^+$ from generic asymptotically flat vacuum spacetimes, *e.g.* BBH spacetimes.

---

[14] If the spacetime contains singularities then some geodesics will end at the singularity and not at $\mathscr{J}^+$. Also, if spacetime contains event horizons, some null geodesics are closed and hence will never terminate [75].

One can formalize the above considerations in terms of a definition. This is given in the next subsection.

Asymptotic simplicity

To characterize the fall-off behavior of asymptotically flat solutions at infinity in terms of geometric concepts, Penrose introduced the notion of *asymptotic simplicity* [113, 115–119].

Definition 1.3.1. *A smooth spacetime $(\tilde{M}, \tilde{g})$ is called* ***asymptotically simple*** *if there exists a smooth, oriented, time-oriented, causal spacetime (M, g) and a smooth function Ω on M such that*

1. *M is a manifold with boundary $\mathscr{I} \equiv \partial \tilde{M}$,*
2. *$\Omega > 0$ on $M \setminus \mathscr{I}$ and $\Omega = 0$, $d\Omega \neq 0$ on $\mathscr{I}$,*
3. *there exists an embedding Φ of $\tilde{M}$ onto $\Phi(\tilde{M}) = M \setminus \mathscr{I}$ which is conformal such that* $\Omega^2 \Phi^{-1*} \tilde{g} = g$ (with the * denoting the pullback operation),
4. *every null geodesic of $(\tilde{M}, \tilde{g})$ has two distinct end points on $\mathscr{I}$.*

$(\tilde{M}, \tilde{g})$ is called the physical spacetime, and (M, g) is the unphysical spacetime.

In this definition, only the conformal class of $(\tilde{M}, \tilde{g})$ enters the definition and it is only the conformal structure of (M, g) which is determined here. The set $\mathscr{I} = \mathscr{I}^+ \cup \mathscr{I}^-$ is referred to as the *conformal boundary* of $(\tilde{M}, \tilde{g})$ at *null infinity.*

Note that definition (1.3.1) does not include BHs because of condition 4. It is clear that spacetimes containing BHs contain future-directed null geodesics that will not end at $\mathscr{I}^+$ but at the singularity of the BH.

For this reason, one can weaken the definition of asymptotic simplicity requiring it to hold essentially only in a neighborhood of $\Omega = 0$.

Definition 1.3.2. *$(\tilde{M}, \tilde{g})$ is* ***weakly asymptotically simple*** *if there exists an asymptotically simple spacetime $(\tilde{M}', \tilde{g}')$ and a neighborhood $\tilde{U}'$ of $\mathscr{I}'$ in $\tilde{M}'$ such that $\tilde{U}' \cap \tilde{M}'$ is isometric to an open subspace $\tilde{U}$ of $\tilde{M}$.*

These definitions are the mathematical basis for the

Penrose Proposal: *Far fields of isolated gravitating systems behave like that of (weakly) asymptotically simple spacetimes in the sense that they can be smoothly extended to null infinity, as indicated above, after suitable conformal rescalings.*

This proposal suggests a sharp characterization of the fall-off behavior implied by the Einstein field equations in terms of the purely geometrical definitions (1.3.1) and (1.3.2). To be able to analyze the gravitational far-field and especially gravitational radiation, we will be interested in only those solutions of the Einstein equations which satisfy the conditions of (1.3.1) and (1.3.2).

If the vacuum field equations hold near $\mathscr{I}$, the latter defines a smooth null hypersurface of M (for details please refer to *e.g.* [116]), and, as already mentioned, splits into the two components $\mathscr{I}^+$ and $\mathscr{I}^-$ which are generated by the past and future endpoints of the null geodesics in M and which have topology $\mathbb{R} \times S^2$.

The Weyl tensor

The Weyl tensor and the Sachs peeling property play a crucial role in defining and implementing gravitational-wave extraction methods from generic (weakly) asymptotically simple spacetimes. It is a certain component of the Weyl tensor, Ψ_4, which can be uniquely defined as the outgoing gravitational radiation field at $\mathscr{J}^+$, and we base some of our wave-extraction methods (see Chapter 5) on this component.

The Weyl tensor arises from the fact that in more than three dimensions, the Riemann tensor contains more independent components than the Ricci tensor. That means, when decomposing the Riemann tensor $R_{\mu\nu\lambda\rho}$ in terms of the Ricci tensor $R_{\mu\nu}$, one has to introduce an additional object, the Weyl tensor $C_{\mu\nu\lambda\rho}$, in order to account for the information missing in the Ricci tensor. In a four-dimensional spacetime, the Weyl tensor is defined as

$$\begin{aligned} C_{\mu\nu\lambda\rho} &:= R_{\mu\nu\lambda\rho} - \left[g_{\mu[\lambda}R_{\rho]\nu} - g_{\nu[\lambda}R_{\rho]\mu}\right] \\ &+ \frac{1}{3}g_{\mu[\lambda}g_{\rho]\nu}R\,. \end{aligned} \tag{1.3.2}$$

The Weyl tensor has the same symmetries as the Riemann tensor, is traceless

$$C^{\mu}{}_{\lambda\mu\rho} = 0\,, \tag{1.3.3}$$

has 10 independent components in four-dimensional spacetimes, and in vacuum, where the Ricci tensor vanishes, coincides with the Riemann tensor. Furthermore, the Weyl tensor is invariant under conformal transformations, *i.e.* given two metrics $\boldsymbol{g}$, $\tilde{\boldsymbol{g}}$ related by (1.3.1), the Weyl tensors coincide

$$\tilde{C}^{\mu}{}_{\nu\lambda\rho} = C^{\mu}{}_{\nu\lambda\rho}\,, \tag{1.3.4}$$

although the Riemann tensors might be different. Because of this property, the Weyl tensor is also called the *conformal Weyl tensor*.

Given that the Weyl tensor has zero divergence in vacuum[15], one can define the *electric* $E_{\mu\nu}$ and *magnetic* $B_{\mu\nu}$ parts of the Weyl tensor as

$$E_{\mu\nu} := n^{\alpha}n^{\beta}C_{\alpha\mu\beta\nu}\,, \tag{1.3.5}$$

$$B_{\mu\nu} := n^{\alpha}n^{\beta}C^{*}_{\alpha\mu\beta\nu}\,, \tag{1.3.6}$$

where n^{μ} is an arbitrary timelike unit vector field, and where $C^{*}_{\alpha\mu\beta\nu}$ is the *dual* Weyl tensor defined as

$$C^{*}_{\alpha\beta\mu\nu} := \frac{1}{2}C_{\alpha\beta\lambda\sigma}\epsilon^{\lambda\sigma}{}_{\mu\nu}\,, \tag{1.3.7}$$

where $\epsilon_{\lambda\sigma\mu\nu}$ is the completely anti-symmetric Levi-Cevita symbol. In terms of the electric and magnetic parts, the Weyl tensor can be expressed as

$$C_{\mu\nu\lambda\rho} = 2\left[l_{\mu[\lambda}E_{\rho]\nu} - l_{\nu[\lambda}E_{\rho]\mu} - n_{[\lambda}B_{\rho]\alpha}\epsilon^{\alpha}{}_{\mu\nu} - n_{[\mu}B_{\nu]\alpha}\epsilon^{\alpha}{}_{\lambda\rho}\right]\,, \tag{1.3.8}$$

with

$$l_{\mu\nu} := g_{\mu\nu} + 2n_{\mu}n_{\nu}\,. \tag{1.3.9}$$

This will be useful when calculating the Weyl tensor at a given timeslice during a numerical simulation because the electric and magnetic parts of the Weyl tensor can easily be expressed in terms of the Arnowitt-Deser-Misner quantities (see Section 2.1) on the slice.

In the next two subsections, we will briefly discuss the asymptotic properties of the Weyl tensor.

---

[15] By writing the Bianchi identities in terms of the Weyl tensor and applying the vacuum Einstein equations, it follows that the Weyl tensor must have zero divergence in vacuum.

The Newman-Penrose formalism

When analyzing the asymptotic properties of spacetime fields it is more convenient to work in a null frame (or *Newman-Penrose*) formalism. One can reduce the complexity of the equations by expressing the various tensor quantities in terms of spinors and spin-weighted scalars. Spin-weighted scalars arise from spinor calculus and have first been introduced by Newman and Penrose [114] and are also discussed in [120][16]. By fully contracting the components of a tensor with a suitably defined null tetrad, one ends up with pseudo-scalars that transform under the change of tetrad in a particular way.

To be more specific, one can introduce a tetrad of vectors $(\boldsymbol{l}, \boldsymbol{n}, \boldsymbol{m}, \overline{\boldsymbol{m}})$ which are null

$$l^\mu l_\mu = n^\mu n_\mu = m^\mu m_\mu = \overline{m}^\mu \overline{m}_\mu = 0, \tag{1.3.10}$$

and which will be called a *Newman-Penrose null tetrad* or just a null tetrad, if the vectors satisfy

$$l_\mu n^\mu = -m^\mu \overline{m}_\mu = 1. \tag{1.3.11}$$

All other contractions vanish. It can be shown that a metric can be constructed according to

$$g_{\mu\nu} = 2 l_{(\mu} n_{\nu)} - 2 m_{(\mu} \overline{m}_{\nu)}, \qquad g^{\mu\nu} = 2 l^{(\mu} n^{\nu)} - 2 m^{(\mu} \overline{m}^{\nu)} . \tag{1.3.12}$$

Using this tetrad, we can construct scalars from a tensor $\eta_{\mu..\nu\lambda..\rho\alpha..\beta\gamma..\delta}$ by contracting all components with elements of the null tetrad, *i.e.*

$$\eta = m^\mu \cdots m^\nu \overline{m}^\lambda \cdots \overline{m}^\rho l^\alpha \cdots l^\beta n^\gamma \cdots n^\delta \eta_{\mu..\nu\lambda..\rho\alpha..\beta\gamma..\delta} \,. \tag{1.3.13}$$

Interestingly, there is now a two-dimensional gauge-freedom, namely the 2-parameter subgroup of the Lorentz group preserving the two null directions l^μ and n^μ as well as the product $l_\mu n^\mu$. This group is generated by the boosts

$$l^\mu \to r l^\mu, \qquad n^\mu \to r^{-1} n^\mu \,, \tag{1.3.14}$$

and the spatial rotations

$$m^\mu \to \mathrm{e}^{i\theta} m^\mu \,, \tag{1.3.15}$$

where r and θ are two arbitrary real parameters. Boosts (1.3.14) and rotations (1.3.15) form the *spin-boost transformations.* This particular transformation is also known as the *null rotation of class III.*

By defining the complex number $\lambda^2 = r \exp{(i\theta)}$, we observe that the scalar η as defined by (1.3.13) undergoes transformation

$$\eta \to \lambda^p \overline{\lambda}^q \eta \tag{1.3.16}$$

whenever the null tetrad is changed according to (1.3.14) and (1.3.15). Such a scalar is called a *spin- and boost-weighted scalar of type* (p, q) with spin-weight $s = \frac{1}{2}(p - q)$ and boost-weight $b = \frac{1}{2}(p+q)$. Pure spin-weighted quantities with zero boost-weight can be obtained by contracting the components of a tensor with $\boldsymbol{m}, \overline{\boldsymbol{m}}$ only. Particularly, spin-weighted quantities will be of special interest, because the $\boldsymbol{m}, \overline{\boldsymbol{m}}$ can be used to represent the intrinsic metric of a spacelike 2-surface according to (1.3.12) and can therefore be utilized when formulating the characteristic Einstein field equations (see Chapter 3).

The formalism above can now be applied to conveniently represent the 10 independent components of the Weyl tensor by five complex scalar spin and boost-weighted quantities known as the *Weyl scalars.* We define the various contractions with elements of the Newman-Penrose null tetrad as

$$\Psi_0 := C_{\mu\nu\lambda\rho} l^\mu m^\nu l^\lambda m^\rho \,, \tag{1.3.17}$$

$$\Psi_1 := C_{\mu\nu\lambda\rho} l^\mu n^\nu l^\lambda m^\rho \,, \tag{1.3.18}$$

$$\Psi_2 := C_{\mu\nu\lambda\rho} l^\mu m^\nu \bar{m}^\lambda n^\rho \,, \tag{1.3.19}$$

$$\Psi_3 := C_{\mu\nu\lambda\rho} l^\mu n^\nu \bar{m}^\lambda n^\rho \,, \tag{1.3.20}$$

$$\Psi_4 := C_{\mu\nu\lambda\rho} n^\mu \bar{m}^\nu n^\lambda \bar{m}^\rho \,. \tag{1.3.21}$$

---

[16] A detailed presentation can be found in [117, 121].

These quantities are scalars with respect to coordinate transformations but are clearly tetrad-dependent and transform according to (1.3.16).

It is useful to note that there are also two other classes of possible tetrad transformations that maintain orthonormality of the null tetrad.

Null rotations of class I leave the vector l^μ unchanged:

$$\begin{gathered} l^\mu \to l^\mu \,, \qquad m^\mu \to m^\mu + a l^\mu \,, \qquad \bar{m}^\mu \to \bar{m}^\mu + \bar{a} l^\mu \,, \\ n^\mu \to n^\mu + \bar{a} m^\mu + a \bar{m}^\mu + a\bar{a} l^\mu \,. \end{gathered} \tag{1.3.22}$$

Null rotations of class II leave the vector n^μ unchanged:

$$\begin{gathered} n^\mu \to n^\mu \,, \qquad m^\mu \to m^\mu + b n^\mu \,, \qquad \bar{m}^\mu \to \bar{m}^\mu + \bar{b} n^\mu \,, \\ l^\mu \to l^\mu + \bar{b} m^\mu + b \bar{m}^\mu + b\bar{b} n^\mu \,. \end{gathered} \tag{1.3.23}$$

The complex parameters (a, b) in class I and class II null rotations are the transformation parameters of the group. Together with class III null rotations, *i.e.* the spin-boost transformations with the real parameters (r, θ), we have 6 degrees of freedom in the tetrad: arbitrary rotation in space plus a Lorentz boost in a given direction, *i.e.* the 6 parameters that form the Lorentz group.

In the next subsection, we will come to an interpretation of the 5 Weyl scalars where the null rotations play an important role.

The Petrov classification and the Sachs peeling property

The *Petrov classification* [117, 122, 123] is a way of classifying the algebraic structure of the Weyl tensor in terms of the null directions of a given spacetime.

Depending on the null tetrad, one can define the Weyl scalars (1.3.17)-(1.3.21) which completely determine the Weyl tensor. It is then possible to apply the null rotations (1.3.14),(1.3.15),(1.3.22),(1.3.23) to the null tetrad, and one can analyze the behavior of the Weyl scalars with respect to such transformations.

Particularly, under a class II null rotation we find that

$$\Psi_0 \quad \to \quad \Psi_0 + 4b\Psi_1 + 6b^2\Psi_2 + 4b^3\Psi_3 + b^4\Psi_4 \,, \tag{1.3.24}$$

$$\Psi_1 \quad \to \quad \Psi_1 + 3b\Psi_2 + 3b^2\Psi_3 + b^3\Psi_4 \,, \tag{1.3.25}$$

$$\Psi_2 \quad \to \quad \Psi_2 + 2b\Psi_3 + b^2\Psi_4 \,, \tag{1.3.26}$$

$$\Psi_1 \quad \to \quad \Psi_3 + b\Psi_4 \,, \tag{1.3.27}$$

$$\Psi_4 \quad \to \quad \Psi_4 \,. \tag{1.3.28}$$

According to (1.3.24), one can make Ψ_0 vanish if the parameter b is chosen as one of the complex roots of

$$\Psi_0 + 4b\Psi_1 + 6b^2\Psi_2 + 4b^3\Psi_3 + b^4\Psi_4 = 0 \,, \tag{1.3.29}$$

and according to (1.3.23), the new null vector l^μ becomes

$$l^\mu \to l^\mu + \bar{b} m^\mu + b \bar{m}^\mu + b\bar{b} n^\mu \,. \tag{1.3.30}$$

The new null vectors corresponding to the roots of (1.3.29) are the *principal null directions* of the Weyl tensor. If some of the roots coincide, the spacetime is said to be *algebraically special.* One can then classify the Weyl tensor according to the roots of equation (1.3.29) in the following Petrov classification.

Petrov type I. All four roots are distinct: b_1, b_2, b_3, b_4. It turns out that in this case, we can always find a null tetrad such that only (Ψ_1, Ψ_2, Ψ_3) are non-vanishing.

Petrov type II. Two roots coincide: $b_1 = b_2$, b_3, b_4. In this case, there exists a null tetrad such that only (Ψ_2, Ψ_3) are different from zero.

Petrov type III. Three roots coincide: $b_1 = b_2 = b_3$, b_4. There exists a null tetrad such that only Ψ_3 is non-vanishing.

Petrov type N. All four roots coincide: $b_1 = b_2 = b_3 = b_4$. One can choose a null tetrad such that only Ψ_4 is non-zero.

Petrov type D. Two pairs of roots coincide: $b_1 = b_2$, $b_3 = b_4$. One can find a null tetrad such that only Ψ_2 is non-zero.

Petrov type O. The Weyl tensor vanishes identically and the spacetime is conformally flat.

It is clear that the most general spacetime has Petrov type I and the various other types represent increasing specialization.

More formally, these classifications can also be elegantly expressed in terms of spinor calculus [117].

The Petrov classification can be used to determine which Weyl scalars are non-zero for a given type of spacetime. Yet, there is another property of the Weyl scalars that is known as the *Sachs peeling property* [114, 115, 117, 119, 124, 125]. It can be shown (see, *e.g.* [117]) that the pseudo-scalars formed by contracting the various components of any spin-s zero rest mass field that is regular at $\mathscr{J}$ with elements of the null tetrad similar to the Weyl scalars, obey a certain fall-off property in the physical spacetime depending on the spin and the boost of the scalar. This is known as the *peeling theorem*, and when applying this to the Weyl tensor, one finds that the Weyl scalars must scale with the radius r to the source as

$$\Psi_n \sim \frac{1}{r^{5-n}}\,, \tag{1.3.31}$$

if the null tetrad is chosen to be in a *Bondi frame.* The Bondi frame is a particular choice of conformal gauge at $\mathscr{J}$. Because the conformal factor in (1.3.1) is not explicitly fixed, it can be multiplied by any strictly positive real scalar field without changing any of its properties. This results in a gauge freedom that allows one to choose a null tetrad that is adapted to $\mathscr{J}$. Since $\mathscr{J}$ is topologically $\mathbb{R} \times S^2$, the easiest way is to fix it such that it represents the flat metric of $\mathbb{R} \times S^2$ via (1.3.12).

One can also express the peeling behavior of the Weyl tensor in terms of the Petrov type

$$C_{\mu\nu\lambda\rho} = \frac{[N]}{r} + \frac{[III]}{r^2} + \frac{[II]}{r^3} + \frac{[I]}{r^4} + \mathcal{O}(r^{-5})\,. \tag{1.3.32}$$

It is possible to show that the leading order term corresponds to plane waves with Petrov type N. Therefore, far from an isolated source in the asymptotic field, (weakly) asymptotically simple spacetimes are asymptotically of type N, that is the only non-zero component is Ψ_4 representing the outgoing radiation field.

There is, however, a word of caution required. The Sachs peeling property only holds for spacetimes that are (weakly) asymptotically simple and extend smoothly to $\mathscr{J}$. It is far from immediate that the required smooth fall-off behavior is in harmony with the fall-off behavior imposed by the Einstein field equations, and there is an ongoing ‘debate whether the conditions imposed might be too strict and exclude interesting physics [126–130].

By now, we know that the conditions can be satisfied by non-trivial solutions. What is not clear, however, is how the solutions satisfying these conditions are to be characterized in terms of their Cauchy initial data (see Chapter 2 and Section 2.4) and whether these conditions exclude solutions modeling important physical phenomena. In fact, it is not clear whether a certain class of Cauchy initial data, namely Bowen-York BHs with non-vanishing linear momentum (see Section 2.4) satisfy the Sachs peeling property [131]! Possible implications for BBHs that are based on Bowen-York initial data are therefore also unclear!

Asymptotic mass and momentum

In this subsection, we briefly repeat expressions for the asymptotic mass and momentum of an asymptotically flat spacetime. A particular result has been found in [132, 133] and is based on the "3+1" splitting of spacetime as to be discussed in Section 2.1. The starting point is to consider weak gravitational fields for which the metric can be written as flat Minkowski plus some linear perturbation $g_{\mu\nu} = \eta_{\mu\nu} + h_{\mu\nu}$, with $|h_{\mu\nu}| \ll 1$. We can then define the total mass and momentum of an isolated system through its gravitational effects on faraway test masses. To ensure that the weak field limit holds, the expressions must be evaluated at spatial infinity I^0, *i.e.* $r \to \infty$. These quantities were first derived by Arnowitt, Deser and Misner [132] and are known as the Arnowitt-Deser-Misner (ADM) mass M_{ADM}, linear momentum P^i_{ADM} and angular momentum J^i_{ADM}. For general asymptotically flat spacetimes we have

$$\begin{aligned} M_{\mathrm{ADM}} &= \frac{1}{16\pi} \lim_{r\to\infty} \oint_S \left(\delta^{ij}\partial_i h_{jk} - \partial_k h\right) dS^k \,, && (1.3.33) \\ P^i_{\mathrm{ADM}} &= \frac{1}{8\pi} \lim_{r\to\infty} \oint_S \left(K^i{}_j - \delta^i{}_j K\right) dS^j \,, && (1.3.34) \\ J^i_{\mathrm{ADM}} &= \frac{1}{8\pi} \lim_{r\to\infty} \oint_S \epsilon^{ijk} x_j K_{kl} dS^l \,, && (1.3.35) \end{aligned}$$

where the surface integral is calculated with $dS^i = s^i dA$, with s^i the unit outward-pointing normal vector to the surface S and dA the area element. In these expressions, only spatial components contribute and the given expressions assume Cartesian coordinates x_j. Apart from the perturbation h, also the *extrinsic curvature* K_{ij} contributes. The extrinsic curvature will be defined in Section 2.1 where we describe the "3+1" splitting of spacetime. As detailed there, the full 4D spacetime is decomposed into a foliation of spatial 3D hypersurfaces parametrized in terms of a timelike vector field. One single hypersurface can be regarded as one instance in time, and on each of these instances, one can calculate (1.3.33), (1.3.34) and (1.3.35). As these quantities represent global properties of spacetime, they must be identical on each hypersurface. In other words, although these quantities are derived from spatial quantities only (and in fact can be computed on 3D hypersurfaces), they hold for the full 4D spacetime, *i.e.* $M_{\mathrm{ADM}}, P^i_{\mathrm{ADM}}$ and J^i_{ADM} are constants in time. However, during numerical simulations, it is usually not possible to calculate the integrals at spatial infinity I^0 as the spatial hypersurfaces do usually not extend to I^0, but terminate at a finite radius[17]. The resulting cut-off introduces an uncertain error.

1.4 Gravitational waves

Gravitational waves can be thought of as ripples of spacetime that, as we will see, travel at the speed of light and cause local distortions of spacetime that can be measured by gravitational-wave detectors, *e.g.* via laser-interferometers. Gravitational waves are physical, and as any other physical wave, *e.g.* in electromagnetism, they carry energy, linear and angular momentum. But unlike electromagnetism where the radiating source, *i.e.* the charge, is always preserved, this is no longer true in the gravitational case as radiating energy through gravitational waves means a diminishing of the mass of the source. This mass-loss has first been investigated by Bondi [134, 135].

Also unlike in electromagnetism where usually a clear seperation is possible between near-field, *e.g.* induction, and far-field interactions, *i.e.* electromagnetic waves, the high non-linearity of the gravitational field makes it difficult to clearly identify the far-field region and something like a wave from a given spacetime. In fact, it turns out that gravitational waves are mathematically well defined only at future null-infinity where spacetime is asymptotically flat, *i.e.* approaches Minkowski spacetime, and where it is possible to clearly separate the wave as small perturbations from the background geometry.

---

[17] As we will see in Section 2.4 and 8.1, the construction of our initial data allows to evaluate these integrals at I^0 on the initial hypersurface.

Similar to electromagnetic waves that are produced by accelerated charges, gravitational waves arise from accelerated masses and unlike electromagnetic waves where the lowest order is of dipole nature, the lowest order gravitational waves must have quadrupole nature, *i.e.* are given by $\ell = 2$ spherical harmonics. The reasons are firstly due to Birkhoff's theorem stating that spherically symmetric spacetimes contain no radiation. This prohibits $\ell = 0$ modes. Secondly, conservation of momentum leads to vanishing dipole modes $\ell = 1$.

Since the gravitational force is the weakest of all fundamental interactions, the generation of gravitational waves is extremely difficult as very large masses moving at relativistic speeds are needed. Nevertheless, gravitational waves are known to be the carriers of the strongest emission of energy through the entire Universe as some of their generating sources are interacting NSs, BHs and SMBHs. These release a tremendous amount of energy through gravitational radiation which can be of the order of 10^{55} ergs when emitted during a $100M_\odot$ BBH merger. However, due to the weakness of the gravitational interaction, the local distortions of spacetimes due to gravitational waves far away from the source are tiny, *e.g.* $h \sim \times 10^{-21}$ as for a $100M_\odot$ BBH merger at a distance of 100Mpc, and are thus extremely difficult to detect. In fact, gravitational waves, although already measured indirectly via the "Hulse-Taylor" pulsar B1913+16 [136] in 1975 and subsequently in [137–139], are another outstanding piece of experimental evidence required to verify GR on an experimental level.

Moreover, gravitational wave observations will open up an entirely new window on the Universe as it will become possible to directly observe the sky in the gravitational regime. Since the dominating force in astrophysical and cosmological interactions, *i.e.* stellar, galactic and even universal dynamics such as the big-bang, is the gravitational force, it will thus become possible to make inferences about the dynamics of such systems from direct measurements [140] and might even give further insight into the fundamental nature of gravity beyond GR [76].

In this section, we will introduce the concept of gravitational waves and will postpone the different concepts and methods of extracting the radiation content from a spacetime to Chapter 5.

Gravitational waves in linearized gravity

Gravitational waves can be viewed as small perturbations around a fixed (and eventually curved) background spacetime. As a first Ansatz, they can be described by using the linearized theory of gravity

$$g_{\mu\nu} = \eta_{\mu\nu} + h_{\mu\nu}\,, \qquad |h_{\mu\nu}| \ll 1\,, \tag{1.4.1}$$

where $\eta_{\mu\nu}$ is the flat Minkowski metric and $h_{\mu\nu}$ its small (linear) perturbations. We use $\eta_{\mu\nu}$ to raise and lower indices, and since this is just the flat Minkowski metric where the spatial part of a tensor and its spatial dual are identical, we are sometimes sloppy and sum over adjacent spatial indices in the same position.

Starting from (1.4.1), one can now calculate the Christoffel symbols of the perturbed metric

$$\begin{aligned} \Gamma^{\mu}{}_{\nu\lambda} &= \frac{1}{2}\eta^{\mu\rho}\left(\partial_\lambda h_{\rho\nu} + \partial_\nu h_{\rho\lambda} - \partial_\rho h_{\nu\lambda}\right) \\ &= \frac{1}{2}\left(\partial_\lambda h^{\mu}{}_{\nu} + \partial_\nu h^{\mu}{}_{\lambda} - \partial^{\mu} h_{\nu\lambda}\right)\,, \end{aligned} \tag{1.4.2}$$

and using this for constructing the Riemann tensor yields

$$\begin{aligned} R^{\mu}{}_{\nu\lambda\rho} &= \partial_\lambda \Gamma^{\mu}{}_{\nu\rho} - \partial_\rho \Gamma^{\mu}{}_{\nu\lambda} \\ &= \frac{1}{2}\left(\partial_\lambda\partial_\nu h^{\mu}{}_{\rho} + \partial_\rho\partial^{\mu} h_{\nu\lambda} - \partial_\lambda\partial^{\mu} h_{\nu\rho} - \partial_\rho\partial_\nu h^{\mu}{}_{\lambda}\right)\,. \end{aligned} \tag{1.4.3}$$

From this, one can construct the Ricci tensor

$$R_{\mu\nu} = R^{\lambda}{}_{\mu\lambda\nu} = \frac{1}{2}\left(\partial_\lambda\partial_\nu h^{\lambda}{}_{\mu} + \partial^{\lambda}\partial_\mu h_{\nu\lambda} - \Box h_{\mu\nu} - \partial_\mu\partial_\nu h\right)\,, \tag{1.4.4}$$

where $h = h^{\mu}{}_{\mu}$ is the trace of the metric perturbation, and $\Box = \partial_\lambda \partial^\lambda = \nabla^2 - \partial_t^2$ is the wave operator. Another contraction yields the curvature scalar

$$R = R^{\mu}{}_{\mu} = \left(\partial_\lambda \partial^\mu h^\lambda{}_\mu - \Box h\right) , \tag{1.4.5}$$

which can be used to finally construct the Einstein tensor

$$\begin{aligned} G_{\mu\nu} &= R_{\mu\nu} - \frac{1}{2}\eta_{\mu\nu} R \\ &= \frac{1}{2}\big(\partial_\lambda \partial_\nu h^\lambda{}_\mu + \partial^\lambda \partial_\mu h_{\nu\lambda} - \Box h_{\mu\nu} - \partial_\mu \partial_\nu h \\ &\qquad - \eta_{\mu\nu}\partial_\lambda \partial^\rho h^\lambda{}_\rho + \eta_{\mu\nu}\Box h\big) \ . \end{aligned} \tag{1.4.6}$$

This expression can be simplified by introducing the *trace-reversed* perturbation

$$\bar{h}_{\mu\nu} = h_{\mu\nu} - \frac{1}{2}\eta_{\mu\nu} h \, , \tag{1.4.7}$$

which satisfies $\bar{h}^{\mu}{}_{\mu} = -h$.

Making use of (1.4.7) by plugging it into 1.4.6 yields

$$G_{\mu\nu} = \frac{1}{2}\left(\partial_\lambda \partial_\nu \bar{h}^\lambda_\mu + \partial^\lambda \partial_\mu \bar{h}_{\nu\lambda} - \Box \bar{h}_{\mu\nu} - \eta_{\mu\nu}\partial_\lambda \partial^\rho \bar{h}^\lambda{}_\rho\right) \ . \tag{1.4.8}$$

A further simplification can be achieved by making use of the Lorenz gauge-condition

$$\partial^\mu \bar{h}_{\mu\nu} = 0 \, , \tag{1.4.9}$$

so that (1.4.8) reduces to

$$G_{\mu\nu} = -\frac{1}{2}\Box \bar{h}_{\mu\nu} \ , \tag{1.4.10}$$

which, in vacuum, is simply

$$\Box \bar{h}_{\mu\nu} = 0 \ . \tag{1.4.11}$$

But this is just an ordinary wave equation and solutions in the form of a superposition of plane waves can be found to be

$$\bar{h}_{\mu\nu}(\mathbf{x}, t) = \mathrm{Re} \int d^3k \ A_{\mu\nu}(\mathbf{k}) e^{i(\mathbf{k}\cdot\mathbf{x} - \omega t)} \ , \tag{1.4.12}$$

where $\omega = |\mathbf{k}|$ and $A_{\mu\nu}(\mathbf{k})$ depend on the wave-vector $\mathbf{k}$. The constraint $k^\mu A_{\mu\nu} = 0$ with $k^a = (\omega, \mathbf{k})$ follows from the Lorenz gauge-condition. These solutions are gravitational waves and as they obey one wave-equation (1.4.11), they travel with the speed of light.

However, this can be further reduced. By imposing asymptotic flatness, *i.e.* $h_{\mu\nu} \to 0$ for $r \to \infty$, one can further restrict the gauge to spatial perturbations only, *i.e.*

$$h_{tt} = h_{ti} = 0 \ , \tag{1.4.13}$$

and also require it to be traceless

$$h = h_i{}^i = 0 \ . \tag{1.4.14}$$

The Lorentz gauge-condition then implies

$$\partial_i h_{ij} = 0 \ , \tag{1.4.15}$$

which means that the metric perturbation h is transverse.

This further restriction to the metric perturbation is called the *transverse-traceless (TT)* gauge which is now completely fixed. Quantities that are written in TT gauge are sometimes written as A^{TT}. The advantage of the TT gauge is that the metric perturbation h^{TT} is free of any gauge

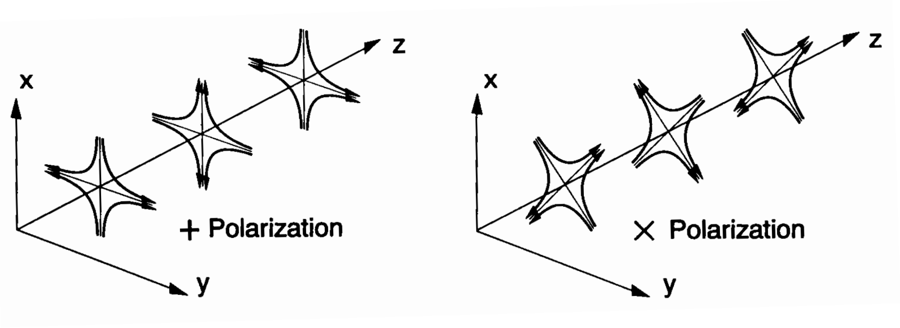

Figure 1.2: Lines of force for a purely + polarized gravitational wave (left), and for a purely × polarized gravitational wave (right). Figure originally published in Ref. [142].

freedoms and contains purely physical information. It unveils that the gravitational-wave field contains two polarization states. This can be seen as follows. If we consider a gravitational plane-wave which is a solution to $\Box h_{ij}^{TT} = 0$ and travels along the z-direction $h_{ij}^{TT} = h_{ij}^{TT}(t-z)$, then the Lorenz condition $\partial_z h_{ij}^{TT} = 0$ implies that $h_{zj}^{TT} = \text{const.}$. Since in asymptotically flat spacetimes $h_{\mu\nu} \to 0$ for $r \to \infty$, the only non-zero components of the metric are h_{xx}^{TT}, h_{xy}^{TT}, h_{yx}^{TT} and h_{yy}^{TT}. Symmetry and tracefree condition now yield that there are only two of the components that are independent. We have

$$h_{+} \equiv h_{xx}^{TT} = -h_{yy}^{TT} \,, \tag{1.4.16}$$

$$h_{\times} \equiv h_{xy}^{TT} = h_{yx}^{TT} \,. \tag{1.4.17}$$

In fact, it can be shown [141] that only these two metric perturbation components satisfy a wave-equation in *all* gauges. All other metric components are pure gauge and can be gathered into a set that obeys Poisson equations. This clarifies that only the components h_+ and $h_\times$ are true radiative degrees of freedom. The fact that in Lorenz-gauge, the non-TT part of the metric also obeys a wave-equation is just a gauge artifact.

The two polarization states h_+ and $h_\times$ are depicted in Figure 1.2. Linear polarizations can be constructed if + and × polarizations are in phase, circular or elliptically polarized waves can be constructed if + and × polarizations are phase shifted by $\pi/2$.

Energy, linear and angular momentum of gravitational waves

As any other physical wave, gravitational waves also carry energy, linear and angular momentum. An important role in this is played by the so-called Isaacson stress-energy tensor [143, 144] which is an effective stress-energy tensor for the gravitational-wave field. However, it is well known that due to the non-locality of GR there is nothing like a well defined stress-energy tensor for the gravitational field in general. Nevertheless in certain limits it is possible to derive a very similar notion of a stress-energy tensor, and especially for the gravitational-wave field it is possible to introduce the so-called *short-wavelength* approximation or “high frequency limit” [143–145].

The short-wavelength approximation relies on the fact that at a fundamental level, gravitational waves can be identified from a possibly curved background spacetime simply by the different length-scales of the system. It is assumed that the gravitational perturbations which represent gravitational waves have a much shorter wavelength λ than the characterizing length-scale L of the background metric, $\lambda \ll L$, which is also known as the *geometric optics regime.*

We therefore consider the perturbation

$$g_{\mu\nu} = g_{\mu\nu}^{\mathrm{B}} + \varepsilon h_{\mu\nu} + \varepsilon^2 j_{\mu\nu} + O(\varepsilon^3) \,, \tag{1.4.18}$$

where $g_{\mu\nu}^{\mathrm{B}}$ is the (curved) background metric, $h_{\mu\nu}$ a perturbation to linear order, $j_{\mu\nu}$ a perturbation to second order and ε a formal expansion parameter. We can then follow the procedure for obtaining the perturbed Einstein equations as outlined for the perturbation around a Minkowski spacetime. Notice however that $\eta_{\mu\nu}$ has to be replaced by $g^{\rm B}_{\mu\nu}$ and partial derivatives have to be replaced by covariant derivatives with respect to the background metric.

After calculating the Christoffel symbols, the Riemann, Ricci and Einstein tensor, and by imposing the transverse-traceless gauge, one obtains for the linearized (*i.e.* neglecting the term $\varepsilon^2 j_{\mu\nu}$ in (1.4.18)) Einstein equations in this gauge a wave-type equation

$$-\frac{1}{2}\Box^B h_{\nu\rho} + R^B_{\mu\rho\nu\lambda} h^{\mu\lambda} = 0 \, , \tag{1.4.19}$$

whose solutions can be interpreted as gravitational waves. Comparing this equation to the result obtained from a flat background (1.4.11) leads to two obvious differences. In (1.4.19) we now also have a coupling to the background Riemann tensor $R^B_{\mu\rho\nu\lambda}$, and in addition to that we also have a coupling to the background connection coefficients that are hidden in the covariant wave operator $\Box^B$.

Now it is possible to do the following. Assuming we are in the geometric optics regime for some given metric $g^{\mu\nu}$, *i.e.* $\lambda \ll L$ applies, we can take this metric and identify the background metric to first order by introducing a covariant averaging procedure [146] by averaging over length-scales large compared to λ but small compared to L, *i.e.*

$$g^B_{\mu\nu} \equiv \langle g_{\mu\nu} \rangle \, . \tag{1.4.20}$$

The gravitational-wave perturbation is then to first order

$$\varepsilon h_{\mu\nu} \equiv g_{\mu\nu} - g^B_{\mu\nu} \, . \tag{1.4.21}$$

It should be noted that the notion of a gravitational wave as given by the flat spacetime perturbation (1.4.1) does not necessarily coincide with the results from the Ansatz with a curved background (1.4.18). Fortunately, far away from the source, *i.e.* in distances where observers are usually sitting, the two definitions coincide since the metric perturbations always are at length-scales λ whereas the background scales with the distance to the source r.

The short-wavelength perturbation (1.4.21) now gives rise to an effective stress energy tensor which can be derived by also including the second-order perturbation in (1.4.18) which was irrelevant for the identification of gravitational waves (1.4.19), but becomes important here because the first-order perturbation will always vanish when averaging over its oscillations.

This time including the term $\varepsilon^2 j_{\mu\nu}$, one can derive the second-order perturbation Einstein equations by inserting (1.4.18) into the vacuum Einstein equations. One ends up with the effective Einstein equations

$$G_{\mu\nu}[g^{\rm B}_{\lambda\rho} + \varepsilon^2 \langle j_{\lambda\rho} \rangle] = 8\pi T^{\rm GW,eff}_{\mu\nu} + O(\varepsilon^3) \, , \tag{1.4.22}$$

where the effective gravitational-wave stress-energy tensor in TT gauge can be written as

$$T^{\rm GW,eff}_{\mu\nu} = \frac{1}{32\pi} \langle \partial_\mu h^{\rm TT}_{ij} \partial_\nu h^{\rm TT}_{ij} \rangle \, . \tag{1.4.23}$$

For a complete derivation, we refer the reader to [141, 143, 144]. The effective Einstein equations (1.4.22), and especially the effective Einstein tensor $G_{\mu\nu}$, are made up of quantities that vary only on length-scales $\sim L$ and change slowly. The effective gravitational-wave stress-energy tensor represents the corrections to the background metric through gravitational waves and is conserved with respect to the metric perturbation $g^{\rm B}_{\lambda\rho} + \varepsilon^2 \langle j_{\lambda\rho} \rangle$. On long length-scales therefore, the action of gravitational waves on a given background spacetime can be viewed as any other source of matter-energy acting on the spacetime.

The effective stress-energy tensor (1.4.23) can now be used for calculating the radiated energy, linear and angular momentum of gravitational waves. For explicit expressions relating the gravitational-wave strain to these radiation quantities, we postpone the reader to Chapter 5.

Gravitational waves in the full non-linear theory

Instead of using linearized gravity, which has obvious limitations, another way of approaching the gravitational-wave emission problem is the use of a suitably defined coordinate system that is adapted to the outgoing gravitational-wave field [124, 125, 134, 135] and that leads to the so-called Bondi-Sachs metric [134]. In terms of this metric, the resulting Einstein equations (or *characteristic* field equations) form a reduced hierarchical set of hypersurface, evolution and constraint equations, which we will discuss in more detail in Chapter 3. This system becomes useful in defining a wave-extraction method that is rigorously defined in a sense that it can yield gravitational waves which are calculated properly at future null-infinity.

Bondi *et al.* [124, 125, 134, 135] used this system to study the behavior of the gravitational field of a radiating source. Using expansions of the characteristic equations in negative powers of a suitably defined radial coordinate r, it is possible to analyze the behavior of the gravitational field at large distances to the source by taking into account possible non-linear interactions that might not be captured by linearized gravity. As general relativity is a highly non-linear theory, it is possible that some of the crucial properties of the field show themselves only through the non-linear terms, and moreover, it might be possible that the solutions to the linearized Einstein equations are not necessarily approximations to the solutions of the full non-linear theory.

In fact, Bondi *et al.* were able to derive the change of mass of a radiating system that is static at an initial and final state [125, 135] some years before the introduction of the Isaacson stress energy tensor, by introducing the Bondi *news-function* which encodes the gravitational radiation at future null-infinity. Among other interesting results such as the Bondi-Sachs-Metzner (BMS) asymptotic symmetry group, this led to the insight that gravitational radiation will always diminish the mass of an excited source when compared to the (stationary) initial state.

Interaction of gravitational waves with a detector

As described in the previous sections, gravitational waves far away from the source appear as small perturbations of a given (flat) background spacetime. Although these perturbations are tiny and can only be measured by highly sensitive instruments, it has become possible [147–149] to be technically able[18] to detect and measure gravitational wave signals.

The starting point is the natural assumption that an observer on Earth is located in an asymptotically flat regime of spacetime, *i.e.* the gravitating source is always many light-years away and its gravitational field is therefore negligible. For the moment, we will also neglect the gravitational field of Earth itself and assume that the entire non-flat part of the metric is only due to a gravitational wave.

Suppose we want to measure the distance between two points located at coordinates $x = 0$ and $x = L_c$ at $z = 0$. The proper distance between these points is given by

$$L = \int_0^{L_c} dx \sqrt{g_{xx}} \ . \tag{1.4.24}$$

Suppose now a gravitational wave in TT gauge is traveling along the z-axis. The proper distance becomes

$$\begin{aligned} L &= \int_0^{L_c} dx \sqrt{1 + h^{TT}_{xx}(t, z = 0)} \\ &\simeq L_c \left(1 + \frac{1}{2} h^{TT}_{xx}(t, z = 0)\right) \ . \end{aligned} \tag{1.4.25}$$

A gravitational wave would therefore result in a measurable change given by

$$\frac{\delta L}{L} \simeq \frac{1}{2} h^{TT}_{xx}(t, z = 0) \ . \tag{1.4.26}$$

---

[18] Although detectors are already operational, a gravitational wave has not been measured yet.

This change can be made observable by means of laser interferometry. A photon that travels between the two points in one of the arms of a Michelson interferometer would acquire a phase-shift of $\delta\phi = 4\pi\delta L/\lambda$ with λ being the photon's wavelength. Another photon that travels the same coordinate distance perpendicular to the other photon would not experience such a phase-shift, and this would lead to measurable interference.

In reality, however, also near-zone gravitational fields have effects on a detector and there is no way to separate the contribution coming from gravitational waves or from other sources. This, among other influences, results in noise which in turn lowers the sensitivity to gravitational waves in certain frequency bands. On top of that, the technique of measuring gravitational waves itself introduces non-trivial contents of noise, *e.g.* seismic, thermal or photon shot noise. Seismic noise is generated from all kinds of ground vibrations (*e.g.* , cars and people moving around) and must be compensated for with sophisticated suspension systems such as multi-stage pendulums. Thermal noise is caused by thermal fluctuations of the mirrors and the suspending pendula and may also mask the gravitational signal. Photon shot noise on the other hand, is due to the quantum nature of light: the laser beam does not represent a continuous beam of light, but consists of small packets, the photons, that make up the beam. Consequently, the interference signal is made up of random fluctuations which can look like a gravitational wave signal. To limit this effect, one can increase the number of photons to limit the photon shot noise. However, by increasing the position certainty of the photons, due to the Heisenberg uncertainty principle, we increase the momentum uncertainty resulting in random momentum transfer to the mirrors. This effect is known as quantum noise and can be avoided by using squeezed quantum states of light. Finally, there is the gravity-gradient noise. This noise is caused by changes in the local Newtonian field and can be induced by atmospheric fluctuations or seismic waves. This noise is also the reason why space-based detectors or underground detectors need to be built as gravity-gradient noise prevents the measurement of gravitational waves below 1 Hz. However, the frequency band below 1 Hz is known to be the band of SMBH mergers and is astrophysically very important.

Therefore, each detector has a characteristic sensitivity curve which is tuned to a certain frequency range, *i.e.* where we expect to find signals from certain astrophysical sources such as binary black holes or binary neutron stars in a certain mass range and configuration. Figure 1.3 shows the sensitivity curve of the LIGO detector [147, 148] and the sources of noise that limit the bandwidth.

In practice, in order to detect a waveform, only one detector would be necessary. However, for getting the full signal, *i.e.* plus and cross polarization modes, two detectors with different orientations to each other are necessary. This is because the two modes are linearly independent, and the current ground-based detectors with their two arms represent a projection to one polarization state only. In addition, it is also a matter of confidence. Two detectors will have uncorrelated noises and false alarms can thus be minimized.

In Chapter 14, we will determine the detectability of BBH mergers with current ground-based as well as the planned advanced and the space-based LISA detector.

1.5 Binary black hole systems

When talking about BBH systems, we usually mean two BHs that orbit each other. Any two orbiting objects represent accelerated masses, and it is well known that accelerated masses will emit gravitational radiation, similar to accelerated charges in electro-dynamics that emit electromagnetic radiation. As the emission of radiation means loss of energy, the two masses will move closer as they orbit each other. In the case of compact objects such as BHs, this effect is so strong that it significantly alters the trajectories after some time, so that we cannot talk about a stable orbiting system anymore. Rather, the two compact objects will inspiral and finally merge.

BBH systems are among the most powerful sources of gravitational radiation in the Universe. As we shall see in Chapter 14, up to 10% of the total mass of the binary can be emitted in a BBH coalescence and one can ask how well a given binary can be seen with current gravitational-wave detectors.

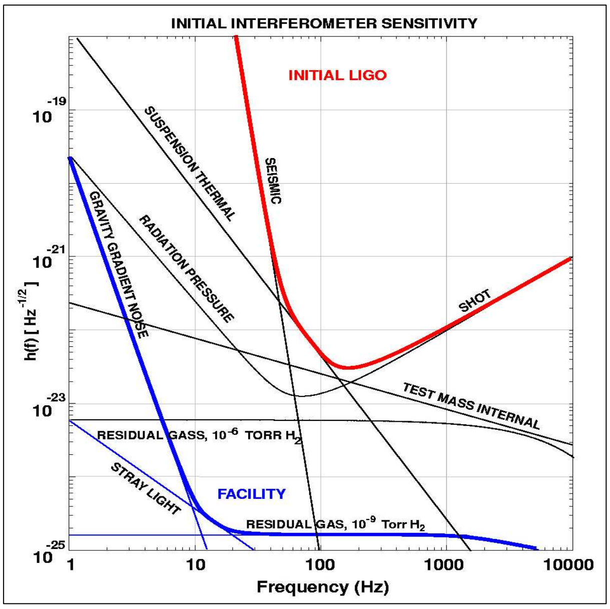

Figure 1.3: This figure shows the initial LIGO sensitivity curve (red) and contributing noise sources. The major noise contributions come from seismic noise, thermal noise and photon shot noise. This figure also shows the lowest noise levels that can be achieved in principle within a ground-based interferometer facility (blue curve). The main limit in this case is the gravity gradient noise and noise from residual gas in the interferometer vacuum system. Figure taken from [150].

BH binaries are assumed to exist in all mass ranges. SBH and IMBH binaries are most probably formed and contained in stellar clusters [23]. SMBH binaries are a result of galaxy mergers and are therefore found at the center of the merged galaxy [8–10].

The three stages of binary black hole coalescence

The evolution of BBH system proceeds in three stages. The initial stage is the inspiral phase and can last for millions of years. During that stage, the two BHs are on nearly circular orbits [151], continuously emitting radiation with increasing amplitude and frequency as they move closer to each other. This process continues up until the final orbit with a certain separation, the innermost stable circular orbit (ISCO[19]). Past this point, no stable orbit is possible anymore, and the BHs fall towards each other, *i.e.* they plunge together and merge. This is the second stage of a BBH system and is called the plunge and merger phase.

What is left behind is a highly excited single BH. As already mentioned in Section 1.2, an excited BH will undergo a ring-down, *i.e.* it will emit all modes away from spherical or axial symmetry in the form of exponentially damped gravitational radiation with a discrete set of frequencies, the quasi-normal modes (QNMs), depending on the spin and mass of the newly formed BH (compare Section 11.3 for an analysis of QNMs).

After some time, the BH will have asymptoted sufficiently to stationarity, *i.e.* its horizon is in equilibrium and becomes *isolated* (see Chapter 4). Most generally, one can expect that the remnant converges to a single Kerr BH, but this has not yet been established mathematically. The problem is that the Kerr solution does not admit any gravitational radiation, whereas in BBH spacetimes, we always have radiation due to the merger process. However, there are ways of measuring how much the horizon of the remnant differs from that of a Kerr horizon [153, 154], and a recent study on curvature invariants finds that the final spacetime is within numerical accuracy identifiable as Kerr [155]. Also, comparing the quasi-normal mode frequencies with the spin determined on an isolated horizon (see Chapter 4) reveals that within numerical accuracy, the final BH must be Kerr (see Section 11.3, and also [156]). Similar behavior has also been found in Section 11.2 (Figure 11.13) [56], where we compare the final spin calculated according to the isolated horizon formalism (see Chapter 4) and according to the circumference function assuming a Kerr geometry. Both methods agree within numerical accuracy.

---

[19] The concept of an ISCO is valid only for test particles. Numerical relativity simulations have shown that the (gauge-dependent) trajectories continue as smooth spirals up until merger (see left panel of Figure 12.7). There is no point in time where the two bodies just fall towards each other. Nevertheless, the ISCO is a useful concept especially for data analysis techniques or in phenomenological theories such as the effective one-body (EOB) approach [152].

During evolution, the binary will emit gravitational radiation which is characteristic for each of the three stages. The inspiral wave is nearly sinusoidal. However, as time proceeds, the frequency and amplitude strictly monotonically increase up until the ISCO. If the initial orbits of the two BHs are eccentric, then the radiation reaction damping will circularize the orbits, so that after a rather short time (approx. 100 orbits) the eccentricity will have been completely removed from the system [151]. On todays supercomputers, we are able to simulate BBH mergers starting from the late inspiral phase with up to 15 orbits prior to merger. At that time, the binary has had enough time during the previous thousands of orbits to circularize its orbit. Therefore, almost all simulations of BBHs use initial data that are on circular orbits, with ideally no initial eccentricity. In the plunge and merger phase, the radiation will result in a peak emission and then exponentially fall off during ring-down[20]. This is depicted in Figure 1.4, where we show the leading order $\ell = m = 2$ gravitational wave-mode of the gravitational-wave strain h for a complete BBH coalescence and its three stages. In this figure, the first upper panel shows the + and × polarization of the wave-mode h_{22}, the panel below shows the amplitude A of the wave-mode, and the two bottom panels show the corresponding phase ϕ and instantaneous frequency ω, respectively, *i.e.* the waveform is written in the form

$$\mathbf{h} \equiv h_+ - i h_\times = A(t) \mathrm{e}^{i\phi(t)} = A(t) \mathrm{e}^{i\omega(t)t} \,, \tag{1.5.1}$$

where $\omega = \dot{\phi}$. One can clearly see how the amplitude and frequency of the wave monotonically increase towards the peak (the merger). Afterwards, during ring-down, the amplitude falls off exponentially, while the frequency remains constant (the high frequency noise in the lower panel comes from numerical artifacts).

Parameter space and properties of the remnant

The final merger remnant has a number of interesting properties. As already mentioned in the previous subsection, the remnant is within numerical accuracy identifiable as a boosted Kerr BH [155, 156].

Despite a certain final mass due to the mass-loss to gravitational radiation, it can attain a significant recoil velocity due to the asymmetric emission of gravitational waves which can be so large that the BH can eventually be "kicked" out of its host object. We will present work on this topic in Chapter 12.

Another interesting property is the final spin of the merger remnant as it can lead to a better understanding of the spin distribution of BHs in our and other galaxies. A detailed analysis of the final spin will be given in Chapter 13.

All of these properties can be analyzed in terms of the parameters of the initial BHs, and one can try to understand which initial configurations lead to what properties of the remnant. In this respect, one can think of a BBH merger as a "mechanism" which takes as input two BHs and has as output one single BH [160]. Indeed, in Chapter 12, 13 and 14, we try to find the mapping of the initial parameter space of the two initial BHs to certain properties of the merger remnant, particularly the recoil velocity, the spin and the final mass.

The parameter space of a BBH simulation is 7-dimensional: there are the two spin vectors $\mathbf{S}_1$ and $\mathbf{S}_2$ of BH number one and two, respectively, and the mass ratio $q = M_1/M_2$, or equivalently, the *symmetric* mass ratio $\nu = M_1 M_2/(M_1 + M_2)^2$. It is possible to consider simply the mass ratio

---

[20] Generally, the wave-signal does not necessarily fall-off to zero during ring-down. Due to non-linear gravitational wave-memory, the amplitude may settle to a constant non-zero value [157–159].

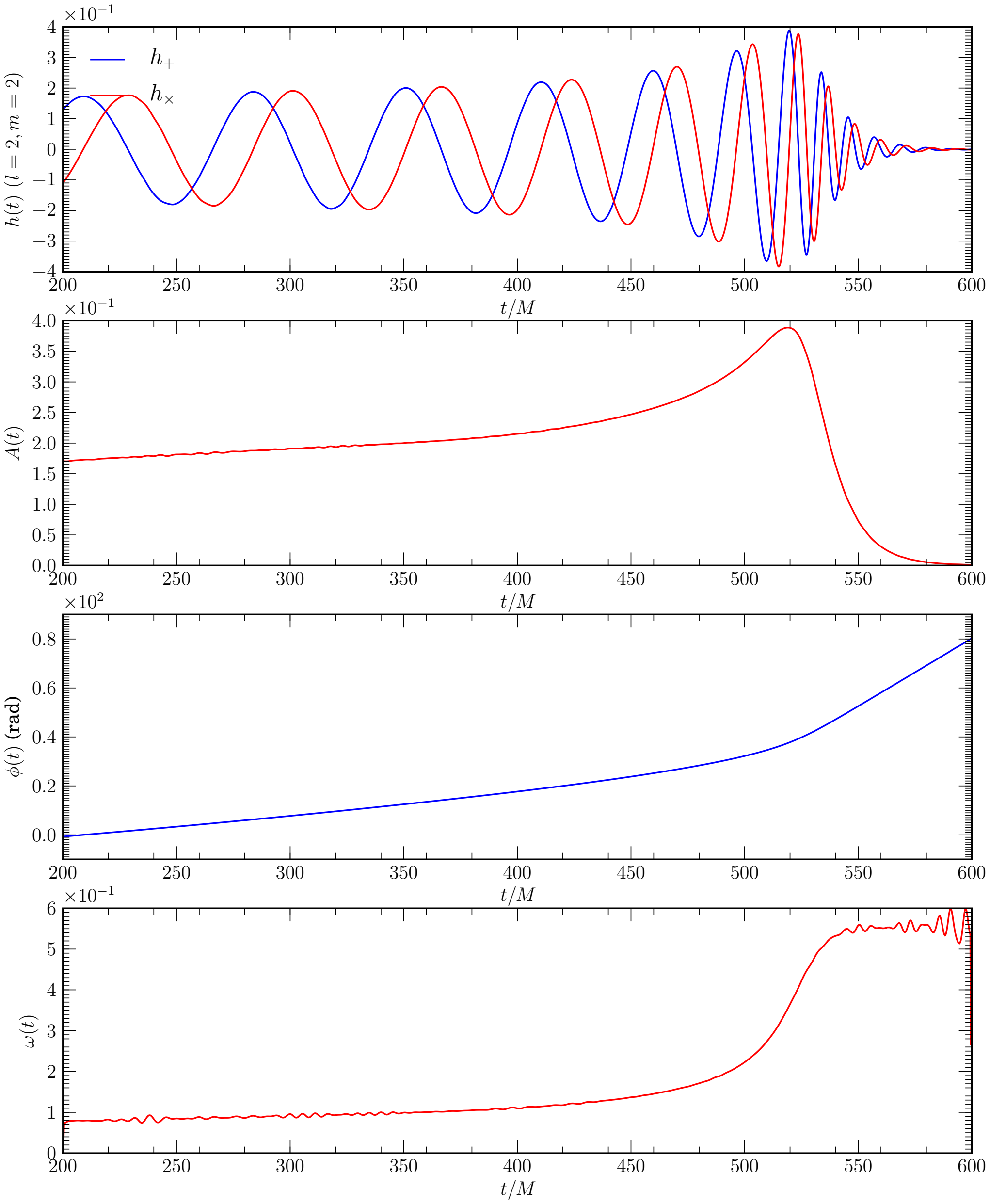

Figure 1.4: A typical BBH merger waveform. The first upper panel shows the + and × polarization of the wave-mode h_{22}, the panel below shows the amplitude A of the wave-mode, and the two bottom panels show the corresponding phase ϕ and instantaneous frequency ω. Data generated by using the CCATIE code (see Section 8.1). The high frequency noise at the bottom panel can be attributed to numerical artifacts. It can be drastically decreased by applying *e.g.* multiblock techniques, which allow for much higher spatial and time resolutions in the wave-zone (compare Figure 11.22).

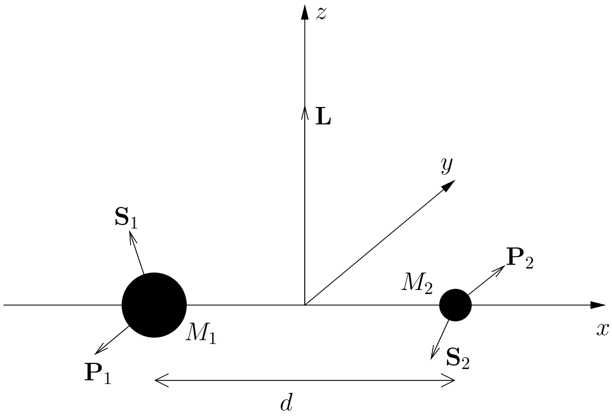

Figure 1.5: This figure shows an initial configuration of a BBH merger. Ideally, the binary would have infinite initial separation. For obvious reasons, this is not possible in numerical simulations. One therefore typically starts the simulation at an initial separation of $d = 8M$ and, if possible, even larger, depending on the computational resources that are available. The coordinate system is chosen such that its origin is located at the center of mass, the z-axis aligns with the initial orbital angular momentum $\mathbf{L}$ and the BHs with masses $M_{1,2}$ are located on the x-axis. The components of the initial spin vectors $\mathbf{S}_{1,2}$ are chosen with respect to this coordinate frame. According to the finite initial separation, one has to choose initial linear momenta $\mathbf{P}_{1,2}$ such that the BHs are on circular orbits. Details on how to obtain these parameters are given in Section 2.4.

instead of the individual masses because the entire system is formulated in terms of geometrized units (see Appendix A.1) and therefore scales with the total mass of the spacetime. An illustration of a typical initial configuration is given in Figure 1.5.

Ideally, the inspiral of the two BHs starts with an infinite initial separation and, as already mentioned, we can therefore think of a BBH merger as the following mapping

$$(\mathbf{S}_1, \mathbf{S}_2, q) \to (\mathbf{v}_{\text{kick}}, \mathbf{a}_{\text{fin}}, M_{\text{fin}})\,. \tag{1.5.2}$$

In practice, we have to start the simulations at a finite initial separation d of the BHs, and we thus also have to choose appropriate initial linear momenta $\mathbf{P}_1$ and $\mathbf{P}_2$ so that the BHs are on circular orbits. However, the outcome must be invariant under these additional parameters, since these parameters mimic the behavior of the BHs at that separation. In other words, if we had started the simulation at a larger initial separation, the trajectories of the BHs would coincide (modulo spin evolution). Again, in practice, due to the imperfection of current methods for obtaining these additional parameters (see Section 2.4), this is not exactly true, but becomes better the larger the initial separation is chosen.

We will consider the mapping (1.5.2) in Part III of this thesis. However, we mostly restrict attention to the 2D parameter subspace of spin-aligned equal-mass binaries[21], *i.e.* equal-mass binaries with initial spins that are aligned with the orbital angular momentum. This is due to the enormous computational power that is needed for exploring the full parameter space numerically. We will give an introduction to this parameter space in Chapter 11.

---

[21] The expression obtained for the final spin, however, is generic and takes the whole 7D parameter space into account.

Chapter 2

The Cauchy evolution system

The Einstein equations describe the entire 4D geometry of a spacetime where time is not treated differently than any spatial direction. In other words, the Einstein equations do not represent a system that describes the gravitational dynamics parametrized in terms of time. In GR, time has lost its preferred meaning over any spatial direction[1].

However, in certain situations it is helpful and even necessary to have the equations in a form that allows one to parametrize it in terms of a "time" parameter. In particular, this is very handy for the numerical evolution of BBH spacetimes where one has knowledge of an initial state of the black holes at a given time instance and is interested in the future development of the system. Such a system that can be evolved from an initial state is sometimes called a Cauchy initial value problem (CIVP). The main characterization of a CIVP is to determine in a suitable subset of the *future* a solution to a hyperbolic PDE where the individual timeslices of the space on which the solutions are defined are spacelike [75, 117, 163]. These surfaces are sometimes called *Cauchy surfaces*. That is, the Cauchy surface is a spacelike hypersurface which every non-spacelike curve intersects only once. The idea of a CIVP is shown in Figure 2.1. On a closed subset S on an initial Cauchy surface Σ, we want to determine all causally related events that are to the future of S and can be uniquely determined from S. The union of all events to the future of S is called the *future Cauchy development* or *the domain of dependence* $D^+(S)$. The domain of dependence is bounded by the *future Cauchy horizon* $H^+(S)$, which represents a boundary to the set of events that we can determine from the subset S on the initial Cauchy surface Σ. Stated differently, given the subset S as initial data on a given Cauchy surface, we want to determine its domain of dependence $D^+(S)$.

The Cauchy problem in GR is rather delicate: the Einstein field equations are *non-linear* and the gravitational field is *self-interacting*, *i.e.* it is non-linear even in the absence of other fields. This is due to the fact that the gravitational field defines the spacetime over which it propagates. Furthermore, gauge-invariance makes it impossible to define a unique (*i.e.* gauge independent) solution. Rather, one determines a unique solution only up to a diffeomorphism, and in order to obtain a definite member of the equivalence class of spacetime metrics, one has to impose gauge conditions to fix the remaining degrees of freedom. For the numerical evolution, finding suitable gauge-conditions is highly non-trivial as they should be *singularity avoidant* and resist *slice stretching.* We will give more details related to this in Section 2.3.

One of the first attempts to recast the Einstein equations into a CIVP was the "3+1" decomposition of the Einstein equations developed by Arnowitt, Deser and Misner [132, 164–166]. Essentially, the whole 4D spacetime is foliated along a timelike vector field by spatial 3D hypersurfaces as depicted in Figure 2.2.

The so called Arnowitt-Deser-Misner (ADM) system of the Einstein equations is then a reformulation in an equivalent set of six evolution and four constraint equations. This system gives a prescription for the evolution and embedding of the 3-metric of the spatial hypersurfaces along a timelike vector field that parametrizes the hypersurface foliation. However, by virtue of the Bianchi identities, only six of the ten spacetime metric components are independent, and hence the ADM evolution system is overdetermined. It is therefore sufficient to consider only six of the equations, and a convenient choice are the six (hyperbolic) evolution equations. The remaining

---

[1] It is interesting to notice that "time" might actually play a preferred role in a unified theory, for space might not exist at all at the fundamental level [161, 162].

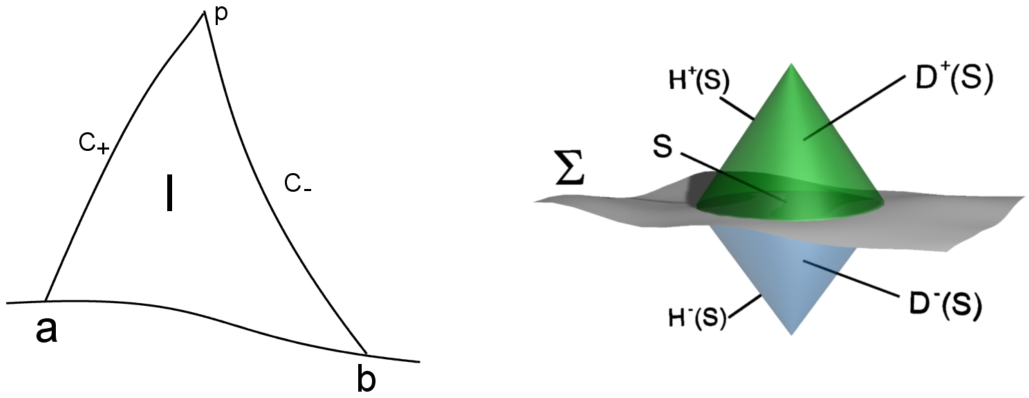

(a) Domain of dependence between a, b along the initial slice of a point p in hyperbolic PDEs. The future domain of dependence I, sometimes called the domain of determinacy, is bounded by the *characteristic lines* C_+, C_- of the hyperbolic equation.

(b) Cauchy development in GR. Given initial data on a closed subset S of the initial hypersurface Σ, these will determine future events in a region $D^+(S)$ to the future of S called the future domain of dependence bounded by the future Cauchy horizon $H^+(S)$. $D^+(S)$ is defined as the set of all points $p \in M$ such that every past-inextendible non-spacelike curve through p intersects S. Similarly, the past domain of dependence $D^-(S)$ is defined by every future-inextendible non-spacelike curve through p intersecting S.

Figure 2.1: The Cauchy problem for hyperbolic PDEs.

four (elliptic) constraint equations have to be satisfied at some initial time, but are otherwise automatically satisfied at later times.

As this system looks very appealing for numerical evolution, it was only a matter of computational power until these equations were coded up in a computer and used for numerical studies of spacetimes [37, 39, 43].

However, it has turned out that the ADM system has a severe drawback. It can be proven that it is only weakly hyperbolic thus allowing the existence of exponentially growing modes and therefore resulting in genuinely unstable discretized evolution schemes.

Especially for the numerical evolution, where it is necessary to discretize the equations, one is interested in a continuous evolution system that can be shown to be strongly hyperbolic. The reason for this is a very well developed underlying mathematical machinery that can be used to implement numerical schemes that are evidently stable. We shall review some aspects of this in Chapter 6. For the Einstein equations, an evolution system in the strong hyperbolic form [167] has been found by Baumgarte, Shapiro, Shibata, Nakamura, Oohara and Kojima (BSSNOK) [168–171]. This system is extremely successful in the numerical evolution of spacetimes and especially in BBH merger simulations. Although in this thesis, we employ the BSSNOK system, it should be mentioned that there are dozens of other formulations as well, one of which, a variant of the generalized harmonic system [172–175], has been used to accomplish the first successful BBH merger simulation [47].

In the next sections, we will first describe the ADM decomposition of the Einstein equations and proceed with the introduction of the BSSNOK system.

2.1 The ADM formalism

The ADM formalism describes the decomposition of the full 4-geometry and corresponding Einstein equations into a set of spatial 3-quantities and their embedding in the 4-geometry. As depicted in Figure 2.2, the spacetime is foliated in terms of spatial hypersurfaces along a timelike vector field. Although this system is not used for the numerical evolution of BBH spacetimes, it is nevertheless

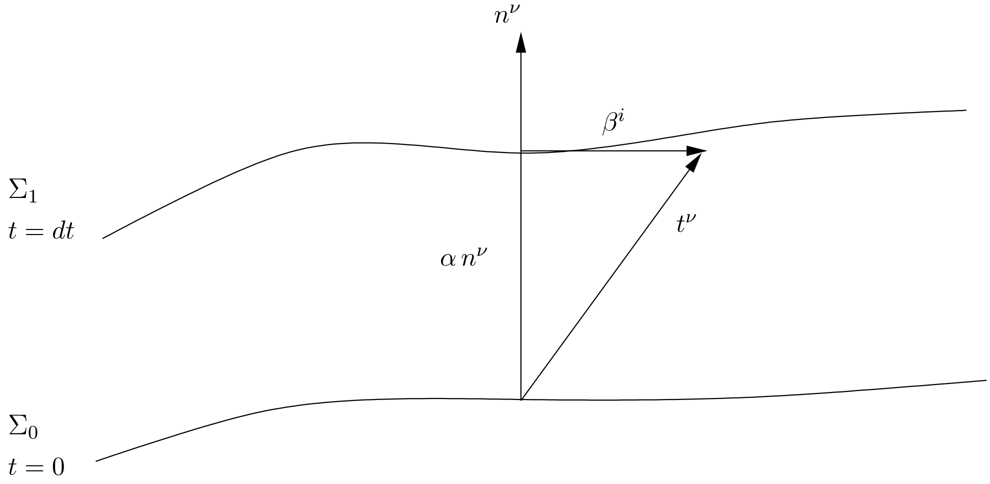

Figure 2.2: The foliation of spacetime into space-like hypersurfaces in the 3+1 decomposition.

instructive and the basic quantities, the *ADM variables*, are used for many other calculations so that it is useful to repeat it here. Most of what follows is taken from [166].

3+1 decomposition

Given two successive arbitrary spatial hypersurfaces Σ_t and Σ_{t+dt} as depicted in Figure 2.2, we can determine the 4D geometry by the following basic quantities:

- The 3-metric γ_{ij} intrinsic to the spatial hypersurface. This metric determines the 3D geometry confined to the particular choice of spatial hypersurface. Note that the indices ij only run over spatial components $1, .., 3$.
- The timelike unit normal vector n^μ of the spatial hypersurfaces is defined as

  $$n^\mu = -\alpha g^{\mu\nu} \nabla_\nu t \,, \tag{2.1.1}$$

  where $g^{\mu\nu}$ is the full 4-metric, and the function t is a *universal time function.* The spatial hypersurfaces Σ_t emerge as spatial level sets of the time function t. The parameter α is known as the *lapse function* and is defined as

  $$\alpha^{-2} \equiv -g^{\mu\nu} \nabla_\mu t \nabla_\nu t \,. \tag{2.1.2}$$

  The lapse function is a gauge parameter, because the choice of a spatial hypersurface, *i.e.* the foliation, is not unique. The lapse of proper time between successive hypersurfaces is given by

  $$d\tau = \alpha(t, x^i) dt \,, \tag{2.1.3}$$

  where x^i denote spatial coordinates confined to the hypersurfaces.
- We can construct a time vector field t^μ which is tangent to the time lines, *i.e.* the lines of constant spatial coordinates x^i as

  $$t^\mu = \alpha n^\mu + \beta^\mu \,, \tag{2.1.4}$$

  where the spatial vector $\beta^\mu = (0, \beta^i)$ is known as the *shift vector.* This vector determines the relative velocity between Eulerian observers and the lines of constant spatial coordinates, *i.e.*

  $$x^i_{t+dt} = x^i_t - \beta^i(t, x^j) dt \,. \tag{2.1.5}$$

  The shift is a gauge parameter, too, because the choice of spatial coordinates is not unique.

Given the functions $\{\alpha, \beta^i, \gamma_{ij}\}$, it is possible to reconstruct the full 4-metric

$$ds^2 = -\alpha^2 dt^2 + \gamma_{ij}(dx^i + \beta^i dt)(dx^j + \beta^j dt)\,, \tag{2.1.6}$$

and its inverse

$$g^{\mu\nu} = \begin{pmatrix} -\alpha^{-2} & \alpha^{-2}\beta^i \\ \alpha^{-2}\beta^j & \gamma^{ij} - \alpha^{-2}\beta^i\beta^j \end{pmatrix}. \tag{2.1.7}$$

In this coordinate basis, the normal vector n^μ takes the form

$$n_\mu = (-\alpha, 0, 0, 0)\,, \qquad n^\mu = \frac{1}{\alpha}(1, -\beta^i)\,. \tag{2.1.8}$$

Using the normal vector n_μ, the 3-metric can be written as

$$\gamma_{\mu\nu} = g_{\mu\nu} + n_\mu n_\nu\,. \tag{2.1.9}$$

Given the 3-metric γ_{ij}, it is possible to define a covariant derivative that is compatible with the 3-metric of the hypersurfaces. This allows to define the Riemann curvature tensor describing the geometry *intrinsic* to the spatial hypersurfaces. However, the 3-curvature tensor does not describe the embedding of the hypersurfaces in the full spacetime. The missing information can be obtained by introducing the *extrinsic curvature* tensor.

Extrinsic curvature

The extrinsic curvature describes the embedding of the spatial hypersurfaces Σ_t in the spacetime. It is defined by

$$K_{\mu\nu} = -\gamma_\mu{}^\sigma \gamma_\nu{}^\rho \nabla_{(\sigma} n_{\rho)}. \tag{2.1.10}$$

By construction, $K_{\mu\nu}$ is symmetric and has only spatial components. The extrinsic curvature can also be expressed in terms of the Lie derivative $\mathcal{L}_n$ of the spatial metric along the vector-field n_μ normal to Σ

$$K_{\mu\nu} = -\frac{1}{2}\mathcal{L}_n \gamma_{\mu\nu}\,. \tag{2.1.11}$$

This clarifies the meaning of the extrinsic curvature. It measures the rate of change of the spatial metric in Σ as it moves along the normal vector-field which we can relate to the flow of time. Thus, $K_{\mu\nu}$ is the time derivative of the spatial metric $\gamma_{\mu\nu}$, and brings us close to an evolution equation for the spatial metric γ_{ij}.

The ADM equations

The ADM equations represent the Einstein equations in 3+1 form by using the quantities

$$\alpha, \qquad \beta^i, \qquad \gamma_{ij}, \qquad K_{ij}\,, \tag{2.1.12}$$

as introduced in the previous two subsections, and are equivalent to the original Einstein equations.

The $3+1$ decomposition of the Einstein equations can be derived by performing a 3+1 splitting of the 4-Ricci tensor $R_{\mu\nu}$ by using the *Gauss*, *Codazzi* and *Ricci equations.* The result of this procedure are the ADM equations which relate three-dimensional curvature quantities to projections of the stress-energy tensor. This yields two different sets of equations. One set describes the dynamical evolution of the spatial metric and the extrinsic curvature whereas the other represents constraint equations which need to be satisfied on each hypersurface. However, if they are satisfied initially, they will always be satisfied at all later times[2].

---

[2] This is only true in the continuous case. In numerically simulations, this is only approximatively true. Due to the discretization error, the numerical solution leaves the *constraint hypersurface* defined by the field variables $\{\gamma_{ij}, K_{ij}\}$. The constraint equations can therefore be regarded as a measure of the accuracy of the numerical result.

The constraint equations read

$$\begin{aligned} R + K^2 - K_{ij}K^{ij} &= 16\pi\rho \qquad \text{Hamiltonian constraint,} && (2.1.13)\\ D_j K^j{}_i - D_i K &= 8\pi j_i \qquad \text{momentum constraint,} && (2.1.14)\end{aligned}$$

where D_i is the covariant derivative operator compatible with the spatial 3-metric γ_{ij}, and where the *total energy density* ρ of a normal observer n^μ is defined as

$$\rho := n^\mu n^\nu T_{\mu\nu}\,, \tag{2.1.15}$$

and the *momentum density* j_μ as measured by a normal observer n^μ is given by

$$j_\mu = -\gamma^\nu{}_\mu n^\rho T_{\nu\rho}\,. \tag{2.1.16}$$

In vacuum, both, the energy density and momentum density are zero, *i.e.* $\rho = 0$ and $\jmath_\mu = 0$.

The evolution equation for the spatial metric reads

$$\partial_t \gamma_{ij} = -2\alpha K_{ij} + D_i\beta_j + D_j\beta_i\,, \tag{2.1.17}$$

and the evolution equation for the extrinsic curvature is

$$\begin{aligned} \partial_t K_{ij} \;=\; & -D_i D_j \alpha + \alpha(R_{ij} - 2K_{ik}K^k{}_j + KK_{ij})\\ & -\alpha 8\pi (S_{ij} - \frac{1}{2}\gamma_{ij}(S - \rho))\\ & +\beta^k D_k K_{ij} + K_{ik} D_j \beta^k + K_{kj} D_i \beta^k\,. \end{aligned} \tag{2.1.18}$$

Since the lapse α and the shift β^i are not determined by the equations, they can be given freely, *i.e.* they are pure gauge. Lapse and shift describe how the coordinates evolve from one slice to the next and it is a crucial point in numerical relativity to choose a 'friendly' gauge that allows for a well-behaved and successful simulation. For example, since any forms of singularities have to be avoided, one could try to drive the lapse such that successive spatial slices will not reach the singularities of BH spacetimes.

It turns out however that the standard ADM formulation is not very well suited for numerical relativity since it is numerically unstable if one discretizes in a straight forward manner. In the next section we will therefore discuss another evolution system, which is used in current state-of-the-art BBH evolution codes.

2.2 The BSSNOK formulation

The evolution equations as given by the ADM equations are not yet in their most desirable form. In their discretized version, the equations develop severe instabilities thus making it very impracticable to apply this system to BBH simulations.

The main reason for this unstable behavior is hidden in the Ricci tensor. The Ricci tensor introduces mixed second derivatives of the spatial metric. Without these, the system would be manifestly hyperbolic since it could be written as wave equations for the components of the spatial metric [176]. Hyperbolicity is a desired feature because mathematical theorems would guarantee the existence and uniqueness of solutions. Furthermore, stability theorems for the discretized problem could be applied, assuring (strictly) stable evolution schemes. Finally, hyperbolic problems have families of characteristics lines along which solutions are propagated with a finite speed. This can be used to analyze and construct boundary conditions.

These considerations suggest that it might be desirable to get rid of the mixed derivative terms occurring in the Ricci tensor and this was first done by Nakamura, Oohara and Kojima [168] and extended by Shibata and Nakamura [169] and Baumgarte and Shapiro [170] and is consequently abbreviated by BSSNOK. In addition to that, we use the modifications introduced in [48, 171, 177].

It can be shown that the BSSNOK system is strongly hyperbolic [167] and is therefore superior to the ADM system which is only weakly hyperbolic. Understanding *completely* why the BSSNOK system has a much better long-term stability behavior than the ADM formulation is still ongoing research. Some of the work analyzing the hyperbolicity and stability properties can be found in [167, 178–181].

It should be mentioned that there also exist many other different approaches to the problem of finding a stable evolution system. One of these is a variant of the generalized harmonic system [172–175] which has been used for the first stable BBH simulation [47] or the Friedrich-Nagy system which is based on a spin-frame formalism [182]. The different formulations are reviewed in[183].

However, as the results in this thesis were all produced using the BSSNOK formulation, we will restrict attention to this system only.

Conformal-traceless 3+1 representation

We can eliminate the mixed derivatives in the Ricci tensor by introducing auxiliary variables. More specifically, we are introducing a conformal metric with conformal factor $\psi = e^{\phi}$ so that

$$\tilde{\gamma}_{ij} = e^{-4\phi}\gamma_{ij}, \tag{2.2.1}$$

and choosing it such that the determinant of the conformally related metric $\tilde{\gamma}_{ij}$ is unity, $\phi = (\ln\gamma)/12$ with $\gamma = \det\gamma_{ij}$. We can split the trace from the extrinsic curvature and conformally rescale the traceless part A_{ij} and choose a conformal rescaling for A_{ij} like the metric itself

$$\tilde{A}_{ij} = e^{-4\phi}(K_{ij} - \frac{1}{3}\gamma_{ij}K). \tag{2.2.2}$$

Here, tildes denote conformally rescaled quantities. Indices of $\tilde{A}_{ij}$ are raised and lowered with the conformal metric $\tilde{\gamma}_{ij}$, so that $\tilde{A}^{ij} = e^{4\phi}A^{ij}$

By taking the trace of the ADM evolution equation (2.1.17) and (2.1.18), and together with $\partial_t \ln\gamma = \gamma^{ij}\partial_t\gamma_{ij}$, we can write

$$\partial_t \ln\gamma^{1/2} = -\alpha K + D_i\beta^i\,. \tag{2.2.3}$$

In addition, we can combine the Hamiltonian constraints (2.1.13) with the trace of the evolution equation for the extrinsic curvature (2.1.18). We get

$$\partial_t K = -D^2\alpha + \alpha\left(K_{ij}K^{ij} + 4\pi(\rho + S)\right) + \beta^i D_i K\,. \tag{2.2.4}$$

Evolution equations for ϕ and K can now be found from equation (2.2.3), yielding

$$\partial_t\phi = -\frac{1}{6}\alpha K + \beta^i\partial_i\phi + \frac{1}{6}\partial_i\beta^i \tag{2.2.5}$$

and (2.2.4)

$$\partial_t K = -\gamma^{ij}D_jD_i\alpha + \alpha(\tilde{A}_{ij}\tilde{A}^{ij} + \frac{1}{3}K^2) + 4\pi\alpha(\rho + S) + \beta^i\partial_i K. \tag{2.2.6}$$

Subtracting these from the evolution equations (2.1.17) and (2.1.18) yields the traceless evolution equations for $\tilde{\gamma}_{ij}$

$$\partial_t\tilde{\gamma}_{ij} = -2\alpha\tilde{A}_{ij} + \beta^k\partial_k\tilde{\gamma}_{ij} + \tilde{\gamma}_{ik}\partial_j\beta^k + \tilde{\gamma}_{kj}\partial_i\beta^k - \frac{2}{3}\tilde{\gamma}_{ij}\partial_k\beta^k. \tag{2.2.7}$$

and $\tilde{A}_{ij}$

$$\begin{aligned}\partial_t\tilde{A}_{ij} \;=\; & e^{-4\phi}\left(-(D_iD_j\alpha)^{TF} + \alpha(R_{ij}^{TF} - 8\pi S_{ij}^{TF})\right) \\ & +\alpha(K\tilde{A}_{ij} - 2\tilde{A}_{il}\tilde{A}^l{}_j) \\ & +\beta^k\partial_k\tilde{A}_{ij} + \tilde{A}_{ik}\partial_j\beta^k + \tilde{A}_{kj}\partial_i\beta^k - \tfrac{2}{3}\tilde{A}_{ij}\partial_k\beta^k.\end{aligned} \tag{2.2.8}$$

In the last equation, the superscript TF denotes the trace-free part of a tensor, e.g. $R^{TF}_{ij} = R_{ij} - \gamma_{ij}R/3$. Note also that in equations (2.2.5) through (2.2.8) the shift terms arise from Lie derivatives of the respective variable. The divergence of the shift, $\partial_i\beta^i$, appears in the Lie derivative because the choice $\tilde\gamma = 1$ makes ϕ a tensor density of weight $1/6$, and $\tilde\gamma_{ij}$ and $\tilde A_{ij}$ tensor densities of weight $-2/3$.

We can now define the "conformal connection functions" to eliminate the mixed derivatives in the Ricci tensor

$$\tilde\Gamma^i \equiv \tilde\gamma^{jk}\tilde\Gamma^i{}_{jk} = -\tilde{\gamma}^{ij}{}_{,j}, \tag{2.2.9}$$

where the $\tilde\Gamma^i_{jk}$ are the connection coefficients associated with $\tilde\gamma_{ij}$. In terms of these, the Ricci tensor can be written

$$\begin{aligned} \tilde R_{ij} \;=\; & -\tfrac12\tilde\gamma^{lm}\tilde\gamma_{ij,lm} + \tilde\gamma_{k(i}\partial_{j)}\tilde\Gamma^k + \tilde\Gamma^k\tilde\Gamma_{(ij)k} + \\ & \tilde\gamma^{lm}\left(2\tilde\Gamma^k{}_{l(i}\tilde\Gamma_{j)km} + \tilde\Gamma^k{}_{im}\tilde\Gamma_{klj}\right). \end{aligned} \tag{2.2.10}$$

The only second derivatives of $\tilde\gamma_{ij}$ left over in this operator is the Laplace operator $\tilde\gamma^{lm}\tilde\gamma_{ij,lm}$ – all others have been absorbed in first derivatives of $\tilde\Gamma^i$.

We now treat the $\tilde\Gamma^i$ as independent functions, and hence need to derive their evolution equation. By permuting a time and space derivative in the definition (2.2.9), we get

$$\partial_t\tilde\Gamma^i = -\partial_j\Big(2\alpha\tilde A^{ij} - 2\tilde\gamma^{m(j}\beta^{i)}{}_{,m} + \frac{2}{3}\tilde\gamma^{ij}\beta^l{}_{,l} + \beta^l\tilde\gamma^{ij}{}_{,l}\Big). \tag{2.2.11}$$

The divergence of the extrinsic curvature can now be eliminated with the help of the momentum constraint (2.1.14), which yields the evolution equation

$$\begin{aligned} \partial_t\tilde\Gamma^i \;=\; & -2\tilde A^{ij}\partial_j\alpha + 2\alpha\Big(\tilde\Gamma^i{}_{jk}\tilde A^{kj} - \tfrac23\tilde\gamma^{ij}\partial_j K - 8\pi\tilde\gamma^{ij}S_j + 6\tilde A^{ij}\partial_j\phi\Big) \\ & +\beta^j\partial_j\tilde\Gamma^i - \tilde\Gamma^j\partial_j\beta^i + \tfrac23\tilde\Gamma^i\partial_j\beta^j + \tfrac13\tilde\gamma^{li}\beta^j{}_{,jl} + \tilde\gamma^{lj}\beta^i{}_{,lj}. \end{aligned} \tag{2.2.12}$$

Equations (2.2.5) through (2.2.8) together with (2.2.12) form a new system of evolution equations that is equivalent to (2.1.17) and (2.1.18). Since the $\tilde\Gamma^i$ are evolved as independent functions, their original definition (2.2.9) serves as a new constraint equation, in addition to (2.1.13) and (2.1.14). Thus, the BSSNOK prescription evolves the variables

$$\phi, \quad \tilde\gamma_{ab}, \quad K, \quad \tilde A_{ab}, \quad \tilde\Gamma^a\,. \tag{2.2.13}$$

We now consider the changes introduced in [48, 177] which advocate the use of a different conformal factor

$$\hat\phi_\kappa := (\det\gamma_{ab})^{-1/\kappa}, \tag{2.2.14}$$

where $\kappa > 0$ is a parameter to be set and the traditional form of BSSNOK differs from this system in the use of $\phi = \ln\det\gamma_{ij}/12$ as an evolution variable, in place of $\hat\phi$.

The new variable $\hat\phi_\kappa$ has been found to improve the behavior of the numerics near the black hole punctures. In [48], it is noted that certain singular terms in the evolution equations for Bowen-York initial data (see Section 2.4) can be corrected using $\chi := \hat\phi_3$. Alternatively, [177] notes that $W := \hat\phi_6$ has the additional benefit of ensuring γ remains positive, a property which needs to be explicitly enforced with χ.

The final set of evolution equations that were used for obtaining the results in this thesis read[3]

$$\begin{aligned}
\partial_t\hat{\phi}_\kappa =& -\frac{2}{\kappa}\hat{\phi}_\kappa\alpha K + \beta^i\partial_i\hat{\phi}_\kappa - \frac{2}{\kappa}\hat{\phi}_\kappa\partial_i\beta^i, && (2.2.15a)\\
\partial_t\tilde{\gamma}_{ab} =& -2\alpha\tilde{A}_{ab} + \beta^i\partial_i\tilde{\gamma}_{ab} + 2\tilde{\gamma}_{i(a}\partial_{b)}\beta^i && (2.2.15b)\\
& - \frac{2}{3}\tilde{\gamma}_{ab}\partial_i\beta^i, &&\\
\partial_t K =& - D_iD^i\alpha + \alpha(A_{ij}A^{ij} + \frac{1}{3}K^2) + \beta^i\partial_i K, && (2.2.15c)\\
\partial_t\tilde{A}_{ab} =& (\hat{\phi}_\kappa)^{\kappa/3}(-D_aD_b\alpha + \alpha R_{ab})^{\mathrm{TF}} + \beta^i\partial_i\tilde{A}_{ab} && (2.2.15d)\\
& + 2\tilde{A}_{i(a}\partial_{b)}\beta^i - \frac{2}{3}A_{ab}\partial_i\beta^i, &&\\
\partial_t\tilde{\Gamma}^a =& \tilde{\gamma}^{ij}\partial_i\beta_j\beta^a + \frac{1}{3}\tilde{\gamma}^{ai}\partial_i\partial_j\beta^j - \tilde{\Gamma}^i\partial_i\beta^a && (2.2.15e)\\
& + \frac{2}{3}\tilde{\Gamma}^a\partial_i\beta^i - 2\tilde{A}^{ai}\partial_i\alpha &&\\
& + 2\alpha(\tilde{\Gamma}^a{}_{ij}\tilde{A}^{ij} - \frac{\kappa}{2}\tilde{A}^{ai}\frac{\partial_i\hat{\phi}_\kappa}{\hat{\phi}_\kappa} - \frac{2}{3}\tilde{\gamma}^{ai}\partial_i K), &&
\end{aligned}$$

with the definitions

$$\tilde{\gamma}_{ab} := \gamma^{-1/3}\gamma_{ab}, \qquad (2.2.16)$$

$$K := \gamma^{ab}K_{ab}, \qquad (2.2.17)$$

$$\tilde{A}_{ab} := \gamma^{-1/3}(K_{ab} - \frac{1}{3}\gamma_{ab}K), \qquad (2.2.18)$$

$$\tilde{\Gamma}^a := \tilde{\gamma}^{ij}\tilde{\Gamma}^a{}_{ij}\,. \qquad (2.2.19)$$

A more comprehensive discussion can be found in [48, 177, 179, 180, 184, 185]. We will discuss the discretization of these equations in Section 8.1.

Note that the evolution equations require proper initial data and boundary conditions. However, there are currently no known exact and constraint-preserving boundary conditions for the Einstein equations. Although there are promising attempts to model proper outgoing radiative and constraint preserving boundary conditions (see *e.g.* [186–188]), in this thesis, we use a simple outgoing radiative (Sommerfeld) boundary condition[4]. This condition will lead to constraint violations at the outer boundary and will spoil the solution in the interior of the computational domain. We therefore have to ensure that the outer boundary is causally disconnected from the interior solution (see Figure 7.7), otherwise there is no guarantee that the solution is a valid one. Unfortunately, enlarging the computational domain comes at a high computational expense. For this reason, we have implemented a new infrastructure with adapted grids to be discussed in Section 7.3.

The generation of proper BBH initial data is discussed in Section 2.4.

Constraint treatment

This specific choice of evolution variables in the previous subsection introduces five additional constraints,

$$\begin{aligned}
\mathrm{tr}\tilde{A}_{ij} &= 0, && (2.2.20)\\
\det\tilde{\gamma}_{ij} &= 1, && (2.2.21)\\
\tilde{\Gamma}^i &= \tilde{\gamma}^{jk}\tilde{\Gamma}^i{}_{jk}\,. && (2.2.22)
\end{aligned}$$

---

[3] Note however, that some results obtained in this thesis, particularly those obtained in Chapter 12, 13 and 14, have made use of the "traditional" BSSNOK evolution system with $\phi = \ln\det\gamma_{ij}/12$ as the evolved conformal factor.

[4] This is because the more sophisticated boundary conditions rely on the harmonic formulation of the evolution system, which is not used here.

It can be shown that by actively enforcing the first of these during the evolution the stability of the numerical simulation is drastically improved [179].

We notice that during evolution due to numerical error the traceless condition is not exactly satisfied at later times. However, in order to enforce it, we can remove the trace by recalculating $\tilde{A}_{ij}$ according to

$$\tilde{A}_{ij}^{TF} = \tilde{A}_{ij} - \frac{1}{3}\tilde{A}\tilde{\gamma}_{ij} \tag{2.2.23}$$

after each evolution step.

The remaining constraints, and especially the Hamiltonian constraint, can be used to monitor the accuracy of the numerical evolution.

2.3 Choosing the right gauge

General relativity is a diffeomorphism invariant theory. This means that different spacetimes can only be distinguished up to diffeomorphic transformations. A set of spacetimes that can be transformed into each other via diffeomorphisms is therefore equivalent. This is a result of the built in gauge-invariance of general relativity, meaning that no coordinate system is preferred over any other coordinate system. In the previous sections, we already encountered the gauge variables α and β^i which determine the way the spacetime is foliated. They can be chosen freely, but have to be fixed. This is necessary when representing the evolution equations on a computer because numerically calculating the components of the metric requires the choice of a coordinate basis by fixing the gauge variables. It has even turned out that the choice of gauge is crucial to the success of BH simulations.

A naive approach would be to take the simplest gauge possible (known as *geodesic slicing*) and start the computation. This, however, will not lead to successful simulations. After a finite amount of time (compare subsection on "geodesic slicing"), the computational grid will fall into the singularity. For this reason, in the first attempts to model colliding BHs on a computer [37, 39, 40, 42–45], one has introduced the so-called *maximal slicing condition* [189] which is known to be singularity avoiding, that is, starting from BH initial data where the physical singularity is to the future of the initial hypersurface, the lapse function α approaches the Minkowski value of unity in the asymptotic regions, but approaches zero near the physical singularity. Unfortunately, this means that while time marches on in the asymptotic regions, it is frozen at the singularity, which in turn leads to a severe "slice stretching" near the singularity during evolution. This inevitably leads to unstable evolution because the stretched region will be under-resolved after some time thus limiting the time span one can numerically evolve [46, 190].

Generally, one would like to find a gauge condition that has the following properties:

- The gauge should be adapted to the underlying symmetries of the problem, *i.e.* the gauge condition should automatically seek exact, or at least approximate symmetries of the spacetime so that they become apparent in the evolution.
- The formation of coordinate singularities has to be avoided. If the spacetime contains singularities, these should also be avoided by hindering the slices from hitting the singularity.
- The gauge should be well behaved mathematically and it should be easy to implement in numerical simulations, *i.e.* hyperbolic equations should be prefered over elliptic equations for the gauge.
- The application of 3-covariance ensures that the conditions on the gauge are not coordinate dependent and can be used in different coordinate systems.

One can find such gauge conditions by relating the gauge to the various geometric quantities computed during evolution or by imposing certain conditions on the geometric quantities themselves. Generally, one can end up with simple algebraic slicing conditions, where the gauge is directly calculated in terms of the geometric quantities, or one can have elliptic, parabolic, or hyperbolic PDEs for the gauge variables.

In the next subsections, we will briefly describe the two already mentioned slicing conditions above until we come to the nowadays widely used *hyperbolic slicing* conditions, and especially the *1+log* slicing condition. These conditions have the advantage of being computationally not as expensive as the maximal slicing condition while still being singularity avoiding, but they still face the problem of slice-stretching near the singularity. A major achievement was the introduction of the $\tilde{\Gamma}$-driver condition [184, 191] which kept the slices from stretching and allowed for long-term simulations. The description of this method finalizes this section.

Geodesic slicing

Geodesic slicing is the simplest of all gauge choices. It amounts to setting

$$\alpha = 1, \qquad \beta^i = 0\,, \tag{2.3.1}$$

which means that proper time equals coordinate time and the coordinates have zero velocity. With this slicing condition, one can show that a point initially located on the black hole throat must fall into the singularity after a proper time $\tau = t = \pi M$ [67]. This means that a numerical computer code must crash after $t = \pi M$ because the numerical grid has fallen into the singularity. Hence, this slicing condition is unusable in numerical simulations. However, it can be exploited for code tests [44]. A better slicing condition is the maximal slicing condition as discussed in the next subsection.

Maximal slicing

Maximal slicing has been used extensively for some time in numerical relativity [37, 39, 40, 42–45] since it allowed the evolution of BHs for longer then $t = \pi M$ by avoiding the BH singularity [189]. This is achieved by starting from BH initial data where the singularity is to the future of the initial hypersurface. By freezing the lapse, *i.e.* $\alpha = 0$ at the singularity, but keeping it at $\alpha > 0$ in the exterior region, the hypersurfaces will never "hit" the singularity but allow for evolution of the spacetime outside of the black hole (see Figure 2.3).

The name maximal slices is derived from the property that the hypersurfaces by which spacetime is foliated have maximal volume. They are characterized by

$$K \equiv \gamma^{ij} K_{ij} = 0 = \frac{\partial K}{\partial t}\,. \tag{2.3.2}$$

The condition $\partial_t K = 0$ is sometimes called *K-freezing* and maximal slicing with $K = 0$ is a special case of that.

Inserting this condition in the evolution equation for the trace of the extrinsic curvature (2.1.18) yields a condition on the lapse

$$D^i D_i \alpha = \alpha R, \tag{2.3.3}$$

or, using the Hamiltonian constraint,

$$D^i D_i \alpha = \alpha K^{ij} K_{ij}\,. \tag{2.3.4}$$

This represents an elliptic equation for α that has to be solved numerically at each time-step during evolution in order to remain in the maximal slicing gauge. Apart from the computational expense of solving an elliptic equation, maximal slicing has the undesired feature of stretching the grid since the time is frozen at the singularity (see Figure 2.3). This inevitably leads to an unstable scheme and limits the total evolution time until the simulation crashes [46, 190]. However, as we will discuss later (see subsection on the hyperbolic $\tilde{\Gamma}$ driver), this slice stretching can be avoided by imposing a condition on the shift vector.

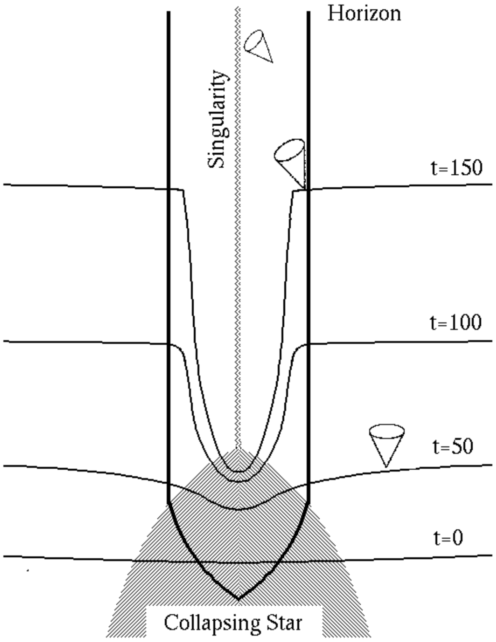

Figure 2.3: This figure illustrates some singularity avoiding slices that wrap up around the singularity inside the horizon. The singularity is never "hit" and is to the future of the slices. This slicing allows a long-term evolution of BHs, but the slice stretching that occurs close to the singularity leads to stretching of the numerical grid. Figure taken from [192].

Hyperbolic slicing

One particular drawback of the maximal slicing condition is the fact that we would have to solve an elliptic equation for the lapse which is computationally extremely expensive. We therefore seek for a condition that still incorporates the singularity avoiding feature of maximal slicings while at the same time being computationally efficient. This has been achieved by the Bona-Massó family of slicing conditions [193] which result in a hyperbolic equation for the lapse which is easy to solve numerically.

But before we consider these type of slicings, let us step back and consider again the maximal slicing condition which resulted in an elliptic equation for the lapse (2.3.4). One problem hides in the fact that the condition $K = 0$ is not actively enforced, *i.e.* if the lapse is perturbed at any time such that K becomes non-zero, the condition (2.3.4) can never put it back to zero. Especially if numerical error builds up, the lapse might be perturbed such that this will be the case. Therefore, the *K-driver* condition has been introduced [194] and reads

$$\frac{\partial K}{\partial t} + cK = 0\,, \tag{2.3.5}$$

where $c > 0$ is a constant in time. This condition will exponentially drive K to zero and therefore actively enforces the condition $K = 0$. By using the Hamiltonian constraints, condition (2.3.5) can be written as a condition for the lapse

$$D^i D_i \alpha = \beta^i \partial_i K + \alpha K^{ij} K_{ij}\,, \tag{2.3.6}$$

which is an elliptic equation.

But it is preferable of having a condition in parabolic, or even better, hyperbolic form.

This can be accomplished by departing from the idea of K-freezing with $\partial_t K = 0$ and instead relating the time derivative of the trace of the extrinsic curvature to the first or second time-derivative of the lapse. In addition to that, it has been found empirically that a certain algebraic slicing condition, the so called "1+log" condition

$$\alpha = 1 + \ln\gamma \tag{2.3.7}$$

is very robust in practice and mimics the behavior of singularity avoidance of maximal slicing [44].

A family of slicing conditions that comprises both ingredients, *i.e.* hyperbolic K-driver slicing conditions that result in a lapse of the form (2.3.7), have been found by Bona and Massó [193] where the lapse is chosen to satisfy the following equation

$$\frac{\partial}{\partial t}\alpha = -\alpha^2 f(\alpha) K\,. \tag{2.3.8}$$

If $f > 0$, we can see that (2.3.8) is hyperbolic by taking an extra time derivative of (2.3.8). We get

$$\frac{\partial^2}{\partial t^2}\alpha = -\alpha^2 f\left[\frac{\partial}{\partial t}K - \alpha(2f + \alpha f')K^2\right], \tag{2.3.9}$$

with $f' := \partial f/\partial\alpha$. By using the ADM evolution equation for the extrinsic curvature K, we find that

$$\frac{\partial^2}{\partial t^2}\alpha - \alpha^2 f D^i D_i \alpha = -\alpha^3 f\left[K_{ij}K^{ij} - (2f + \alpha f')K^3\right]\,. \tag{2.3.10}$$

This equation for the lapse is a wave-equation with a quadratic source-term in K_{ij} if $f > 0$, and with a *gauge-speed* of

$$v_g = \alpha\sqrt{f\gamma^{ii}} \tag{2.3.11}$$

along direction x^i. Wave-equations are hyperbolic, and therefore the lapse is evolved with a hyperbolic equation if it obeys condition (2.3.8).

In addition, if we set $f = 2/\alpha$ in (2.3.8), the solution of the lapse is of the form

$$\alpha = h(x^i) + \ln\gamma\,, \tag{2.3.12}$$

where $h(x^i)$ is a positive function that is constant in time and depends only on the coordinates. But this is the desired form of the lapse that has been found empirically to be very robust and singularity avoidant [44]. The singularity avoidance features of the Bona-Massó slicings have been studied in more detail in [195, 196].

We can also write

$$\partial_t\alpha - \beta^i\partial_i\alpha = -n\alpha(K - K_0)\,, \tag{2.3.13}$$

where $K_0 = K(t = 0)$ is the initial value of the trace of the extrinsic curvature, n is some constant, usually chosen to be $n = 2$. This is a slight generalization to the Bona-Massó family of slicing conditions (2.3.8) and is the condition to the lapse that is used in todays numerical relativity codes known as "1+log" slicing. Note that the shift term was added [197] in order to remove unphysical gauge modes that arise when using the original implementation of (2.3.13) as given in [196].

At the beginning of the simulation, we have to specify initial data for the lapse. The form that we use is described in Section 2.4 and given by (2.4.25). During evolution, boundary data is given by an outgoing Sommerfeld condition.

However, although the slicing condition (2.3.13) is computationally very inexpensive and at the same time singularity avoiding, it still suffers from slice stretching near the singularity. This can be compensated by introducing a condition for the shift which we will discuss in the next subsection.

Hyperbolic $\tilde{\Gamma}$-driver condition

Both, maximal and hyperbolic slicing conditions result in a severe stretching of the grid near the singularity causing the black hole horizon to grow in coordinate space. This usually results in a loss of resolution and thus ultimately in a crash of the simulation. One is therefore interested in finding a gauge that counters the infalling of the spatial coordinates into the black hole.

This can be achieved by choosing a shift that is outward pointing. Since the shift is the velocity of the coordinates, it can be chosen such that it cancels the infalling coordinate velocity therefore resulting in an almost static coordinate system. However, the dynamic evolution of black holes is so complex that it is impossible to choose a shift such that the desired effect on the coordinates is achieved.

One breakthrough has been made with the introduction of hyperbolic $\tilde{\Gamma}$-driver condition [184, 191]. Similar to the lapse, this condition imposes a hyperbolic equation on the shift which results in the desired effect on the coordinates.

Consider the definition of the $\tilde{\Gamma}$-variable of the BSSNOK system (2.2.9). One can easily derive an elliptic condition for the shift by setting $\partial_t \tilde{\Gamma} = 0$ (*Gamma freezing*) which is closely related to the well known *minimal distortion* shift condition [41]. The minimal distortion shift condition is a very natural (but elliptic) condition that will minimize the changes in the shape of volume elements during an evolution and is therefore exactly what we want. In the weak-field limit, it can even be shown that this condition results in the TT-gauge [40] which is another desirable feature when extracting gravitational waves from the spacetime.

However, as for the lapse, solving an elliptic equation for the minimal distortion condition is computationally too expensive. Again, one seeks for a condition that is manifestly hyperbolic and therefore easy to solve numerically.

When solving elliptic equations, one usually makes use of a fictitious time coordinate and then evolves the resulting parabolic equation until the solution relaxes to a stationary state so that it satisfies the original elliptic equation. One can also reformulate the problem in terms of an hyperbolic equation. Now, in practice we do not necessarily need highly accurate gauge conditions since the gauge is arbitrary [194]. As long as it is behaving approximately the way we would like to see it, there is no need to relax the solution of the hyperbolic equation until it becomes stationary so that a solution to the original elliptic solution has been found. We therefore consider the first relaxation step as accurate enough and have effectively transformed the elliptic problem to a hyperbolic one.

The hyperbolic-driver can be written as

$$\begin{aligned} \partial_t \beta^i - \beta^j \partial_j \beta^i &= \frac{3}{4} \alpha B^i, && (2.3.14) \\ \partial_t B^i - \beta^j \partial_j B^i &= \partial_t \tilde{\Gamma}^i - \beta^j \partial_j \tilde{\Gamma}^i - \eta B^i \,, && (2.3.15) \end{aligned}$$

where η is a damping parameter which can be chosen freely and is there for avoiding strong oscillations in the shift. At the beginning of the simulation, we normally choose $\beta = 0$ as initial data for the shift and outgoing radiative (Sommerfeld) boundary conditions during evolution.

Note that the advection terms on the LHS of these equations were not present in their original definitions in [184, 191], where co-rotating coordinates were used, but have been added following the experiences of [49, 197], and are required for correct advection of the puncture in "moving-puncture" evolutions. In fact, the orbital motion of the punctures is completely induced by these additional terms. This can be understood by recalling that the shift is evolved in such a way that it counteracts any slice stretching effect, *i.e.* the coordinates shall reflect the geometry of the spacetime as closely as possible. Hence, the shift condition not only avoids longitudinal slice stretching effects close at the singularity of a single BH but also automatically adapts to the tangential motion of the spacetime geometry in the case of two orbiting BHs. Furthermore, if the shift vanishes at the punctures, the punctures, *i.e.* the conformal metric $\tilde{\gamma}_{ij}$ and the conformal factor $\hat{\phi}$ at the punctures, will not move in space either.

2.4 Initial data

The evolution problem of GR requires the specification of appropriate initial data. These data, however, cannot be specified freely, because the Einstein equations give rise to four constraint equations, *i.e.* three momentum constraints and the Hamiltonian constraint that the initial data have to satisfy.

For the evolution of BBH, we are interested in initial data that represents BHs in vacuum with momenta and spins, and which are eventually put on quasi-circular orbits. Important aspects of BH data sets are the choice of the spatial hypersurface and how the singularity inside the BHs is treated (see also Section 2.5).

In order to obtain multi-BH initial data, a non-trivial topology is usually introduced. The first of such non-trivial topologies have been found by Einstein and Rosen [198], so-called *Einstein-Rosen bridges*, in their work on point particles. Subsequently, various constructions for Einstein-Rosen bridges, or *wormholes*, were given in [199–203]. As we will see in the next subsections, the spatial slice of such solutions typically consists of two or more copies of $\mathbb{R}^3$ with several spheres removed, *i.e. excising* a ball in each throat, and identifications of various spherical inner boundaries. In this way several asymptotically flat regions are connected via bridges or "throats" (Figure 2.4). The removal, or *excision*, of the throat interiors, and hence the other asymptotically flat ends, is possible because they are causally disconnected from the remaining part of spacetime.

By using the idea of wormholes and throats, one can employ sophisticated methods for solving the constraint equations for two asymptotically flat spaces that are connected by as many throats as there are black holes, and are isometric copies of each other (known as Misner data [202]). Since the constraints are elliptic equations, one has to specify a computational domain and associated inner and outer boundary conditions for the remaining part of spacetime. For example, at the spherical excision boundary, one can impose boundary conditions based on an isometry condition as proposed by Misner [201, 202], which have been used in [204] and also in [205].

By means of a method called *conformal-imaging* [206–214], one can generalize the Misner data as a time-symmetric solution of the momentum and Hamiltonian constraints to more realistic BH initial data known as Bowen-York data. Unfortunately, this method is rather complex and results in an infinite series solution.

It is also possible to use the apparent horizon of the BH as an excision boundary surface [215] with no reference to wormhole topologies at all. However, as we will briefly discuss in Section 2.5, these proposed excision methods are connected to several complications.

An alternative to excision boundaries and conformal-imaging is to work with a generalization to the throat solution in the form proposed by Brill and Lindquist [203] on flat three-space $\mathbb{R}^3$ in the absence of time-symmetry by compactifying the internal asymptotically flat regions. In this way, a simple domain of integration is obtained [216–220], and the singular points that correspond to the other asymptotically flat infinities in this solution are called *punctures*. This will be the method of choice for constructing BBH initial data since it is easy to implement and removes the necessity of defining inner boundary conditions. Furthermore, punctures are a powerful way of dealing with the singularities in the simulation during evolution. We will discuss this further in Section 2.5.

A key ingredient when constructing initial data is the *conformal transverse-traceless* decomposition of the metric on the initial slice [221–225] and the solution of the momentum constraints by making use of Bowen-York extrinsic curvature [206, 207]. This will be subject of the next two subsections. Another way of constructing initial data is given by the so-called *thin-sandwich* decomposition [226]. Similar to the conformal transverse-traceless decomposition, one prescribes initial data in terms of a conformal metric, but this time on two nearby hypersurfaces, or equivalently, the metric and its time derivative on a given hypersurface. In principle this method is known to give more control over the expected dynamics of the spacetime as the quantities that are specified have a direct physical meaning. However, it can be shown that the two methods are equivalent [227] and in practice [228], it is easier to follow the former approach.

Finally, in the last two subsections, we will describe two methods that are used in order to generate initial data parameters for arbitrary mass and spinning BHs that are inspiralling. A common method produces initial data parameters by defining an effective potential whose minimization would lead to quasi-circular orbits in Newtonian gravity [229, 230]. However, these parameters result in a certain amount of eccentricity that cannot be removed easily. It is more efficient to make use of post-Newtonian inspirals starting from a much larger initial separation allowing to circularize the orbits via radiation-reaction [231]. After post-Newtonian evolution, the obtained set of spin and momentum parameters is used to solve the constraint equations on the initial hypersurface.

Although some of the results produced in this thesis have made use of the effective potential method[5], the current method of choice is the post-Newtonian method.

The numerical implementation of the generation of BBH initial data is not discussed here, but will be postponed to Section 8.1.

Conformal transverse-traceless initial data construction

The starting point for constructing initial data is an Ansatz for solving the Hamiltonian and momentum constraints on the initial slice. One successful method was introduced by Lichnerowicz, York and others [221–225], and is known as the conformal transverse-traceless decomposition. This method allows to specify initial data in terms of the conformal 3-metric and the extrinsic curvature. As mentioned above, another but similar way of prescribing data is known as the thin-sandwich decomposition [226] and lets one specify initial data in terms of the conformal 3-metric and its time derivative instead of using extrinsic curvature. This, however, can be shown to be equivalent [227] and is not used in practice [228] for the work done in this thesis.

We start off by decomposing the 3-metric γ_{ij} in terms of a conformal factor ψ and an auxiliary metric $\tilde{\gamma}_{ij}$ so that

$$\gamma_{ij} = \psi^4 \tilde{\gamma}_{ij} \tag{2.4.1}$$

and which is conformally flat:

$$\gamma_{ij} = \psi^4 \delta_{ij} \tag{2.4.2}$$

where δ_{ij} is the Kronecker delta. The extrinsic curvature is separated into its trace K and its tracefree part given by

$$A^{ij} = K^{ij} - \frac{1}{3}\gamma^{ij} K\,, \tag{2.4.3}$$

and we introduce the conformal transformation on A^{ij} in the following way

$$\tilde{A}^{ij} = \psi^{10} A^{ij}\,. \tag{2.4.4}$$

We now take advantage of an algebraic relation for any symmetric and traceless tensor S^{ij}, which can be split in the following way

$$S^{ij} = S^{ij}_{*} + (\mathbf{L}W)^{ij}\,, \tag{2.4.5}$$

where S^{ij}_{*} is a symmetric, traceless and *transverse* tensor (*i.e.* with zero divergence $D_j S^{ij}_{*} = 0$), W^i is a vector, and $\mathbf{L}$ is an operator defined as

$$(\mathbf{L}W)^{ij} := D^i W^j + D^j W^i - \frac{2}{3}\gamma^{ij} D_k W^k\,. \tag{2.4.6}$$

The quantity $(\mathbf{L}W)^{ij}$ is known as the *conformal Killing form* associated with the vector W^i, and its contribution is called the *longitudinal part* of S^{ij}.

Applying this relation to $\tilde{A}^{ij}$ yields

$$\tilde{A}^{ij} = \tilde{A}^{ij}_{*} + (\tilde{\mathbf{L}}\tilde{W})^{ij}\,, \tag{2.4.7}$$

and we need to construct the transverse tensor $\tilde{A}^{ij}_{*}$. Such a tensor can be constructed from an arbitrary symmetric-tracefree tensor $\tilde{M}^{ij}$ which is not necessarily transverse. Using this new tensor, one can show that A^{ij} can be written as

$$\tilde{A}^{ij} = \tilde{M}^{ij} + (\tilde{\mathbf{L}}\tilde{V})^{ij}\,, \tag{2.4.8}$$

---

[5] Specifically, the results reported in Chapter 12 and 13 make use of the effective potential method. All other results make use of the post-Newtonian method.

where V^i is a new vector related to W^i. For details refer to [123, 225].

This allows to transform the Hamiltonian and momentum constraints in terms of $\tilde{A}^{ij}$, $\tilde{V}^i$ and $\tilde{M}^{ij}$ in the following form

$$\begin{aligned} 8\tilde{D}^2\psi - \tilde{R}\psi + \psi^{-7}\tilde{A}_{ij}\tilde{A}^{ij} - \frac{2}{3}\psi^5 K^2 + 16\pi\psi^5\rho &= 0\,, && (2.4.9)\\ \tilde{\Delta}_{\tilde{\mathbf{L}}}\tilde{V}^i + \tilde{D}_j\tilde{M}^{ij} - \frac{2}{3}\psi^6\tilde{D}^i K - 8\pi\psi^{10}j^i &= 0\,. && (2.4.10) \end{aligned}$$

These four equations are to be solved for ψ and $\tilde{V}^i$, with free data given in the form of the conformal 3-metric $\tilde{\gamma}_{ij}$, a symmetric-tracefree tensor $\tilde{M}^{ij}$, the trace of the extrinsic curvature K, and the energy and momentum densities ρ and j. The physical quantities are then reconstructed as

$$\begin{aligned} \gamma_{ij} &= \psi^4\tilde{\gamma}_{ij}\,, && (2.4.11)\\ K^{ij} &= \psi^{-10}\tilde{A}^{ij} + \frac{1}{3}\gamma^{ij}K\,, && (2.4.12) \end{aligned}$$

with

$$\tilde{A}^{ij} = (\tilde{\mathbf{L}}\tilde{V})^{ij} + \tilde{M}^{ij}\,. \qquad (2.4.13)$$

In the next subsection, we will discuss how to obtain solutions to equations (2.4.9) and (2.4.10).

Bowen-York extrinsic curvature

In the previous subsection, we have found a form of the momentum and Hamiltonian constraints that need to be solved for the four unknowns ψ and $\tilde{V}^i$. One simple way of finding a solution to equations (2.4.9) and (2.4.10) is to impose *time-symmetric* data in vacuum, *i.e.* $K_{ij} = 0$ and the matter source-terms $j^i = \rho = 0$. However, the time-symmetry imposes a situation that is momentarily static which is not very physical because astrophysical systems such as BHs will be orbiting each other and therefore are not static at any time. It would hence be useful to find a solution which represents BHs that have clearly defined linear momentum and spin. Such solutions were constructed by Bowen and others [206–213], and especially important to us is the solution to the momentum constraint known as the Bowen-York extrinsic curvature [206, 207].

We can consider the momentum constraint in the form (2.4.10) in vacuum $\rho = j^i = 0$ and maximal slicing $K = 0$. If we choose $\tilde{M}^{ij} = 0$, the constraints reduce to

$$\tilde{\Delta}_{\tilde{\mathbf{L}}}\tilde{V}^i = \tilde{D}^2\tilde{V}^i + \frac{1}{3}\tilde{D}^i\tilde{D}_j\tilde{V}^j = 0\,. \qquad (2.4.14)$$

One can show that an analytic solution can be found as

$$\tilde{V}^i = -\frac{1}{4r}[7P^i + n^i n_j P^j] + \frac{1}{r^2}\epsilon^{ijk}n_j S_k\,, \qquad (2.4.15)$$

with P^i and S^i constant vectors, n^i the outward-pointing unit radial vector, and ϵ^{ijk} the anti-symmetric Levi-Cevita symbol in three dimensions. Having found the vector $\tilde{V}^i$, the conformal tracefree extrinsic curvature is given by

$$\begin{aligned} \tilde{A}_{ij} = (\tilde{\mathbf{L}}\tilde{V})_{ij} &= \frac{3}{2r^2}[n_i P_j + n_j P_i + n_k P^k(n_i n_j - \delta_{ij}]\\ &- \frac{3}{r^3}(\epsilon_{ilk}n_j + \epsilon_{jlk}n_i)n^l S^k\,, && (2.4.16) \end{aligned}$$

with $K_{ij} = \psi^{-2}\tilde{A}_{ij}$. Equation (2.4.16) defines what is known as the Bowen-York extrinsic curvature [206, 207].

The constant vectors P^i and S^i have clear physical interpretations. By making use of the ADM integrals (see Section 1.3), one can see that the linear and angular momenta at spatial infinity can be calculated as

$$P^i = \frac{1}{8\pi} \lim_{r\to\infty} \oint (K^i{}_l - \delta^i{}_l K) n^l dS \qquad (2.4.17)$$

$$S^i = \frac{1}{16\pi} \lim_{r\to\infty} \oint \epsilon^{ijk} x_j K_{kl} n^l dS \qquad (2.4.18)$$

where the integrals are evaluated over spheres of constant r, with n^i the outward-pointing normal vector to the sphere, and where the $\{x^i\}$ are taken to be asymptotically Cartesian coordinates.

By plugging the Bowen-York extrinsic curvature $K_{ij} = \psi^{-2}\tilde{A}_{ij}$ as given by (2.4.16) into the above equations for P^i and S^i and assuming that the conformal factor behaves as $\psi \to 1$ for $r \to \infty$, we find that after some algebra the parameters P^i and S^i are the linear and angular momenta of the spacetime and thus represent linear momentum and spin of a “particle” or BH. Because the momentum constraints are a set of linear equations, one can add an infinite number of solutions of the type (2.4.16) at different centers $r = r_i$ to represent two or more “particles” with given momenta and spins.

This method, however, has a drawback. While a single BH with zero linear momentum and zero spin reduces to a Schwarzschild BH in isotropic coordinates, it can be shown that a single zero-linear-momentum and spinning BH does not reduce to a Kerr spacetime in general [232]. A Bowen-York BH does not describe a stationary spacetime as is the case for Kerr spacetimes. Rather, it represents a dynamical spacetime that corresponds to Kerr plus some spurious gravitational radiation field. The same is true for a non-spinning non zero-linear-momentum Bowen-York BH which does not reduce to a boosted Schwarzschild spacetime. The fact that spinning Bowen-York BHs do not reduce to Kerr also imply that it is not possible to construct initial data with BHs that are maximally spinning, *i.e.* $|a| = 1$, as this limiting case can only be achieved by Kerr spacetimes [86]. This is due to the fact that the junk radiation will generally also carry away angular momentum, and as a single spinning Bowen-York BH will settle to a Kerr solution, the initial spin of the Bowen-York BH must be generally smaller than 1. Otherwise, Bowen-York initial data would falsify the cosmic censorship conjecture [78]. However, tests have shown that cosmic censorship is maintained for these kind of initial data (*e.g.* [233]).

Although the effect of this spurious gravitational-wave content is small, there are other approaches to get rid of this spurious effect such as the Kerr-Schild type data [234]. Nevertheless, the solution just described is widely used in the construction of initial data for BH simulations.

What remains to be solved is the Hamiltonian constraint equation. Bowen and collaborators proceeded in their original work [206–213] by a method called conformal-imaging, but this method involves certain complications such as defining inner boundaries. A much easier method is known as the puncture method which we will describe in the next subsection.

The puncture method

In the previous subsection, we have obtained a solution to the momentum constraint of the form (2.4.10) which represents a “particle” with a given linear momentum and spin. What remains to be solved is the Hamiltonian constraint equations of the form (2.4.9). Unfortunately, this cannot be done analytically anymore due to the presence of a non-trivial extrinsic curvature, so that numerical methods are required.

One method that has been successful is known as the puncture method developed by Brandt and Brügmann [216] and circumvents the necessity of defining inner boundary conditions at the singularities. The absence of inner boundary conditions, however, is a feature that makes this method particularly appealing as it greatly simplifies the numerical solution of the Hamiltonian constraint equation and removes certain accompanying technical problems such as the “lego” sphere problem.

The starting point for the puncture method is Brill-Lindquist type initial data [203] of which the puncture method represents a generalization. Brill-Lindquist data [203], and also Misner data [202], represent a certain topology of the initial hypersurface as depicted in Figure 2.4. The simplest of such topologies is derived from the Schwarzschild spacetime in quasi-isotropic coordinates. Considered as a problem on $\mathbb{R}^3$ except the point $r = 0$, the constraint equations (2.4.9) and (2.4.10) can be solved by

$$\psi = 1 + \frac{m}{2r}\,, \qquad K_{ij} = 0\,, \tag{2.4.19}$$

where m is the mass, r the isotropic radius and where we have set the extrinsic curvature to zero (*i.e.* no Bowen-York extrinsic curvature).

There exists an isometry given by

$$r \rightarrow \frac{m^2}{4r} \tag{2.4.20}$$

which leaves the coordinate sphere $r = m/2$ invariant and which maps the entire exterior asymptotically flat space into that sphere. Consequently, there exists a second asymptotically flat region near $r = 0$. Equivalently, one can represent this solution to the constraints on a space consisting of two copies of $\mathbb{R}^3$ with a sphere excised and appropriate identifications at the spheres. This is shown in Figure 2.4(a). A generalization two N black holes for time-symmetric initial data, *i.e.* $K_{ij} = 0$, is possible by exploiting the linearity of the Hamiltonian constraint. The solution takes the form

$$\psi = 1 + \sum_{i=1}^{N} \frac{m_{(i)}}{2|\mathbf{r} - \mathbf{r}_i|}\,, \qquad K_{ij} = 0\,, \tag{2.4.21}$$

where $m_{(i)}$ characterizes the *bare* mass of the ith BH and $\mathbf{r}_i$ is the location of the ith BH in the conformally flat 3-space. The resulting topology for $N = 2$ is depicted in Figure 2.4(b). Each of the throats connects to a different asymptotically flat region which are independent of each other. This solution is known as Brill-Lindquist data [203]. Note that the isometry between upper sheet and lower sheet is lost due to the presence of three sheets. Because of this, it is worth mentioning work done by Misner [201, 202] who constructed similar data via an infinite series expansion so that the isometry when multiple BHs are present can be recovered. This is known as Misner type data and is depicted in Figure 2.4(c). Interestingly, this solution reduces to the wormhole solution as found by Misner [201] if the invariant spheres have the same radius (see Figure 2.4(d)). The latter Misner type solutions were generalized by York and others by the *conformal-imaging* method [206–213] and were used in the first simulations together with excision techniques, but due to complications by the presence of inner spherical boundaries and the isometry condition, these solutions are hardly used anymore.

We therefore consider Brill-Lindquist type data (2.4.21). This solution contains exactly one singular point for each throat, namely the point $\mathbf{r}_i$ and due to the loss of isometry, there is no inner boundary where one can stop the integration. This means we must integrate through the complete $\mathbb{R}^3$ interior region and deal with the singularities in the solution for the conformal factor directly. The basic idea behind the puncture method [216] is to write the conformal factor with the singular piece explicitly separated as

$$\psi = \psi_{\mathrm{BL}} + u\,, \qquad \psi_{\mathrm{BL}} = \sum_{i=1}^{N} \frac{m_{(i)}}{2|\mathbf{r} - \mathbf{r}_i|}\,, \tag{2.4.22}$$

where ψ_{BL} represents Brill-Lindquist data minus 1 (the 1 is absorbed in the function u). The term ψ_{BL} has zero Laplacian on $\mathbb{R}^3$ with the points $\mathbf{r} = \mathbf{r}_i$ excised, *i.e.* on a "punctured" $\mathbb{R}^3$. The Hamiltonian constraint then reduces to

$$D^2_{\text{flat}} u + \eta \left(1 + \frac{u}{\psi_{\mathrm{BL}}}\right) = 0\,, \tag{2.4.23}$$

where D^2_{flat} is the Laplacian associated to the flat 3-metric and with

$$\eta = \frac{1}{8\psi_{\mathrm{BL}}^7} \tilde{A}_{ij} \tilde{A}^{ij}\,, \tag{2.4.24}$$

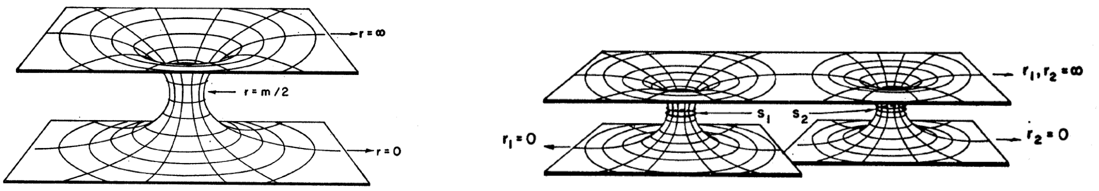

(a) This figure shows the two-dimensional analog of the Schwarzschild-Kruskal manifold as isometrically embedded in flat three-space. The sheets at the top and bottom of the funnel continue to infinity and represent the asymptotically flat regions of the manifold ($r \to 0, r \to \infty$).

(b) This figure shows the topology of a manifold containing two "throats" as isometrically embedded in flat three-space. Each "throat" connects to a different asymptotically flat region (Brill-Lindquist data [203]). This is in contrast to Misner-type data [202] where the throats are connected to the same isometric copy of $\mathbb{R}^3$.

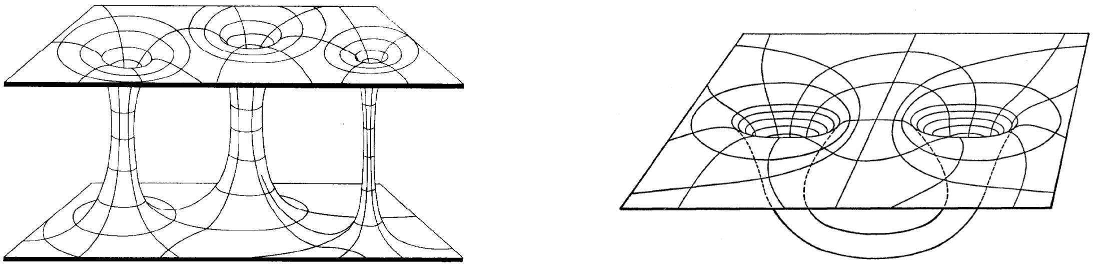

(c) This figure shows the topology of Misner type data [202] containing three "throats" connecting to the same isometric copy of $\mathbb{R}^3$.

(d) This figure shows the topology of a Misner wormhole [201] which is obtained when the spheres in the construction of Misner type data have the same radii.

Figure 2.4: Illustration of the throat topologies as induced by Brill-Lindquist and Misner type initial data on the first slice. Figures taken from [201–203].

where we have used the fact that we have a maximal slice, *i.e.* $K = 0$, and also that the spatial metric is conformally flat so that $\tilde{R} = 0$. This equation must now be solved for u. To solve it, we need to impose boundary conditions. At infinity, asymptotic flatness implies that we must have $u = 1 + k/r$ for some constant k. The key observation of the puncture method is that we can in fact solve for u with no special boundary condition at the punctures. This can be seen by performing the limit $\mathbf{r} \to \mathbf{r}_i$. The term $\tilde{A}_{ij}\tilde{A}^{ij}$ with Bowen-York extrinsic curvature (2.4.16) diverges as $|\mathbf{r} - \mathbf{r}_i|^{-6}$ for non-zero spin and for zero spin as $|\mathbf{r} - \mathbf{r}_i|^{-4}$, so that η goes to zero as $|\mathbf{r} - \mathbf{r}_i|$ for non-zero spin and as $|\mathbf{r} - \mathbf{r}_i|^3$ for zero spin. This implies that for $\mathbf{r} \to \mathbf{r}_i$, *i.e.* near the punctures, the Hamiltonian constraint (2.4.23) reduces to $D^2_{\text{flat}} = 0$. In [216] it is shown that under these conditions there exists a unique C^2 solution u to the Hamiltonian constraint in all of $\mathbb{R}^3$, so that we can ignore the punctures when solving for u. A solution can be obtained numerically by using a single-domain pseudo-spectral solver for the elliptic equation for u. Details can be found in [228] and a brief summary of the procedure is described in Section 8.1.

In addition to the metric components, we also have to specify initial data for the lapse and shift variables. In our case, the initial shift is simply $\beta = 0$. Initial data for the lapse evolution can be specified in pre-collapsed form, *i.e.* we choose the lapse according to [235]

$$\tilde{\alpha} = \frac{1 - \left(\frac{m_1}{2r_1} + \frac{m_2}{2r_2}\right)}{1 + \frac{m_1}{2r_1} + \frac{m_2}{2r_2}} , \tag{2.4.25}$$

where $r_{1,2}$ and $m_{1,2}$ are the locations and masses of the two punctures, respectively. A subsequent averaging of the lapse $\alpha = (1 + \tilde{\alpha})/2$ ensures that the lapse takes values $\alpha \in [1, 0]$.

Recent work on punctures [236–239] suggest that the above throat construction leads to unnecessary gauge motion at the beginning of the evolution. This is because when the simulation begins, the "1+log" slicing and $\tilde{\Gamma}$-driver condition transform the initial throat topology to a "trumpet" topology (see Figure 2.5 and Section 2.5), and also generate an advection component to the shift vector, which moves the trumpets across the grid [236]. It is therefore suggested to construct initial data directly in the form of a trumpet topology [240]. The hope is to thus minimize gauge motion and noise artifacts that are inherent in current numerical relativity waveforms at the beginning of the evolution. The effect of this, however, has still to be estimated numerically.

Now that we have found a solution to the constraint equations, we have to choose the freely specifiable vectors P^i and S^i such that they correspond to a physical scenario of interest. Most interesting in this thesis is a BBH configuration which is inspiralling with a minimum amount of initial eccentricity. In the next two subsections, we will describe two methods for obtaining such parameters.

Quasi-circular orbits and the effective potential method

In the previous subsections, we have found a solution to the Hamiltonian and momentum constraints that corresponds to BHs with freely specifiable bare mass m, linear momentum P^i, spin S^i and coordinate location $\mathbf{r}$. The problem is now to find a set of parameters that corresponds to BBHs that are orbiting each other with the minimum amount of eccentricity, *i.e.* they are put in *quasi-circular* orbits. This is an astrophysically motivated choice because it is well known that the gravitational-radiation damping circularizes the BBH orbit. By quasi-circular, it is meant that the radial component of the BH momenta is small compared to the angular momentum, *i.e.* we have an inspiral in an adiabatic stage and are far from the plunge. In other words, the time-scale for energy loss due to gravitational-wave emission is considerably larger than the orbital time-scale. In this case, we can make use of the *effective potential* method in Newtonian gravity as a reasonable approximation. This method is based on the fact that minimizing the total energy of the system, while keeping the total angular momentum of the system fixed, results in circular orbits in Newtonian gravity [229, 230]. This approach defines an effective potential based on the binding energy

$$E_b := M_{\text{ADM}} - M_1 - M_2 , \tag{2.4.26}$$

where M_{ADM} is the total ADM mass of the spacetime as measured at infinity, and M_1 and M_2 are the masses of the individual BHs. Quasi-circular orbits can then be found by minimizing the effective potential as a function of separation, while keeping the ratio of the masses of the BHs, the spins, and the total angular momentum constant. The effective potential is defined by E_b/μ with $\mu = M_1 M_2/(M_1 + M_2)$ being the reduced mass. The problem that arises now is how one defines the individual masses of BHs when they are relatively close to each other. In practice, we make use of the irreducible mass as calculated on an apparent horizon (see Section 4.2).

In order to choose the input parameters that correspond to the desired physical parameters we have to use a non-linear root finding procedure, since the physical parameters depend non-linearly on the input parameters and it is not possible to invert the problem analytically.

As detailed in [230], when the black-hole spins are taken as parameters, it is possible to reduce the number of independent input variables, so that at a given separation $\bar{\boldsymbol{r}} \equiv |\mathbf{r}_2 - \mathbf{r}_1|/m_1$, the independent input parameters are: $\bar{q} \equiv m_1/m_2$ and the dimensionless magnitude of the linear momentum p/m_1, where $p \equiv P_1 = P_2$ is equal to the magnitudes of the input momenta $\mathbf{P}_1$, $\mathbf{P}_2$. It is sufficient to work with this single momentum parameter, because we work in the zero momentum frame so that $\mathbf{P}_1 = -\mathbf{P}_2$, and because we also choose the $\mathbf{P}_{1,2}$ to be perpendicular to the x-axis[6] in order to realize quasi-circular orbits. Using a Newton-Raphson method, we can solve for $\bar{q}$ and p/m_1 so that $M_1/M_2 = 1$ and the system has a given dimensionless orbital angular momentum, $L/(\mu M)$. For such a configuration the initial data solver [228] returns a very accurate value for M_{ADM}, which together with the accurate *irreducible mass* (4.3.5) calculated on the apparent horizon (see Section 4.3) [241, 242] makes it possible to calculate an accurate value of the dimensionless binding energy

$$E_b/\mu = (M_{\mathrm{ADM}} - M_1 - M_2)/\mu. \tag{2.4.27}$$

The quasi-circular initial data parameters are then obtained by finding the minimum in E_b/μ for varying values of $\bar{\boldsymbol{r}}$ while keeping the required orbital angular momentum $L/(\mu M)$ constant.

However, as this method was used in early work during this thesis, it is much better to find BBH initial parameters in terms of post Newtonian evolutions as this will result in less eccentric data. This will be the subject of the next subsection.

Initial parameters from post-Newtonian inspiral

In order to reduce the remaining amount of eccentricity inherent in the initial data parameters as found by the effective potential method, one can take advantage of post-Newtonian (PN) evolutions following the scheme outlined in [231] which can be regarded as part of the process of matching the numerical BBH computations to the long-term inspiral described by PN approximations. The eccentricity present in the quasi-circular orbit parameters is mainly due to the approximate "circularity" condition[7]. However, a spiral motion must contain a radial component and we wish to find initial tangential and radial momenta that, for a given initial separation, lead to non-eccentric inspiral.

One way of producing such parameters is to numerically integrate the PN equations [243] to highest PN order available [244] and read off the particles' momenta once they have reached a separation that we wish to use as initial configuration for the numerical relativity simulation. The essential idea is to exploit the fact that any initial eccentricity will decay over time due to circularizing effects of gravitational-wave emission on the time-scale of hundreds of orbits, not the < 10 orbits typically simulated in numerical codes. One starts off with a much larger initial separation (in practice $d = 40M$) when integrating the PN equations and allows the radiation-reaction to circularize the orbits.

The integration of the PN equations of motion are used in the ADM-TT gauge as described in [244] as this agrees with the Bowen-York puncture initial data up to 2PN order [245]. The conservative part of the Hamiltonian is given up to third PN order, and was originally derived in [245, 246] and also in [247–249]. Radiation-reaction flux terms can be calculated up to 3.5PN order beyond the quadrupole order, which can be achieved by averaging the radiation flux over one orbit by assuming quasi-circular inspiral [250–252]. Additionally, one can include the leading-order spin-spin and spin-orbit coupling terms for the conservative part of the Hamiltonian [253–255] and spin-induced radiation flux terms as described in [244] which are again averaged over one orbit.

---

[6] We always place our initial BHs on the x-axis (see Figure 1.5).

[7] Another contribution comes from the conformal flatness assumption on the initial Cauchy hypersurface. This assumption results in the generation of an uncontrollable amount of spurious junk radiation which carries away angular and linear momentum from the two BHs and thus perturbs the orbits.

In the non-spinning case, the PN equations of motion are a system of six coupled ordinary differential equations of the form

$$\frac{dx^i}{dt} = \frac{\partial H}{\partial p_i}\,, \tag{2.4.28}$$

$$\frac{dp_i}{dt} = -\frac{\partial H}{\partial x^i} + F_i\,, \tag{2.4.29}$$

where H is the PN-Hamiltonian responsible for the conservative part of the dynamics, x^i is the separation vector between the tow particles and p^i is the momentum of one particle in the center-of-mass frame. In the spinning case the system is augmented by the evolution equations for the spins. The term F_i is the radiation-reaction flux-term.

One can then numerically integrate the equation of motions, by using initial momenta using the 3PN formula as given in [256] for a sufficiently large initial separation, *e.g.* $d = 40M$. The initial data parameters for the numerical relativity simulation are then read off once the particles have reached the desired separation, *e.g.* $d = 8M$.

It can be shown that these parameters result in at least a factor of five less eccentricity as the ones obtained by the effective potential method described in the previous subsection [231] and has therefore become our standard method for generating initial data parameters.

An alternative way of obtaining initial data parameters with very low orbital eccentricity has been reported in [257, 258]. Here, initial data obtained via quasi-circular parameters are evolved for about 1.5 orbits. By correcting the quasi-circular parameters with components that counter the measured eccentricity, the data is evolved again, but this time with the corrected set of parameters. The whole procedure is iterated until the measured eccentricity in the BH trajectories is sufficiently small.

2.5 Dealing with spacetime singularities

The first problem that arises when one tries to represent and evolve BHs on a computer is the question how to deal with the singularity of a BH. At a singularity, geometric quantities become infinite and it is impossible to cope with that in numerical simulations. One therefore has to introduce techniques of hiding the singularity from the numerics. One of the most straightforward ways is to simply cut out the interior of the BH, *i.e.* everything that lies inside the event horizon. This is possible because the spacetime inside the BH is causally disconnected from the outside and therefore never contributing to the physics in the exterior spacetime. The first successful simulations that made use of this *black hole excision* technique were done by Seidel and Suen [259] and later in [192]. However, while this method is successful in spherical symmetry, it is cumbersome in general. The reason is that most of current 3D GR codes are based on Cartesian coordinates whereas a BH horizon is topologically spherical so that the horizon boundary points are not aligned with the grid and one has to construct appropriate stencils for a “lego” sphere [204, 260, 261]. Alternatively, one can work with adapted coordinates which match the spherical boundary such as multiple coordinate patches with spherical coordinates [215, 262]. As this already results in complication, additionally, if the black holes are moving, one has to introduce a complicated logic in order to move the excision region with the black holes [263]. This method is therefore hardly used in current BBH merger simulations.

The current method of choice for removing spacetime singularities is know as the *puncture evolution* method. In this method, one conformally decomposes the spacetime metric such that the singularity of the BH is absorbed in the conformal factor, and the resulting conformal metric is free of irregularities. This approach is even more attractive in case of the BSSNOK formulation of the evolution system where one also uses a conformal decomposition of the metric. A convenient picture of this is given by Figure 2.4(b). In this topology, the BH data are represented in coordinates such that they never reach the physical singularities, but instead follow a wormhole through to another copy of the flat exterior spacetime. These extra copies are compactified so that their infinities are represented by single points on a numerical grid, which are called "punctures" [203, 216]. This has been discussed as a choice for solving the initial data equations in Section 2.4 already, and since its introduction in [216] the first BBH computer codes early this decade employed it as the *static* puncture evolution, *i.e.* the singular part of the conformal factor was factored out analytically and kept static so that the punctures were held fixed at an initial coordinate location [46, 190]. By making use of static puncture evolution, however, the simulations were not very successful and there was a huge effort in trying to have at least one orbit (see *e.g.* [264, 265]) before the code crashed. Fortunately, in 2005, there was a major breakthrough by abandoning the static approach and introducing *moving* punctures [48, 49]. Here, the idea is to maintain the singular part of the conformal factor, *i.e.* it is not factored out analytically. Instead the conformal factor is evolved freely like all other metric components. We will discuss this method in the next subsection of this section.

Puncture evolution

Puncture evolutions [48, 49, 197] are todays most preferred way of dealing with spacetime singularities. Especially when used together with the BSSNOK formalism, this method combines easily with the evolution system.

In the traditional puncture implementation (2.4.22), $\psi_{\rm BL}$ is factored out and handled analytically so that only the regular parts of the metric are evolved. In this case, the punctures remain fixed on the grid while the binary evolves. However, this may lead to severe coordinate stretching. While the black holes are moving closer to each other and eventually approaching zero physical distance, certain metric components must become zero hence causing other quantities to grow uncontrollably. Additionally, a co-rotating coordinate frame, *i.e.* a coordinate system with rotates with the orbiting BHs, needs to be introduced so that the BHs are kept fixed on the grid. This may lead to superluminal coordinate speeds at large distances from the BHs and may result in noise artifacts being reflected from the outer boundary of the Cartesian grid.

However, instead of factoring out the singular part $\psi_{\rm BL}$ of the conformal factor analytically and hence keeping it fixed, one can maintain it together with the regular part and evolve it freely on the grid by ensuring that the singular part is not located at a grid point initially.

The free evolution of punctures is made possible by a modification to the hyperbolic $\tilde{\Gamma}$-driver condition (2.3.14), (2.3.15). In the traditional implementation,

$$\partial_t\beta^i = \frac{3}{4}\alpha\psi_{\rm BL}^{-2}B^i, \qquad \partial_t B^i = \partial_t\tilde{\Gamma}^i - \eta B^i\,, \tag{2.5.1}$$

a vanishing shift vector is ensured at the puncture by adding a factor $\psi_{\rm BL}$ of the conformal factor to the equations. This term has been removed in order to allow the punctures to evolve. In addition, a new term $\beta^j\partial_j\tilde{\Gamma}^i$ has been added which facilitates more stable and accurate evolution of moving punctures by eliminating a zero-speed mode (compare (2.3.14), (2.3.14)).

With this new $\tilde{\Gamma}$-driver condition, it can be shown for single non-spinning BHs that the singular part quickly becomes regular [236]. Instead of keeping the throat topology out to another asymptotic flat end, it quickly asymptotes to a stationary regular solution of small but constant radius R inside the horizon so that the other end becomes an infinitely long cylinder, or a "trumpet" (Figure 2.5). This change in the appearance of the numerical slices is achieved by the gauge conditions, especially by the hyperbolic $\tilde{\Gamma}$-driver [238]. The $\tilde{\Gamma}$-driver drags all data points near the puncture from the other asymptotically flat end into the BH horizon and due to the lack of resolution, the slice terminates close to the singularity. This therefore represents some type of "natural excision" with the advantage that it does not require the introduction of an interior boundary

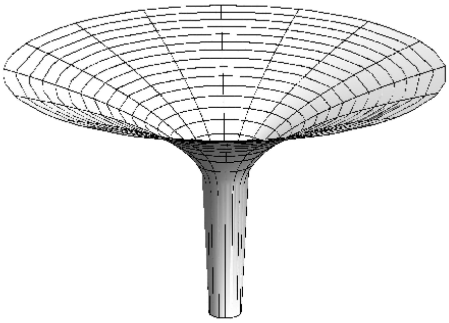

Figure 2.5: Illustration of the trumpet topology as adopted by the punctures during evolution. In contrast to the initial topologies as depicted in figs. 2.4(a), 2.4(b), 2.4(c), there is only one asymptotically flat end. The other end is an infinitely long cylinder. Figure taken from [240].

where boundary conditions and special finite difference stencils must be applied. In view of this, it has been suggested to directly make use of the trumpet topology in the initial data to limit gauge motion at the beginning of the simulation [240]. Subsequent work [266] even shows that the set of initial parameter construction simplifies. For example, the puncture bare mass m turns out to be directly linked to the physical mass M of the BH, and in contrast to the puncture data in terms of a throat representation therefore does not need to be obtained by solving a non-linear equation.

By the comparison of two curvature 4-scalars for an excision based simulation and a moving puncture based simulation, it has been shown that both methods result in the same spacetime [267] and therefore provide convincing evidence that puncture evolutions and excised black holes are equivalent.

Chapter 3

The characteristic evolution system

The characteristic evolution system of the Einstein field equations is a different formulation in the sense that it does not belong to the family of 3+1 decompositions like the ADM or BSSNOK systems of the previous chapter. More specifically, instead of foliating spacetime by means of spatial hypersurfaces along a timelike vector field, it is foliated in terms of null hypersurfaces with constant retarded time $u = r - t$ as depicted in Figure 3.1. Since the null hypersurfaces represent the characteristics of the Einstein equations, such a system is sometimes called a *characteristic initial value problem* (cIVP) [117]. One main feature of representing PDEs along their characteristics is a simplification, or reduction, of the set of equations and variables.

The characteristic reduction of the Einstein equations was first introduced by Bondi [134, 135] when analyzing the properties of gravitational radiation in the non-linear regime as outlined in Section 1.4 and has also shown to be extremely useful when studying gravitational radiation numerically (see *e.g.* [268]). In fact, characteristic evolutions were the first long-time stable evolution schemes that made it possible to evolve moving BHs in 3D [269].

One of the main advantages inherent to this system is the possibility of compactifying the radial coordinate without rendering the numerical scheme unstable, and thus making it possible to analyze the behavior of gravitational waves at future null infinity, where they are unambiguously defined.

The main drawback of characteristic evolution is the possible formation of coordinate singularities that arise due to focusing of null rays (caustics). This effect especially occurs in strong field regions so that characteristic evolution is not well suited for simulating BBH mergers[1]. However, it can be used to accurately represent the gravitational wave-zone out to future null infinity $\mathscr{J}^+$, and the coupling to Cauchy evolutions makes it possible to evolve the entire spacetime of any strongly gravitating source, especially BBH mergers. This coupling results in a new wave-extraction method whose theory we will describe in Section 5.3.

In this chapter, we describe the characteristic formulation of the Einstein equations as well as the evolution system that is implemented in the numerical code used for extracting waves at future null infinity. This code has already been described and used in [60, 268, 269, 272–277] and another code based on the same formalism has been developed in [278, 279]. Here, we mainly repeat what has already been published there.

3.1 The Bondi-Sachs metric

The formulation of the Einstein equations along characteristic lines relies on the specification of a suitably defined coordinate system, the so called Bondi coordinates $y^\mu = (r, y^A, u)$, which are parametrized by angular coordinates y^A with $A = 1, 2$, a surface area coordinate $y^0 = r$ and a retarded time coordinate $y^4 = u = r - t$ labeling the family of outgoing null hypersurfaces emanating from a world-tube Γ. This was first done in [134, 135], and in terms of these coordinates, the *Bondi-Sachs line element* for a spacetime $(\mathcal{M}, g)$ can be written as

$$ds^2 = -\left(\mathrm{e}^{2\beta}\frac{V}{r} - r^2 h_{AB} U^A U^B\right) du^2 - 2\mathrm{e}^{2\beta} du dr - 2r^2 h_{AB} U^B du dy^A + r^2 h_{AB} dy^A dy^B \,, \quad (3.1.1)$$

---

[1] It is principally possible to deal with the development and structure of caustics during characteristic evolution [270, 271]. However, this complication is avoided by simply not considering the parts of spacetime that contain caustics.

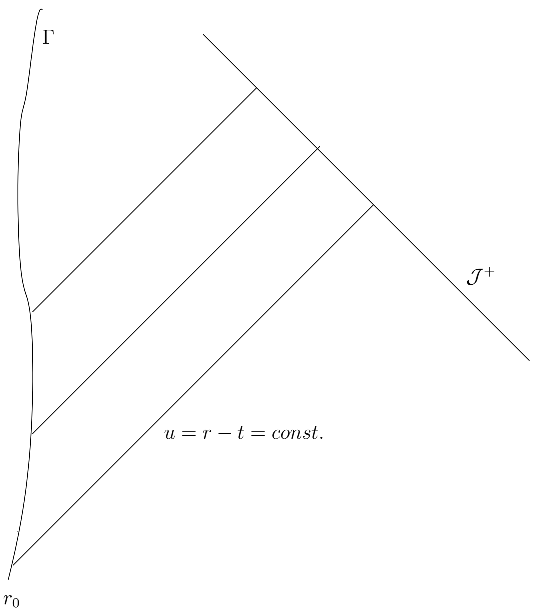

Figure 3.1: Null foliation of space time along $u =$ const. hypersurfaces. The characteristic evolution is carried out in the region between an inner boundary, *i.e.* the world-tube Γ at radius r_0, and future null infinity $\mathscr{J}^+$.

where h_{AB} satisfies

$$h^{AB}h_{BC} = \delta^A{}_C, \qquad \det(h_{AB}) = \det(q_{AB}), \tag{3.1.2}$$

with q_{AB} the unit sphere metric.

The free variables in the Bondi-Sachs metric are V, β, U^A and h_{AB}. The symmetric 2-tensor h_{AB} represents the conformal geometry of the 2-surfaces defined by $dr = du = 0$ (Bondi-spheres), which foliate the world-tube and represent the angular part of the given spacetime metric g by $g_{AB} = r^2 h_{AB}$. This is deduced from the intrinsic metric of $r =$ const. surfaces (2+1 decomposition) which is obtained by setting $dr = 0$ in (3.1.2). We get

$$\gamma_{ij}dy^i dy^j = -\mathrm{e}^{2\beta}\frac{V}{r}du^2 + r^2 h_{AB}(dy^A - U^A du)(dy^B - U^B du). \tag{3.1.3}$$

In addition, the requirement $\det(h_{AB}) = \det(q_{AB})$ fixes h_{AB} such that there are only two independent components. These components are the two radiative degrees of freedom of the gravitational field. The scalar β measures the *expansion* $\mathrm{e}^{2\beta}$ of the light cone between an asymptotic frame and the world-tube. Furthermore, V is the analog of the Newtonian potential and $-U^A$ can be identified from (3.1.3) as the shift vector. The square of the lapse function is $\mathrm{e}^{2\beta}V/r$ as can be seen from (3.1.3).

The next step is to apply line element (3.1.1) to the Einstein equations.

3.2 The Einstein equations in a characteristic formulation

By making use of the Bondi-Sachs line element (3.1.1), it is possible to perform the characteristic reduction of the Einstein equations. The full derivation is given in [135]. Here, we state the results for the vacuum Einstein equations $R_{\mu\nu} = 0$ which split into three groups:

1. main equations,
   a) hypersurface equations (4 equations),
   b) standard (evolution) equations (2 equations),

2. trivial equation (1 equation),
3. supplementary conditions (conservation laws) (3 equations).

The hypersurface equations, given by R_{rr}, R_{rA} and $h^{AB}R_{AB}$, can be written as

$$\begin{aligned}
\beta_{,r} &= \frac{1}{16} r h^{AC} h^{BD} h_{AB,r} h_{CD,r} \,, && (3.2.1)\\
\left(r^4 \mathrm{e}^{-2\beta} h_{AB} U^B{}_{,r}\right)_{,r} &= 2r^4 \left(r^{-2}\beta_{,A}\right)_{,r} - r^2 h^{BC} D_C h_{AB,r} \,, && (3.2.2)\\
2\mathrm{e}^{-2\beta} V_{,r} &= R - 2D^A D_A \beta - 2D^A \beta D_A \beta && \\
&\quad + r^{-2}\mathrm{e}^{-2\beta} D_A \left(r^4 U^A\right)_{,r} - \frac{1}{2} r^4 \mathrm{e}^{-4\beta} h_{AB} U^A{}_{,r} U^B{}_{,r} \,. && (3.2.3)\\
& && (3.2.4)
\end{aligned}$$

They involve the metric components only within $u = \text{const.}$ hypersurfaces.

The evolution equations, given by $R_{AB} - h_{AB} h^{CD} R_{CD}/2$, yield

$$\begin{aligned}
r(r h_{AB,u})_{,r} - \frac{1}{2}(r V h_{AB,r})_{,r} &= \Bigg(2\mathrm{e}^{\beta} D_A D_B \mathrm{e}^{\beta} - r^2 h_{AC} D_B U^C{}_{,r} - \frac{r^2}{2} h_{AB,r} D_C U^C \\
&\quad + \frac{r^4}{2} \mathrm{e}^{-2\beta} h_{AC} h_{BD} U^C{}_{,r} U^D{}_{,r} - r^2 U^C D_C h_{AB} \\
&\quad - 2r h_{AC} D_B U^C + r^2 h_{AC} h_{BE} \left(D^C U^E - D^E U^C\right)\Big) \\
&\quad - \frac{1}{2} h_{AB} \left(r^2 h^{CD}{}_{,r} \left(h_{CD,u} - \frac{V}{2r} h_{CD,r} \right) - 2\mathrm{e}^{\beta} D_C D^C \mathrm{e}^{\beta} \right. \\
&\quad \left. + D_C (r^2 U^C)_{,r} - \frac{1}{2} r^4 \mathrm{e}^{-2\beta} h_{CD} U^C{}_{,r} U^D{}_{,r} \right) \,, \qquad (3.2.5)
\end{aligned}$$

where D_A is the covariant derivative and R the Ricci scalar of the 2-metric h_{AB}. These equations describe the motion of the gravitational field, especially the propagation of gravitational radiation.

Still, there are remaining components, $R_{u\alpha}$ or $R^r{}_\alpha$, that together with the hypersurface and evolution equations form a complete set of components of the vacuum Einstein equations. Given that the main equations are satisfied, one arrives at the trivial equation

$$R^r{}_r = 0. \qquad (3.2.6)$$

This equation is automatically satisfied if one applies the Bianchi identities to the main equations.

The supplementary equations

$$R^r{}_u = 0, \qquad R^r{}_A = 0 \qquad (3.2.7)$$

are then satisfied on a complete outgoing null cone if they hold on a single spherical cross-section. In his derivation, Bondi has chosen this sphere to be at infinity and identified these equations as conservation laws for energy and angular momentum.

We can sum this up by the constraint equations

$$R^r{}_\alpha = 0, \qquad \text{or} \qquad R_{u\alpha} = 0. \qquad (3.2.8)$$

The evolution equations (3.2.5) can be discretized and evolved numerically. However, it is advantageous to recast these equations in terms of spin-weighted quantities. This is discussed in the next subsection.

Formulation in terms of spin-weighted scalars

The characteristic equations (3.2.5) and (3.2.8) are currently in a form that is rather complex. One can reduce the complexity of the equations by reformulating the angular components of the various tensor quantities in terms of spin-weighted scalars. Spin-weighted scalars arise from spinor calculus and have first been introduced by Newman and Penrose [114] and are also discussed in [120].

We use the Newman-Penrose formalism as introduced in Section 1.3 to define spin-weighted scalars on spatial 2-surfaces. Since the angular coordinate directions in the Bondi-Sachs line-element define a manifestly spatial 2-surface (the Bondi-spheres), we can remove angular tensor components by taking advantage of spin-weighted scalars, thus cleaning up the characteristic equations significantly.

Correspondingly, we introduce a spatial dyad q^A, $\bar{q}^A$, which according to (1.3.10), (1.3.11) and (1.3.12) obeys

$$q_{AB} = \frac{1}{2} q_{(A}\bar{q}_{B)}, \qquad q^A q_A = 0, \qquad q^A \bar{q}_A = 2 \tag{3.2.9}$$

where q_{AB} is the unit sphere metric. Note that we normalize to 2 so that we get rid of awkward factors of $1/\sqrt{2}$ in the numerics.

We can now contract all angular tensor components with combinations of q_A and $\bar{q}_A$. As a result, tensors with one angular index might either have spin-weight $s = -1$ or $s = +1$. The choice is left arbitrary since both spin-weighted scalars are mapped into each other via complex conjugation which is an anti-isomorphism. Tensors with two angular indices can either have spin-weight $s = -2$, $s = 0$ or $s = 2$. It turns out that every rank-2 tensor is completely represented by a spin-weight $s = 0$ field and by either a $s = 2$ or $s = -2$ field [280]. We therefore introduce

$$J = \frac{1}{2} q^A q^B h_{AB}, \qquad K = \frac{1}{2} q^A \bar{q}^B h_{AB}, \qquad U = U^A q_A. \tag{3.2.10}$$

The determinant condition in (3.1.2) implies

$$K^2 = 1 + J\bar{J}. \tag{3.2.11}$$

Therefore K contains no additional information and J completely incorporates the two degrees of freedom of h_{AB}.

As these new pseudo-scalars have a well-defined transformation property (see Section 1.3, (1.3.16)), we have to introduce a new covariant derivative operator since the usual derivative operator does not preserve this property. This operator is known as the 'eth'-operator $\eth$ and it can be defined as

$$\eth\eta = q^A \partial_A \eta + s\Gamma\eta, \qquad \bar{\eth}\eta = \bar{q}^A \partial_A \eta - s\bar{\Gamma}\eta \tag{3.2.12}$$

for a spin-weighted scalar η with spin s, where

$$\Gamma = -\frac{1}{2} q^A \bar{q}^B \nabla_A q_B \, . \tag{3.2.13}$$

The $\eth$ ($\bar{\eth}$) operator acting on a spin-weighted scalar has the effect of spin raising (lowering), *i.e.* the spin is increased (decreased) by 1 [281]. An example is given by the spin-weighted spherical harmonics. Spin-s spherical harmonics (7.4.10) can be obtained from the scalar spherical harmonics by applying the $\eth$-operator s times.

By means of computer algebra systems, it is now straight-forward to express the characteristic equations in terms of the new variables U and J and the eth-derivative operator. The equations in their final form are reported after the next two subsections.

Another advantage of the spin-weighted formalism is the separation of the angular coordinate basis from the characteristic equations. As we will see in the next subsection, it is now very easy to introduce any kind of angular coordinate basis.

Angular coordinate basis

What has been left out so far is the choice of angular coordinates. The introduction of the dyad (3.2.9) and the definition of the spin-weighted scalars make the formulation of the equations independent of angular coordinates. However, in order to do actual computations, it is necessary to know the coordinate representation of the dyad q_A, since it enters through the definition of the eth-derivative operators.

In order to avoid singularities at the poles, it is convenient to introduce a 2-patch covering of the Bondi-spheres. This can be accomplished, *e.g.* by using stereographic coordinates (see Figure 8.2(*left*)) defined by

$$\xi_{\text{North}} = \sqrt{\frac{1-\cos\theta}{1+\cos\theta}}e^{i\phi}, \quad \xi_{\text{South}} = \sqrt{\frac{1+\cos\theta}{1-\cos\theta}}e^{-i\phi}. \tag{3.2.14}$$

We choose for the complex coordinate representation $\xi = q + ip$ so that $y^A = (q, p)$ for $A = 1, 2$. In these coordinates, the unit sphere metric reads

$$ds^2 = \frac{4}{(1+q^2+p^2)^2}(dq^2 + dp^2)\,, \tag{3.2.15}$$

and hence, the dyad is represented by

$$q^A = \frac{1+q^2+p^2}{2}(1, i), \qquad q_A = \frac{2}{1+q^2+p^2}(1, i)\,. \tag{3.2.16}$$

The quantity Γ used in the definition of the eth-operator (3.2.12) becomes

$$\Gamma = q + ip\,, \tag{3.2.17}$$

so that it is straight-forward to evaluate the eth-derivatives.

It is important to note that the dyad q_A constitutes a local frame, *i.e.* it represents a different tensor basis for different patches with different coordinates. Because the spin-weighted scalars do not transform like scalars under a change of basis, it is necessary to apply a transformation in order to be able to represent spin-weighted scalars of the north patch in the south patch and vice versa.

This is done as follows. We know that a spin-weighted scalar transforms as (1.3.16)

$$\eta \rightarrow \eta' = \mathrm{e}^{is\theta}\eta\,, \tag{3.2.18}$$

where s is the spin-weight and θ an unknown rotation angle. The task is now to find the unknown angle θ.

Accordingly, we consider the transformation between “Old” (O) and “New” (N) patch. The Jacobian $J^a{}_b$ from the old patch to the new patch is defined as

$$J^A{}_B = \frac{\partial x^A_{(N)}}{\partial x^B_{(O)}}\,. \tag{3.2.19}$$

The components of the dyad $q^A_{(O)}$ of the old patch in the coordinates of the new patch are related by

$$q^A_{(O)[N]} = q^B_{(O)}J^A{}_B. \tag{3.2.20}$$

Now, according to the gauge transformation (1.3.15), $q^A_{(N)}$ and $q^A_{(O)[N]}$ are related by a spin frame transformation. We have

$$q^A_{(N)(\pm)} = \mathrm{e}^{i\theta}q^A_{(O)[N]}\,. \tag{3.2.21}$$

Furthermore, by construction, we have

$$q_{AB(N)}q^A_{(N)}\bar{q}^B_{(N)} = 2 \qquad \Rightarrow \qquad q^A_{(N)} = \frac{2}{q_{AB(N)}\bar{q}^B_{(N)}} = \frac{2}{q_{AB(N)}\bar{q}^B_{(N)}q^A_{(O)[N]}}q^A_{(O)[N]}\,. \tag{3.2.22}$$

Comparison of (3.2.21) and (3.2.22) leads to

$$\mathrm{e}^{i\theta} = \frac{2}{q_{AB(N)}\bar{q}^B_{(N)}q^A_{(O)[N]}}\,. \tag{3.2.23}$$

which completes the basis transformation.

In [60], another angular coordinate basis using 6-patch coordinates has been introduced. Although this method results in a more accurate numerical scheme [60], it is not used here because its implementation has not been parallelized.

Before proceeding with the evolution equations in terms of the spin-weighted scalars, we next introduce a radial compactification scheme.

Radial compactification

In the numerical computation of a system of equations, one always faces the problem of finite domains. This becomes a problem when it comes to the description of the asymptotic behavior of fields, and especially to gravitational-wave extraction defined at future null infinity $\mathscr{J}^+$ ($r \to \infty$, $u = \text{const.}$).

This problem can be solved by a remapping of the radial surface area coordinate into a compact interval

$$x := \frac{r}{r + r_{\text{wt}}}, \qquad r \in [0, \infty[\qquad \Rightarrow \qquad x \in [0, 1]\,. \tag{3.2.24}$$

where $r_{\text{wt}} > 0$ is a compactification parameter that can be chosen freely, and which can be interpreted as the location of the world-tube in the physical radial coordinate r.

This simple transformation is made possible by the conformal invariance of the light-cone foliation which allows an infinite shrinkage of the surface area r. Accordingly, this gives rise to the conformal transformation of the metric, where the physical spacetime (M, g) is related to an unphysical $(\tilde{M}, \tilde{g})$ by a conformal rescaling of the metric $\tilde{g}_{\mu\nu} = \Omega^2 g_{\mu\nu}$. By means of asymptotic simplicity (see Section 1.3), future null infinity $\mathscr{J}^+$ is identified with the compactified boundary $\Omega = 0$ which, in terms of the unphysical spacetime, is located at $x = 1$.

In order to re-express our equations in terms of the compactified coordinate x, we need to replace radial derivatives by derivatives with respect to x. The relations are

$$r = r_{\text{wt}} \frac{x}{1-x}, \qquad dr = r_{\text{wt}}(1-x)^{-2} dx, \qquad \frac{\partial}{\partial r} = \frac{\partial x}{\partial r}\frac{\partial}{\partial x} = \frac{(1-x)^2}{r_{\text{wt}}}\frac{\partial}{\partial x}. \tag{3.2.25}$$

As one can read off from the second equation, the conformal factor in our case becomes $\Omega = (1-x)^2 / r_{\text{wt}}$. This is non-singular throughout the entire spacetime between the world-tube and future null infinity. Therefore, our compactification is suitable for solving the cIVP globally.

The evolution system

One can obtain the spin-weighted hypersurface and evolution equations by starting off from the Ricci tensor

$$R_{\mu\nu} = \Gamma^{\rho}{}_{\nu\mu,\rho} - \Gamma^{\rho}{}_{\rho\mu,\nu} + \Gamma^{\rho}{}_{\rho\sigma}\Gamma^{\sigma}{}_{\nu\mu} - \Gamma^{\rho}{}_{\nu\sigma}\Gamma^{\sigma}{}_{\rho\mu}. \tag{3.2.26}$$

The Christoffel symbols can be written as

$$\Gamma^{\rho}{}_{\mu\nu} = \frac{1}{2} g^{\rho\sigma} \left(g_{\nu\sigma,\mu} + g_{\mu\sigma,\nu} - g_{\mu\nu,\sigma} \right). \tag{3.2.27}$$

By recovering the tensor components of the spin-weighted fields, *e.g.*

$$\begin{aligned} U_B = U^A q_{AB} &= \frac{1}{2}(U^A q_A \bar{q}_B + U^A \bar{q}_A q_B) \\ &= \frac{1}{2} U \bar{q}_B + \frac{1}{2} \bar{U} q_B\,, \end{aligned} \tag{3.2.28}$$

where we have used the first equation of (3.2.9), one can express the metric in terms of the spin-weighted fields. By using the second two relations of (3.2.9), one obtains a metric which is free of any tetrad elements. By inserting (3.2.28) and (3.2.27) into the Ricci tensor (3.2.26), this is then expressed in terms of the spin-weighted fields and their derivatives. The partial derivatives in the angular directions have to be replaced by their eth counterparts. This is done by considering (3.2.12) in

$$\begin{aligned} \partial_B = q_{AB}\partial^A &= \frac{1}{2}q_A\overline{q}_B\partial^A + \frac{1}{2}\overline{q}_A q_B\partial^A \\ &= \frac{1}{2}\overline{q}_B(\eth - is\Gamma) + \frac{1}{2}(\overline{\eth} + is\overline{\Gamma}). \end{aligned} \tag{3.2.29}$$

These simple algebraic transformations are ideally suited for computer algebra systems such as Maple.

The resulting hypersurface equations read

$$\begin{aligned} \beta_{,r} &= N_\beta\,, && (3.2.30)\\ U_{,r} &= r^{-2}\mathrm{e}^{2\beta}Q + N_U\,, && (3.2.31)\\ (r^2Q)_{,r} &= -r^2\left(\overline{\eth}J + \eth K\right)_{,r} + 2r^4\eth\left(r^{-2}\beta\right)_{,r} + N_Q\,, && (3.2.32)\\ W_{,r} &= \frac{1}{2}\mathrm{e}^{2\beta}R - 1 - \mathrm{e}^{\beta}\eth\overline{\eth}\mathrm{e}^{\beta} + \frac{1}{4}r^{-2}\left(r^4\left(\eth\overline{U} + \overline{\eth}U\right)\right)_{,r} + N_W\,, && (3.2.33) \end{aligned}$$

where the Ricci scalar takes the form

$$R = 2K - \eth\overline{\eth}K + \frac{1}{2}\left(\overline{\eth}^2 J + \eth^2\overline{J}\right) + \frac{1}{4K}\left(\overline{\eth}\overline{J}\eth J - \overline{\eth}J\eth\overline{J}\right)\,, \tag{3.2.34}$$

and where

$$Q \equiv q^A Q_A = r^2\mathrm{e}^{-2\beta}q^A h_{AB}U^B{}_{,r} \tag{3.2.35}$$

is a new variable which obeys

$$(r^2Q)_{,r} = 2r^4\left(r^{-2}q^A\beta_{,A}\right)_{,r} - r^2q^Ah^{BC}D_Ch_{AB,r}\,, \tag{3.2.36}$$

and which is introduced to eliminate the second radial derivatives in the equation for U. Also note that we have replaced the more usual Bondi variable V by $W := V - r$, since $V = r$ in Minkowski space.

The evolution equation reads

$$\begin{aligned} 2(rJ)_{,ur} - \left(r^{-1}V(rJ)_{,r}\right)_{,r} &= \\ -r^{-1}(r^2\eth U)_{,r} &+ 2r^{-1}\mathrm{e}^{\beta}\eth^2\mathrm{e}^{\beta} - \left(r^{-1}W\right)_{,r}J + N_J. \end{aligned} \tag{3.2.37}$$

In the above equations, the symbols N_β, N_U, N_Q, N_W and N_J represent non-linear aspherical terms, *i.e.* terms that are quadratic in the deviation from spherical symmetry (quasi-spherical approximation) [272]. They are given by

$$N_\beta = \frac{r}{8}\left(J_{,r}\overline{J}_{,r} - (K^2)_{,r}\right)\,, \tag{3.2.38}$$

$$N_U = \frac{\mathrm{e}^{2\beta}}{r^2}\left(KQ - Q - J\overline{Q}\right)\,, \tag{3.2.39}$$

$$\begin{aligned} N_Q = {} & r^2\big((1-K)(\eth K_{,r} + \eth(\overline{J}J_{,r}) + \overline{\eth}(JK_{,r}) - J_{,r}\overline{\eth}K \\ & + \frac{1}{2K^2}\left(\eth\overline{J}\left(J_{,r} - J^2\overline{J}_{,r}\right) + \eth J\left(\overline{J}_{,r} - \overline{J}^2J_{,r}\right)\right)\big)\Big)\,, \end{aligned} \tag{3.2.40}$$

$$\begin{aligned} N_W = {} & e^{2\beta}\Bigg((1-K)(\eth\overline{\eth}\beta + \eth\beta\overline{\eth}\beta) + \frac{1}{2}\left(J(\overline{\eth}\beta)^2 + \overline{J}(\eth\beta)^2\right) \\ & - \frac{1}{2}\left(\eth\beta(\overline{\eth}K - \eth\overline{J}) + \overline{\eth}\beta(\eth K - \overline{\eth}J)\right) + \frac{1}{2}\left(J\overline{\eth}^2\beta + \overline{J}\eth^2\beta\right)\Bigg) \\ & - \mathrm{e}^{-2\beta}\frac{r^4}{8}(2KU_{,r}\overline{U}_{,r} + J\overline{U}^2_{,r} + \overline{J}U^2_{,r})\,, \end{aligned} \tag{3.2.41}$$

$$N_J = N_{J1} + N_{J2} + N_{J3} + N_{J4} + N_{J5} + N_{J6} + N_{J7} + \frac{J}{r}(P_1 + P_2 + P_3 + P_4)\,, \tag{3.2.42}$$

where

$$\begin{aligned}
N_{J1} &= -\frac{\mathrm{e}^{2\beta}}{r}\left(K(\eth J\bar{\eth}\beta + 2\eth K\eth\beta - \bar{\eth}J\eth\beta) + J(\bar{\eth}J\bar{\eth}\beta - 2\eth K\bar{\eth}\beta) - \overline{J}\eth\beta\right)\,,\\
N_{J2} &= -\frac{1}{2}\left(\eth J(r\overline{U}_{,r} + 2\overline{U}) + \bar{\eth}J(rU_{,r} + 2U)\right)\,,\\
N_{J3} &= (1-K)(r\eth U_{,r} + 2\eth U) - J(r\eth\overline{U}_{,r} + 2\eth\overline{U})\,,\\
N_{J4} &= \frac{r^3}{2}\mathrm{e}^{-2\beta}\left(K^2U_{,r}^2 + 2JKU_{,r}\overline{U}_{,r} + J^2\overline{U}_{,r}^2\right)\,,\\
N_{J5} &= -\frac{r}{2}J_{,r}(\eth\overline{U} + \bar{\eth}U)\,,\\
N_{J6} &= r\left(\frac{1}{2}(\overline{U}\eth J + U\bar{\eth}J)(J\overline{J}_{,r} - \overline{J}J_{,r})\right.\\
&\quad +(JK_{,r} - KJ_{,r})\overline{U}\bar{\eth}J - \overline{U}(\eth J_{,r} - 2K\eth KJ_{,r} + 2J\eth KK_{,r})\\
&\quad \left. -U(\bar{\eth}J_{,r} - K\eth\overline{J}J_{,r} + J\eth\overline{J}K_{,r})\right)\,,\\
N_{J7} &= r(J_{,r}K - JK_{,r})\left(\overline{U}(\bar{\eth}J - \eth K) + U(\bar{\eth} - \eth\overline{J})\right.\\
&\quad \left. +K(\bar{\eth}U - \eth U) + (J\overline{\eth U} - \overline{J}\eth U)\right)\,,
\end{aligned} \tag{3.2.43}$$

$$\begin{aligned}
P_1 &= r^2\left(\frac{J_{,u}}{K}(\overline{J}_{,r}K - \overline{J}K_{,r}) + \frac{\overline{J}_{,u}}{K}(J_{,r}K - JK_{,r})\right) - 8V\beta_{,r}\,,\\
P_2 &= e^{2\beta}\left(-2K(\eth\bar{\eth}\beta + \bar{\eth}\beta\eth\beta) - (\bar{\eth}\beta\eth K + \eth\beta\bar{\eth}K)\right.\\
&\quad \left. + \left(J(\bar{\eth}^2\beta + (\bar{\eth}\beta)^2) + \overline{J}(\eth^2\beta + (\eth\beta)^2)\right) + (\bar{\eth}J\bar{\eth}\beta + \eth\overline{J}\eth\beta)\right)\,,\\
P_3 &= \frac{r}{2}\left((r\bar{\eth}U_{,r} + 2\bar{\eth}U) + (r\eth\overline{U}_{,r} + 2\eth\overline{U})\right)\,,\\
P_4 &= -\frac{r^4}{4}\mathrm{e}^{-2\beta}(2KU_{,r}\overline{U}_{,r} + J\overline{U}_{,r}^2 + \overline{J}U_{,r}^2)\,.
\end{aligned} \tag{3.2.44}$$

By using the second expression in (3.2.24), one can easily replace radial derivatives in terms of the compactified coordinate. The equations can then be discretized. This will be discussed in Section 8.2.

The constraint equations

As in the Cauchy case, the constraint equations can be used to monitor the accuracy of the numerical evolution. This is because the hypersurface and evolution equations already completely determine the evolving fields. Insertion of J, K, W, β, U should then satisfy the constraint equations, *i.e.* give $R_{0\alpha} = 0$ up to truncation error.

The spin-weighted versions are obtained by expanding $R_{0\alpha}$ in terms of the metric and its derivatives whose components in turn are expressed with the spin-weighted fields J, K, W, β, U [60]. Contracting the two angular components of $R_{0\alpha}$ with one of the tetrad elements then gives rise to three constraint equations for the spin-weighted fields

$$R_{00}, \qquad R_{01}, \qquad q^AR_{0A}\,. \tag{3.2.45}$$

The full expressions can be easily obtained by using computer algebra systems. However, as the equations are rather complicated, we skip their presentation here.

Finally, the conservation conditions (3.2.8) impose constraints on the integration constants $\beta|_\Gamma$, $Q|_\Gamma$ on the world-tube, *i.e.* they cannot be chosen freely. The equations read [273]

$$\begin{aligned} \beta_{,u} &= \mathcal{K}_\beta\,, \\ Q_{,u} &= -2\eth\beta_{,u} - q^A\mathcal{K}_A\,, \end{aligned} \tag{3.2.46}$$

where $\mathcal{K}_\beta$ and $\mathcal{K}_A$ are terms that are purely made out of hypersurface quantities containing β, U^A, V, h_{AB} and their r and x^A derivatives. These equations determine the evolution of the integration constants $\beta|_\Gamma$, $Q|_\Gamma$ on the world-tube. Another way of obtaining the integration constants $\beta|_\Gamma$, $Q|_\Gamma$ in a constraint preserving manner is to match them to an interior solution, *e.g.* in Cauchy-characteristic extraction (Section 5.3). The remaining integration constants can be given freely.

Chapter 4

Horizons

The formation of horizons in GR play a crucial role in defining the causal structure of spacetime. For example, the hyperbolic properties of GR induce a causal relationship between events in spacetime, and *Cauchy horizons* define which events in spacetime are causally influenced by each other in the Cauchy problem of GR (see Figure 2.1).

In the case of BHs, the *event horizon* determines the region of spacetime that is "inside" the BH and is causally disconnected from the "external" region of spacetime. The event horizon is defined as the past causal boundary of future null infinity and thus is a global property of spacetime, *i.e.* it can only be located once the entire future Cauchy development of a given spatial hypersurface is known. This indicates that an event horizon can only be traced after we have completed our simulation, and worse than that, it is even necessary to know the *entire* future development of the initial slice out to timelike infinity. Otherwise it is not possible to determine which null rays are trapped, and which have made it to future null infinity. It is the teleological notion of an event horizon that makes it impossible to uniquely locate and define BHs during numerical simulations[1].

For this reason, it is useful to introduce a different sort of horizon, the *apparent horizon*, which can be computed locally on the hypersurface[2], and can be used to characterize BHs in compact spacetimes that represent only a portion of the entire spacetime. In 1970, Hawking and Penrose were able to show [75, 282, 283] that the existence of an apparent horizon implies the existence of a singularity and an event horizon outside or coinciding with the apparent horizon by means of cosmic censorship [78], and hence the existence of a BH. Unfortunately, the converse is not necessarily true as there may exist slicings of spacetimes with event horizons that do not contain any apparent horizons. On the other hand, it is debatable whether the definition of a BH must relate to an event horizon (see *e.g.* [79]). It may be sufficient to define a BH in terms of the existence of an apparent horizon on a given spatial hypersurface, otherwise it would be impossible to find a BH experimentally as we can technically only do local measurements! Nonetheless, numerical experiments have shown that the issue of slicings that contain event horizons but no apparent horizons does not arise in practice for BH spacetimes that are under consideration here [241, 284–290].

On the apparent horizons, one can define a number of *quasi-local* measurements, *i.e.* from the spacetime geometry of the horizons, it is possible to deduce the spin and mass of a BH *during* a numerical simulation by only taking into account quantities that are defined on the current spatial hypersurface.

However, most of these quasi-local definitions rely on the concept of *isolated horizons* [291], *i.e.* horizons that are not undergoing dynamical interaction, but reside in equilibrium. In practice, however, there are two classes of BH horizons: in addition to the isolated horizons, there is also the class of *dynamical horizons* which arise whenever the horizon is evolving and its properties are varying in time, *e.g.* during inspiral, merger and ring-down of a BBH coalescence.

Fortunately, we can regard the individual horizons in a BBH system during inspiral, when the BHs are well separated, to be approximately isolated. The same is true after ring-down. Within

---

[1] It is possible to make use of characteristic evolutions to determine the event horizon "on-the-fly". Large red-shifts from the source, *i.e.* from the inner world-tube, to $\mathscr{J}^+$ are an indication for the possible formation of an event horizon.

[2] As we will see in Section 4.3 the apparent horizon is in some sense an arbitrary notion, as it is tied too rigidly to the choice of spatial hypersurface.

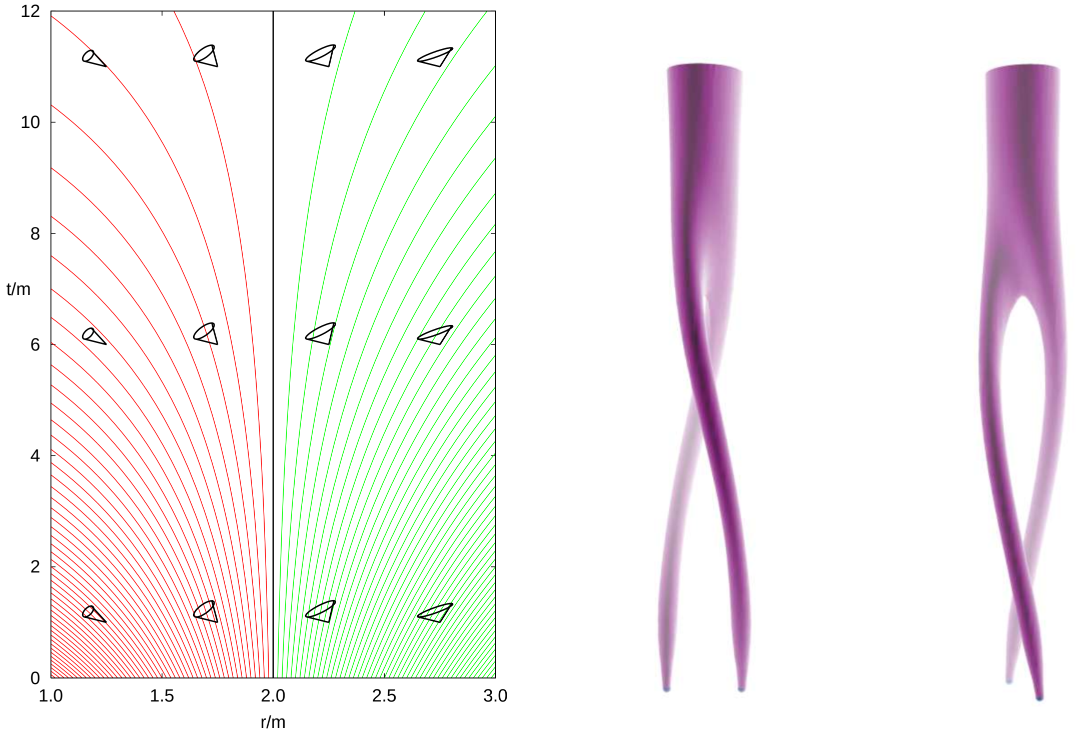

Figure 4.1: The *left panel* shows a number of future directed outgoing null geodesics in the neighborhood of the event horizon in Schwarzschild spacetime and plotted in ingoing Edington-Finkelstein coordinates. The *right panel* depicts the horizon surface(s), the “pair of pants”, of the late inspiral phase of two orbiting and merging BHs. Left figure taken from [295]. Right figure by Peter Diener.

our numerical accuracy, we can reach a point in time after ring-down at which we can regard the final BH as being stationary and hence isolated. In fact, it has been shown that the quasi-local definitions of spin and mass are also valid in dynamical situations [292, 293].

In the next sections, we will give definitions for the event horizon, apparent horizon as well as introduce the concepts of dynamical and isolated horizons. Especially the latter are important, because many of our calculations regarding the spin and mass of a BH rely on isolated and dynamical horizon computations.

4.1 Event horizons

Event horizons are usually defined as the past causal boundary of future null infinity [75]. This definition captures the idea that the event horizon is a surface on which all outgoing null rays define closed curves and can never reach future null infinity. Everything that is inside the horizon is then causally disconnected from the exterior spacetime, *i.e.* nothing can leak out of this horizon. The fact that null geodesics define closed curves on the horizon implies that the event horizon is a null hypersurface. It is necessarily continuous, but need not be differentiable anywhere [294].

The teleological nature of the definition of an event horizon implies that it “knows” about the future, *i.e.* its dynamical evolution reacts to processes that may not have registered in the past light cone yet. As such, this definition is highly non-local, and trying to find an event horizon locally in time is impossible. It can only be determined once the entire future development of the complete spacetime is known. This is because the null rays are exponentially diverging away from the horizon towards future null infinity, but the closer one gets to the horizon from the outside, the slower this divergence will be, until one finally hits the surface where no null ray can make it to future null infinity anymore (see left panel in Figure 4.1).

An event horizon finder has for example been implemented in [296] and makes use of an algorithm that integrates null surfaces backwards in time. This particular approach has proven to be robust because, if viewed backwards from future null infinity, the null geodesics are now converging at the horizon (see left panel in Figure 4.1). For more details on how to determine an event horizon please refer to [295].

However, in numerical relativity, event horizons are hardly used. Due to the global nature of these horizons, it is impractical to search for horizons after the evolution is completed. Usually, one is interested in the position, as well as spin and mass of a BH *during* evolution. For this reason, it is much better to rely on the concepts of apparent horizons, which can be defined during BH evolution. This is described in the next section.

4.2 Apparent horizons

The idea for introducing a notion like an apparent horizon is to have something like an instantaneous "surface" of a BH, *i.e.* a surface that can be calculated from quantities on a given spatial hypersurface only. It relies on the concept of surface *expansion* along a null direction, which is calculated for a given surface on the given hypersurface.

Apparent horizons can be defined as the outer boundary of a *trapped region* on a given spatial hypersurface. A trapped region is defined as the union of all *trapped surfaces* in that hypersurface, and a trapped surface is defined as a smooth closed 2-surface, whose future-pointing outgoing null geodesics have negative *expansion*. However, there is also an alternate definition. It can be shown [297] that the above is equivalent to the following definition. The apparent horizon is the outermost *marginally outer trapped surface* in a hypersurface, and a marginally outer trapped surface is defined as a smooth closed 2-surface whose future-pointing outgoing null geodesics have zero expansion.

The expansion of a 2-surface can be defined as follows.

Expansion

Given a smooth closed spacelike 2-surface S located in a spatial hypersurface Σ, *i.e.* $S \subset \Sigma$, we can define the surface normals R^a to the 2-surface which are tangent to Σ. The spatial hypersurface Σ defines timelike surface normals T^a (see Figure 4.2). Both, T^a and R^a must be linearly independent, and we can construct outgoing and ingoing null vectors as

$$\ell^a := \frac{1}{\sqrt{2}}(T^a + R^a)\,, \qquad n^a := \frac{1}{\sqrt{2}}(T^a - R^a)\,. \tag{4.2.1}$$

Let q_{ab} be the surface metric intrinsic to the 2-surface S. The expansion along outgoing and ingoing null directions at the 2-surface is then defined as

$$\theta_{(\ell)} := q^{ab}\nabla_a \ell_b\,, \qquad \theta_{(n)} := q^{ab}\nabla_a n_b\,. \tag{4.2.2}$$

Note that the derivatives involve only quantities that live on the surface $S \subset \Sigma$ and can thus be calculated at each time-step during a numerical simulation. However, $S \subset \Sigma$ represents a restriction on more general cases.

The expansion lets one define a number of interesting surfaces as listed in the next subsection.

Trapped surfaces

Depending on the expansions $\theta_{(\ell)}$ and $\theta_{(n)}$ of S, one can define the following surfaces.

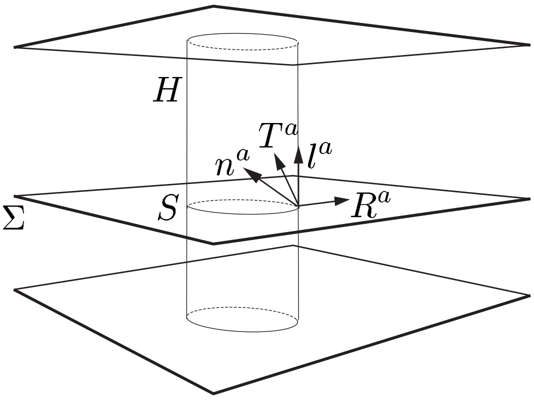

Figure 4.2: Illustration of some quantities defined at the worldtube H of apparent horizons. The apparent horizon S is embedded in the Cauchy hypersurface Σ, T^a is the unit timelike normal to Σ, R^a the outward pointing unit normal to S, and ℓ^a and n^a are outgoing and ingoing null vectors, respectively. Figure taken from [298].

- As a reference, a closed 2-surface S in flat space has

$$\theta_{(\ell)} > 0\,, \qquad \theta_{(n)} < 0\,, \tag{4.2.3}$$

  i.e. in flat space, the outgoing expansion is always positive and the ingoing expansion is always negative.

- The closed 2-surface S is said to be *trapped*, if

$$\theta_{(\ell)} < 0\,, \qquad \theta_{(n)} < 0\,, \tag{4.2.4}$$

  i.e. both expansions are strictly negative. This is very different to the behavior of a 2-surface in flat space. Penrose recognized that a trapped surface implies the existence of a singularity [75, 282, 283].

- The closed 2-surface S is said to be *marginally trapped*, if

$$\theta_{(\ell)} = 0 \qquad \text{or} \qquad \theta_{(n)} = 0\,. \tag{4.2.5}$$

- The closed 2-surface S is said to be *marginally outer trapped*, if

$$\theta_{(\ell)} = 0\,. \tag{4.2.6}$$

The apparent horizon is then defined as the outermost marginally outer trapped surface in the hypersurface Σ.

Properties

Because the apparent horizon is a trapped surface, the existence of an apparent horizon implies the existence of a singularity [75, 282, 283], and by means of cosmic censorship [78], we can expect that there is also an event horizon and hence a BH. In contrast to the event horizon, the apparent horizon of a BH can be computed directly from quantities that are defined on a spatial hypersurface without knowledge of the future development of the spacetime. This makes apparent horizons a perfect candidate for locating and defining BHs in numerical simulations. However, the apparent horizon is slicing dependent, *i.e.* if the spatial hypersurface is wiggled even slightly, new outer trapped regions may appear or disappear and hence alter the shape of the apparent horizon. It is the “outermost” in the definition of an apparent horizon, which makes its notion to be still very global.

The world-tube that is formed by a succession of apparent horizons in time is generally non-timelike. It can become null (and thus slicing independent), if no matter or radiation is crossing the horizon anymore. In that case, apparent horizon and event horizon coincide.

An algorithm of how an apparent horizon can be located during our numerical simulations is given in Section 8.1. Once the apparent horizon is known, we are interested in definitions for the BH mass and spin in terms of the apparent horizon. This has been addressed by the isolated and dynamical horizon formalism to be described in the next section.

4.3 Isolated and dynamical horizons

The isolated and dynamical horizon framework [291–293, 298, 299] offers a convenient way of defining the mass and spin of a BH.

Isolated horizons can model BHs whenever the horizon itself is in equilibrium, but the remaining part of spacetime may still contain dynamics such as gravitational radiation. The extension to dynamical horizons may even be used for BHs that are not in equilibrium, *i.e.* BHs that are orbiting each other, and radiation and matter may cross the horizon.

An example of an isolated horizon is given by the late-time behavior of a BH remnant in a BBH merger simulation. The back-scattered radiation that is still falling into the final BH at late-times can be regarded as so small that the event horizon of that BH becomes approximately isolated. In this case, the apparent horizon becomes a null-surface and coincides with the event horizon. If one constructs a world-tube H from a time-succession of apparent horizons, the intrinsic 2-metric q_{ab} of the apparent horizon surface S induces a degenerate 3-metric on the surface of H. As the apparent horizon is topological spherical [300], the topology of the apparent horizon world-tube is $S^2 \times \mathbb{R}$. The outgoing null vectors ℓ (4.2.1) then define null normals of H which have zero expansion.

Isolated horizons

The considerations above motivate the following definitions.

Definition 4.3.1. *A three dimensional sub-manifold Δ of a space-time $(\mathcal{M}, g_{ab})$ is said to be a non-expanding horizon (NEH) if it satisfies the following conditions:*

1. *Δ is topologically $S^2 \times \mathbb{R}$ and null;*
2. *The expansion $\theta_{(\ell)} := q^{ab}\nabla_a \ell_b$ of ℓ vanishes on Δ, where ℓ is any null normal to Δ;*
3. *All equations of motion hold at Δ and, if any matter fields are present with T_{ab} as the stress energy tensor, then we require $-T^a_b \ell^b$ to be future directed and causal for any future directed null normal ℓ^b.*

Condition 3 is satisfied by all classical matter fields and is *e.g.* implied by the null-energy condition, but does not play any role in the vacuum case. Condition 2 is equivalent to requiring that every cross-section of Δ be marginally trapped, and if it holds for one null normal, it holds for all.

The definition of a NEH exactly models the late-time behavior of an apparent horizon when it equilibriates, *i.e.* the world-tube H represents a NEH, Δ. A NEH is an invariant notion in the full 4D spacetime and is completely independent on the slicing of the spacetime and it turns out that the definitions of spin or mass on the NEH are independent of the spatial hypersurface as well.

Every cross-section of a NEH with a spatial slice is potentially an apparent horizon. However, apparent horizons are not necessarily NEHs. This is true especially in dynamical situations when the apparent horizon is non-isolated.

In order to define the mass M_S and angular momentum J_S on a spatial cross-section S of Δ, one needs to go beyond the definition of a NEH and introduce additional structures on the horizon. This is done via the definition of a *weakly isolated horizon* [301, 302]. The Hamiltonian analysis which leads to the definitions of mass and angular momentum requires this extra structure.

Fortunately, it turns out that the *formulae* for M_S and J_S do not depend on this extra structure and hold true for non-expanding horizons. We could therefore omit these definitions entirely and simply state the results of the calculation. For the sake of completeness, we shall give the basic idea behind (weakly) isolated horizons.

First, we note that two null normals ℓ^a and $\tilde{\ell}^a$ to a NEH Δ are said to belong to the same equivalence class $[\ell]$ if $\tilde{\ell} = c\ell$ for some positive constant c. Then we can define weakly isolated horizons as follows:

Definition 4.3.2. *The pair* $(\Delta, [\ell])$ *is said to constitute a weakly isolated horizon (WIH) provided* Δ *is a NEH and each null normal* ℓ^a *in* $[\ell]$ *satisfies*

$$(\mathcal{L}_\ell D_a - D_a \mathcal{L}_\ell)\ell^b = 0\,. \tag{4.3.1}$$

In this definition, D_a is the derivative operator on Δ compatible with the degenerate 3-metric q_{ab} of Δ [301]. WIHs are therefore characterized by the property that, in addition to q_{ab}, the connection component $D_a \ell^b$ is also time-independent. This can be further restricted by requiring that the full connection D should be time-independent. This leads to the notion of an isolated horizons:

Definition 4.3.3. *A WIH is said to constitute an isolated horizon (IH) if*

$$(\mathcal{L}_\ell D_a - D_a \mathcal{L}_\ell)V^b = 0 \tag{4.3.2}$$

for arbitrary vector fields V^a *tangent to* Δ.

Thus, IHs are a restriction over WIHs. This is because any NEH can be turned into a WIH by making a suitable choice of the null normal ℓ, which is always possible. However, not any WIH admits an IH structure.

The definitions of (weakly) isolated horizons make it possible to define angular momentum and mass on an apparent horizon that is in equilibrium without implicitly assuming that the geometry close to the horizon of a BH is isometric to Kerr.

However, as isolated horizons model an apparent horizon only in equilibrium, *i.e.* when the horizon is null, we need a different concept in dynamical situations when the apparent horizon becomes spacelike. This is described in the next subsection.

Dynamical horizons

The spin and mass of a BH are of special interest also in dynamical environments, *e.g.* when radiation is crossing the horizon during ring-down or when two BHs are in close orbit with each other. In these cases, the horizons cannot be modeled in terms of isolated horizons as they are not in equilibrium anymore. For this reason, it is useful to introduce the concept of dynamical horizons [292, 299].

Definition 4.3.4. *A smooth, three-dimensional, spacelike submanifold (possibly with boundary)* H *of spacetime is said to be a dynamical horizon (DH) if it can be foliated by a family of closed 2-manifolds such that*

1. *on each leaf* S *the expansion* $\theta_{(\ell)}$ *of one null normal* ℓ^a *vanishes; and*
2. *the expansion* $\theta_{(n)}$ *of the other null normal* n^a *is negative.*

Thus, a DH H is basically a world-tube foliated by closed, marginally trapped 2-surfaces. This definition is a truly quasi-local definition and as such does not require asymptotic flatness at infinity as the definition of an event horizon requires. However, a DH does not necessarily describe BHs, because stationary spacetimes do not admit DHs. On the other hand, in time-dependent situations, there may be many DHs inside the event horizon of a BH. Usually, we associate the apparent horizon with a DH. This makes it possible to calculate the mass and spin as a quasi-local measure on the apparent horizon.

How to obtain the mass and spin on DHs or IHs is described in the next subsection.

Mass and spin

The quasi-local definitions of mass and spin of a BH can be defined on apparent horizons through the isolated and dynamical horizon framework. If the apparent horizon is in equilibrium, then it can be described by IHs. Otherwise, it can be described as a DH.

It turns out that the expressions for mass and spin are the same, whether the dynamical or the isolated horizon formalism is used.

Let us denote the mass and spin on a slice S of the horizon Δ by M_S and J_S, respectively. The formula for angular momentum reads [302]

$$J_S = \frac{1}{8\pi} \oint_S (\varphi^a R^b K_{ab})\, \mathrm{d}^2V\,, \tag{4.3.3}$$

where the integral is taken over the closed, spacelike 2-surface S, R^b is the unit outward pointing normal on S, K_{ab} the extrinsic curvature on S, and φ^a a tangent, rotational Killing vector field of the intrinsic metric q_{ab} of S. In order to define angular momentum at all, it is necessary that S is axisymmetric so that we can always find the Killing vector φ^a. There are various methods to find this Killing vector. Usually, this is done by solving the Killing transport equations. For details, please refer to [298]. It is worthwhile to note that expression (4.3.3) reduces to the ADM expression for the angular momentum (1.3.35) when evaluated at infinity.

The mass on the horizon reads [301, 302]

$$M_S = \frac{1}{2R_S}\sqrt{R_S^4 + 4J_S^2}\,, \tag{4.3.4}$$

where $R_S = (A_S/4\pi)^{1/2}$ is the areal radius and J_S the angular momentum on a cross-section S of the horizon Δ. This formula is identical to the relationship between mass, radius and angular momentum in the Kerr spacetime [303, 304]. However, expression (4.3.4) is not an assumption, but a result from Hamiltonian analysis.

The *irreducible mass* is defined as the mass (4.3.4) minus the rotational energy of the BH [303, 304], *i.e.*

$$M_{\mathrm{irr}} = \frac{1}{2}R_S\,. \tag{4.3.5}$$

Chapter 5

Gravitational wave extraction: Theory

Gravitational wave extraction is one of the key goals of numerical relativity since it is not possible to obtain a complete waveform for generic BBH spacetimes on an analytical level, neither via exact solutions nor by using perturbative approaches. Black hole perturbation theory, on the one hand, is based on perturbations around a Schwarzschild or Kerr background and hence cannot be used to describe the dynamics in highly distorted geometries such as the inspiral and plunge phase of BBHs. However, it is perfectly suited for modeling the dynamics of a single distorted BH, and has led to important discoveries about the stability and oscillation properties of BH spacetimes [96], such as quasi-normal mode ringing of Schwarzschild [103–108] and Kerr geometries [109–111], and the 'no hair theorem' stating that all perturbations away from spherical or axial symmetry will be radiated away [99–101] (see Section 11.3 for an analysis of the quasi-normal mode ringing of the merger remnant).

Post-Newtonian theory, on the other hand, models the field equations in terms of the expansion parameter $v/c \ll 1$, which means that it is only valid in regimes with non-relativistic (internal) speeds and weak gravitational fields inside the source [305]. This is the case for the inspiral phase of a BBH coalescence, but excludes the subsequent plunge and ring-down phases.

Both approximate approaches can therefore be used to study the inspiral and the ring-down phases of a wave-signal, but fail in the highly non-linear dynamics during the plunge.

Numerical schemes, on the other hand, do not rely on any perturbative expansion parameter and can capture the plunge phase as well, so that a complete waveform including inspiral, plunge and ring-down can be obtained.

There are two commonly used ways in numerical relativity of determining the gravitational wave-signal which we will shortly review. One is based on the curvature component Ψ_4 of the Weyl tensor (Section 5.1) while the other makes use of gauge-invariant perturbations of Schwarzschild spacetimes (Section 5.2). Since our computational domain is finite but gravitational waves are defined unambiguously only at future null infinity $\mathscr{J}^+$, we have to work with some large but finite extraction radius r_{extr} which introduces some unknown systematic error in the waves. Another proposed method called Cauchy-characteristic extraction (CCE) is based on compactified characteristic evolution of the wave-zone using the metric data of a Cauchy evolution as boundary data for the characteristic evolution. Due to the compactification of the radial coordinate, future null infinity can be represented on the computational grid and leads to mathematically well-defined wave extraction. Although the theory of CCE (see Section 5.3) is already known for some time, this method is applied for the first time to BBH merger simulations in this thesis (see Section 9.1 for the computational implementation and Section 15.2 for results).

This chapter concludes with expressions for the gravitational-wave strain h, radiated energy, as well as radiated linear and angular momentum in terms of Ψ_4 and the gauge-invariant master functions encountered in Section 5.2.

5.1 Extraction I: Complex Weyl scalars

The Newman-Penrose formalism [114] provides a convenient representation for a number of radiation related quantities as spin-weighted scalars. In particular, the curvature component

$$\Psi_4 \equiv -C_{\alpha\beta\gamma\delta} n^\alpha \bar{m}^\beta n^\gamma \bar{m}^\delta, \tag{5.1.1}$$

is defined as a particular component of the Weyl curvature, $C_{\alpha\beta\gamma\delta}$, projected onto a given null frame, $\{\boldsymbol{l}, \boldsymbol{n}, \boldsymbol{m}, \bar{\boldsymbol{m}}\}$.

As already discussed in Section 1.3, the identification of the Weyl scalar Ψ_4 with the gravitational radiation content of the spacetime is a result of the peeling theorem [113, 114, 117, 124], which states that in an appropriate frame the Ψ_4 component of the curvature has the slowest fall-off with radius, $\mathcal{O}(1/r)$.

The most straight-forward way of evaluating Ψ_4 in numerical (Cauchy) simulations is to define an orthonormal basis in the three space $(\hat{\boldsymbol{r}}, \hat{\boldsymbol{\theta}}, \hat{\boldsymbol{\phi}})$, centered on the Cartesian grid center and oriented with poles along $\hat{\boldsymbol{z}}$. The normal to the slice defines a time-like vector $\hat{\boldsymbol{t}}$, from which we construct the null frame

$$\boldsymbol{l} = \frac{1}{\sqrt{2}}(\hat{\boldsymbol{t}} - \hat{\boldsymbol{r}}), \quad \boldsymbol{n} = \frac{1}{\sqrt{2}}(\hat{\boldsymbol{t}} + \hat{\boldsymbol{r}}), \quad \boldsymbol{m} = \frac{1}{\sqrt{2}}(\hat{\boldsymbol{\theta}} - \mathrm{i}\hat{\boldsymbol{\phi}}) \; . \tag{5.1.2}$$

Note that in order to make the vectors $\{\boldsymbol{l}, \boldsymbol{n}, \boldsymbol{m}, \bar{\boldsymbol{m}}\}$ null (1.3.10), $(\hat{\boldsymbol{r}}, \hat{\boldsymbol{\theta}}, \hat{\boldsymbol{\phi}})$ have to be orthonormal relative to the spacetime metric. In practice, we fix $\hat{\boldsymbol{r}}$ and then apply a Gram-Schmidt orthonormalization procedure to determine $\hat{\boldsymbol{\theta}}$ and $\hat{\boldsymbol{\phi}}$.

It is then possible to calculate Ψ_4 via a reformulation of (5.1.1) in terms of ADM variables on the slice [306] by using the electric and magnetic parts (1.3.5),(1.3.6) of the Weyl tensor,

$$\Psi_4 = C_{ij}\bar{m}^i\bar{m}^j \; , \tag{5.1.3}$$

where

$$C_{ij} \equiv E_{ij} - iB_{ij} = R_{ij} - KK_{ij} + K_i{}^k K_{kj} - \mathrm{i}\epsilon_i{}^{kl}\nabla_l K_{jk} \; . \tag{5.1.4}$$

The remaining Weyl scalars can be similarly obtained and read

$$\Psi_3 = \frac{1}{\sqrt{2}} C_{ij}\bar{m}^i e_r^j \; , \tag{5.1.5}$$

$$\Psi_2 = \frac{1}{2} C_{ij} e_r^i e_r^j \; , \tag{5.1.6}$$

$$\Psi_1 = -\frac{1}{\sqrt{2}} C_{ij} m^i e_r^j \; , \tag{5.1.7}$$

$$\Psi_0 = C_{ij} m^i m^j \; , \tag{5.1.8}$$

where $(e_r^j) \equiv \hat{\boldsymbol{r}}$ is the radial unit vector.

Practically, when relating Ψ_4 to gravitational radiation, one has to live with a finite cut-off radius since the simulation domain is finite. But then it should be noted that the conditions of the Peeling theorem are only valid in an asymptotic frame and are not satisfied exactly at a small radius and in the chosen frame. However, there are proposals for how this situation can be improved [307] by at least relating Ψ_4 as calculated using the frame (5.1.2) at finite radius to the asymptotic Bondi frame thus removing some potential gauge-ambiguities.

Even better, one can calculate Ψ_4 directly at $\mathcal{J}^+$. This is detailed in Section 5.3, where the traditional approach (which is gauge dependent and has a finite-radius cut-off error) presented in this Section is abandoned, and a characteristic formulation of the Einstein equations is used to determine the fields out to future null infinity.

Details on the numerical implementation on this particular extraction method can be found in Section 9.2.

5.2 Extraction II: Gauge-invariant perturbations of Schwarzschild

The method of extracting gravitational waves from a spacetime using gauge-invariant perturbations of a Schwarzschild background is, as the name implies, based on black hole perturbation theory [96, 308–311]. This method has recently been reviewed in [312] and we follow this reference closely. The underlying assumption is that "far away" from the source in the wave-zone, the spacetime, or more specifically the gravitational wave-signal, can be described in terms of linear[1] perturbations around a Schwarzschild background metric. Upon knowledge of the perturbation coefficients within the numerical simulation, one can readily obtain a waveform via gauge-invariant odd-parity (or axial) current multipoles $Q^{\times}_{\ell m}$ and even-parity (or polar) mass multipoles $Q^{+}_{\ell m}$ of the metric perturbation [310]. The problem is then to determine the perturbation coefficients relating the numerically obtained spacetime in the wave-zone to a perturbed Schwarzschild background [317, 318].

Within this formalism, one important issue is the problem of distinguishing infinitesimal 'physical' perturbations from infinitesimal coordinate transformations (or gauge-transformations) due to the coordinate freedom of GR. One can circumvent this problem by either fixing the gauge as done by Regge-Wheeler [96], or by introducing linearly gauge-invariant perturbations as done by Moncrief [310] who related the original Regge-Wheeler current and mass multipoles (or *master functions*) to gauge-invariant variables. The advantage of the latter is the exclusion of possible gauge-dependent contributions and the natural relationship to physical observables, especially energy and momentum of the gravitational waves.

Gauge-invariance can be enforced by the following. Consider a tensor field $\boldsymbol{X}$ in a background metric $\overset{0}{\boldsymbol{g}}$ and $\delta\boldsymbol{X}$ its infinitesimal perturbation. The perturbation is said to be gauge-invariant if under an infinitesimal coordinate transformation $x^\mu \rightarrow x^{\mu'} \equiv x^\mu + \xi^\mu$ with $\xi^\mu \ll 1$ it remains unchanged, i. e.

$$\delta\boldsymbol{X} \rightarrow \delta\boldsymbol{X}' = \delta\boldsymbol{X} + \mathcal{L}_{\boldsymbol{\xi}}\boldsymbol{X} = \delta\boldsymbol{X}\,, \tag{5.2.1}$$

which implies that $\mathcal{L}_{\boldsymbol{\xi}}\boldsymbol{X} = 0$, where $\mathcal{L}_{\boldsymbol{\xi}}$ is the Lie derivative along $\boldsymbol{\xi}$ in the metric $\overset{0}{\boldsymbol{g}}$. The vanishing Lie derivative implies that $\boldsymbol{\xi}$ inducing the coordinate transformation must be the consequence of symmetries in the background metric $\overset{0}{\boldsymbol{g}}$ which cannot be imposed generically. However, in our case, we are interested in perturbing around the Schwarzschild metric which possess a spherical Killing symmetry thus allowing us to take full advantage of the gauge-invariant approach and which will result in expansions in terms of multipoles with $\ell \geq 2$.

Multipolar expansion

We make the Ansatz

$$g_{\mu\nu} = \overset{0}{g}_{\mu\nu} + h_{\mu\nu}, \tag{5.2.2}$$

where $\overset{0}{g}_{\mu\nu}$ represents the components of the background Schwarzschild metric

$$\overset{o}{g}_{\mu\nu}= \begin{pmatrix} -N^2 & 0 & 0 & 0 \\ 0 & A^2 & 0 & 0 \\ 0 & 0 & r^2 & 0 \\ 0 & 0 & 0 & r^2\sin^2\theta \end{pmatrix}\,, \tag{5.2.3}$$

and where the functions N, A, and r are functions of our coordinate radius and time and $h_{\mu\nu}$ its small non-spherical perturbations with $|h_{\mu\nu}|/|\overset{0}{g}_{\mu\nu}| \ll 1$.

It is important to notice that because our background manifold $\mathcal{M}$ is spherically symmetric, it can be split into the product $\mathcal{M} = M^2 \times S^2$ of a 2-dimensional submanifold M^2 with Lorentzian signature and coordinates (t, r) and the submanifold of a 2-sphere S^2 with coordinates[2] (θ, ϕ). This allows us to consider the perturbations regarding these submanifolds independently and it gives rise to an expansion in terms of even and odd-parity multipoles. The difference between even and odd-parity multipoles is manifested in their transformation behavior under parity transformations. Even-parity (or polar) multipoles transform as $(-1)^{\ell}$ and odd-parity (or axial) multipoles transform as $(-1)^{\ell+1}$ under the coordinate change $(\theta,\phi)\to(\pi-\theta,\pi+\phi)$.

---

[1] There exist also perturbations to second-order [313, 314] which enable one to study QNM coupling, the non-linear stability of the Schwarzschild solution and recent results point out the relevance for extreme-mass ratio inspirals [315]. The gauge-invariant formalism presented in this section has recently been extended in [316] to second-order and enables the study of non-linear features in gravitational waves and mode-mode coupling as well as assessing the error inherent in first-order perturbations.

[2] Within this Section, our convention for labeling tensor indices will depart from what has been introduced in the Introduction of this thesis to make the notation consistent with existing literature. We use capital Latin indices $A, B, \ldots$ to label components confined to $\mathcal{M}$ while small case Latin indices $a, b, \ldots$ label components confined to S^2.

We can write

$$h_{\mu\nu}=\sum_{\ell m}\left[\left(h^{\ell m}_{\mu\nu}\right)^{(o)}+\left(h^{\ell m}_{\mu\nu}\right)^{(e)}\right] \ , \tag{5.2.4}$$

where the label (o) and (e) denote odd and even parity perturbations, respectively.

Decomposing $\left(h^{\ell m}_{\mu\nu}\right)^{(o)}$ and $\left(h^{\ell m}_{\mu\nu}\right)^{(e)}$ in terms of spherical harmonics $Y^{\ell m}$ and the axial vector harmonics $S^{\ell m}_c$ defined as

$$S^{\ell m}_c\equiv\epsilon_{cd}\gamma^{de}\nabla_e Y^{\ell m} \ , \tag{5.2.5}$$

where ϵ_{cd} is the volume form on S^2 as defined by the condition $\epsilon_{cd}\epsilon^{ce}={\gamma_d}^{e}$ and such that $\nabla_c\epsilon_{ab}=0$, we are able to write

$$\left(h^{\ell m}_{\mu\nu}\right)^{(\mathrm{o})}=\begin{pmatrix} 0 & h^{(\mathrm{o})}_A S^{\ell m}_c \\ h^{(\mathrm{o})}_A S^{\ell m}_c & h\nabla_{(d}S^{\ell m}_{c)} \end{pmatrix} \tag{5.2.6}$$

for the odd-parity perturbations and

$$\left(h^{\ell m}_{\mu\nu}\right)^{(\mathrm{e})}=\left(\begin{array}{cc|c} NH_0Y^{\ell m} & H_1Y^{\ell m} & h^{(\mathrm{e})}_A\nabla_cY^{\ell m} \\ H_1Y^{\ell m} & AH_2Y^{\ell m} & \\ \hline h^{(\mathrm{e})}_A\nabla_cY^{\ell m} & & r^2\left(KY^{\ell m}\gamma_{cd}+G\nabla_d\nabla_cY^{\ell m}\right) \end{array}\right) \tag{5.2.7}$$

for the even-parity perturbations. In both expressions, we have omitted the indices ℓ, m for the odd-parity coefficient functions $h^{(o)}_A$ which are functions of the coordinates (t,r) in the submanifold M^2 and the even-parity coefficient functions H_0, H_1, H_2, $h^{(\mathrm{e})}_0$, $h^{(\mathrm{e})}_1$ K, G which are functions of the coordinates (θ,ϕ) in the submanifold S^2.

A similar decomposition can be made for the stress-energy tensor describing the matter-sources, but here, we restrict our attention to the pure vacuum problem.

Given the Hamiltonian of the perturbed Einstein equations in ADM form [132], it is now possible to derive variational principles for the odd and even-parity perturbation sector [310] to give equations of motions that are similar to wave-equations with a scattering potential.

Odd (axial) perturbations

The odd (or axial) perturbations have been first studied by Regge and Wheeler [96] in a fixed gauge and have been re-derived by Moncrief [310] in a gauge invariant notion.

By introducing the gauge-invariant multipoles [319]

$$k_A\equiv h_A-\nabla_A h+2h\frac{\nabla_A r}{r} \ , \tag{5.2.8}$$

one can construct the gauge-invariant Regge-Wheeler master functions [310]

$$Q^{(\mathrm{o})}\equiv\frac{\nabla_A r}{r}\overset{0}{g}{}^{AB}k_B=\frac{1}{r}\left(1-\frac{2M}{r}\right)\left[h^{(\mathrm{o})}_1+\frac{r^2}{2}\partial_r\left(\frac{h_2}{r^2}\right)\right] \ , \tag{5.2.9}$$

which satisfy the “Regge-Wheeler” equations

$$\partial^2_t Q^{(\mathrm{o})}-\partial^2_{r_*}Q^{(\mathrm{o})}+V^{(\mathrm{o})}_{\ell}Q^{(\mathrm{o})}=0, \tag{5.2.10}$$

where

$$r_* \equiv r + 2M \ln\left(\frac{r}{2M} - 1\right) \tag{5.2.11}$$

is the 'tortoise coordinate' [101] and $V_\ell^{(\mathrm{o})}$ is the odd-parity scattering potential, defined as

$$V_\ell^{(\mathrm{o})} \equiv \left(1 - \frac{2M}{r}\right)\left(\frac{\Lambda}{r^2} - \frac{6M}{r^3}\right) \tag{5.2.12}$$

with $\Lambda = \ell(\ell+1)$. Equation (5.2.10) is the equation of motion derived from the variational principle of the perturbed Einstein equations and (5.2.9) is the solution to this wave-like equation with scattering potential (5.2.12).

Following convention [317] which is nowadays commonly used, we introduce an additional master function that is related to (5.2.9) by

$$Q^\times_{\ell m} = \sqrt{\frac{2(\ell+1)!}{(\ell-2)!}} Q^{(\mathrm{o})}_{\ell m}. \tag{5.2.13}$$

This function can be calculated from a numerically obtained spacetime and can be related to gravitational wave modes (Section 5.4), radiated energy (Section 5.5), linear (Section 5.6) and angular momentum (Section 5.7).

Even (polar) perturbations

The even (or polar) perturbations are more complicated than the odd ones, and have been derived by Zerilli [308, 309] 13 years after the Regge-Wheeler master functions were discovered. As for the odd perturbations, Moncrief also applied his analysis [310] to the even-parity sector to yield a gauge-invariant formalism. Following Moncrief, one can introduce the gauge-invariant multipoles [310]

$$\kappa_1 \equiv K + \frac{1}{A}\left(r\partial_r G - \frac{2}{r} h_1^{(\mathrm{e})}\right) , \tag{5.2.14}$$

$$\kappa_2 \equiv \frac{1}{2}\left[R H_2 - \sqrt{A}\partial_r\left(r\sqrt{A}K\right)\right] , \tag{5.2.15}$$

where both κ_1 and κ_2 are gauge-invariant functions, as well as the following linear combination

$$q_1 \equiv r\Lambda\kappa_1 + \frac{4r}{A^2}\kappa_2 . \tag{5.2.16}$$

In the same fashion as for the odd-parity sector, one can construct the function

$$\Psi^{(\mathrm{e})} \equiv \frac{r q_1}{\Lambda\left[r\left(\Lambda - 2\right) + 6M\right]} , \tag{5.2.17}$$

which is known as the Zerilli master function [308] and which is a solution to the even-parity master equation or "Zerilli" equation

$$\partial_t^2 \Psi^{(\mathrm{e})} - \partial^2_{r_*}\Psi^{(\mathrm{e})} + V_\ell^{(\mathrm{e})}\Psi^{(\mathrm{e})} = S^{(\mathrm{e})} , \tag{5.2.18}$$

and, again, is a wave-like equation in the scattering Zerilli potential [308]

$$V_\ell^{(\mathrm{e})} \equiv \left(1 - \frac{2M}{r}\right) \frac{\Lambda(\Lambda-2)^2 r^3 + 6(\Lambda-2)^2 M r^2 + 36(\Lambda-2)M^2 r + 72M^3}{r^3\left[(\Lambda-2)r + 6M\right]^2} . \tag{5.2.19}$$

Following again convention [317], we introduce an additional master function that is related to (5.2.18) by

$$Q^+_{\ell m} = \sqrt{\frac{2(\ell+1)!}{(\ell-2)!}} \Psi^{(\mathrm{e})}_{\ell m}. \tag{5.2.20}$$

This function can again be calculated from a numerically obtained spacetime and can be related to gravitational wave modes (Section 5.4), radiated energy (Section 5.5), linear (Section 5.6) and angular momentum (Section 5.7).

Obtaining the master functions from numerical spacetimes

The even and odd-parity master functions can be straight-forwardly evaluated by relating the numerical spacetime to the perturbation (5.2.2).

The spherical part of the metric, given in the functions N, A, and r, can be obtained by projecting the full numerical metric against Y_{00}, yielding the following expressions [318]:

$$N^2 = -\frac{1}{4\pi}\int g_{tt}d\Omega \tag{5.2.21}$$

$$A^2 = \frac{1}{4\pi}\int g_{rr}d\Omega \tag{5.2.22}$$

$$r^2 = \frac{1}{8\pi}\int\left(g_{\theta\theta} + \frac{g_{\phi\phi}}{\sin^2\theta}\right)d\Omega \tag{5.2.23}$$

Each ℓm-mode of $h_{\mu\nu}$ can then be obtained by projecting the full numerical metric against the appropriate $Y_{\ell m}$. For example:

$$H_2^{(\ell m)} = \frac{1}{A^2}\int g_{rr}Y_{\ell m}d\Omega\,. \tag{5.2.24}$$

Expressions for the other functions are provided in [320]. In practice, we do not extract A to compute $H_2^{(\ell m)}$, but rather we assume it to have the form $1 - \frac{2M}{r}$, where we take M to be the ADM mass of the spacetime.

Once the perturbation coefficients have been retrieved, they can be directly inserted into (5.2.9) and (5.2.17) to obtain the even and odd master functions.

Details on the numerical implementation on this particular extraction method can be found in Section 9.3.

5.3 Extraction III: Cauchy-characteristic extraction

In the previous sections, we have reviewed two commonly used methods in numerical relativity to extract gravitational waves from numerically obtained spacetimes: a method based on the complex Weyl component Ψ_4 and another one based on gauge-invariant metric perturbations. Both of these methods have one practical drawback: they are related to outgoing radiation, *i.e.* gravitational waves, only in the limit of infinite radius to the source (see Section 5.4). On a finite computational domain and with our evolution system as described in Chapter 2 (and particularly in Section 2.2), however, it is not feasible to include infinity on our finite-sized numerical grid.

Thus, when using these extraction methods, one has to introduce an artificial "cut-off" radius at which the extraction is performed and hope that the method has sufficiently converged to the answer at infinity. In reality, this systematic error is hard to address as it is a-priori unknown how the signal would look like at infinity. In Chapter 15, we will discuss how "good" this approximation introduced by a finite-radius extraction is.

On the other hand, there exist various approaches to obtain a wave-signal at infinity by evolving the full non-linear Einstein equations out to $\mathscr{J}^+$. One of these methods utilizes hyperboloidal slicings [321–327] that allow to include infinity via spatial compactification techniques. Another method is called Cauchy-characteristic extraction (CCE) [272, 275, 276, 328–330], which utilizes characteristic evolution of the Einstein equations (see Chapter 3) also allowing for the inclusion of $\mathscr{J}^+$ in the numerical computation. However, none of these methods have been successfully applied to the binary black hole problem. In this thesis and for the first time in numerical relativity, we apply Cauchy-characteristic extraction to BBH inspiral and merger simulations and obtain an unambiguously defined and gauge-invariant gravitational wave. For the implementation and results, please refer to Sections 9.1 and 15.2, respectively. In this section, we focus on the underlying theory of CCE and will mainly repeat what has been written in [330], *i.e.* we follow this reference closely. At the end of this section, we also describe the steps that are necessary to obtain the *Bondi news function* and Ψ_4 from the characteristic evolution which contain the radiation content at future null infinity.

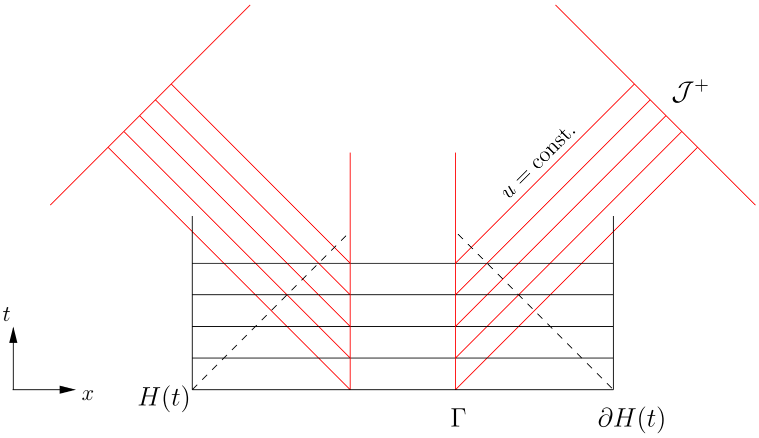

Figure 5.1: This figure illustrates the concept of CCE. The world-tube Γ on which boundary data for the characteristic evolution is constructed intersects consecutive Cauchy hypersurfaces $H(t)$. While the Cauchy hypersurfaces have a finite extent, the characteristic hypersurfaces $u = \text{const.}$ emanate from the world-tube out to future null infinity $\mathcal{J}^+$. The dotted lines indicate the causal influence from the outer boundary $\partial H(t)$, *i.e.* it represents the future Cauchy horizon of the domain of dependence on the initial data set.

Outline of the procedure

Cauchy-characteristic extraction combines the strengths of two evolution schemes. While Cauchy evolution (see Chapter 2) has proven to be robust and accurate for interior strong-field regions, the standard approaches do not allow the inclusion of spatial or future null infinity in the computation which is necessary for unambiguous gravitational-wave extraction. Characteristic evolution (see Chapter 3) on the other hand can accurately represent the weak-field regions of a spacetime. The possibility of applying spatial compactification allows to include future null infinity $\mathcal{J}^+$ on the computational grid without rendering the numerical evolution scheme unstable as would be the case in Cauchy evolution schemes. Thus, characteristic evolution can be used to describe the entire wave-zone of a given spacetime out to $\mathcal{J}^+$. However, current characteristic evolution schemes fail to model the strong-field regions since these regions may cause focusing of light rays. The resulting caustics of the null cones lead to coordinate singularities which, at present, cannot be handled numerically[3]. It is therefore natural to try to combine both evolution schemes and obtain a numerical solution that accurately represents the entire spacetime from the source to $\mathcal{J}^+$.

The prescription for this technique is sketched in Figure 5.1. During each Cauchy evolution step, we construct boundary data on a world-tube Γ necessary for the following characteristic time-step. After the characteristic time-step is completed, we have a numerical solution to the entire spacetime up to the current evolution step. As described a bit later in this section, we can then calculate the gravitational-wave signal, *i.e.* the *news* at $\mathcal{J}^+$.

While characteristic extraction appears to be only a coordinate transformation, it is actually rather more complicated. The difficulty is that Bondi-Sachs coordinates use a surface area radial coordinate, and this coordinate can be constructed only once the angular coefficients of the metric have been found. Thus the construction proceeds in two stages.

In the first stage (see Figure 5.2), we use an affine coordinate λ in the radial direction, and find the transformed metric and its first λ-derivatives at angular grid-points of the extraction world-tube Γ. The process can be summarized as follows.

- Define a world-tube Γ by $x^2+y^2+z^2 = R^2$ with R constant, and induce angular coordinates ϕ^A on Γ as though in Euclidean space.

---

[3] The situation might be improved by dealing with the development and structure of caustics during evolution [270, 271].

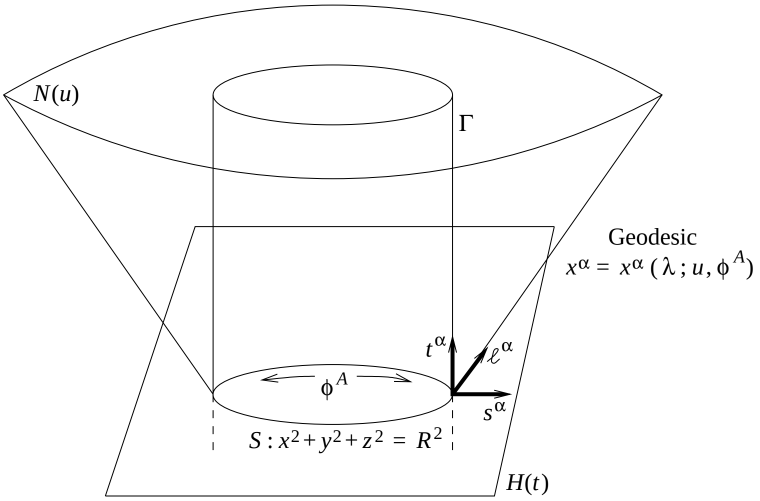

Figure 5.2: Schematic illustration of the (first stage) construction of the characteristic coordinates and metric.

- Let H be a hypersurface of constant t, and define the 2-surface $S = H \cap \Gamma$.
- Let t^α be a unit normal to H, and let s^α be normal to S in H.
- Construct outgoing null vectors $\ell^\alpha = t^\alpha + s^\alpha$, and then outgoing null geodesics in direction ℓ^α with affine parameter λ.
- The union of such geodesics is the null cone N, labeled by u being the Cauchy time t where N meets Γ.
- Construct the Jacobian for the coordinate transformation $(t, x, y, z) \to (u, \lambda, \phi^A)$.
- Find the transformed metric at the angular grid-points of Γ.
- Find the first λ-derivatives of the transformed metric at the angular grid-points of Γ.

In the second stage, we make the transformation to a surface area coordinate r. The difficulty here is that, in general, r is not constant on Γ. Thus in order to set data on an inner world-tube of the characteristic grid, we need the metric quantities on the world-tube, as well as their first derivatives off the world-tube. The process can be summarized as follows.

- Make the coordinate transformation $\lambda \to r = r(u, \lambda, \phi^A)$ with r defined by the condition that it is a surface area coordinate.
- Find r and $r_{,\lambda}$ at the grid points of Γ.
- Find the metric and its first λ-derivatives at the grid points of Γ.
- Find J, U, W and β at the grid points of Γ.
- Using $\partial_r = \partial_\lambda / r_{,\lambda}$, find $J_{,r}$, $U_{,r}$, $W_{,r}$ and $\beta_{,r}$ at the grid points of Γ.
- Set J, U, W_c and β on an inner world-tube of the characteristic grid.

In the following subsections, we will describe in detail the steps necessary to obtain characteristic boundary data from a Cauchy timeslice $H(t)$. This is more or less a copy of what has been written in [330] and is reported here for completeness.

Coordinate parametrization of the world-tube

The intersections $S_t = \Gamma \cap H(t)$ of the world-tube with the Cauchy timeslice $H(t)$ have spherical topology and can be parametrized by angular labels $\tilde{y}^A$ with $A = 2, 3$ on the sphere. These intersections are labeled by the time coordinate of the Cauchy foliation with $x^4 = t$. The future oriented null cones emanating from the world-tube are parametrized by the labels on the sphere

$\tilde{y}^A$ and an affine parameter λ along the radial direction and with $\lambda = 0$ on the world-tube. We can define an affine null coordinate system $\tilde{y}^\alpha = (\tilde{y}^1, \tilde{y}^A, \tilde{y}^4)$ with $\tilde{y}^1 \equiv y = t$ being the retarded time, $\tilde{y}^1 = \lambda$ and $\tilde{y}^A = \tilde{\phi}^A$ angular coordinates. A second null coordinate system (the Bondi coordinate system) is defined by $y^\alpha = (y^1, y^A, y^4)$ with $y^1 = r$ being a surface area coordinate, and $y^A = \tilde{y}^A$ and $y^4 = \tilde{y}^4$. According to the angular coordinate patches used in the characteristic evolution scheme (see Chapter 3), we cover the unit sphere with two stereographic coordinate maps

$$\xi_{\text{North}} = \sqrt{\frac{1-\cos\theta}{1+\cos\theta}}e^{i\phi}\,, \quad \xi_{\text{South}} = \sqrt{\frac{1+\cos\theta}{1-\cos\theta}}e^{-i\phi}\,, \tag{5.3.1}$$

where the complex coordinate ξ labels angular stereographic coordinates and (θ, ϕ) are the usual spherical polar coordinates. We introduce the notation $\tilde{y}^A \equiv \tilde{\phi}^A = (q,p)$ with $A = 2,3$ for the angular coordinates so that the complex coordinate ξ can be written as $\xi = q + ip$.

On each patch, we can furthermore introduce a complex dyad q^A which represents the unit sphere (compare Chapter 3)

$$q_{AB} = \frac{1}{2}(q_A\bar{q}_B + \bar{q}_A q_B) = \frac{4}{P^2}\begin{bmatrix} 1 & 0 \\ 0 & 1 \end{bmatrix} \tag{5.3.2}$$

with determinant $\det(q_{AB}) = 16/P^4$, and where $P = 1 + \xi\bar{\xi}$.

Next, we need to relate the Cartesian coordinates $x^i = (x, y, z)$ of the Cauchy timeslice $H(t)$ to the stereographic null coordinate system on its intersection with the world-tube Γ. Since we fix the location of the world-tube to be coordinates spheres $x^2 + y^2 + z^2 = R^2$ with R constant, we have

$$\begin{aligned} f^x(\tilde{y}^A) &= 2R\left(\frac{\text{Re}\,(\xi)}{1+\xi\bar{\xi}}\right)\,, \\ f^y(\tilde{y}^A) &= \pm 2R\left(\frac{\text{Im}\,(\xi)}{1+\xi\bar{\xi}}\right)\,, \\ f^z(\tilde{y}^A) &= \pm R\left(\frac{1-\xi\bar{\xi}}{1+\xi\bar{\xi}}\right)\,, \end{aligned} \tag{5.3.3}$$

where the positive (negative) sign corresponds to the north (south) patch.

4D geometry around the world-tube

The 4D geometry around the world-tube is fully determined by the 4D-metric and its derivatives. One can then define the unit normal n^α to the $t =$ const. slices, the outward pointing normal s^α to the world-tube and the generator of the outgoing null radial geodesics ℓ^α through the world-tube (see Figure 5.2). This completes the coordinate transformation from Cartesian to affine null coordinates $x^\alpha \to \tilde{y}^\alpha$ in a neighborhood of the world-tube.

In terms of the 3+1 ADM variables, *i.e.* the 3-metric g_{ij}, lapse α and shift β^i (see Section 2.1), the 4-metric $g_{\mu\nu}$ and its derivatives $g_{\mu\nu,\sigma}$ can be written as

$$\begin{aligned} g_{it} &= g_{ij}\beta^j\,, \\ g_{tt} &= -\alpha^2 + g_{it}\beta^i\,, \\ g_{it,\mu} &= g_{ij,\mu}\beta^j + g_{ij}\beta^j_{,\mu}\,, \\ g_{tt,\mu} &= -2\alpha\alpha_{,\mu} + g_{ij,\mu}\beta^i\beta^j + 2g_{ij}\beta^i\beta^j_{,\mu}\,. \end{aligned} \tag{5.3.4}$$

The unit normal n^μ to the hypersurface $H(t)$ is determined from the lapse and shift

$$n^\mu = \frac{1}{\alpha}\left(1, -\beta^i\right). \tag{5.3.5}$$

The outward pointing unit normal s^α to the intersection S_t of the world-tube at time t by construction lies in the slice $H(t)$ and reads $s^\alpha = (s^i, 0)$, *i.e.* is completely spacelike. This vector depends on the 3-metric of the Cauchy timeslice and the parametrization of the world-tube $x^i(\tilde{y}^A)$

$$q^i = \frac{\partial x^i}{\partial \tilde{y}^2}, \quad p^i = \frac{\partial x^i}{\partial \tilde{y}^3}. \tag{5.3.6}$$

which can be obtained from (5.3.3).

To obtain the components s^i, one defines the spatial normal 1-form σ_i and its norm which are given by

$$\sigma_i = \epsilon_{ijk}\, q^j p^k, \quad \sigma = \sqrt{g^{ij}\sigma_i\sigma_j}\,. \tag{5.3.7}$$

The components are then given by

$$s^i = g^{ij}\frac{\sigma_j}{\sigma}. \tag{5.3.8}$$

Finally, the generators ℓ^α of the outgoing null cone $N(t)$ through the intersection S_t are given on the world-tube by

$$\ell^\alpha = \frac{n^\alpha + s^\alpha}{\alpha - g_{ij}\beta^i s^j}\,, \tag{5.3.9}$$

which is normalized so that $\ell^\alpha t_\alpha = -1$, where $t^\alpha = \alpha n^\alpha + \beta^\alpha$ is the Cauchy evolution vector.

This completes the description of the 4D-geometry around the world-tube. Since the quantities in this subsection are all defined in a Cartesian coordinate basis, the next step is to represent these quantities in the null coordinate basis.

Coordinate transformation

This subsection describes the transformation of the 4D quantities introduced in the previous subsection from the Cartesian coordinate basis to the affine null coordinate basis in a neighborhood of the world-tube. Afterwards, we transform from the affine null coordinate basis to the Bondi coordinate basis which uses a Bondi areal radius coordinate r. This indirect route is necessary, since the Bondi surface area coordinate r is actually unknown until the angular coordinates are defined. The angular coordinates on the other hand can only be obtained after the null rays have been found.

Directly calculating the null rays which generate the hypersurface foliation of the characteristic evolution would require the numerical solution of a nonlinear PDE (the eikonal equation), and in order to avoid this, we instead prefer to solve the null geodesic equation in Cartesian coordinates in order to find the rays $x^\mu(\lambda)$ generating the null hypersurfaces. The solution $x^\alpha(\lambda)$ to the geodesic equation around the world-tube in Cartesian coordinates can be obtained analytically to second order as

$$x^\alpha = x^{(0)\alpha} + \ell^{(0)\alpha}\lambda + O(\lambda^2), \tag{5.3.10}$$

where

$$x^{(0)\alpha} = x^\alpha_{|\Gamma} \quad \text{and} \quad \ell^{(0)\alpha} = x^\alpha_{,\lambda\,|\Gamma} \tag{5.3.11}$$

are the coordinates of the points and the generators of the null cone at the intersection S_t of the world-tube.

Along each outgoing null geodesics $x^\alpha(\lambda)$ emanating from S_t, we can define angular and time coordinates by setting their values to be constant along the rays, and equal to their values on the world-tube

$$\tilde{y}^A = y^A_{|\Gamma} \quad \text{and} \quad \tilde{y}^4 \equiv \tilde{u} = t. \tag{5.3.12}$$

Upon definition of this affine null coordinate system, we can perform the basis transformation of the 4-metric from the Cartesian to affine null coordinate basis. The 4-metric in affine null coordinates $\tilde{\eta}_{\alpha\beta}$ is obtained from

$$\tilde{\eta}_{\tilde{\alpha}\tilde{\beta}} = \frac{\partial x^\mu}{\partial \tilde{y}^\alpha}\frac{\partial x^\nu}{\partial \tilde{y}^\beta} g_{\mu\nu}, \tag{5.3.13}$$

and will be computed in the next subsection. But first, we have to evaluate the Jacobians in the equation above.

Plugging in expansion (5.3.10) into $\partial x^\mu/\partial\tilde{y}^\alpha$ yields for the Jacobians

$$x^\mu_{,\tilde{\alpha}} \equiv \frac{\partial x^\mu}{\partial \tilde{y}^\alpha} = x^{(0)\mu}_{\ \ ,\tilde{\alpha}} + x^{(1)\mu}_{\ \ ,\tilde{\alpha}}\lambda + O(\lambda^2), \quad x^{(1)\mu}_{\ \ ,\tilde{\alpha}} \equiv \ell^{(0)\mu}_{\ \ ,\tilde{\alpha}}, \quad \text{for} \quad \tilde{\alpha} = (\tilde{A}, \tilde{u}). \tag{5.3.14}$$

Because the radial coordinate λ is an affine parameter of the null geodesics, radial derivatives in (5.3.14) can be omitted and the $\tilde{\eta}_{\lambda\tilde{\mu}}$ components of the null metric are fixed and read

$$\tilde{\eta}_{\lambda\lambda} = \tilde{\eta}_{\lambda\tilde{A}} = 0, \quad \tilde{\eta}_{\lambda\tilde{u}} = -1, \tag{5.3.15}$$

which follows from the conditions $s^\alpha n_\alpha = 0$, $\ell^\alpha \ell_\alpha = 0$, $s^\alpha s_\alpha = 1$, $n^\alpha n_\alpha = -1$ and $t^\alpha \ell_\alpha = -1$.

Furthermore, the world-tube was setup such that the intersections S_t are at $t =$ const. so that time derivatives vanish and only the angular derivatives of the $x^{(0)i}$ for $i = 1, 2, 3$ contribute. This means that the leading order part $\mathcal{O}(\lambda^0)$ of the Jacobian is then given by the condition $\partial t/\partial\tilde{u}_{|\Gamma} = 1$ and by

$$x^{(0)i}{}_{,\tilde{A}} = \frac{\partial f^i(\tilde{y}^B)}{\partial \tilde{y}^A}, \tag{5.3.16}$$

which is known analytically by means of expressions (5.3.3). The next higher order term $\mathcal{O}(\lambda)$ of the Jacobian obeys

$$x^\mu_{,\lambda\tilde{A}} = \ell^\mu_{,\tilde{A}}, \quad x^\mu_{,\lambda\tilde{u}} = \ell^\mu_{,\tilde{u}}, \tag{5.3.17}$$

which follows from (5.3.10) and (5.3.11).

From (5.3.9), we see that in order to evaluate the derivatives of ℓ^μ, we have to calculate the derivatives of n^μ and s^i. This can be done by directly using the 3+1 ADM quantities, *i.e.* lapse α, shift β^i and the 3-metric g_{ij}.

The 3+1 derivatives in Cartesian coordinates are given by

$$\begin{aligned} n^i_{,j} &= \frac{1}{\alpha^2}\left(\alpha_{,j}\beta^i - \alpha\beta^i_{,j}\right), \\ n^t_{,j} &= -\frac{1}{\alpha^2}\alpha_{,j}. \end{aligned} \tag{5.3.18}$$

The retarded time derivative $\partial_{\tilde{u}}$ at $\lambda =$ const. is simply the $3+1$ time derivative ∂_t, therefore $n^\mu_{,\tilde{u}} = n^\mu_{,t}$ where

$$\begin{aligned} n^i_{,t} &= \frac{1}{\alpha^2}\left(\alpha_{,t}\beta^i - \alpha\beta^i_{,t}\right), \\ n^t_{,t} &= -\frac{1}{\alpha^2}\alpha_{,t}. \end{aligned} \tag{5.3.19}$$

From (5.3.8), and since the σ_k are time-independent, the time derivative of s^i is given by

$$\begin{aligned} s^i_{,t} &= g^{ik}_{,t}\frac{\sigma_k}{\sigma} - g^{ik}\frac{\sigma_k\sigma_{,t}}{\sigma^2} = -g^{im}g^{kn}g_{mn,t}\frac{\sigma_k}{\sigma} - s^i\frac{\sigma_{,t}}{\sigma} \\ &= -g^{im}g_{mn,t}s^n - s^i\frac{\sigma_{,t}}{\sigma}, \end{aligned} \tag{5.3.20}$$

where the time derivative of σ can be calculated from

$$2\sigma\sigma_{,t} = \left(\sigma^2\right)_{,t} = g^{kl}_{,t}\sigma_k\sigma_l = -g^{km}g^{ln}g_{mn,t}\sigma_k\sigma_l = -s^m s^n g_{mn,t}\sigma^2, \tag{5.3.21}$$

with the resulting expression

$$s^i_{,t} = \left(-g^{im} + s^i\frac{1}{2}s^m\right)g_{mn,t}s^n. \tag{5.3.22}$$

Since all these derivatives are in terms of Cartesian coordinates, we now have to transform them to the null coordinate basis. For $\lambda =$ const., this can be accomplished by using the leading order term $\mathcal{O}(\lambda^0)$ in the Jacobian (5.3.14) so that

$$n^\mu_{,\tilde{A}} = n^\mu_{,j}x^j_{,\tilde{A}}. \tag{5.3.23}$$

By using (5.3.8), we can write the angular derivatives of s^i as

$$\begin{aligned} s^i{}_{,\tilde{A}} &= g^{ik}_{,j}\, x^j{}_{,\tilde{A}} \frac{\sigma_k}{\sigma} + g^{ik} \frac{\sigma_{k,\tilde{A}}}{\sigma} - g^{ik} \frac{\sigma_k \sigma_{,\tilde{A}}}{\sigma^2} \\ &= -\, g^{in} g^{km} g_{mn,j}\, x^j{}_{,\tilde{A}} \frac{\sigma_k}{\sigma} + g^{ik} \frac{\sigma_{k,\tilde{A}}}{\sigma} - s^i \frac{\sigma_{,\tilde{A}}}{\sigma} \,, \end{aligned} \tag{5.3.24}$$

where the $\sigma_{k,\tilde{A}}$ are obtained from the analytic expressions (5.3.3), and $\sigma_{,\tilde{A}}$ from

$$\begin{aligned} 2\sigma\sigma_{,\tilde{A}} &= \left(\sigma^2\right)_{,\tilde{A}} = \left(g^{kl}\sigma_k\sigma_l\right)_{,\tilde{A}} = g^{kl}_{,j}\, x^j{}_{,\tilde{A}}\sigma_k\sigma_l + 2\, g^{kl}\sigma_l\sigma_{k,\tilde{A}} \\ &= -\, g^{km} g^{ln} g_{mn,j} x^j_{,}\sigma_k\sigma_l + 2\, g^{kl}\sigma_l\sigma_{k,\tilde{A}} \\ &= -\, s^m s^n g_{mn,j} x^j{}_{,\tilde{A}}\sigma^2 + 2 s^k \sigma\sigma_{k,\tilde{A}} \,. \end{aligned} \tag{5.3.25}$$

Collecting (5.3.24) and (5.3.25), we arrive at the angular derivatives of the normal to the world-tube

$$\begin{aligned} s^i{}_{,\tilde{A}} &= -g^{in} s^m g_{mn,j}\, x^j{}_{,\tilde{A}} + g^{ik} \frac{\sigma_{k,\tilde{A}}}{\sigma} + s^i \left(\frac{1}{2} s^m s^n g_{mn,j} x^j{}_{,\tilde{A}} - s^k \frac{\sigma_{k,\tilde{A}}}{\sigma} \right) \\ &= \left(g^{in} - s^i s^n\right) \frac{\sigma_{n,\tilde{A}}}{\sigma} + \left(-g^{in} + \frac{1}{2} s^i s^n \right) s^m g_{mn,j} x^j{}_{,\tilde{A}} \,. \end{aligned} \tag{5.3.26}$$

Null metric

We are now ready to apply the Jacobian transformation (5.3.13) to obtain the 4-metric in the affine null coordinate basis.

However, before we proceed, we note that it is necessary to know the null-metric not only on, but also slightly off the world-tube. The reason is that the coordinates of the gridpoints of our world-tube do not necessarily coincide with the gridpoints of the characteristic evolution code. This is because the coordinates of the world-tube have been chosen to be fixed at $R^2 = x^2 + y^2 + z^2 =$ const. whereas the characteristic code uses a surface area radius coordinate which depends on the geometry on the world-tube.

In order to avoid the rather complicated implementation of a full 4D interpolation scheme, we can alternatively introduce an expansion of the null metric along the affine parameter λ:

$$\tilde{\eta}_{\tilde{\alpha}\tilde{\beta}} = \tilde{\eta}^{(0)}_{\tilde{\alpha}\tilde{\beta}} + \tilde{\eta}_{\tilde{\alpha}\tilde{\beta},\lambda}\lambda + O(\lambda^2). \tag{5.3.27}$$

This allows us to represent the null metric slightly off the world-tube to second-order accuracy in order to be able to assign its values to the gridpoints of the null code. By applying the Jacobian transformation, we can then express the coefficients

$$\begin{aligned} \tilde{\eta}^{(0)}_{\tilde{u}\tilde{u}} &= g_{tt|\Gamma} \,, \\ \tilde{\eta}^{(0)}_{\tilde{u}\tilde{A}} &= x^i{}_{,\tilde{A}} g_{it|\Gamma} \,, \\ \tilde{\eta}^{(0)}_{\tilde{A}\tilde{B}} &= x^i{}_{,\tilde{A}} x^j{}_{,\tilde{B}} g_{ij|\Gamma} \,, \end{aligned} \tag{5.3.28}$$

and, for the λ derivative

$$\begin{aligned} \tilde{\eta}_{\tilde{u}\tilde{u},\lambda} &= \Big[g_{tt,\lambda} + 2\, \ell^\mu{}_{,\tilde{u}} g_{\mu t} \Big]_{|\Gamma} + O(\lambda) \,, \\ \tilde{\eta}_{\tilde{u}\tilde{A},\lambda} &= \Big[x^k{}_{,\tilde{A}} \Big(\ell^\mu{}_{,\tilde{u}} g_{k\mu} + g_{kt,\lambda} \Big) + \ell^k{}_{,\tilde{A}} g_{kt} + \ell^t{}_{,\tilde{A}} g_{tt} \Big]_{|\Gamma} + O(\lambda), \\ \tilde{\eta}_{\tilde{A}\tilde{B},\lambda} &= \Big[x^k{}_{,\tilde{A}} x^l{}_{,\tilde{B}} g_{kl,\lambda} + \Big(\ell^\mu{}_{,\tilde{A}} x^l{}_{,\tilde{B}} + \ell^\mu{}_{,\tilde{B}} x^l{}_{,\tilde{A}} \Big) g_{\mu l} \Big]_{|\Gamma} + O(\lambda), \end{aligned} \tag{5.3.29}$$

where

$$g_{\alpha\beta,\lambda|\Gamma} = g^{(0)}_{\alpha\beta,\mu}\ell^{(0)\mu}\,. \tag{5.3.30}$$

The contravariant null metric $\tilde{\eta}^{\alpha\beta}$ can be similarly obtained by expanding it in powers of λ,

$$\tilde{\eta}^{\tilde{\mu}\tilde{\nu}} = \tilde{\eta}^{(0)\,\tilde{\mu}\tilde{\nu}} + \tilde{\eta}^{\tilde{\mu}\tilde{\nu}}_{,\lambda}\lambda + O(\lambda^2), \tag{5.3.31}$$

with coefficients given by

$$\tilde{\eta}^{(0)\,\tilde{\mu}\tilde{\alpha}}\tilde{\eta}^{(0)}_{\tilde{\alpha}\tilde{\nu}} = \delta^{\tilde{\mu}}_{\tilde{\nu}}, \quad \tilde{\eta}^{\tilde{\mu}\tilde{\nu}}_{,\lambda} = -\tilde{\eta}^{\tilde{\mu}\tilde{\alpha}}\,\tilde{\eta}^{\tilde{\beta}\tilde{\nu}}\,\tilde{\eta}_{\tilde{\alpha}\tilde{\beta},\lambda}. \tag{5.3.32}$$

It follows from (5.3.15) that the following components of the contravariant null metric in the $\tilde{y}^\alpha$ coordinates are fixed

$$\tilde{\eta}^{\lambda\tilde{u}} = -1, \quad \tilde{\eta}^{\tilde{u}\tilde{A}} = \tilde{\eta}^{\tilde{u}\tilde{u}} = 0, \tag{5.3.33}$$

therefore the contravariant null metric can be computed by

$$\begin{aligned} \tilde{\eta}^{\tilde{A}\tilde{B}}\tilde{\eta}_{\tilde{B}\tilde{C}} &= \delta^{\tilde{A}}_{\tilde{C}}\,, \\ \tilde{\eta}^{\lambda\tilde{A}} &= \tilde{\eta}^{\tilde{A}\tilde{B}}\tilde{\eta}_{\tilde{B}\tilde{u}}\,, \\ \tilde{\eta}^{\lambda\lambda} &= -\tilde{\eta}_{\tilde{u}\tilde{u}} + \tilde{\eta}^{\lambda\tilde{A}}\tilde{\eta}_{\tilde{A}\tilde{u}}\,, \end{aligned} \tag{5.3.34}$$

and similarly for its λ derivative

$$\begin{aligned} \tilde{\eta}^{\tilde{A}\tilde{B}}_{,\lambda} &= -\tilde{\eta}^{\tilde{A}\tilde{C}}\tilde{\eta}^{\tilde{B}\tilde{D}}\tilde{\eta}_{\tilde{C}\tilde{D},\lambda}\,, \\ \tilde{\eta}^{\lambda\tilde{A}}_{,\lambda} &= \tilde{\eta}^{\tilde{A}\tilde{B}}\left(\tilde{\eta}_{\tilde{u}\tilde{B},\lambda} - \tilde{\eta}^{\lambda\tilde{C}}\tilde{\eta}_{\tilde{C}\tilde{B},\lambda}\right)\,, \\ \tilde{\eta}^{\lambda\lambda}_{,\lambda} &= -\tilde{\eta}_{\tilde{u}\tilde{u},\lambda} + 2\,\tilde{\eta}^{\lambda\tilde{A}}\tilde{\eta}_{\tilde{u}\tilde{A},\lambda} - \tilde{\eta}^{\lambda\tilde{A}}\tilde{\eta}^{\lambda\tilde{B}}\tilde{\eta}_{\tilde{A}\tilde{B},\lambda}\,. \end{aligned} \tag{5.3.35}$$

The next step is the final transformation of the null metric to Bondi coordinates.

Metric in Bondi coordinates

The surface area coordinate $r(u,\lambda,\tilde{y}^A)$ is defined by

$$r = \left(\frac{det(\tilde{\eta}_{\tilde{A}\tilde{B}})}{det(q_{AB})}\right)^{\frac{1}{4}}\,, \tag{5.3.36}$$

where, for our choice of stereographic coordinates $\xi = q + ip$, we use $\tilde{y}^A \equiv y^A = (q,p)$ and $\det(q_{AB}) = 16/(1+q^2+p^2)^4$. To carry out the final coordinate transformation $\tilde{y}^\alpha \to y^\alpha$ for the null metric, we need to know $r_{,\lambda}$, $r_{,\tilde{A}}$ and $r_{,\tilde{u}}$. From (5.3.36) it follows

$$r_{,\lambda} = \frac{r}{4}\tilde{\eta}^{\tilde{A}\tilde{B}}\tilde{\eta}_{\tilde{A}\tilde{B},\lambda}\,. \tag{5.3.37}$$

Similarly,

$$r_{,\tilde{C}} = \frac{r}{4}\left(\tilde{\eta}^{\tilde{A}\tilde{B}}\tilde{\eta}_{\tilde{A}\tilde{B},\tilde{C}} - \frac{det(q_{\tilde{A}\tilde{B}})_{,\tilde{C}}}{det(q_{\tilde{A}\tilde{B}})}\right)\,, \tag{5.3.38}$$

where

$$\begin{aligned} \frac{det(q_{\tilde{A}\tilde{B}})_{,\tilde{C}}}{det(q_{\tilde{A}\tilde{B}})} &= -\frac{8}{1+q^2+p^2}\tilde{y}^{\tilde{C}}\,, \\ \tilde{\eta}_{\tilde{A}\tilde{B},\tilde{C}} &= \left(x^i_{,\tilde{A}\tilde{C}}\,x^j_{,\tilde{B}} + x^i_{,\tilde{A}}\,x^j_{,\tilde{B}\tilde{C}}\right)g_{ij} + x^i_{,\tilde{A}}\,x^j_{,\tilde{B}}\,x^k_{,\tilde{C}}\,g_{ij,k}\,, \end{aligned} \tag{5.3.39}$$

with the $x^i_{,\tilde{A}\tilde{C}}$ given functions of (q, p). From (5.3.36) and (5.3.28)

$$r_{,\tilde{u}} = \frac{r}{4}\,\tilde{\eta}^{\tilde{A}\tilde{B}}\tilde{\eta}_{\tilde{A}\tilde{B},\tilde{u}}\,, \tag{5.3.40}$$

where

$$\tilde{\eta}_{\tilde{A}\tilde{B},\tilde{u}} = \left[x^i_{,\tilde{A}}\,x^j_{,\tilde{B}}\,g_{ij,t}\right]_{|\Gamma} + O(\lambda)\,. \tag{5.3.41}$$

The null metric $\eta^{\alpha\beta}$ in Bondi coordinates is defined on the world-tube Γ by

$$\eta^{\alpha\beta} = \frac{\partial y^\alpha}{\partial \tilde{y}^\mu}\frac{\partial y^\beta}{\partial \tilde{y}^\nu}\tilde{\eta}^{\tilde{\mu}\tilde{\nu}}\,. \tag{5.3.42}$$

Note that the metric of the sphere is unchanged by this coordinate transformation, i.e. $\eta^{AB} = \tilde{\eta}^{\tilde{A}\tilde{B}}$, so it is only necessary to compute the components η^{rr}, η^{rA} and η^{ru} on Γ, or equivalently the metric functions β, U^A and V (compare Section 3.1). From (5.3.33),

$$\begin{aligned}
\eta^{rr} &= r_{,\tilde{\alpha}}\,r_{,\tilde{\beta}}\,\tilde{\eta}^{\tilde{\alpha}\tilde{\beta}} = (r_{,\lambda})^2\,\tilde{\eta}^{\lambda\lambda} + 2\,r_{,\lambda}\left(r_{,\tilde{A}}\,\tilde{\eta}^{\lambda\tilde{A}} - r_{,\tilde{u}}\right) + r_{,\tilde{A}}\,r_{,\tilde{B}}\,\tilde{\eta}^{\tilde{A}\tilde{B}}\,,\\
\eta^{rA} &= r_{,\tilde{\alpha}}\,\tilde{\eta}^{\tilde{\alpha}\tilde{A}} = r_{,\lambda}\,\tilde{\eta}^{\lambda\tilde{A}} + r_{,\tilde{B}}\,\tilde{\eta}^{\tilde{A}\tilde{B}}\,,\\
\eta^{ru} &= r_{,\tilde{\alpha}}\,\tilde{\eta}^{\tilde{\alpha}\tilde{u}} = -r_{,\lambda}\,.
\end{aligned} \tag{5.3.43}$$

The contravariant Bondi metric can be written in the form

$$\eta^{\alpha\,\beta} = \begin{bmatrix} e^{-2\,\beta}\dfrac{V}{r} & -e^{-2\,\beta}U^2 & -e^{-2\,\beta}U^3 & -e^{-2\,\beta} \\ -e^{-2\,\beta}U^2 & r^{-2}\,h^{22} & r^{-2}\,h^{23} & 0 \\ -e^{-2\,\beta}U^3 & r^{-2}\,h^{32} & r^{-2}\,h^{33} & 0 \\ -e^{-2\,\beta} & 0 & 0 & 0 \end{bmatrix}, \tag{5.3.44}$$

where h_{AB} is a metric on the sphere of surface area 4π, such that $h_{AB}h^{BC} = \delta_A^C$ and $det(h_{AB}) = det(q_{AB}) = q$, for q_{AB} a unit sphere metric.

The remaining task is to express the metric functions in terms of the variables that are used by the characteristic evolution code.

Bondi variables for starting up the null code at the world-tube

As described in Chapter 3, the characteristic evolution equations are written in terms of the spin-weighted quantities β, U, W and J and it is the necessary final step to express the null metric in terms of these quantities. As we need to know these variables slightly off the world-tube due to the discretization of the equations, we will again make use of the expansion in powers of λ.

We start with the metric function

$$J \equiv \frac{1}{2}q^A q^B h_{AB}\,, \tag{5.3.45}$$

where q^A is the complex dyad representing the unit sphere. We know that

$$\eta_{AB} = \tilde{\eta}_{AB} \equiv r^2 h_{AB}\,, \tag{5.3.46}$$

$$\begin{aligned}
h_{AB} &= \frac{1}{r^2}\eta_{AB}\,,\\
h_{AB,\lambda} &= \frac{1}{r^2}\left(\eta_{AB,\lambda} - \frac{2\,r_{,\lambda}}{r}\,\eta_{AB}\right),
\end{aligned} \tag{5.3.47}$$

and we can expand

$$J(y^\alpha) = J + J_{,\lambda}\lambda + O(\lambda^2)\,, \tag{5.3.48}$$

where the coefficients are given by

$$\begin{aligned} J &= \frac{1}{2\,r^2} q^A q^B \eta_{AB}\,, \\ J_{,\lambda} &= \frac{1}{2\,r^2} q^A q^B \eta_{AB,\lambda} - 2\,\frac{r_{,\lambda}}{r} J\,. \end{aligned} \tag{5.3.49}$$

Next, we consider the "expansion factor" β. From (5.3.43) we see that metric function β can be expressed as

$$\beta = -\frac{1}{2}\log(r_{,\lambda}). \tag{5.3.50}$$

Since again, we want to expand in terms of λ, we would require the second derivative $r_{,\lambda\lambda}$ and in order to circumvent this we make use of the characteristic equation

$$\beta_{,r} = \frac{r}{8}\left(J_{,r}\bar{J}_{,r} - (K_{,r})^2\right)\,, \tag{5.3.51}$$

where K is defined as

$$K \equiv \frac{1}{2} q^A \bar{q}^B h_{AB}\,. \tag{5.3.52}$$

At constant angles (q,p), the relation $\partial_\lambda = r_{,\lambda}\partial_r$ holds, and we know from (5.3.49) J and $J_{,\lambda}$ for each outgoing radial null geodesic through the world-tube. Thus we can write

$$\beta_{,\lambda} = \frac{r}{8\,r_{,\lambda}}\left(J_{,\lambda}\bar{J}_{,\lambda} - (K_{,\lambda})^2\right)\,. \tag{5.3.53}$$

By means of definition (5.3.52), it follows that

$$K_{,\lambda} = \frac{1}{K}\mathrm{Re}\,\left(\bar{J}J_{,\lambda}\right)\,, \tag{5.3.54}$$

so that finally

$$\beta_{,\lambda} = \frac{r}{8\,r_{,\lambda}}\left(J_{,\lambda}\bar{J}_{,\lambda} - \frac{1}{1+J\bar{J}}\left[\mathrm{Re}\,\left(\bar{J}J_{,\lambda}\right)\right]^2\right)\,. \tag{5.3.55}$$

Then, β is found to second-order accuracy by:

$$\beta(y^\alpha) = \beta + \beta_{,\lambda}\lambda + O(\lambda^2). \tag{5.3.56}$$

Next we consider the "shift" U. This function is related to the Bondi metric (5.3.44) by using (5.3.43) by

$$U \equiv U^A q_A = \frac{\eta^{rA}}{\eta^{ru}} q_A = -\left(\tilde{\eta}^{\lambda\tilde{A}} + \frac{r_{,\tilde{B}}}{r_{,\lambda}}\tilde{\eta}^{\tilde{A}\tilde{B}}\right) q_{\tilde{A}}\,. \tag{5.3.57}$$

Again we need the λ-derivative for the world-tube-expansion. In order to eliminate the second derivative $r_{\lambda\lambda}$ we make use of relation

$$\beta_{,\lambda} = -\frac{\eta^{ru}_{,\lambda}}{2\,\eta^{ru}} = -\frac{r_{,\lambda\lambda}}{2\,r_{,\lambda}}\,, \tag{5.3.58}$$

so that we get

$$\begin{aligned} U_{,\lambda} &= -\left[\tilde{\eta}^{\lambda\tilde{A}}_{,\lambda} + \left(\frac{r_{,\lambda\tilde{B}}}{r_{,\lambda}} - \frac{r_{,\tilde{B}}\,r_{,\lambda\lambda}}{r^2_{,\lambda}}\right)\tilde{\eta}^{\tilde{A}\tilde{B}} + \frac{r_{,\tilde{B}}}{r_{,\lambda}}\tilde{\eta}^{\tilde{A}\tilde{B}}_{,\lambda}\right] q_{\tilde{A}}, \\ &= -\left(\tilde{\eta}^{\lambda\tilde{A}}_{,\lambda} + \frac{r_{,\lambda\tilde{B}}}{r_{,\lambda}}\tilde{\eta}^{\tilde{A}\tilde{B}} + \frac{r_{,\tilde{B}}}{r_{,\lambda}}\tilde{\eta}^{\tilde{A}\tilde{B}}_{,\lambda}\right) q_{\tilde{A}} + 2\,\beta_{,\lambda}\left(U + \tilde{\eta}^{\lambda\tilde{A}} q_{\tilde{A}}\right)\,. \end{aligned} \tag{5.3.59}$$

Then, U is found to second-order accuracy by:

$$U(y^\alpha) = U + U_{,\lambda}\lambda + O(\lambda^2). \tag{5.3.60}$$

Finally, we need to relate the "mass aspect" W. This variable is related to V in the Bondi-metric (5.3.44) by $W \equiv (V - r)/r^2$. The reasons for introducing this variable is the fact that $V = r$ in Minkowski space and hence it is not regular at null infinity as $r \Rightarrow \infty$. In terms of the contravariant null metric (with the affine parameter λ as the radial coordinate)

$$W = \frac{1}{r}\left(\frac{\eta^{rr}}{r_{,\lambda}} - 1\right) = \frac{1}{r}\left(r_{,\lambda}\tilde{\eta}^{\lambda\lambda} + 2\left(r_{,\tilde{A}}\,\tilde{\eta}^{\lambda\tilde{A}} - r_{,u}\right) + \frac{r_{,\tilde{A}}\,r_{,\tilde{B}}}{r_{,\lambda}}\,\tilde{\eta}^{\tilde{A}\tilde{B}} - 1\right). \tag{5.3.61}$$

The λ derivative of W is given by

$$\begin{aligned}
W_{,\lambda} \;&=\; -\frac{r_{,\lambda}}{r}W + \frac{1}{r}\left(r_{,\lambda}\tilde{\eta}^{\lambda\lambda} + 2\left(r_{,\tilde{A}}\,\tilde{\eta}^{\lambda\tilde{A}} - r_{,u}\right) + \frac{r_{,\tilde{A}}\,r_{,\tilde{B}}}{r_{,\lambda}}\,\tilde{\eta}^{\tilde{A}\tilde{B}} - 1\right)_{,\lambda} \\
&=\; -\frac{r_{,\lambda}}{r}\left(\left(\frac{r_{,\lambda}}{r} + 2\,\beta_{,\lambda}\right)\tilde{\eta}^{\lambda\lambda} - \tilde{\eta}^{\lambda\lambda}_{,\lambda} - \frac{1}{r}\right) + \frac{2}{r}\left(\frac{r_{,\lambda}r_{,u}}{r} - r_{,\lambda u}\right) \\
&\quad + \frac{2}{r}\left(r_{,\lambda\tilde{A}} - \frac{r_{,\lambda}r_{,\tilde{A}}}{r}\right)\tilde{\eta}^{\lambda\tilde{A}} + 2\frac{r_{,\tilde{A}}}{r}\,\tilde{\eta}^{\lambda\tilde{A}}_{,\lambda} \\
&\quad + \frac{r_{,\tilde{B}}}{r\,r_{,\lambda}}\left(2\,r_{,\lambda\tilde{A}}\tilde{\eta}^{\tilde{A}\tilde{B}} + 2\,\beta_{,\lambda}r_{,\tilde{A}} + r_{,\tilde{A}}\tilde{\eta}^{\tilde{A}\tilde{B}}_{,\lambda}\right) - \frac{r_{,\tilde{A}}\,r_{,\tilde{B}}}{r^2}\,\tilde{\eta}^{\tilde{A}\tilde{B}}\,.
\end{aligned} \tag{5.3.62}$$

Then, W is found to second-order accuracy by:

$$W(y^\alpha) = W + W_{,\lambda}\lambda + O(\lambda^2). \tag{5.3.63}$$

It should be noted that the characteristic code actually uses the variable $W_c = r^{-2}W$.

It is now possible to provide $J_{|\Gamma}, U_{|\Gamma}, \beta_{|\Gamma}, W_{|\Gamma}$ as boundary data for the characteristic evolution at each time-step. The code is then evolved according to the system as described in chapter (3). However, in order to extract the gravitational-wave signal at $\mathscr{J}^+$, one has to relate the characteristic variables to the extraction quantities, *i.e.* Ψ_4 and the Bondi news function, at future null infinity. This will be described in the next subsection.

Obtaining the Bondi news and Ψ_4

The final step for obtaining the gravitational-radiation signal at future null infinity after the construction of the boundary data from a Cauchy evolution step and the subsequent characteristic evolution step is the computation of the Bondi news function and the complex Weyl component Ψ_4 at $\mathscr{J}^+$. As already outlined in previous sections, these two functions describe the radiation content of a spacetime. In this subsection, we summarize the procedure for obtaining these functions and will mainly repeat what has already been published in [273, 277, 331].

The mathematical theory relating metric quantities at future null infinity, $\mathscr{J}^+$, to gravitational radiation, and using the present formalism, is given in [273, 277, 331]. In the original work of Bondi *et al.* [135], it was possible to assume that the coordinates at $\mathscr{J}^+$ were such that $\beta = J = 0$ there, and in that case the gravitational news takes the very simple form

$$N = \frac{1}{2}\partial_u\partial_\ell J\,, \tag{5.3.64}$$

where ℓ is an inverse radial coordinate to be defined later. However, the coordinates used in the characteristic code are fixed at the inner boundary Γ, and in general the Bondi gauge conditions are not true. Previous work has presented the formalism for calculating, in a general gauge, the gravitational news [273], as well as Ψ_4 [277].

Geometrically, the Bondi gauge condition $J = 0$ means that, for large r, a 2-surface of constant (u, r) is really spherical rather than being, for example, an ellipsoid; this condition can be expressed algebraically by saying that the 2-surface has constant curvature. An expression for the news, in a general gauge, must take (implicit) account of the transformation to Bondi gauge coordinates,

$$r \to r_B = \omega(u, y^A)r, \qquad y^A \to y_B^A = y_B^A(u, y^A). \tag{5.3.65}$$

The Bondi gauge condition $\beta = 0$ at $\mathscr{J}^+$ means that, for large r, coordinate time is the same as proper time, and the implementation of this condition is straightforward.

While the transformation to Bondi gauge coordinates can be done explicitly [331], in the present code it is done implicitly leading to an expression for the news in terms of the code metric variables and coordinates.

In order to construct the Bondi news function at null infinity, it is useful to introduce the conformal compactification of the Bondi metric (5.3.44) $d\hat{s}^2 = \ell ds^2$ where $\ell = 1/r$ is an inverse radial coordinate so that $\mathscr{J}^+$ is located at $\ell = 0$. By using the coordinates (ℓ, y^A, u), the compactified Bondi metric reads

$$\begin{aligned} d\hat{s}^2 &= -\left(e^{2\beta}V\ell^3 - h_{AB}U^AU^B\right)du^2 + 2e^{2\beta}dud\ell - 2h_{AB}U^Bdudy^A + h_{AB}dy^Ady^B \\ &= \hat{g}_{\mu\nu}dy^\mu dy^\nu \,. \end{aligned} \tag{5.3.66}$$

The news function can be constructed from the leading coefficients in an expansion of (5.3.66) in powers of the inverse radial coordinate ℓ. The coefficients are functions of the time u and angular coordinates y^A and read

$$h_{AB} = H_{AB} + \ell c_{AB} + O(\ell^2)\,, \tag{5.3.67}$$

$$\beta = H + O(\ell^2)\,, \tag{5.3.68}$$

(where the $O(\ell)$ term vanishes),

$$U^A = L^A + 2\ell e^{2H} H^{AB} D_B H + O(\ell^2)\,, \tag{5.3.69}$$

and

$$\ell^2 V = D_A L^A + \ell(e^{2H}\mathcal{R}/2 + D_A D^A e^{2H}) + O(\ell^2)\,, \tag{5.3.70}$$

where $\mathcal{R}$ and D_A are the 2-dimensional curvature scalar and covariant derivative associated with the metric h_{AB}. The expansion coefficients H, H_{AB}, c_{AB} and L^A completely determine the radiation field. In an inertial Bondi coordinate system at $\mathscr{J}^+$, *i.e.* when the coordinates have Minkowski form, these coefficients would reduce to $H = L^A = 0$ and $H_{AB} = q_{AB}$ (where q_{AB} is the unit sphere metric) and the radiation would be completely contained in c_{AB}. Unfortunately, the null coordinates at $\mathscr{J}^+$ are determined by the induced coordinates at the world-tube (see previous subsections) so that generally, we do not have an inertial Bondi frame. However, we can always find an inertial Bondi coordinate system (ℓ_B, q_B, p_B, u_B) and an associated conformal metric $d\tilde{s}_B^2 = \omega^2 d\hat{s}^2$ with $\omega > 0$ such that

1. $\frac{\partial}{\partial u_B}$ is null and affine and points along the null generators at $\mathscr{J}^+$,
2. $\ell_B = \omega\ell + \mathcal{O}(\ell^2)$,
3. the conformal metric $d\tilde{s}_B^2$ in the subspace ($u_B =$ const., $\ell_{\rm B} =$ const.) is the unit sphere metric on $\mathscr{J}^+$.

We can fix a null tetrad on $\mathscr{J}^+$ in the inertial Bondi coordinates by setting

$$\tilde{n}^a = (1, 0, 0, 0)\,, \tag{5.3.71}$$

$$\tilde{\ell}^a = (0, 0, 0, 1)\,, \tag{5.3.72}$$

$$\tilde{m}^a = (0, \tilde{P}/2, i\tilde{P}/2, 0)\,. \tag{5.3.73}$$

Here, $\tilde{P} = 1 + q_B^2 + p_B^2$, and we note that $\tilde{m}^{(A}\bar{\tilde{m}}^{B)} = q^{AB}$ as required. We define a dyad adapted to the coordinates in the code, *i.e.* related to H^{AB} by $F^{(A}\bar{F}^{B)} = H^{AB}$, which reads

$$F^A = q^A \sqrt{\frac{K_0 + 1}{2}} - J_0 \bar{q}^A \sqrt{\frac{1}{2(K_0 + 1)}}\,, \tag{5.3.74}$$

where q_A is the dyad (5.3.2) representing the unit sphere metric and $J_0 = q^A q^B H_{AB}/2$, and $K_0 = q^A \bar{q}^B H_{AB}/2$.

We write $F^a = (0, F^A, 0)$, and F^a is related to $\tilde{m}^a$ by

$$\tilde{m}^a = e^{-i\delta}\omega^{-1}F^a + \gamma\tilde{n}^a \,. \tag{5.3.75}$$

Using the new dyad (5.3.74), the Bondi news function is then given by

$$N = \frac{1}{4}\mathrm{e}^{-2i\delta}\omega^{-2}e^{-2H}F^A F^B\Big(\left(\partial_u + \mathcal{L}\right)c_{AB} - \frac{1}{2}c_{AB}D_C L^C + 2\omega D_A[\omega^{-2}D_B(\omega e^{2H})]\Big)\,, \tag{5.3.76}$$

where D_A is the covariant derivative with respect to H_{AB}.

In order to calculate this function, one needs to evolve two scalar quantities, the phase factor δ introduced in (5.3.75) and the conformal factor ω. Additionally, one needs to evaluate the angular code coordinate function as a function of the inertial angular coordinates $\xi(\xi_B)$, as well as the Bondi time in terms of null coordinate time and angular inertial coordinates $u_B(u, \xi_B)$. We can introduce the ODEs along the null generators of $\mathcal{J}^+$

$$\frac{d\delta}{du} = \frac{1}{2}\mathrm{Im}\left(\frac{\bar{J}_{0,u}J_0}{K_0+1} + \frac{J_0\left(U_0\bar{\eth}\bar{J}_0 + \bar{U}_0\eth\bar{J}_0\right)}{2(K_0+1)} + J_0\bar{\eth}\bar{U}_0 + K_0\bar{\eth}U_0 + 2U_0\bar{\xi}\right)\,, \tag{5.3.77}$$

$$\frac{d\xi}{du} = \frac{1}{2}(1+\xi\bar{\xi})U_0\,, \tag{5.3.78}$$

$$\frac{du_B}{du} = \omega e^{2H}\,, \tag{5.3.79}$$

where $U_0 = q_A\,L^A$ and the PDE for ω

$$\partial_u \log\omega = -\mathrm{Re}\left(\bar{U}\,\eth\log\omega + \frac{1}{2}\eth\bar{U}\right)\,. \tag{5.3.80}$$

The Bondi news function can then be calculated in three steps:

1. Evaluation of (5.3.76) by ignoring the phase factor $\exp(-2i\delta)$ and by using the evolution coordinates (u, ξ).
2. Interpolation of the news onto a fixed inertial grid $N(u, \xi_B)$ and multiplication by the phase factor $\exp(-2i\delta)$ which is only known on the inertial grid.
3. Interpolation of the news onto fixed inertial time slices $N(u_B, \xi_B)$.

Note that we set $J = 0$ at $\mathcal{J}^+$ at $u = 0$, so that $\omega = 1$ at $u = 0$. We now have the news in the inertial Bondi frame.

Finally, we can get Ψ_4 from the Bondi news via[4]

$$\Psi_4 = \partial_u N\,. \tag{5.3.81}$$

However, this relation only holds in an inertial Bondi frame. As for the news, this assumption does not hold in general by the coordinate choice in the code, and we have to use a more general expression when in an arbitrary frame. This expression reads

$$\Psi_4 = \frac{1}{2}\omega^{-3}e^{-2i\delta}\hat{n}^\mu F^A F^B\Big(\partial_\mu\hat{\Sigma}_{AB} - \partial_A\hat{\Sigma}_{\mu B} - \hat{\Gamma}^\alpha_{\mu B}\hat{\Sigma}_{A\alpha} + \hat{\Gamma}^\alpha_{AB}\hat{\Sigma}_{\mu\alpha}\Big)|_{\mathcal{I}^+}\,, \tag{5.3.82}$$

where

$$\ell\hat{\Sigma}_{\mu\nu} := \hat{\nabla}_\mu\hat{\nabla}_\nu\ell - \frac{1}{4}\hat{g}_{\mu\nu}\hat{\Theta}\,, \tag{5.3.83}$$

and

$$\hat{\Theta} := \hat{\nabla}^\mu\hat{\nabla}_\mu\ell = e^{-2\beta}\Big(\partial_\ell(\ell^3 V) + \partial_A U^A\Big)\,. \tag{5.3.84}$$

For the derivation of this result, please refer to [277]. However, (5.3.81) can be used once the Bondi news function is known in terms of the inertial coordinates (ℓ_B, q_B, p_B, u_B) as described above.

---

[4] In characteristic work, it is conventional to work with a quantity Ψ_4 that is related to the usual Ψ_4^0 (1.3.21) via $\Psi_4 = -(1/2)\bar{\Psi}_4^0$.

5.4 The gravitational-wave strain

All quantities of the three methods described in the previous sections for extracting the radiation content in the spacetime have a direct relationship to the gravitational-wave strain $h(t)$, *i.e.* the actual distortions of spacetime that a gravitational-wave detector would measure in the asymptotic wave-zone far away from the source.

The first (Section 5.1) and third method (Section 5.3) both calculate the Weyl scalar Ψ_4, whereas the second method (Section 5.2) relies on gauge-invariant master-functions (5.2.20) and (5.2.13).

The strain from the Weyl component Ψ_4

The complex Weyl component Ψ_4 is related to the gravitational-wave strain by [101, 141, 332]

$$\frac{1}{2}\left(\ddot{h}_+ - i\ddot{h}_\times\right) = \lim_{r\to\infty} \Psi_4\,, \tag{5.4.1}$$

where "+" and "×" denote the two polarization states of the strain.

This is a result from linearized theory of gravity and it is therefore only valid at large distances to the source, *i.e.* in the wave-zone. In TT-gauge there is a close relationship between the metric perturbations (1.4.1) to the linearized Riemann tensor by

$$R_{itjt} = -\frac{1}{2}\ddot{h}^{\mathrm{TT}}_{ij}\,. \tag{5.4.2}$$

Since in vacuum, the Riemann tensor is identical to the Weyl tensor $R_{\mu\nu\lambda\rho} \equiv C_{\mu\nu\lambda\rho}$ and by using (5.1.1), we get (5.4.1).

In terms of spin-weighted spherical harmonic modes, the strain can be calculated according to

$$h_+ - \mathrm{i}h_\times = 2\lim_{r\to\infty}\sum_{\ell,m}\int_0^t dt' \int_0^{t'} dt''\Psi_4^{\ell m}\,{}_{-2}Y_{\ell m}\,. \tag{5.4.3}$$

The strain from gauge invariant master-functions

The advantage of using gauge-invariant perturbations [310] over the originally implemented Regge-Wheeler [96] and Zerilli [308, 309] variables is that these are directly related to the gravitational-wave strain [333, 334].

The underlying procedure for relating the even and odd-parity master-functions (5.2.20), (5.2.13) to the strain relies on the following conditions. Firstly, it is necessary to evaluate each multipole of the decomposed metric perturbations in the tetrad $\mathbf{e}$ of stationary observers in the background Schwarzschild spacetime, *i.e.* $h_{\hat{\mu}\hat{\nu}} = \mathbf{e}^\mu{}_{\hat{\mu}}\mathbf{e}^\nu{}_{\hat{\nu}}h_{\mu\nu}$, where $\mathbf{e}$ is diagonal with components $\mathbf{e}^\mu{}_{\hat{\mu}} \equiv \left\{A, A^{-1}, r^{-1}, (r\sin\theta)^{-1}\right\}$ and where the indices $\hat{\mu}$ refer to the locally "flat" coordinates. Secondly, we have to impose the radiation gauge, *i.e.* all quantities need to be evaluated far away from the source in the wave-zone which leads to the requirement that the components $h_{\hat{\theta}\hat{\theta}}$, $h_{\hat{\phi}\hat{\phi}}$ and $h_{\hat{\theta}\hat{\phi}}$ must fall off as $\mathcal{O}(1/r)$ whereas the remaining components obey a more rapid decay of $\mathcal{O}(1/r^2)$. Thirdly, the metric has to be traceless to linear order, *i.e.* $h_{\hat{\theta}\hat{\theta}} + h_{\hat{\phi}\hat{\phi}} = 0 + \mathcal{O}(1/r^2)$.

For a detailed derivation please refer to [333, 334] and [312] for a review. Here, we just state that (5.2.20), (5.2.13) are related to the two polarization states of the gravitational-wave strain by

$$h_+ - \mathrm{i}h_\times = \frac{1}{\sqrt{2}r}\sum_{\ell,m}\left(Q^+_{\ell m} - \mathrm{i}\int_{-\infty}^t Q^\times_{\ell m}(t')dt'\right)\,{}_{-2}Y^{\ell m}(\theta,\phi) + \mathcal{O}\left(\frac{1}{r^2}\right)\,, \tag{5.4.4}$$

where ${}_{-2}Y^{\ell m}(\theta,\phi)$ are the spin-weight $s=-2$ spherical harmonics.

5.5 Radiated energy

The energy loss due to gravitational radiation is important particularly in BBHs since this can be used, *e.g.* to determine the final mass of the merger remnant (see Chapter 14). As for the gravitational-wave strain, all extraction quantities also have a direct relationship to the energy that is carried by the gravitational wave. Moreover, once an expression in terms of the gravitational-wave strain is known, one can use (5.4.1) and (5.4.4) to get expressions in terms of the extraction quantities Ψ_4 and $Q^{+}_{\ell m}$ and $Q^{\times}_{\ell m}$.

We therefore consider now the radiated energy in terms of the gravitational-wave strain h. An expression for the radiated energy can be derived by considering the gauge-invariant Isaacson stress-energy tensor in the TT gauge [143, 144]

$$T_{\mu\nu} = \frac{1}{32\pi}\langle \partial_\mu h^{\mathrm{TT}}_{ij} \partial_\nu h^{\mathrm{TT}}_{ij} \rangle \,, \tag{5.5.1}$$

where a sum over the indices ij is implied and where $\langle\,\rangle$ denotes an average over several wavelengths which means that it holds in the "limit of high-frequency" (or *short-wave* approximation), *i.e.* whenever the wavelength of the gravitational-wave field is short compared to the background geometry. By using the explicit form of the h^{TT}_{ij} in terms of h_{+} and $h_{\times}$, and introducing $H := h_{+} - i h_{\times}$, the Isaacson stress-energy tensor can be rewritten as

$$T_{\mu\nu} = \frac{1}{16\pi}\mathrm{Re}\,\langle \partial_\mu H \partial_\nu \bar{H} \rangle \,. \tag{5.5.2}$$

By making use of the asymptotic property $\partial_r h \sim -\partial_t h$ for outgoing waves and integrating the components T^{0i} over a 2-surface at infinity, one obtains

$$\frac{dE}{dt} = \lim_{r\to\infty} \frac{r^2}{16\,\pi} \int_{S^2} |\dot{H}|^2 d\Omega \,, \tag{5.5.3}$$

where $d\Omega = \sin\theta d\theta d\phi$ and S^2 a 2-surface at infinity.

The radiated energy from the Weyl component Ψ_4

The radiated energy flux can be calculated from the Weyl component Ψ_4 as follows [135, 332, 335, 336]

$$\frac{dE}{dt} = \lim_{r\to\infty} \left\{ \frac{r^2}{4\pi} \int_{S^2} d\Omega \left| \int_{-\infty}^{t} d\tilde{t}\Psi_4 \right|^2 \right\} \,, \tag{5.5.4}$$

where $d\Omega = \sin\theta d\theta d\phi$ and S^2 a 2-surface at infinity This is a result of substituting (5.4.1) into Eq. (5.5.2). Note that this can also be obtained by using the definition of the Bondi-mass [117, 134, 135].

In terms of spin-weighted spherical harmonic coefficients $\Psi_4^{\ell m}$ the radiated energy reads [336]

$$\frac{dE}{dt} = \lim_{r\to\infty} \left\{ \frac{r^2}{4\pi} \sum_{\ell,m} \left| \int_{-\infty}^{t} d\tilde{t}\Psi_4^{\ell m} \right|^2 \right\} \,, \tag{5.5.5}$$

which is due to the orthonormality property of the spin-weighted spherical harmonics.

The radiated energy from gauge-invariant master-functions

In the same way as for the radiated energy flux in terms of Ψ_4, we consider the Isaacson stress-energy tensor (5.5.2) [333, 334]. By making use of relation (5.4.4), we obtain

$$\frac{dE}{dt} = \frac{1}{32\pi} \sum_{\ell,m} \left(\left| \frac{dQ^{+}_{\ell m}}{dt} \right|^2 + \left| Q^{\times}_{\ell m} \right|^2 \right) \tag{5.5.6}$$

as the radiated energy flux in terms of the master-functions $Q^{+}_{\ell m}$ and $Q^{\times}_{\ell m}$.

5.6 Radiated linear momentum

The linear momentum is important especially in binary interactions as the net-linear momentum that is carried away by asymmetrically emitted radiation can lead to a significant recoil of the merger remnant of BBHs. In Chapter 12, we will quantify this effect on various BBH configurations and discuss astrophysical implications.

As in the previous sections, we can relate the extraction quantities to the linear momentum carried by the gravitational waves by first deriving an expression for the radiated linear momentum in terms of the gravitational-wave strain h and then making use of the relationship of the extraction quantities to the gravitational-wave strain to obtain explicit expressions in terms of the extraction quantities Ψ_4 and $Q^{+}_{\ell m}$ and $Q^{\times}_{\ell m}$.

By considering the components T^{ir} of the Isaacson stress-energy tensor (5.5.2) and by neglecting angular derivatives of the wave-strain in the wave-zone, *i.e.* $\partial_i H \sim (x_i/r)\partial_r H$, one arrives at [144, 337]

$$\frac{dP_i}{dt} = \lim_{r\to\infty} \frac{r^2}{16\pi} \int_\Omega l_i\, |\dot{H}|^2\, d\Omega\,. \tag{5.6.1}$$

The vector l_i is the radial unit vector in flat space

$$l_i = (\sin\theta\cos\phi, \sin\theta\sin\phi, \cos\theta). \tag{5.6.2}$$

The radiated linear momentum from the Weyl component Ψ_4

The linear momentum flux in terms of Ψ_4 reads [336]

$$\frac{dP_i}{dt} = \lim_{r\to\infty}\left\{\frac{r^2}{16\pi}\int_{S^2} d\Omega l_i \left|\int_{-\infty}^{t} d\tilde{t}\Psi_4\right|^2\right\}, \tag{5.6.3}$$

and can be obtained by inserting (5.4.1) into (5.6.1).

In terms of spin-weighted spherical harmonic coefficients $\Psi_4^{\ell m}$ the radiated linear momentum flux reads [336]

$$\begin{aligned}
\frac{dP_+}{dt} &= \lim_{r\to\infty}\frac{r^2}{8\,\pi}\sum_{\ell,m}\int_{-\infty}^{t} dt'\Psi_4^{\ell,m} \\
&\times \int_{-\infty}^{t} dt'\left(a_{\ell,m}\,\bar{\Psi}_4^{\ell,m+1} + b_{\ell,-m}\,\bar{\Psi}_4^{\ell-1,m+1}\right. \\
&- \left. b_{\ell+1,m+1}\,\bar{\Psi}_4^{\ell+1,m+1}\right)\,, \qquad (5.6.4)\\
\frac{dP_z}{dt} &= \lim_{r\to\infty}\frac{r^2}{16\pi}\sum_{\ell,m}\int_{-\infty}^{t} dt'\Psi_4^{\ell,m} \\
&\times \int_{-\infty}^{t} dt'\left(c_{\ell,m}\,\bar{\Psi}_4^{\ell,m} + d_{\ell,m}\,\bar{\Psi}_4^{\ell-1,m}\right. \\
&+ \left. d_{\ell+1,m}\,\bar{\Psi}_4^{\ell+1,m}\right)\,, \qquad (5.6.5)
\end{aligned}$$

where $P_+ := P_x + iP_y$ and where the coefficients $(a_{\ell,m}, b_{\ell,m}, c_{\ell,m}, d_{\ell,m})$ are given by

$$\begin{aligned}
a_{\ell,m} &= \frac{\sqrt{(\ell-m)\,(\ell+m+1)}}{\ell\,(\ell+1)}\,,\\
b_{\ell,m} &= \frac{1}{2\,\ell}\sqrt{\frac{(\ell-2)\,(\ell+2)\,(\ell+m)\,(\ell+m-1)}{(2\ell-1)(2\ell+1)}}\,,\\
c_{\ell,m} &= \frac{2\,m}{\ell\,(\ell+1)}\,,\\
d_{\ell,m} &= \frac{1}{\ell}\sqrt{\frac{(\ell-2)\,(\ell+2)\,(\ell-m)\,(\ell+m)}{(2\ell-1)(2\ell+1)}}\,.
\end{aligned}$$

This can be obtained by decomposing (5.6.2) in scalar (*i.e.* spin zero) spherical harmonics as

$$\begin{aligned} l_x &= \sin\theta\cos\varphi = \sqrt{\frac{2\pi}{3}}\left[Y^{1,-1} - Y^{1,1}\right] , \\ l_y &= \sin\theta\sin\varphi = i\sqrt{\frac{2\pi}{3}}\left[Y^{1,-1} + Y^{1,1}\right] , \\ l_z &= \cos\theta = 2\sqrt{\frac{\pi}{3}}\,Y^{1,0} . \end{aligned} \tag{5.6.6}$$

By substituting

$$\Psi_4 = \sum_{\ell m} \bar{\Psi}_4^{\ell m}\,{}_{-2}Y_{\ell m} \tag{5.6.7}$$

and (5.6.6) into (5.6.3), we can see that the flux of linear momentum involves integrals over three spin-weighted spherical harmonics. Such integrals are given in terms of the Wigner 3-lm symbols with $l_3 = 1$ and are explicitly given in the Appendix of [336].

The radiated linear momentum from gauge-invariant master-functions

As for the linear momentum flux in terms of Ψ_4, one can obtain an expression in terms of the gauge-invariant master-functions $Q^{+}_{\ell m}$ and $Q^{\times}_{\ell m}$ by inserting (5.4.4) into (5.6.1). By decomposing (5.6.2) in spherical harmonics (5.6.6) one can then perform the angular integral similar to the procedure described in [145].

In [145] the even-parity (or *electric*) multipoles are indicated with $I_{\ell m}$ and the odd-parity (or *magnetic*) ones with $S_{\ell m}$. They are related to our notation by

$$ {}^{(\ell)}I_{\ell m} = Q^{+}_{\ell m} , \tag{5.6.8}$$

$$ {}^{(\ell+1)}S_{\ell m} = Q^{\times}_{\ell m} , \tag{5.6.9}$$

where ${}^{(\ell)}f_{\ell m} \equiv d^{\ell} f_{\ell m}/dt^{\ell}$. From the well known property $(Q^{+,\times}_{\ell m})^{*} = (-1)^m Q^{+,\times}_{\ell\,-m}$, where the asterisk indicates complex conjugation, one can rewrite (4.20) of [145] in a more compact form. Following [338] where the lowest multipolar contribution was explicitly computed in this way, it is convenient to combine the components of the linear momentum flux in the equatorial plane in a complex number as $\mathcal{F}_x + \mathrm{i}\mathcal{F}_y$. The multipolar expansion of the flux vector can be written as

$$\mathcal{F}_x + \mathrm{i}\mathcal{F}_y = \sum_{\ell=2}^{\infty}\sum_{m=0}^{\ell} \delta_m \left(\mathcal{F}_x^{\ell m} + \mathrm{i}\mathcal{F}_y^{\ell m}\right) , \tag{5.6.10}$$

$$\mathcal{F}_z = \sum_{\ell=2}^{\infty}\sum_{m=0}^{\ell} \delta_m \mathcal{F}_z^{\ell m} , \tag{5.6.11}$$

where $\delta_m = 1$ if $m \neq 0$ and $\delta_m = 1/2$ if $m = 0$. Each multipole reads

$$\begin{aligned} \mathcal{F}_x^{\ell m} + \mathrm{i}\mathcal{F}_y^{\ell m} \equiv \frac{(-1)^m}{16\pi\ell(\ell+1)}\Bigg\{ &- 2\mathrm{i}\left[a^{+}_{\ell m}\dot{Q}^{+}_{\ell-m}Q^{\times}_{\ell\,m-1} + a^{-}_{\ell m}\dot{Q}^{+}_{\ell m}Q^{\times}_{\ell\,-(m+1)}\right] \\ &+ \sqrt{\frac{\ell^2(\ell-1)(\ell+3)}{(2\ell+1)(2\ell+3)}}\bigg[b^{-}_{\ell m}\left(\dot{Q}^{+}_{\ell\,-m}\dot{Q}^{+}_{\ell+1\;m-1} + Q^{\times}_{\ell\,-m}\dot{Q}^{\times}_{\ell+1\;m-1}\right) \\ &+ b^{+}_{\ell m}\left(\dot{Q}^{+}_{\ell m}\dot{Q}^{+}_{\ell+1\;-(m+1)} + Q^{\times}_{\ell m}\dot{Q}^{\times}_{\ell+1\;-(m+1)}\right)\bigg]\Bigg\} , \end{aligned} \tag{5.6.12}$$

$$\begin{aligned} \mathcal{F}_z^{\ell m} \equiv \frac{(-1)^m}{8\pi\ell(\ell+1)}\Bigg\{ &2m\,\mathrm{Im}\left[\dot{Q}^{+}_{\ell\,-m}Q^{\times}_{\ell m}\right] \\ &+ c_{\ell m}\sqrt{\frac{\ell^2(\ell-1)(\ell+3)}{(2\ell+1)(2\ell+3)}}\mathrm{Re}\left[\dot{Q}^{+}_{\ell\,-m}Q^{+}_{\ell+1\,m} + Q^{\times}_{\ell\,-m}\dot{Q}^{\times}_{\ell+1\,m}\right]\Bigg\} , \end{aligned} \tag{5.6.13}$$

and

$$\begin{aligned} a^{\pm}_{\ell m} &\equiv \sqrt{(\ell \pm m)(\ell \mp m + 1)}\ , \\ b^{\pm}_{\ell m} &\equiv \sqrt{(\ell \pm m + 1)(\ell \pm m + 2)}\ , \\ c_{\ell m} &\equiv \sqrt{(\ell - m + 1)(\ell - m + 1)}\ . \end{aligned}$$

Note that here both $\mathcal{F}^{\ell m}_x$ and $\mathcal{F}^{\ell m}_y$ are *real* numbers and are obtained as the real and imaginary part of the right-hand-side of (5.6.12). As a remark, we note that for $\ell = m = 2$, (5.6.12) [56] reduces to (9) of [338].

5.7 Radiated angular momentum

In accordance with radiated energy and linear momentum, one can also relate the strain and the extraction quantities to the radiated angular momentum. However, it is more delicate to deal with angular momentum because one has to be careful when using the short-wave approximation and the Isaacson stress-energy tensor. In fact, the result from averaging over a number of wavelength and neglecting angular derivatives will lead to wrong results since this ignores terms that are of order $1/r^3$, and it is exactly these terms that contribute to the angular momentum carried by the gravitational waves. An expression for the angular momentum flux was first derived by DeWitt in 1971 and is also given in [145]. For a review also consider [336] and in TT gauge the flux reads

$$\frac{dJ_i}{dt} = -\lim_{r\to\infty} \frac{r^2}{16\pi}\,\mathrm{Re}\int_{S^2} \hat{J}_i H\, \partial_t \bar{H}\, d\Omega\ , \tag{5.7.1}$$

with the angular momentum operators $\hat{J}_i$ defined as

$$\begin{aligned} \hat{J}_x &= \frac{1}{2}\left(\hat{J}_+ + \hat{J}_-\right) \\ &= -\sin\varphi\,\partial_\theta - \cos\varphi\left(\cot\theta\,\partial_\varphi + i\,s\csc\theta\right)\ , \\ \hat{J}_y &= -\frac{i}{2}\left(\hat{J}_+ - \hat{J}_-\right) \\ &= +\cos\varphi\,\partial_\theta - \sin\varphi\left(\cot\theta\,\partial_\varphi + i\,s\csc\theta\right)\ , \\ \hat{J}_z &= \partial_\varphi\ . \end{aligned} \tag{5.7.2}$$

The radiated angular momentum from the Weyl component Ψ_4

Making use again of (5.4.1) and plugging this into the expression for the angular momentum flux (5.7.1), one obtains an expression in terms of Ψ_4 that reads

$$\begin{aligned} \frac{dJ_i}{dt} &= -\lim_{r\to\infty} \frac{r^2}{16\pi}\,\mathrm{Re}\Bigg\{\int_{S^2}\left(\int_{-\infty}^{t} \bar{\Psi}_4\, dt'\right) \\ &\quad \times \hat{J}_i\left(\int_{-\infty}^{t}\int_{-\infty}^{t'} \Psi_4\, dt'' dt'\right) d\Omega\Bigg\}\ . \end{aligned} \tag{5.7.3}$$

In terms of spin-weighted spherical harmonic coefficients $\Psi_4^{\ell m}$ the radiated linear momentum flux reads [336]

$$\begin{aligned}
\frac{dJ_x}{dt} &= \lim_{r\to\infty} \frac{r^2}{32\pi} \operatorname{Im}\Bigg\{ \sum_{\ell,m} \int_{-\infty}^{t} \int_{-\infty}^{t'} \Psi_4^{\ell,m}\, dt'' dt' \\
&\times \int_{-\infty}^{t} \Big(f_{\ell,m}\, \bar{\Psi}_4^{\ell,m+1} + f_{\ell,-m}\, \bar{\Psi}_4^{\ell,m-1} \Big) \Bigg\} dt', \qquad (5.7.4) \\
\frac{dJ_y}{dt} &= -\lim_{r\to\infty} \frac{r^2}{32\pi} \operatorname{Re}\Bigg\{ \sum_{\ell,m} \int_{-\infty}^{t} \int_{-\infty}^{t'} \Psi_4^{\ell,m}\, dt'' dt' \\
&\times \int_{-\infty}^{t} \Big(f_{\ell,m}\, \bar{\Psi}_4^{\ell,m+1} - f_{\ell,-m}\, \bar{\Psi}_4^{\ell,m-1} \Big) \Bigg\} dt', \qquad (5.7.5) \\
\frac{dJ_z}{dt} &= \lim_{r\to\infty} \frac{r^2}{16\pi} \operatorname{Im}\Bigg\{ \sum_{\ell,m} m \int_{-\infty}^{t} \int_{-\infty}^{t'} \Psi_4^{\ell,m}\, dt' dt'' \\
&\times \int_{-\infty}^{t} \bar{\Psi}_4^{\ell,m}\, dt' \Bigg\}, \qquad (5.7.6)
\end{aligned}$$

with

$$\begin{aligned}
f_{\ell,m} &:= \sqrt{(\ell-m)(\ell+m+1)} \\
&= \sqrt{\ell(\ell+1) - m(m+1)}\,. \qquad (5.7.7)
\end{aligned}$$

This can be obtained from the action of the angular momentum operators on the spin-weighted spherical harmonics which are given in the Appendix of [336]. One ends up with surface integrals over spin-weighted spherical harmonics where one can make use of the usual orthonormality relations to arrive at (5.7.4), (5.7.5) and (5.7.6).

The radiated angular momentum from gauge-invariant master-functions

Similar to the results for Ψ_4, one can make use of (5.7.1) by plugging in the relation of $Q^{+}_{\ell m}$ and $Q^{\times}_{\ell m}$ to the gravitational-wave strain to obtain an expression for the radiated angular momentum flux in terms of the gauge-invariant master-functions. One finds [336]

$$\begin{aligned}
\frac{dJ_x}{dt} &= -\frac{1}{32\pi} \operatorname{Im} \sum_{\ell,m} f_{\ell,m} \left(\bar{Q}^{+}_{\ell,m}\, \dot{Q}^{+}_{\ell,m+1} + \bar{P}^{\times}_{\ell,m}\, Q^{\times}_{\ell,m+1} \right), \qquad (5.7.8) \\
\frac{dJ_y}{dt} &= -\frac{1}{32\pi} \operatorname{Re} \sum_{\ell,m} f_{\ell,m} \left(\bar{Q}^{+}_{\ell,m}\, \dot{Q}^{+}_{\ell,m+1} + \bar{P}^{\times}_{\ell,m} Q^{\times}_{\ell,m+1} \right), \qquad (5.7.9) \\
\frac{dJ_z}{dt} &= -\frac{1}{32\pi} \sum_{\ell,m} m \left(\dot{Q}^{+}_{\ell,m}\, \bar{Q}^{+}_{\ell,m} + Q^{\times}_{\ell,m}\, \bar{P}^{\times}_{\ell,m} \right), \qquad (5.7.10)
\end{aligned}$$

with the definition

$$P^{\times}_{\ell,m} := \int_{-\infty}^{t} Q^{\times}_{\ell,m}\, dt'\,. \qquad (5.7.11)$$

Part II

Numerics and Implementation

Chapter 6

Discretization of hyperbolic PDEs

Underlying to the computational implementation of hyperbolic PDEs such as the Einstein equations is the question how the continuous representation of the equation can be transformed into a discrete formulation that can be implemented on computers. There are many possible answers and depending on the complexity of the set of considered equations, this is usually not too difficult. In case of the Einstein equations, unfortunately, one faces one of the most complicated set of equations possible. The Einstein equations are a set of ten coupled non-linear second-order hyperbolic PDEs with hundreds of terms. However, the main reason for the difficulties is given by its strong non-linearity. If a PDE is non-linear, this usually means that the stability of the discretized equation is hard to analyze analytically if not impossible. But numerical stability is a crucial point for computer simulations as it determines whether a certain discretization scheme will be condemned to lead to exponentially growing modes and hence to unpredictable crashes of the simulation or whether it will lead to solutions that are bounded over time and hence useful for numerical computations.

A key concept for numerical stability is the understanding of the hyperbolicity of the equations. For a certain class of hyperbolic equations, there is a powerful mathematical set of theorems guaranteeing the stability of the discretized equations. The straight-forward 3+1 split of the Einstein equations, *i.e.* the ADM equations, for example did not lead to stable numerical behavior when making them discrete. It was necessary to cast the equations in a different form, *e.g.* the BSSNOK system, in order to meet certain requirements for numerical stability.

Apart from these issues, there are more fundamental points that have to be considered when selecting a certain discretization method. It can be shown that not all discretization schemes lead to a stable numerical evolution and some are conditionally stable while others are always unstable. The stability of a discrete approximation to a PDE can be analyzed in terms of von Neumann stability analysis. Here, the application of the *method of lines* (MoL) allows for the separate treatment of time and space discretization hence simplifying the analysis considerably, while at the same time offering a greater flexibility in the choice of discretization schemes.

Finally, any numerical solution must be convergent, *i.e.* in the limit of infinite solution it must represent the continuous solution. This important aspect of the approximate solution has to be tested for each computation because otherwise the error due to numerics is unknown. An unknown numerical error however, means that the approximate solution is meaningless.

In the next few sections, we briefly discuss the underlying concepts such as stability, convergence and hyperbolicity when discretizing PDEs as well as the discretization scheme itself.

6.1 Finite differences

The key ingredient when considering the discretized version of a given PDE is to replace the partial derivatives

$$f'(x) := \lim_{h\to 0} \frac{f(x+h) - f(x)}{h} \tag{6.1.1}$$

by some method that approximates the limit in the equation above. The obvious way is to just leave the limit aside and choose a sufficiently small h to approximate the equation above. This is what is called *finite difference* and is the easiest and most efficient way of discretizing PDEs.

In order to approximate the derivatives, it is necessary to have the function values at a discrete set of points $\{x_i\}$ with spacing h so that $f_i = f(x_i)$. The $\{x_i\}$ are usually uniformly spaced and we call the set of points sampling our domain the *numerical grid.* Due to its simplicity, it would be preferable to represent PDEs as finite difference equations. However, it should be mentioned that other physical models are defined only on complicated topologies, such as *e.g.* the heat transfer problem, or the mechanical deformation of cars in a crash test simulations. In these models it is unfeasible to apply finite differences simply because the grid cannot be adapted easily to complicated boundary topologies. Here, other methods such as *finite volumes* (see *e.g.* [339]), *finite elements* or *discontinuous Galerkin* [340] have to be used. Another problem with equations in partial differential form is the requirement that the solution to the equation must belong to a certain class of functions, namely the class of continuous differentiable functions C^q. Otherwise, taking derivatives would be ill-defined. However, some equations admit discontinuous solutions such as shocks. It is therefore not possible to catch certain phenomena when the equation is written as a PDE. In this case, one can transform the PDE to its *weak form*, *i.e.* replacing the derivatives with the help of test-functions by integrals so that no derivatives are involved anymore. Now, one has to solve for integrals. For example, schemes based on this procedure are the finite volume, finite element or discontinuous Galerkin method, and are used in (relativistic) hydrodynamics.

Fortunately, in case of the vacuum Einstein equations, all of these points do not apply and it is possible to stick to finite differences. This greatly simplifies the implementational complexity and is at the same time highly efficient as everything simply reduces to additions and subtractions. However, there are attempts to use methods that offer higher accuracies than finite differences. Coming along as a special case of finite elements, one of these methods is known as the spectral method. For BBH simulations, spextral schemes have been implemented by the Caltech/Cornell group [156, 341]. Unfortunately, the implementation appears to be cumbersome and convincing results of the superiority in the accuracy over finite differences have not been produced so far (compare Section 11.2).

Another route is taken by the attempt of constructing a scheme based on discontinuous Galerkin methods departing from the Einstein-Hilbert action [342]. This would guarantee a numerical scheme that can be easily analyzed with respect to its error and associated convergence. However, investigations in that direction have just started and are far from a usable production code.

In the next subsection, we will briefly describe finite difference discretization stencils that are used in the implementation of our BBH code.

Difference operators

Difference operators are approximations to derivative operators, and the simplest can be written as

$$f'(x) := \frac{f(x+h) - f(x)}{h} + \mathcal{O}(h^2) \tag{6.1.2}$$

by simply leaving away the limit in the definition of the derivative of a function. This approximation can be shown to be first-order accurate, *i.e.* the error will decrease linearly when increasing the resolution of the underlying computational grid. With the help of Taylor expansions, we can construct higher-order approximations, *e.g.* by subtracting

$$\begin{aligned} f(x+h) &= f(x) + f'(x)(x+h-x) + \frac{1}{2}f''(x)(x+h-x)^2 + \mathcal{O}(f^{(3)})\,, \\ f(x-h) &= f(x) + f'(x)(x-h-x) + \frac{1}{2}f''(x)(x-h-x)^2 + \mathcal{O}(f^{(3)})\,, \end{aligned}$$

we obtain

$$f'(x) = \frac{f(x+h) - f(x-h)}{2h} + \mathcal{O}(h^3)\,, \tag{6.1.3}$$

which is second-order accurate since we have used Taylor expansion up to second-order for the construction of this difference operator. Note that in the construction of a difference approximation, we assume that the function is continuously differentiable up to order q, *i.e.* $f \in C^q$, where q is the order of accuracy of the finite difference operator.

Apart from the order of accuracy, there is one significant difference between (6.1.2) and (6.1.3). While the first-order difference operator is side-winded, the latter is centered. This important difference can have dramatic impact on the stability of a numerical scheme. An example of this is depicted in Figure 6.1 and a more detailed explanation is given in the corresponding subsection.

Both types, side-winded and centered, can be extended to arbitrary high order of accuracy [343]. In practice, we use fourth and eighth-order finite differencing (see Appendix A.3). This is possible because the solution to the Einstein equations are sufficiently smooth. Higher order schemes have the advantage that they produce less high frequency noise and converge much faster to the exact solution, *i.e.* for a sufficiently high resolution they are generally more accurate if the solution is smooth up to order q. However, in order to remove spurious high-frequency noise from the numerical approximation, one can introduce artificial dissipation operators. These is discussed in the next subsection.

Dissipation operators

After a finite difference operator has been applied to a numerical function, the result will usually exhibit spurious high-frequency noise. This uncontrollable amount of noise is due to the lack of resolution to properly resolve the higher frequency components on the numerical grid and can in the worst case lead to unstable behavior of the simulation. To lessen this effect, artificial dissipation operators have been constructed that can be used together with a given finite difference operator. The underlying idea is to damp the high-frequency components down to a harmless amount similar to a low-pass filter. The standard way of adding artificial dissipation to a finite difference approximation is known as *Kreiss-Oliger dissipation* [344].

Consider a finite difference scheme of the form

$$u_m^{n+1} = u_m^n + \Delta t S(u_m^n)\,, \tag{6.1.4}$$

where n denotes the time-step m the gridpoint and $S(u_m^n)$ is some spatial finite difference operator. We can modify this scheme by adding a term of the form

$$u_m^{n+1} = u_m^n + \Delta t S(u_m^n) - \epsilon \frac{\Delta t}{\Delta x}(-1)^N \Delta_x^{2N}(u_m^n)\,, \tag{6.1.5}$$

with $\epsilon > 0$, $N \geqslant 1$ an integer, and where Δ_x^{2N} is a centered difference operator of differential order $2N$.

A von Neumann stability analysis (see Section 6.3) shows [123] that the extra term very strongly damps frequencies close to the grid spacing Δx, and leaves longer wavelengths unaffected.

When considering the continuum limit of (6.1.5), we get

$$\partial_t u = S(u) - \epsilon(-1)^N (\Delta x)^{2N-1} \partial_x^{2N} u\,. \tag{6.1.6}$$

This shows that we have effectively added an extra term to our original PDE that vanishes if $\Delta x \to 0$. The extra term mimics the behavior of dissipation as, *e.g.* in the heat equation. In order to maintain the original order of accuracy m of the difference approximation, it is necessary that the dissipative term satisfies $2N-1 \geqslant m$. A fourth-order difference scheme therefore requires fifth-order dissipation. The various dissipation operators used in this thesis are given in Appendix A.3.

6.2 Method of lines

The *method of lines* (MoL) [345] involves the separate discretization of space and time which enables one to independently analyze the stability properties of the time evolution scheme with the same spatial derivative operator S. In other words, this method allows for different discretization techniques of the time integration and the spatial derivative operators. Usually, we start with the discretization of the latter, which can be any of finite differences, finite volumes, finite elements or spectral methods. It is most common to split the time derivatives in a system of PDEs to first order, and since MoL is equivalent of transforming the PDEs to ordinary differential equations ODEs, we can apply ODE integrators like the iterative Crank Nicholson or the Runge-Kutta scheme to perform the time-integration. To illustrate the idea, we consider the semi-discrete system in which only the time derivative is discretized and the spatial derivatives are left continuous. Let $\mathbf{u}$ be an array of dynamical fields and S a continuous spatial differential operator. The evolution of $\mathbf{u}$ can be written as

$$\partial_t \mathbf{u} = S(\mathbf{u})\,. \tag{6.2.1}$$

The continuous flow of time is then replaced by a succession of discrete time instants $\{t_n\}$ and we label $\mathbf{u}^n = \mathbf{u}(t_n)$. The Euler step (forward time difference) is a first-order scheme and can be used as a simple approximation. It reads

$$\mathbf{u}^{n+1} = \mathbf{u}^n + \Delta t S(t_n,\, \mathbf{u}^n)\,. \tag{6.2.2}$$

This however, is not very accurate and can lead to unstable behavior (in a sense made clear later). A better approximation is given in the next subsection.

Runge-Kutta time integration

Since the Euler step is an insufficient approximation and is also unconditional unstable [345] in most cases, we need better approximations. A scheme that is sufficient in most cases, and which we employ in our BBH simulations, is the classical fourth-order Runge-Kutta scheme

$$\begin{aligned}
k_1 &= S(t_{n-1},\, \mathbf{u}^{n-1})\,,\\
k_2 &= S\left(t_{n-1} + \frac{\Delta t}{2},\, \mathbf{u}^{n-1} + \frac{\Delta t}{2}k_1\right)\,,\\
k_3 &= S\left(t_{n-1} + \frac{\Delta t}{2},\, \mathbf{u}^{n-1} + \frac{\Delta t}{2}k_2\right)\,,\\
k_4 &= S(t_{n-1} + \Delta t,\, \mathbf{u}_{n-1} + \Delta t\, k_3)\,,\\
\mathbf{u}^n &= \mathbf{u}^{n-1} + \frac{\Delta t}{6}(k_1 + 2k_2 + 2k_3 + k_4) + \mathcal{O}(\Delta t^5)\,.
\end{aligned} \tag{6.2.3}$$

The scheme involves the evaluation of the RHS terms at various intermediate (or sub) steps. Using these substeps, a higher order approximation can be achieved by a proper combination of them.

Of course, the time integrator should have at least the same accuracy as the spatial discretization. Otherwise the overall accuracy would be limited by the time integrator. Practically, however, in our BBH merger simulations, we seem to be dominated by the 8th-order spatial finite difference error as we observe convergence of higher order than the fourth-order Runge-Kutta scheme (see convergence of the Llama code, Section 11.2).

Another important issue is the fact that not all time integrators provide an (un)conditional stable scheme. By means of Fourier mode analysis [345] of the discretized PDE, one can determine the stability regions of a given time integrator scheme and decide whether it provides a stable scheme or not. For example, the wave equation fails to work with the Euler step or with a second-order Runge-Kutta scheme.

We briefly give an overview of stability properties in the next section.

6.3 Stability and well-posedness

Stability and *well-posedness* are important properties of PDE problems including proper initial data, boundary conditions and the discretization scheme with respect to growth of the analytical and numerical solution at later times. While well-posedness is concerned with the properties of the continuous problem, stability is its discrete analogue, and a problem that is known to be well-posed does not necessarily result in a stable numerical implementation as this depends on the discretization scheme that has been used. If we say that a numerical scheme is *stable* then we mean that the continuous problem is well-posed and that the discretization does not allow arbitrary growth of the numerical solution at later times. The stability of a numerical scheme can be analyzed according to von Neumann [345–347]. In essence, transforming the discrete equation to the Fourier domain reveals whether the solution will grow arbitrarily over time or will remain bounded. Finally, another important result for numerical stability is the *Courant-Friedrichs-Lewy* (CFL) *condition* [345, 348] which places limits on the maximal time-step size that one is allowed to choose for a given spatial separation of gridpoints.

In the next four subsections, we briefly state the concept of well-posedness, stability, and stability analysis as well as the CFL condition.

Well-posedness

Well-posedness is a reasonable requirement for any given problem. Roughly speaking, it states that a well-posed problem should have a solution, that this solution is unique and that it should depend continuously on the problem's data. For a given system of PDEs, an initial boundary value problem on the domain $x \in [0,1]$ is given by

$$\begin{aligned} \mathbf{u}_t &= P\left(x, t, \frac{\partial}{\partial x}, \frac{\partial^2}{\partial x^2}, \ldots\right)\mathbf{u} + F, \qquad t \geq t_0, \\ \mathbf{u}(x,t_0) &= \mathbf{f}(x) \\ L_0\left(t, \frac{\partial}{\partial x}, \frac{\partial^2}{\partial x^2}, \ldots\right)\mathbf{u}(0,t) = g_0, &\qquad L_1\left(t, \frac{\partial}{\partial x}, \frac{\partial^2}{\partial x^2}, \ldots\right)\mathbf{u}(1,t) = g_1 \end{aligned} \tag{6.3.1}$$

where L_0 and L_1 are differential operators that incorporate the boundary conditions and F is a forcing function. This results in the following definition for homogeneous boundary conditions $F = g_0 = g_1 = 0$ [345].

Definition 6.3.1. *The problem (6.3.1) with $F = g_0 = g_1 = 0$ is **well-posed** if, for every $\mathbf{f} \in C^\infty$ that vanishes in a neighborhood of $x = 0, 1$, it has a unique solution that satisfies the estimate*

$$\|\mathbf{u}(\cdot,t)\| \leq K e^{\alpha(t-t_0)} \|\mathbf{u}(\cdot,t_0)\| \tag{6.3.2}$$

where K and α do not depend on $\mathbf{f}$ and t_0.

For general inhomogeneous boundary data, we have

Definition 6.3.2. *The problem (6.3.1) is **strongly well-posed** if it is well-posed and instead of (6.3.2), the solution satisfies the estimate*

$$\|\mathbf{u}(\cdot,t)\|^2 \leq K(t,t_0)\left(\|\mathbf{u}(\cdot,t_0)\| + \int_{t_0}^{t} (\|F(\cdot,\tau)\|^2 + |g_0(\tau)|^2 + |g_1(\tau)|^2) d\tau\right) \tag{6.3.3}$$

$K(t,t_0)$ is supposed to be a function that is bounded in every finite time interval, i.e. $\infty > \|K(t,t_0)\|_\infty$ and does not depend on the data.

In particular cases, stronger estimates might be obtained such that the functional growth in each step can even be suppressed entirely.

It is important to note, that it is not the PDE itself that is well-posed (or ill-posed), but the entire problem including initial and boundary data.

Stability

Analyzing the numerical stability properties of any finite difference scheme is an important issue for numerical approximations to PDEs and is the discrete analog of well-posedness. Stability analysis helps to determine whether a given difference scheme can principally run for ever or blows up and crashes. Blow-ups usually occur because exponentially growing modes develop which ultimately lead to overflow errors.

A general difference approximation of a linear system of PDEs can be written as [345]

$$\begin{aligned} Q_{-1}\mathbf{u}^{n+1} &= \sum_{\sigma=0}^{q} Q_\sigma \mathbf{u}^{n-\sigma}, \qquad n = q,\, q+1, ... \\ \mathbf{u}^\sigma &= \mathbf{f}^{(\sigma)}, \qquad \sigma = 0, 1, ..., q \end{aligned} \tag{6.3.4}$$

where the Q_σ are difference operators. By assuming that Q_{-1} is uniformly bounded[1] and has a uniformly bounded inverse Q_{-1}^{-1} as grid and time-step size $h, k \to 0$, we can advance the solution step by step in time. For simplicity, we restrict ourselves to the case $q = 0$, which means that the discretized time scheme only involves the current and next time-level. A more general discussion can be found in [345], although the following statements do not lose any validity.

We can rewrite (6.3.4) as

$$\begin{aligned} \mathbf{u}^{n+1} &= Q(t_n)\mathbf{u}^n\,, \qquad n = 0, 1, ... \\ \mathbf{u}^0 &= \mathbf{f} \end{aligned} \tag{6.3.5}$$

where $Q(t_n) = Q_{-1}^{-1}Q_0$ and f defines the initial data on the initial time-step. The discrete solution operator can be defined as

$$\mathbf{u}^n = S_h(t_n,\, t_\nu)\mathbf{u}^\nu\,. \tag{6.3.6}$$

We then have the following definition

Definition 6.3.3. *Given the constants α_S, C and K_S, the difference approximation (6.3.5) is called **stable** for $h \leq h_0$, if for all h the discrete operator norms satisfy*

$$\|Q_{-1}^{-1}\|_h \leq C, \qquad \|S_h(t_n,\, t_\nu)\|_h \leq K_S \mathrm{e}^{\alpha_S(t_n - t_\nu)}. \tag{6.3.7}$$

The stability requirement results in the estimate

$$\|\mathbf{u}^n\|_h \leq K(t_n)\|\mathbf{f}\|_h, \qquad K(t_n) = K_S \mathrm{e}^{\alpha_S t_n}, \tag{6.3.8}$$

stating that the growth of the solution at later times is bounded by the initial data times some exponential factor. We allow here for an exponential factor in order to factor in possible exponential solutions. However, in specialized cases where the continuum problem contains no exponentially growing solutions, more restrictive definitions might be used and the functional growth might even be suppressed entirely.

For practical purposes, a more refined stability definition is useful.

Definition 6.3.4. *Suppose the continuous solution operator $S(t, t_0)$ is bounded by the estimate*

$$\|S(t,\, t_0)\|_{op} \leq K\mathrm{e}^{\alpha(t-t_0)}. \tag{6.3.9}$$

*A difference approximation is then said to be **strictly stable** if in addition to (Definition 6.3.3), we have*

$$\|S_h(t_n,\, t_0)\|_h \leq K_S \mathrm{e}^{\alpha_S(t_n - t_0)} \tag{6.3.10}$$

where

$$\alpha_S \leq \alpha + \mathcal{O}(k) \tag{6.3.11}$$

---

[1]

Theorem 6.3.1. *(5th principle of linear functional analysis: principle of uniformly boundedness) [349]* *Let $(V, \|\cdot\|_V)$, $(W, \|\cdot\|_W)$ be normed K-vector-spaces, $S \subseteq V$ a set of second category in $(V, \tau_{\|\cdot\|_V})$ and $F \subseteq L(V, W)$. Then it is equivalent:*

1. $\forall s \in S: \quad \sup\{\|f(s)\|_W \,|\, f \in F\} < \infty$
   (i.e. F is pointwise bounded in S)
2. $\sup\{\|f\|_{op} \,|\, f \in F\} < \infty$
   (i.e. F is bounded in $(L(V, W), \|\cdot\|_{op})$)

This aims for difference operators that are of order k because it is possible to show [345] that perturbations to a difference operator of order k, e.g. $\mathbf{u}^{n+1} = (Q_0 + k\mathbb{1})\mathbf{u}^n$ automatically satisfy Definition 6.3.3 if their unperturbed part satisfies Definition 6.3.3. But this may lead to an unwanted behavior, since terms of order k can indeed play an important role for stability. The functional growth of (6.3.9) and (6.3.10) can be adapted to the problem resulting in a more restrictive estimate.

Von Neumann stability analysis

Different analysis techniques exist where the most popular certainly is the *Fourier mode analysis* [345–347]. Using the method of lines, the stability properties of the PDE can be analyzed in two steps. First, the semi-discretized PDE in space is transformed to Fourier space, *i.e.* the spatial difference operators are applied to Fourier modes of the form $\xi \exp(i\omega h x_j)$, where ξ is the amplitude of the Fourier mode, ω is the wave number, h is the grid spacing and j is the index of the grid point. For example, with the discrete Fourier mode $\widehat{u}_j = \xi \exp(i\omega h x_j)$, the centered finite difference operator approximating $\partial/\partial x$ becomes

$$\widehat{D}_0 \widehat{u}_j = \frac{\xi \exp(i\omega h x_{(j+1)}) - \xi \exp(i\omega h x_{(j-1)})}{2h} = \xi \exp(i\omega h x_j) i \frac{\sin(\omega h)}{h}. \tag{6.3.12}$$

Solving the Fourier-transformed PDE (which in the semi-discretized sense is an ODE)

$$\partial_t \widehat{\mathbf{u}} = \widehat{Q} \widehat{\mathbf{u}} \tag{6.3.13}$$

reveals whether we get solutions of type

$$\widehat{u} = \mathrm{e}^{\lambda t}, \qquad \mathrm{Re}(\lambda) = 0\,, \tag{6.3.14}$$

where the λ are the eigenvalues of $\widehat{Q}$.

It is a necessary condition for stability that these eigenvalues satisfy

$$|\lambda| \leq \mathrm{e}^{\alpha s k}. \qquad \text{(the von Neumann condition)} \tag{6.3.15}$$

An ODE method will then give a stable evolution if the λk lie within the method's region of stability. It is beyond the scope of this section to describe how these regions can be determined but it is clear for the case (6.3.14) that it should encompass parts of the imaginary axis. In this case, the Euler step or low-order Runge-Kutta schemes fail to give an (un-)conditional stable scheme since they have stability regions tangent to the imaginary axis at the origin.

Another technique is the *energy method* [345]. It provides a different way of proving stability and is simpler to apply than Fourier analysis in cases of PDEs with non-constant coefficients. In this approach, no transformations are used and the calculations are carried out in physical space. Instead, one constructs a suitable norm such that the growth in each step will not exceed $\mathrm{e}^{\alpha k}$. With the help of this method, it is possible to construct difference schemes that are strictly stable [350].

The Courant-Friedrichs-Lewy condition

Another necessary condition for numerical stability is the Courant-Friedrichs-Lewy (CFL) condition [345, 348] stating that the numerical domain of dependence should always contain the theoretical domain of dependence. This can be derived as a consequence from the von Neumann stability analysis for *explicit* schemes. The idea is depicted in Figure 6.1. The theoretical domain of dependence of the value of a solution at one point only depends on the characteristic lines crossing through that point. In other words, the largest characteristic speed v_{max} along every given direction n_i can not exceed the corresponding numerical speed

$$v_{\max} < n_i v^i_{\mathrm{num}}, \qquad v^i_{\mathrm{num}} = \frac{s \Delta x^i}{\Delta t}\,, \tag{6.3.16}$$

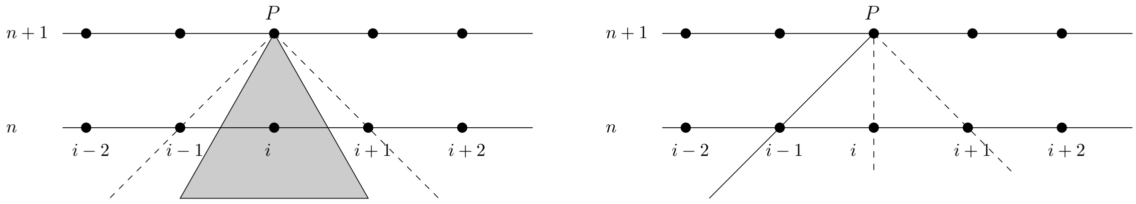

(a) Suppose a problem like the wave equation. In a correct discretization, the theoretical (gray triangle) is enclosed by the numerical domain of dependence (dashed triangle). Here, the difference scheme approximates the value at P with a spatial stencil that spans over the grid points $i-1, i, i+1$.

(b) Incorrect discretization, *e.g.* for an advection equation. The theoretical domain of dependence (straight line) does not coincide with the numerical one (dashed triangle). A correct discretization would involve $i-1, i$ (upwind scheme) instead of $i, i+1$ (downwind scheme).

Figure 6.1: Two examples of the theoretical domain of dependence and the numerical domain of dependence. It becomes apparent that since the numerical domain of dependence has to encompass the theoretical domain of dependence and is therefore usually bigger, acausal information from outside the theoretical domain of dependence can influence the simulation. This effect will grow for very stretched stencils.

where s is the stencil width, *i.e.* the maximum number of points involved in a difference scheme along any direction [351].

Stated differently, we can put a limit on the time-step size

$$\Delta t \leq C \Delta x \,, \tag{6.3.17}$$

where $C = s/v_{\mathrm{num}}$.

Note that implicit schemes do not obey such requirements and therefore allow for much larger time-steps. In physical situations where one is interested in stationary solutions, implicit methods are therefore preferable. In our BBH simulations however, we are interested in all of the non-linear motion from inspiral over merger to ring-down. As this requires a certain minimum time resolution in order to resolve these dynamics, the CFL condition for explicit schemes is in practice no real limit and one can take full advantage of the efficiency of explicit methods.

6.4 Hyperbolicity

In this section, we will briefly mention the concept of *hyperbolicity* since this aspect has been rather important for finding a 3+1 formulation of the Einstein equations that is numerically stable. Roughly speaking, hyperbolicity is a condition on the coefficients of a system of PDEs which grants that the Cauchy formulation of the problem is well-posed; that is, if appropriate data for that system is given on an appropriate hypersurface, then a unique solution can be found in a neighborhood of that hypersurface, and that solution depends continuously on the values of the initial data [183]. Apart from this natural requirement for any given system describing physical interactions, hyperbolicity also implies finite propagation velocities, *i.e.* the past domain of dependence is finite.

Consider a first order system of evolution equations of the form

$$\partial_t u + M^i \partial_i = 0 \,, \tag{6.4.1}$$

where the M^i are $n \times n$ matrices, with the index i running over spatial dimensions. The concept of hyperbolicity can now be defined in terms of the matrices M^i, which are also called *characteristic matrices*. By defining an arbitrary unit vector n_i, one can construct the matrix $P(n_i) := M^i n_i$, which is also known as the *principal symbol* of the system of equations.

A system is then called *strongly hyperbolic* if the principal symbol has real eigenvalues and a complete set of eigenvectors for all n_i. In the weaker case, when P does not have a complete set of eigenvectors but the eigenvalues are still real for all n_i, then the system is called *weakly hyperbolic*. In the case when the system is strongly hyperbolic, but in addition all M^i are symmetric, we say the system is *symmetric hyperbolic*. Finally, we say that a system is *strictly hyperbolic*, if the eigenvalues are not only real but also distinct for all n_i.

Note that in the case when the principal symbol has purely imaginary eigenvalues then the system is called *elliptic*, and if it contains mixed values, *i.e.* real and imaginary, then the system is called *parabolic*. However, these case are of no interest to us here.

Consider now a strongly hyperbolic system. For this system, we can always find a positive definite Hermitian matrix $H(n_i)$ such that

$$HP - P^T H^T = HP - P^T H = 0\,, \tag{6.4.2}$$

where the super-index T represents the transposed matrix. In other words, the new matrix HP is symmetric, and H is called the symmetrizer. We can now use this symmetrizer H to construct an inner product and norm for the solutions of the differential equation in the form

$$\begin{aligned} \langle u, v\rangle &:= u^\dagger H v\,, & (6.4.3)\\ \|u\|^2 &:= \langle u, u\rangle = u^\dagger H u\,, & (6.4.4) \end{aligned}$$

where $u^\dagger$ is the adjunct of u. The norm above is usually called an energy norm and H plays the role of a metric tensor in the space of solutions to the differential equation.

This energy norm can now be taken to estimate the growth of the solution over time. If we write the solution u as a Fourier mode of the form

$$u(x,t) = \tilde{u}(t) e^{ik\vec{x}\vec{n}}\,, \tag{6.4.5}$$

we can then use the evolution equation (6.4.1) together with the time derivative of the energy norm to get

$$\begin{aligned} \partial_t \|u\|^2 &= \partial_t(u^\dagger H u) = \partial_t(u^\dagger) H u + u^\dagger H \partial_t(u) \\ &= ik\tilde{u}^T P^T H \tilde{u} - ik\tilde{u}^T H P \tilde{u} \\ &= ik\tilde{u}^T (P^T H - HP)\tilde{u} = 0\,. & (6.4.6) \end{aligned}$$

Clearly, (6.4.6) represents the growth of the energy norm over time which is only zero for strongly and symmetric hyperbolic systems for which condition (6.4.2) holds. A vanishing growth of this norm shows that the system is well-posed.

When applying the analysis above to the ADM formulation[2] of the Einstein equations one finds in fact, that the system is only weakly hyperbolic. In contrast, as analyzed in [167], the BSSNOK formulation used in this thesis can be shown to be strongly hyperbolic. This is the main reason why the BSSNOK system behaves much better than the ADM system when evolving the set of equations numerically. For a detailed analysis on various formulation of the Einstein equations consider [123].

6.5 Convergence and consistency

Any numerical solution is meaningless without proper studies of how the solution behaves if the resolution is increased. This is because the numerical calculations are approximations to the underlying differential equations, and unless the size of the error of this approximation is known, there is no way of telling whether the numerical calculation is already close to the correct solution or if it is useless.

Suppose we have a differential equation of the form

$$\mathcal{L}u = 0\,, \tag{6.5.1}$$

---

[2] This refers to the version constructed by York.

where $\mathcal{L}$ is some differential operator acting on a function u. Let us write the finite difference version of this equation as

$$\mathcal{L}_\Delta u_\Delta = 0\,, \tag{6.5.2}$$

where Δ denotes the finite step-size of a given finite difference scheme. Clearly, the finite difference version depends on the step size Δ.

We are interested in the behavior of the numerical approximation u_Δ with respect to the exact continuum solution u of the original equations, *i.e.* in the limit when Δ vanishes.

For this, we can define the *truncation error* of our finite difference approximation as

$$\tau_\Delta := \mathcal{L}_\Delta u\,, \tag{6.5.3}$$

which represents the residuum of applying the finite difference operator $\mathcal{L}_\Delta$ to the exact solution u of the original continuum equation.

Typically, the truncation error τ_Δ will not be zero, but it should approach zero as Δ becomes smaller, *i.e.*

$$\lim_{\Delta\to 0} \tau_\Delta = 0\,. \tag{6.5.4}$$

We can then check if the finite difference approximation to the original equation will result in the continuum equation *locally*, *i.e.* at each gridpoint. If this is the case, we call our numerical approximation *consistent*. Consistency is fundamental for any finite difference approximation. Clearly, if it fails, even at one single gridpoint, we will never be able to recover the correct solution to the original equation in the limit of infinite resolution.

If the finite difference scheme is consistent, the truncation error of the difference approximation will approach zero as a power of the discretization parameter Δ. Any given difference approximation is said to be of order n if

$$\lim_{\Delta\to 0} \tau_\Delta \sim \Delta^n\,. \tag{6.5.5}$$

This, however, is only a local property. At any point in space and time, the difference approximation reduces to the original differential equation in the continuum limit.

It is also possible to consider a *global* property of the numerical approximation: *convergence*. Here, instead of considering the truncation error, we introduce the *solution error*,

$$\epsilon_\Delta := u - u_\Delta\,, \tag{6.5.6}$$

which is the difference between exact continuum solution of the original differential equation and numerical solution of the discretized equation. The approximation is then said to be convergent, if the solution error ϵ_Δ goes to zero as the resolution is increased.

Convergence is different from consistency. A numerical approximation can be consistent, but can fail to converge and even diverge. One can check whether a numerical solution converges by considering a set of solutions using different resolutions. However, it is rather difficult to find out whether the numerical solution converges to the exact solution and not to something else. Fortunately, there is a theorem that can be proven, known as the *Lax equivalence theorem*:

Theorem 6.5.1. *Given an initial value problem that is mathematically well posed, and a finite difference approximation to it that is consistent, then stability is a necessary and sufficient condition for convergence.*

This fundamental theorem relates convergence to the exact solution to a property that is usually much easier to prove: stability. If we can show that our numerical scheme is stable, then we can be sure that our numerical solution will not converge to some wrong solution, but to the exact continuum solution.

A detailed analysis of the convergence and consistency of the numerical implementation of the Einstein equations is given in [352].

Testing for convergence

In order to actually quantify the error of our numerical approximation, we have to carry out a convergence test. One fundamental observation made by Richardson [353] is that the solution of a stable finite difference scheme can be interpreted as a continuum function with a power series expansion in the discretization parameter, *i.e.* the grid spacing Δ,

$$u_\Delta(t,x) = u(t,x) + \Delta e_1(t,x) + \Delta^2 e_2(t,x) + \cdots , \tag{6.5.7}$$

where $u(t,x)$ is the solution of the original differential equation, and the $e_i(t,x)$ are error functions at different orders in Δ. If we know the order of accuracy of our numerical approximation, we can expect some of these error functions to vanish, *i.e.* for a first order scheme we would expect $e_1(t,x) \neq 0$, but all other terms should vanish.

Suppose now we have an exact solution to the continuum equation. We can test for convergence by taking two resolutions, Δ_1 and Δ_2, with $r \equiv \Delta_1/\Delta_2 > 1$. By calculating the solution error for both resolution

$$\epsilon_{\Delta_1} = u - u_{\Delta_1} , \qquad \epsilon_{\Delta_2} = u - u_{\Delta_2} , \tag{6.5.8}$$

we can define the *convergence factor* as

$$c := \frac{\|\epsilon_{\Delta_1}\|}{\|\epsilon_{\Delta_2}\|} . \tag{6.5.9}$$

By using Richardson extrapolation, one can find that a finite difference approximation of order n will obey

$$\lim_{\Delta\to 0} c = \left(\frac{\Delta_1}{\Delta_2}\right)^n \equiv r^n . \tag{6.5.10}$$

If resolution Δ_2 is twice as high as Δ_1 then we can expect $c \sim 2^n$, so that a fourth-order scheme $n = 4$ has a convergence factor of $c = 16$. In practice, one can take several resolutions and check that c approaches the expected convergence factor when increasing the resolution. If this is the case, we say that the numerical solution is in the *convergence regime.*

In more general cases, one does not have an exact solution to test for convergence. In this case, it is possible to use three different resolutions $\Delta_1 > \Delta_2 > \Delta_3$ and the convergence factor reads

$$c := \frac{\|u_{\Delta_1} - u_{\Delta_2}\|}{\|u_{\Delta_2} - u_{\Delta_3}\|} . \tag{6.5.11}$$

In the continuum limit, the convergence factor then behaves as

$$\lim_{\Delta\to 0} c = \frac{\Delta_1^n - \Delta_2^n}{\Delta_2^n - \Delta_3^n} . \tag{6.5.12}$$

It should be noted that although we have taken the norms in (6.5.9) and (6.5.11), we can also consider the above pointwise at each gridpoint.

Finally, by using the Richardson expansion (6.5.7), we can estimate the remaining error in the numerical solution by taking two solutions on two different resolutions Δ_1 and Δ_2. The Richardson expansion implies

$$\begin{aligned} u_{\Delta_1} - u_{\Delta_2} &= e_n(\Delta_1^n - \Delta_2^n) + \mathcal{O}(\Delta^{n+1}) \\ &= e_n \Delta_2^n (r^n - 1) + \mathcal{O}(\Delta^{n+1}) \\ &\sim \epsilon_{\Delta_2}(r^n - 1) , \end{aligned} \tag{6.5.13}$$

where ϵ_{Δ_2} is the estimated solution error on our highest resolution grid. We can also write

$$\epsilon_{\Delta_2} \sim \frac{1}{r^n - 1}(u_{\Delta_1} - u_{\Delta_2}) , \tag{6.5.14}$$

which is an estimate for the solution error that is at least accurate to order $n+1$. Given (6.5.14), we can now put an error bar to the numerical solution.

Chapter 7

Computational infrastructure

Any computation relies on some sort of infrastructure such as the discrete representation of variables, I/O methods, parallelization schemes and other items managing the flow of computations as well as the computation itself. This can be very simple when data is represented on a uniform grid. It can become extremely complicated when dealing with heavily nested, arbitrarily shaped grids that overlap each other and have to be split among thousands of processors. This is the case in numerical relativity simulations, where methods such as adaptive mesh refinement (AMR) and multiblock schemes are employed and distributed across parallel supercomputers to be able to deliver the accuracy necessary when simulating BBHs.

A substantial effort has therefore been made over the past 10 years in order to provide tools to numerical relativity scientists that enable the use of state-of-the-art numerical methods and schemes. One major step was the birth of *Cactus* [354–356]. Cactus is meant as a unified programming environment offering enough basic infrastructure such as discrete representation of variables, I/O and multi-processor parallelization. The physicist willing to implement new equations and routines then does not have to carry the burden of writing I/O methods for his or her need and can focus on the main task.

The next major achievement was the implementation of an adaptive mesh refinement (AMR) driver to Cactus, called *Carpet* [357, 358]. Mesh refinement becomes necessary when the field variables require higher resolutions in some regions but can get around with less resolution in other regions. Adding resolution only in regions where necessary is a tremendous saving in computing time and greatly enhances the efficiency. However, this comes at the cost of complicated computer logic, as one needs to keep track of multiple refinement regions spread across many processors.

Finally, another important step is the implementation of multiblock schemes as this allows to take advantage of grid topologies other than the standard Cartesian ones. Part of the achievement of this thesis is the implementation of a fully parallel, multiblock-capable AMR driver. This allows to adapt the grids of the wave-zone to its spherical topology while at the same time using efficient Cartesian AMR grids at the BHs. The advantages are obvious. First, and foremost, as opposed to standard Cartesian grids, the angular resolution of the spherical grid in the wave-zone is now fixed. This means that as one increases the outer boundary located at $R_{\rm max}$, the scaling in computational effort goes as $R_{\rm max}$ and not as $R^3_{\rm max}$ so that it becomes possible to use large wave-zones with high radial resolutions. Second, this allows to reduce the amount of refinement levels so that back-reflection artifacts at mesh-refinement boundaries are minimized and thus allowing for a higher computational accuracy. Third, the computational scaling across multiple processors is greatly improved so that supercomputers on the peta scale can easily be utilized for BH physics. The presented code therefore represents leading state-of-the-art technology in the field of numerical relativity.

Another common problem in the current distribution of Cactus is the lack of proper representation of spherical surfaces. Spherical surfaces are important because many analysis tools such as apparent horizon finding, isolated horizon computations or wave extraction methods make use of the same type of grid topology. Up to now, a scientist willing to implement physics routines operating on such spheres has to manually implement interpolation calls to get the data from the 3D grid to the sphere, has to implement his own surface integration routines and most important, faces the problem of proper and efficient parallelization. We have therefore implemented a grid driver for spheres similar to Carpet, called *Spherical Slice*, which offers a set of easy to use routines in order to manipulate distributed data on spheres. This driver is not limited to the standard spherical polar grids, but does also know about inflated-cube 6-patch grids allowing for equally balanced gridpoint distribution across the sphere and regular derivatives at the poles.

All of these infrastructural items will now be discussed in the next sections.

7.1 The Cactus computational toolkit

Cactus [354–356] is an *application framework* allowing users to work together and develop simulations that run on large-scale supercomputers. Application frameworks represent an abstraction of computational operations and bundle many important aspects when dealing with software development of complex problems. As the computational power advances, computational tools, libraries, and computing paradigms themselves also advance and it can become a difficult task to maintain a running code infrastructure throughout different architectures even for experienced computer scientists. It becomes therefore more and more necessary to develop a common code development framework instead of rewriting essential code from scratch. The main advantage of such an application framework is obvious: the physics inclined programmer does not need to bother with computer science problems and can rely on working and efficient code that is based on the latest computational technologies without being exposed to the raw details of their implementation. The application programmer is interested in an *abstracted* view of the operations needed for data distribution, message passing, parallel IO, scheduling or operations on the numerical grid and not the particular implementation. For example, the application programmer does not need to know about what kind of particular flavor of message passing or some future replacement is used, and a properly designed application framework is future-proof in the sense that it will work on todays as well as on future computer systems. Cactus is designed to meet all of these requirements, and in the next subsections, we will briefly describe the structure of Cactus. For a more detailed insight please refer to [354–356].

Structure

The core of Cactus is made up by the "flesh", and modules which can be be developed by an application programmer are referred to as "thorns". The flesh is independent of all thorns and provides the main program, *i.e.* it parses simulation parameters from a parameter file, activates the appropriate thorns and passing control to thorns as required. Despite this, it does very little, and any computation needs to be provided via thorns. A thorn is the basic working module within Cactus. All user-supplied code goes into thorns, which are, by and large, independent of each other. Thorns mainly communicate within each other via calls to the flesh API. The connection from a thorn to the flesh or to other thorns is specified in configuration files which are parsed at compile time and when the code is build, a separate build tree, referred to as a "configuration", is created for each distinct combination of architecture and configuration options. Associated with each configuration is a list of thorns that are supposed to be compiled into the resulting executable which is referred to as a "thornlist". At run time, the executable reads a parameter file which details which thorns are to be active, and specifies values for the control parameters for these thorns. The main program flow is shown in Figure 7.1 and Figure 7.2.

Modularity

Cactus introduces a separate name space for each thorn and encapsulates the thorn's variable definitions and function declaration which are registered within the flesh. The application programmer can decide which variables and functions should be accessible from other thorns. There are two important pieces of terminology used in the Cactus language. *Grid variables* are variables which can be passed between thorns or routines belonging to the same thorn through the defined flesh interface; this implies it is related to the computational grid rather than being an internal variable of the thorn or one of its routines. An *implementation* is an abstract name for the functionality

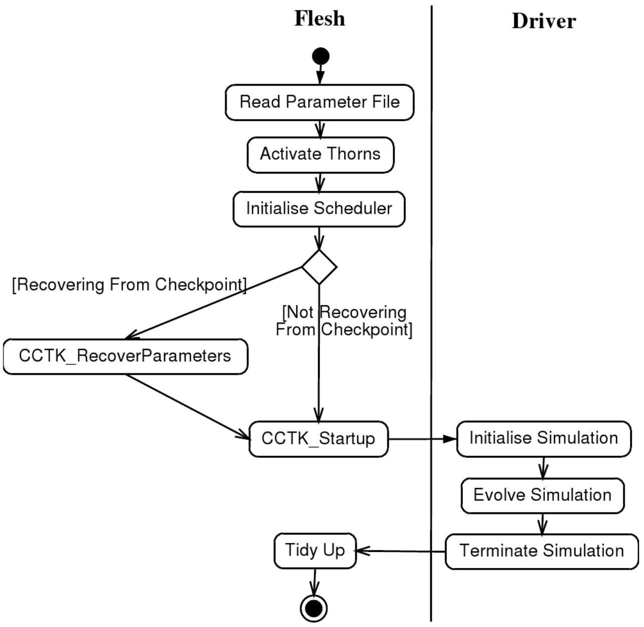
Flesh
Driver
Read Parameter File
Activate Thorns
Initialise Scheduler
[Recovering From Checkpoint]
[Not Recovering From Checkpoint]
CCTK_RecoverParameters
CCTK_Startup
Initialise Simulation
Evolve Simulation
Terminate Simulation
Tidy Up

Figure 7.1: This figure illustrates the main flow of control in the Cactus framework. The flesh initializes the code, then hands control to the driver thorn. Figure taken from [354].

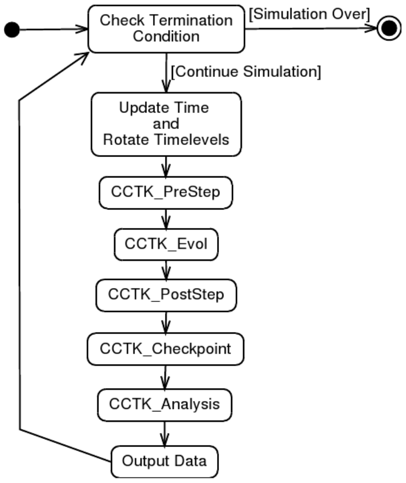
Check Termination Condition
[Simulation Over]
[Continue Simulation]
Update Time and Rotate Timelevels
CCTK_PreStep
CCTK_Evol
CCTK_PostStep
CCTK_Checkpoint
CCTK_Analysis
Output Data

Figure 7.2: This figure illustrates the evolution action item (corresponding to the *evolve simulation* action in Figure 7.1). Figure taken from [354].

offered by a thorn; all thorns providing the same implementation expose the same interfaces to the outside world, and only one such thorn may be active at a time. Grid variables fall into three categories: grid scalars, which are single numbers (per processor); grid functions, which are distributed arrays with a size fixed to the problem size (all grid functions have the same size); and grid arrays which are similar to grid functions but may have any size. The variable scope of these grid variables may be private, *i.e.* visible only to routines from this thorn; protected, *i.e.* visible to all thorns in the group of friends of this thorn's implementation; or public, *i.e.* visible to all thorns which inherit from this thorn's implementation. The thorn's parameters have a similar scope and may be numeric, boolean, keywords, strings or lists.

Routines from a thorn are scheduled within the Cactus' scheduling mechanism. This is described in the next subsection.

Scheduling mechanism and control inversion

An important aspect when writing Cactus thorns is the time at which a routine is called by the Cactus flesh. Usually, there are routines that evolve the field variables, *e.g.* the metric components in our case, that are contained in one thorn, and then there may be additional thorns that do analysis operations on the evolved field variables such as, *e.g.* calculating Ψ_4 after one evolution loop. For this reason, the application programmer has to schedule the thorn's routines at various time bins and relative to the times when other routines from this thorn or other thorns are run. For example, the metric evolution of the Einstein equations may be scheduled in the time bin CCTK_Evol and the computation of Ψ_4 may be scheduled in the time bin CCTK_Analysis which is called after CCTK_Evol (see Figure 7.2). Additionally, routines within one time bin may be scheduled *before* or *after* any other routine registered in the flesh. These specifications form a directed acyclic graph, and a topological sort is carried out to determine the order of execution of all routines registered in the flesh. This defines the concept of *control inversion*. In traditional programming the flow is controlled by a central piece of code. Using control inversion, this central control as a design principle is left behind. Although the caller will eventually get its answer, how and when is out of control of the caller. It is the callee who decides to answer how and when. Control inversion as a design guideline serves the following purposes: *(i)* There is a decoupling of the execution of a certain task from implementation. *(ii)* Every system can focus on what it is designed for. *(iii)* Every system does not make assumptions about what other systems do or should do. *(iv)* Replacing systems will have no side effect on other systems.

Memory management, multi-processor distribution and message passing

In order to take full advantage of parallel multi-processor supercomputing, it is necessary to split the work load into smaller subsets of the original computational domain so that each processor works on a subset of the original data only. Optimally, if the computational domain can be split into n equal chunks of data, the computational gain should be n times larger when using n processors as compared to a single processor execution. Usually, this requires the allocated memory to be split across multiple processors as most architectures currently make use of distributed memory. This means that one processor is aware only of its assigned subset of the total domain, and as usually information from adjacent domains is required for the current computation, this data needs to be obtained from the neighboring processor owning the data. This is done by setting up interprocessor boundary zones which hold copies of adjacent grid points from the neighboring processor (see Figure 7.3). The boundary zones usually need to be updated after each computational step, and this particular task is done by some parallelization layer that takes care of inter-processor communication. In practice, there are different implementations for such a layer, and the most commonly used one is the *message passing interface* (MPI) [359] standard. The MPI standard defines a set of routines that enable one to, *e.g.* copy data buffers between processors by setting up a single MPI *process* per processor core. Altogether, the MPI processes are then able to communicate among each other to *e.g.* update the interprocessor boundary zones.

However, higher order methods require a substantial amount of interprocessor boundary zones, leading to a significant memory overhead for each MPI process. This can be counteracted by using

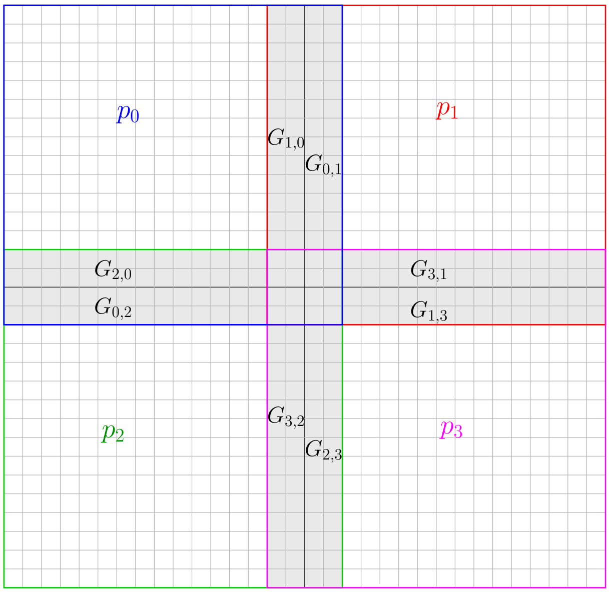

Figure 7.3: This figure illustrates how a 2D domain is split across 4 processors p_n. Each of the processors contains only a subsection of the grid indicated by the colored boxes. The gray regions indicate the interprocess-boundary zones for processor p_n denoted by $G_{n,m}$ which hold copies of the data of the neighboring processor p_m in the given direction. The boundary zones overlap at the corners of the local grids. By first updating all boundary zones in one direction and then in another direction, it is possible to avoid multiple copying of the data at the corners.

OpenMP [360] within a multi-core node, which is especially attractive on modern systems with eight or 16 cores per node; all performance critical parts of Cactus support OpenMP. Instead of running one MPI process per core, the resulting hybrid code divides one MPI process into several *threads*. Similar to MPI processes, threads represent execution of the code on a subset of the original data in parallel. Since on one node all processor cores have access to the entire memory of that node, it is not necessary for threads to introduce additional interprocessor boundary zones. Depending on the interprocessor boundary size, this can result in non-trivial amounts of memory that can be saved. Additionally, as interprocessor communication is obsolete, there is also a non-negligible speed advantage over plain MPI parallelization. Furthermore, the implementation of a thread reduces to a simple pre-processor statement telling the compiler to tile a loop into several threads.

In Cactus, all of the above is of course hidden to the application programmer. However, these operations are not introduced by the flesh. Rather, there is the concept of a Cactus *driver* implementation, which is a thorn that takes care of memory management, multi-processor domain decomposition and interprocessor communication. The driver is free to allocate memory for variables and set up the data layout in whatever way is most appropriate. The application routines just get a block of data that can be computationally processed. The driver is also the place which holds the parallelization logic and defines how and in what way interprocessor boundary zones need to be updated. An example of a Cactus driver is described in the next section.

7.2 Adaptive mesh refinement

In physical systems, it is often the case that the most interesting phenomena, *e.g.* regions with large gradients in the field variables, occur only in a small subset of a spatial and temporal domain. In contrast, other regions may not be subject to large variations and change only over a large-scale interval. For a numerical simulation, this means that there are large-gradient regions where

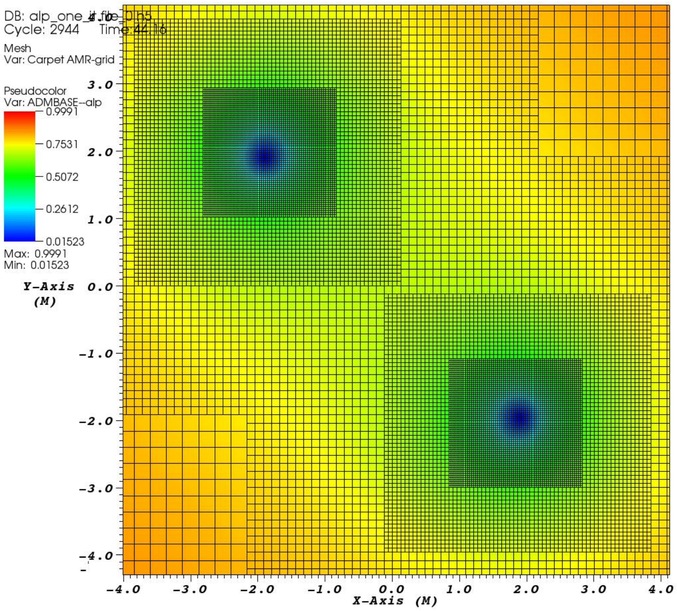

Figure 7.4: Illustration of AMR used in BBH simulations. The BHs are indicated by the blue spots through the lapse function which approaches zero at the singularity. A hierarchy of nested refined grids is located at each of the BHs. The refinement centers move with the BHs during evolution.

a rather high resolution is required compared to the large-scale dynamics of other regions where it is possible to get away with less resolution. In the brute force approach, when using finite difference approximations, one can introduce a single uniform grid on which the field variables are represented, and choose the associated resolution according to the minimal resolution necessary to resolve the dynamics in the large-gradient regions. While this approach is rather easy to implement numerically, it has one significant drawback: a large percentage of computational resources is spend in regions that can get away with far less resolution and a less perfect approximation might already be sufficiently good compared to a higher resolution computation. To circumvent this problem, one can introduce a *non-uniform* computational domain, using a finer mesh resolution in the "interesting" regions and a coarser resolution in other areas. This method is known as *mesh refinement*. It allows to significantly reduce the efforts in computational time and memory, especially when dealing with large-scale simulations on massive parallel computers as is the case for BBH simulations. In this way, the resolution can effectively be increased by an amount that would have been impossible otherwise.

In many situations, it may be desirable to *adaptively* refine the computational mesh according to the evolution of the field variables such that a certain local target truncation error is maintained. For example, in BBH simulations, the orbiting BHs represent regions of strong curvature which require mesh refinement (see Figure 7.4), but as the BHs are moving, the refined regions need to move as well, *i.e.* the refinement needs to adapt during the evolution. This is known as *adaptive mesh refinement* (AMR) and has been used for decades [361], especially in the fluid dynamics community [362, 363]. In 2004, Schnetter and collaborators introduced *fixed mesh refinement* to 3D numerical relativity [357] which was later extended to moving refinement boxes and therefore adaptive mesh refinement[1]. In the following subsections, we will describe the underlying concept of mesh refinement, where most of which is based on [357].

---

[1] Note that as there is no proper refinement criterion based on some local truncation error, strictly speaking, this is only moving fixed mesh refinement

Carpet: The Cactus AMR driver

AMR has been introduced by Schnetter and collaborators [357] in the form of a Cactus driver called *Carpet* [358], which interacts with the Cactus scheduler in order to determine which routines are applied to which grid at which time. As Cactus is based on the concept of control inversion (cf. Section7.1), it is straight-forward to change an existing Cactus application with physics computations on uniform grids to mesh refinement without rewriting any of the physics thorns. The main changes are minor technicalities such as changing the execution rule, *i.e.* whether a given routine should be called only once for a single time-step or whether it should be called for each refined piece of the grid individually. For example, the computation of the evolution equations have to be executed on each refined piece of the grid, while the interpolation of a field variable on to a sphere is a global operation that needs to be executed only once per time-step. The Carpet mesh refinement driver makes use of the methods described in the next subsections.

Mesh refinement method

Carpet applies the Berger-Oliger approach to mesh refinement [361], where the computational domain as well as all refined subdomains consists of a set of rectangular grids. More specifically, it makes use of a simplified Berger-Oliger method ("minimal Berger-Oliger") where the grid points are located on a grid with Cartesian topology, and the grid boundaries are aligned with the grid lines. Fine grid boundaries, however, are allowed to occur in between coarse grid points, and a properly nested example is shown in Figure 7.5. Here, the notation is the following. The grids are grouped into *refinement levels* (or simply "levels") L^k, each containing an arbitrary number of grids ${G^k}_j$. Each grid on refinement level k has the grid spacing (in one dimension) Δx^k. The grid spacings are related by the relation $\Delta x^k = \Delta x^{k-1}/N_{\text{refine}}$ with the integer *refinement factor* N_{refine}. In what follows we will assume that N_{refine} is always set to 2. The base level L^0 covers the entire domain (typically with a single grid) using a coarse grid spacing. The base level need neither be rectangular nor connected. The refined grids have to be *properly nested.* That is, any grid ${G^k}_j$ must be completely contained within the set of grids L^{k-1} of the next coarser level, except possibly at the outer boundaries.

The crucial question how the grids should refine is deferred to the user, *i.e.* the user has to manually specify where the refinement boxes have to be placed initially. For BBH simulations, one ideally chooses the refinement centers to be located at the BHs. During evolution, the refinement centers are moved according to either tracking the punctures or the centers of the individual apparent horizons.

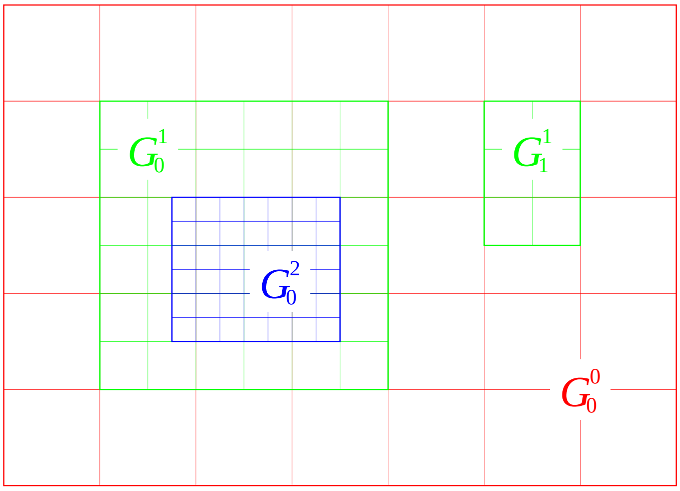

Figure 7.5: Base level G_0^0 and two refined levels G_j^1 and G_j^2, showing the grid alignments and demonstrating proper nesting. Figure taken from [357].

Time evolution scheme

The time evolution scheme is implemented according to the Berger-Oliger AMR scheme [361]. In this scheme, one first evolves coarse grid data forward in time before evolving any data on the finer grids. These evolved coarse grid data can then be used to provide (Dirichlet) boundary conditions for the evolution of data on the finer grids via *prolongation*, *i.e.* polynomial interpolation in time and space[2]. This is depicted in Figure 7.6(a). For hyperbolic systems, where a Courant-like criterion holds, a refinement by a factor of N_{refine} requires time step sizes that are smaller by a factor N_{refine}, and hence N_{refine} time steps on level $k+1$ are necessary for each time step on level k. At time steps in which the coarse and fine grids are both defined, the fine grid data are *restricted* onto the coarse grid (via a simple copy operation) after it has been evolved forward in time. If there are more than two grid levels, then one proceeds recursively from coarsest to finest, evolving data on the coarsest grid first, interpolating this data in time and space along boundaries of finer grids, evolving the finer grid data, and restricting evolved data from finer to coarser grids whenever possible. This is illustrated in Figure 7.6(b).

For time evolution schemes that consist only of a single iteration (or step), the fine grid boundary condition needs to be applied only once. Most higher-order time integrations schemes, such as Runge-Kutta or iterative Crank-Nicholson, are actually multi-step schemes and correspondingly require the fine grid boundary condition to be applied multiple times. If this is not done in a consistent manner at each iteration, then the coarse and the fine grid time evolution will not couple correctly, and this can introduce a significant error.

There are several ways to guarantee consistent boundary conditions on fine grids. The method presented in [357] involves not providing any boundary condition to the individual integration substeps, but instead using a larger fine grid boundary, as demonstrated in Figure 7.6(c). That is, each of the integration substeps is formally applied to a progressively smaller domain, and the prolongation operation re-enlarges the domain back to its original size. Note that this “buffering” is done only for prolongation boundaries; outer boundaries are handled in the conventional way. Also, this is done only for the substeps due to the time integration scheme, so that the prolongation *is* applied at fine grid times when there is no corresponding coarse grid time. Note also that the use of buffer zones is potentially more computationally efficient.

7.3 Multiblock schemes

Of particular topical relevance is the construction of long waveforms which can be used for gravitational-wave analysis of the binary [51], and also to construct a family of templates [33–35, 63], so to inform and improve gravitational wave detection algorithms. Here the requirements are particularly challenging for numerical simulations, requiring waveforms which are accurate in phase and amplitude over multiple cycles to allow for an unambiguous matching to post-Newtonian waveforms at large separation. Some recent studies have shown very promising results in this direction for particular binary black hole models [257, 364–371]. However, they have also highlighted the problems associated with producing long waveforms of sufficient accuracy.

First of all, for binaries with a larger separation, systematic errors associated with gravitational waveform extraction at a finite radius become more pronounced. Typically a number of extraction radii are used, and the results extrapolated to infinite radius (assuming such a consistent extrapolation exists given potential issues of gauge). In order to have some confidence in the results, the outermost “extraction sphere” needs to be at a large radius, say on the order of $150-200M$ (see Section 15.1). Even at this radius, the amplitude of the extrapolated waveform differs significantly from the measured waveform. Unfortunately, extracting at larger radii comes at a computational expense. One of the standard methods in use today is finite differencing in conjunction with “mesh refinement”, in which the numerical resolution is chosen based on the length scale of the problem. A minimum number of discrete data points are required to resolve a feature of a given size accurately, which sets a limit on the minimum resolution which should be applied in a region.

---

[2] Carpet uses quadratic interpolation in time and fifth-order interpolation in space.

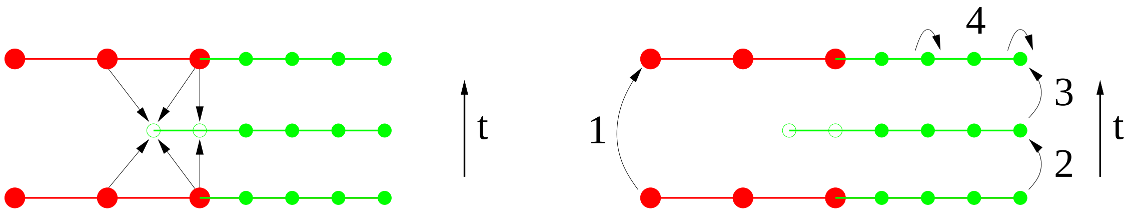

(a) Schematic for the prolongation scheme, in $1+1$ dimensions, for a two-grid hierarchy. The large filled (red) circles represent data on the coarse grid, and smaller filled (green) circles represent data on the fine grid. The arrows indicate interpolation of coarse grid data in space and time, necessary for the boundary conditions on the fine grid. Figure taken from [357].

(b) Schematic for the time evolution scheme, in $1+1$ dimensions, for a two-grid hierarchy. The large filled (red) circles represent data on the coarse grid, and smaller filled (green) circles represent data on the fine grid. The algorithm uses the following order. 1: Coarse grid time step, 2 and 3: fine grid time steps, 4: restriction from fine grid to coarse grid. Since the fine grid is always nested inside a coarse grid, there are also coarse grid points (not shown) spanning the fine grid region (at times when the coarse grid is defined) at the locations of "every other" fine grid point; the data at these coarse grid points are restricted (copied directly) from the fine grid data. Figure taken from [357].

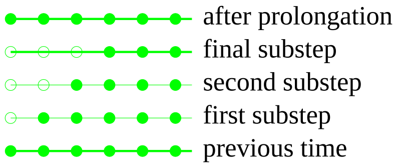

(c) Schematic for the "buffering" during time integration. Shown is the left edge of a refined region, which extends further to the right, which is integrated in time with a 3-step iterative Crank-Nicholson method. At the filled points (in the interior), time integration proceeds as usual. The empty points (near the boundary) are left out, because no boundary condition is given during time integration. A prolongation after the time integration fills the empty points again. This whole scheme corresponds to either of the steps labeled 2 and 3 in Figure 7.6(b). Figure taken from [357].

Figure 7.6: Schematics of aspects of AMR logic.

Thus, even with mesh refinement there is a limit on the coarseness of the grid which can be allowed in the wave-zone. For a Cartesian grid, the number of computational points scales as r^3, so that requiring a sufficient resolution to $200M$ already comes at significant expense, and increasing this distance further becomes impractical.

An additional difficulty arises from the requirement that the outer boundary have minimal influence on the interior evolution, since it is (in all current binary black hole codes) an artificial boundary, that is, the wave-zone, *i.e.* the extraction world-tubes, shall be causally disconnected from the artificial outer boundary for the duration of the simulation (see Figure 7.7). This places an additional requirement on the size of the computational grids, so that even outside the wave-zone region where the physics is accurately resolved, it is conventional to place several even coarser grids. This is done in the knowledge that the physical variables can not be resolved in these regions, but the grids are helpful as a numerical buffer between the outer boundary and interior domain. Again, adding these outer zones comes at a computational expense. The boundaries with under-resolved regions also lead to unphysical reflections which can contaminate the solution. The problem of increasing the grid size can be significantly reduced if, rather than a Cartesian coordinate system, one uses a discretization which has a radial coordinate. Then, for a fixed angular resolution, the number of points on the discrete grid increases simply as a linear function of r, rather than the r^3 of the Cartesian case. This has two advantages. The gravitational wave-zone has spherical topology and therefore, a numerical approximation would be most efficiently represented by employing a spherical grid. A further computational motivation comes from the fact that non-synchronous mesh-refinement (such as the Berger-Oliger algorithm) can greatly complicate the parallelization of an evolution scheme, and thus having many levels of refinement clearly has an impact on the efficiency of large scale simulations. This will become particularly relevant for the coming generations of peta-scale machines which strongly emphasize parallel execution (possibly over several thousand cores) over single processor performance.

The use of spherical-polar coordinates has largely been avoided in 3-dimensional general relativity due to potential problems associated with the coordinate singularity at the poles. Additionally, even if regularization were simple, the inhomogeneous areal distribution of latitude-longitude grid points over the sphere make spherical-polar coordinates sub-optimal. A number of alternative coordinate systems have been proposed and implemented for studies of black holes in 3D. The Pittsburgh null code avoids the problem of regularization at the poles by implementing a 2D stereographic patch system (see Section 8.2). Cornell/Caltech have developed a multipatch system which has been used for long binary black hole evolutions [156, 372] [3]. This code, using spectral spatial differentiation, uses an intricate patch layout in order to reduce the overall discretization error. The boundary treatment between patches is based on the transfer of characteristic variables. A similar approach was implemented by the LSU group, for the case of finite differences with penalty boundary conditions [375], and used to successfully evolve single perturbed black holes with a fixed background [376] and have recently been attempted for binary black hole systems [377].

In this section, we present the computational infrastructure for a BBH evolution code “Llama” based on adapted radial coordinates in the wave zone, for generic evolution systems. The grids follow a prescription which was first used by Thornburg, in which six regular patches cover the sphere. Data at the boundaries of the patches are filled by interpolation. The six patch wave zone is coupled to an interior Cartesian code, which contains the zone in which the binary system moves, and optionally allows for mesh refinement around the individual bodies. The resulting code has the advantages of making use of established techniques for moving puncture evolutions on Cartesian grids, while having excellent efficiency and accuracy in the wave zone due to the adapted spherical grids.

Details on the convergence and accuracy, as well as first results based on this code can be found in Section 11.2 and Section 15.1, respectively. Further details on the evolution scheme are given in Section 8.1.

In the following subsections, we will focus on the details of the coordinate structures that are employed, and the setup of the multiblock scheme.

---

[3] Multi-domain spectral methods have previously been applied to the problem of generating initial data for binaries in [205, 373, 374].

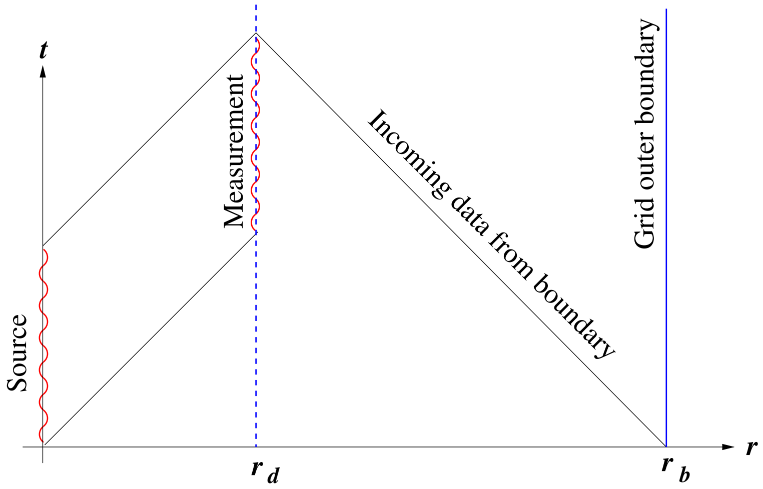

Figure 7.7: Schematic of the causal propagation of information during the evolution. The gravitational wave source is located in the vicinity of $r = 0M$, with waves propagating outward at the speed of light $c = 1$, and are measured at radius r_d for a time of interest which would include the inspiral, merger and ring-down of a binary system. The unphysical outer boundary of the grid is located at r_b, which is chosen to be sufficiently far removed so that the future Cauchy horizon of the domain of dependence of the initial slice does not reach r_b until the measurement is complete.

Multiple grid patches, local and global coordinates

In numerous computational applications, it becomes impractical to model the problem at hand with just one single grid. A perfect example is the wave-zone problem of BBH simulations. Usually, one can gain computational efficiency by employing multiple *curvi-linear* grid patches with adapted coordinates that cover the computational domain. Each patch may have its own local coordinate system (a, b, c) and a well-defined mapping to global Cartesian coordinates (x, y, z), so that the grid of a given patch is uniform in local coordinates, but may be curved in the global coordinate frame. If the patches cover a simply-connected domain, they must, depending on the method, overlap or at least touch in order to be able to pass data from patch to patch. The transfer of data between patches is necessary because information may travel in certain directions depending on the characteristics of the PDE. One method that leads to a provable mathematically stable scheme and that requires the patches to be touching is the *penalty method* (or *simultaneous approximation term* (SAT) technique) [378–380]. This method has been applied to numerical relativity in *e.g.* [377, 381]. The drawback of this method is that it requires a detailed analysis of the characteristics of the evolution system, and by construction cannot handle any shocks or other discontinuities. In order to circumvent this, we prefer interpolating boundary conditions. In this method, the patches are required to overlap, but gridpoints do not need to coincide. In the overlap regions, or ghost-zones, the fields are updated via Lagrange interpolation polynomials[4]. The depth of the ghost-zones is determined by the stencil width of the finite difference operators.

The problem may then be modeled locally on each patch, and a coordinate transformation can be used to represent the field variables in each of the local coordinate patches in the overlap region. As this works well for scalar fields, the extension to tensor fields is cumbersome. For tensor fields, a change in coordinates must be accompanied with a basis transformation, and depending on the number of overlap zones and individual local coordinate systems, this can become quite a bit of work.

However, it is possible to represent all tensor fields in the same global coordinate frame, *i.e.* the fields are parametrized by local coordinates (a, b, c), but the global coordinate basis (x, y, z) is

---

[4] The coupling of this scheme to relativistic hydrodynamics simulations and the associated appearance of shocks requires the use of (weighted) essentially non-oscillatory ((W)ENO) interpolation.

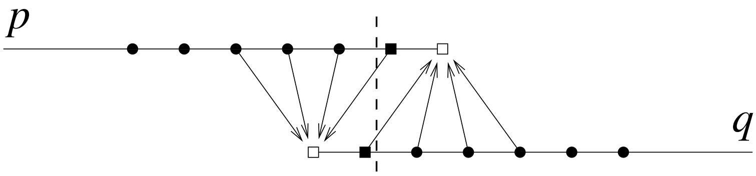

Figure 7.8: Schematic of interpolating patch boundaries in 1-dimension, assuming 4-point finite difference and interpolation stencils. Points in the nominal zones, $\mathcal{N}_{p,q}$, are indicated by filled circles, points in ghost zones, $\mathcal{G}_{p,q}$, by open squares, and points in overlap zones, $\mathcal{O}_{p,q}$, by closed squares. The vertical dotted line demarcates the boundary between nominal zones on each patch. Ghost points on patch p are evaluated by centered interpolation operations from points in $\mathcal{S}_q$ on the overlapping patch (arrows) and *vice versa*.

never changed. This makes it possible to represent all fields in terms of the local coordinates of each patch without ever applying a basis transformation. Thus, each tensor component can be treated like a scalar field in the overlap regions.

By finding the global (Cartesian) coordinates of the ghost-points from the overlap region of one patch, it is possible to determine the nearby points of the interpolation molecule given the global-to-local coordinate mapping of the other patch. This is described in the next subsection.

Interpatch interpolation

Data is communicated between patches by interpolating onto overlapping points. Each patch, p, is responsible for determining the numerical solution for a region of the spacetime. The boundaries of these patches can overlap neighboring patches, q, (and in fact must do so for the case of the interpolating boundaries considered here), creating regions of the spacetime which are covered by multiple patches. We define three sets of points on a patch. The *nominal* regions, $\mathcal{N}_p$, contain the points where the numerical solution is to be determined. The nominal regions of the patches do not overlap, $\bigcap_p \mathcal{N}_p = \emptyset$, so that if data is required at any point in the spacetime, it can be obtained without ambiguity by referencing the single patch in whose nominal region it resides. A patch, p, is bounded by a layer of *ghost* points, $\mathcal{G}_p$, which overlap the nominal zones of neighboring patches, q, $\mathcal{G}_p \cap \bigcup_q \mathcal{N}_q = \mathcal{G}_p$, and are filled by interpolation. (These points are conceptually similar to the inter-processor ghost-zones used by domain decomposition parallelization algorithms in order to divide grids over processors.) The size of these regions is determined by the width of the finite difference stencil to be used in finite differencing the evolution equations on the nominal grid. Finally, an additional layer of *overlap* points, $\mathcal{O}_q$, is required: i) to ensure that the set of stencil points, $\mathcal{S}_q \subset \mathcal{O}_q \cup \mathcal{N}_q$, used to interpolated to the ghost zone does not itself originate from the ghost zone of the interpolating patch, $\mathcal{S}_q \cap \mathcal{G}_q = \emptyset$, $\mathcal{O}_q \cap \bigcup_p \mathcal{N}_p = \mathcal{O}_q$; and ii) to compensate for any difference in the grid spacing between the local coordinates on the two patches. An illustration of the scheme in 1-dimension the scheme is provided in Fig. 7.8.

Note that points in $\bigcup_q \mathcal{O}_q \subset \bigcup_p \mathcal{N}_p$ are not interpolated, but rather are evolved in the same way as nominal grid points within $\bigcup_p \mathcal{N}_p$. That is, in these regions points on each grid are evolved independently, and is in principle multi-valued. However, since the union of set of nominal points on each patch $\bigcup_p \mathcal{N}_p$ uniquely and unambiguously covers the entire simulation domain, *i.e.* $\bigcap_p \mathcal{N}_p = \emptyset$, and since the overlap regions are a subset of the nominal grid, if data is required at a point within these overlap zones, there is exactly one patch owing this point on its nominal grid, and it will be returned uniquely from this patch. The differences between evolved field values evaluated in these overlap points converge away with the finite difference order of the evolution scheme.

The use of additional overlap points makes this inter-patch interpolation algorithm somewhat simpler than the one implemented by Thornburg in [262]. That algorithm required inter-patch boundary conditions to be applied in a specific order to ensure that all interpolation stencils are evaluated without using undefined grid points, and requires off-centering interpolation stencils under certain circumstances, which is not necessary when overlap points are added. It also relies on the particular property of the inflated-cube coordinates which ensured that the ghost-zones could be filled using 1-dimensional interpolation in a direction orthogonal to the boundary. This property would be non-trivial (and often impossible) to generalize to match arbitrary patch boundaries, such as that between the Cartesian and radially oriented grids of Fig. 7.11.

Another significant difference between Thornburg's approach and the approach presented here is that former stores tensor components in the patch-local frame, while we store them in the global coordinate frame. Evaluating components in the patch-local frame requires a basis transformation while interpolating. This is further complicated in the case of non-tensorial quantities (such as the $\tilde{\Gamma}^i$ of the BSSNOK formulation) which have quite complicated basis transformation rules involving spatial derivatives. Instead, we store tensor components in the global coordinate frame, which requires no basis transformation during inter-patch interpolations.

The number of ghost points in $\mathcal{G}_p$ can be reduced using finite difference stencils which become lop-sided towards the boundaries of the patch, and may provide an important optimization since interpolation between grids can be expensive, particularly if processor communication is involved. However, this tends to be at the cost of increased numerical error in the finite difference operations towards the grid boundaries. We have generally found it preferable to use centered stencils throughout the nominal, $\mathcal{N}_p$, and overlap, $\mathcal{O}_p$, zones and have applied certain optimizations to the interpolation operators as described below. Another optimization can be achieved by using lower order interpolation so that it is possible to reduce the number of overlapping points in $\mathcal{O}_p$.

The interpolation scheme for evaluating data in ghost zones is based on Lagrange polynomials using data from the overlapping patch. In 1-dimension, the Lagrange interpolation polynomial can be written as

$$\mathcal{L}_x[\phi](x) = \sum_i^N b_i(x)\,\phi_i\,, \tag{7.3.1a}$$

where the coefficients are

$$b_i(x) = \prod_{k\neq i} \frac{(x - x_k)}{(x_i - x_k)}\,. \tag{7.3.1b}$$

In these expressions, $x \in \mathcal{G}_p$ is the coordinate of the interpolation point and $\phi_i \in \mathcal{S}_q \subset \mathcal{N}_q \cup \mathcal{O}_q$ are the values at grid-points in the interpolation molecule surrounding x. The number of grid-points in the interpolation molecule, N, determines the interpolation order, and interpolation of n-th order accuracy is given by $N = n + 1$ stencil points in the molecule.

For interpolation in d-dimensions, the interpolation polynomial can be constructed as a tensor product of 1-dimensional Lagrange interpolation polynomials along coordinate directions, $\mathbf{x} = (x^1, ..., x^d)$:

$$\begin{aligned}\mathcal{L}[\phi](\mathbf{x}) &= \mathcal{L}_{x^1}[\phi](x^1) \otimes \ldots \otimes \mathcal{L}_{x^d}[\phi](x^d) \\ &= \left(\sum_i^N b_i(x^1)\,\phi_i\,,\right) \cdots \left(\sum_j^N c_j(x^d)\,\phi_j\right)\,.\end{aligned} \tag{7.3.2}$$

Therefore, for d-dimensional interpolation of order n, one has to determine N^d neighboring stencil points and associated interpolation coefficients, Eq. (7.3.1b), *for each* point in the ghost-zone of a given patch. Most generally, full 3-dimensional interpolation is required, though in particular cases coordinates between two patches can be constructed such that they align locally so that only 1-dimensional interpolation is needed. This is, for instance, the case for the overlap region between the inflated-cube spherical patches used here (see Fig. 7.11). We have optimized the current code to automatically take advantage of this.

In order to interpolate to a point for which the coordinates a_i^p given in the basis of patch p are given, we need to know the patch owning the nominal region containing this point. For this we first convert a_i^p to the global coordinate basis x_i, then determine which patch q owns the corresponding nominal region $\mathcal{N}_q$, and then convert x_i to the local coordinate bases this patch a_i^q. By construction, patch q has sufficient overlap points to evaluate the interpolation stencil there:

$$x_i := \text{local-to-global}_p(a_i^p)\,, \tag{7.3.3a}$$

$$q := \text{owning-patch}(x^i)\,, \tag{7.3.3b}$$

$$a_i^q := \text{global-to-local}_q(x^i)\,. \tag{7.3.3c}$$

The three operations "local-to-global", "owning-patch", and "global-to-local" depend on the patch system and their local coordinate systems.

We can then find the points of patch q that are closest to the interpolation point a_i^q in the local coordinates this patch. In order to find these points, we exploit the uniformity of the grid in local coordinates. The grid indices of the stencil points in a given direction are determined via

$$i \in \left\{ \text{floor}(j+k) \;\middle|\; j = \frac{x - x_0}{\Delta x},\ k = -\frac{n}{2}, \cdots, \frac{n}{2} \right\}\,, \tag{7.3.4}$$

where x_0 is the origin of the local grid, n is the interpolation order, and "floor" denotes rounding downwards to the nearest integer.

There remains to be determined the refinement level which contains the region surrounding the interpolation point, as well as the processor that owns this part of the grid. For this purpose, an efficient tree-search algorithm has been implemented. In this algorithm, the individual patches and refinement levels are defined as "super-regions", i.e., bounding boxes that delineate the global grid extent before processor decomposition. Each of these super-regions is recursively split into smaller regions. The leaves of the resulting tree structure represent the individual local components of the processor decomposition. Locating a grid point in this tree structure requires $O(\log n)$ operations on n processors, whereas a linear search (that would be necessary without a tree structure) would require $O(n)$ operations.

While the corresponding tree structure is generic, the actual algorithm used in `Carpet` splits the domain into a kd tree of depth d in $d = 3$ dimensions. That is, the domain is first split into k sub-domains in the x direction, each of these sub-domains is then independently split into several in the y direction, and each of these is then split in the z direction. This leads to cuboid sub-domains for each processor, where the sub-domains do not overlap, and where each sub-domain can have a different shape. `Carpet` balances the load so that each processor receives approximately the same number of grid points, while keeping the sub-domains' shapes as close to a cube as possible.

Our implementation pre-calculates and stores most of the above information when the grid structure is set up, saving a significant amount of time during interpolation. In particular, the following are stored:

- For each ghost-point, the source patch (where the interpolation is performed), and the local coordinates on this patch;
- For each ghost-point, the interpolation stencil coefficients (7.3.1b);
- For each processor, the communication schedule specifying which interpolation points need to be sent to what other processor.

When the grid structure changes, for example, when a mesh-refinement grid is moved or resized, these quantities have to be recalculated.

Altogether, the inter-patch interpolation therefore consists of applying processor-local interpolation stencils, sending the results to other processors, receiving results from other processors, and storing these results in the local ghost-points. These are all operations requiring no look-up in complex data structures, and which consequently execute very efficiently on modern hardware.

Global derivatives

In order to work in the global Cartesian coordinate frame, it is necessary to take derivatives with respect to the Cartesian coordinate basis. Otherwise, the system would be mathematically ill-defined.

However, we can only approximate the derivative operators of the local coordinate frame by finite differences since it is generally only the local coordinates that define a uniform grid. In the global coordinates, the grid is generally curvi-linear and does not have an equidistant distribution of gridpoints.

Fortunately, we can construct "global" derivatives from the "local" ones by applying a Jacobi transformation, *i.e.*

$$\frac{\partial}{\partial x^k} = \frac{\partial a^i}{\partial x^k}\frac{\partial}{\partial a^i}\,, \tag{7.3.5}$$

where x^k are the global coordinates and a^i are the local coordinates. The Jacobians $J^i{}_k \equiv \partial a^i/\partial x^k$ are most often known analytically, and can be stored for each point on the grid as separate grid functions to speed up the computation.

Similarly, second derivatives are obtained via

$$\hat{\partial}_i\hat{\partial}_j = J^k{}_i\partial_k(J^l{}_j)\partial_l + J^k{}_iJ^l{}_j\partial_k\partial_l\,, \tag{7.3.6}$$

where the hat denotes derivatives in global coordinates. The second derivatives make it necessary of also knowing the derivatives of the Jacobians $\partial_k(J^l{}_j)$ at each gridpoint. The Jacobians employed in our particular choice of coordinates as described in the next subsection are given in the Appendix A.4.

The global finite difference derivative operators are implemented as inlined pointwise functions in a separate Cactus thorn and can be called within the main evolution loop or other computations on the grid. The finite difference functions then take as argument also the Jacobians at a given point. These have to be set up at the beginning of the simulation and are derived from the particular local coordinate systems that are used. In our case, these are known analytically and are stored in grid functions initially and must be recalculated whenever the grid structure changes.

The wave-zone: six-patch "inflated cube" system

The main difficulty that Cartesian coordinates face is that they are not very well suited for modeling radial waves at large radii. The essential problem is that in order to resolve the wave profile, a certain minimum radial resolution is required and must be maintained as the wave propagates to large radii. The angular resolution, however, can remain fixed – if a wave is resolved at a certain angular resolution as small radii, then it is unlikely to develop significant angular features as it propagates to large distances from the compact source. Cartesian grids with fixed spacing, however, resolve spheres with increasing angular resolution according to r^2. That is, to maintain a given required radial resolution, the angular directions are extremely over-resolved at large radii, and this comes at a large computational cost. Namely, for a Cartesian grid to extend in size or increase it's resolution by a factor n, the cost in memory and number of computations increase by n^3, while for a radial grid with fixed angular resolution, the increase is linear, n.

For this reason, it is desirable to employ a spherical coordinate system in the wave-zone. However, the use of standard spherical polar coordinates is impractical due to the non-regularity at the poles. Also, the angular distribution of points is not homogeneous. In order to maintain regularity everywhere on the sphere, the angular coordinates can be split into several maps, *i.e.* we regard S^2 as a manifold and introduce a suitable coordinate atlas. The obvious choice would be the well-known stereographic coordinate mapping. Unfortunately, this mapping does not offer a homogeneous angular distribution of points. Furthermore, the distortions in the overlap zones become rather big and may prevent high accuracy.

A coordinate mapping that has proven to be accurate corresponds to the "inflated cube" coordinates which has been used in a number of relativity applications, and is displayed in Figure 7.9. In this mapping, S^2 is covered by six coordinate patches in a way that allows for a homogeneous distribution of angular points and with minimal distortions in the overlap zone.

The local angular coordinates (ρ, σ) range over $(-\pi/4, +\pi/4) \times (-\pi/4, +\pi/4)$ and can be related to global angular coordinates (μ, ν, ϕ) which are given by

$$\mu \equiv \text{rotation angle about the x-axis} = \arctan(y/z), \tag{7.3.7a}$$

$$\nu \equiv \text{rotation angle about the y-axis} = \arctan(x/z), \tag{7.3.7b}$$

$$\phi \equiv \text{rotation angle about the z-axis} = \arctan(y/x). \tag{7.3.7c}$$

For example, on the $+z$ patch, the mapping between the local (ρ, σ, R) and Cartesian (x, y, z) coordinates is given by:

$$\rho \equiv \nu = \arctan(x/z), \tag{7.3.8a}$$

$$\sigma \equiv \mu = \arctan(y/z), \tag{7.3.8b}$$

$$R = f(r), \tag{7.3.8c}$$

with appropriate rotations for each of the other cube faces, and where $r = \sqrt{x^2 + y^2 + z^2}$. As emphasized by Thornburg [262], aside from avoiding pathologies associated with the axis of standard spherical polar coordinates, this choice of local coordinates has a number of advantages. In particular, the angular coordinates on neighboring patches align so that interpolation is only one dimensional, which can be at least expected to improve the efficiency of the interpolation operation as well as improved accuracy.

The local radial coordinate, R, is determined as a function of the global coordinate radius, r. We can use this degree of coordinate freedom to increase the physical (global) extent of the wave-zone grids, at the cost of some spatial resolution. In practise, we use a function of the form

$$f(r) = A(r - r_0) + B\sqrt{1 + (r - r_0)^2/\epsilon}, \tag{7.3.9a}$$

with

$$R = f(r) - f(0). \tag{7.3.9b}$$

in order to transition between two almost constant resolutions (determined by the parameters A and B) over a region whose width is determined by ϵ, centered at r_0.

The effect of the radial transformation is illustrated in Fig. 7.10. The coordinate R is a nearly constant rescaling of r at small and large radii. The change in the scale factor is largely confined to a transition region. Note that since we apply the same global derivative operators (described below) to analysis tools as are used for the the evolution, it is possible to do analysis (e.g., measure waveforms, horizon finding) within regions where the radial coordinate is non-uniform. The regions of near-constant resolution are, however, useful in order to make comparisons of measurements at different radii without the additional complication of varying numerical error due to the underlying grid spacing.

All of the implemented finite differences take into account the Jacobians of the global to local coordinate transformations, and thus analysis tools such as wave extraction have no difficulty with the curvi-linear coordinates.

Adding AMR: Seven-patch system

The above coordinate setup and multiblock structure has already been implemented in *e.g.* [60, 262, 377, 381]. However, new is the coupling of the multiblock infrastructure to an Cartesian AMR grid (see Section 7.2) and the formulation of the evolution equations in terms of global coordinates. In our implementation, the spherical grid is centered around a Cartesian patch capable of AMR (see Figure 7.11) and overlaps with the central Cartesian grid by the required minimum number of overlap points depending on the finite difference operator and interpolation polynomial. This combines the strengths of two systems. The BHs are orbiting each other on the standard Cartesian AMR grid, hence taking advantage of reliable and established methods in the strong field region around the BHs. The spherical multiblock grid of the wave-zone is attached as an overlapping

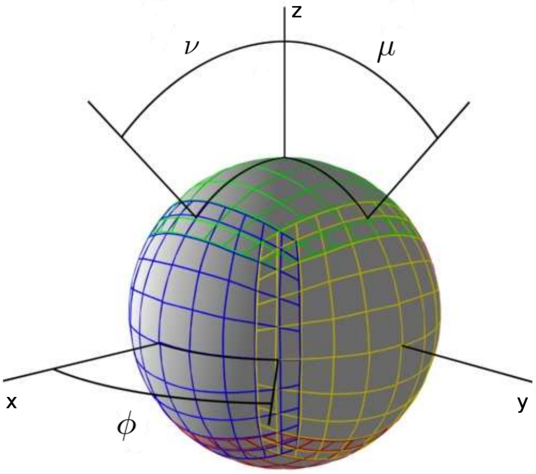

Figure 7.9: This figure shows the angular "inflated cube" coordinate patches for one spherical shell $r =$ const. in the wave-zone as well as the "global" angles (μ, ν, ϕ). The patches overlap in the ghost-zones. Only 1D interpolation is necessary since one of the coordinate lines always coincides.

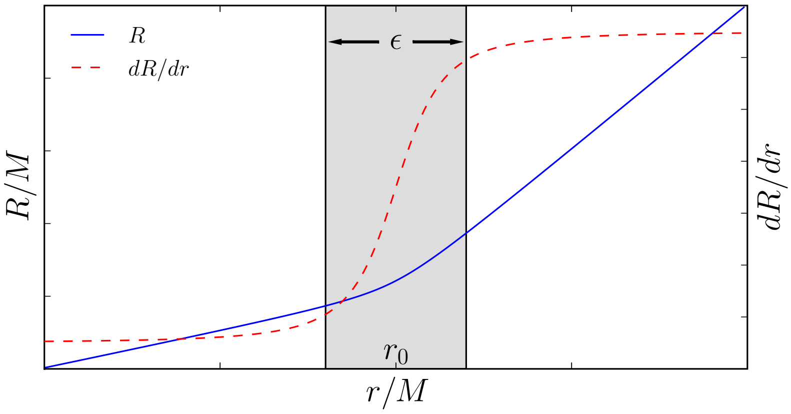

Figure 7.10: The radial resolution can be smoothly stretched in a region around r_0 whose width is determined by ϵ. The global outer boundary is located at $r_{\max} > R_{\max}$. The effective resolutions are h_0 at the inner local radius, and h_1 towards the outer boundary, as shown by the dashed (red) line dR/dr. The solid (blue) line indicates the global radial coordinate R in terms of the local coordinate r.

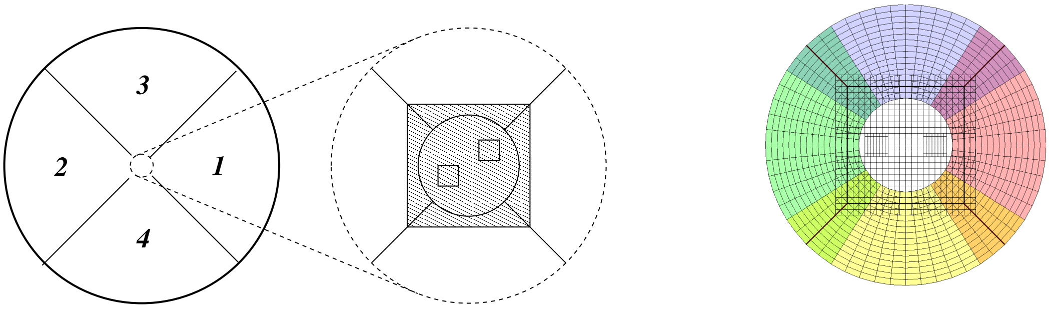

Figure 7.11: Schematic depiction of the grid structure in the $z = 0$ plane. Four radial grids surround the equator. The right figure shows an expanded inset of the Cartesian grid covering the near-zone around the individual BHs. The boundaries of the nominal grids owned by each patch are indicated by thick lines.

patch system so that we adapt to the spherical topology of the wave-zone in the far-field region at the same time.

The use of global Cartesian coordinates on each patch simplifies the treatment and makes the scheme independent on the particular type of patch system that is used. For example, existing implementations like the construction of initial data or the gauge drivers do not need to be re-implemented for a different coordinate basis.

The Llama-code

In order to model a BBH system, we would like to follow the most straight-forward procedure which is currently in use, namely the moving puncture approach (see Section 2.5). By this method, initial data for conformally flat Brill-Lindquist-type black holes with a compactified throat ("puncture") are specified on an initial slice (see Section 2.4). The coordinate singularity at the location of the punctures is effectively ignored, and the solution evolved over the entire grid without excising the black hole interiors. Given a suitable gauge condition, numerical dissipation is sufficient to keep the evolutions stable at the non-differential points, and causality prevents errors from contaminating the exterior spacetime.

To carry out the evolution, we use a conformal-traceless formulation commonly called "BSSNOK" (see Section 2.2), including the usual "$1 + \log$" and "$\tilde{\Gamma}$-driver" gauge conditions (see Section 2.3). This formulation has proven to constitute a robust evolution scheme, especially when coupled to AMR.

The AMR multiblock scheme as described in the previous subsections, together with the established methods for solving the Cauchy evolution problem as detailed in Chapter 2, form the "Llama" code.

The only modification to the evolution equations which is required for the multiblock framework is that the spatial derivative operators work in the global coordinate basis. Since the original "CCATIE" code made use of hardcoded local derivative operators and hence instead of modifying the existing code, it had been easier to rewrite a new implementation of the evolution system from scratch. This also allowed for the application of state-of-the-art computational science aspects like hybrid MPI/OpenMP parallelization.

Details on the numerical implementation of the evolution system are given in Section 8.1. Results based on this code regarding the asymptotic fall-off structure of the Weyl scalars are given in Section 15.1. The convergence of the code is reported in Section 11.2.

7.4 Spherical slices

Spherical Slice is a new infrastructure for dealing with data on spheres. As opposed to the existing framework to *Spherical Surface*, which defines a set of spherical grids but does not allocate memory, the new infrastructure takes care of memory management and parallel multi-domain decomposition as well. Stated differently, it automatically allocates distributed memory for each new registered variable that is defined on a sphere. Additionally, it offers frequently used functions such as interpolation, surface integration, harmonic decomposition, finite differencing, easy to use data iterators for traversing the data and much more. These operations are used in many physics computations such as wave-extraction or apparent horizon finding so that a common framework when dealing with data on such spherical surfaces simplifies the process of developing physics programs. Having faced this problem ourselves, we realized that a good portion of time spent for implementing physics went into inventing the wheel again and again. On top of that, some parallelization issues can become tricky, and the physics inclined implementor should not be bothered with the question of how to implement an optimal parallel code. Therefore, we have created *Spherical Slice* which is represented through a set of easy to use and fast template C++ classes and aliased Cactus functions. In the next few subsections, we will explain the main functionality.

Variable registration

The first thing to do when working with data on spheres is to register a new variable within the *Spherical Slice* framework. This is accomplished by calling the aliased Cactus function

```
CCTK_INT FUNCTION
    SphericalSlice_RegisterVariable
         (CCTK_POINTER_TO_CONST IN varname,
          CCTK_INT IN sn,
          CCTK_INT IN timelevels,
          CCTK_POINTER_TO_CONST IN distrib_method)
```

where `varname` is an arbitrary variable name, `sn` is the number of a defined spherical slice, `timelevels` is the number of time-levels and `distrib_method` denotes the parallelization rule. This deserves some more comment. Although the argument `varname` can be arbitrary, if it coincides with a 3D Cactus grid function, *Spherical Slice* automatically interpolates the data of the Cactus function onto the given sphere number when calling another offered aliased function `SphericalSlice_SyncVariable`. The sphere number `sn` refers to a set of previously defined spheres. Similar to *Spherical Surface*, the number of spheres, their shapes and radii are defined in a Cactus parameter file. Upon execution of Cactus, *Spherical Slice* internally stores these definitions and `sn` is simply the “sn”-th sphere that has been defined in the parameter file. If more then one time-level is requested, *Spherical Slice* will also store past time-levels. The first time-level always represents the current time-step. On each synchronization call, all time levels are cycled to the past level so that the newly synchronized data is on the current time-level and the former data is on the previous time-level. Finally, `distrib_method` can be either of the following: `constant`, `single` or `split`. If `distrib_method=constant`, the complete spherical data slice will be allocated and copied on each processor so that each processor knows about the complete data. This is useful for computations that cannot be parallelized and where each processor needs to know about all data. If `distrib_method=single`, the complete spherical data is only known on one processor and if `distrib_method=split`, the data will be parallely distributed across processors.

Internally, a variable defined on a spherical slice is represented and accessible via arrays of a certain type-class. The type-class can be either of `spheredata_1patch` or `spheredata_6patch` and is determined according to the chosen grid-type for the current sphere as defined in the Cactus parameter file. As the name suggests, `spheredata_1patch` represents the usual spherical polar parametrization of the sphere while `spheredata_6patch` utilizes the six-patch coordinate system as also described in [262] and also utilized in our new multiblock code[5] (Section 7.3). Both of these type-classes are derived from an interface abstraction `spheredata` which defines the common interface functionality such as getting the current radius of the current gridpoint or its Cartesian coordinates and much more. For a detailed overview on the interface abstraction layer, please refer to the accompanied Doxygen class documentation.

Once a variable is registered, an instance of the sphere type is either put to the array containing all slices of type `spheredata_1patch` or of type `spheredata_6patch`. The array number for a registered variable is obtained from the return value of the registration function `SphericalSlice_RegisterVariable`. Through these two arrays, one can access all variables and its data as well as associated operators. However, for the most common operations such as interpolation or harmonic decomposition, there are higher level aliased Cactus functions that can be called without knowing about these arrays. Access to these becomes necessary in cases where pointwise mathematical operations are needed such as in computations of a quantity on the sphere given quantities on the same or on other spheres.

Parallelization

According to the selected distribution method for a registered variable, the data is either stored on all processors, on one processor or split across multiple processors. The latter deserves some more comment. The user usually defines the grid settings of the spherical slices and also specifies a number of processors on which the code is supposed to run. According to these settings, *Spherical Slice* tries to uniformly distribute the grid across processors so that each processor contains an equal load. This is accomplished by first deriving the number of processor per spatial direction from the total number of processors and then splitting the number of gridpoints per direction across the number of processors in that direction (compare Figure 7.3). However, it can happen that the grid in one direction is smaller than the number of processors in that direction. In that case, the distribution is limited to a subset of all available processors only. For simplicity, the six-patch sphere is simultaneously parallelized for each patch, *i.e.* each of the patches is distributed on exactly the same processors.

Note that the `distrib_method=single` implementation keeps track of how many spheres are registered on one processor. In this way it is ensured that not all registered spheres with `distrib_method=single` are located on the same processor but that the load is shared among all processors.

Data is communicated across processors by invoking MPI commands. The most common operations are reduction operations such as taking the sum over all data-points, *e.g.* when integrating. These reduction operations are unfortunately rather expensive and can add a significant overhead to the computation. For this reason, we have implemented a communication stack class which can be used to postpone execution of communication. In essence, instead of directly invoking the MPI layer to perform the reduction, the programmer invokes the `commstack` class which collects all reduction requests in a buffer. Afterwards, a single reduction on the whole buffer is performed which significantly improves the communication latency.

Interface

In this subsection, we will briefly describe some of the main interface routines that are frequently used. The most important routines are the already mentioned `SphericalSlice_RegisterVariable` and the routine

```
CCTK_INT FUNCTION
    SphericalSlice_SyncVariable
         (CCTK_POINTER_TO_CONST IN cctkGH_,
          CCTK_INT IN varno) .
```

---

[5] Note that slices using six-patches can automatically adapt to the grid setup of the Llama code if requested. This allows to directly copy gridpoints to the spherical slices without the need of interpolation.

The former registers a new variable and allocates distributed memory for it. The latter invokes interpolation calls to interpolate data from a Cactus grid function onto the sphere and takes arguments `cctkGH_` which contains a pointer to the Cactus grid hierarchy and `varno` which is the variable number that one obtains when registering a variable within *Spherical Slice*. Alternate to this routine, there is a function `SphericalSlice_CollectiveSyncVariable` which synchronizes a whole set of variables at once thus speeding up the interpolation process significantly since the search for adjacent gridpoints on the Cartesian 3D grid and the construction of Lagrange interpolation polynomials has to be performed only once.

With only these two function calls, one is able to immediately have interpolated data on an arbitrary sphere that was customly defined in the Cactus parameter file. This already shows the significant reduction of programming time over the traditional Cactus approach.

There are two additional offered aliased functions. These are `SphericalSlice_IntegrateVariable` and `SphericalSlice_ContractVariableWithsYlm` and perform surface integration and decomposition in terms of spin-weighted spherical harmonics, respectively. We will describe them briefly in the next two subsections.

The aliased functions offer the most basic global reduction operations and are convenient to use since they require only one function call. However, if one needs to manipulate data in a pointwise manner, there is no other way than diving deeper into the interface routines as defined in the `spheredata` class. These functions are self-explanatory and are well documented in the accompanied Doxygen function-guide.

Surface integration

As already mentioned, there is a function

```
CCTK_REAL FUNCTION
    SphericalSlice_IntegrateVariable
         (CCTK_INT IN varno,
          CCTK_INT IN time-level)
```

which, given the variable number `varno` and its time-level, returns the surface integral over the sphere.

The surface integral is defined as

$$A = \int d\Omega \sqrt{-g} f(\Omega)\,, \tag{7.4.1}$$

where g is the determinant of the surface metric and Ω angular coordinates. For standard spherical polar coordinates (θ, ϕ), this is simply

$$A = r^2 \int d\theta d\phi \sin^2\theta f(\theta,\phi)\,, \tag{7.4.2}$$

and for 6-patch local coordinates (ρ, σ) as defined in Section 7.3,

$$A = r^2 \sum_{i=0}^{5} \int d\rho d\sigma \sqrt{\frac{\sec^4\sigma(\rho\sec^2\rho - \sigma\tan\rho\tan^2\sigma)^2}{(\rho^2+\sigma^2)^2(\sec^2\sigma + \tan^2\rho)^3}} f_i(\rho,\sigma)\,, \tag{7.4.3}$$

where the index i refers to the i-th patch.

However, for spheres whose radius depends on the angular coordinates, this is more complicated and the determinant of the metric is not know analytically anymore. For the spherical polar angular coordinate system with non-constant radius, the determinant becomes

$$\det g = \sqrt{r^2\left(r^2\sin^2\theta + \frac{\partial r^2}{\partial\phi} + \sin^2\theta\frac{\partial r^2}{\partial\theta}\right)}\,, \tag{7.4.4}$$

which involves angular derivatives of the radius as a function $r = r(\theta, \phi)$. For 6-patch coordinate systems, the arising extra terms in the determinant are quite messy and not worth repeating here.

The angular derivatives of the radius r are obtained numerically by applying fourth-order accurate finite differencing as given in Appendix A.3.

The integral is solved numerically as follows. In the spherical polar case, we can take advantage of an highly accurate Gauss quadrature scheme which is exact for polynomials of order up to $N_\theta/2 - 1$, where N_θ is the number of gridpoints along the θ-direction. On a staggered grid, *i.e.* $\theta_j = (j + 1/2)\pi/N_\theta$, $j = 0, ..., N_\theta - 1$, the scheme can be written as

$$\int d\Omega f(\Omega) = \sum_{i}^{N_\theta} \sum_{j}^{N_\phi} f_{ij} w_j + \mathcal{O}(N_\theta)\,, \tag{7.4.5}$$

where N_θ and N_ϕ are the number of angular gridpoints and w_j is the weight function expressed as [382, 383]

$$w_j = \frac{2\pi}{N_\phi} \frac{4}{N_\theta} \sum_{l=0}^{N_\theta/2-1} \frac{1}{2l+1} \sin\left([2l+1]\theta_j\right)\,, \tag{7.4.6}$$

for N_θ even, and

$$w_j = \frac{2\pi}{N_\phi} \frac{4}{N_\theta} \left(\frac{1}{2N_\theta} \sin(N_\theta \theta_j) + \sum_{l=0}^{(N_\theta-1)/2-1} \frac{1}{2l+1} \sin\left([2l+1]\theta_j\right) \right)\,, \tag{7.4.7}$$

for N_θ odd.

Internally, the weight function is pre-calculated for fast surface integration.

In the 6-patch case, we make use of a 4-th order variant Simpson's rule [384] defined as

$$\begin{aligned} \int_{x_0}^{x_N} dx\, f(x) \quad \approx \quad & \Delta x \left[\frac{17}{48} f_0 + \frac{59}{48} f_1 + \frac{43}{48} f_2 + \frac{49}{48} f_3 \right. \\ & + \langle f_k \rangle \\ & \left. + \frac{49}{48} f_{N-3} + \frac{43}{48} f_{N-2} + \frac{59}{48} f_{N-1} + \frac{17}{48} f_N \right]\,. \end{aligned} \tag{7.4.8}$$

where Δx denotes the spacing of the grid.

This completes the subsection on surface-integration. Having routines for calculating these integrals, it is straight-forward to calculate spherical harmonic modes of a function on a sphere. This will be discussed in the next subsection.

Harmonic decomposition

An important tool for *e.g.* analyzing gravitational waves is the decomposition of the signal on the sphere into harmonic modes

$$h_{\ell m} = \int d\Omega_s \bar{Y}_{\ell m}(\Omega) h(\Omega)\,. \tag{7.4.9}$$

where ${}_s\bar{Y}_{\ell m}$ is the spin-weighted spherical harmonic with spin s. *Spherical Slice* offers a function

```
CCTK_COMPLEX FUNCTION
    SphericalSlice_ContractVariableWithsYlm
         (CCTK_INT IN varno,
          CCTK_INT IN time-level,
          CCTK_INT IN s,
          CCTK_INT IN l,
          CCTK_INT IN m)
```

which performs the integral above given a variable number `varno`, a time-level, the spin s, and the mode parameters ℓ and m. Usually, one is interested in the entire decomposition of a function for $\ell \leq \ell_{\max}$. For this reason, there is a function `SphericalSlice_ContractVariableWithAllsYlm` which returns all contractions with spin-weighted spherical harmonics in the form of an array. If one is interested in the simultaneous decomposition of multiple variables, for speed reasons, it is recommended to use yet another function `SphericalSlice_ContractAllVariablesWithAllsYlm` which does exactly this.

The spin-weighted spherical harmonics are calculated as given in the appendix of [385].

They are defined in terms of the usual spherical harmonics Y_{lm} by

$${}_sY_{lm} \equiv \sqrt{\frac{(l-|s|)!}{(l+|s|)!}}\, \eth^s\, Y_{lm}, \tag{7.4.10}$$

where $\eth^{-|s|} \equiv (-1)^s\, \bar{\eth}^{|s|}$. They are non-zero for $|s| \leq l, |m| \leq l$.

We adopt the Condon-Shortley phase for the spherical harmonics, which differs from that used by Goldberg et al. [281] by a factor of $(-1)^m$ so that with the conventions adopted here, ${}_sY^*_{lm} = (-1)^{s+m}{}_{-s}Y_{l(-m)}$.

The spin weighted harmonics are separable and can be written as

$${}_sY_{lm}(\theta,\phi) = {}_s\lambda_{lm}(\cos\theta)e^{im\phi}\,, \tag{7.4.11}$$

where ${}_s\lambda_{lm}$ can be evaluated recursively for $m \geq |s|$ starting with

$${}_s\lambda_{mm}(x) = (-2)^{-m}\sqrt{\frac{(2m+1)!}{4\pi(m+s)!(m-s)!}}(1-x)^{(m+s)/2}(1+x)^{(m-s)/2}, \tag{7.4.12}$$

and the recursion relation (derived from standard results for the Wigner D-matrices; see *e.g.* [386])

$${}_s\lambda_{lm} = \left(x + \frac{sm}{l(l-1)}\right) C_{slm}\, {}_s\lambda_{(l-1)m} - \frac{C_{slm}}{C_{s(l-1)m}}\, {}_s\lambda_{(l-2)m}, \tag{7.4.13}$$

where

$$C_{slm} \equiv \sqrt{\frac{l^2(4l^2-1)}{(l^2-m^2)(l^2-s^2)}}. \tag{7.4.14}$$

The harmonics for $m \leq -|s|$ can be obtained from ${}_s\lambda_{l(-m)} = (-1)^{s+m}{}_{-s}\lambda_{lm}$. A straightforward way to evaluate ${}_s\lambda_{lm}$ for $|m| < |s|$ is to compute ${}_{\pm n}\lambda_{l|s|}$ for $0 \leq n < |s|$ and then use the symmetry ${}_s\lambda_{lm} = (-1)^{m+s}{}_m\lambda_{ls}$. Further useful results for the spin weight harmonics can be found in [387], and expressions for the spin-weight ±2 harmonics in terms of the associated Legendre functions are given in [388].

The functionality of *Spherical Slice* to decompose quantities on the sphere in terms of spin-weighted spherical harmonics has been used in the Cactus thorns *Harmonic Decomposition*, *Psiclops* and *Worldtube*. *Harmonic Decomposition* is a general purpose decomposition tool. In the Cactus parameter file, any Cactus variable can be registered for harmonic decomposition on any defined spherical slice. *Psiclops* on the other hand, calculates the complex Weyl components $\Psi_{0,..,4}$, and decomposing these quantities on spheres is important for wave analysis. Therefore, *Psiclops* offers hard-coded harmonic decomposition of these variables on any sphere defined in the Cactus parameter file. Finally, *Worldtube* decomposes the entire 3-metric, lapse and shift to be used for CCE or other post-processing metric-based calculations (see Section 9.1).

In the traditional Cactus approach, if one of these thorns wanted to make use of this functionality, this would have to be re-implemented. These examples therefore show the great amount of code redundancy that is avoided through the use of *Spherical Slice*.

Chapter 8

Discretization of the evolution systems

Once a proper computational infrastructure such as the AMR and multiblock drivers as described in the last chapter is in place, it can be used as a building block for representing the discretized fields of a PDE or any other equation that needs to be solved on a computer.

In this chapter, we will focus on the particular implementations used for the evolution systems. The first Section deals entirely with the Cauchy evolution system as introduced in Chapter 2 while the second Section describes the discretization scheme of the characteristic evolution system as introduced in Chapter 3. Furthermore, we will describe additional numerical implementations such as the generation of initial data, *puncture tracking* and *apparent horizon finding*. Both, puncture tracking and apparent horizon finding can be used to determine the position of the orbiting BHs, and hence are used for moving the AMR fine-grid boxes with the position of the BHs so that each BH sits on a hierarchy of 2:1 refined grid-boxes to maintain maximal accuracy. Additionally, apparent horizon finding means determining the shape of the apparent horizon surface which can be used to calculate various quasi-local measures such as the mass and the spin of the BH that are defined on the horizon.

The generation of BH initial data involves solving the constraint equations as described in Section 2.4 and is based on a single-domain spectral method [228].

Since there are two distinct Cauchy codes that have been used in this thesis, the *CCATIE* and the *Llama* code, we will describe both of them. The two evolution systems, Cauchy and characteristic evolutions, are based on standard finite difference techniques. However, due to the nature of the characteristic equations, a more refined discretization scheme is used for the time evolution. The characteristic code makes use of a *null parallelogram* scheme, which needs to be adapted in the full non-linear case. The Cauchy systems on the other hand can be discretized by employing the MoL scheme as described in Section 6.2.

8.1 The Cauchy system

In this thesis, two Cauchy codes have been used to carry out the simulations presented in Part III of this thesis. The CCATIE code is a Cartesian AMR code which has been collaboratively developed over the past years by the AEI and LSU group. This code has been the main working horse for most of the physics results presented in Chapter 12, 13 and 14. However, as detailed in Section 7.3, this code is limited in terms of computational scalability and accuracy. The Llama code on the other hand is based on the newly developed multiblock infrastructure that enables the application of large wave-zones with superior accuracy and efficiency (see Section 7.3). This code represents an evolution of the CCATIE code, but has been completely rewritten from scratch to make use of current computational science aspects such as OpenMP parallelization and efficient loop tiling. Furthermore, it is much more modular in terms of augmenting the code with additional features, *i.e.* implementing a new gauge driver would be trivial to achieve.

Both codes are based on the same 3+1 formulation of the Einstein equations, *i.e.* they utilize a formulation of the BSSNOK system described in Section 2.2 and both codes use a very similar MoL discretization scheme. Furthermore, additional procedures for tracking the motion of the punctures, finding apparent horizons and generating initial data are identical in both codes. In the next two subsections, we will therefore now describe the aspects that are common to both codes and will describe the differences in the subsequent two subsections. The final three subsections are then devoted to the generation of puncture initial data, puncture tracking and apparent horizon finding, respectively.

Structure of the numerical grid

The numerical grid consists of uniform 3D grids with spatial indices i, j, k where the spatial step size h is the same for all coordinate directions. In the simplest scenario, the numerical grid consists of only one single uniform 3D grid with Cartesian coordinates $x^\mu = (x, y, z)$. The coordinates are then labeled according to

$$x_i^l = x_0^l + (i-1)h, \qquad i = 1 \ldots N_l\,, \tag{8.1.1}$$

where x_0^l defines the lower boundary of the domain in coordinate direction l, and N_l denotes the associated number of gridpoints. A grid function g can then be labeled as

$$g_{ijk} \equiv g(x_{ijk}^\mu) \equiv g(x_i, y_j, z_k) \tag{8.1.2}$$

on the grid.

In reality, however, this is not as simple. The application of one single uniform 3D grid is a waste of resources and as explained in Section 7.2, one can introduce mesh refinement to circumvent this situation. As a consequence, there is not just one grid, but there are many grids assembled in a nested hierarchy of increasing resolution.

Fortunately, the design of Cactus allows the programmer to work with simple uniform grids only. This is because Cactus relies on the concept of control inversion, *i.e.* a scheduled evolution routine is called for each *subgrid*. In other words, the rather complex AMR grid is *a priori* split by the driver into many smaller uniform grid chunks (the subgrids) with given resolution and domain boundaries according to the refinement levels and boxes. Each scheduled routine working on some 3D grid is then locally implemented as if the grid functions are represented on simple uniform grids. The Cactus driver thorn, *i.e.* Carpet, ensures that the scheduled routine is called for each subgrid with the correct grid parameters so that after having called the scheduled routine for all subgrids, the driver has processed the complete data on the entire AMR grid.

On top of that, as described in Section 7.3, the Llama code adds grids with spherical topology surrounding the interior AMR grid. However, locally, the patches of the spherical grid also represent uniform 3D grids. Following the same logic as for the AMR subgrids, the scheduled routines are called for these additional subgrids so that once again the driver has ensured that all data have been traversed.

Discretization of the equations

The MoL scheme allows to treat the time and space discretization independently (see Section 6.2). It is therefore convenient to discretize the RHSs of the evolution equations (2.2.15a)-(2.2.15e) before bothering with the time discretization.

The RHSs are first fully expanded in terms of the individual components via Mathematica. Accordingly, there are the main evolution variables $\hat{\phi}$, $\tilde{\gamma}_{ab}$, K, $\tilde{A}_{ab}$ and $\tilde{\Gamma}^a$ as well as the gauge-variables α and β^i, which are stored as 21 individual grid functions, and many intermediate variables that are valid on one gridpoint only and are calculated for each gridpoint from the evolution variables or other intermediate variables. For example, the spatial derivatives of a grid function at a point are calculated and stored for the current gridpoint only. In order to perform the subsequent time-integration step, the RHSs of all evolution equations are calculated by looping over all points on the spatial grid and are stored in intermediate helper grid functions. Afterwards, these grid functions are passed to the Runge-Kutta time-integrator (see Section 6.2) which then advances the evolution variables in time. To make the scheme more transparent, we can consider the equation for $\hat{\phi}$ as an example. The remaining equations are evolved in the same way, but not reported here due to the complexity of the equations.

We first write

$$\partial_t \hat{\phi}_\kappa \equiv \hat{\phi}_{\rm RHS} = \frac{2}{\kappa}\hat{\phi}_\kappa \alpha K + \beta^i \partial_i \hat{\phi}_\kappa - \frac{2}{\kappa}\hat{\phi}_\kappa \partial_i \beta^i \,. \tag{8.1.3}$$

The partial derivatives ∂_i can now be approximated by finite difference operators. This is usually done via centered finite differences. In this particular case, however, we deal with the shift-advection term which has to be approximated by an off-centered difference operator for stability reasons. Whether the two partial derivatives $\partial_i \hat{\phi}$ and $\partial_i \beta^i$ use forward or backward stencils is determined by the sign of the shift vector in a given direction so that we always have an upwind scheme. We choose forward finite differences for ∂_i if $\beta^i > 0$ and backward finite differences if $\beta^i < 0$. If $\beta^i = 0$, we choose a centered stencil.

The discretized equation reads

$$\begin{aligned}(\hat{\phi}_{\rm RHS})^n_{ijk} &= \frac{2}{\kappa}(\hat{\phi}_\kappa)^n_{ijk}\alpha^n_{ijk}K^n_{ijk} \\ &+ \left[(\beta^x)^n_{ijk}D_x + (\beta^y)^n_{ijk}D_y + (\beta^z)^n_{ijk}D_z\right](\hat{\phi}_\kappa)^n_{ijk} \\ &- \frac{2}{\kappa}(\hat{\phi}_\kappa)^n_{ijk}\left(D_x(\beta^x)^n_{ijk} + D_y(\beta^y)^n_{ijk} + D_z(\beta^z)^n_{ijk}\right) ,\end{aligned} \tag{8.1.4}$$

where the index n denotes the current time-step and the indices i, j, k denote the current grid-point in the 3D uniform grid. The finite difference operators D_x, D_y, D_z (see Section 6.1 and Appendix A.3) represent partial derivatives in the global Cartesian x, y, z coordinate frame and are either off-centered or centered as mentioned above. Additionally, one can add dissipation (see Section 6.1 and Appendix A.3) to the main evolution variables. Dissipation is added as an extra term, one for each variable[1], to the RHSs of the equations. The amount of dissipation can vary from refinement level to refinement level, and usually we apply more dissipation to the wave-zone to limit back-reflection artifacts from refinement boundaries.

By looping over all points, one can calculate the RHS term for each grid point and the outcome of the RHS is stored in the intermediate grid function $\hat{\phi}_{\rm RHS}$ and passed on to the Runge-Kutta time-integrator. As the Runge-Kutta scheme requires the calculation of intermediate time-steps (6.2.3), the RHS calculation is repeated on these steps for the construction of $\hat{\phi}$ on the next time-step.

Finally, after one evolution step, both codes convert the internal evolution variables to the well known ADM variables. This makes it simple for external analysis thorns which can rely on a common variable specification and interface. In addition and behind the scenes, the AMR multiblock driver takes care of prolongation and restriction of the refinement levels (see Section 7.2), as well as interpatch and interprocessor boundary zone updates (see Section 7.1 and 7.3, respectively).

This completes one evolution step. It should be noted that it is insufficient to consider the evolution equations only. As outlined in Section 2.3, we also need to evolve the gauge variables α and β^i according to some appropriate conditions. Such gauge conditions are implemented via the "1+log" slicing condition and the hyperbolic $\tilde{\Gamma}$-driver condition. The additional equations are evolved together with the main evolution equations.

In the next two subsections, we will describe the differences between the CCATIE and the Llama code.

The CCATIE code

The CCATIE code is the legacy AEI/LSU code that employs Cartesian AMR grids to evolve BBHs. The finite difference operators are fourth-order accurate (see Appendix A.3) and hardcoded, *i.e.* it is not possible to change the order of accuracy without regenerating the code. The type of evolved conformal factor is the traditional variable $\phi = \ln \det \gamma_{ij}/12$. Again this particular choice in the formulation is hardcoded.

As this code is based on Cartesian AMR, the outer boundary of the simulation domain can be pushed further out by setting up additional coarse grid refinement levels with a larger spatial extent. However, having many refinement boundaries introduces additional back-reflection noise and lowers the accuracy of the simulation. Furthermore, there are limits on the number of refinement levels that can be used for a given resolution. This is because at one point, the outgoing wave-train is not resolved anymore at the resolution of the coarsest refinement levels hence resulting in dramatic back-reflection artifacts.

---

[1] We apply dissipation to the variables $\hat{\phi}$, $\tilde{\gamma}_{ab}$, K, $\tilde{A}_{ab}$, $\tilde{\Gamma}^a$, α and β^a.

For this reason, we have taken advantage of multiblock schemes (see Section 7.3) and have implemented the Llama code.

The Llama code

The Llama code is a new code that makes use of multiblock schemes coupled to a Cartesian AMR driver. As detailed in Section 7.3, this code sets up a Cartesian AMR central patch, similar to the CCATIE code. In addition to that, it also sets up a spherical grid that consists of a six-patch mapping of S^2 allowing to maintain a high spatial resolution in the wave-zone with large outer boundaries.

The finite difference operators are not hardcoded so that it is possible to choose between different orders of accuracy. It is possible to select second, fourth, sixth and eighth-order accurate difference operators (see Appendix A.3). It should be noted that on the spherical grid, the difference operators need to be transformed from the local coordinate basis to the global Cartesian coordinate frame. As described in Section 7.3, it is sufficient to apply a Jacobian transformation to the difference operators. That is, the routine for calculating the finite difference operators takes as an additional argument also the Jacobians at that point, and a linear combination of local derivatives in terms of the Jacobians results in the proper global Cartesian derivative so that the evolution system itself is not affected by the different choices of coordinate systems.

The type of evolved conformal factor can also be freely selected. The possible choices are listed in Section 2.2. A comparison of the different conformal factors is given in Section 11.2.

Calculation of puncture initial data

In this subsection, we briefly describe a numerical technique for solving the constraint equations for the computation of black hole puncture data with linear momentum and spin. We summarize work that has been achieved in [228] and is implemented as a Cactus thorn called *TwoPunctures*.

In order to find BBH initial data, one has to solve the Hamiltonian and momentum constraint equations. As described in Section 2.4, a procedure for tackling this problem is to perform a conformal decomposition of the spacetime so that the Hamiltonian constraint equation reduces to an equation for the conformal factor. A solution to the momentum constraint has been found by Bowen and others and is known as Bowen-York extrinsic curvature (2.4.16). This solution represents a "particle", *i.e.* a BH with clearly defined linear momentum and spin. By virtue of the puncture method, it is possible to find an equation for the Hamiltonian equation in a form such that no further boundary conditions at the singularities have to be imposed. This greatly simplifies the process of solving the constraint equation numerically.

Concretely, the equations that have to be solved numerically are Equation (2.4.23) with Bowen-York extrinsic curvature (2.4.16). The key numerical elements that have been used for solving this elliptic equation are a pseudo-spectral collocation method for representing the derivatives and a preconditioned biconjugate gradient stabilized (BICGSTAB) Krylov subspace method [389] for solving the arising linear system of equations. The linear system arises as a consequence from the decomposition of the non-linear system by means of Newton-Raphson iterations. Another noteworthy feature is the choice of coordinates mapping $\mathbb{R}^3$, including spatial infinity and the two puncture points, to a *single* rectangular coordinate patch (see Figure 8.1). With this particular choice of coordinates, the punctures are functions C^∞ as opposed to the C^2 differentiability in Cartesian coordinates. This fact is important because pseudo-spectral methods are exponentially convergent only if the function to be solved for is C^∞. For C^2 functions, the pseudo-spectral method would reduce to a fourth-order accurate scheme at most. However, the fall-off behavior for $r \to \infty$ of the Bowen-York extrinsic curvature is C^4 [220][2], and therefore limits the overall accuracy of this scheme to sixth-order in the limit of infinite resolution.

---

[2] This is true only if the total linear momentum of the spacetime vanishes. Otherwise, the function is only C^2.

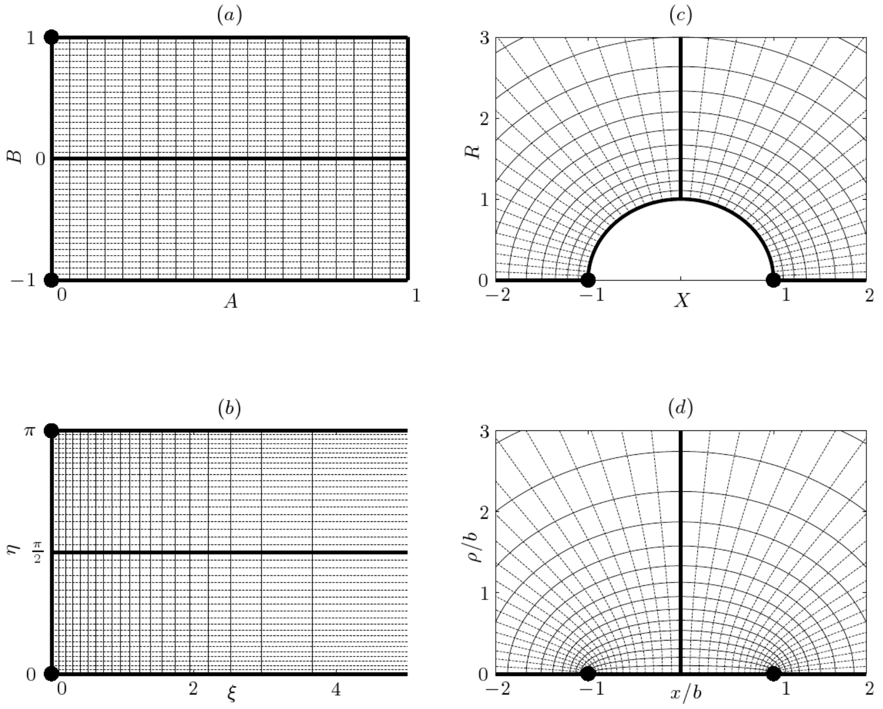

Figure 8.1: This figure depicts the coordinate patch used for the two-puncture initial data problem in four different coordinates. Shown are (a) equidistant coordinate lines in the system of spectral coordinates (A, B), as well as (b) their images in prolate spheroidal coordinates (ξ, η), (c) in the coordinates (X, R), and (d) in cylindrical coordinates (x, ρ). The punctures are indicated by bullets. The $(x = 0)$-plane, several sections of the x-axis and their corresponding images in the other coordinate systems as well as spatial infinity given by $A = 1$ are emphasized by thick lines. Figure taken from [228].

To be more specific, we have to solve an elliptic equation of the form

$$f(u) \equiv \triangle u + \varrho(u) = 0 \tag{8.1.5}$$

for the function u. Here, $\triangle$ denotes the Laplace operator, and ϱ is a source term which in general depends on u. This equation can be solved numerically on gridpoints (A_i, B_j, φ_k), where (A, B, φ) is a coordinate system to be introduced later, with

$$A \in [0,1], \quad B \in [-1,1], \quad \varphi \in [0, 2\pi), \tag{8.1.6}$$

in which u is well-defined within the spatial domain, in particular at its boundaries.

In practice, due to the choice of coordinates, we introduce the function $U = u/(A-1)$ which is then represented on gridpoints according to

$$U_{ijk} = U(A_i, B_j, \varphi_k)\,, \tag{8.1.7}$$

where

$$0 \le i < n_A, \quad 0 \le j < n_B, \quad 0 \le k < n_\varphi\,. \tag{8.1.8}$$

Crucial now is the way on how we approach the discrete representation. As mentioned earlier, we make use of a pseudo-spectral collocation method, *i.e.* we represent the function to be solved in terms of an infinite series expansion of the coefficients (8.1.7) of certain basis functions

$$U = \sum_{ijk} U_{ijk} T_i T_j F_k\,, \tag{8.1.9}$$

where the basis functions in our case are chosen to be the Chebyshev polynomials $T_{n_A}(1-2x)$ and $T_{n_B}(-x)$ for the coordinates A and B respectively, and a Fourier expansion in terms of $F = \sin(n_\varphi \varphi)$ with respect to φ.

The locations of the gridpoints are chosen such that they coincide with the roots of these basis functions, *i.e.*

$$\begin{aligned} A_i &= \sin^2\left[\frac{\pi}{2n_A}\left(i+\frac{1}{2}\right)\right], && (8.1.10)\\ B_j &= -\cos\left[\frac{\pi}{n_B}\left(j+\frac{1}{2}\right)\right], && (8.1.11)\\ \varphi_k &= 2\pi\frac{k}{n_\varphi}\,, && (8.1.12) \end{aligned}$$

where the A_i and B_j are also known as *Chebyshev nodes.*

Derivatives may then be calculated by simply differentiating the basis functions, *i.e.* if we plug (8.1.9) into (8.1.5), partial derivatives are replaced by an infinite series expansion. In practice, the series has to be stopped after a finite number of terms, and the number of coefficients determines the level of accuracy in the approximation. Thus, for a vector

$$\vec{U} = (U_{000}, \ldots, U_{(n_A-1)(n_B-1)(n_\varphi-1)})^T \tag{8.1.13}$$

we may fill another vector

$$\vec{f}(\vec{U}) = (f_{000}, \ldots, f_{(n_A-1)(n_B-1)(n_\varphi-1)})^T \tag{8.1.14}$$

by the evaluation of $f(u)$ at the grid points (A_i, B_j, φ_k).

The non-linear elliptic equation is thus transformed to a non-linear set of algebraic equations

$$\vec{f}(\vec{U}) = 0 \tag{8.1.15}$$

for the unknown U_{ijk} which can be decomposed in terms of linear equations by means of Newton-Raphson iterations, *i.e.* we write

$$\begin{aligned} \vec{U} &= \lim_{N\to\infty} \vec{U}_N, && (8.1.16)\\ \vec{U}_{N+1} &= \vec{U}_N - \vec{V}_N, && (8.1.17) \end{aligned}$$

where $\vec{V}_N$ satisfies the linear problem

$$J_N \vec{V}_N = \vec{b}_N \qquad (8.1.18)$$

with

$$J_N = \frac{\partial \vec{f}}{\partial \vec{U}}(\vec{U}_N)\,, \quad \vec{b}_N = \vec{f}(\vec{U}_N)\,. \qquad (8.1.19)$$

The linear system (8.1.18) may now be solved efficiently with the BICGSTAB method, which requires a careful choice of a preconditioning scheme in order to maintain the overall efficiency of this method. Details on the preconditioner are given in [228], and here it is sufficient to mention that it is based on a linearized form of (8.1.5) that is solved via finite differences on a uniform grid.

What remains to be described is the particular choice of coordinate mapping used. The coordinate mapping that is envisioned here covers the entire domain out to spatial infinity and becomes spherical at *each* puncture in order to maintain regularity of u at the punctures. Particularly, regularity of u can be achieved if we use specific coordinates in which the distances r to the punctures are analytic functions there [220], and it is possible to define a coordinate system such that the puncture initial data is C^∞ instead of C^2. This feature allows for a higher convergence order of the pseudo-spectral method.

For the two-puncture initial data problem, we apply this idea by introducing a specific mapping

$$(A, B, \varphi) \mapsto (x, y, z), \qquad (8.1.20)$$

which is composed of several transformations (see Figure 8.1),

$$\begin{aligned} (A, B, \varphi) &\mapsto (\xi, \eta, \varphi) \mapsto (X, R, \varphi) \mapsto (x, \rho, \varphi)\\ &\mapsto (x, y, z). && (8.1.21) \end{aligned}$$

These transformations are chosen to realize the two different aspects of the desired entire transformation, (i) regularity of the distance function r at both punctures, and (ii) mapping of a compact rectangular domain in $\mathbb{R}^3$ to the entire space of (x, y, z)-coordinates. Details on the construction of this coordinate mapping are given in [228]. The final transformation from (A, B, φ) to (x, y, z) takes the form

$$\begin{aligned} x &= b\,\frac{A^2+1}{A^2-1}\,\frac{2B}{1+B^2},\\ y &= b\,\frac{2A}{1-A^2}\,\frac{1-B^2}{1+B^2}\cos\varphi, && (8.1.22)\\ z &= b\,\frac{2A}{1-A^2}\,\frac{1-B^2}{1+B^2}\sin\varphi\,. \end{aligned}$$

Using these coordinates, it is straightforward to apply the single-domain pseudo-spectral method that has just been described. Finally, boundary conditions for (8.1.5) are necessary at infinity $r \to \infty$ or $A \to 1$

$$\lim_{r\to 0} = 0\,, \qquad (8.1.23)$$

but otherwise no further boundary conditions need to be imposed.

Note that the final solution must be represented on the computational grid of the Cauchy evolution code. Fortunately, the solution is expressed as an expansion in terms of Chebyshev polynomials on the Chebyshev nodes (8.1.10) and (8.1.11) and as such defines an interpolation polynomial with the nice property of minimizing the problem of Runge's phenomenon. Furthermore, it provides an approximation that is close to the polynomial of best approximation to a continuous function under the maximum norm. Upon knowledge of the coefficients U_{ijk}, one therefore knows the function everywhere.

Puncture tracking

Puncture tracking is a way of localizing the BHs, *i.e.* the punctures, on the computational domain. This information can be used to move the mesh refinement boxes with the BHs so that the BHs are always maximally resolved.

One can follow the puncture's coordinate location by integrating the shift vector in time, *i.e.* we use the coordinate equation of motion

$$\partial_t x^i = -\beta^i \,. \tag{8.1.24}$$

It is sufficient to consider (8.1.24) since the location of the puncture would remain fixed at one coordinate location if we would not evolve the shift vector according to the hyperbolic $\tilde{\Gamma}$-driver condition. That is, the orbital motion of the BHs is completely induced by the hyperbolic $\tilde{\Gamma}$-driver condition as discussed in Section 2.2.

Equation (8.1.24) can be discretized as

$$x^i_n = x^i_{n-1} - \Delta t \beta^i_n(x^i_{n-1}) \,, \tag{8.1.25}$$

where n denotes the current time-step, Δt is the time-step size and $\beta^i_n(x^i_{n-1})$ is the shift vector at the current time-step and the old puncture location. Given the puncture locations on the initial timeslice, one can then integrate this equation during evolution to get a first-order accurate solution.

Note that generally, the position of the punctures are not coinciding with any of the gridpoints. For this reason, since the shift vector is only known at the gridpoints i, j, k, the shift vector has to be interpolated to the position x^i_{n-1}. This is done via fourth-order Lagrange interpolation.

Apparent horizon finding

As discussed in Chapter 4, the apparent horizon can be used to locate a BH as well as defining the spin and mass of the BH in terms of the isolated horizon framework. It is therefore crucial to know the exact shape of the apparent horizon to be able to compute the spin and mass of a BH. In this subsection, we briefly outline the procedure for numerically locating the apparant horizon 2-surface from a numerically generated spacetime. There are many possible approaches [295], and in this thesis, we use the computational implementation as given in [242].

The apparent horizon is defined as the outermost marginally outer trapped surface, where a marginally outer trapped surface is a 2-surface whose future-pointing outgoing null geodesics have zero expansion $\theta_{(\ell)} = 0$. In terms of the 3+1 ADM variables, this condition can be written as [242]

$$\theta_{(\ell)} \equiv \nabla_i n^i + K_{ij} n^i n^j - K = 0 \,, \tag{8.1.26}$$

where n^i is the outward pointing unit normal to the 2-surface and K_{ij} the extrinsic curvature. Finding an apparent horizon then reduces to solving (8.1.26), and selecting the "outermost" of the marginally outer trapped surfaces.

Technically, this is done as follows. First we choose a point inside of the apparent horizon[3]. By assuming that the apparent horizon is a star-shaped region about this point, we can define the radius $r \equiv \left[\sum_i (x - x_i)^2\right]^{1/2}$ as a function of generic angular coordinates (ρ, σ), *i.e.* $r = h(\rho, \sigma)$. As shown in [242], it is possible to rewrite (8.1.26) in terms of the apparent horizon's shape function $h(\rho, \sigma)$, *i.e.* we can rewrite it as a function

$$\theta_{(\ell)}(h, \partial_u h, \partial_{uv} h, g_{ij}, \partial_k g_{ij}, K_{ij}) = 0 \,, \tag{8.1.27}$$

---

[3] This requires an initial guess. At the beginning of the simulation, this guess is known from the initial data. During evolution, the previous location of the apparent horizon can be used as a starting point for the current time provided that it did not change too quickly. By making use of *pre-tracking* algorithms [295, 390, 391], one can further improve the initial guess.

where ∂_u, ∂_{uv} denote first and second angular derivatives, respectively. This equation can be viewed as an elliptic PDE for h on S^2. In this particular implementation, we use six-patch "inflated cube" angular coordinates as described in Section 7.3 to discretize S^2 with N_{ang} total points on the sphere. Approximating the angular derivatives ∂_u and ∂_{uv} via finite differences then results in N_{ang} algebraic equations for h which are solved via Newton's method. Details on the exact procedure are presented in [242].

8.2 The characteristic system

In this section, we review the discretization of the characteristic equations as implemented in the PITT null code that has been used for producing the results of this thesis and which has been introduced in Chapter 3. After having described the structure of the numerical grid, we repeat the numerical discretization scheme as already presented in [272, 273, 350, 392, 393]. For this, it is instructive to consider the quasi-spherical approximation, which involves less terms but captures the essential idea. However, as the discretized hypersurface equations can be easily extended to the full non-linear set of equations, the evolution equation requires some extra treatment.

Structure of the numerical grid

As described in Chapter 3, the characteristic code uses a coordinate parametrization of spherical topology.

The compactified radial coordinate x is discretized as

$$x_i = x_1 + (i-1)\Delta x, \qquad i = 1 ... N_x, \qquad \Delta x = \frac{1-x_1}{N_x - 1}\,, \tag{8.2.1}$$

where the point $x_{N_x} = 1$ is located at future null infinity $\mathscr{I}^+$. The point x_1 is expected to lie on or inside the world-tube Γ, so that the world-tube is located on the characteristic grid.

The local angular 2-patch coordinates take values in the closed set $(q,p) \in [-1-\epsilon_q, 1+\epsilon_q] \times [-1-\epsilon_p, 1+\epsilon_p]$ where ϵ_q and ϵ_p denote the size of the overlap region (ghost-zones) between the patches. Note that there is also a 6-patch version of the code [60]. As this code has not been parallelized, it is not used for the results of this thesis. The two mappings of S^2 are shown in Figure 8.2.

A recent development makes use of circular instead of square stereographic patches [277]. However, in practice this does not give significant advantages in numerical accuracy and here we stick to the square patch version of the code. In practice, the ghost-zone width depends on the size of the stencil of the angular difference operators that are contained within the expressions for the eth-operators, *e.g.* a second order approximation requires a ghost-zone width of one gridpoint and a fourth order stencil a width of two ghostpoints.

The angular discretization reads

$$q_i = -1 - \epsilon_q + (i-1)\Delta q, \qquad i = 1 ... N_q, \qquad \epsilon_q = 1, 2, ..., \qquad \Delta q = \frac{2}{N_q - 2\epsilon_q - 1}\,, \tag{8.2.2}$$

and

$$p_i = -1 - \epsilon_p + (i-1)\Delta p, \qquad i = 1 ... N_p, \qquad \epsilon_p = 1, 2, ..., \qquad \Delta p = \frac{2}{N_p - 2\epsilon_p - 1}\,. \tag{8.2.3}$$

The evolution proceeds along the retarded time coordinate u with time-step Δu. This time-step is subject to the CFL condition (see Section 6.3).

The continuum spin-weighted field variables are then reduced to their numerical counterparts on the rectangular grid. These grid-variables depend on the gridpoints and can be labeled by

$$J^n_{ijk} = J(u_n, x_i, q_j, p_k)\,. \tag{8.2.4}$$

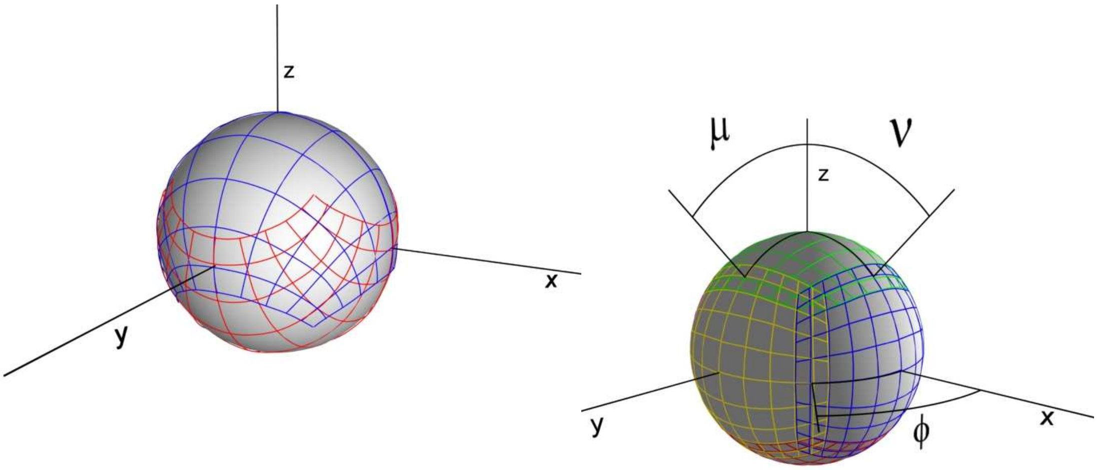

Figure 8.2: These figures show stereographic (left) and six-patch mapping (right) covering S^2. Large distortions in the overlap region of the stereographic mapping may cause inaccuracies. Furthermore, 2D interpolation is necessary. Six-patches on the other hand reduce the distortions and only 1D interpolation is necessary. However, as the six-patch code has not been parallelized, we are not using it in this thesis.

However, as shown in [392, 394], von Neumann stability analysis (see Section 6.3) reveals that U should be represented by values at the midpoints $x_{i=\frac{1}{2}} = x_i + \Delta x/2$ on a radially staggered grid

$$U^n_{ijk} = (u_n, x_{i+\frac{1}{2}}, \rho_j, \sigma_k)\,. \tag{8.2.5}$$

Additionally, all grid-functions need to be regular and smooth throughout the entire grid including $\mathscr{J}^+$ $(x = 1)$ which requires that $W(x)$ is replaced by $\widehat{W}(x) = r^{-2}W(x)$ [395] in the numerical scheme.

Numerical implementation of the quasi-spherical approximation

The discretized version of the characteristic equations are obtained by essentially replacing the differential operators by finite difference operators [272]. However, as it is rather straight-forward to discretize the hypersurface equations, it is more complicated to discretize the evolution equation. For the quasi-spherical approximation, *i.e.* by neglecting the non-linear terms, the discretized evolution equation can be written in terms of a null-parallelogram scheme, which needs to be replaced by an Iterative-Crank Nicholson scheme in the full non-linear version.

In this section, we give the discrete versions of the characteristic equations in the quasi-spherical approximation. Note that we will leave the ð-operators untouched[4]. Only difference approximations of derivatives along the radial and time coordinate are given explicitly. The discretization of the ð-operator can be done by simply replacing the differential operators contained in the ð-derivative with an appropriate finite difference operator as given in Appendix A.3. In practice, we use second-order finite difference operators for the angular ð-derivatives.

The non-linear aspherical terms can later be discretized in a straight forward manner.

1. *The hypersurface equations.* Before solving the evolution equation for a given time step, the hypersurface equations have to be computed in the hierarchical order given below.
    a) Equation for β: By neglecting the aspherical term N_β, we end up with $\beta_{,r} = 0$ implying that β is independent of r. Therefore β is completely determined by its boundary value at the world-tube Γ
    $$\beta_i = \beta_{|\Gamma}\,. \tag{8.2.6}$$

---

[4] This allows us to drop the angular indices of the grid. The discretization of the ð-operators can be treated independently

b) Equation for Q: By re-expressing radial derivatives in terms of the compactified radial coordinate x (3.2.25) and omitting the aspherical term N_Q, one obtains

$$2Q + x(1-x)Q_{,x} = -x(1-x)(\bar{\eth}J + \eth K)_{,x} - 4\eth\beta\,. \tag{8.2.7}$$

By replacing the derivative operators with respect to x by their second-order difference approximation, we obtain an expression of the fields on the gridpoints x_i and x_{i-1}. Remember that Q had been introduced as an intermediate variable for U, and as U operates on midpoints, Q has to follow the same logic, *i.e.* Q is represented on midpoints $Q_{i-\frac{1}{2}}$. The midpoint value can be approximated by $(Q_i + Q_{i-1})/2$ so that we obtain

$$\begin{aligned} Q_i \quad + \quad & Q_{i-1} + x_{i-\frac{1}{2}}\left(1 - x_{i-\frac{1}{2}}\right)\frac{Q_i - Q_{i-1}}{2\Delta x} = \\ & -x_{i-\frac{1}{2}}\left(1 - x_{i-\frac{1}{2}}\right)\left(\bar{\eth}\frac{J_i - J_{i-1}}{2\Delta x} + \eth\frac{K_i - K_{i-1}}{2\Delta x}\right) \\ & -2\eth(\beta_i + \beta_{i-1}) + \mathcal{O}(\Delta^3)\,. \end{aligned} \tag{8.2.8}$$

c) Equation for U: As before, we neglect the aspherical terms contained in N_U and re-express the derivatives by means of (3.2.25) and obtain

$$U_{,x} = \frac{\mathrm{e}^{2\beta}Q}{r_{\mathrm{wt}}x^2}\,, \tag{8.2.9}$$

where r_{wt} is the location of the innermost radial gridpoint in terms of the non-compactified radial coordinate r, *i.e.* the compactification parameter as introduced in (3.2.24). Discretization yields

$$U_i = U_{i-1} + \frac{\mathrm{e}^{2\beta_i}Q_i}{r_{\mathrm{wt}}x_i^2}\Delta x + \mathcal{O}(\Delta^3)\,. \tag{8.2.10}$$

Due to the staggering of U, this leads to an algorithm for U at the point $x_{i+\frac{1}{2}}$ in terms of values of Q at the points x_i that lie on the same angular ray. The value of U at the $world-tube$ is evaluated from the Taylor expansion at the boundary

$$U_1 = U_{|\Gamma} + U_{,x|\Gamma}\left(x_{\frac{3}{2}} - x_1\right) + \mathcal{O}(\Delta^2)\,. \tag{8.2.11}$$

d) Equation for W: Re-expressing this equation in terms of $\widehat{W} = r^{-2}W$ (for maintaining regularity at $\mathcal{J}^+$), taking the x-derivative and neglecting the aspherical term N_W gives

$$\begin{aligned} x^2\widehat{W}_{,x} + 2\frac{x}{1-x}\widehat{W} \quad = \quad & \frac{1}{2}\mathrm{e}^{2\beta}R - 1 - \mathrm{e}^{\beta}\eth\bar{\eth}\mathrm{e}^{\beta} \\ & +\frac{1}{4}x^2\left(\eth\overline{U} + \bar{\eth}U\right)_{,x} \\ & +\frac{x}{1-x}\left(\eth\overline{U} + \bar{\eth}U\right). \end{aligned} \tag{8.2.12}$$

The finite difference equation becomes

$$\begin{aligned} x_{i-\frac{1}{2}}^2\left(1 - x_{i-\frac{1}{2}}\right)\frac{\widehat{W}_i - \widehat{W}_{i-1}}{\Delta x} \quad + \quad & x_{i-\frac{1}{2}}\left(\widehat{W}_i + \widehat{W}_{i-1}\right) = \\ & \frac{1}{2}\left(1 - x_{i-\frac{1}{2}}\right)\left(\frac{1}{2}\mathrm{e}^{2\beta_i}R_i + \frac{1}{2}\mathrm{e}^{2\beta_{i-1}}R_{i-1}\right. \\ & \left.-2 - \mathrm{e}^{\beta_i}\eth\bar{\eth}\mathrm{e}^{\beta_i} - \mathrm{e}^{\beta_{i-1}}\eth\bar{\eth}\mathrm{e}^{\beta_{i-1}}\right) \\ & +\frac{1}{4}x_{i-\frac{1}{2}}^2\left(1 - x_{i-\frac{1}{2}}\right)\left(\eth\frac{\overline{U}_i - \overline{U}_{i-2}}{2\Delta x} + \bar{\eth}\frac{U_i - U_{i-2}}{2\Delta x}\right) \\ & +x_{i-\frac{1}{2}}\left(\eth\overline{U}_{i-1} + \bar{\eth}U_{i-1}\right) + \mathcal{O}(\Delta^3)\,. \end{aligned} \tag{8.2.13}$$

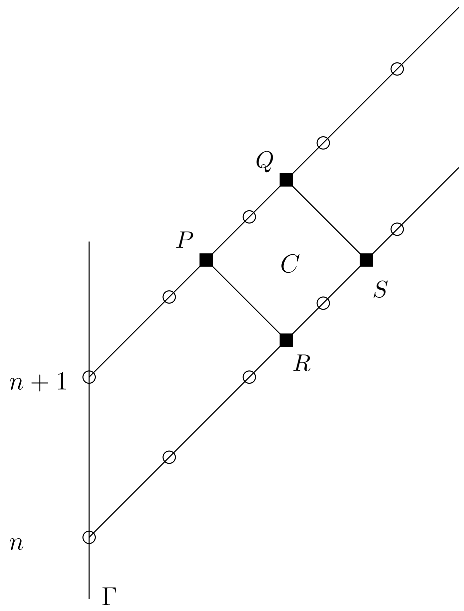

Figure 8.3: The null-parallelogram scheme.

2. *The evolution equations.* Once the hypersurface variables are known at a given time-step, one can solve the evolution equation for the metric variable J. The numerical implementation of the evolution equation is based on a *null-parallelogram algorithm.* The underlying idea is to integrate the 2-dimensional wave operator over the null-parallelogram $\mathcal{A}$ spanned by the points P, Q, R, S (Figure 8.3) and to make use of the flat space identity (8.2.22).

   For this, we first consider the 2-dimensional covariant scalar wave operator

$$\Box^{(2)}_{\gamma}\psi = e^{-2\beta}\left[2\psi_{,ru} - \left(\frac{V}{r}\psi_{,r}\right)_{,r}\right], \tag{8.2.14}$$

   which corresponds to the intrinsic metric γ' in the (u, r) submanifold with line element

$$d\sigma^2 = \mathrm{e}^{2\beta}du\left[\frac{V}{r}du + 2dr\right]. \tag{8.2.15}$$

   Note that although γ' is identical to (3.1.3) with vanishing shift vector $-U^A$, this is introduced because it is now possible to express the LHS of (3.2.37) in terms of the 2-dimensional covariant wave operator (8.2.14) corresponding to γ' (8.2.15).

   By neglecting the aspherical term N_J and inserting the wave operator (8.2.14) one can rewrite the evolution equation (3.2.37) as

$$\mathrm{e}^{2\beta}\Box^{(2)}_{\gamma'}(rJ) = \mathcal{H}, \tag{8.2.16}$$

   where

$$\mathcal{H} = -r^{-1}(r^2\eth U)_{,r} + 2r^{-1}\mathrm{e}^{\beta}\eth^2\mathrm{e}^{\beta} - \left(r^{-1}W\right)_{,r}J. \tag{8.2.17}$$

   The reason for introducing the 2-dimensional wave operator is due to the property of being conformally flat with conformal weight -2. This allows us to use the flat space identity (8.2.22) which in turn gives an evolution equation for J.

   The conformal weight can be derived by the following implication [396]

$$\begin{aligned}
\widehat{\Box}\psi &= \frac{1}{\sqrt{-\widehat{g}}}\partial_\mu\left(\sqrt{-\widehat{g}}\,\widehat{g}^{\mu\nu}\partial_\nu\psi\right)\\
\Rightarrow \qquad \widehat{\Box}^{(2)}\psi &= \Omega^{-2}\frac{1}{\sqrt{-g^{(2)}}}\partial_\mu\left(\Omega^2\sqrt{-g^{(2)}}\,\Omega^{-2}g^{(2)\mu\nu}\partial_\nu\psi\right) = \Omega^{-2}\Box^{(2)}\psi\,, \quad (8.2.18)
\end{aligned}$$

in which we have used a conformal rescaling of the metric g and the associated implication

$$\begin{aligned} \widehat{g}^{(2)}_{\mu\nu} = \Omega^2 g^{(2)}_{\mu\nu} \qquad & \Rightarrow \qquad \det \widehat{g}^{(2)} \propto (\widehat{g}^{(2)}_{\mu\nu})^2 \propto \Omega^4 (g^{(2)}_{\mu\nu})^2 \\ & \Rightarrow \qquad \sqrt{-\widehat{g}^{(2)}} = \Omega^2 \sqrt{-g^{(2)}} \, . \end{aligned} \tag{8.2.19}$$

Because any two dimensional metric $g^{(2)}$ is conformally flat, the 2-dimensional wave operator is also conformally flat by means of (8.2.18). Due to the conformal weights 2 and -2 of $g^{(2)}$ and $\Box^{(2)}$ respectively, the conformal factors cancel out and any surface integral over $\Box^{(2)}\psi$ is identical to the flat space result which can easily be evaluated in our case. We can therefore write

$$\int_{\mathcal{A}} d^2x \Box^{(2)}_{\gamma'}(rJ) = \int_{\mathcal{A}} dudv \sqrt{-m} \Box^{(2)}_{flat}(rJ) \, , \tag{8.2.20}$$

where $d^2x = \sqrt{-\gamma'} du \wedge dr$ is the surface element corresponding to γ', and where we have introduced the flat (Minkowski-)metric m in terms of the (double-)null coordinates u and v

$$ds^2 = -dudv, \qquad (m_{\mu\nu}) = \begin{pmatrix} 0 & -\frac{1}{2} \\ -\frac{1}{2} & 0 \end{pmatrix} . \tag{8.2.21}$$

The corresponding d'Alembertian is $\Box^{(2)}_{flat} = -4\partial_u \partial_v$.

The reason for choosing this particular (flat) metric is that the integral (8.2.20) can now easily be evaluated [396]

$$\begin{aligned} \int_{\mathcal{A}} dudv \sqrt{-m} \Box^{(2)}_{flat}(rJ) &= -2 \int_{\mathcal{A}} dudv (rJ)_{,uv} \\ &= -2 \int_{v_0}^{v_1} dv \left((rJ)_{,v}|_{u_1} - (rJ)_{,v}|_{u_0} \right) \\ &= -2 \left((rJ)|_{u_1,v_1} - (rJ)|_{u_1,v_0} - (rJ)|_{u_0,v_1} + (rJ)|_{u_0,v_0} \right) \\ &= -2 (rJ)_Q - (rJ)_S - (rJ)_P + (rJ)_R \, , \end{aligned} \tag{8.2.22}$$

where we have introduced the gridpoints P, Q, R and S as shown in (Figure 8.3). With (8.2.16), (8.2.20) and the surface element $d^2x = \sqrt{-\gamma'} du \wedge dr$, one finally obtains

$$(rJ)_Q = (rJ)_P + (rJ)_S - (rJ)_R + \frac{1}{2} \int_{\mathcal{A}} dudr \mathcal{H} \tag{8.2.23}$$

as the integral form of the evolution equation (3.2.37). The integrand can be approximated by its value at the center C of the parallelogram which leads to

$$(rJ)_Q = (rJ)_P + (rJ)_S - (rJ)_R + \frac{1}{2} \Delta u (r_Q - r_P + r_S - r_R) \mathcal{H}_C \, . \tag{8.2.24}$$

However, it turns out that the corners of the null-parallelogram cannot be chosen to lie exactly on the grid because the segments (RP, SQ) are ingoing null geodesics which change their orientation with respect to the fixed numerical gridpoints. This is due to the compactification of the radial direction which yields a non-constant velocity of light in terms of the x-coordinate [272]. Numerical analysis and experimentation have shown that a stable algorithm results by placing the parallelogram in a way that the sides formed by the ingoing rays intersect adjacent u-hypersurfaces at equal but opposite x-displacement from the neighboring gridpoints. The values of (rJ) at the vertices of the parallelogram are then approximated to second order accuracy by linear interpolation between nearest neighbor gridpoints on the same outgoing characteristic.

The final discretized version of (8.2.16) reads

$$\begin{aligned} (rJ)^{n+1}_i &= \mathcal{F} \left((rJ)^{n+1}_{i-1}, (rJ)^{n+1}_{i-2}, (rJ)^n_{i+1}, (rJ)^n_i, (rJ)^n_{i-1} \right) \\ & \quad + \frac{1}{2} \Delta u (r_Q - r_P + r_S - r_R) \mathcal{H}_C \, , \end{aligned} \tag{8.2.25}$$

with $\mathcal{F}$ being a linear function of the (rJ)'s. Since the value of (rJ) on the world-tube is known, it is now possible to obtain all values of (rJ) in the interior of the radial domain by an explicit radial march. Special care has to be taken at radial gridpoints next to the boundary point because $(rJ)^{n+1}_{-1}$ and $(rJ)^{n}_{i=N_x+1}$ are not known. For the second radial gridpoint, this can be overcome by placing the parallelogram such that P and Q lie exactly on the gridpoints $(n+1,1)$ and $(n+1,2)$, respectively. Analogously, the point $(rJ)^{n+1}_{i=N_x}$ is obtained by choosing Q and S to lie exactly on $(n+1,N_x)$ and (n,N_x), respectively.

However, there arise technical problems regarding the order of accuracy near $\mathscr{J}^+$ [272]. It is therefore convenient to renormalize (8.2.25) by introducing the variable $\Phi = xJ$. This new variable remains finite at $\mathscr{J}^+$ and the evolution equation now reads

$$\begin{aligned}\Phi_Q &= \frac{1}{4}x_Q\Delta u\mathcal{H}_C + \frac{1-x_Q}{1-x_P}\left(\Phi_P - \frac{1}{4}x_P\Delta u\mathcal{H}_C\right)\\ &\quad + \frac{1-x_Q}{1-x_S}\left(\Phi_S + \frac{1}{4}x_S\Delta u\mathcal{H}_C\right) - \frac{1-x_Q}{1-x_R}\left(\Phi_R + \frac{1}{4}x_R\Delta u\mathcal{H}_C\right). \qquad (8.2.26)\end{aligned}$$

Since the variables at point Q are obtained by linear interpolation, the final value at the gridpoints $(2 < i < N_x)$ is

$$J^{n+1}_i = \frac{\Phi_Q\Delta x - \Phi^{n+1}_{i-1}(x_Q - x_i)}{x_i(x_i - x_Q)}\,, \qquad (8.2.27)$$

and for $i = 2$ and $i = N_x$

$$J^{n+1}_i = \frac{\Phi_Q}{x_i}\,. \qquad (8.2.28)$$

The full non-linear discretization

In the last section, we gained numerical expressions for the equations in the quasi-spherical approximation. As described in [273, 392], the full non-linear hypersurface equations can be obtained by simply discretizing the aspherical terms N_β, N_W, N_U, N_Q and N_J and evaluating them at the midpoint of an integration cell, *e.g.* in (8.2.8) we add the discretized aspherical term $N_{Q_{i-1/2}}$. However, as this works well for the hypersurface equations, it is impossible to follow this approach for the evolution equation. In this case, the term P_1 in N_J introduces a time derivative of the evolution variable J in the RHS thus requiring the value of J at the $(n+1)$-th time-step. This, however, is exactly what we try to find and hence, another strategy has to be pursuited. As described in [273, 392, 397], the null-parallelogram algorithm is dropped and an iterative approach is applied. For this, the evolution equation can be rewritten as

$$2(rJ)_{,ur} - \left(r^{-1}V(rJ)_{,r}\right)_{,r} = \frac{J}{r}P_1 + \widehat{\mathcal{H}}\,, \qquad (8.2.29)$$

similar to the quasi-spherical approximation

$$\widehat{\mathcal{H}} = -r^{-1}(r^2\eth J)_{,r} + 2r^{-1}\mathrm{e}^{\beta}\eth^2\mathrm{e}^{\beta} - (r^{-1}W)_{,r}J + N_J - \frac{J}{r}P_1\,, \qquad (8.2.30)$$

where the term containing the u-derivative is subtracted such that $\widehat{\mathcal{H}}$ is free of u-derivatives. By using the variable $\Phi = xJ$, one gets

$$\begin{aligned}2(\Phi_{,x}(1-x) &+ \Phi)_{,u} - \mathcal{F}_1(\Phi_{,x}(1-)x + \Phi) - \mathcal{F}_2\Phi_{,xx} = \\ &J(1-x)\left(\frac{2}{K}Re[\overline{\Phi}_{,u}(J_{,x}K - JK_{,x})] - 8\beta_{,x}(1-x+x\widehat{W})\right) + \widehat{\mathcal{H}}\,, \qquad (8.2.31)\end{aligned}$$

where

$$\begin{aligned}\mathcal{F}_1 &= \widehat{W}_{,x}x(1-x) + \widehat{W}\,,\\ \mathcal{F}_2 &= (1-x)^2\left((1-x) + x\widehat{W}\right). \qquad (8.2.32)\end{aligned}$$

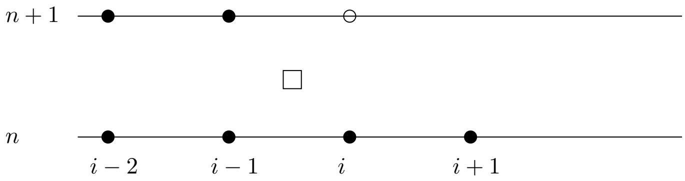

Figure 8.4: The difference molecule for approximating the field value of the full problem at the cell midpoint (square). Black dots indicate where the field values are known. The unknown value at $(n+1, i)$ is iteratively obtained.

By approximating the occurring derivatives of Φ at the cell midpoints $(n+\frac{1}{2}, i-\frac{1}{2})$ with one-sided 'half-way' point differences of second order [343], *e.g.*

$$\left.\frac{\partial\Phi}{\partial x}\right|_{i}^{n} = \frac{\Phi^n_{i+1/2} - \Phi^n_{i-1/2}}{\Delta x} \qquad \Rightarrow \qquad \left.\frac{\partial\Phi}{\partial x}\right|_{i-\frac{1}{2}}^{n} = \frac{\Phi^n_i - \Phi^n_{i-1}}{\Delta x}\,,$$

we get

$$\left.\frac{\partial\Phi}{\partial x}\right|_{i-\frac{1}{2}}^{n+\frac{1}{2}} = \frac{1}{2}\left(\left.\frac{\partial\Phi}{\partial x}\right|_{i-\frac{1}{2}}^{n+1} + \left.\frac{\partial\Phi}{\partial x}\right|_{i-\frac{1}{2}}^{n}\right) = \frac{1}{2\Delta x}\left(\Phi^{n+1}_i - \Phi^{n+1}_{i-1} + \Phi^n_i - \Phi^n_{i-1}\right)\,,$$

and likewise

$$\begin{aligned}
\Phi_{,xx}\,\Big|^{n+\frac{1}{2}}_{i-\frac{1}{2}} &= \frac{1}{2\Delta x^2}(\Phi^{n+1}_i - 2\Phi^{n+1}_{i-1} + \Phi^{n+1}_{i-2} + \Phi^n_{i+1} - 2\Phi^n_i + \Phi^n_{i-1})\,,\\
\Phi_{,u}\,\Big|^{n+\frac{1}{2}}_{i-\frac{1}{2}} &= \frac{1}{2\Delta u}(\Phi^{n+1}_i + \Phi^{n+1}_{i-1} - \Phi^n_i - \Phi^n_{i-1})\,,\\
\Phi_{,xu}\,\Big|^{n+\frac{1}{2}}_{i-\frac{1}{2}} &= \frac{1}{\Delta x\Delta u}\left((\Phi^{n+1}_i - \Phi^{n+1}_{i-1}) - \frac{1}{4}(\Phi^n_i - \Phi^n_{i-2} + \Phi^n_{i+1} - \Phi^n_{i-1})\right)\,.
\end{aligned} \tag{8.2.33}$$

For further reading on the stability analysis of these stencils please consider [392] and [397]. It turns out that using four gridpoints on the n-th time-level introduces some dissipation which helps to avoid instabilities even in the high amplitude regime. Since $\widehat{\mathcal{H}}$ is independent of the yet to be calculated value of J^{n+1}_i, it can be evaluated by

$$\widehat{\mathcal{H}} = \frac{1}{2}(\widehat{\mathcal{H}}^{n+1}_{i-3/2} + \widehat{\mathcal{H}}^n_{i+1/2})\,. \tag{8.2.34}$$

Now it is possible to use an outward radial march to obtain successive radial field values from previously calculated ones at time levels n and $n+1$. However, in order to achieve this, it is not sufficient to use the null-parallelogram algorithm since this involves the yet unknown value of Φ^{n+1}_i. Instead, a modified Crank-Nicholson scheme [345] can be applied which proceeds iteratively to the next time-level rather then doing an implicit calculation. We proceed as follows:

1. As an initial guess, the value of Φ^n_i is copied to Φ^{n+1}_i first. The resulting error is of order $\mathcal{O}(\Delta)$.
2. Second, we provide this value to the RHS of (8.2.31) which requires knowledge of Φ^{n+1}_i. After being evaluated with the initial guess, the resulting value of Φ^{n+1}_i is a correction to the initial guess.
3. The newly attained value of Φ^{n+1}_i can be inserted in the RHS of (8.2.31) again and we repeat step (1) and (2) until the difference between successive steps is within a certain threshold which ensures second order convergence.

Chapter 9

Gravitational wave extraction: Implementation

The theoretical methods for computing gravitational radiation as discussed in Chapter 5 have to be discretized and implemented in terms of computer code. Here, we describe various implementational aspects of these methods. The most important method is the implementation of CCE as it allows for the first time to calculate gravitational radiation at future null infinity for BBH merger simulations. The code that has been developed is general purpose, in that it is independent of the Cauchy code and can be applied to calculate the gravitational radiation, at $\mathscr{J}^+$, given data at a finite radius calculated in another computation. Thus its application to other astrophysical problems than BBHs will be straightforward.

Second, we discuss the implementation of calculating the energy, linear and angular momentum carried by gravitational waves given the waves as harmonic modes of the Weyl scalar Ψ_4. Early during his PhD, the author has implemented similar code to allow for the calculation of the kick velocity that the BH remnant can acquire due to the asymmetric emission of gravitational radiation. This code was implemented as an online-calculation during the simulation. However, as we at the same time output the harmonic modes of Ψ_4, it is more convenient and also computationally more efficient to calculate these quantities with post-processing tools. As the online calculation proceeds in a similar manner and does not contain any techniques that are different from the post-processing tool, we will therefore limit the description to the latter.

We also briefly outline the numerical procedure for calculating the Weyl scalars Ψ_n on the Cauchy domain as well as obtaining the gauge invariant master-functions Q^+ and $Q^\times$. The former is implemented as a thorn called *Psiclops* while the latter is implemented as a thorn called *WaveExtract*. Both methods are commonly used during Cauchy evolution on finite extraction radii, and hence are now superseded by CCE. Nevertheless, since many results in this thesis were obtained by using these two methods, it is still worth mentioning their implementation.

9.1 Cauchy characteristic extraction

One major source of error in the extraction methods mentioned in Sections 5.1 and 5.2 is due to the fact that they are unambiguously defined only at an infinite distance to the source. However, our computing resources are finite and hence our simulation domain can only cover a finite subset of the whole spacetime. This forces us to extract waves according to our available extraction methods at a finite distance which introduces an unknown systematic error in our simulations.

As mentioned in Section 5.3, one possible way of circumventing this problem is CCE. In CCE, one uses a Cauchy evolution system in the inner strong field region and a characteristic evolution system in the exterior weak-field region. The characteristic evolution system as discussed in Chapter 3 has the advantage of allowing a compactification of the radial coordinate. This allows the inclusion of future null infinity on the numerical grid while at the same time still remaining numerically stable. Unfortunately, it has the disadvantage of forming coordinate singularities - caustics - in strong field regions such as in the vicinity of black holes. This problem renders it useless for the numerical simulation of BBH mergers as a stand-alone evolution. However, it is possible to couple the characteristic evolution to a Cauchy evolution system by providing characteristic boundary data on a world-tube from a Cauchy evolution as already discussed in Section 5.3.

Here, we focus on the numerical implementation of the CCE problem. The essential idea is to use the characteristic evolution as a stand-alone post-processing evolution. During Cauchy evolution, we dump the metric variables decomposed into harmonic modes on a fixed coordinate sphere to disk. Afterwards, we reconstruct the metric quantities from the harmonic modes for each time-step during characteristic evolution to obtain BBH boundary data for the radiation propagation to future null infinity. Since we obtain the fields at $\mathscr{J}^+$ in terms of coordinate time u, we finally have to transform the fields to constant Bondi time u_B. Furthermore, due to the rather complicated procedure of calculating the conformal factor ω for the calculation of the news, we have implemented a linearized approximation that turns out to be numerically more accurate than the full non-linear computation.

In the next subsections, we describe these procedures in more detail.

World-tube boundary data

Boundary data for the characteristic evolution are constructed during Cauchy evolution in terms of the ADM variables on coordinates spheres with fixed radius R. The time succession of this coordinate sphere is known as our world-tube Γ.

In order to be able to transform the full 4-metric as given by (2.1.7) and (2.1.6) in terms of the ADM variables to a representation of the 4-metric in terms of Bondi coordinates and in terms of the characteristic evolution variables in a neighborhood of the world-tube (see Section 5.3), we have to compute the following quantities: the ADM metric components γ_{ij}, as well as the time-derivatives $\partial_t\gamma_{ij}$ and Cartesian derivatives $\partial_k\gamma_{ij}$, the lapse α, as well as time and Cartesian derivatives $\partial_t\alpha$ and $\partial_i\alpha$, the shift vector β^i, and again time and Cartesian derivatives $\partial_t\beta^i$ and $\partial_i\beta^k$.

In the specific formulation of the evolution system that is used in this thesis, we can compute these quantities as follows. As mentioned in Section 8.1, the BSSNOK evolution variables are transformed to the ADM variables after each evolution step and are therefore known everywhere. Particularly, given the conformal factor ϕ, the relation of the conformal metric $\tilde{\gamma}_{ij}$ of the BSSNOK evolution system to the ADM 3-metric γ_{ij} is given by (2.2.1). What remains is the calculation of time and spatial derivatives.

The time derivatives of the lapse and shift vector are known directly from the RHS of the "1+log" slicing condition (2.3.13) and the hyperbolic $\tilde{\Gamma}$-driver condition (2.3.14), (2.3.15). The RHSs of these equations have to be computed at each time-step in order to evolve the gauge variables with a MoL scheme, similar to the evolution equations (see Section 8.1).

The time derivatives of the metric components can be obtained via the ADM relation

$$\partial_t\gamma_{ij} = -2\alpha K_{ij} + D_i\beta_j + D_j\beta_i\,, \tag{9.1.1}$$

where D_i is the covariant derivative operator compatible with the spatial 3-metric γ_{ij} and K_{ij} the extrinsic curvature. In order to compute the covariant derivative, it is necessary to invert the 3-metric and to calculate the Christoffel symbols on each grid point. Because the shift vector is given in contravariant form, we have to transform it to its covariant representation with index down. After looping over all points on the computational grid, we store the outcome in grid functions, *i.e.* one per metric component.

Next, we have to obtain the Cartesian derivatives of the metric, lapse and shift. This is straightforwardly done by applying finite difference operators to the variables. Note that in case of non-Cartesian local coordinates, the derivatives are calculated via the global derivatives as described in (Section 7.3). For practical reasons, *i.e.* mainly storage and memory requirements, it is sufficient to calculate the radial instead of the Cartesian derivatives. The Cartesian derivatives can later be reconstructed in terms of angular derivatives of the spherical harmonics which are known analytically. This saves two additional grid functions per ADM variable. We obtain the radial derivatives in terms of the Cartesian derivatives as

$$\begin{aligned}
\partial_r \gamma_{ij} &= \frac{1}{r}\left(x\partial_x\gamma_{ij} + y\partial_y\gamma_{ij} + z\partial_z\gamma_{ij}\right) , && (9.1.2)\\
\partial_r \alpha &= \frac{1}{r}\left(x\partial_x\alpha + y\partial_y\alpha + z\partial_z\alpha\right) , && (9.1.3)\\
\partial_r \beta^i &= \frac{1}{r}\left(x\partial_x\beta^i + y\partial_y\beta^i + z\partial_z\beta^i\right) . && (9.1.4)
\end{aligned}$$

This completes the first step of calculating all variables that are necessary for the construction of characteristic boundary data. What remains is the projection of these variables on to a coordinate sphere with fixed radius R and a subsequent decomposition in terms of scalar spherical harmonics. To project the variables on to the sphere, we use fourth-order Lagrange interpolation. Afterwards, the variables are decomposed as

$$\alpha_{\ell m} = \int_{S^2} d\Omega\, \bar{Y}_{\ell m}\alpha(\Omega) . \qquad (9.1.5)$$

The projection and decomposition are both done via Spherical Slice (see Section 7.4) and the resulting array of spherical harmonic modes is stored in a file for further processing. The reconstruction from the data in that file will be described in the next subsection.

Reconstruction from harmonic modes

Once the boundary data in terms of the ADM variables and their time and radial derivatives are known on a coordinate sphere with radius R and stored in a file, the characteristic boundary module can interpret the data in that file and reconstruct the variables on S^2. This means that the characteristic code can be run as a post-processing tool to obtain the gravitational radiation at $\mathcal{J}^+$.

The advantage of reconstructing from harmonic modes is the independence in terms of angular coordinates[1] , as well as resolution. In addition, the necessary finite-mode cut-off can be regarded as a filter that factors out angular high-frequency noise.

The variables can be reconstructed via

$$\alpha = \sum_{\ell,m} \alpha_{\ell m} Y_{\ell m} . \qquad (9.1.6)$$

Note that for practical reasons, we have preferred to calculate the radial instead of the Cartesian derivatives of the ADM variables. As a consequence, we have the harmonic modes of the radial derivatives. In order to obtain the Cartesian derivatives instead, one can take angular derivatives of the spherical harmonics and then apply a Jacobian transformation from stereographic to Cartesian coordinates

$$\frac{\partial}{\partial x^i}\alpha = \frac{\partial r}{\partial x^i}\,\partial_r \alpha_{\ell m} Y_{\ell m}(q,p) + \alpha_{\ell m}\frac{\partial q}{\partial x^i}\frac{\partial Y_{\ell m}}{\partial q} + \alpha_{\ell m}\frac{\partial p}{\partial x^i}\frac{\partial Y_{\ell m}}{\partial p} , \qquad (9.1.7)$$

where q, p denote the stereographic coordinates as introduced in Section 3.2. By using the relation

$$A_{,q} = \frac{\eth A + \bar{\eth} A - 2ipsA}{1+q^2+p^2} , \qquad A_{,p} = \frac{i(\bar{\eth} A - \eth A + 2qsA)}{1+q^2+p^2} , \qquad (9.1.8)$$

for a quantity A with spin-weight s, we can express partial derivatives with respect to angular coordinates in terms of the eth-derivative

$$\begin{aligned}
\frac{\partial}{\partial x^i}\alpha &= \frac{\partial r}{\partial x^i}\,\partial_r \alpha_{\ell m} Y_{\ell m}\\
&+ \alpha_{\ell m}\frac{\partial q}{\partial x^i}\left(\frac{\eth Y_{\ell m} + \bar{\eth} Y_{\ell m}}{1+q^2+p^2}\right) + \alpha_{\ell m}\frac{\partial p}{\partial x^i} i\left(\frac{\bar{\eth} Y_{\ell m} - \eth Y_{\ell m}}{1+q^2+p^2}\right) , \qquad (9.1.9)
\end{aligned}$$

---

[1] On the Cauchy side, the ADM quantities are represented in spherical polar coordinates on S^2. The characteristic code, on the other hand, works with a stereographic coordinate mapping of S^2.

where we have used the fact that the scalar spherical harmonics have spin-weight $s = 0$.

This can be further simplified by replacing the eth-derivatives of the spherical harmonics by spin-weight $s = \pm 1$ spherical harmonics as given by (7.4.10). We can finally write

$$\frac{\partial}{\partial x^i}\alpha = \frac{\alpha^{\ell m}\sqrt{\ell(\ell+1)}}{1+q^2+p^2}\left[{}_1Y_{\ell m}(q_{,i} - ip_{,i}) - {}_{-1}Y_{\ell m}(q_{,i} + ip_{,i})\right] + r_{,i}\alpha^{\ell m}_{,r}Y_{\ell m}\,, \tag{9.1.10}$$

where

$$\begin{aligned} r_{,i} &= \partial_i\sqrt{x^2+y^2+z^2} = \frac{x_i}{r}\,, & (9.1.11)\\ q_{,i} &= \partial_i\left(\frac{x}{\sqrt{x^2+y^2+z^2}\pm z}\right) = \frac{1}{(r\pm z)^2}\left(r\pm z - x^2/r,\ -xy/r,\ -xz/r \mp x\right), & (9.1.12)\\ p_{,i} &= \partial_i\left(\frac{\pm y}{\sqrt{x^2+y^2+z^2}\pm z}\right) = \frac{1}{(r\pm z)^2}\left(\mp xy,\ \pm r + z \mp y^2/r,\ -y \mp yz/r\right), & (9.1.13) \end{aligned}$$

where the upper sign is valid for the north patch and the lower sign is valid for the south patch.

This means that we do not have to calculate any extra derivatives numerically and by virtue of (9.1.10), we immediately obtain the Cartesian derivatives from the radial derivatives.

Once the ADM variables and their derivatives are reconstructed on the coordinate sphere S^2, the code executes the computations already discussed in Section 5.3 to obtain the boundary data in terms of the characteristic evolution variables and in terms of the Bondi coordinates. After completion of this step, the code can use these boundary data to evolve the characteristic evolution variables according to Section 8.2 further in time.

Results for the application of this method to a BBH merger are presented in Section 15.2. However, the fields at $\mathscr{J}^+$ first have to be transformed to constant Bondi time u_B. This is described in the next subsection.

Interpolation to constant Bondi time and mode decomposition

Subsequent to an evolution time-step of the characteristic variables out to future null infinity is the computation of the news function N and the Weyl scalar Ψ_4 in terms of inertial spatial Bondi coordinates (r_B, p_B, q_B). These, however, are not yet given in terms of the inertial Bondi time coordinate u_B, *i.e.* we have $N = N(r_B, p_B, q_B, u)$, where u is the code coordinate time. Also, one deals with the complete 2D data at $\mathscr{J}^+$, but for analysis purposes, it is more convenient to have the data decomposed in terms of spherical harmonic modes.

In an earlier implementation, the transformation to constant u_B was achieved by outputting the news function as a function on S^2 at each time-step to a file. In a post-processing step, these timeslices were then read in and interpolated to constant Bondi time. This, however, is rather inconvenient to use in practice. Rather, one would like to have the variables automatically transformed to the correct time coordinate and decomposed in terms of spherical harmonic modes instead of fiddling around with additional post-processing tools. For this reason, we have extended the module for calculating the news function and the Weyl scalar Ψ_4 by routines that get rid of these inconveniences.

During characteristic evolution, we know the inertial Bondi time in terms of coordinate time and angular coordinates $u_B = u_B(u, p, q)$ at each time-step at $\mathscr{J}^+$. By keeping five time levels of u_B, N and Ψ_4 in memory at each time-step, it is possible to interpolate N and Ψ_4 to $u_B =$ const. for each point on S^2 by means of fourth-order Lagrange interpolation on the fly during evolution.

In practice, we average the Bondi time over S^2 on the past-past time-level to find the target time $u_B =$ const.. We use the past-past time-level to have the interpolation stencil centered around the target interpolation time to maintain maximal accuracy in the interpolation. Once the target time is known, N and Ψ_4 are interpolated for each point on S^2 to $u_B =$ const. so that we finally have $N = N(r_B, p_B, q_B, u_B)$ and $\Psi_4 = \Psi_4(r_B, p_B, q_B, u_B)$.

Afterwards, and if requested by the user, the code has been extended to automatically decompose the two functions in terms of spin-weighted spherical harmonic modes.

Therefore, the data is available in a format that is convenient for analysis without any further post-processing. Tools like *Psi4Lab* (see Section 9.4) can read in the harmonic modes of Ψ_4 and calculate radiated energy, linear and angular momentum as well as the wave-strain h.

Linearized conformal factor

For the computation of the news N and Ψ_4, it is necessary to calculate the conformal factor ω of the conformal compactification of the Bondi metric at $\mathcal{J}^+$ (see Section 5.3). However, the full non-linear computation of this factor turns out to be numerically not as accurate, *i.e.* there are spurious contents of noise. Since in some cases that we consider the fields at $\mathcal{J}^+$ are in a linear regime, we can make use of a relation between the conformal factor ω and J at $\mathcal{J}^+$ in the linearized approximation.

Given J at $\mathcal{J}^+$ in terms of $s = 2$ spin-weighted spherical harmonics, *i.e.*

$$J|_{\mathcal{J}^+}(u, x^A) = \sum_{\ell \geq 2, m} J_{\ell,m}(u) {}_2Y_{\ell,m} \,, \tag{9.1.14}$$

we can write ω in terms of scalar spherical harmonics as [398]

$$\omega(u, x^A) = 1 + \sum_{\ell \geq 2, m} \omega_{\ell,m}(u) Y_{\ell,m} \,, \tag{9.1.15}$$

where

$$\omega_{\ell,m}(u) = -\frac{1}{4}\sqrt{\frac{\ell(\ell+1)}{(\ell-1)(\ell+2)}}\left(J_{\ell,m}(u) + (-1)^m \bar{J}_{\ell,-m}(u)\right) \,. \tag{9.1.16}$$

As we also need the angular eth-derivative of ω, we additionally have

$$\eth\omega(u, x^A) = \sum_{\ell \geq 2, m} \omega_{\ell,m}(u) \sqrt{\ell(\ell+1)} {}_1Y_{\ell,m} \,. \tag{9.1.17}$$

The linearized computation has been implemented as an alternative to the full non-linear computation of ω and can be selected by the user if necessary.

9.2 Psiclops

Psiclops is a Cactus implementation for the computation of the Weyl scalars Ψ_n. These scalars are straight-forwardly calculated from the relations (5.1.3)-(5.1.8) as described in Section 5.1. In practice, one first defines a proper null tetrad $\{\boldsymbol{l}, \boldsymbol{n}, \boldsymbol{m}, \bar{\boldsymbol{m}}\}$. By computing first and second spatial derivatives of the 3-metric components γ_{ij}, one can construct the Ricci tensor R_{ij} necessary for the computation of C_{ij} (5.1.4) which is then contracted with the elements of the null tetrad to finally obtain the Weyl scalars. Furthermore, it is also necessary to compute the spatial derivatives of the extrinsic curvature K_{ij} to evaluate C_{ij}.

By looping over all points on the numerical grid, one can compute the Weyl scalars everywhere, and the derivatives are all approximated by centered finite difference operators as given in Appendix A.3. It is possible to select the order of accuracy as necessary. One can choose between second, fourth, sixth and eighth-order accurate finite differences.

As one is interested in the values of the Weyl scalars on given extraction spheres, Psiclops is also able to decompose the Weyl scalars in terms of spin-weighted spherical harmonics on user-defined spheres by using the interpolation and decomposition routines offered by Spherical Slice (see Section 7.4). This makes further analysis convenient and post-processing tools such as Psi4Lab (see Section 9.4) can easily compute the various radiation quantities related to gravitational radiation.

9.3 WaveExtract

A second method for obtaining gravitational radiation is based on gauge-invariant perturbations of Schwarzschild as described in Section 5.2. The computation of the even and odd master-functions Q^+ and $Q^\times$ is implemented as a Cactus thorn called *WaveExtract*.

To compute the master-functions, it is first necessary to interpolate the metric variables onto a user-defined extraction sphere. Particularly, we interpolate the components of the ADM 3-metric γ_{ij} as well as their radial derivatives $\partial_r\gamma_{ij}$ by using fourth-order Lagrange polynomials. The radial derivatives are obtained by first looping over all points on the numerical grid and applying centered finite difference operators up to eighth-order accuracy (see Appendix A.3) to the 3-metric components to obtain their Cartesian derivatives, and afterwards using a Jacobian transformation, *i.e.*

$$\partial_r\gamma_{ij} = \frac{1}{r}\left(x\partial_x\gamma_{ij} + y\partial_y\gamma_{ij} + z\partial_z\gamma_{ij}\right) . \tag{9.3.1}$$

Once we have these quantities in terms of the spherical polar coordinates on the extraction sphere, we have to transform the tensor components to this local coordinate basis. This is done by applying a Jacobi transformation, *i.e.*

$$\hat{\gamma}_{kl} = \frac{\partial y^k}{\partial x^i}\frac{\partial y^l}{\partial x^j}\gamma_{ij} , \tag{9.3.2}$$

where the x^i are the Cartesian coordinates (x, y, z) and the y^l are the spherical polar coordinates (r, θ, ϕ).

To separate the spherical part of the metric from its perturbation, *i.e.* to obtain h_{ij} from the full numerical metric, we follow what has been described in Section 5.2. Afterwards we can proceed to compute the harmonic modes of the even and odd master-functions Q^+ and $Q^\times$ given by expressions (5.2.9), (5.2.17). Here, all occurring integrals are approximated according to (7.4.5). The implementation of this integration method as well as eighth-order accurate radial finite differences is a modification to the original code which we have added to obtain higher accuracy and less noise in the result. Also, we have adapted the interpolation routines to a new set of Carpet internal interpolation routines that parallelize much better. The original code became unusable when using more than 256 processors, *i.e.* WaveExtract dominated the total evolution time by more than a factor of 1/3. With the new interpolation routines, the execution time is now negligible with respect to the main evolution loop.

9.4 Psi4Lab

Psi4Lab is a post-processing tool that, given the harmonic modes of Ψ_4, calculates the various quantities associated with gravitational radiation. As discussed in Chapter 5, Ψ_4 can be related to the gravitational-wave strain h (Section 5.4), its energy $E_{\rm rad}$ (Section 5.5), linear momentum $P_{\rm rad}$ (Section 5.6) and angular momentum $J_{\rm rad}$ (Section 5.7). Here, we will describe how these equations are integrated numerically.

As an example, let us consider the gravitational-wave strain h. In that case, the equation reads (see Section 5.4)

$$h_+ - \mathrm{i}h_\times = 2\lim_{r\to\infty}\sum_{\ell,m}\int_0^t dt'\int_0^{t'} dt''\Psi_4^{\ell m}\,{}_{-2}Y_{\ell m} . \tag{9.4.1}$$

The time integrals are generically calculated by using the fourth-order variant Simpson's rule in such a way that the integral for the time step k uses only past time steps i with $0 \le i \le k$. We have

$$\begin{aligned}\int_{x_0}^{x_N} dx\, f(x) \quad \approx \quad \Delta x \Bigg[& \frac{17}{48}f_0 + \frac{59}{48}f_1 + \frac{43}{48}f_2 + \frac{49}{48}f_3 \\ & +\langle f_k\rangle \\ & +\frac{49}{48}f_{N-3} + \frac{43}{48}f_{N-2} + \frac{59}{48}f_{N-1} + \frac{17}{48}f_N\Bigg] .\end{aligned} \tag{9.4.2}$$

Care is required for the very first time steps, for which we have less than 7 evaluations of the integrand. In this case, we use the 2nd-order accurate trapezoid rule if $N = 1, 3$, or 5

$$\int_{x_0}^{x_N} dx\, f(x) \approx \Delta x \left[\frac{1}{2} f_0 + \langle f_k \rangle + \frac{1}{2} f_N\right] , \tag{9.4.3}$$

or the fourth-order accurate Simpson's rule

$$\begin{aligned} \int_{x_0}^{x_N} dx\, f(x) \quad &\approx \quad \Delta x \left[\frac{1}{3} f_0 + \frac{4}{3} f_1 \right. \\ &\qquad \left. + \langle \frac{2}{3} f_{2k} + \frac{4}{3} f_{2k+1} \rangle + \frac{1}{3} f_N \right] , \end{aligned} \tag{9.4.4}$$

if $N = 2, 4$ or 6. For $N \geq 7$, we simply use Simpson's rule in the form (9.4.2). It should be noted that the use of a higher-order time integration scheme improves the overall accuracy in the calculation of the final recoil velocity by more than a factor of 10.

By applying the integration scheme twice to each harmonic mode, we obtain the second time integrals of $\Psi_4^{\ell m}$. Unfortunately, this generally introduces a drift in the strain, *i.e.* the wave is not oscillating about zero. This is due to the unknown integration constants that are implicitly set to zero in our case. Therefore, we eventually have a linear drift of the form

$$\int_0^x \left(\int_0^{x'} f(x'') dx'' + C \right) dx' = F(x) + Cx \,. \tag{9.4.5}$$

In practice, we can get rid of this effect by shifting the first integral so that it essentially oscillates about zero. This can be achieved by noting that the wave must settle to zero after ring-down. The resulting residual due to the integration constant can be used to manually shift the wave back to zero. Practically, as the wave will contain spurious oscillations coming from numerical noise, one can average over an interval after ring-down to obtain the correct shift value.

Another error that is introduced to the integrated wave-mode is coming from the fact that the wave will contains junk radiation at the beginning. This radiation is caused by the imperfection of the initial data and does not represent the physical behavior of a BBH merger waveform at the beginning of the wave-train. To circumvent any problems arising from this imperfection, one can cut away the time interval that contains the initial part of the wave-train, and start the time integration after the junk radiation has left the system.

With these words of caution in mind, one can easily integrate expression (9.4.1). The other radiation quantities are obtained similarly. Particularly, we integrate (5.5.5), (5.6.4), (5.6.5) and (5.7.4)-(5.7.6). We note that these expressions contain occurrences of the isotropic coordinate radius r. In tests it has turned out that when using wave-modes obtained from a finite radius computation the outcome is better approximated by replacing the isotropic radius r with the Schwarzschild coordinate radius $r_{\rm sch}$, *i.e.* we set

$$r = r_{\rm sch} = r_{\rm iso} \left(1 - \frac{M}{2 r_{\rm iso}}\right)^2 , \tag{9.4.6}$$

where M is the total ADM mass of the spacetime. This behavior can be attributed to the fact that at finite radii $r < 100M$, the spacetime of a BBH merger is more similar to a Schwarzschild metric than to flat Minkowski space.

In a similar manner as what has been described in this Section one proceeds when computing the radiation quantities from the gauge-invariant master-functions. In that case, one integrates (5.4.4), (5.5.6), (5.6.12), (5.6.13), (5.7.8)-(5.7.10). It is worth noting that these expressions contain one time integral less than the ones using Ψ_4. Therefore, one obtains integrated wave-data that does not need to be corrected for spurious drifts in the wave.

Chapter 10

Visualization of simulation data

Visualizing simulation output is a very important tool for getting an insight into physical phenomena that occur in a simulation, and not only that, it is of great help for debugging codes or getting an idea of regions where the accuracy is lowered due to the generation of noise or other artifacts. However, there are only few (freely-available) software solutions that offer powerful data rendering of the typically huge datasets of parallel simulations that can easily comprise hundreds of gigabytes. One of these software packages is called *VisIt* [399] and is developed and maintained by the Lawrence Livermore National Laboratory, University of California.

VisIt is a uniquely powerful, full-featured software package based on the open source visualization class-library VTK [400] for the visualization of scientific, engineering and analytical data: Its open system design is built on a standard interface environment. And its sophisticated data model provides users with great flexibility in creating visualizations.

In contrast to the visualization package OpenDX [401], VisIt does not offer a data flow-based programming environment. Instead, plots are generated by creating "plot objects" from variables contained in a data file and adding modifiers to the corresponding plot stack. In this way, sophisticated visualizations including complicated data transformations can be created within a few mouse-clicks making it the software of choice for quick and efficient data inspection. In addition, parallel rendering with multiple processor cores enables for the processing of huge datasets. Various features include

- Import and export of a large number of different data formats
- Data transformation / expressions
- High-end rendering
- Graphics output
- Full parallel support
- Online visualization
- Debugging

A priori, VisIt is unable to read the HDF5 [402] data format as generated by Carpet output. In order to take full advantage of VisIt, it is necessary to develop a database plugin in the form of a dynamic runtime-library. In the next subsection, we briefly describe the database plugin for Cartesian AMR grids and general curvi-linear meshes that we have implemented.

10.1 A Visit database plugin for Carpet AMR and curvi-linear meshes

Datafiles written in the HDF5 file format (as created by various I/O methods in Cactus) cannot be read by one of the built-in VisIt database plugins. For that reason appropriate readers must be provided as external database plugins.

The *visitCarpetHDF5* package [66] as developed by me provides such readers as runtime-loadable plugins to be used in a standard installation of VisIt. *visitCarpetHDF5* reads arbitrary N-dimensional datasets from (parallel) HDF5 output generated by the Carpet adaptive mesh-refinement

(AMR) driver for Cactus. The datasets in the HDF5 datafile are assumed to describe Carpet-AMR data, *i.e.* one or multiple regular nested grids with different resolutions (see Section 7.2). Since in parallel runs one usually deals with chunked HDF5 files, the reader is capable of transparent recombination on-the-fly. In order to be able to visualize general multiblock grids (see Section 7.3), we have later extended the plugin to general curvi-linear meshes.

From a development point of view, it is relatively easy to make VisIt understand simulation data stored in a file. As described in [403], one has to overload certain routines that are derived from a class abstraction that represents an interface to database plugins. VisIt knows about four database types: single-domain and single time-step databases, single-domain and multi time-step databases, multi-domain and single time-step databases and multi-domain and multi time-step databases. Since Carpet dumps multi-grid data of successive time-steps to the same set of files in parallel data output, we are interested in the latter type of database.

In the next few subsections, we briefly describe the underlying procedure and overloaded routines for this kind of database. In the last subsection, we present a small selection of visualizations done with VisIt extended by the *visitCarpetHDF5* reader.

Construction of metadata

The first necessary task when loading data is to construct suitable metadata such as gridsizes of the individual data chunks, their spacing, their offset in space, their time and their variable name. When opening a file, the reader therefore first checks how many processors were involved in a simulation data output and then browses through all available multi-processor output files in order to collect the information that is attached to each of the HDF5 dataset in the form of HDF5 attributes.

Once these information are available, the overloaded routine `PopulateDatabaseMetaData` is invoked to provide the VisIt metadata server with these informations.

Particularly, VisIt needs to know about the mesh type, *e.g.* Cartesian AMR grids or curvi-linear grids, the number of mesh pieces (blocks), *i.e.* the different mesh components from different processors including refined mesh sections, variables and associated data-type, and additional information like the units of the coordinate system. Based on a mesh-type attribute attached to a Carpet HDF5 dataset, the reader registers two different mesh types: AMR grids and general curvi-linear meshes. At this stage, the number of individual processor and refinement components are given to the VisIt database for each of the two mesh types. Because data can be complex or real-valued, the variables are set to scalar or vector types since complex-valued variables can be regarded as real-valued 2-vectors. Upon knowledge of these information, meshes and variables can be constructed.

Construction of meshes

Having obtained the relevant metadata, VisIt invokes the overloaded routine `GetMesh` for each of the registered grid components in order to construct the mesh. As mentioned earlier, grid components can be anything: chunks of a decomposed parallel grid or individual refinement components. In the `GetMesh` routine, a set of gridpoints with associated coordinate locations is created and returned to the compute engine. Based on the mesh type, it is decided whether to create a rectilinear Cartesian grid component for the Cartesian AMR grid, or whether to create a curvi-linear mesh as is the case for the spherical 6-patch “inflated-cube” grid used in Llama (see Section 7.3). After mesh construction, overlapping interprocessor ghost-points or buffer-points are blanked out to prevent visualization artifacts in non-opaque renderings. Finally, the compute engine knows the exact grid extends of the current block and is ready to assign data values to the gridpoints.

Reading of data

Once an individual mesh block is constructed, the VisIt compute engine invokes the overloaded routine `GetVar`. Similar to the routine `GetMesh`, this routine is called for each of the registered

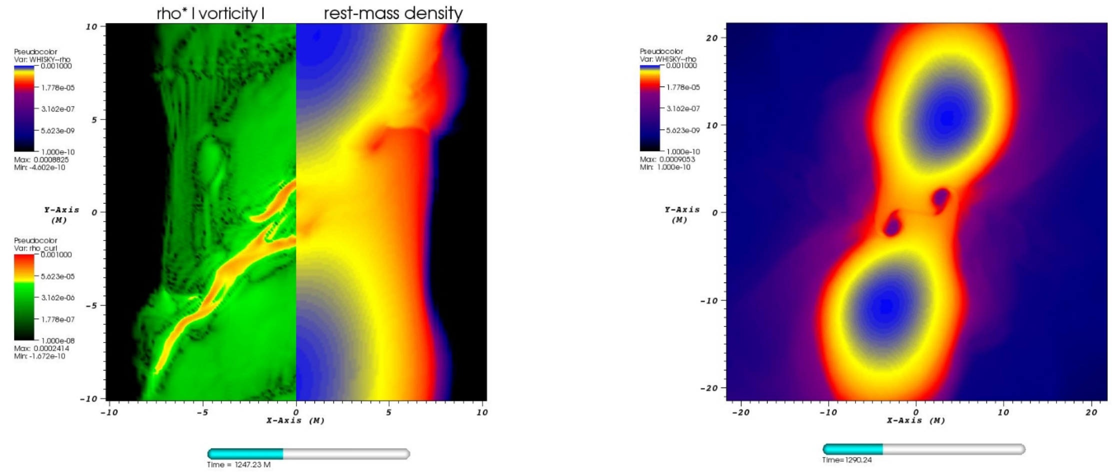

(a) High-mass polytropic equal mass neutron star binary. Here we show on the equatorial plane the value of the weighted vorticity, i.e. $\rho \cdot curl(v)$ (left panel) and on the right panel the rest-mass density rho, both using a logarithmic scale. The time is the one at which the two neutron stars merger after having inspiralled for almost 2.5 orbits. This is a still images of a movie used to study the development of a Kelvin-Helmholtz instability during the merger of binary neutron stars. In the left panel one can clearly see that the vorticity is some order of magnitudes larger on the line along which the two NSs are in contact. This image has been very useful to prove the development of this instability and of the turbulent motions it triggers [404, 405].

(b) High-mass ideal-fluid equal-mass neutron star binary. Here we show in a log scale the value of the rest-mass density on the equatorial plane at the time of the merger of the two neutron stars. It is evident the development of vortexes along the line where the two neutron stars enter in contact.[404, 405]

Figure 10.1: Two examples of visualizations done with VisIt and the *visitCarpetHDF5* database plugin.

mesh blocks. Upon execution, the actual real-valued data is read from the associated Carpet HDF5 dataset output for the current time-step and the current block. This is the only time after browsing for metadata that the HDF5 file is accessed by the reader.

Additionally, *visitCarpetHDF5* is also capable of reading complex-valued data. Based on the associated "type" metadata attribute for each variable, the compute engine alternatively invokes the routine `GetVectorVar`. In this case, the real and imaginary part are assigned to the first and second vector component, respectively.

This completes the process of generating plot objects. Plots can be of any type: pseudo-colored, volume-rendered, elevated, and much more. Two examples of visualizations are shown in the next subsection.

Examples

In this subsection, we give two examples of work that has been done with the help of VisIt. This work is not related to any of the work done in this thesis, but represents a good example of how visualization tools can help in understanding important physics. Both images as shown in Figure 10.1 make use of pseudo-color plots. These type of plots are based on 2D slices through a 3D dataset and different data values are marked by different colors. The work from which these examples are taken is detailed in [404] and the Figure captions are due to [405].

Another example of a VisIt visualization is the title figure of this thesis.

Part III

Simulations and Physics

Chapter 11

Binary black hole merger simulations

In this chapter, we discuss computer simulations that have been performed for this thesis. We introduce the 2D subspace of the 7D parameter space (see Section 1.5) that has been mainly considered: the 2D parameter space of equal-mass, spinning binaries whose spins are aligned or anti-aligned with the orbital angular momentum. These spin-configurations might be preferred by nature as there exist several mechanisms to align the spins of the binaries with the orbital angular momentum [406, 407].

In view of this, two sets of simulations have been performed. One set comprises 38 initial binary configurations which complete about one or two orbits before merger. Although rather short, these simulations give a deeper insight on the nature of the recoil-velocities that the merger remnant acquires during evolution. This effect is due to the asymmetric emission of gravitational radiation and has its largest contribution from the plunge phase of the BHs. It is therefore sufficient to consider the last orbit during inspiral, the merger and ring-down phases of a binary evolution. The same is valid for computations of the final spin of the merger remnant as this effect depends only on the total individual spins of the BHs in this parameter subspace.

However, for data analysis related problems as reported in Chapter 14, it is necessary to include as much of the inspiral phase as possible. For this reason, we have performed a second set of simulations that start with a larger initial separation of the BHs. In this way, the gravitational-wave frequency spectrum becomes broader because the initial frequency in the resulting waveforms is lower. In turn, this allows to consider binaries with smaller masses. Furthermore, the matching procedure to PN waveforms becomes more accurate (see Chapter 14).

Any numerical simulation is meaningless without proper error estimates and convergence tests. By performing two-level or three-level convergence checks (see Section 6.5), it is possible to verify the correctness as well as the accuracy of the simulations. For getting further insight on the accuracy, one can perform additional tests, such as the conservation of mass and angular momentum, or the correct peeling properties that the Weyl scalars have to obey. We report on this for exemplaric simulations from the given set of configurations in Section 11.2.

An important achievement in this thesis is the implementation of the Llama multiblock simulation code (see Section 7.3, 8.1). In Section 11.2, we show convergence of wave-modes up to $(\ell, m) = (6, 6)$ and determine the phase and amplitude accuracy of the code. We find comparable accuracy to the Caltech/Cornell spectral code [156] and determine the irreducible mass $M_{\text{irr}} = 0.884355 \pm 20 \times 10^{-6}$ and spin $S_f / M_f^2 = 0.686923 \pm 10 \times 10^{-6}$ of the remnant. We have estimated the phase and amplitude to numerical accuracies better than 0.010% and 0.090% during inspiral, respectively, and 0.003% and 0.153% during merger.

We also compare the QNM frequencies of $(\ell, m) \leq (6, 6)$ wave-modes found in the literature [102, 408] to the frequencies that are obtained numerically from the wave-modes during ring-down of the simulation. We find excellent agreement to the QNM frequencies of a single Kerr BH up to $(\ell, m) = (6, 6)$, and conclude that the final BH must be a Kerr BH.

Finally, we will also briefly state results from the comparison of different simulation codes from different numerical relativity groups [61] in which it has been shown that for current ground-based detectors, the differences in the simulation results, *i.e.* the waveforms, are sufficiently small to be unimportant. In other words, current numerical relativity codes are accurate enough to be used for templates in gravitational-wave searches in current detectors.

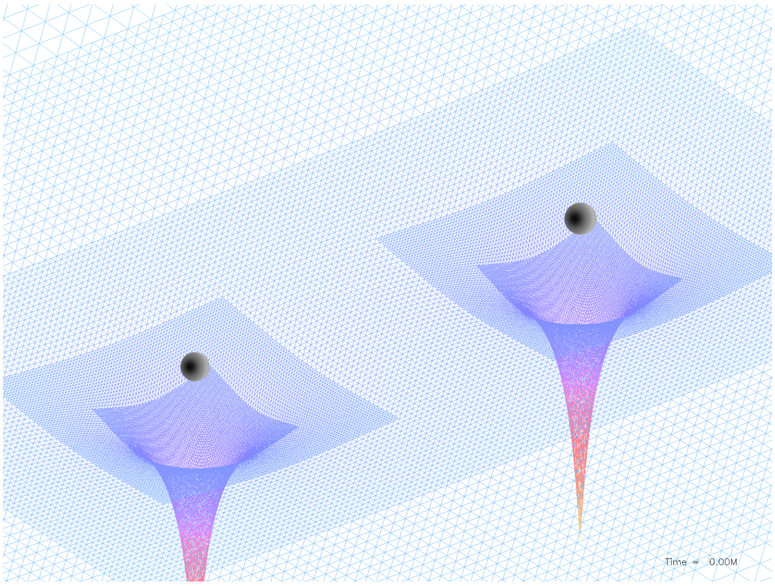

Figure 11.1: Initial grid setup of a BBH simulation. Depicted is a 2D slice of the the lapse function α as well as the BH apparent horizons (black spheres). At the punctures, α approaches zero. A schematic representation is shown in Figure 1.5.

11.1 Spin-aligned binaries

Our interest in spin-aligned binaries stems from the fact that there are indications they may represent preferred configurations in nature, at least if the BHs are supermassive. Post-Newtonian studies have shown that in vacuum, the gravitational spin-orbit coupling has a tendency to align the spins when they are initially close to the orbital one [406]. Furthermore, it has been shown, that when the binary is surrounded by a massive circumbinary disc, as the one expected by the merger of two galaxies, the dissipative dynamics of the matter exerts a torque with the effect of aligning the spins to the orbital angular momentum [407]. In addition, and as found in this thesis, the merger of binaries with aligned spins yields recoil velocities which are sufficiently small (*i.e.* $\lesssim 450\,\mathrm{km/s}$ [55, 409, 410], Chapter 12) to prevent the final BH from being expelled from the host galaxy. This would then be compatible with the overwhelming astronomical evidence that massive BHs reside at the centers of most galaxies [1–3]. Finally, a recoiling SMBH could retain the inner part of its accretion disc and thus the fuel for a continuing QSO phase lasting millions of years as it moves away from the galactic nucleus [411]. Yet, the analysis of QSOs from the Sloan Digital Sky Survey shows no evidence for BHs carrying an accretion disc and hence for very large recoiling velocities [412].

Our parameter space is therefore 2-dimensional, parametrized by the projections a_1, a_2 of the dimensionless spins $\boldsymbol{a}_i \equiv \boldsymbol{S}_i/M_i^2$ of the individual BHs on to the direction of the angular momentum (chosen as the z-axis). As a result, spins that are aligned with the orbital angular momentum are characterized by positive values of a_1, a_2, while anti-aligned spins have negative values.

Spin-kick configurations

The numerical simulations have been carried out using the CCATIE code (Section 8.1) The initial data consists of five sequences with constant orbital angular momentum, which is however different from sequence to sequence. In the r and ra-sequences, the initial spin of one of the BHs $\mathbf{S}_2$ is held fixed along the z-axis and the spin of the other black hole is varied so that the spin ratio a_1/a_2 takes the values between -1 and $+1$, with $a_i \equiv \mathbf{S}_i/M_i^2$. In the t-sequence, instead, the spin with a negative z-component is held fixed, while in the s and u-sequences $a_1/a_2 = 1$ and -1, respectively.

Table 11.1: Binary sequences for which numerical simulations have been carried out, with different columns referring to the puncture initial location $\pm x/M$, the linear momenta $\pm p/M$, the mass parameters m_i/M, the dimensionless spins a_i, the normalized ADM mass $\widetilde{M}_{\rm ADM} \equiv M_{\rm ADM}/M$ measured at infinity, and the normalized ADM angular momentum $\widetilde{J}_{\rm ADM} \equiv J_{\rm ADM}/M^2$. Finally, the last six columns contain the numerical and fitted values for $|v_{\rm kick}|$ (in km/s), $a_{\rm fin}$ and the corresponding errors as discussed in Chapter 12.

	$\pm x/M$	$\pm p/M$	m_1/M	m_2/M	a_1	a_2	$\widetilde{M}_{\rm ADM}$	$\widetilde{J}_{\rm ADM}$	$\lvert v_{\rm kick}\rvert$	$\lvert v^{\rm fit}_{\rm kick}\rvert$	err. (%)	$a_{\rm fin}$	$a^{\rm fit}_{\rm fin}$	err. (%)
$r0$	3.0205	0.1366	0.4011	0.4009	-0.584	0.584	0.9856	0.825	261.75	258.09	1.40	0.6891	0.6883	0.12
$r1$	3.1264	0.1319	0.4380	0.4016	-0.438	0.584	0.9855	0.861	221.38	219.04	1.06	0.7109	0.7105	0.06
$r2$	3.2198	0.1281	0.4615	0.4022	-0.292	0.584	0.9856	0.898	186.18	181.93	2.28	0.7314	0.7322	0.11
$r3$	3.3190	0.1243	0.4749	0.4028	-0.146	0.584	0.9857	0.935	144.02	146.75	1.90	0.7516	0.7536	0.27
$r4$	3.4100	0.1210	0.4796	0.4034	0.000	0.584	0.9859	0.971	106.11	113.52	6.98	0.7740	0.7747	0.08
$r5$	3.5063	0.1176	0.4761	0.4040	0.146	0.584	0.9862	1.007	81.42	82.23	1.00	0.7948	0.7953	0.06
$r6$	3.5988	0.1146	0.4638	0.4044	0.292	0.584	0.9864	1.044	45.90	52.88	15.21	0.8150	0.8156	0.07
$r7$	3.6841	0.1120	0.4412	0.4048	0.438	0.584	0.9867	1.081	20.59	25.47	23.70	0.8364	0.8355	0.11
$r8$	3.7705	0.1094	0.4052	0.4052	0.584	0.584	0.9872	1.117	0.00	0.00	0.00	0.8550	0.855	0.00
$ra0$	2.9654	0.1391	0.4585	0.4584	-0.300	0.300	0.9845	0.8250	131.34	132.58	0.95	0.6894	0.6883	0.16
$ra1$	3.0046	0.1373	0.4645	0.4587	-0.250	0.300	0.9846	0.8376	118.10	120.28	1.85	0.6971	0.6959	0.17
$ra2$	3.0438	0.1355	0.4692	0.4591	-0.200	0.300	0.9847	0.8499	106.33	108.21	1.77	0.7047	0.7035	0.17
$ra3$	3.0816	0.1339	0.4730	0.4594	-0.150	0.300	0.9848	0.8628	94.98	96.36	1.46	0.7120	0.7111	0.13
$ra4$	3.1215	0.1321	0.4757	0.4597	-0.100	0.300	0.9849	0.8747	84.74	84.75	0.01	0.7192	0.7185	0.09
$ra6$	3.1988	0.1290	0.4782	0.4602	0.000	0.300	0.9850	0.9003	63.43	62.19	1.95	0.7331	0.7334	0.04
$ra8$	3.2705	0.1261	0.4768	0.4608	0.100	0.300	0.9852	0.9248	41.29	40.55	1.79	0.7471	0.7481	0.13
$ra10$	3.3434	0.1234	0.4714	0.4612	0.200	0.300	0.9853	0.9502	19.11	19.82	3.72	0.7618	0.7626	0.11
$ra12$	3.4120	0.1209	0.4617	0.4617	0.300	0.300	0.9855	0.9750	0.00	0.00	0.00	0.7772	0.7769	0.03
$s0$	2.9447	0.1401	0.4761	0.4761	0.000	0.000	0.9844	0.8251	0.00	0.00	0.00	0.6892	0.6883	0.13
$s1$	3.1106	0.1326	0.4756	0.4756	0.100	0.100	0.9848	0.8749	0.00	0.00	0.00	0.7192	0.7185	0.09
$s2$	3.2718	0.1261	0.4709	0.4709	0.200	0.200	0.9851	0.9251	0.00	0.00	0.00	0.7471	0.7481	0.13
$s3$	3.4098	0.1210	0.4617	0.4617	0.300	0.300	0.9855	0.9751	0.00	0.00	0.00	0.7772	0.7769	0.03
$s4$	3.5521	0.1161	0.4476	0.4476	0.400	0.400	0.9859	1.0250	0.00	0.00	0.00	0.8077	0.8051	0.33
$s5$	3.6721	0.1123	0.4276	0.4276	0.500	0.500	0.9865	1.0748	0.00	0.00	0.00	0.8340	0.8325	0.18
$s6$	3.7896	0.1088	0.4002	0.4002	0.600	0.600	0.9874	1.1246	0.00	0.00	0.00	0.8583	0.8592	0.11
$t0$	4.1910	0.1074	0.4066	0.4064	-0.584	0.584	0.9889	0.9002	259.49	258.09	0.54	0.6868	0.6883	0.22
$t1$	4.0812	0.1103	0.4062	0.4426	-0.584	0.438	0.9884	0.8638	238.37	232.62	2.41	0.6640	0.6658	0.27
$t2$	3.9767	0.1131	0.4057	0.4652	-0.584	0.292	0.9881	0.8265	200.25	205.21	2.48	0.6400	0.6429	0.45
$t3$	3.8632	0.1165	0.4053	0.4775	-0.584	0.146	0.9879	0.7906	174.58	175.86	0.73	0.6180	0.6196	0.26
$t4$	3.7387	0.1204	0.4047	0.4810	-0.584	0.000	0.9878	0.7543	142.62	144.57	1.37	0.5965	0.5959	0.09
$t5$	3.6102	0.1246	0.4041	0.4761	-0.584	-0.146	0.9876	0.7172	106.36	111.34	4.68	0.5738	0.5719	0.33
$t6$	3.4765	0.1294	0.4033	0.4625	-0.584	-0.292	0.9874	0.6807	71.35	76.17	6.75	0.5493	0.5475	0.32
$t7$	3.3391	0.1348	0.4025	0.4387	-0.584	-0.438	0.9873	0.6447	35.36	39.05	10.45	0.5233	0.5227	0.11
$t8$	3.1712	0.1419	0.4015	0.4015	-0.584	-0.584	0.9875	0.6080	0.00	0.00	0.00	0.4955	0.4976	0.42
$u1$	2.9500	0.1398	0.4683	0.4685	-0.200	0.200	0.9845	0.8248	87.34	88.39	1.20	0.6893	0.6883	0.15
$u2$	2.9800	0.1384	0.4436	0.4438	-0.400	0.400	0.9846	0.8249	175.39	176.78	0.79	0.6895	0.6883	0.17
$u3$	3.0500	0.1355	0.3951	0.3953	-0.600	0.600	0.9847	0.8266	266.39	265.16	0.46	0.6884	0.6883	0.01
$u4$	3.1500	0.1310	0.2968	0.2970	-0.800	0.800	0.9850	0.8253	356.87	353.55	0.93	0.6884	0.6883	0.01
$r0l$	4.1924	0.1073	0.4066	0.4065	-0.584	0.584	0.9889	0.8997	-	-	-	-	-	-
$r0s$	2.8186	0.1441	0.3997	0.3994	-0.584	0.584	0.9849	0.8123	-	-	-	-	-	-

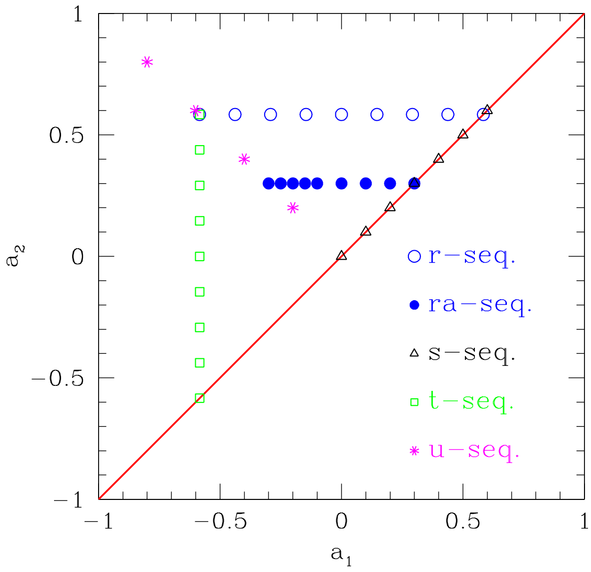

Figure 11.2: Position in the (a_1, a_2) space of the five sequences r, ra, s, t, and u for which the inspiral and merger has been computed.

In order to check the influence of the evolution time before plunge on the kick measurements of the $r0$ model as discussed in Chapter 12, we also calculated initial data for a $r0$ configuration at larger initial separation $r0l$ and at smaller initial separation $r0s$. In all cases, the masses are $M_i = M/2 = 1/2$. For the orbital initial data parameters we use the effective-potential method, which allows one to choose the initial data parameters such that the resulting physical parameters (*e.g.,* masses and spins) describe a BBH system on a quasi-circular orbit. The free parameters are: the coordinate locations $\mathbf{C}_i$, the mass parameters m_i, the linear momenta $\mathbf{p}_i$, and the spins $\mathbf{S}_i$. Quasi-circular orbits are then selected by setting $\mathbf{p}_1 = -\mathbf{p}_2$ to be orthogonal to $\mathbf{C}_2 - \mathbf{C}_1$, so that $\mathbf{L} \equiv \mathbf{C}_1 \times \mathbf{p}_1 + \mathbf{C}_2 \times \mathbf{p}_2$ is the orbital angular momentum. The initial parameters are collected in the left part of Table 11.1, while the right part reports the results of simulations. For all of them we have employed 8 levels of refinement and a minimum fine-grid resolution $h/M = 0.024$, which has been reduced to $h/M = 0.018$ for binaries $r5$, $r6$. An exemplaric initial grid setup including the apparent horizons of the BHs is depicted in Figure 11.1. Shown is a 2D slice of the lapse function indicating the proper time which becomes zero at the punctures. One can also see the hierarchical 2:1 mesh refinement around the two BHs.

Binaries with equal masses and aligned but otherwise arbitrary spins, can be parametrized uniquely by the dimensionless spins of the two BHs a_1, a_2 and can therefore be summarized in the portion of the (a_1, a_2) plane in which the two spins vary. It is therefore convenient to think in terms of "spin diagrams", which summarize in a simple way all of the relevant information (Figure 11.2). In addition, since the labeling "1" and "2" is arbitrary, we have a line of symmetry indicated by the red line $a_1 = a_2$ in the spin diagram. This symmetry not only allows us to consider only one portion of the (a_1, a_2) space (*cf.* Figure 11.2), thus halving the computational costs (or doubling the statistical sample), but it can also be exploited later on to improve our fits for various physical quantities of interest, such as the final spin or recoil velocity of the merger remnant. The position of the five sequences within the (a_1, a_2) space is shown in Figure 11.2.

Configurations with larger initial separation

The drawback of the configurations in the previous subsection is their rather small initial separation. As small initial separations are sufficient for kick and final spin computations, instead, if one tries to address data analysis problems, one needs to have the broadest gravitational-wave frequency band-width possible. This is achieved by configurations with larger initial separations. The further the BHs are apart initially, the lower is the initial gravitational-wave frequency and hence the frequency spectrum becomes broader. In addition, if one tries to match PN waveforms to the numerical relativity ones, it is necessary to have as many gravitational wave cycles prior to merger as possible, mainly because the PN approximation breaks down at some point close to the plunge phase.

In this subsection, we report the initial configurations that are used for the analysis of gravitational-wave detectability of these binaries. The difference to the previous initial data parameters is mainly the larger initial separation between the BHs. However, one other important difference is the method that is used to obtain these initial parameters. Here, we make use of PN evolutions as described in Section 2.4 to obtain initial parameters with significantly reduced orbital eccentricity. This is important because eccentricity introduces frequency components that would not be contained in the wave-signal otherwise. Also, when matching to PN waveforms, the spurious amount of eccentricity results in a significant lowering in quality of the match and has therefore be avoided as much as possible.

The numerical simulations have been carried out using the `CCATIE` code (Section 8.1). Specific to these simulations, is the numerical grid setup. For the simulations presented here, we have used 9 levels of mesh refinement with a fine-grid resolution of $h/M = 0.02$ and fourth-order finite differencing. The wave-zone grid has a resolution of $h/M = 0.128$ and extends from $r = 24\,M$ to $r = 180\,M$, in which the wave extraction is carried out. The outer (coarsest) grid extends to a spatial position which is $819.2\,M$ in each coordinate direction. Furthermore, because the BHs spins are all directed along the z-axis of our Cartesian grids, it is possible to use a reflection symmetry condition across the $z = 0$ plane.

The initial data are constructed applying the "puncture" method as described Section 2.4. We have considered four different sequences labeled as *"r", "s," "t"*, and *"u"* along straight lines in the (a_1, a_2) parameter space, also referred to as the "spin diagram". As shown in Figure 11.3, these sequences allow us to cover the most important portions of the space of parameters which, we recall, is symmetric with respect to the $a_1 = a_2$ diagonal.

As mentioned earlier, similar sequences have also been considered in [55–59] (Section 11.1) but have here been recalculated both using a higher resolution and with improved initial orbital parameters. More specifically, we use post-Newtonian (PN) evolutions following the scheme outlined in Section 2.4, which provides a straightforward prescription for initial-data parameters with small initial eccentricity, and which can be interpreted as part of the process of matching our numerical calculations to the inspiral described by the PN approximations. The free parameters to be chosen for the puncture initial data are therefore: the puncture coordinate locations $\boldsymbol{C}_i$, the puncture bare mass parameters m_i, the linear momenta $\boldsymbol{p}_i$, and the individual spins $\boldsymbol{S}_i$. The initial parameters for all of the binaries considered are collected in the left part of Table 11.2. The initial separations are fixed at $d = 8\,M$, where M is the total initial BH mass, chosen as $M = 1$ (note that the initial ADM mass of the spacetime is not exactly 1 due to the binding energy of the BHs), while the individual asymptotic initial BH masses are therefore $M_i = 1/2$. The only exception is binary s_{-8}, for which $d = 10\,M$.

Equal-mass non-spinning reference configuration

Equal-mass non-spinning BBHs have become a standard benchmark in numerical relativity. For this reason, we have carried out numerical evolutions of this binary in order to assess the convergence and accuracy of the newly developed simulation code "Llama" (see Section 7.3), as well as the new CCE code (see Section 9.1).

The numerical evolution starts from an initial separation $d/M = 11.0$ and goes through approximately 8 orbits (a physical time of around $1360M$), merger and ring-down. The masses of the punctures are set to $m = 0.4872$ and are initially placed on the x-axis with momenta $p = (\pm 0.0903, \mp 0.000728, 0)$, giving the initial slice an ADM mass $M_{\mathrm{ADM}} = 0.99052$. These initial data parameters were determined using a post-Newtonian evolution from large initial separation,

Table 11.2: Binary sequences for which numerical simulations have been carried out, with various columns referring to the puncture initial location $\pm x/M$, the mass parameters m_i/M, the dimensionless spins a_i, and the normalized ADM mass $\widetilde{M}_{\text{ADM}} \equiv M_{\text{ADM}}/M$ measured at infinity. Finally, the last four columns contain the numerical values of the energy radiated during the simulation using the two methods described in the text and the corresponding errors between them, as well as the error to the fitted values.

	$\pm x/M$	m_1/M	m_2/M	a_1	a_2	$(p_x,\ p_y)_1 = -(p_x,\ p_y)_2$	$\widetilde{M}_{\text{ADM}}$	$E^{\text{NR}}_{\text{rad}}$	$E^{Q^{\times,+}}_{\text{rad}}$	err. (%)	fit err. (%)
r_0	4.0000	0.3997	0.3998	−0.600	0.600	(0.002103, −0.112457)	0.9880	0.0366	0.0356	2.8	1.6
r_2	4.0000	0.3997	0.4645	−0.300	0.600	(0.002024, −0.111106)	0.9878	0.0407	0.0394	3.3	0.6
r_4	4.0000	0.3998	0.4825	0.000	0.600	(0.001958, 0.001958)	0.9876	0.0459	0.0445	3.1	1.9
r_6	4.0000	0.3999	0.4645	0.300	0.600	(0.001901, −0.108648)	0.9876	0.0523	0.0504	3.8	2.2
s_{-8}	5.0000	0.3000	0.3000	−0.800	−0.800	(0.001300, −0.101736)	0.9894	0.0240	0.0231	3.8	3.0
s_0	4.0000	0.4824	0.4824	0.000	0.000	(0.002088, −0.112349)	0.9877	0.0360	0.0354	1.7	0.2
s_2	4.0000	0.4746	0.4746	0.200	0.200	(0.001994, −0.110624)	0.9877	0.0421	0.0410	2.7	1.7
s_4	4.0000	0.4494	0.4494	0.400	0.400	(0.001917, −0.109022)	0.9876	0.0499	0.0480	4.0	2.5
s_6	4.0000	0.4000	0.4000	0.600	0.600	(0.001860, −0.107537)	0.9876	0.0609	0.0590	3.2	0.2
s_8	4.0000	0.4000	0.4000	0.800	0.800	(0.001816, −0.106162)	0.9877	0.0740	0.0744	0.5	2.2
t_0	4.0000	0.3995	0.3995	−0.600	−0.600	(−0.002595, 0.118379)	0.9886	0.0249	0.0243	2.5	1.1
t_1	4.0000	0.3996	0.4641	−0.600	−0.300	(−0.002431, 0.116748)	0.9883	0.0271	0.0264	2.7	1.8
t_2	4.0000	0.3997	0.4822	−0.600	0.000	(−0.002298, 0.115219)	0.9881	0.0295	0.0289	2.1	2.2
t_3	4.0000	0.3998	0.4642	−0.600	0.300	(−0.002189, 0.113790)	0.9880	0.0326	0.0317	2.8	1.8
u_2	4.0000	0.4745	0.4745	−0.200	0.200	(0.002090, −0.112361)	0.9878	0.0361	0.0354	2.0	0.2
u_4	4.0000	0.4492	0.4494	−0.400	0.400	(0.002095, −0.112398)	0.9879	0.0363	0.0355	2.3	0.7
u_8	4.0000	0.2999	0.2999	−0.800	0.800	(0.002114, −0.112539)	0.9883	0.0374	0.0363	3.0	3.7

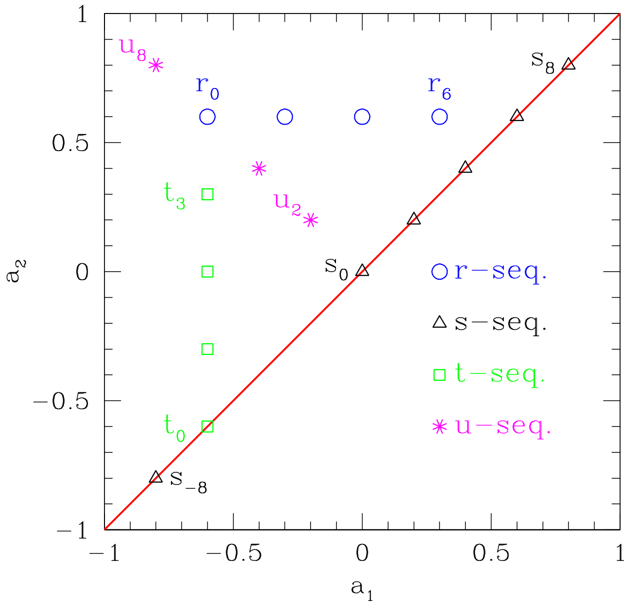

Figure 11.3: Schematic representation in the (a_1, a_2) plane, also referred to as the "spin diagram", of the initial data collected in Table 11.2. These sequences cover most important portions of the space of parameters which is symmetric with respect to the $a_1 = a_2$ diagonal.

following the procedure outlined in Section 2.4, with the conservative part of the Hamiltonian accurate to 3PN, and radiation-reaction to 3.5PN, and determines orbits with eccentricity less than $e = 0.004 \pm 0.0005$.

The grids are made up of the central Cartesian patch with 2:1 AMR as described in Section 7.2 and a surrounding spherical 6-patch system as described in Section 7.3.

The central patch is made up of 6 levels of refinement with a coarse grid Cartesian resolution that is equal to the radial resolution of the spherical grid.

In order to determine the order of convergence and accuracy, we have carried out three different resolutions with radial spacing $h = 0.64M$, $h = 0.80M$ and $h = 0.96M$ on the coarse grid. We use $N = 31$, $N = 25$ and $N = 21$ points on the nominal grid per spherical patch per direction, respectively. The CFL factor is chosen as $C = 0.45$ for each refinement level, except for the coarsest level where it reads $C = 0.225$. That is, for stability reasons, the coarse grid and the next finer refinement level are evolved with the same time-step.

Derivatives on each grid are locally computed using standard finite differences at 8th-order. Data is passed between patches by interpolation, in this case via centered 5th-order Lagrange polynomials. A 4th-order Runge-Kutta integrator is used to evolve the solution. Further details on the convergence order of various numerical aspects of the code are shown in Table 11.3.

Results on the convergence of the Llama code are reported in the next Section 11.2. The accuracy in the wave-extraction, and a detailed analysis of the asymptotic behavior of the Weyl scalars is presented in Section 15.1. An analysis of ring-down quasi-normal modes is given in Section 11.3. Finally, the invariance of the CCE algorithm with respect to the world-tube location and a comparison to finite-radius wave-extraction is given in Section 15.2.

Numerical method	Order
Grid interior finite differencing	8
Inter-patch interpolation	5
Kreiss-Oliger dissipation	9
Time integration (RK4)	4
Mesh-refinement:	
Spatial prolongation	5
Spatial restriction	n/a
Time interpolation	2
Analysis tools:	
Interpolation	4
Finite differencing	8
Surface integration	$N_\theta/2-1$

Table 11.3: Table of convergence order of various numerical aspects of the Llama evolution code that was used for the evolution of the equal-mass non-spinning reference configuration. The surface integration is exact for polynomials up to degree $N_\theta/2-1$, where $N_\theta=120$ is the number of gridpoints along the θ-direction on the sphere.

11.2 Convergence and accuracy tests

For the results in this thesis, we have used the CCATIE code, the newly developed Llama multi-block code, as well as the PITT characteristic code. In this section, we report on convergence of all codes and find that all codes converge at their theoretical order of accuracy. In addition to that, we have assessed the level of accuracy of the CCATIE code by testing for angular momentum and mass conservation during the simulations and find excellent agreement of the expected relations between initial, final and radiated mass and angular momentum. As the Llama code offers much higher resolution with grids adapted to the problem, it is expected that this code will perform even better in these tests. The error in the CCATIE code can therefore be regarded as an upper limit, *i.e.* the error in the Llama code will be much smaller. However, to date, the same quantities have not yet been looked at for the Llama code, and a rigorous test has to be postponed to the future. However, the errors in the amplitude and phase of an extracted wave already sufficiently demonstrate the superiority of this code.

Convergence of the CCATIE code

As described in Section 8.1, the finite difference error of the derivative stencils used in the numerical algorithm is $O(h^4)$, while the error in the time-interpolation stencils used for mesh refinement boundary points is $O(\Delta t^3)$ (see Section 7.2). Thus the expected theoretical convergence rate is three. However, it is only time-related operations which are at third order, and since the time step which we use is smaller than the grid spacing and much smaller than the dynamical timescales, we can expect that the error coefficient of the leading order term is quite small. Third order convergence is expected during time-periods when the system goes through rapid dynamical changes, such as the plunge or merger.

The proper convergence of the code was established using the binary system $r0$, for which we have carried out evolutions using 8 levels of mesh refinement with fine grid-spacings of $h/M=0.024$, 0.018, and 0.012, *i.e.* resolutions “medium”, “high”, and “very-high”, respectively, where “low” refers to $h/M=0.030$, which was deemed to be of insufficient accuracy for the results presented in Chapter 12 and 13. Other refinement levels have resolutions that are half of the next finest grid. The refinement levels on the initial slice are set up to be identical for the three resolutions and their locations and sizes evolve according to the same algorithm in each case.

We focus on the convergence of a number of different aspects of the code. The first of these is the degree of satisfaction of the Einstein equations, which can be partially determined by examining the Hamiltonian and momentum constraints (2.1.13) and (2.1.14). A more stringent requirement is to evaluate how well the Einstein tensor satisfies the vacuum condition, $G_{\alpha\beta} = 0$. For this we define the positive definite quantity

$$\boldsymbol{G} \equiv \left\{ \begin{array}{ll} \sqrt{G_{00}^2 + G_{01}^2 + \cdots + G_{33}^2} & \text{outside appar. horizons} \\ 0 & \text{inside appar. horizons .} \end{array} \right. \tag{11.2.1}$$

In computing norms over the entire grid, we find it useful to mask out the interiors of the horizons, where the error at the puncture locations – which is not expected to converge – can dominate over more relevant errors in the physically observable domain. In order to compute $G_{\alpha\beta}$ we compute the 4-derivatives of the ADM metric, lapse and shift, then construct the 4-derivatives of the 4-metric from which we can compute the Riemann tensor and then finally obtain $G_{\alpha\beta}$. Time-derivatives are taken using three time-levels, centered around the past time-level. Spatial derivatives are taken using fourth-order accurate centered stencils. Thus the finite-difference error in computing $G_{\alpha\beta}$ is $\mathcal{O}(\Delta t^2)$ in time and $\mathcal{O}(h^4)$ in the space dimensions. Effectively we see a minimum of third order accuracy for this quantity, indicating that the coefficient of the $\mathcal{O}(\Delta t^2)$ error term is small compared to the higher-order terms.

Since the metric gradients and hence the truncation errors are the largest near the BHs, through the L_∞ norm of (11.2.1) we effectively monitor that the Einstein tensor converges near the horizons for the duration of the evolution. We regard this as a rather stringent test in comparison with the common use of the L_2 norm, as the latter tends to dilute errors in small regions or 2D surfaces such as grid boundaries, as they are normalized over the entire grid volume. By contrast, the L_∞ norm measures the worst error on the grid, which by propagation of error will also suffer if there are any non-convergent regions on the grid.

This convergence of $\boldsymbol{G}$ is summarized in Figure 11.4, which reports the time evolution of the L_∞ norm of (11.2.1) at the medium and very-high resolutions. Also indicated with dashed and dotted lines are the expression for the L_∞ norm of (11.2.1) at the very-high resolution when rescaled for third (dotted line) and fourth-order convergence (dashed line).

There is a period at the beginning of the evolutions where the initial data construction prevents fourth-order convergence. This is due to the fact that the initial data is computed by an interpolation of the results of a spectral solver onto the finite difference grid which is used for evolution. An error is introduced because we keep fixed the number of spectral coefficients and because the Cartesian grid points do not coincide with the spectral collocation points of the Chebyshev polynomials, resulting in a certain amount of high-frequency noise that spoils the convergence for some time at the beginning of the simulation. Numerical dissipation and the constraint damping built into the evolution system implies that the evolution quickly adjusts itself to actually solving the Einstein equations to a good accuracy. The effects of these initial transient modes can last for different amounts of time for the different resolutions, *e.g.* $\sim 10\,M$ for the medium resolution and $\sim 30\,M$ for the very-high resolution.

Soon after this transient has disappeared, the code shows the expected fourth-order convergence, with the largest values of the violation found in the vicinity of the apparent horizons, where the gradients in the metric are the steepest. The violations grow rapidly with time as the binary inspirals and the largest values of the violation of the Einstein tensor are seen at the time of the merger, $t \approx 109\,M$, with values as large as $\mathcal{O}(300)$. Such violations are essentially confined to a *single* grid point on the trailing edge of the apparent horizon and are produced by the very steep gradients in the shift. Clearly, violations of this magnitude would not be revealed when looking at the L_2 norms and are a source of concern. However, as we will show later, such violations do not propagate away from the horizon to affect the fourth-order convergence of the waveforms.

At the time of the merger the excision of a common apparent horizon from the calculation of the L_∞ norm is responsible for the decrease by about four orders of the violation. After this, the L_∞ do not grow further in time for the very-high resolution simulation, while a modest increase is seen in the simulation run at medium resolution. During this time the code shows a convergence which is between third-order (right after the merger) and fourth-order (during the ring-down).

In addition to convergence in the Einstein tensor, we also validate the correctness of the physically relevant information contained in the waveforms. We do this by computing convergence rate of

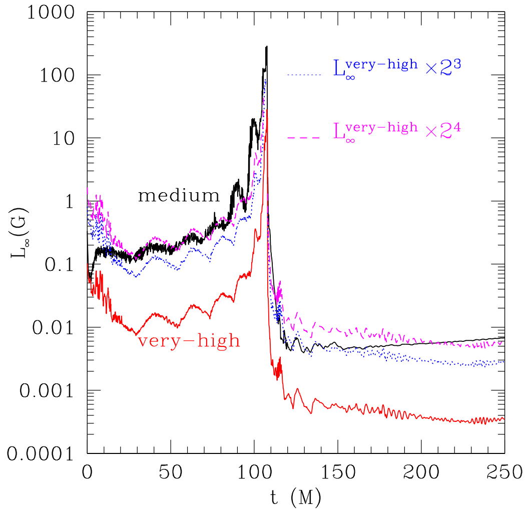

Figure 11.4: The L_∞ norm of the Einstein tensor (11.2.1) as a function of time. During the periods of strong dynamics (*i.e.*, when the time derivatives of the evolution variables are large) the convergence order is dominated by the accuracy of the time-interpolation algorithm used at mesh refinement boundaries, thus yielding third-order accuracy. At the times when these time-derivatives are small, the fourth-order finite-differencing algorithm becomes the dominant source of the error. Note that the very large violations (of $\mathcal{O}(300)$ at the medium resolution) are confined to a *single* grid point on the trailing edge of the apparent horizon and are produced by the very steep gradients in the shift. As discussed later, this does not affect the fourth-order convergence of the waveforms. At the time of the merger a common apparent horizon forms and its excision from the calculation of the L_∞ norm is responsible for the drop in the violation.

the waveforms Q^+_{22}, Q^+_{33}, and $Q^\times_{21}$ using the ratio of the integrated differences between the medium and high resolutions, and the high and very-high resolutions

$$\rho(Q) \equiv \frac{\sqrt{\int_{u_1}^{u_2} |Q_{0.024} - Q_{0.018}|^2 du}}{\sqrt{\int_{u_1}^{u_2} |Q_{0.018} - Q_{0.012}|^2 du}}\,, \tag{11.2.2}$$

where $u \equiv t - r_{\rm E}$ is the retarded time at a given detector, Q stands for either Q^+_{22}, Q^+_{33} or $Q^\times_{21}$ and refers to either its amplitude or the phase. As indicated in (11.2.2), the integrals are evaluated over the retarded interval $[u_1, u_2]$ which does not include the initial spurious burst of radiation (which we do not expect to converge) but contains otherwise the complete waveform including the ring-down.

Assuming a truncation error $\mathcal{O}(h^p)$ and that the coefficient of this error does not depend on resolution, the function ρ becomes to leading order (see Section 6.5 and compare (6.5.12))

$$\rho = \frac{(h_{0.024})^p - (h_{0.018})^p}{(h_{0.018})^p - (h_{0.012})^p}\,, \tag{11.2.3}$$

where $h_{0.024} = 0.024\,M$ and we we underline the importance of having used a full doubling of the resolution between the smallest and largest resolution to improve the accuracy of this estimate over more narrowly spaced resolution steps. In practice, we measure ρ and then solve for the *"effective"* convergence order p using (11.2.3).

In Table 11.4 we report the convergence rates as calculated from (11.2.2) for the time interval $0 \le u \le 190$ (u is the retarded time as defined in Section 11.2) which excludes the initial burst but

Table 11.4: Integrated convergence rates of the Zerilli-Moncrief gauge-invariant variables providing the dominant contribution in the kick-velocity measurements. As the numbers indicate, we achieve at least third order convergence both in amplitude and phase. A time-shift as given by (11.2.5)–(11.2.7) was made on the raw data to remove the near cancellation of the lowest-order error terms.

Q	$Q^{\times}_{21}$		Q^{+}_{22}		Q^{+}_{33}	
$r_{\rm E}/M$	amp	phase	amp	phase	amp	phase
30	4.51	3.95	4.65	4.31	4.32	2.13
40	4.08	3.70	4.61	4.34	4.26	2.62
50	3.83	4.44	4.35	4.76	4.02	2.39

contains the rest of the waveform. We see close to fourth-order convergence for the $\ell = 2$ modes Q^{+}_{22} and $Q^{\times}_{21}$. The $\ell = m = 3$ mode Q^{+}_{33}, on the other hand, shows second order convergence in phase, which is most likely related to the fact that the magnitude of this mode is the same size as the finite difference error in Q^{+}_{22} and is a factor of 40 smaller than the magnitude of Q^{+}_{22} itself.

The final kick-velocity magnitude in units of km/s is

$$|v|_{\rm kick} = 263.49, \quad 259.75, \quad \text{and} \quad 261.00 \tag{11.2.4}$$

for the medium, high and very-high resolutions. This gives $\rho(|v|_{\rm kick}) = 2.98$ which can be inserted into (11.2.3) to obtain a calculated convergence rate of 4.32.

It should be noted that the above definition of convergence rate naturally results in non-integer values for the exponent ρ, even though our methods are explicitly polynomial. This is because the derivation of (11.2.3) assumes a coefficient of one in the leading order error term that extrapolates between the resolutions. If the coefficient is in practice different for a given set of resolutions, then a non-integer value results which is larger if the coefficient is smaller. As such, values obtained in this way should not be considered literal polynomial extrapolation orders. By “convergence order 3.8” we rather mean that our results are consistent with third-order finite differencing where the leading third-order error coefficient is quite small so that at the given resolutions the convergence appears to be closer to a fourth-order approximation. Very high convergence exponents are a likely indication that the lowest resolution is not in the convergent regime for the measured quantity. Non-integer convergence orders obtained in this way are resolution dependent, and should themselves converge to the lowest order finite difference approximation used in the code in the limit of infinite resolution.

An important property of the waveforms which has emerged when performing these convergence tests is that the dominant source of error is a de-phasing which causes the lower resolution evolutions to “lag” behind the higher resolution. This delay is usually rather small and between $0.1\,M$ and $0.5\,M$, but it is clearly visible when comparing the total amplitude of Q as a function of time. The most important consequence of this error is that it can spoil the convergence tests if not properly taken into account: the residuals errors seem, in fact, to indicate over-convergence. This is shown in the upper panel of Figure 11.5, which reports the differences between Q^{+}_{22} when computed at different resolutions scaled for fourth-order convergence. Clearly the overlap is rather poor and even indicating that the truncation error is smaller than expected. This is obviously an artifact of the near cancellation of the lowest-order terms in the truncation error and induced by the small time-differences at different resolutions.

We remove this effect by shifting the time coordinate of the medium and high resolution runs by the time interval needed to produce an alignment of the maxima of the emitted radiation. This is done by by manually shifting the time-coordinate of the medium and high resolution runs

$$t \to t + \delta t. \tag{11.2.5}$$

The value of δt is set for the medium and high resolution runs independently, using the minimization condition

$$\frac{\partial}{\partial(\delta t)} \int_{150}^{170} |Q(t \to t + \delta t) - Q_{\rm vhigh}|^2 dt = 0. \tag{11.2.6}$$

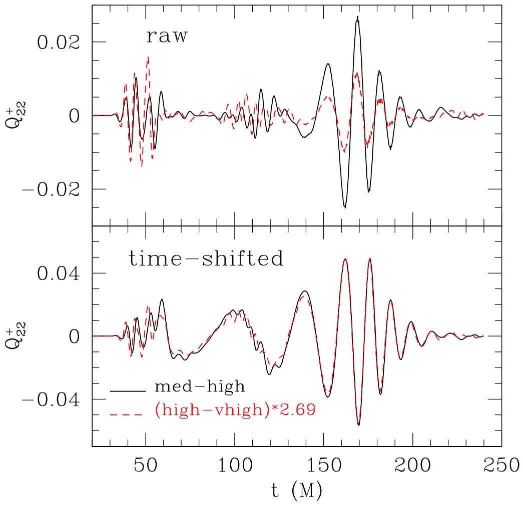

Figure 11.5: Convergence of the fiducial waveform Q^+_{22} for the binary system $r0$ before and after the time-shift defined in (11.2.5)–(11.2.7). In the upper graph we show the difference between Q^+_{22} when computed at different resolutions, scaled for fourth-order convergence and using raw data, *i.e.* without time-shifting). The overlap between the curves is rather poor indicating an over-convergence, *i.e.* the truncation error appears to be smaller than expected). In the lower panel we show the same data but after time-shifting. The very good overlap of the scaled curves on the indicates that the time-shifting is essential for obtaining properly scaling differences between runs of various resolutions.

This effectively means aligning in time the peak amplitude of the three runs, at $t \approx 160\,M$. Solving (11.2.6) numerically for the Q^+_{22} waveforms gives

$$\delta t_{0.024} = 0.4756 \quad \text{and} \quad \delta t_{0.018} = 0.1078. \tag{11.2.7}$$

Applying the time-shifting condition (11.2.5) to the coarse and medium resolution data, and inserting the result into (11.2.2)–(11.2.3) gives convergence rates that are consistent with the theoretical expectations.

We report in the lower panel of Figure 11.5 the same data shown in the upper panel, but after the time-shifting. Clearly, the overlap is now extremely good suggesting that the time-shifting is essential for obtaining the expected fourth-order convergence in the waveforms. In accord with the convergence in the waveforms we also see fourth order convergence in the final kick value.

The final kick-velocity magnitude in units of km/s is

$$|v|_{\rm kick} = 263.49, \quad 259.75, \quad \text{and} \quad 261.00 \tag{11.2.8}$$

for the medium, high and very-high resolutions. This gives $\rho(|v|_{\rm kick}) = 2.98$ which can be inserted into (11.2.3) to obtain a calculated convergence rate of 4.32.

As a final note we remark that besides validating a proper convergence of the code, it is also important to assess the accuracy of any measurable quantity at the relevant resolutions considered here. As a representative and physically meaningful quantity we have considered the accuracy of the fiducial waveform Q^+_{22} for the binary system $r0$. This is shown in Figure 11.6, where in the upper graph we report the waveforms at the three different resolutions: very-high (continuous line), high (dashed line) and medium (dotted line). Already with the lowest of these resolutions the accuracy is sufficiently high so that the curves are essentially indistinguishable from each other

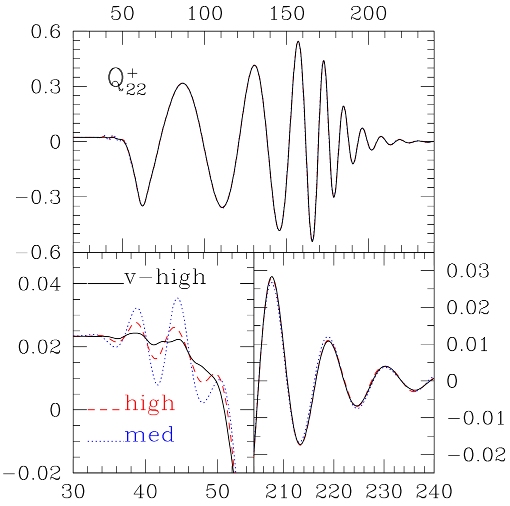

Figure 11.6: Accuracy of the fiducial waveform Q^{+}_{22} for the binary system $r0$. In the upper graph we show the waveforms at the three different resolutions: very-high (continuous line), high (dashed line), medium (dotted line). The accuracy is very good already with the lowest resolution and the curves cannot be distinguished. The lower panels show magnifications of some relevant portions of the waveform, with the lower-left panel concentrating on the initial transient radiation produced by the truncation error. The lower-right panel, on the other hand, refers to the quasi-normal ringing and shows that it is well-captured at all resolutions.

by eye. The lower panels show magnifications of the relevant portions of the waveform, with the lower-left panel concentrating on the initial transient radiation produced by the truncation error. The latter clearly is rather large at the medium resolution, but it nicely converges away when the grid spacing is decreased. The lower-right panel, on the other hand, refers to the quasi-normal ringing and shows that it is well-captured at all resolutions.

Convergence and accuracy of the Llama code

The newly implemented multiblock code “Llama” is tested for convergence by considering the phase and amplitude convergence of the $(\ell, m) = (2, 2)$ and $(\ell, m) = (6, 6)$ modes of the Weyl scalar Ψ_4 for an equal-mass non-spinning binary starting from an initial separation $d = 11M$. The evolution lasts for approximately $T = 1350M$ and encompasses inspiral, merger and ring-down. Figure 11.7 and 11.8 show the error in phase $\Delta\phi$ and amplitude ΔA for the $\ell = m = 2$ wave-mode extracted at $r = 100M$ and $r = 1000M$, respectively, between medium $h = 0.80M$ and low $h = 0.96M$ resolutions and high $h = 0.64M$ and medium $h = 0.80M$ resolutions in the wave-zone scaled for fourth-order convergence. Figure 11.9 shows the same, but for the $(\ell, m) = (6, 6)$ wave-mode at $r = 100M$ scaled for third-order convergence. The scaling factor is determined according to (6.5.12), *i.e.* we have

$$c = \frac{(h_{0.96})^p - (h_{0.80})^p}{(h_{0.80})^p - (h_{0.64})^p}\,, \tag{11.2.9}$$

and assuming fourth-order convergence $p = 4$, this becomes $c \approx 1.8$, while third-order convergence requires $c \approx 1.4$.

Stated differently, for convergence of order p and the associated convergence factor c, the relations

$$\Delta\phi_1 = c\Delta\phi_2\,, \qquad \Delta A_1 = c\Delta A_2 \tag{11.2.10}$$

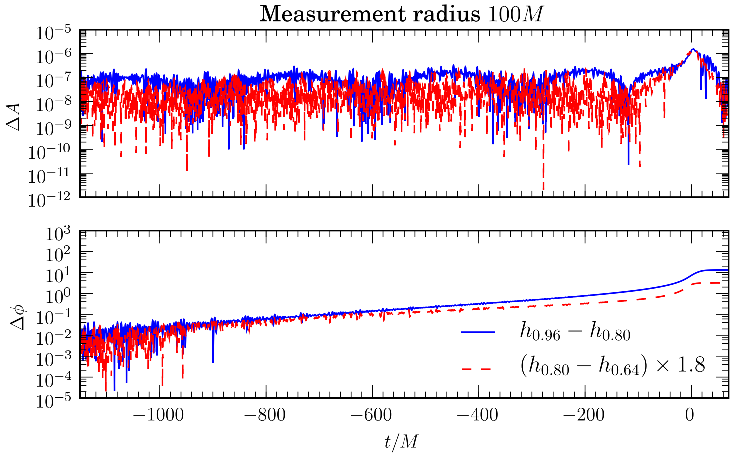

Figure 11.7: Convergence in amplitude A (*top*) and phase ϕ (*bottom*) of the $(\ell, m) = (2, 2)$ harmonic mode of the Weyl scalar Ψ_4 at an extraction radius $r = 100M$. The differences $\Delta\phi$ and ΔA in high $h = 0.64M$ and medium $h = 0.80M$ and medium $h = 0.80M$ and low $h = 0.96M$ resolution are scaled for fourth-order convergence.

must hold, where

$$\Delta\phi_1 = |\phi_{0.96} - \phi_{0.80}| \,, \qquad \Delta\phi_2 = |\phi_{0.80} - \phi_{0.64}| \,, \tag{11.2.11}$$

$$\Delta A_1 = |A_{0.96} - A_{0.80}| \,, \qquad \Delta A_2 = |A_{0.80} - A_{0.64}| \,. \tag{11.2.12}$$

In order to take the pointwise differences of the waveforms at different resolutions, we first align the maxima in the amplitude of the waves by using a bisection root-finding algorithm for the first derivatives of a 2nd-order Lagrange polynomial constructed from points around the maximum on the grid. This is necessary because the maximum is rather sharp, and the true maximum may be located inbetween gridpoints. Once we have found the exact location of the maxima, we align the medium and coarse resolution waves with the high resolution one. Since generally, the gridpoints of the waves do not line up, we calculate pointwise differences by fourth-order interpolating the waves to a common set of points. Note that the interpolation procedures do not affect the convergence of the waves. By chosing a different interpolation polynomial of higher or lower order, the convergence order of the waves remains the same. This is because the additional interpolation error introduced in the procedure for constructing pointwise differences is neglegible compared to the error in the evolution itself.

During merger at $t = 0M$, we clearly have at least fourth-order convergence, while during inspiral $t < 0M$ we have approximately eighth-order convergence (the convergence factor in that case is larger, and rescaling with this factor lines all curves up). The different theoretical convergence orders are summarized in Table 11.3, and we note that the lowest order error is due to the mesh-refinemnt time-interpolation scheme which is of second-order accuracy. Therefore, we can expect at least global second-order convergence. However, the time-interpolation error is small compared to the remaining errors so that its contribution to the measured convergence rate is neglegible. As the dynamics in the inspiral phase happen on a longer timescale compared to the strong temporal dynamics during merger, the dominant error during inspiral comes from the eighth-order accurate spatial discretization. During merger, the fourth-order error of the time-integration becomes evident and we measure fourth-order convergence in the $\ell = m = 2$ wave-mode. The higher modes appear to be more sensitive to lower-order errors, and the $\ell = m = 6$ mode exhibits clear third-order convergence during late inspiral, merger and ring-down.

The spherical multiblock structure in the wave-zone allows us to maintain a high radial, angular as well as time resolution all the way out to the outer boundary of the computational domain. Thus, we are able of accurately resolving spherical harmonic modes up to $\ell = 8$ at a detector

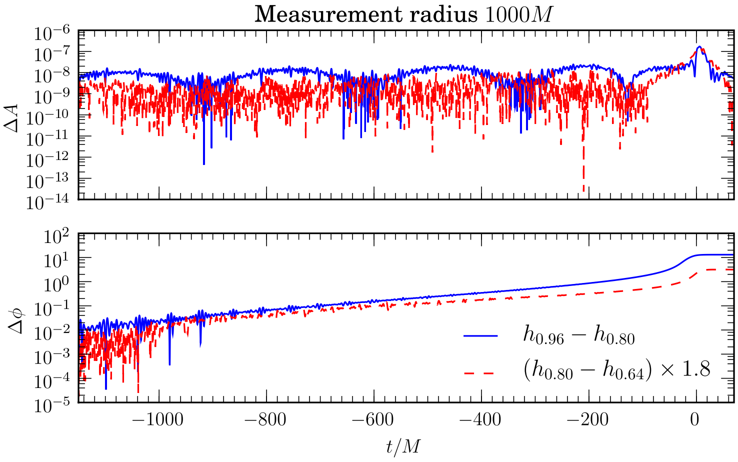

Figure 11.8: Convergence in amplitude A (*top*) and phase ϕ (*bottom*) of the $(\ell, m) = (2, 2)$ harmonic mode of the Weyl scalar Ψ_4 at an extraction radius $r = 1000M$. The differences $\Delta\phi$ and ΔA in high $h = 0.64M$ and medium $h = 0.80M$ and medium $h = 0.80M$ and low $h = 0.96M$ resolution are scaled for fourth-order convergence.

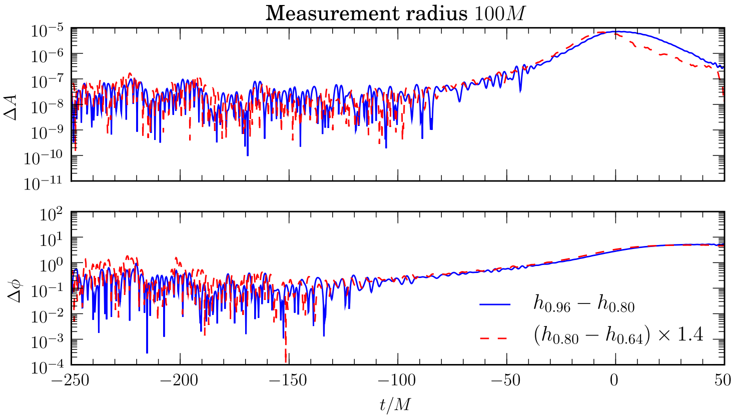

Figure 11.9: Convergence in amplitude A (*top*) and phase ϕ (*bottom*) of the $(\ell, m) = (6, 6)$ mode of Ψ_4 for a detector at $r = 100M$. The differences $\Delta\phi$ and ΔA in high $h = 0.64M$ and medium $h = 0.80M$ and medium $h = 0.80M$ and low $h = 0.96M$ resolution are scaled for third-order convergence.

Total ADM mass, M_{ADM}	$0.99051968 \pm 20 \times 10^{-9}$
Total ADM angular momentum, J_{ADM}	$0.99330000 \pm 10 \times 10^{-17}$
Irreducible mass, M_{irr}	$0.884355 \pm 20 \times 10^{-6}$
Spin, S_f/M_f^2	$0.686923 \pm 10 \times 10^{-6}$
Christodoulou mass, M_{f}	$0.951764 \pm 20 \times 10^{-6}$
Angular momentum, S_f	$0.622252 \pm 10 \times 10^{-6}$
Radiated energy, E_{rad}	$0.0387146 \pm 2 \times 10^{-6}$
Radiated angular momentum, J_{rad}	$0.370007 \pm 68 \times 10^{-6}$

Table 11.5: Properties of the merger remnant as measured on the apparent horizon (M_{irr}, S_f/M_f^2) and from the gravitational radiation (E_{rad}, J_{rad}). Ranges indicate the estimated numerical error. For the error in J_{ADM}, we have simply quoted machine precision (it is an analytical expression of the input momenta on the conformally flat initial slice).

radius of $r = 1000M$, which is further supported by the convergence of the $(\ell, m) = (6,6)$ mode (see Figure 11.9). Figure 11.11 shows the real part of the $\ell = m = 2,4,6,8$ harmonic modes of Ψ_4 extracted at $r = 1000M$ over the course of the evolution.

We can estimate the remaining phase and amplitude error by means of Richardson expansion (6.5.14). During the inspiral phase (which for this purpose we regard as being the period $t \leq -100M$), we have found roughly 8th-order convergence in the amplitude and phase, as described above. The remaining relative error for the $(\ell, m) = (2,2)$ mode can be estimated as

$$\max_{t\in[-1350,-100]} \mathrm{err}(A)_{\mathrm{inspiral}} = 0.090\%\,, \tag{11.2.13a}$$

$$\max_{t\in[-1350,-100]} \mathrm{err}(\phi)_{\mathrm{inspiral}} = 0.010\%\,. \tag{11.2.13b}$$

where $\mathrm{err}(A) := \Delta A/A$ and $\mathrm{err}(\phi) := \Delta\phi/\phi$, i.e., the rate of loss of phase with ϕ. During merger and ring-down ($t > -100M$), we observe 4th-order convergence in the amplitude, while maintaining 8th-order convergence in the phase. This results in the estimate

$$\max_{t\in(-100,150]} \mathrm{err}(A)_{\mathrm{merger}} = 0.153\%\,, \tag{11.2.14a}$$

$$\max_{t\in(-100,150]} \mathrm{err}(\phi)_{\mathrm{merger}} = 0.003\%\,. \tag{11.2.14b}$$

The time evolution of the numerical error in phase and amplitude is shown in Figure 11.10.

We note that these errors are of comparable order to the errors inherent in the extrapolation (see Section 15.1). Moreover, as is pointed out in Section 15.2, the error between extrapolated waveforms and those determined at future null infinity, $\mathcal{J}^+$, by characteristic extraction, is an order of magnitude larger than the numerical error determined here. This highlights the importance of reducing systematic errors inherent in finite radius measurements of Ψ_4.

This demonstrates the superiority of the multiblock code over standard Cartesian-based codes, since (i) the accurate and convergent resolution of a waveform at $r = 1000M$ has not been possible before and is shown at that distance to the source for the first time, and (ii) the accurate resolution of higher harmonic modes beyond $\ell \geq 4$, especially during merger and ring-down is a particular strength of the multiblock code and has not yet been demonstrated by other numerical relativity groups. In addition, it should be stressed that the artificial outer boundary is causally disconnected from the wave-zone (see Figure 7.7), thus minimizing unphysical contaminations of the computation.

A detailed analysis of the ring-down quasi-normal mode frequencies is given in Section 11.3.

Finally, Table 11.5 lists the properties of the remnant to high precision as measured via the isolated horizon formalism (see Section 4.3). The results agree well with previous high-accuracy measurements, such as those obtained by spectral evolution [61, 156], with the spin and irreducible mass agreeing within three decimal and four decimal places, respectively. While this is larger than the reported errors, we note that we have evolved a different initial data set than [156]. As reported in Section 11.1 our evolution has somewhat more eccentricity, and the level of agreement can be used to judge the influence of small amounts of eccentricity on the result.

By comparing the properties of the merger remnant with the integrated radiated energy, E_{rad}, and angular momentum, J_{rad}, determined from the gravitational waveforms, we find the residuals

$$|M_f + E_{\mathrm{rad}} - M_{\mathrm{ADM}}| = 4.1 \times 10^{-5}, \tag{11.2.15a}$$

$$|S_f + J_{\mathrm{rad}} - J_{\mathrm{ADM}}| = 1.0 \times 10^{-3}. \tag{11.2.15b}$$

Here we have used the extrapolations of the gravitational waveforms to $r \to \infty$ based on the 6 outermost measurement radii. The extrapolated values were obtained by taking the radiated energy and angular momentum on the three extraction spheres, and doing a linear extrapolation by fitting a function of the form

$$Q(r) = Q_0 + Q_1/r\,, \tag{11.2.16}$$

where Q is either E_{rad} or J_{rad}.

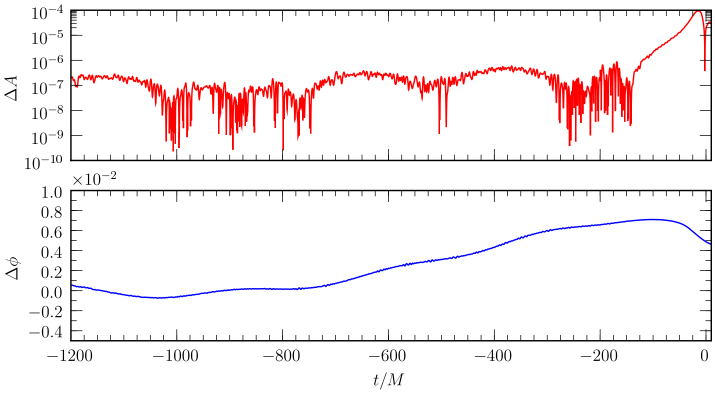

Figure 11.10: Absolute numerical error in the amplitude (top) and phase (bottom) accumulated over the course of the evolution for the highest resolution run, determined according to (6.5.14) for the point-wise differences in amplitude and phase between medium and high resolution runs. For the phase we assume the measured 8th-order convergence over the entire evolution, while for the amplitude we use 8th-order before $t \leq -100$, and 4th-order thereafter (see text).

Convergence of the characteristic code

In this section, we repeat results regarding the convergence of the characteristic code as obtained in [60]. In this paper, we have analyzed the convergence and accuracy behavior of 2-patch versus 6-patch mapping of S^2. Although we have not used the 6-patch version of the code in this thesis, the convergence results for the 6-patch mapping, which makes use of second-order and fourth-order accurate angular finite difference operators, are reported as well.

We first specify the linearized solutions against which the code is tested, as well as the various parameters that describe a numerical solution and its output. Then we present the results of testing the comparative performance of the second order six-patch, fourth order six-patch and stereographic codes against the linearized solutions. We will also report convergence of the constraint equations.

A class of solutions, in Bondi-Sachs form, to the linearized Einstein equations in vacuum was presented in [413], and we use these solutions to test the accuracy of the numerical evolutions described later. More specifically, the solutions to be used are those given in Section 4.3 of [413] for the case of a dynamic spacetime on a Minkowski background. We write

$$\begin{aligned} J &= \sqrt{(\ell-1)\ell(\ell+1)(\ell+2)}\ {}_2Z_{\ell m}\mathrm{Re}\,(J_\ell(r)e^{i\nu u}), \\ U &= \sqrt{\ell(\ell+1)}\ {}_1Z_{\ell m}\mathrm{Re}\,(U_\ell(r)e^{i\nu u}), \\ \beta &= Z_{\ell m}\mathrm{Re}\,(\beta_\ell e^{i\nu u}), \\ W_c &= Z_{\ell m}\mathrm{Re}\,(W_{c\ell}(r)e^{i\nu u}), \end{aligned} \tag{11.2.17}$$

where $J_\ell(r)$, $U_\ell(r)$, β_ℓ, $W_{c\ell}(r)$ are in general complex, and taking the real part leads to $\cos(\nu u)$ and $\sin(\nu u)$ terms. The quantities β and W_c are real; while J and U are complex due to the terms $\eth^2 Z_{\ell m}$ and $\eth Z_{\ell m}$, representing different terms in the angular part of the metric. We require a solution that is well-behaved at future null infinity, and is well-defined for $r \geq 2$, at which surface

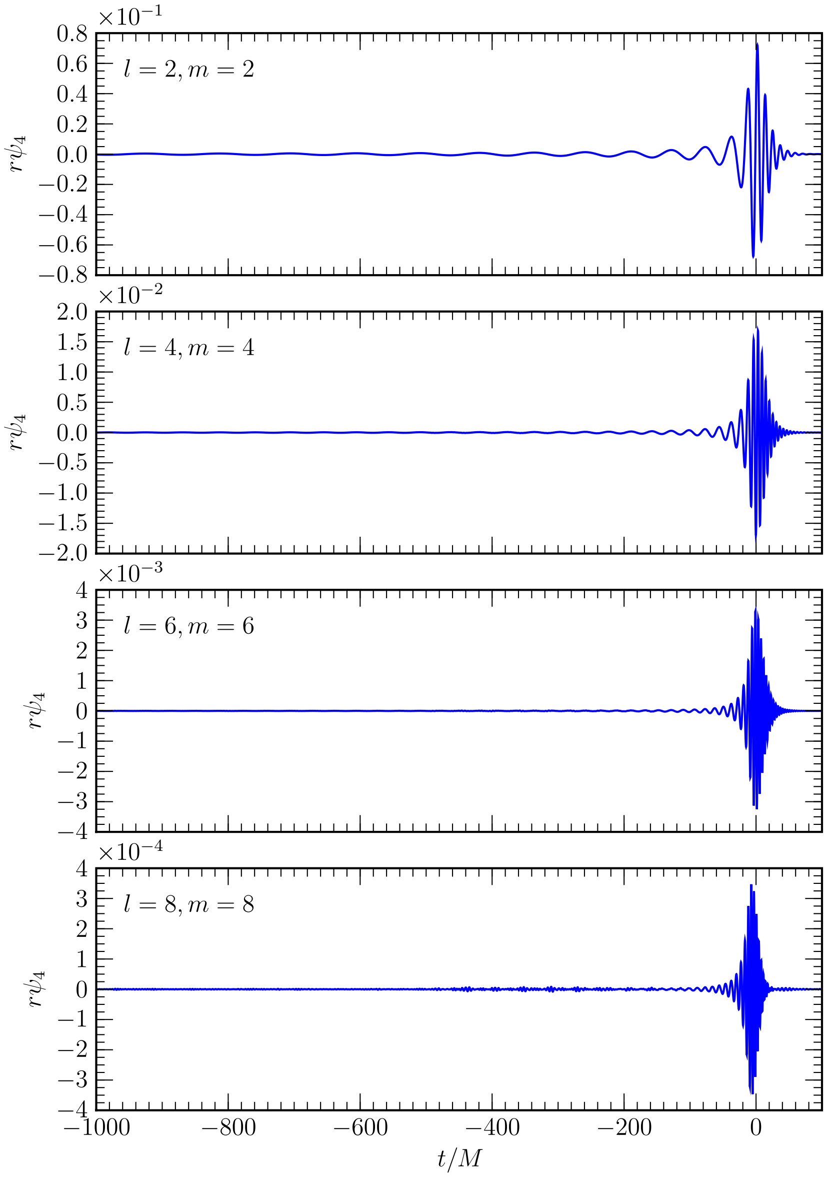

Figure 11.11: Dominant spherical harmonic modes of ψ_4 for $\ell \leq 8$ as computed for an equal-mass non-spinning reference configuration using the Llama multiblock code. Compare also Figure 11.22.

we set the inner boundary. We find in the case $\ell = 2$

$$\begin{aligned}
\beta_2 &= \beta_0, \\
J_2(r) &= \frac{24\beta_0 + 3i\nu C_1 - i\nu^3 C_2}{36} + \frac{C_1}{4r} - \frac{C_2}{12r^3}, \\
U_2(r) &= \frac{-24i\nu\beta_0 + 3\nu^2 C_1 - \nu^4 C_2}{36} + \frac{2\beta_0}{r} + \frac{C_1}{2r^2} + \frac{i\nu C_2}{3r^3} + \frac{C_2}{4r^4}, \\
W_{c2}(r) &= \frac{24i\nu\beta_0 - 3\nu^2 C_1 + \nu^4 C_2}{6} + \frac{3i\nu C_1 - 6\beta_0 - i\nu^3 C_2}{3r} \\
&- \frac{\nu^2 C_2}{r^2} + \frac{i\nu C_2}{r^3} + \frac{C_2}{2r^4}, \qquad (11.2.18)
\end{aligned}$$

with the (complex) constants β_0, C_1 and C_2 freely specifiable.

We find in the case $\ell = 3$

$$\begin{aligned}
\beta_2 &= \beta_0, \\
J_3(r) &= \frac{60\beta_0 + 3i\nu C_1 + \nu^4 C_2}{180} + \frac{C_1}{10r} - \frac{i\nu C_2}{6r^3} - \frac{C_2}{4r^4}, \\
U_3(r) &= \frac{-60i\nu\beta_0 + 3\nu^2 C_1 - i\nu^5 C_2}{180} + \frac{2\beta_0}{r} + \frac{C_1}{2r^2} - \frac{2\nu^2 C_2}{3r^3} + \frac{5i\nu C_2}{4r^4} + \frac{C_2}{r^5}, \\
W_{c3}(r) &= \frac{60i\nu\beta_0 - 3\nu^2 C_1 + i\nu^5 C_2}{15} + \frac{i\nu C_1 - 2\beta_0 + \nu^4 C_2}{3r} \\
&- \frac{i2\nu^3 C_2}{r^2} - \frac{4i\nu^2 C_2}{r^3} + \frac{5\nu C_2}{r^4} + \frac{3C_2}{r^5}. \qquad (11.2.19)
\end{aligned}$$

The emitted gravitational radiation, that is the news N, takes a simple form in the linearized limit when the metric satisfies (11.2.17)

$$N = \mathrm{Re}\left(e^{i\nu u}\lim_{r\to\infty}\left(\frac{\ell(\ell+1)}{4}J_\ell - \frac{i\nu}{2}r^2 J_{\ell,r}\right) + e^{i\nu u}\beta_\ell\right)\sqrt{(\ell-1)\ell(\ell+1)(\ell+2)}\; {}_2Z_{\ell m}. \quad (11.2.20)$$

For the cases ℓ =2 and 3,

$$\ell = 2: \quad N = \mathrm{Re}\left(\frac{i\nu^3 C_2}{\sqrt{24}}e^{i\nu u}\right)\, {}_2Z_{2m}; \quad \ell = 3: \quad N = \mathrm{Re}\left(\frac{-\nu^4 C_2}{\sqrt{30}}e^{i\nu u}\right)\, {}_2Z_{3m}. \quad (11.2.21)$$

Using these solutions, we can test the accuracy and convergence of the code. In all cases we take $\nu = 1$ and $m = 0$. We present results for the cases $\ell = 2$ and $\ell = 3$ with

$$C_1 = 3\cdot 10^{-6}, \quad C_2 = 10^{-6}, \quad \beta_0 = i\cdot 10^{-6} \quad (\ell = 2) \quad (11.2.22)$$

$$C_1 = 3\cdot 10^{-6}, \quad C_2 = i\cdot 10^{-6}, \quad \beta_0 = i\cdot 10^{-6} \quad (\ell = 3) \quad (11.2.23)$$

in (11.2.18) in the case $\ell = 2$, and in (11.2.19) in the case $\ell = 3$.

All the numerical simulations use a compactified radial coordinate $x = r/(r_{wt} + r)$ with $r_{wt} = 9$. Data is prescribed at time $u = 0$ as well as at the inner boundary $r = 2$ (which is equivalent to $x = 0.1888$). The stereographic grids (with ghost zones excluded) are

$$\text{Coarse: } n_x = n_q = n_p = 41, \qquad \text{Fine: } n_x = n_q = n_p = 81; \quad (11.2.24)$$

and there is no overlap between the two patches, *i.e.* we set the code parameter $q_{\text{size}} = 1$ which means that on the nominal grid, the holomorphic coordinate function $\zeta = q + ip$ takes values in $q, p \in [-1, 1]$. The six-patch grids are such that, over the whole sphere, the total number of angular cells is equivalent. We take

$$\text{Coarse: } n_x = 41, \quad n_\sigma = n_\rho = 24, \qquad \text{Fine: } n_x = 81, \quad n_\sigma = n_\rho = 47. \quad (11.2.25)$$

Six-patch results are reported for both second-order and fourth order differencing of the angular derivatives. In all cases, the fine grid has $\Delta u = 0.0125$ and the coarse grid has $\Delta u = 0.025$. Runs are performed for two complete periods, *i.e.* starting at $u = 0$ and ending at $u = 4\pi$. Results are reported for the errors of the quantities shown using the L_2 (root-mean-square) norm, evaluated at the time shown, averaged over all non-ghost grid-points over the whole sphere and between the inner boundary and future null infinity. The norm of the error in the news is averaged over the whole sphere at future null infinity.

Given a quantity Ψ, the error ε and the associated convergence factor C are defined as

$$\varepsilon = \|\Psi_{numeric} - \Psi_{analytic}\|, \quad C = \frac{\varepsilon_{coarse}}{\varepsilon_{fine}}. \tag{11.2.26}$$

Thus [352] (see Section 6.5), $C = 2$ corresponds to first order, and $C = 4$ to second order, convergence. We expect the code to exhibit second order convergence ($C = 4$) in the limit of infinite resolution, even when using fourth-order accurate angular derivatives.

Figure 11.12 shows the the error norms $\varepsilon(t)$ for the metric quantity J, and for the Bondi news N, plotted against time in the case $\ell = 2$. Each panel of the figure plots $\varepsilon(t)$ for the three schemes stereographic, six-patch second order, and six-patch fourth order; and in each case, we plot $4 \cdot \varepsilon(t)$ at fine resolution (points), and $\varepsilon(t)$ at coarse resolution (solid line), so that for second order convergence the points and solid line coincide. Table 11.6 gives the error norm ε (coarse resolution) and the convergence rate C, in both cases averaged over the whole run, for the quantities indicated.

It is clear that all schemes give (approximate) second order convergence of the metric quantity J. However, the news and the constraints (all of which contain second derivatives of metric quantities) exhibits, in some cases, degradation of the order of convergence. Referring to the plot of the news N in Figure 11.12, we see that the six-patch schemes were approximately second order convergent throughout the run, but that the stereographic scheme exhibits convergence degradation that is periodic in time (Although not shown in the figure, the convergence rate is at all times better than first order). The analytic solution has period 2π, and it is interesting that degradation peaks when the analytic solution is zero. We should also mention that this type of behavior has shown up in previous performed runs of the stereographic code and may be related to high-frequency error modes coming from angular patch interfaces or corners.

The convergence rates of the constraints appear problematic. However, the fact that the convergence rates of R_{0A} (stereographic case) and of R_{01} (all cases) are nearly second order is important. This implies that the problem is not due either to (a) a simple mis-coding of the finite difference representation of derivatives, or to (b) the expressions generated by the computer algebra. This issue will require further investigation in order to be able to use constraint violation as a reliable indicator of code accuracy.

The comparative behavior of the error norm is particularly interesting. On average, the error norm of second order six-patch is smaller than that of stereographic by a factor of order two (although there were cases in which the error was slightly larger). However, the fourth order six-patch scheme exhibit a dramatic reduction in the error norm, by a factor of up to 47 compared to that of the stereographic case.

Although we use the full nonlinear version of the code, we are not able to test nonlinear effects because the analytic solution against which we measure the error is valid only in a linearized regime. Even so, it is highly expected that the improvement in accuracy associated with the six-patch fourth order scheme, carries over to the non-linear regime.

Conservation of mass and angular momentum

In this section we discuss the radiated angular momentum and energy during the evolution of the different initial-data sets. Note that this is restricted to the r-sequence of the first set of spin-aligned binaries as reported in Section 11.1. However, as the remaining binaries of that same set have similar resolutions, we expect to have approximately the same accuracy for the remaining

$\ell = 2$ test data

Quantity	Stereographic	Six-patch, 2nd order	Six-patch, 4th order
$C(J)$	3.8456	3.8286	3.9112
$\varepsilon(J)$	3.3039×10^{-9}	1.5491×10^{-9}	6.9157×10^{-11}
$C(N)$	3.3119	3.9642	3.5528
$\varepsilon(N)$	2.2785×10^{-8}	1.0913×10^{-8}	8.4414×10^{-10}
$C(R_{00})$	1.2487	1.5000	2.0319
$\varepsilon(R_{00})$	3.1942×10^{-9}	2.8779×10^{-9}	5.7668×10^{-10}
$C(R_{01})$	3.5560	3.5936	3.1296
$\varepsilon(R_{01})$	3.9214×10^{-11}	1.6988×10^{-11}	2.7331×10^{-12}
$C(R_{0A})$	3.4285	1.7558	2.0043
$\varepsilon(R_{0A})$	5.2549×10^{-9}	6.6397×10^{-9}	2.1543×10^{-9}

$\ell = 3$ test data

Quantity	Stereographic	Six-patch, 2nd order	Six-patch, 4th order
$C(J)$	3.9783	3.9106	4.0777
$\varepsilon(J)$	4.6461×10^{-9}	3.2784×10^{-9}	1.3677×10^{-10}
$C(N)$	2.1201	3.9134	3.6262
$\varepsilon(N)$	4.9174×10^{-8}	2.8182×10^{-8}	1.7996×10^{-9}
$C(R_{00})$	1.2743	1.7963	2.0330
$\varepsilon(R_{00})$	7.2594×10^{-9}	4.5824×10^{-9}	1.1744×10^{-9}
$C(R_{01})$	3.5144	3.5383	3.3824
$\varepsilon(R_{01})$	1.3262×10^{-10}	7.5501×10^{-11}	6.0924×10^{-12}
$C(R_{0A})$	3.4326	1.9510	2.0156
$\varepsilon(R_{0A})$	9.0299×10^{-9}	1.0076×10^{-8}	2.9654×10^{-9}

Table 11.6: This table shows the error norm ε for the low resolution runs, and the convergence factor C, both averaged over space and time, for each version of the code and for each of five diagnostic quantities: the metric variable J, the news function N, and the constraints R_{00}, R_{01}, and R_{0A}.

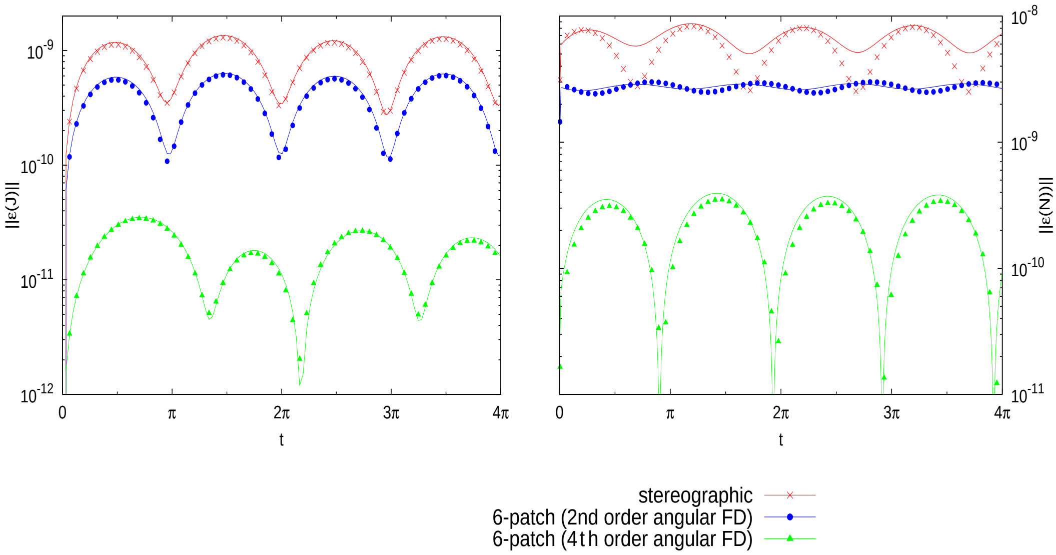

Figure 11.12: This figure shows an example of the convergence and accuracy of the various versions of the code. The left panel shows results for the metric variable J, while the right panel shows results for the news function N; the same key applies to both parts. In all cases, the solid line shows the coarse resolution results, while the points show the fine resolution results multiplied by 4.

members of the set. The second set of spin-aligned binaries as reported in Section 11.1 has a much higher numerical resolution and hence, conservation is expected to be satisfied to a much higher accuracy. The numbers reported here are therefore to be considered as an upper bound and the simulation carried out in this thesis will have errors that are not larger than the errors reported here.

We compute the radiated angular momentum and mass by calculating their difference between the initial data and that of the final BH, and then compare these quantities with the corresponding ones measured in terms of the emitted gravitational radiation. The differences in the two independent estimates serve therefore as stringent indicators of the conservative properties of our code.

The radiated angular momentum can be simply written as the difference between the initial and final values

$$\boldsymbol{J}_{\rm rad} = \boldsymbol{J}_{\rm fin} - \boldsymbol{J}_{\rm ini}\,, \tag{11.2.27}$$

where, as a result of the conformal flatness of the initial-data slice (see Section 2.4), $\boldsymbol{J}_{\rm ini}$ is given by the simple expression

$$\boldsymbol{J}_{\rm ini} \equiv \boldsymbol{J}_{\rm ADM} = \boldsymbol{C}_1 \times \boldsymbol{p}_1 + \boldsymbol{C}_2 \times \boldsymbol{p}_2 + \boldsymbol{S}_1 + \boldsymbol{S}_2\ . \tag{11.2.28}$$

Here $\boldsymbol{C}_i$, $\boldsymbol{p}_i$ and $\boldsymbol{S}_i$ are the position, the linear momentum and the spin of the i-th BH. The final angular momentum $\boldsymbol{J}_{\rm fin}$, on the other hand, is set to be equal to the spin of the final BH after all the radiation has left the computational domain. Two different methods are used to obtain this measure, both of which are based on properties of the apparent horizon of the final hole.

The first method employs the isolated/dynamical horizon formalism and searches for a rotational Killing vector ϕ^a on the final apparent horizon so as to measure the spin of the final BH as (see Chapter 4)

$$J = -\frac{1}{8\pi}\oint_S K_{ab}\phi^a \hat{r}^b d^2V\,. \tag{11.2.29}$$

We note that this expression (11.2.29) is valid on any sphere where a Killing vector ϕ^a can be found, and is therefore a quasi-local measure of the angular momentum. In particular, at large distances

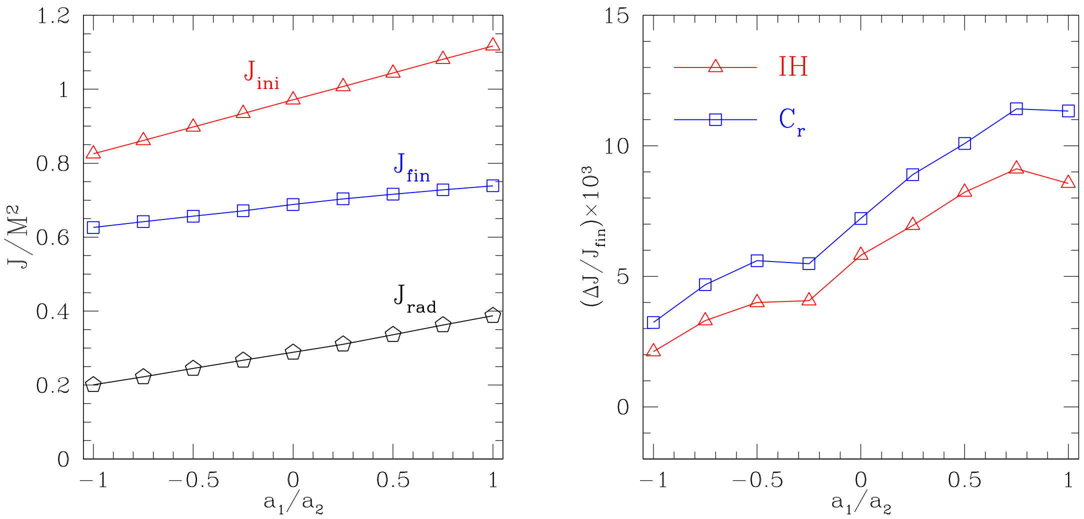

Figure 11.13: *Left panel:* Dependence on the spin ratio of the initial total angular momentum $J_{\rm ini}$ [as computed from (11.2.28)], of the radiated angular momentum $J_{\rm rad}$ [as computed through the gauge-invariant waveforms], and of the final spin of the BH $J_{\rm fin}$. All quantities show a linear behavior, whose coefficient are collected in Table 11.7. *Right panel:* Relative error $\Delta J/J_{\rm ini}$ in the conservation of the angular momentum [*cf.*, (11.2.35)]. Different curves refer to whether the final spin of the BH is computed using the isolated/dynamical horizon formalism (triangles) or the distortion of the apparent horizon (squares). In both cases the error is of about 1% at most for simulations at the medium resolution.

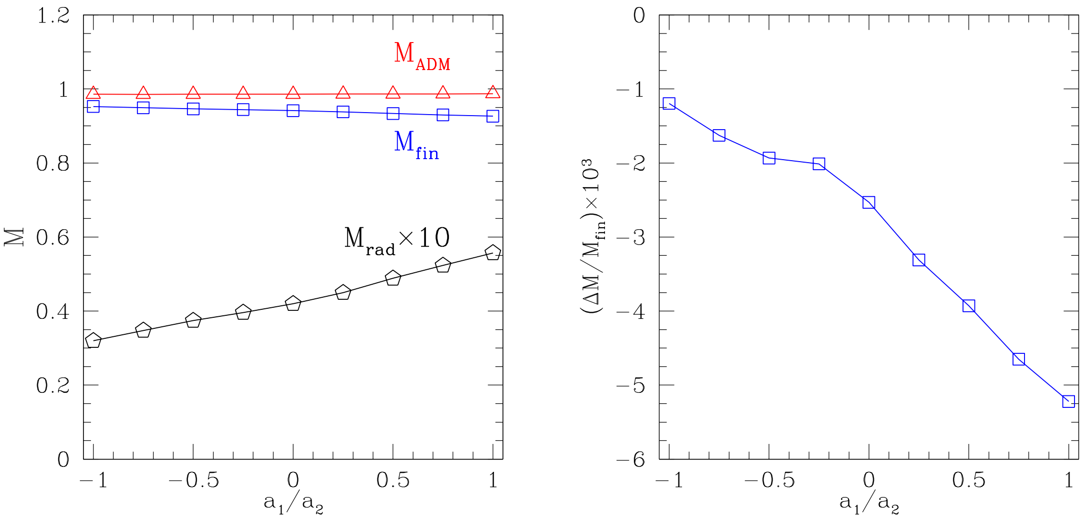

Figure 11.14: *Left panel:* Dependence on the spin ratio of the ADM mass $M_{\rm ADM}$, of the scaled radiated energy $M_{\rm rad}$ [as computed through the gauge-invariant waveforms and scaled by a factor of 10 to make it visible], and of the final mass of the BH $M_{\rm fin}$. All quantities show linear behaviors, whose coefficients are collected in Table 11.7. *Right panel:* Relative error $\Delta M/M_{\rm ini}$ in the conservation of the energy [*cf.*, (11.2.37)]. Note that the error is of about 0.5% at most for simulations at the medium resolution.

where the spacetime is close to axisymmetric, there is a good approximation to an angular Killing vector, and we can apply this expression to determine the angular momentum of the spacetime. Note also that (11.2.29) is identical to the ADM angular momentum when evaluated at spacelike infinity. (Refs. [293, 299] also give a quasi-local formula for the angular momentum flux due to gravitational radiation.)

The second method instead, assumes that the final BH has settled to a Kerr one and uses the rotational-induced distortion of the apparent horizon of the final BH to estimate its spin. Defining C_p and C_e to be respectively the apparent horizon's polar and equatorial proper circumferences, their ratio $C_r \equiv C_p/C_e$ will undergo damped oscillations as the perturbed BH settles to a Kerr state through the quasi-normal ringing. The final value of C_r can be expressed as a nonlinear function of the dimensionless spin parameter $a = J/M^2$ as [185, 414, 415]

$$C_r(a) = \frac{1+\sqrt{1-a^2}}{\pi} E\left(-\frac{a^2}{(1+\sqrt{1-a^2})^2}\right) , \tag{11.2.30}$$

where $E(k)$ is the complete elliptic integral of the second kind

$$E(k) = \int_0^{\pi/2} \sqrt{1-k\sin^2\theta}d\theta \, . \tag{11.2.31}$$

By inverting numerically (11.2.30) we obtain a from the late time C_r that is measured from the apparent horizon shape. Note that for computing J we need to multiply a by the square of the final mass, which we take to be $M_{\text{ADM}} - M_{\text{rad}}$. An alternative choice involving the total mass (4.3.4) (see Section 4.3) as measured from the apparent horizon would lead to essentially the same results.

As mentioned at the beginning of this section, the determination of the radiated angular momentum can also be done using directly the asymptotic waveform amplitudes h_+ and $h_\times$ as (see Section 5.7)

$$\frac{d^2 J}{dt\, d\Omega} = -\frac{r^2}{16\pi}\left(\partial_t h_+ \partial_\phi h_+^* + \partial_t h_\times \partial_\phi h_\times^*\right) , \tag{11.2.32}$$

where the amplitude h_+ and $h_\times$ themselves can be expressed either in terms of the Zerilli-Moncrief gauge-invariant variables $Q^+_{\ell m}$, $Q^\times_{\ell m}$ or, alternatively, in terms of the Newman-Penrose scalar Ψ_4. A comparison between the two approaches is presented in the next Subsection, where it is shown that the differences are minute. Because of this, hereafter we will refer to asymptotic amplitudes measured in terms of the gauge-invariant variables only.

The left panel of Figure 11.13 summarizes this comparison by showing, as functions of the spin ratio a_1/a_2, J_{fin} from (11.2.29), J_{rad} from (11.2.32) both adding nicely to yield J_{ini}. Note that J_{ini} is growing linearly as it is obvious from (11.2.28), but also that that a similar behavior is shown by the radiated angular momentum (and hence by the final spin of the BH). Using a linear fitting we can derive phenomenological expressions for the relative losses of angular momentum

$$\frac{J_{\text{rad}}}{J_{\text{ini}}} = \xi^J_{\text{rad}}\left(\frac{a_1}{a_2}\right) + \chi^J_{\text{rad}} , \tag{11.2.33}$$

and the relative spin-up of the final BH

$$\frac{J_{\text{fin}}}{J_{\text{ini}}} = \xi^J_{\text{fin}}\left(\frac{a_1}{a_2}\right) + \chi^J_{\text{fin}} \, . \tag{11.2.34}$$

The fitted values for $\xi^J_{\text{rad, fin}}$ and $\chi^J_{\text{rad, fin}}$ are presented in Table 11.7 and readily indicate that the system looses 24% of its initial orbital angular momentum in the case of anti-aligned spins and up to 34% for aligned spins.

To the best of our knowledge expressions (11.2.33) and (11.2.34) do not have a PN counterpart and yet, since they depend only on the spin-ratio, they represent simple and powerful ways of estimating both the efficiency in the extraction of angular momentum and the spin of the final black in a binary merger when the spins are orthogonal to the orbital plane. This information

Table 11.7: Coefficients for the phenomenological expressions (11.2.33) and (11.2.34) (and the corresponding coefficients for $\Delta M_{\rm rad,\,fin}/M$) by means of which it is possible to compute the relative losses of energy and angular momentum, as well as the final mass and spin of the BH in binary mergers in which the spins are orthogonal to the orbital plane.

$\xi^J_{\rm rad}$	0.0513	$\xi^M_{\rm rad}$	0.0118
$\chi^J_{\rm rad}$	0.2967	$\chi^M_{\rm rad}$	0.0437
$\xi^J_{\rm fin}$	-0.0513	$\xi^M_{\rm fin}$	-0.0118
$\chi^J_{\rm fin}$	0.7033	$\chi^M_{\rm fin}$	0.9563

Table 11.8: Final and radiated angular momenta and masses, computed from the gauge-invariant waveforms. Shown is also the radiated spin and mass relative to their initial values, which are listed in Table 11.1.

	a_1/a_2	$J_{\rm fin}$	$J_{\rm rad}$	$J_{\rm rad}/J_{\rm ADM}$	$M_{\rm fin}$	$M_{\rm rad}$	$M_{\rm rad}/M_{\rm ADM}$
$r0$	-1.00	0.6244	0.2008	0.2434	0.9536	0.0320	0.0325
$r1$	-0.75	0.6391	0.2222	0.2580	0.9507	0.0348	0.0353
$r2$	-0.50	0.6530	0.2449	0.2727	0.9482	0.0374	0.0380
$r3$	-0.25	0.6676	0.2670	0.2857	0.9461	0.0396	0.0402
$r4$	0.00	0.6827	0.2886	0.2971	0.9439	0.0420	0.0426
$r5$	0.25	0.6966	0.3106	0.3084	0.9412	0.0450	0.0456
$r6$	0.50	0.7075	0.3363	0.3222	0.9376	0.0488	0.0495
$r7$	0.75	0.7181	0.3626	0.3355	0.9344	0.0523	0.0530
$r8$	1.00	0.7292	0.3878	0.3471	0.9315	0.0557	0.0564

could be easily injected in those N-body simulations in which the interaction of BBHs is taken into account [416] and thus yield accurate estimates on final distribution of BH spins.

Since we have two independent and different ways of computing $J_{\rm rad}$ [*i.e.*, either from (11.2.32) or from (11.2.27)] we can quantify our ability to conserve angular momentum by measuring the normalized residual

$$\frac{\Delta J}{J_{\rm ini}} \equiv \frac{J_{\rm fin} + J_{\rm rad} - J_{\rm ini}}{J_{\rm ini}} \,. \tag{11.2.35}$$

This is shown in the right panel of Figure 11.13 and the two different lines refer to the two measures of the final spin of the BH, *i.e.*, either via the isolated-horizon formalism (triangles) or via the distortion of the apparent horizon (squares). In both cases the error is extremely small, ranging between 1.1% and 0.2% for simulations at the medium resolution, and thus providing convincing evidence of our accuracy in the preservation of angular momentum. It should be noted that while there seems to be a small advantage in using the isolated horizon measure, the differences are too small to be significant. Indeed, a small change in the procedure, such as the use of the mass measured via the apparent horizon via (11.2.30) in place of $M_{\rm ini} - M_{\rm fin}$ (as we are doing in this figure), would revert the advantage.

We proceed next to a similar analysis for the conservation of the mass-energy of the system by considering the difference between the the initial mass and final plus the radiated masses. As for the initial mass we obviously consider the ADM mass of the system $M_{\rm ADM}$, while the radiated energy $M_{\rm rad}$ is computed through the gravitational waveforms (see Section 5.5)

$$\frac{d^2E}{dt d\Omega} = \frac{r^2}{16\pi}\left(\left|\dot{h}_+\right|^2 + \left|\dot{h}_\times\right|^2\right) \,. \tag{11.2.36}$$

As for the angular momenta, we have chosen to express the right hand side of (11.2.36) in terms of the Zerilli-Moncrief functions and to use as final mass of the BH $M_{\rm fin}$, the one given by (4.3.4) and measured via the apparent horizon (see Section 4.3).

The left panel of Figure 11.14 shows $M_{\rm ADM}$, $M_{\rm fin}$ and $M_{\rm rad}$, with the latter rescaled the radiated by a factor of ten to make it more visible. Also in this case there is a clear linear behavior of both the radiated energy and of the final mass of the BH in terms of the spin ratio. As a result, phenomenological expressions of the type (11.2.33) and (11.2.34) are possible also for $M_{\rm fin}$ and $M_{\rm rad}$. The corresponding values of the coefficients $\xi^{M}_{\rm rad,\,fin}$ and $\chi^{M}_{\rm rad,\,fin}$ are also presented in Table 11.7.

Finally, to check the precision at which the energy is conserved, and in analogy to (11.2.35), we have computed the relative error

$$\frac{\Delta M}{M_{\rm ADM}} \equiv \frac{M_{\rm fin} + M_{\rm rad} - M_{\rm ADM}}{M_{\rm ADM}}\,, \tag{11.2.37}$$

and plotted this as a function of the spin ratio in the right panel of Figure 11.14. Clearly, also the energy losses are extremely small and for all the binaries in the sequence, the error in the energy balance is below 0.52% at the medium resolution. Table 11.8 summarizes the numerical results for the radiated energy and angular momentum for the members of the sequence.

A comparison of wave-extraction methods and test for peeling

First note, that the results reported in this section relate to an earlier work performed when calculating recoil velocities [56] and here we restrict attention to the quantities that are directly related to gravitational radiation, *i.e.* Ψ_4 and Q^{+}.

A more refined study of the asymptotic behavior of all Weyl scalars is done in [53] and reported in Section 15.1.

The identification of the Newman-Penrose Ψ_4 with the gravitational radiation content of the spacetime is a result of the peeling theorem, which states that in an appropriate frame the Ψ_4 component of the curvature has the slowest falloff with radius, $\mathcal{O}(1/r)$. The conditions of this theorem are not satisfied exactly at a small radius and in the chosen frame. While there are proposals for how this situation can be improved [307], we find that beyond $r_{\rm E} \geq 30\,M$ in fact our measure of Ψ_4 scales well with the different extraction radii $r_{\rm E}$, suggesting that the peeling property is satisfied to a reasonable approximation (see Figure 11.15).

In the course of the same analysis, it is also worth looking at the waveforms as calculated by using the gauge-invariant formalism. In particular, we focus on the real part of the $\ell = 2, m = 2$ even parity wave mode Q^{+}_{22} and check for the correct scaling for the different extraction radii. The right panel of Figure 11.17 shows that Q^{+}_{22} is constant for all extraction radii as expected.

As a final remark, we will also compare the h_{+} and $h_{\times}$ as calculated by using the odd and even master functions in the gauge-invariant formalism according to (5.2.9), (5.2.17) and the spin-weighted spherical harmonic amplitudes of the Weyl component $\Psi_4^{\ell m}$ decomposed on the extraction spheres. Using these amplitudes, the metric perturbations $h_{+}, h_{\times}$ recovered by a double time integral of (5.4.1)

$$h_{+} - {\rm i} h_{\times} = \lim_{r\to\infty} \sum_{\ell,m} \int_0^t dt' \int_0^{t'} dt'' \Psi_4^{\ell m}\ {}_{-2}Y_{\ell m}\ . \tag{11.2.38}$$

The numerical integration of (11.2.38) requires knowledge of an integration constant for the calculation of the second integral to eliminate the linear offset. This constant is determined by searching for minima in the $\Psi_4^{\ell m}$ mode and averaging over them. The resulting value is used as the integration constant. In both cases, we only consider the dominant contribution from mode $\ell = 2\,, m = 2$.

The influence of upwinded advection stencils

It has long been recognized that for BSSNOK evolutions employing a shift vector, β^a, the overall accuracy can be improved by “upwinding” the finite difference stencils for advective terms of the form $\beta^i \partial_i u$ [184] (compare Equations (2.3.14) and (2.3.15)). The upwind derivatives employ

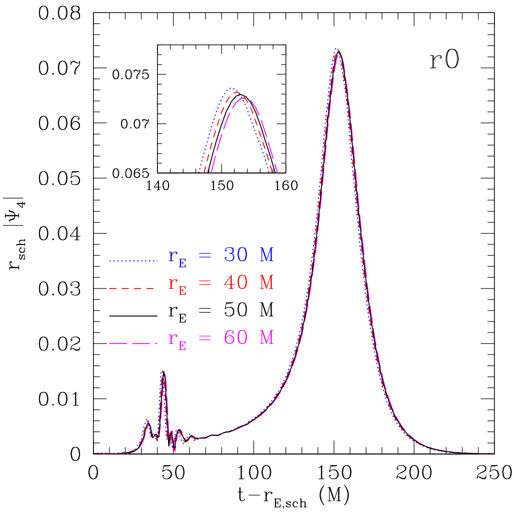

Figure 11.15: Amplitude of $r_{_{\rm E,sch}}|\Psi_4|$ for extraction spheres at $r_{_{\rm E}} = 30\,M$, $40\,M$, $50\,M$ and $60\,M$, demonstrating that Ψ_4 does indeed fall off as required by the peeling property. There is a slight decrease in amplitude with larger radius, suggesting that dissipative effects may become important at larger radii. Results in Chapter 12 use waveforms from the $r_{_{\rm E}} = 50\,M$ extraction sphere, unless indicated otherwise.

stencils which are off-centered by some number of grid points in the direction of β^a. The drawback of the method is that in order to maintain the same order of accuracy in the derivatives, the stencil must have the same width as a centered stencil, but since it is offset in either a positive or negative direction, it effectively requires an additional number of points to be available to the derivative operator equal to the size of the offset. For parallel codes which physically decompose the grid over processors and communicate ghost-zone boundaries, this means that a larger number of points must be communicated and can impact the overall efficiency. Further, a larger number of points must be translated at inter-patch and refinement level boundaries.

The original observation that upwinding is helpful was made with a code that used 2nd-order spatial finite differences. In that case, the centered stencils are small (three points) and the upwind derivatives correspond to sideways derivatives in the direction of the shift, i.e., no “downwind” information is used. For higher order schemes, the importance of upwinding may be less significant, since the stencils are large relative to the size of the shift vector. In practice, some implementations have empirically determined that upwinding by 1 point at 6th-order is helpful [231]. However, this is not done universally, particularly in conjunction with 8th-order centered differencing [417, 418].

We have found upwinding to be important in reducing numerical error in the black hole motion for every order of accuracy we have tried. The effect is demonstrated in Figure 11.18, which plots the motion of the black hole punctures for a data set involving a pair of equal-mass binaries with spins $a_1 = -a_2 = 0.8$ evolved with the Llama multiblock code and at a relatively low resolution with 8th-order spatial finite differencing. The results of two evolutions are plotted, one using fully centered stencils, and the other upwinding the advection terms with a one-point offset. Whereas the latter evolution displays the expected inspiral behaviour, at this resolution the binary evolved with centered advection actually flies apart. The is purely a result of accumulated numerical error, and at higher resolutions both tracks can be made to inspiral and merge. Our observation, however, is that for a given fixed resolution, the one-point offset advection has a significantly reduced numerical error in the phase as compared to the fully centered derivatives.

Based on some limited experimentation with larger offsets, we have the general impression that the one point offset provides the optimal accuracy for each of the finite difference orders we have tried (4th, 6th, 8th). We do not exclude the possibility that there may be situations in which the

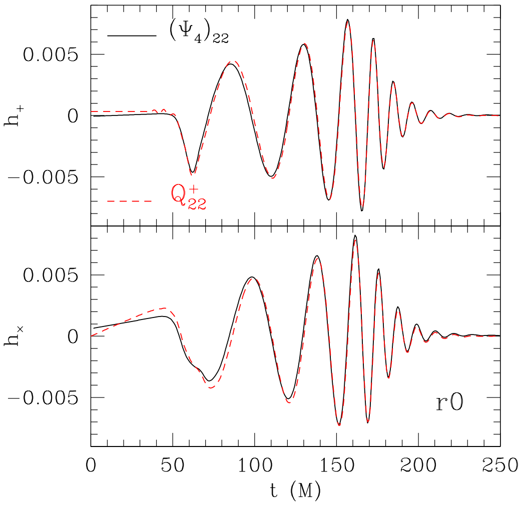

Figure 11.16: Comparison of the two polarization amplitudes h_+ (upper graph) and $h_\times$ (lower graph) as computed with Ψ_4 (continuous black line) or with the gauge invariant quantities $Q^+_{\ell m}$ (dashed red line). Note the two polarizations are computed using the lowest (and dominant) multipole $\ell = 2,\ m = 2$ and are extracted at $r_{\rm E} = 50\,M$.

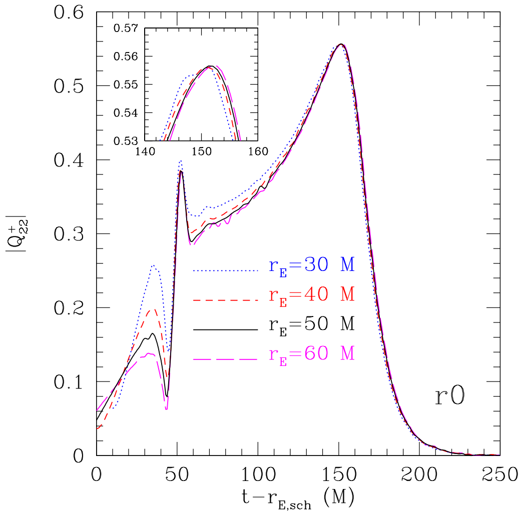

Figure 11.17: Fall-off behavior for the gauge-invariant quantity Q^+_{22}, which is shown to be constant when extracted at isotropic radii $r_{\rm E} = 30\,M$, $40\,M$, $50\,M$, and $60\,M$.

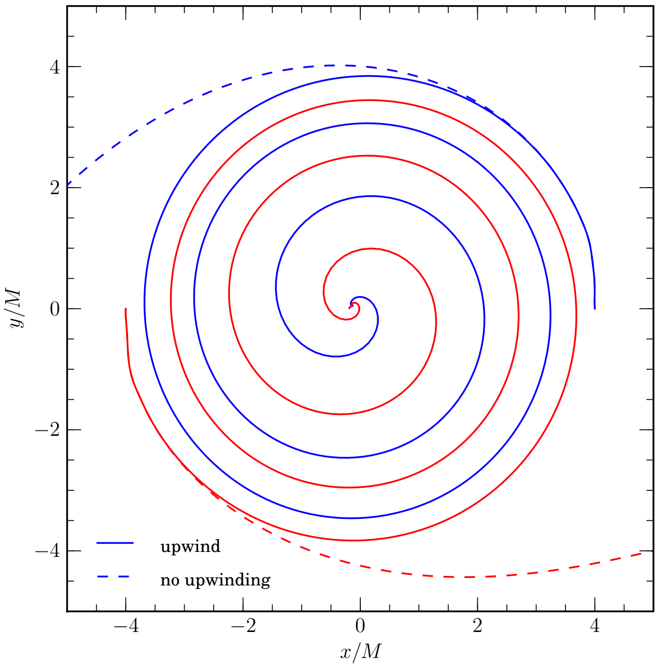

Figure 11.18: Trajectories of the two inspiralling punctures for a spinning configuration $a_1 = -a_2 = 0.8$, with upwinded advection terms (solid lines) and without (dashed lines). In the case where no upwinding has been used, the black holes do not inspiral, due to the accumulation of numerical error.

fully centered stencils perform as well as upwinded advection, however we have not come across a situation where the latter method performs worse.

As an alternative, we have also tested lower order upwinded derivatives as a potential scheme which would allow us to maintain a smaller stencil width. We generally find that the resultant numerical errors are of the same magnitude or larger than if we had not done the upwind at all.

We note parenthetically the fact that the off-centering is most important in the immediate neighborhood of the black holes, where the shift has a non-trivial amplitude. It is possible that a scheme where the stencils are off-centered only on grids where the shift is larger than some threshold would also be effective, and not suffer the drawbacks mentioned above over the bulk of the grid. We have not experimented with such a scheme, however.

High order finite differencing

A recent trend in the implementation of finite difference codes for relativity has been the push towards higher order spatial derivatives, it is now common to use 6th or 8th-order stencils. The benefit of higher order stencils is that the convergence rate can be dramatically increased, so that a small increase in resolution leads to a large gain in accuracy. And while not guaranteed, it is often the case that for a given fixed resolution, a higher order derivative will be more accurate, requiring fewer points to accurately represent a wavelength [345].

In moving to high order stencils, there is a trade-off between the possible accuracy improvements, and the extra computational cost. High order stencils generally involve two extra floating point operations per order. Since they require a larger stencil width, they also incur a cost in communication of larger ghost zones, as well as requiring wider overlap zones at grid boundaries. In practice, we find that higher order stencils can also have a more strict Courant limit, requiring a smaller timestep (and thus more computation to reach a given physical time). While it is possible to demonstrate a large gain in accuracy in switching from 2nd to 4th-order operators, there are diminishing returns in the transition to 6th and higher order [345].

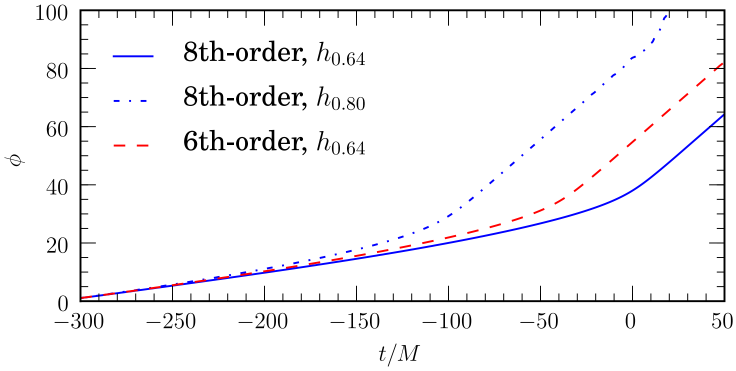

Figure 11.19: Phase evolution of the $(\ell, m) = (2, 2)$ mode Ψ_4 for the aligned-spin model with $a_1 = -a_2 = 0.8$ $h = 0.64M$. The 6th-order case at $h_{0.64}$ has a trajectory between the low resolution ($h_{0.80}$) and high resolution ($h_{0.64}$) 8th-order evolution.

We have experimented with 4th, 6th and 8th-order finite differencing for the evolution equations. Generally we find that the 8th-order operators can indeed provide a notable benefit, particularly in the phase accuracy, at low resolution. In Figure 11.19, we plot the phase evolution for an equal mass model with spins $a_1 = -a_2 = 0.8$ (evolved with the Llama multiblock code). The evolution covers the last three orbits and ring-down. We find that for this high-spin case, even over this short duration, a significant dephasing takes place. Assuming 8th-order convergence, the 6th-order evolution at the $h_{0.64}$ resolution would be comparable to the 8th-order at approximately $h_{0.77}$ resolution. We can get some idea of the relative amount of work required for each calculation by noting there would be $N = (0.64/0.77)^3$ fewer grid points in the $h_{0.77}$ evolution, but the 8th-order derivatives require $9/7$ times as many floating point computations for a derivative in one coordinate direction, and requires a Courant factor which is 0.9 times that of the 6th-order run. Taken together, this suggests an 8th-order run at $h_{0.77}$ would require a factor 0.68 of the amount of work of the 6th-order case to achieve comparable accuracy. Note that this computation does not take into account potential additional communication overhead associated with the wider 8th-order stencils. But assuming this is not dominant, the conclusion seems to be that for this level of accuracy, the 6th-order evolution is somewhat less efficient than the 8th-order version would be.

For a given situation, it may be that these factors change significantly. Implementation, and even hardware, details can shift the balance of costs between various operations. Further, the test case considered here involves a fairly high spin. Lower spin models (such as that considered in the main body of the paper), are accurate at modest resolutions, and in such cases the 6th-order evolutions may in fact prove to be relatively more efficient if the accuracy is already sufficient for a given purpose. On the other hand, if grid sizes and memory consumption are limiting factors, the 8th-order operators do give a consistent accuracy benefit for a fixed grid size. Our expectation, however, is that implementing yet higher order stencils (for example, 10th-order) may not be justified on the basis of efficiency.

As a final point, we note that the required high-order accuracy appears to be largely a consequence of the field gradients in the near-zone, immediately surrounding the black holes. An alternative scheme, then, could be to apply high-order finite differencing in this region, while using a lower order (and thus more efficient) scheme in the wave zone. Results from such a test are displayed in Figure 11.20, where we have used 8th-order only on the finest refinement level, *i.e.* , the mesh surrounding the black holes, but 4th-order on all coarser Cartesian and radial wave-zone grids. This, in turn, allows for a slightly less restrictive Courant limit, so that it becomes possible to run with a slightly larger time-stepping. The phase evolution of Ψ_4 is almost identical to that of the fully 8th-order case, but the we found that the speed of the run was increased by more than 25% (similar to that of the fully 6th-order evolution). Further optimizations, such as decreasing ghost-zone sizes of the 4th-order grids and consequently the communication overhead, might improve this further. While the errors and convergence order of this scheme have not been tested in detail, we suggest it as a potentially quite effective scheme for the impatient.

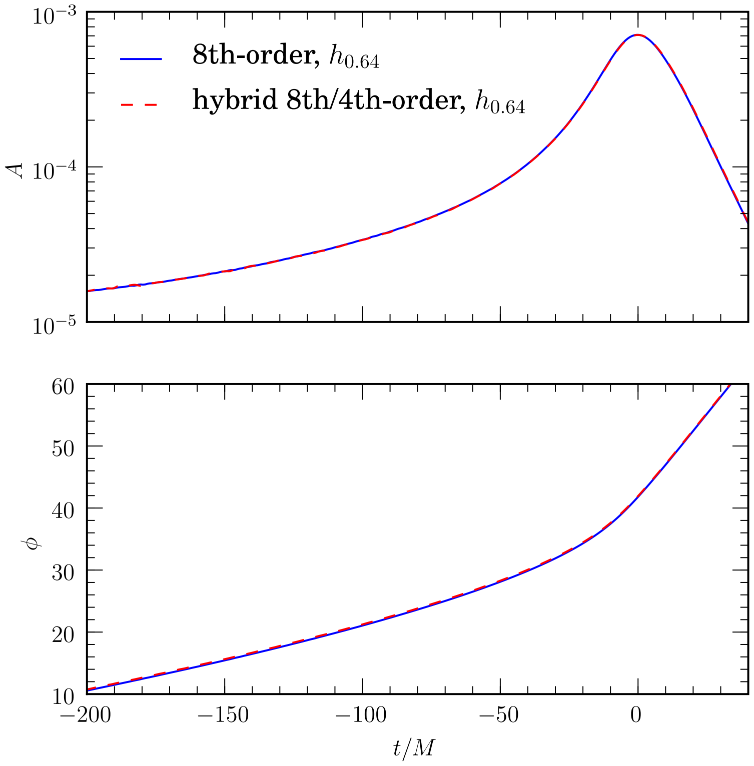

Figure 11.20: Amplitude and phase evolution of the $(\ell, m) = (2, 2)$ mode of Ψ_4 for the equal-mass aligned-spin model, comparing 8th-order spatial finite differencing with a scheme in which 8th-order is used only on the fine meshes surrounding the bodies, and 4th-order on the wave-zone grids.

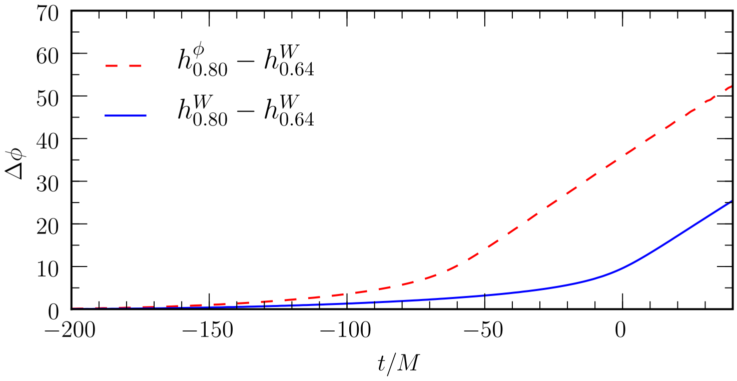

Figure 11.21: Differences in phase of a spinning configuration with resolution $h = 0.80M$ and conformal variables ϕ and W against a simulation with $h = 0.64M$ and conformal variable W. The dephasing is significant as we are on the coarse limit of resolution for this particular configuration.

Choice of conformal variable

In Section 2.2, we have described our implementation of the BSSNOK evolution system, and note that currently three variations are in use, based on the use of different variables to represent the conformal scalar. The original formulation is based on the use of $\phi := \log\gamma/12$. An issue with this variable in the context of puncture evolutions is that it has an $O(\ln r)$ singularity which can lead to large numerical error in finite differences calculated in the neighborhood of the puncture. More recently, the use of alternative variables $\chi = \gamma^{-1/3}$ [48] and $W = \gamma^{-1/6}$ [419] have been proposed as a means of improving this situation by replacing ϕ with variables that are regular everywhere on the initial data slice. In terms of the evolution system outlined in (2.2.15), the χ and W options correspond to the choices $\kappa = 3$ and $\kappa = 6$, respectively.

The influence of this change of variable can be seen in improved phase accuracy of binary evolutions carried out with either χ or W. In Figure 11.21, we show results from an evolution of the equal-mass aligned-spin ($a_1 = -a_2 = 0.8$) test case presented in the previous subsections, using ϕ and W as evolution variables (again we use the Llama multiblock code). Plotted are the phase errors, $\Delta\phi$, between runs at low resolution, $h_{0.80}$, using both ϕ and W with a higher resolution, $h_{0.64}$, evolution using W. The numerical error associated with the low resolution ϕ evolution is significantly larger than that of the corresponding W evolution.

The reason for this may be related to that of the benefit seen from upwind advective differences. The phase accuracy of the waveforms is crucially dependent on correctly modeling the motion of the bodies, and this requires accurate advective derivatives in the neighborhood of the punctures. The reduced numerical error associated with the regular χ and W variables is important.

Note that even in the ϕ case, numerical error generated at the puncture seems to be confined to within the horizon. Quantities such as constraints measured outside the horizon, or the horizon properties itself, are not significantly affected. However, it seems that a clear reduction in phase error can be attained through the use of either the χ or W variants of BSSNOK, and we have used the latter for the tests carried out in this paper.

11.3 Ring-down and quasi-normal modes

In this section, we analyze the ring-down behavior and QNM frequencies of the equal-mass non-spinning binary reference configuration as reported in Section 11.1. This binary has been evolved with the newly implemented Llama multiblock code (see Section 7.3, 8.1) and the convergence and accuracy of the waveforms have been demonstrated in Section 11.2.

Given the phase $\phi(t)$ of the wave-modes, we can calculate the instantaneous frequency given by $\omega(t) = \dot{\phi}(t)$. Figure 11.22 shows the late-time behavior of amplitude and frequency for wave-modes $(\ell, m) \leq (6, 6)$, respectively. We note that during ring-down, the frequencies settle to a constant value. If the final black hole is a Kerr BH, these frequencies are given by the quasi-normal modes of a Kerr BH with given spin a.

In our case, $a = 0.686923 \pm 1 \times 10^{-5}$ (see Table 11.5), and the real part of the prograde QNM frequencies for the different modes in that case is given by [102, 408]. For example, $M\omega_{22} = 0.526891$ for the $(\ell, m) = (2, 2)$ mode, given a final black hole of the measured mass M_f and spin a.

At this point, it is worth noting that the QNM frequencies are given in the spin-weighted *spheroidal* harmonics basis. As our waveforms are represented in a spin-weighted *spherical* harmonic basis, we have to apply a basis transformation to the wave-modes, *i.e.* we have

$$\hat{\Psi}_4^{\ell' m'} = \sum_{\ell, m} \Psi_4^{\ell, m} \langle \ell, m | \ell', m' \rangle \,, \tag{11.3.1}$$

where a dash denotes labeling of the *spheroidal* harmonic modes, and $\langle \ell, m | \ell', m' \rangle$ is the overlap

$$\langle \ell, m | \ell', m' \rangle = \int_\Omega d\Omega_{-2}\bar{S}_{\ell' m'}(c_{\ell' m'})_{-2}Y_{\ell m} \,, \tag{11.3.2}$$

where the spheroidal harmonics parameter[1] $c_{\ell' m'} = a\omega_{\ell' m'}$ depends on the spin a of the BH and the corresponding *prograde* or *retrograde* QNM frequency $\omega_{\ell' m'}$ of the $(\ell' m')$ spheroidal harmonic mode. In our case, we observe prograde QNMs. If $c = 0$ (as is the case for non-spinning BHs), the spheroidal harmonics reduce to the spherical harmonics.

The spin-weighted spheroidal harmonics used here have been implemented following Leaver's method [111] and are reviewed in [420]. In Appendix A.5, we streamline the procedure for computing the spin-weighted spheroidal harmonics as they have been implemented in Mathematica.

The frequencies measured during the ring-down are plotted in Figure 11.23 for the modes $(\ell, m) = (2, 2)$,$(4, 4)$ and $(6, 6)$. We have plotted data for the $r = 1000M$ measurement, as well as the value obtained by extrapolating the waveforms extracted at the outermost 6 measurement spheres to $r \to \infty$, and find that in fact the extrapolation has little effect on the frequency of the lower order modes at these distances from the source. We note that there is a modulation of the ring-down frequency, particularly apparent in the $(2, 2)$ mode. This is a result of mode mixing, which stems from the use of the spherical harmonic basis for the Ψ_4 measurements. By transforming the $r = 1000M$ result to spheroidal harmonics, this modulation visible in the $t < 40M$ signal is largely removed (dashed line).

As the amplitude of the wave declines exponentially to the level of numerical error, the frequencies become difficult to measure accurately. We estimate the ring-down frequency for each mode by performing a least-squares fit of a horizontal line through the measured spheroidal harmonic frequency over the range $t \in [40, 80]M$ (dotted line) with the standard deviation of the fit as a gauge of the error (grey region). These constant lines represent the estimated frequency of the associated QNM modes, and are tabulated as ω^{NR} in Table 11.9. They agree to high precision with the prograde QNM frequencies, $\omega^{\mathrm{lit.}}$, determined Kerr black holes by perturbative methods [421]. We conclude that the merger remnant is compatible with a Kerr black hole within the given error estimates.

11.4 Comparing different simulation codes

In this section, we will briefly state the results of the "Samurai" project [61]. In the "Samurai" project, different simulation codes, including the CCATIE code (see Section 8.1), have been compared to determine the consistency of the waveforms from several numerical relativity groups

---

[1] We restrict attention to the $N = 0$ overtone only.

(ℓ, m)	$M_f\omega^{\text{lit.}}$	$M_f\omega^{\text{NR}}$	$\lvert M_f\omega^{\text{NR}} - M_f\omega^{\text{lit.}}\rvert$
$(2, 2)$	0.526891	0.5267 ± 0.0011	1.9×10^{-4}
$(4, 4)$	1.131263	1.1312 ± 0.0028	6.3×10^{-5}
$(6, 6)$	1.707630	1.7074 ± 0.0662	2.3×10^{-4}

Table 11.9: Prograde $N = 0$ QNM frequencies for different modes and spin $a = 0.6869$ as determined by perturbative methods [421], $\omega^{\text{lit.}}$, and as measured during ring-down in the numerical relativity simulation, ω^{NR}.

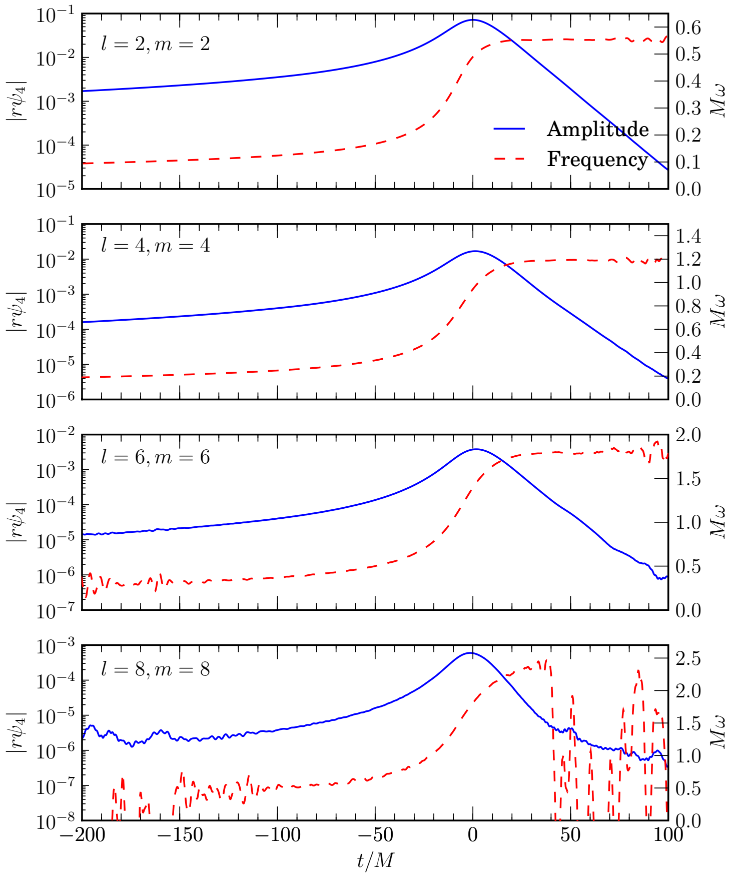

Figure 11.22: Late-time amplitude and frequency evolution for various modes of Ψ_4. The associated waveforms for this equal-mass non-spinning configuration are shown in Figure 11.11.

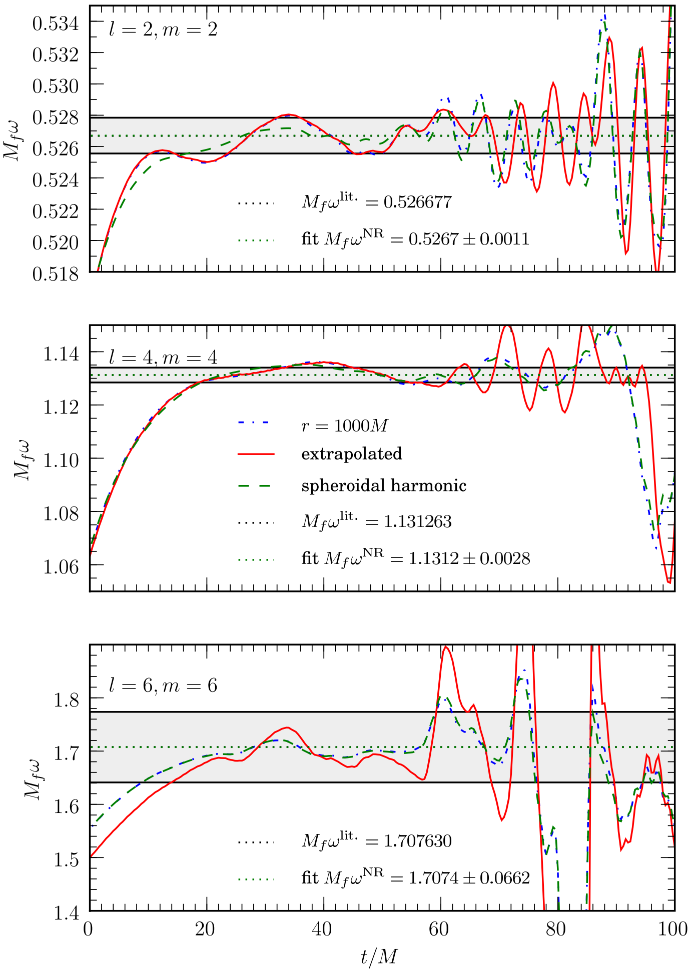

Figure 11.23: Zoom-in of the ring-down frequencies for the dominant Ψ_4 modes. From top to bottom, the plots show the frequencies of the $(\ell, m) = (2, 2)$, $(4, 4)$ and $(6, 6)$ modes respectively, over a timescale from the $(2, 2)$ waveform peak to $100M$ later, at which point the waveform amplitude is too small to measure an accurate frequency. The Ψ_4 data measured at $r = 1000M$ is plotted, in addition to the value extrapolated to $r \to \infty$, and the transformation to spheroidal harmonics. The expected QNM frequency is plotted as a dotted line, as well as a fit to the spheroidal harmonic data between $t \in [40M, 80M]$, with error-bars determined by the standard deviation of the fit.

with an eye towards gravitational-wave detection. This is important to assess because numerical relativity waveforms are eventually used as gravitational-wave templates for matched filtering gravitational-wave searches in the detector data output. For this reason, numerical relativity waveforms generated from different simulation codes have to be in agreement up to a certain minimum error. Generally, the waveforms may be different because they depend on the numerical method used, the construction of the initial data, gauge-conditions and wave-extraction methods. As there are many possible ways and as each group has its own way of implementing these aspects, each code contains different types of errors and uncertainties. If the variations in the waves due to these errors are larger than the minimum error necessary for detection, the numerical relativity waveforms would be useless for current gravitational-wave searches.

Fortunately, it turns out that all codes agree fairly well. The codes that have been compared are the CCATIE code (see Section 8.1), BAM [256, 422], Hahndol [197, 423], MayaKranc [424] and SpEC [372]. Since the SpEC waveforms have the lowest reported internal uncertainties, all waveforms are compared against the SpEC waveform.

In [61], two kinds of comparisons are then performed. The first deals with the phase and amplitude agreement of the Ψ_4 waveforms. It is found that all of the waveforms agree within their claimed internal uncertainty. This acts as a clear validation of the results between different codes, and demonstrates that the variation between waveforms due to different numerical techniques, initial data, gauge conditions and wave-extraction methods is at worst no larger than the internal error estimates in each waveform. The details of the uncertainties in each numerical code are of little direct interest in the practical business of gravitational-wave detection and source parameter estimation. For that reason a second comparison attempts to assess what the apparently small differences between the five waveforms mean for gravitational-wave searches. The relevant quantity to compare for gravitational-wave detection is the match $\mathcal{M}$ between two waveforms, which quantifies their disagreement with respect to the noise spectrum of a given detector (see Chapter 14 for details). In gravitational-wave searches, if the match between the correct physical waveform and the template is greater that 0.965, then no more than about 10% of signals will be lost.

For the Samurai waveforms, the matches are so close to unity that it makes more sense to consider the mismatch, $1 - \mathcal{M}$. Figure 11.24 shows the mismatch between the SpEC waveform and the others for the Enhanced LIGO and Virgo detectors. As is clear from the figure, the matches are well within the standard $1 - M < 0.035$ threshold for detection! One can also make a comparison relevant to parameter estimation. As discussed in [61, 175], if the signal-to-noise ratio of the difference between two waveforms $\delta h(t) = h_1(t) - h_2(t)$ is less than one, then the two waveforms will be indistinguishable in a gravitational wave search (see Section 15.2 for more details). The signal-to-noise ratio (SNR) (see Chapter 14 for a definition) of both the waveforms and their difference decreases in inverse proportion to the distance D of the detector from the source. We can therefore determine the maximum SNR such that, if a signal were detected with a lower SNR, it would not be possible to distinguish whether it was h_1 or h_2. For the Enhanced LIGO and Virgo detectors, a detection will be considered reliable if the SNR is above 5–8, and SNRs above 30 are considered unlikely. (For example, the maximum SNR of injections for the NINJA project is 30 [64].) It turns out that in all cases the waveforms cannot be distinguished if the SNR is below ~ 14. This suggests that these five waveforms are unlikely to be distinguishable (for intrinsic parameters) in single detectors prior to the commissioning of Advanced LIGO and Virgo in 2014.

For a complete analysis on the waveform comparisons, please refer to [61].

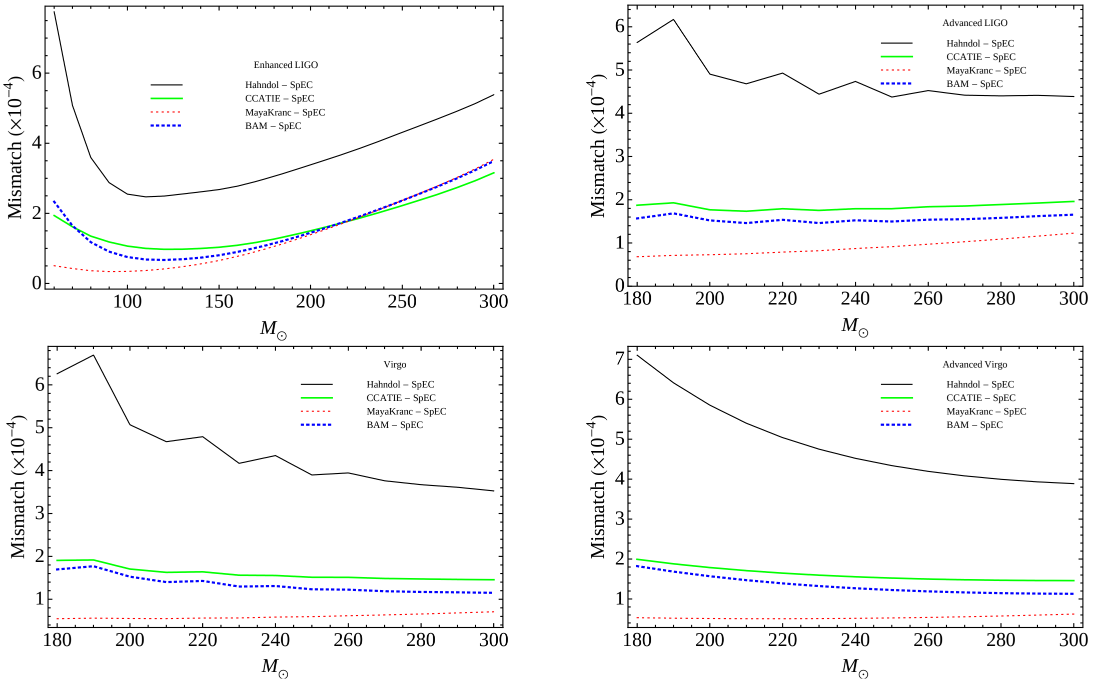

Figure 11.24: The mismatch between the `SpEC` waveform and each of the other codes. The three plots show the results for the Enhanced LIGO, Advanced LIGO, Virgo and Advanced Virgo noise curves. The lower end of the mass range was chosen such that the entire numerical waveform was included in the detector's frequency band.

Chapter 12

Gravitational recoil of binary black hole mergers

Together with energy and angular momentum, gravitational radiation also carries away linear momentum. In the case of a binary system of non-spinning BHs, a physical intuition of this loss of linear momentum can be built rather easily. As the two bodies orbit around the common center of mass, each will emit radiation which is forward-beamed. Unless the two BHs have exactly the same mass, their motion will be different, with the smaller BH moving more rapidly and, hence, being more efficient in beaming its emission. The net momentum gained over an orbit is negligible if the orbit is almost circular (the momentum loss in any direction is essentially balanced by an equal loss in the diametrically opposite direction), but it can become large when integrated over many orbits, leading to a recoil that is a fraction ($\lesssim 10^{-2}$) of the speed of light during the last portion of the orbit prior to the merger. This net linear momentum to the final BH is also often called a "kick" [425, 426]. While estimations of kick velocities have been available for some time [427–429], the largest part of the system's acceleration is generated in the final orbits of the binary system, and as such requires fully relativistic calculations to be determined accurately.

A number of PN/perturbative analyses (see, *e.g.* [429, 430]) have provided estimates of this recoil velocity, while numerical relativity simulations [431, 432] have measured it to rather high precision, predicting a maximal kick of 175 km/s for a binary system of non-spinning BHs with a mass ratio $q \equiv M_1/M_2 \simeq 0.36$, where M_1 and M_2 are the masses of the two BHs. Such a recoil has indeed quite important astrophysical consequences, since it could, provided it is large enough, kick the binary out of its host environment. Clearly, a replaced or an even missing central BH would have dramatic consequences for the further development of the host. Determining accurately what are the expected escape velocities for the most typical environments hosting a BBH system is rather difficult, but the estimates made in [433], for instance, predict that the escape velocities for dwarf galaxies and globular clusters are $\lesssim 100$ km/s, but for giant galaxies these can be ~ 1000 km/s.

Over the past years, a number of numerical relativity simulations have been carried out to determine recoil velocities in various sections of the parameter space of BBH systems. The first systems to be studied were unequal mass systems with moderate mass ratios, where the first calculations were performed by the Penn State [434] and Goddard [431] groups, with simulations at mass ratios near the estimated peak of the Fitchett formula [428]. A more extensive study, exploring a large number of models between mass ratios 0.25 to 1.0, was carried out by the Jena group [435], providing for the first time a mapping of the unequal mass parameter space with fully relativistic simulations. The recoils from systems in which the bodies had spin were first considered by a number of studies in the first half of 2007. The Penn State group examined a sequence of equal mass binaries with spins equal and anti-aligned, determining that the largest recoil possible from such an evolution is of the order of 475 km/s [410]. At the same time, in [55] we studied a sequence of models in which the spins are anti-aligned, but of different magnitude, and arrived at a similar estimate of 450 km/s. The Jena and Brownsville (now Rochester) groups showed that extremely large kicks are possible from particular configurations of misaligned spins, measuring recoils as high as 2500 km/s [436], and extrapolating to 4000 km/s for the maximally spinning case [437, 438]. Such spin configurations have recently been studied in more detail in [439]. Other studies consider hyperbolic encounters where recoil velocities as large as 10000 km/s can occur [440]. Velocities of this magnitude have a number of astrophysical implications for models of galaxy mergers. However, as there are mechanisms in nature to align the spins (*c.f.* Section 11.1), kick velocities of this magnitude will be probably very rare indicating that most merger remnants will not have sufficient kinetic energy to leave their hosts.

In this chapter, we focus on the asymmetrically emitted gravitational radiation from BBH systems with spins aligned with the orbital angular momentum. If the spins of the two bodies differ, there can be a prominent beaming of the gravitational radiation during the late plunge, causing a recoil of the final merged BH. In a first attempt to tackle this problem, we have performed an accurate and systematic study of recoil velocities from a sequence of equal-mass BHs whose spins are aligned with the orbital angular momentum, and whose individual spins range from $a = +0.584$ to -0.584, to arrive at a consistent maximum recoil of $448 \pm 5\,\mathrm{km/s}$ for anti-aligned models.

We have then extended and refined this work to the whole 2D subspace of equal-mass and spin-aligned binaries and by least-square fitting the results of these simulations we have constructed a phenomenological expression, or a "spin diagram", which provides straightforward information about the recoil velocity $|v_{\mathrm{kick}}|$ in terms of the dimensionless spins a_1 and a_2 of the two initial BHs. Overall this suggest a maximum recoil velocity of $|v_{\mathrm{kick}}| = 441.94\,\mathrm{km/s}$.

Quite surprisingly, this relation highlights a nonlinear behavior, not predicted by the PN estimates, and can be readily employed in astrophysical studies on the evolution of BBHs in massive galaxies. An essential result of our analysis, without which no systematic behavior can be found, is the identification of different stages in the waveform, including a transient due to lack of an initial linear momentum in the initial data. Furthermore, by decomposing the recoil computation into coupled modes, we are able to identify a pair of terms which are largely responsible for the kick, indicating that an accurate computation can be obtained from modes up to $\ell = 3$.

The simulation are calibrated with strict convergence tests as presented in Section 11.2, and we verify the correctness of our measurements by using multiple independent methods whenever possible. As shown in Section 11.2, we have excellent conservation of mass and angular momentum thus strengthen the accuracy of our results.

12.1 Systematic studies on a restricted set of spin-aligned binaries

In this section, we report on initial work done on recoiling BBH mergers which is restricted to the r-sequence as listed in Table 11.1, but has been investigated in great systematic detail.

We describe the influence of the initial dynamics on the radiated waveforms and the importance of suitable vector integration constants to remove these effects when determining the final recoil velocity. These vectors, in fact, capture the information about the net linear momentum that the spacetime has built-up during its past evolution and prior to the actual numerical evolution and can result into a significant correction.

Then, we proceed in reporting on evolutions of the aligned-spin sequence and the dependence of the recoil velocity on the spin-ratio. We find that the data show an almost linear behavior at large negative spin-ratios, as predicted by PN calculations. However taking into account also results from positive spin-ratios, the data suggest a nonlinear (quadratic) dependence and we give a phenomenological expression for the recoil velocity as a function of the spin ratio. Extrapolating our results to the case of maximally rotating BHs, we find that the maximum recoil velocity attainable by spin-orbit aligned configurations is $448 \pm 5\,\mathrm{km/s}$.

Initial transients in the waveforms

As given in Section 5.6, both Eqs. (5.6.3) and (5.6.12) provide an expression of the recoil velocity in terms of the radiated (linear) momentum per (infinitesimal) time interval. A time-integration of those equations is needed in order to compute the recoil and this obviously opens the question of determining an integration constant which is in practice a vector. Fortunately, this integration constant has here a clear physical meaning and it is therefore easy to compute. In essence it reflects

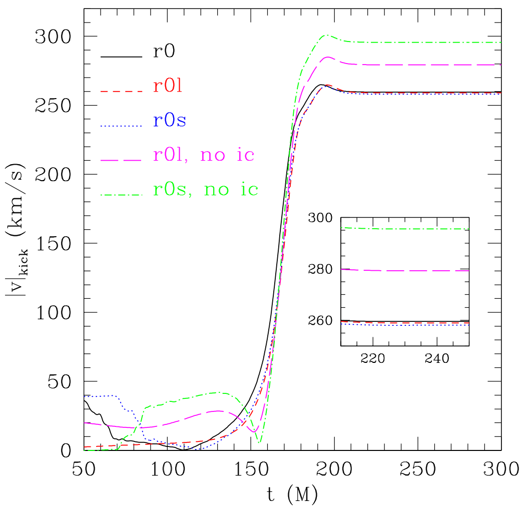

Figure 12.1: The recoil velocity of the binary $r0$ (Table 11.1) is compared to those of the same system but with either a larger or a smaller initial separation (*i.e.* $r0l$ and $r0s$, respectively). Note the same recoil velocity is obtained when the integration constant is properly taken into account, while an error as large as $\sim 13\%$ is made otherwise.

the fact that at the time the simulation is started, the binary system has already accumulated a non-vanishing net momentum as a result of the slow inspiral from an infinite separation.

Since the initial data is constructed so as to have a vanishing linear momentum, there will be a inconsistency between this assumption and the actual evolution of the initial data. Stated differently, the numerical evolution of the Einstein equations will soon tend to a spacetime which is different from the initial one and indeed corresponding to one with a net linear momentum. This momentum is the one that the binary has gained when inspiralling from $t = -\infty$ till $t = 0$. Calculating the integration constant amounts therefore to computing the vector accounting for this mismatch and is essential for a correct measurement of the recoil velocity. The error made when neglecting this constant, as routinely done in numerical relativity calculations, inevitably produces a systematic deviation from the correct answer and, as we will show in the next section, it can altogether prevent from having even the qualitative behavior right.

The relevance of this integration constant depends on the initial separation and it is more important for binaries that start their evolution already quite close. This is rather obvious: the tighter the binary is, the larger the emitted momentum per unit time and the more important is to evaluate the initial mismatch. Figure 12.1 helps to illustrate this point and can be discussed before entering into the details of how we actually compute the integration constant. The figure shows the time evolution of the recoil velocity $|v|_{\rm kick} \equiv \sqrt{v_x^2 + v_y^2}$ for the same binary system having spin ratio $a_1/a_2 = -1$ but with increasing initial separation. More precisely, we consider systems $r0l$, $r0$ and $r0s$ (Table 11.1) which differ only in the initial separation, which is about 8.4, 6.0 and 5.6 M, respectively. The data in Figure 12.1 is properly shifted in time so as to have the curves overlap and shows that *only* when the integration constant is properly taken into account, do the three simulations yield the same recoil velocity (*cf.*, solid, dashed, and dotted lines). On the other hand, when the integration constant is not included in the calculation, different evolutions will yield different estimates, with a systematic error that can be as large as 13% (*cf.*, long-dashed and dot-dashed lines) and is clearly unacceptable given that the overall precision of the simulations is below 1% (*cf.*, Figures 11.13–11.14 and the discussion in Section 11.2).

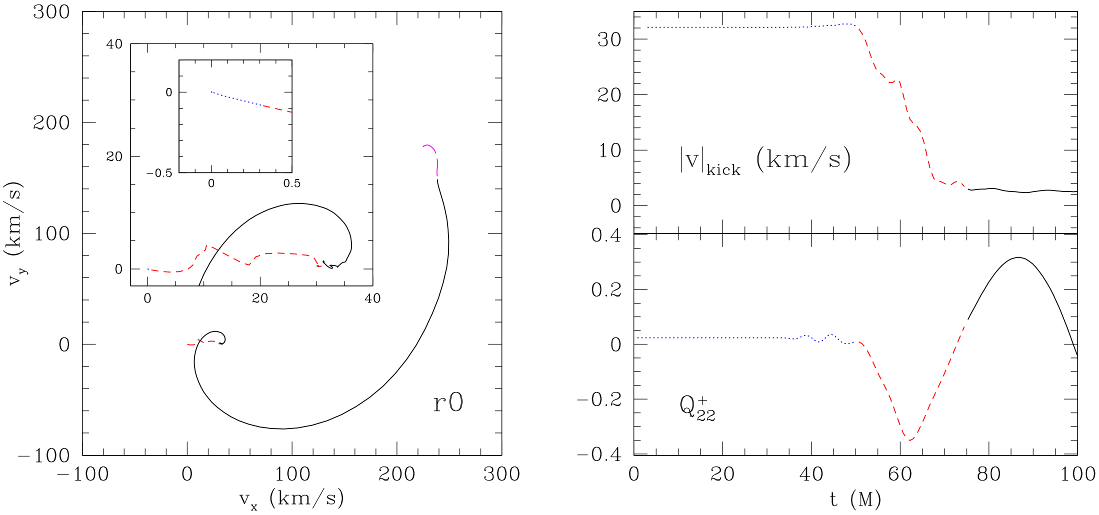

Figure 12.2: *Left panel:* Evolution in velocity space of the recoil-velocity vector. Very little variation is recorded before the radiation reaches the observer at $r_{\rm E} = 50\,M$ (dotted lines in the two insets). The absence of the proper linear momentum in the initial data triggers a rapid and an almost straight-line motion (dashed line) of the center of the spiral away from the origin of coordinates during the initial stages of the evolution. After this transient motion, the evolution is slower, with the spiral progressively opening up (solid line). The vector to the center of the spiral corresponds to the initial linear momentum of the spacetime and is used as integration constant for Eqs. (5.6.3) and (5.6.12). The final part of the evolution is characterized by a change in the spiral pattern (long-dashed line) as a result of the interaction of different modes in the ring-down of the final BH. Note that the figure has been rotated clockwise of about 30° to allow for the two insets. *Right panel:* Initial behavior of the recoil velocity (upper graph) and of the waveform (Q^+_{22}) for model $r0$ (lower graph). This figure should be compared with the initial vector evolution of the recoil velocity shown in the left panel where the same types of lines have been used for the different stages of the evolution.

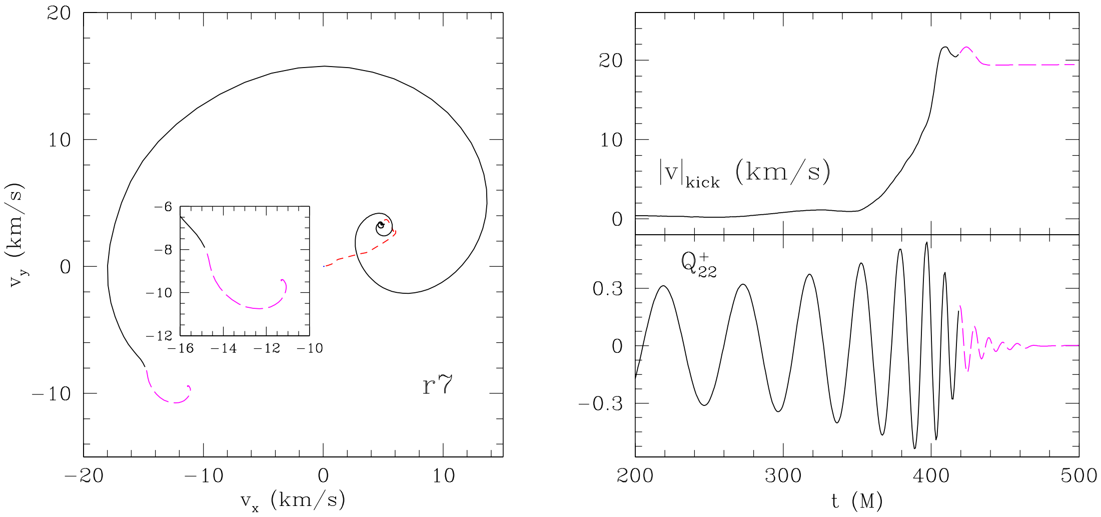

Figure 12.3: *Left panel:* The same as in the left panel of Figure 12.2 but for system $r7$. Shown in the inset is the sudden re-orientation of the recoil velocity vector during ring-down and corresponding to a new spiral with different aperture (long-dashed line). Although more pronounced in $r7$, the appearance of this "hook" at ring-down is seen all the members of the sequence. *Right panel:* The same as in the left panel of Figure 12.2 but for system $r7$. The upper graph concentrates on the final stages of the evolution in of the recoil velocity and on the appearance of a second peak during ring-down (long-dashed curve). The lower graph shows the same but in terms of the Q^+_{22} waveform. A discussion of these final stages of the evolution is made in Section 12.1.

Besides providing the right answer, the calculation of the integration constant also results in a considerable saving in computational costs. The complete dynamics of the binary $r0l$ including the merger and ring-down, in fact, requires simulations for about $600\,M$; the same answer in terms of recoil velocity can be obtained with the system $r0s$, whose dynamics is fully accounted for with a simulation lasting only for $340\,M$.

Having stressed the importance of including the integration constant in the measurement of the recoil velocity, we next illustrate how to actually compute it. In essence, it is sufficient to look carefully at the evolution in the velocity-space of the two components v_x and v_y of the recoil velocity (because of the symmetry the z-component is zero but the method described here can be easily extended to the case in which $v^z \neq 0$). This is shown in the left panel of Figure 12.2, which reports the track of the "center of mass" for system $r0$ in such a space. Different types of line refer to different intervals in time during the evolution and, for an observer at $r_{\rm E} = 50\,M$, the dotted one refers to $t \lesssim 50\,M$, the dashed one to $50\,M \lesssim t \lesssim 75\,M$, the continuous one to $75\,M \lesssim t \lesssim 183\,M$, and finally the long-dashed one to $t \gtrsim 183\,M$.

Clearly, for $t \lesssim 50\,M$ the system undergoes very little evolution in velocity-space (*cf.*, dotted line in the inset within the inset of the left panel) but a rapid change, lasting for about $25\,M$, takes place as the radiation reaches the observer. The radiation received has information about the "correct" linear momentum of the spacetime which is solution of the Einstein equations for system $r0$ as if it had inspiraled from infinity, and thus rapidly moves the center of mass to a net nonzero recoil velocity (*cf.*, almost-straight dashed line in the inset in the left panel). Once the system has adjusted for the proper linear momentum, the evolution proceeds as expected, with the recoil velocity vector slowly tracking a spiral in velocity space. This is an important point which we prefer to underline: the rate of change of linear momentum is very large only initially and this is because as the binary migrates from the initial non-radiating state (the data is conformally flat, see Section 2.4) to the consistent radiating state, it will emit the amount of linear momentum it would have emitted when inspiralling from infinite separation. After this burst of linear momentum, the evolution of the recoil velocity is minute, essentially until it grows very rapidly during the last orbit.

Computing the integration constant consists then in calculating the position of the center of the spiral and this can be done either by a simple inspection of a graph in the velocity-space, from which we compute the center of the spiral or, equivalently, by searching for the initial vector that would lead to an essentially *monotonic* in time growth of the recoil velocity[1]. The latter procedure does not require a human judgment but we have found it to yield the same answer (to less than 1 km/s) as the one guessed by looking at the velocity space.

The right panel of Figure 12.2 shows the same evolution as the left one, but through different quantities. The upper panel, in particular, shows the time evolution of the recoil velocity and the rapid changes it undergoes initially when the radiation first invests the observer. The lower panel, on the other hand, shows the Q^{+}_{22} amplitude and highlights that, while the initial burst of radiation stops after $t \sim 50\,M$ (*cf.*, dotted line), the waveform is still not fully consistent until $t \sim 75\,M$ (*cf.*, dashed line).

The procedure discussed so far for the calculation of the integration constant relative to the binary system $r0$ applies qualitatively to all the other members of the sequence, with differences that are due essentially to the times at which the various stages take place.

It is worth remarking that the evolution of the recoil vector in the velocity-space has another interesting feature during the final stages of the evolution and when the final BH is ringing down. This is marked as a long-dashed line in the left panel of of Figure 12.2 and shows a break in the building of the spiral and the appearance of a new spiral with a different aperture (we refer to this feature as "the hook"). This is more evident in the left panel of Figure 12.3, which shows the evolution of the recoil vector for the binary system $r7$ and offers a magnification of the hook in the inset. A more detailed description of this feature is beyond the scope of this paper and will be presented in a future work, but we can here point out that the hook accounts for a rapid change

---

[1] The presence of a small eccentricity prevents from a strict monotonicity of the recoil velocity for binaries starting from a large separation. In this case, very small oscillations appear over the orbital timescale.

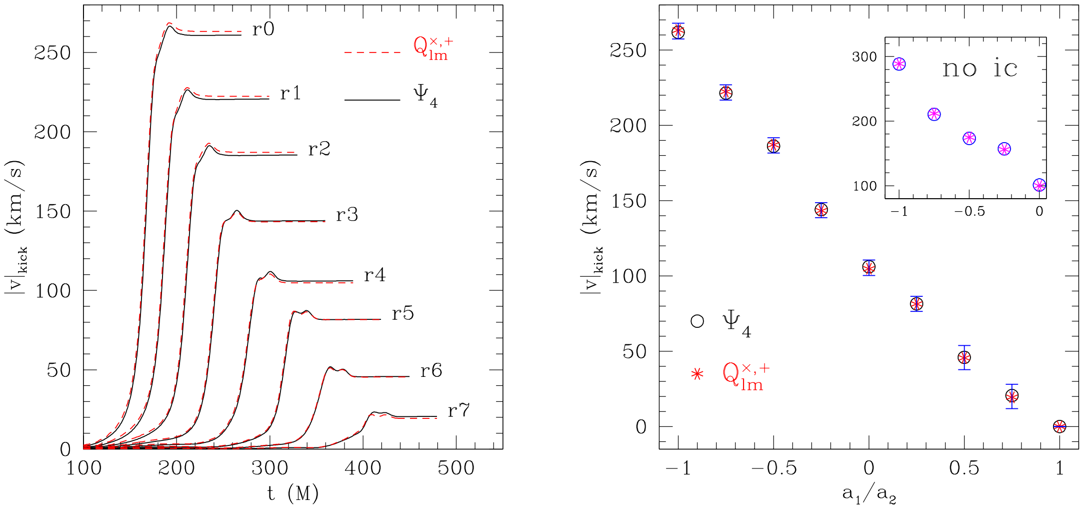

Figure 12.4: *Left panel:* Recoil velocity as a function of the spin asymmetry parameter a_1/a_2 for the r-sequence models listed in Table 11.1. Indicated with a continuous lines are the results obtained via Ψ_4, while a dashed line is used for the gauge-invariant quantities $Q^{+,\times}_{\ell m}$. *Right panel:* Final recoil velocity calculated with both the use Ψ_4 (empty circles) and the gauge-invariant quantities (stars). Shown in the inset is the incorrect scaling obtained when the correction for the integration constant is not made.

in the recoil velocity and it is due to the interplay of different modes during the ring-down. This is clearly illustrated in the right panel of Figure 12.3 which similarly reports the time evolution of the recoil velocity and the final stages of the Q^+_{22} waveform.

Recoil velocities

The recoil velocity has been calculated for the r-sequence of models listed in Table 11.1. As mentioned in Section 11.1, this sequence corresponds to equal-mass BHs, whose initial spins are unequal, though always aligned with the z-axis. The $r0$ model has equal but opposite spins, while the $r8$ model has equal and aligned spins on the BHs, with other models corresponding to intermediate values, as outlined in Section 11.1. Since the total initial orbital angular momentum $\boldsymbol{L}$ of the system is chosen to be constant over the sequence, the initial separations of the BHs increases in the sequence, as well as the time to merger due to spin-spin effects which contribute to an orbital “hang-up” in the aligned case.

We extract gravitational waves by both the gauge-invariant and the Ψ_4 methods described in Sections 5.1 and 5.2 and by interpolating the radiation-related quantities onto 2-spheres at coordinate radii $r_{\rm E} = 30\,M$, $40\,M$, $50\,M$, and $60\,M$. The use of multiple extraction radii is made to check the consistency of the measurement and the precise value of the extraction radius has little influence on the actual kick calculation. In the case of the binary system $r0$ we have verified that the recoil velocity yields the same value with differences that are smaller than 2 km/s for extraction 2-spheres at distances larger than $30\,M$. As a result, we have used $r_{\rm E} = 50\,M$ as the fiducial distance for an observer in the wave-zone and all of the results presented hereafter will be made at this extraction 2-sphere. A validation that the gauge-invariant quantities have the proper scaling with radius is presented in Section 11.2.

The evolution of the recoil velocity for the entire r-sequence listed in Table 11.1 is displayed in the left panel of Figure 12.4. It is apparent that the suitable choice of the integration constant discussed in the previous section yields early evolutions that are always monotonic in time and that, as expected, the largest recoil velocity is generated for the case in which the asymmetry is the

Table 12.1: Final kick velocities in units of km/s for the r-sequence listed in Table 11.1. Columns two and three show the values obtained using the gauge-invariant quantities $Q^{\times,+}_{\ell m}$ and Ψ_4 respectively and taking into account the integration constant. Columns four and five, on the other hand, show the results obtained when ignoring the integration constant. The same data are shown in the right panel of Figure 12.4.

Model	$Q^{\times,+}_{\ell m}$	Ψ_4	$Q^{\times,+}_{\ell m}$, no ic	Ψ_4, no ic
$r0$	263.2	261.8	288.9	288.4
$r1$	222.4	221.4	211.9	210.6
$r2$	187.1	186.2	174.8	173.3
$r3$	143.3	144.0	155.9	157.3
$r4$	104.8	106.1	100.0	101.3
$r5$	81.4	81.5	76.9	77.0
$r6$	45.6	45.9	55.4	56.2
$r7$	19.4	20.6	13.8	14.8
$r8$	0.0	0.0	0.0	0.0

largest, namely for the binary $r0$. The left panel Figure 12.4 also shows that the profile for each case is rather similar, with the largest contribution to the kick velocity being generated in a period of about $80\,M$, corresponding roughly to the timescale of the last orbit and merger. Furthermore, it is notable that 95% of the acceleration occurs $\sim 30\,M$ after the appearance of the first common apparent horizon, indicating that the kick is generated not only by the final stages of the inspiral (*i.e.*, by the "plunge") but also and more significantly by the ring-down of the final BH. This fact helps to explain why accurate recoil velocities can be obtained by evolutions involving very few cycles only, provided the integration constant is properly taken into account.

It is worth noting that during the final stages of the evolution, the recoil velocity is not monotonic but shows at least two peaks, whose relative amplitude depends on the spin ratio. For spin ratios ~ -1 the first peak is hardly visible, while the second one is the most pronounced one. As the spin ratio increases, however, the first peak becomes more prominent and for spin ratios ~ 1 it becomes comparable with the second one or even larger for binaries $r6$ and $r7$. As mentioned in the previous section and further discussed in the following one, the appearance of these peaks is related to the interplay of different mode-contributions during the ring-down. The second peak, in particular, can be associated to a rapid change in the recoil-velocity vector and is behind the characteristic "hook" discussed in the left panels of Figures 12.2 and 12.3. While additional work is needed, especially in thorough perturbative investigations, to fully account for the rich, post-merger properties of the recoil velocities, we believe the double-peak evolution to be physically genuine since it is seen in all binaries and is supported by the highly accurate and convergent simulations. As a representative measure of the accuracy in determining these recoil velocities, we mention that we have carried out simulations also for the binary system $r8$, in which the black holes have identical spin and thus from which no kick should result. The computed recoil velocity has been found to be 10^{-9} km/s, clearly indicating that our evolutions do an excellent job in preserving the orbital symmetry of these binaries.

We have found that the evolution of the recoil velocity generated by spin asymmetries appears to be rather different from the one generated by mass asymmetries [55, 431, 435] and which shows much larger variations between the maximum attained value and the final one. Once again, this different behavior is related to the different interplay of the ring-down modes in the case of mass asymmetries and will be presented in a separate work.

The recoil velocities attained by the final BHs and shown for in the left panel of Figure 12.4 can be studied in terms of their dependence on the spin ratio a_1/a_2, which can also be regarded as the "asymmetry" parameter of the system, being the largest for $a_1/a_2 = -1$ and zero for $a_1/a_2 = 1$. These velocities are collected in Table 12.1 and are shown as a function of a_1/a_2 in the right panel of Figure 12.4, where we have indicated with open circles the values obtained using Ψ_4 and with stars those obtained using the gauge-invariant perturbations.

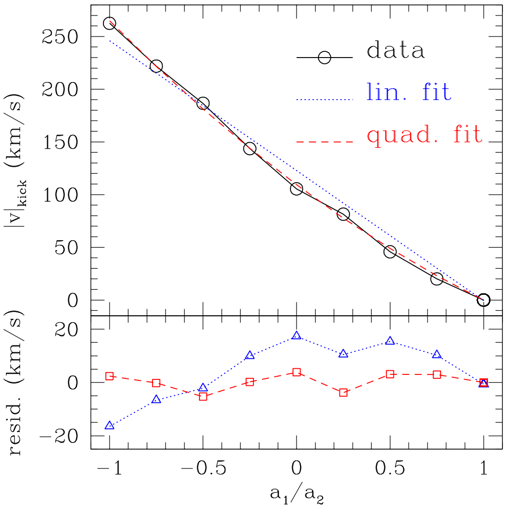

Figure 12.5: *Upper panel:* Comparison of the computed data for the recoil velocity (open circles) with the least-squares fits using either a linear (dotted line) or a quadratic dependence (dashed line). *Lower panel:* Point-wise residuals computed with the linear (dotted line) or a quadratic fit (dashed line).

The data in the right panel of Figure 12.4 is shown together with its error-bars, which include errors from the determination of the integration constants, from the truncation error and from the amount of ellipticity contained in the initial data. We have estimated these errors to be of 5 km/s for binaries $r0$–$r5$ and of 8 km/s for binaries $r6$ and $r7$. Shown also in the inset is the recoil data obtained when ignoring the integration constant. It is remarkable that when the proper evaluation of the initial transient is not made, the data does not show the remarkable correlation with the spin ratio which is instead shown by the corrected data. Quite surprisingly, however, the correlation found the one predicted by PN studies. We recall, in fact, that using PN theory at the 2.5 order, Kidder [441] has concluded that in the case of a circular, non-precessing orbit, the total kick for a binary system of arbitrary mass and spin ratio can be expressed as [429]

$$\begin{aligned} |v|_{\rm kick} &= c_1 \frac{q^2(1-q)}{(1+q)^5} + c_2 \frac{a_2 q^2 (1 - q a_1/a_2)}{(1+q)^5} \\ &= \tilde{c}_2 a_2 \left(1 - \frac{a_1}{a_2}\right) , \end{aligned} \tag{12.1.1}$$

where $q \equiv M_1/M_2$ is the mass ratio and is equal to one for the binaries considered here, thus leading to the second form of (12.1.1). The coefficients c_1 and $\tilde{c}_2 \equiv c_2/32$ depend on the total mass of the system and on the orbital separation at which the system stops radiating, which is intrinsically difficult to determine with precision since it lies in a region where the PN approximation is not very accurate. Indeed, we find that the coefficient c_2 is not really a constant in the case of equal-mass binaries but, rather, it can be seen to depend at least linearly on the spin ratio.

This is shown in Figure 12.5, whose upper panel offers a comparison among the computed data for the recoil velocity (open circles) with the least-squares fits using either a linear (dotted line) or a quadratic dependence (dashed line). It is quite apparent that a linear dependence on a_1/a_2, such as the one expected in (12.1.1) for $c_2 =$ const. does not reproduce well the numerical data and yields point-wise residuals of the order of 20 km/s. These are shown with a dotted line in the lower panel of Figure 12.5. A quadratic dependence on a_1/a_2, on the other hand, reproduces the numerical data very nicely, with residuals that are of the order of 5 km/s, as shown with a dashed line in the lower panel of the same figure, and thus compatible with the reported error-bars.

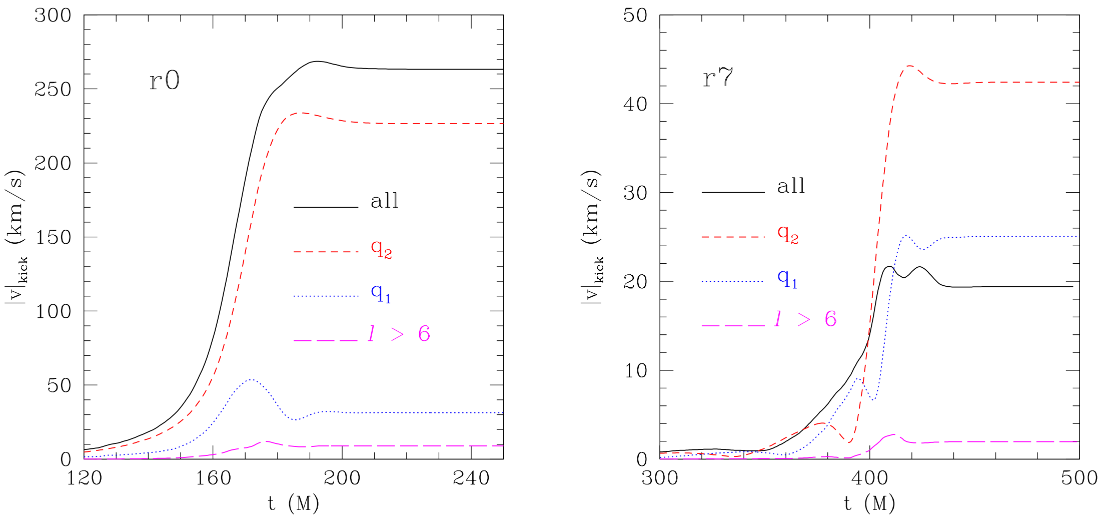

Figure 12.6: The total kick calculated via (5.6.12) up to $\ell = 7$ is compared to the contributions of individual terms q_1 and q_2, as well as the sum of term excluding these. In the case of the $r0$ system (left panel) the spins are anti-aligned and the q_2 term is dominant and the q_1 term does not provide a significant contribution. In the case of the $r7$ system (right panel), on the other hand, the spins are essentially aligned and the while the q_2 term is still dominant, the q_1 term also makes a significant contribution.

We can re-express (12.1.1) in the more generic form

$$|v|_{\rm kick}\left(a_2, \frac{a_1}{a_2}\right) = |a_2| f\left(\frac{a_1}{a_2}\right) \tag{12.1.2}$$

where a_2 plays here the role of a "scale-factor". The function $f(a_1/a_2)$ with $a_1/a_2 \in [-1, 1]$ and maximum at $a_1/a_2 = -1$ can then be seen as to be determined from numerical relativity calculations (or higher-order PN approximations) and our least-squares fit suggests the expression

$$f_{\rm quad.} = 109.3 - 132.5\left(\frac{a_1}{a_2}\right) + 23.1\left(\frac{a_1}{a_2}\right)^2 \ {\rm km/s}\,. \tag{12.1.3}$$

The maximum kick velocity for a given a_2 is then readily calculated even without a detailed knowledge of the function $f(a_1/a_2)$ as

$$(|v|_{\rm kick})^{\rm max}(a_2) = |a_2| f(-1)\,. \tag{12.1.4}$$

Using the data reported in Table 12.1 for $a_2 = -0.584$ we obtain for $|a_2| = 1$ that the maximum recoil velocity attainable from a binary system of equal-mass BHs with spins aligned to the orbital angular momentum is $448 \pm 5\,{\rm km/s}$. This is in very good agreement with our previous estimate made in [55] with a smaller sequence and in equally good agreement with the results reported in [410].

Mode contributions to the recoil velocity

For the models studied in the previous section we have evaluated (5.6.12) including modes up to $\ell = 7$. In practice, however, we find that the recoil is strongly determined by the lower-mode contributions. In particular, the two terms

$$q_1 \equiv \frac{1}{48\pi}\sqrt{\frac{30}{7}}\dot{Q}^{+}_{22}\, Q^{+}_{3-3}, \tag{12.1.5}$$

$$q_2 \equiv -\frac{\mathrm{i}}{48\pi}\dot{Q}^{+}_{2-2}\, Q^{\times}_{2\,1} \tag{12.1.6}$$

are the dominant ones. This can be seen in Figure 12.6, where the time evolutions of the terms q_1 and q_2 are plotted (dotted and dashed lines, respectively) together with the total kick calculated via (5.6.12) (solid line), and with the contributions from all other terms up to $\ell = 7$ excluding q_1 and q_2 (long-dashed line). A rapid inspection of the figure reveals that the kick is dominated in particular by the q_2 term, whereas the q_1 term has a magnitude of the order of all the other modes combined. A similar result holds for each member of the sequence, so that the two contributions determine the final kick to more that 95%. It should be noted that the mode contributions are vector quantities, just as the kick velocity itself, and are not always aligned or even maintain the same angle to each other during the duration of the recoil.

This coupling also goes some way to explain some features of the recoil velocity profiles displayed in Figure 12.4. As mentioned in the previous section, in fact, the binaries $r4$ to $r8$ show a clear double peak in the evolution of the kick velocity before it settles down to the final value. The same feature can also be seen in the more asymmetric $r0$ to $r3$ binaries, where it appears as a flattening of the slope near the maximum. Since the two peaks are shown both by the gauge-invariant and by the Ψ_4-based techniques (which are rather different in both the assumptions they rely on and in the practical implementation) we do not believe them to be a simple numerical artifact. Overall, the properties of the recoil velocity near its maximum, and before it settles to the final value, are determined by the relative phases of the two contributions identified above. An analysis of the terms q_1 and q_2 in vector-space, and which will be presented in a subsequent work, reveals that when they are relatively aligned at the peak of the acceleration, there is a clear single peak in the evolution. For the more symmetric models, on the other hand, the two contributions are more anti-aligned and a double peak results.

These considerations in the vector evolution of the two contributions q_1 and q_2 need also to be linked with the evolution in vector space of the recoil velocity. As stressed in Section 12.1, in fact, there is a distinct kink in the evolution of the velocity vector towards the final stages of the merger (this feature is indicated with a long-dashed line in the v_x vs. v_y plots of Figures 12.2 and 12.3). The presence of the kink corresponds to a local decrease of the recoil velocity and hence to the minimum between the two peaks. Because this decrease is more pronounced for the lower-kick binaries $r4$ to $r8$, the first peak becomes more evident there.

On the influence of orbital eccentricity

A source of potential error in calculating a “physical” kick comes from the choice of initial data parameters. Our evolutions begin from fairly close separations, comprising at most the last 2-3 orbits. As such, parameters for quasi-circular orbits determined by the effective potential method (see Section 2.4), give only approximations to the true orbital parameters for BHs that have spiraled in from infinity, and it is known that the method produces a non-trivial residual eccentricity for initial data at close separation. This eccentricity can have significant effects on the orbital trajectories before merger, and a potential influence on the calculated recoil. To test this we have evolved two modified $r0$ models, one in which the initial linear momenta of the BHs is 3% larger than that specified in Table 11.1, and another in which the linear momenta are 3% smaller. The modified momenta have the effect of changing the orbital energy of the bodies from the minima determined by the effective potential method, introducing an additional eccentricity to the evolution. The resulting BH trajectories and kick determinations are shown respectively in Figure 12.7. We see that although the level of applied eccentricity is large, and in fact much larger than the expected eccentricity due to the intrinsic inaccuracy of the effective potential method, it modifies the recoil by only about 10 km/s, that is, 4%. Further, in both the high and low energy cases, the recoil is increased over the fiducial $r0$ case, suggesting that increased eccentricity generically leads to a slightly larger recoil.

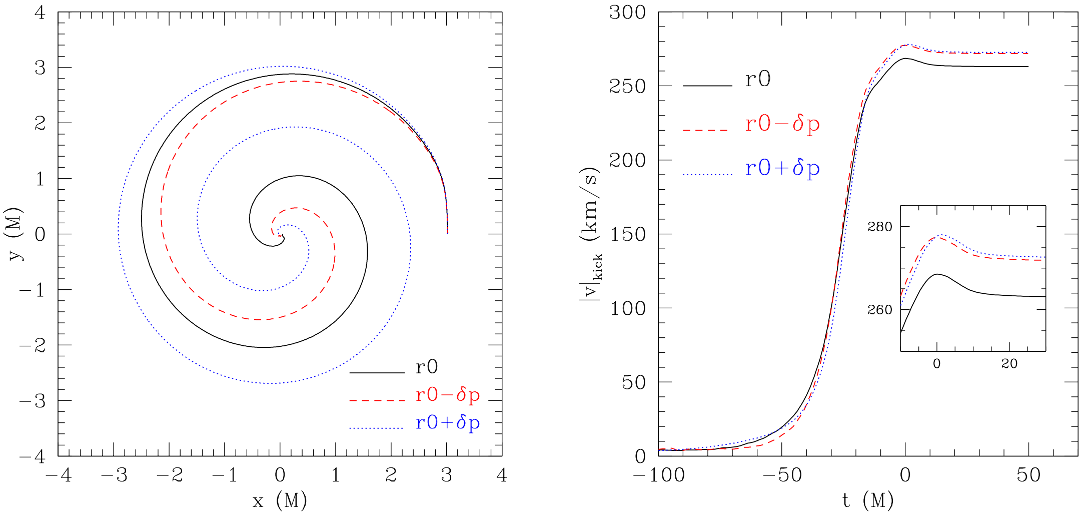

Figure 12.7: *Left panel:* Coordinate trajectories for one of the BHs for the $r0$ compared with similar models where the initial linear momenta have been changed by ±3% in order to modify the eccentricity of the inspiral. *Right panel:* Recoil velocity for the $r0$ case is compared with similar models for which the initial eccentricity has been increased by adding and subtracting 3% of the initial linear momentum of the black holes relative to the $r0$ values. The effect of increased eccentricity in the final merger is to increase the size of the kick, by about 4% in both cases.

Conclusions

We have performed a highly-accurate study of recoil velocities in BBH mergers from a sequence of equal-mass BHs with varying spin configurations. In this sequence, the spins are aligned with the orbital angular momentum since there are strong indications that such alignment is preferred in astrophysical situations. This makes our choice of initial data especially realistic and our results particularly relevant also within an astrophysical context.

In practice, the initial configurations are built so that the spin of one of the BHs is kept at a constant dimensionless value $a_2 = 0.584$ while the other varies from $a_1 = -a_2$ to $a_1 = +a_2$, thus spanning a range between -1 and 1 in spin ratio. We have followed our BH evolutions for about two to four orbits and then throughout the plunge, merger, and ring-down phases. This work thus extends and refines recent results obtained from a reduced but similar initial-data sequence [55].

The main aspects of this work, which revolve around the methods used, the tests performed and the results obtained, can be summarized as follows.

Methods. To increase the significance of our results and our confidence in their accuracy, we have implemented two independent methods for the calculation of the linear momentum from the emitted gravitational radiation. These are based on either the measure the Newman-Penrose scalar Ψ_4 or on the calculation of the gauge-invariant perturbations of a Schwarzschild BH $Q^{\times,+}_{\ell m}$. Overall, we find that both methods of calculating the linear momentum loss agree excellently and we are thus able to obtain accurate recoil measurements with error bars of 5 km/s for the anti-aligned spin binaries and of 8 km/s in the aligned cases.

Such a good agreement, however, is attainable *only* if the initial transient in the waveform is properly taken into account. The transient is produced by the use of initial data not containing the net linear momentum the system has accumulated since inspiralling from infinite separation. We discuss the importance of choosing the correct vector integration constant when calculating the radiated linear momentum and describe an unambiguous method for doing so.

We remark that a proper choice of this constant is essential not only because it influences the final recoil velocity with differences of 10% and more, but also because it allows for a systematic interpretation of the results. Without it, in fact, the correct functional dependence of the final recoil velocity on the spin ratio is irremediably lost and a comparison with the PN prediction impossible. Last but not least, a proper integration constant can result in a significant saving of computational time, allowing simulations to start at much smaller initial separations without sacrificing accuracy.

Tests. In order to show the accuracy of our results, we demonstrate that both the Zerilli-Moncrief gauge invariant waveforms and the Einstein tensor converge with an order between three and four, which is the expected convergence behavior of our numerical methods (see Section 11.2).

Furthermore, because the Newman-Penrose scalar Ψ_4 serves as a measure for the radiation content of the spacetime in appropriately chosen frames and at sufficiently large distances from the source, we show that the peeling property is indeed well satisfied in our numerical simulations. In particular, we demonstrate that both the gravitational wave information Ψ_4 and the gauge-wave information Ψ_3 satisfy the expected scaling with radius. Similarly, we also show that, as expected, the gauge invariant quantity Q^{+}_{22} does not vary with radius (see Section 11.2).

Finally, we investigate those systematic effects that may influence our gravitational-wave measurements. In particular, we study the effects that the choice of the extraction radius has on the final kick velocity and find little influence for $r_{\rm E} \geq 30\,M$. Based on this, we choose $r_{\rm E} = 50\,M$ as the fiducial extraction radius in this paper. Furthermore, to exclude that the effects of the eccentricity in our initial data are significant for this paper, we artificially increase or reduce the eccentricity of the initial data by comparatively large amounts. Also in this case we find that the differences in the recoil velocities are below the estimated error-bars. Altogether, the set of tests carried out gives us confidence that our waveforms and recoil velocities are both correct and accurate.

Results. Using the mathematical and numerical setup as described and tested above, we have investigate the dependence of the recoil velocity on the initial data parameters and most notably on the spin ratio a_1/a_2. As expected, a larger asymmetry in the initial conditions causes a larger recoil, with a velocity of about 262 km/s for a binary of equal and anti-aligned spins, and a numerically computed recoil of 10^{-9} km/s for a binary of equal and aligned spins.

Using such accurate measurements, we have then studied the functional dependence of the recoil velocity on the spin ratio finding that a quadratic behavior reproduces very well the numerical results and corrects the post-Newtonian prediction of a linear dependence. We summarize this behavior in a phenomenological expression that can be readily employed in astrophysical studies on the evolution of binary BHs in massive galaxies.

With a straightforward extrapolation of the quadratic dependence to the maximal spinning case $a_1 = -a_2 = 1$ we obtain 448 ± 5 km/s as the maximal possible recoil velocity attainable from a binary system of equal-mass BHs with spins aligned to the orbital angular momentum. This recoil velocity is in very good agreement with our previous estimate made in [55] with a smaller sequence and in equally good agreement with the results reported in [410].

As mentioned above, the inclusion of the integration constant has been essential to obtain physically consistent results. At the same time, its investigation has allowed to highlight some important features of the evolution of the recoil velocity in vector space. Most importantly, it has shown that even when all non-spherical modes up to $\ell = 7$ are taken into account, the recoil is dominated by lower mode contributions, especially $\ell = 2, m = -2, 1, 2$ and $\ell = 3, m = -3$. The interplay of these contributions in vector space and during ring-down is what is responsible for the rich features observed in the final evolution of the recoil velocity.

Finally, we provide accurate measurements of the radiated energy and angular momentum. These measurements reveal a clear linear dependence on the spin ratio a_2/a_1, and we derive phenomenological expressions for the relative losses of angular momentum and the relative spin-up of the final BH. These relations can be easily used in N-body simulations if the interaction of binary black holes is to be taken into account, and when an accurate estimate on the final distribution of BH spins is important.

12.2 Parameter space of equal-mass spin-aligned binaries

In this section, we extend the analysis of the recoil velocity to the complete 2D parameter space of equal-mass spin-aligned binaries. For this, we have considered a total of 38 different simulations as given in Section 11.1 (Table 11.1). This allows us to construct phenomenological expressions for the recoil velocity of the merger remnant as a function of the spin-parameters of the initial BHs. Note that in the meantime, other groups have published phenomenological expressions for the recoil velocity that take into account the full 7D parameter space of binary-BH initial configurations [417, 442]. Here, however, we will restrict attention to the recoil velocity for binaries with equal masses and aligned but otherwise arbitrary spins. This information depends uniquely on the dimensionless spins of the two BHs a_1, a_2 and can therefore be summarized in the portion of the (a_1, a_2) plane in which the two spins vary. It is therefore convenient to think in terms of "spin diagrams" (Figure 11.2). Since the labeling "1" and "2" is arbitrary, the line $a_1 = a_2$ in the spin diagram has an important symmetry: the recoil velocity vector undergoes a π-rotation, *i.e.* $\vec{v}_{\rm kick}(a_1, a_2) = -\vec{v}_{\rm kick}(a_2, a_1)$ but $|v_{\rm kick}(a_1, a_2)| = |v_{\rm kick}(a_2, a_1)|$. This symmetry not only allow us to consider only one portion of the (a_1, a_2) space (*cf.* Figure 11.2), thus halving the computational costs (or doubling the statistical sample), but they will also be exploited later on to improve our fits. The position of the five sequences within the (a_1, a_2) space is shown in Figure 11.2.

Spin diagrams and fits

Overall, the data sample computed numerically consists of 38 values for $|v_{\rm kick}|$ and for $a_{\rm fin}$ which, for simplicity, we have considered to have constant error-bars of 8 km/s, which represent, the largest errors reported in [56] (see Section 12.1). We have modeled the data with a generic quadratic function in a_1 and a_2 so that for the recoil velocity, the fitting function is

$$|v_{\rm kick}| = |c_0 + c_1 a_1 + c_2 a_1^2 + d_0 a_1 a_2 + d_1 a_2 + d_2 a_2^2| \,. \tag{12.2.1}$$

Note that the fitting function on the right-hand-side of (12.2.1) is smooth everywhere but that its absolute value is not smooth along the diagonal $a_1 = a_2$. Using (12.2.1) and a blind least-square fit of the data, we obtained the coefficients (in km/s)

$$\begin{aligned} c_0 &= 0.67 \pm 1.12\,, & d_0 &= -18.56 \pm 5.34\,,\\ c_1 &= -212.85 \pm 2.96\,, & d_1 &= 213.69 \pm 3.57\,,\\ c_2 &= 50.85 \pm 3.48\,, & d_2 &= -40.99 \pm 4.25\,, \end{aligned} \tag{12.2.2}$$

with a reduced-$\chi^2 = 0.09$. Clearly, the errors in the coefficients can be extremely large and this is simply the result of small-number statistics. However, the fit can be improved by exploiting some knowledge about the physics of the process to simplify the fitting expressions. In particular, we can use the constraint that no recoil velocity should be produced for binaries having the same spin, *i.e.* that $|v_{\rm kick}| = 0$ for $a_1 = a_2$, or the symmetry condition across the line $a_1 = a_2$. Enforcing both constraints yields

$$c_0 = 0\,, \quad c_1 = -d_1\,, \quad c_2 = -d_2\,, \quad d_0 = 0\,, \tag{12.2.3}$$

thus reducing the fitting function (12.2.1) to the simpler expression

$$|v_{\rm kick}| = |c_1(a_1 - a_2) + c_2(a_1^2 - a_2^2)| \,. \tag{12.2.4}$$

Performing a least-square fit using (12.2.4) we then obtain

$$c_1 = -220.97 \pm 0.78\,, \qquad c_2 = 45.52 \pm 2.99\,, \tag{12.2.5}$$

with a comparable reduced-$\chi^2 = 0.14$, but with error-bars that are much smaller on average. Because of this, we consider expression (12.2.4) as the best description of the data at second-order

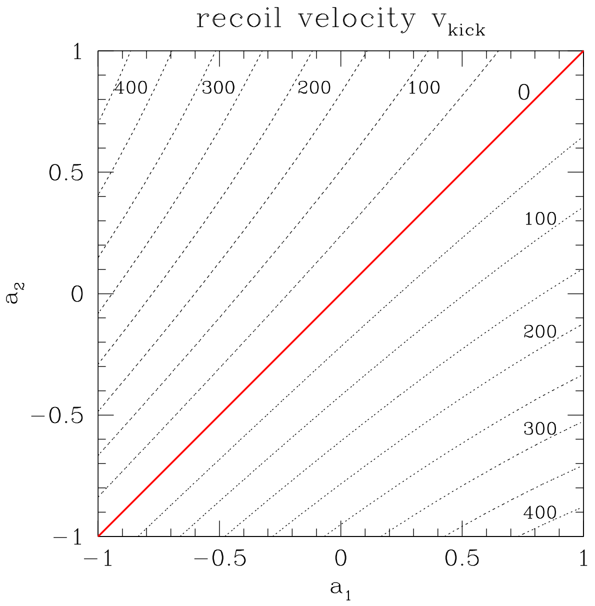

Figure 12.8: Contour plots of $|v_{\rm kick}|$ as a function of the spin parameters a_1 and a_2. The diagram has been computed using expressions (12.2.4) and (12.2.5).

in the spin parameters. Using (12.2.4) and (12.2.5), we have built the contour plots shown in Figure 12.8.

A few remarks are worth making. Firstly, we recall that post-Newtonian calculations have so far derived only the linear contribution in the spin to the recoil velocity (see [337] and references therein). However, the size of the quadratic coefficient (12.2.5) is not small when compared to the linear one and it can lead to rather sizeable corrections. These are maximized when $a_1 = 0$ and $a_2 = \pm 1$, or when $a_1 = \pm 1$ and $a_2 = 0$, and can be as large as $\sim 20\%$; while these corrections are smaller than those induced by asymmetries in the mass, they are instructive in pointing out the relative importance of spin-spin and spin-orbit effects during the merger and can be used as a guide in further refinements of the post-Newtonian treatments. Secondly, expression (12.2.4) clearly suggests that the maximum recoil velocity should be found when the asymmetry is the largest and the spins are antiparallel, *i.e.* $a_1 = -a_2$. Thirdly, when $a_2 = $ const., expression (12.2.4) confirms the quadratic scaling proposed in [56] (see Section 12.1 with a smaller data set). Fourthly, for $a_1 = -a_2$, expression (12.2.4) is only linear and reproduces the scaling suggested by [410]. Finally, using (12.2.4) the maximum recoil velocity is found to be $|v_{\rm kick}| = 441.94 \pm 1.56$ km/s, in very good agreement with the results of [410] and [56].

Reported in the right part of Table 11.1 are also the fitted values for $|v_{\rm kick}|$ obtained through the fitting functions (12.2.4), and the corresponding errors. The latter are of few percent for most of the cases and increase up to $\sim 20\%$ only for those binaries with very small kicks and which are intrinsically more difficult to calculate. As a concluding remark we note that the fitting coefficients computed here have been constructed using overall moderate values of the initial spin; the only exception is the binary $u4$ which has the largest spin and which is nevertheless fitted with very small errors (*cf.* Table 11.1).

Chapter 13

Final spin of the merger remnant

The determination of the final spin of a BBH merger is a question of key importance in several fields. In astrophysics, it provides information on the properties of isolated stellar-mass BHs produced at the end of the evolution of a binary system of massive stars. In cosmology, it can be used to model the distribution of masses and spins of the SMBHs produced through the merger of galaxies (see [443] for an interesting example). In addition, in gravitational-wave astronomy, the a-priori knowledge of the final spin can help the detection of the ring-down.

Modeling the final spin in general is made difficult by the fact that it depends on the 7-dimensional space of parameters characterizing the two initial BHs (see Section 1.5). However, in special cases, when symmetries can be exploited, the description can be much simpler.

Several recent studies have shed light on the remnant of the merger process. Using conservation principles, Hughes and Blandford [444] argued that mergers rarely lead to rapidly rotating objects. [435] numerically evolved a sequence of non-spinning unequal-mass BHs, arriving at detailed estimates of the radiated energy and angular momentum. In a series of papers [55–57] we have studied the parameter space of mergers of equal-mass BH binaries whose spins are aligned with the orbital angular momentum but otherwise arbitrary. The findings agree well with independent numerical evolutions [410, 445], as well as more recent studies of models with initial spins up to $J/M^2 = 0.8$ [419]. An important result of these studies has been the determination of simple (quadratic) fitting formulas for the recoil velocity and spin of the merger remnant as a function of the initial BH parameters [57].

A number of analytical approaches have been developed over the years to determine the final spin of a binary coalescence [244, 446–449]. Very recently, an interesting method, inspired by the dynamics of a test particle around a Kerr BH, has been proposed for generic binaries ([450], BKL hereafter). The approach assumes that the angular momentum of the final BH is the sum of the individual spins and of the orbital angular momentum of a test particle on the last-stable orbit of a Kerr BH with the same spin parameter as that of the final BH.

In this chapter, we present results obtained in [57–59]. In this series of papers, we have developed a phenomenological expression for the final spin of BBH merger remnants which can be used in many-body studies of galactic mergers, or hierarchical models of BH formation, where it is impractical to perform full non-linear BBH merger calculations.

To appreciate the spirit of our approach it can be convenient to think of the inspiral and merger of two BHs as a mechanism which takes, as input, two BHs of initial masses M_1, M_2 and spin vectors $\boldsymbol{S}_1$, $\boldsymbol{S}_2$ and produces, as output, a third BH of mass M_{fin} and spin $\boldsymbol{S}_{\text{fin}}$. In conditions of particular astrophysical interest, the inspiral takes place through quasi-circular orbits since the eccentricity is removed quickly by the gravitational-radiation reaction [151]. Furthermore, at least for non-spinning equal-mass BHs, the final spin does not depend on the value of the eccentricity as long as it is not too large [451].

While the recent possibility of measuring accurately the final spin through numerical relativity calculations represents an enormous progress, the complete coverage of the full parameter space uniquely through simulations is not a viable option. As a consequence, work has been done to derive analytic expressions for the final spin which would model the numerical relativity data but also exploit as much information as possible either from perturbative studies, or from the symmetries of the system [56–58, 419, 449, 452]. In this sense, these approaches do not amount to a blind fitting of the numerical relativity data, but, rather, use the data to construct a physically consistent and mathematically accurate modeling of the final spin.

In a first attempt, we have considered the final spin restricted to the 2D parameter space of equal-mass spin-aligned binaries as reported in Section 11.1. Successively, we have then extended the spin formula to unequal-masses and later to arbitrary spin configurations.

13.1 Spin of equal-mass spin-aligned binaries

In this Section, we discuss the final spin of a BBH merger remnant as a function of the two dimensionless spin-parameters a_1 and a_2 of the initial BHs within the parameter space of equal-mass spin-aligned binaries as motivated in Section 11.1. Similar to the recoil velocity presented in Section 12.2, the information of the final spin can be summarized in the portion of the $(a_1,\, a_2)$ plane in which the two spins vary. The position of the five sequences within the $(a_1,\, a_2)$ space is shown in Figure 11.2. Since the labeling “1” and “2” is arbitrary, the line $a_1 = a_2$ in the spin diagram has an important symmetry: the final spin does not change, *i.e.*, $a_{\rm fin}(a_1,\, a_2) = a_{\rm fin}(a_2,\, a_1)$. As for the kick, this symmetry allows us to consider only one portion of the $(a_1,\, a_2)$ space (*cf.* Figure 11.2).

Fitting formula

Using the data of the final spin from the various simulations presented in Section 11.1, we can try to fit the data to a generic polynomial expression.

In the same way as for the kick-velocity presented in Section 12.2, we have first fitted the data for $a_{\rm fin}$, with a function

$$a_{\rm fin} = p_0 + p_1 a_1 + p_2 a_1^2 + q_0 a_1 a_2 + q_1 a_2 + q_2 a_2^2\,, \tag{13.1.1}$$

and found coefficients with very large error-bars. As a result, also for $a_{\rm fin}$ we resort to physical considerations to constrain the coefficients $p_0 \ldots q_2$. More specifically, we expect that, at least at lowest order, binaries with equal and opposite spins will not contribute to the final spin and thus behave essentially as non-spinning binaries. Stated differently, we assume that $a_{\rm fin} = p_0$ for binaries with $a_1 = -a_2$. In addition, enforcing the symmetry condition across the line $a_1 = a_2$ we obtain

$$p_1 = q_1\,, \quad p_2 = q_2 = q_0/2\,, \tag{13.1.2}$$

so that the fitting function (13.1.1) effectively reduces to

$$a_{\rm fin} = p_0 + p_1(a_1 + a_2) + p_2(a_1 + a_2)^2\,. \tag{13.1.3}$$

Performing a least-square fit using (13.1.3) we then obtain

$$\begin{aligned} p_0 &= 0.6883 \pm 0.0003\,, \qquad p_1 = 0.1530 \pm 0.0004\,,\\ p_2 &= -0.0088 \pm 0.0005\,, \end{aligned} \tag{13.1.4}$$

with a reduced-$\chi^2 = 0.02$.

It should be noted that the coefficient of the quadratic term in (13.1.4) is much smaller then the linear one and with much larger error-bars. Given the small statistics it is hard to assess whether a quadratic dependence is necessary or if a linear one is the correct one (however, see also the comment below on a possible interpretation of expression (13.1.3)). In view of this, we have repeated the least-square fit of the data enforcing the conditions (13.1.2) together with $p_2 = 0$ (*i.e.*, adopting a linear fitting function) and obtained $p_0 = 0.6855 \pm 0.0007$ and $p_1 = 0.1518 \pm 0.0012$, with a worse reduced-$\chi^2 = 0.16$. Because the coefficients of the lowest-order terms are so similar, both the linear and the quadratic fits are well within the error-bars of the numerical simulations. Nevertheless, since a quadratic scaling yields smaller residuals, we consider it to be the best representation of the data and have therefore computed the contour plots in Figure 13.1 using (13.1.3) and (13.1.4).

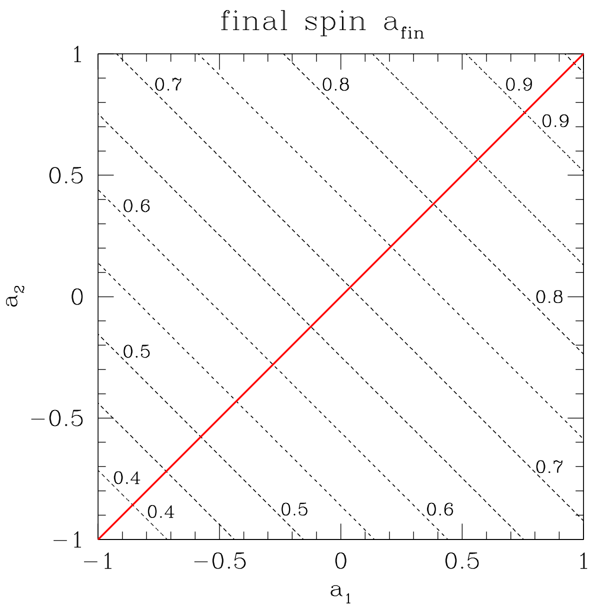

Figure 13.1: Contour plots of $a_{\rm fin}$ as a function of the spin parameters a_1 and a_2. The diagram has been computed using expressions (13.1.3) and (13.1.4).

Here, a few remarks are worth making: Firstly, the fitted value for the coefficient p_0 agrees very well with the values reported by several groups [435, 453] when studying the inspiral of unequal-mass non-spinning binaries. Secondly, expression (13.1.3) has maximum values for $a_1 = a_2$, suggesting that the maximum and minimum spins are $a_{\rm fin} = 0.9591 \pm 0.0022$ and $a_{\rm fin} = 0.3471 \pm 0.0224$, respectively. Thirdly, the quadratic scaling for $a_{\rm fin}$ substantially confirms the suggestions of [454] but provides more accurate coefficients. Finally, although very simple, expression (13.1.4) lends itself to an interesting interpretation. Being effectively a power series in terms of the initial spins of the two BHs, its zeroth-order term can be seen as the orbital angular momentum not radiated in gravitational waves and which amounts, at most, to $\sim 70\%$ of the final spin. The first-order term, on the other hand, can be seen as the contribution to the final spin coming from the initial spins of the two BHs and this contribution, together with the one coming from the spin-orbit coupling, amounts at most to $\sim 30\%$ of the final spin. Finally, the second-order term, which is natural to expect as nonzero in this view, can then be related to the spin-spin coupling, with a contribution to the final spin which is of $\sim 4\%$ at most.

As a side remark we also note that the monotonic behavior expressed by (13.1.4) does not show the presence of a local maximum of $a_{\rm fin} \simeq 0.87$ for $a_1 = a_2 \sim 0.34$ as suggested by [446] in the effective one-body (EOB) approximation. Because the latter has been shown to be in good agreement with numerical relativity simulations of non-spinning black holes [368, 448], additional simulations will be necessary to refute these results or to improve the EOB approximation for spinning BHs.

Reported in the right part of Table 11.1 are the fitted values for $a_{\rm fin}$ obtained through the fitting function (13.1.3), and the corresponding errors. As a concluding remark we note that the fitting coefficients computed here have been constructed using overall moderate values of the initial spin; the only exception is the binary $u4$ which has the largest spin and which is nevertheless fitted with very small errors (*cf.* Table 11.1). In addition, since the submission of [57], another group has reported results from equal-mass binaries with spins as high as $a_1 = a_2 = \pm 0.9$ [419]. Although also for these very high-spin binaries the error in the predicted values is of 1% at most, a larger sample of high-spin binaries is necessary to validate that the fitting expressions (12.2.4) and (13.1.3) are robust also at very large spins.

Table 13.1: Initial parameters of the new binaries computed at the AEI. The different columns contain the initial spin a, the symmetric mass ratio ν, half of the initial separation $x/M = \frac{1}{2}(x_1 - x_2)$, the dimensionless initial angular momentum $\tilde{J} = J/(\mu M)$, the numerical and fitted values for $a_{\rm fin}$ and the corresponding relative error.

	a	ν	x/M	$\tilde{J}$	$a_{\rm fin}$	$a^{\rm fit}_{\rm fin}$	|err.| (%)
$t8$	-0.5840	0.2500	3.1712	2.432	0.4955	0.4981	0.53
$ta8$	-0.3000	0.2500	3.7078	3.000	0.5941	0.5927	0.23
$tb8$	-0.8000	0.2500	3.8082	2.200	0.4224	0.4227	0.08
$tb8\ell$	-0.8000	0.2500	4.8600	2.400	0.4266	0.4227	0.92
$p1$	-0.8000	0.1580	3.2733	0.336	0.0050	0.0046	9.89
$p2$	-0.5330	0.1875	3.3606	1.872	0.2778	0.2794	0.57
$p3$	-0.2667	0.2222	3.4835	2.883	0.5228	0.5216	0.23

13.2 Extension to unequal-mass spin-aligned binaries

In this section, we combine the data obtained in recent simulations to provide a phenomenological but analytic estimate for the final spin in a binary BH system with arbitrary mass ratio and spin ratio, but in which the spins are constrained to be parallel to the orbital angular momentum. In addition to the data presented in Section 11.1 [57], we add three simulations of equal-mass, high-spin binaries and three simulations of unequal-mass, spinning binaries (see Table 13.1). As is the case for the spin-aligned binaries given reported in Section 11.1, these additional simulations have been carried out using the CCATIE code [56] (Section 8.1). Other data is taken from unequal-mass, non-spinning binaries [32, 435, 453], and of equal-mass, spinning binaries [57, 419]; all of the AEI data is summarized in Table 13.1. To avoid the possible contamination from the errors associated with high-spin binaries reported by [419], we have not considered binaries with initial spin $|J/M^2| \geq 0.75$ reported in the literature [419, 445]. We have, however, considered estimates of high-spin binaries (*cf.*, Table 13.1), for which we know the spins remain essentially constant prior to merger, with changes less than 0.5% [56], and that are very well captured by the fit.

Methods and Results

We start by considering the final spin $a_{\rm fin}$ as a function of the two free variables in the problem: the symmetric mass ratio $\nu \equiv M_1 M_2/(M_1+M_2)^2$ and the spin of the initial BHs $a \equiv J/M^2$, *i.e.*, $a_{\rm fin} \equiv J_{\rm fin}/M^2_{\rm fin} = a_{\rm fin}(a,\, \nu)$. (Note a is dimensionless and not the angular momentum per unit mass.) By construction $a_1 = a_2 = a$, and $\vec{a}/|\vec{a}| = \pm\vec{L}/|\vec{L}|$, where $\vec{L}$ is the orbital angular momentum. We next express $a_{\rm fin}$ as a third-order polynomial of ν and a

$$\begin{aligned} a_{\rm fin} = \quad & s_0 + s_1 a + s_2 a^2 + s_3 a^3 + s_4 a^2 \nu + s_5 a \nu^2 + \\ & t_0 a \nu + t_1 \nu + t_2 \nu^2 + t_3 \nu^3\,. \end{aligned} \tag{13.2.1}$$

Expression (13.2.1) is a lowest-order *ansatz*. It intends to capture the behavior of a function known exactly only in the extreme mass-ratio limit (EMRL) and which has support from numerical simulations in two restricted regimes: *i.e.*, $\nu = 1/4$; $0 \leq |a| \lesssim 0.75$ and $0.16 \lesssim \nu \leq 1/4$; $a = 0$. A-priori there is no reason to believe, that the proposed fit $a_{\rm fin}(\nu, a)$ will capture the general behavior well, but in fact it does.

Given the available numerical estimates, it is possible to calculate the coefficients s_0–s_5, and t_0–t_3 by simply performing a 2D least-square fit of the data. This, however, would require a lot of care and is likely to lead to inaccurate estimates. This is because the space of parameters presently accessible to numerical simulations is rather small. Reliable results are in fact available only for spins $|a| \lesssim 0.8$ and mass ratios $q \equiv M_2/M_1 \gtrsim 0.25$ and thus corresponding to $\nu \gtrsim 0.16$. However,

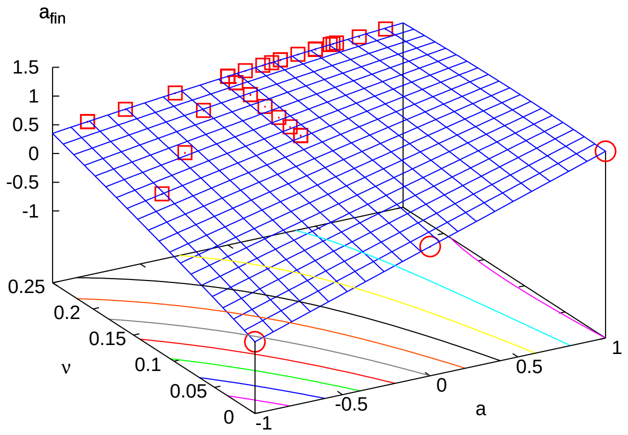

Figure 13.2: Global dependence of the final spin on the symmetric mass ratio and on the initial spins as predicted by expression (13.2.5). Squares refer to numerical estimates while circles to the EMRL constraints.

it is possible to exploit *exact* results which hold in the EMRL, *i.e.*, for $\nu = 0$, to constrain the coefficients in expression (13.2.1). It is worth emphasizing that the EMRL results are not only exact, but also in regimes that numerical relativity simulations cannot probe. More specifically, we can exploit that in the EMRL the final spin cannot be affected by the infinitesimally small BH. In practice, this amounts to requiring that

$$a_{\rm fin}(a, \nu = 0) = a\,, \qquad (13.2.2)$$

which constrains four of the six coefficients

$$s_0 = s_2 = s_3 = 0\,, \qquad s_1 = 1\,. \qquad (13.2.3)$$

Additional but non-exact constraints can also be applied by exploiting the knowledge, near the EMRL, of the functional dependence of $a_{\rm fin}$ on the mass ratio. A convenient way of doing this is suggested by BKL, and within this approach we perform a Taylor expansion of $a_{\rm fin}$ for $\nu \ll 1$ and determine that

$$\begin{aligned} &a'_{\rm fin}|_{(a=1,\nu=0)} = 2(\sqrt{3}/3 - 1)\,, \quad a'_{\rm fin}|_{(a=0,\nu=0)} = 2\sqrt{3}\,, \\ &a'_{\rm fin}|_{(a=-1,\nu=0)} = 2(1 + 19\sqrt{15}/45)\,, \end{aligned} \qquad (13.2.4)$$

where $a'_{\rm fin} \equiv \partial a_{\rm fin}/\partial\nu$. The coefficients in (13.2.1) are then $s_4 = \sqrt{3}(19\sqrt{5} - 75)/45$, $t_1 = 2\sqrt{3}$, $t_0 = [\sqrt{3}(15 - 19\sqrt{5}) - 90]/45$. While this may seem a good idea, it leads to bad fits of the data. We believe this is due to two distinct reasons: *(i)* the lack of accurate numerical data for near-extreme BHs, *i.e.*, $|a| \approx 1$, and which therefore leads to incorrect estimates of the coefficients; *(ii)* expressions (13.2.4) are analytic but not exact and should be used with caution. There are, in fact, deviations from analyticity in ν as $\nu \to 0$, and as revealed by the presence of integer powers of $\nu^{1/5}$ during the transition between the last stable orbit and the plunge (see [447]). In the case of non-spinning binaries ($a = 0$), it is now possible to verify that the deviations are indeed very small [448], but this check is not possible for very large spins. In view of this and to make the minimal number of assumptions, we retain the analytic estimate only for the coefficient t_1, so that (13.2.1) has five out of ten coefficients constrained analytically

$$a_{\rm fin} = a + s_4 a^2 \nu + s_5 a \nu^2 + t_0 a \nu + 2\sqrt{3}\nu + t_2 \nu^2 + t_3 \nu^3\,. \qquad (13.2.5)$$

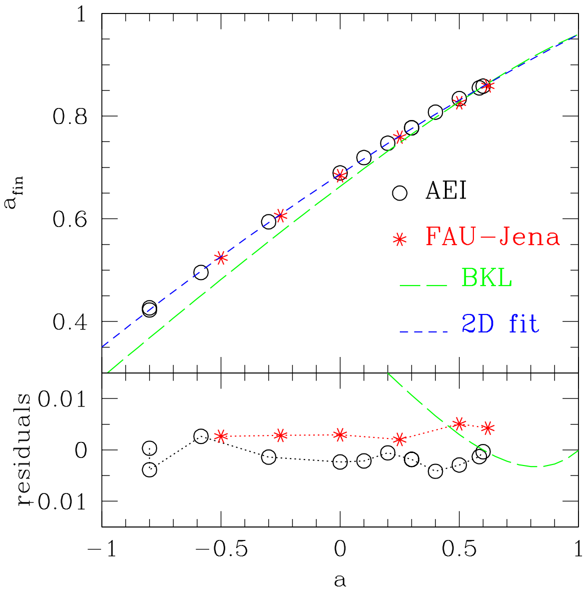

Figure 13.3: *Upper panel:* Comparison of the numerical data with the 2D fit through (13.2.5) in the case of equal-mass binaries, ($\nu = 1/4$). Empty circles indicate the AEI data [57] (see Section 11.1), stars the FAU-Jena data [419]], a long-dashed line the BKL, and a short-dashed one the fit. *Lower panel:* residuals between the different estimates and the fit.

Determining the remaining five coefficients from a least-square fit of the available data yields

$$\begin{aligned} s_4 &= -0.129 \pm 0.012\,, \qquad & s_5 &= -0.384 \pm 0.261\,, \\ t_0 &= -2.686 \pm 0.065\,, \qquad & t_2 &= -3.454 \pm 0.132\,, \\ t_3 &= 2.353 \pm 0.548\,, \end{aligned} \tag{13.2.6}$$

with surprisingly small residuals and large error-bars only for s_5. The functional behavior of expression (13.2.5) and the position of the numerical data points are shown in Figure 13.2.

In the following we discuss the properties of the proposed fit, providing evidence that it represents a very accurate description of the available estimates, and discuss how to use it to make astrophysically interesting predictions.

(i) The estimate for the final spin in the case of equal masses and the comparison with available data and estimates is made in Figure 13.3. The upper panel shows the numerical estimates, [circles for the AEI data [57] (see Section 11.1) and stars for the FAU-Jena data [419]], the BKL estimate and our 2D fit through (13.2.5). The lower panel shows the residuals between the different estimates and the 2D fit; these are always of a few percent only and become larger for the BKL estimate when $a \lesssim 0$.

(ii) Despite the cubic dependence assumed in (13.2.1), expression (13.2.5) is only *quadratic* with a. When $\nu = 1/4$, it confirms what was obtained recently [57] (see Section 13.1), indicating that, for equal-mass binaries, the next order will be four.

(iii) Using (13.2.5) and (13.2.6) we estimate that the minimum and maximum final spins for an equal-mass binary are $a_{\rm fin} = 0.3502 \pm 0.03$ and $a_{\rm fin} = 0.9590 \pm 0.03$, respectively.

(iv) For non-spinning binaries, expression (13.2.5) is cubic in ν and a comparison with the available data and the estimate from the EOB approach combined with test-mass limit predictions for the ring-down [448] is shown in Figure 13.4. In particular, the upper panel shows the numerical values, [empty circles for the Jena data [453] and stars for the Goddard data [32]], a long-dashed line for the quadratic EOB 1D fit [448] and a short-dashed line for our 2D fit. (Because it is very similar

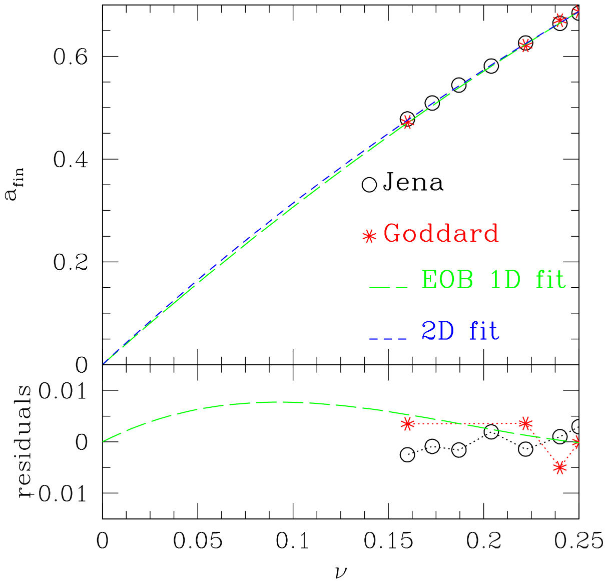

Figure 13.4: *Upper panel:* Comparison of the numerical data with the 2D fit through (13.2.5) in the case of non-spinning binaries. Empty circles indicate the Jena data [453], stars the Goddard data [32]], a long-dashed line the quadratic EOB fit [448] and a short-dashed line our 2D fit. *Lower panel:* residuals between the different estimates and the 2D fit.

to the EOB estimate, we have not shown the BKL prediction.) The residuals are shown in the lower panel.

(v) A physically useful condition that can be deduced from the 2D fit are the values of the initial spin and mass ratio that will lead to a final *Schwarzschild* BH [444, 450]. In practice this amounts to requiring $a_{\rm fin}(a,\nu) = 0$ in (13.2.5) and this curve in the $(a,\,\nu)$ plane is shown in the upper panel of Figure 13.5. Binaries on the curve produce Schwarzschild BHs, while binaries above the curve start with a positive total angular momentum and end with a positive one; binaries below the curve, on the other hand, start with a positive total angular momentum and end with a negative one, *i.e.*, with a global *flip*. Also shown in the upper panel of Figure 13.5 is the prediction from BKL: $a_{\rm Schw.}|_{\rm BKL} = 2\nu\sqrt{3}/(2\nu-1)$. The two estimates are very similar for all values of ν and small differences appear for $\nu \gtrsim 0.15$, where the BKL estimate is less accurate. Shown with a cross is the binary p_1 (*cf.*, Table 13.1) which yields a final BH with spin $a_{\rm fin} = 0.005$. The numerical value is between the BKL prediction and the 2D fit.

(vi) The BKL is expected to be particularly accurate for $\nu \ll 1$ and its prediction in this regime are captured very well by the 2D fit (of course the two predictions are identical for $\nu = 0$). This is shown in the lower panel of Figure 13.5 with different curves referring to $\nu = 0.001\,, 0.01$ and 0.1; interestingly, the differences are small even for $\nu = 0.1$.

(vii) It is simple to derive the value of a which will produce a final BH with the *same* spin as the initial ones. This amounts to requiring that $a_{\rm fin}(a,\nu) = a$ in (13.2.5) and the resulting solution is shown in Figure 13.6; clearly, the axis $\nu = 0$ is a trivial solution and a magnification of the behavior away from the EMRL is shown in the inset. For equal-mass binaries the critical value is $a_{\rm crit} = 0.9460$, in very good agreement with the BKL estimate $a_{\rm crit} \gtrsim 0.948$ [450]. The minuteness of the region for which $a_{\rm fin} < a$ (dashed region) suggests that BHs from aligned-spins binaries are typically spun-up by mergers.

(viii) It is easy to verify that by setting $\nu = 1/4$ and $2a = a_1 + a_2$ in (13.2.5), the coefficients s_1–s_5 and t_0–t_3 coincide, within the error-bars, with the coefficients p_0, p_1 and p_2 reported in [57] for equal-mass, unequal-spin binaries. The fact that the fit here is equivalent to, but has been

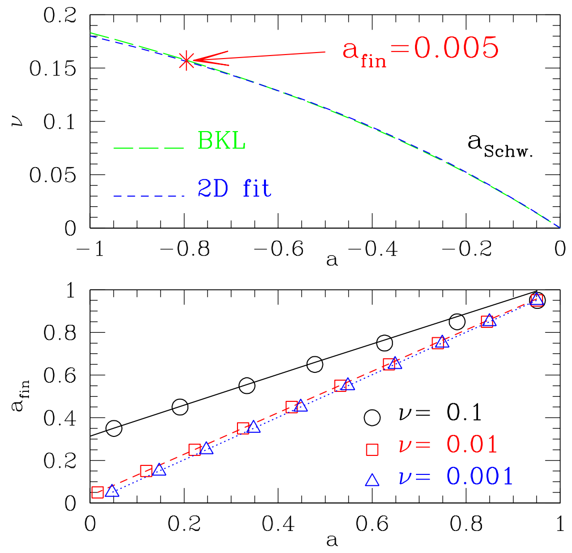

Figure 13.5: *Upper panel:* Set of initial spins and mass ratios leading to a final Schwarzschild BH: *i.e.*, $a_{\rm fin}(a,\nu) = 0$. The two curves refer to the BKL estimate (long dashed) and to the 2D fit (short dashed), respectively. Indicated with a star is a numerical example leading to $a_{\rm fin} = 0.005$. *Lower panel:* Comparison between the BKL prediction (symbols) and the 2D fit (solid, dashed and long-dashed lines) near the EMRL. Different curves refer to different values of ν and the match is complete for $\nu = 0$.

independently derived from, the one for the equal-mass, unequal-spin binaries, is an indication of its robustness. Indeed, it is possible to extend (13.2.5) to the whole (a_1, a_2, ν) space *i.e.*, to describe the final spin of generic aligned, unequal-spin, unequal-mass BH binaries, by replacing a with $(a_1 + a_2 q^2)/(1 + q^2)$. The resulting expression reduces to (13.2.5) for unequal-mass, equal-spin binaries, and to the one in [57] for equal-mass (see Section 13.1), unequal-spin binaries. Our suggested extension of (13.2.5) to the (a_1, a_2, ν) space is the simplest one which recovers, for aligned spins, the well-tested limits of equal-mass, unequal-spins and unequal-mass, equal-spins. Work is in progress to validate this ansatz with numerical simulations.

A final comment is one of caution. The dependence of the final spin on the mass ratio in the case of extreme aligned BHs is particularly challenging to calculate and not yet investigated accurately by numerical calculations. The predictions of expression (13.2.5) in this limit amount to mere extrapolations and are therefore accurate to a few percent at most. As an example, when $a = 1$, the fit (13.2.5) is a non-monotonic function with maximum $a_{\rm fin} \simeq 1.029$ for $\nu \simeq 0.093$; this clearly is an artifact of the extrapolation.

13.3 Extension to generic mass-ratios and spins

Here, we show that without additional fits and with a minimal set of assumptions it is possible to obtain the extension to the complete space of parameters and reproduce all of the available numerical relativity data. Although our treatment is intrinsically approximate, we also suggest how it can be improved.

In the previous sections, analytic fitting expressions for $\boldsymbol{a}_{\rm fin}$ have so far been built using binaries having spins that are either *aligned* or *anti-aligned* with the initial orbital angular momentum. This is because in this case both the initial and final spins can be projected in the direction of the orbital angular momentum and it is possible to deal simply with the (pseudo)-scalar quantities a_1, a_2 and $a_{\rm fin}$ ranging between -1 and $+1$. If the BHs have *equal mass* but *unequal* spins that

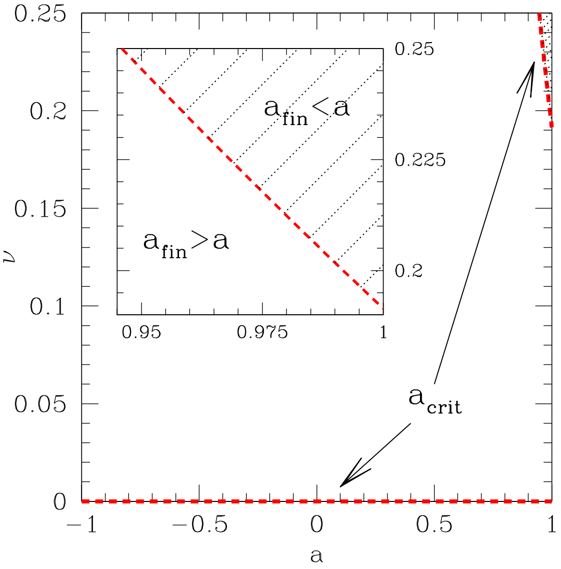

Figure 13.6: Critical values of the initial spin and mass ratio leading to a final BH having the same spin as the initial ones *i.e.*, $a_{\rm fin}(a,\nu) = a$. A magnification is shown in the inset, where the dashed/non-dashed region refers to binaries *spun-down/up* by the merger.

are either *parallel* or *antiparallel*, then the spin of the final BH has been shown to be accurately described by the simple analytic fit [57] (13.1.3)

$$a_{\rm fin}(a_1, a_2) = p_0 + p_1(a_1 + a_2) + p_2(a_1 + a_2)^2\,, \tag{13.3.1}$$

where $p_0 = 0.6883 \pm 0.0003$, $p_1 = 0.1530 \pm 0.0004$, and $p_2 = -0.0088 \pm 0.0005$. When seen as a power series of the initial spins, expression (13.3.1) suggests an interesting physical interpretation. Its zeroth-order term, in fact, can be associated with the (dimensionless) orbital angular momentum not radiated in gravitational waves and amounting to $\sim 70\%$ of the final spin at most. The first-order term, on the other hand, can be seen as the contributions from the initial spins and from the spin-orbit coupling, amounting to $\sim 30\%$ at most. Finally, the second-order term, includes the spin-spin coupling, with a contribution to the final spin which is of $\sim 4\%$ at most.

If the BHs have *unequal mass* but spins that are *equal* and *parallel*, the final spin is instead given by the analytic fit [58] (13.2.5)

$$\begin{aligned} a_{\rm fin}(a, \nu) = a + s_4 a^2 \nu + s_5 a \nu^2 + t_0 a \nu + \\ 2\sqrt{3}\nu + t_2 \nu^2 + t_3 \nu^3\,, \end{aligned} \tag{13.3.2}$$

where ν is the symmetric mass ratio $\nu \equiv M_1 M_2/(M_1 + M_2)^2$, and where the coefficients take the values $s_4 = -0.129 \pm 0.012$, $s_5 = -0.384 \pm 0.261$, $t_0 = -2.686 \pm 0.065$, $t_2 = -3.454 \pm 0.132$, $t_3 = 2.353 \pm 0.548$. Although obtained independently in [57] and [58], expressions (13.3.1) and (13.3.2) are compatible as can be seen by considering (13.3.2) for equal-mass binaries ($\nu = 1/4$) and verifying that the following relations hold within the computed error-bars

$$p_0 = \frac{\sqrt{3}}{2} + \frac{t_2}{16} + \frac{t_3}{64}\,, \quad p_1 = \frac{1}{2} + \frac{s_5}{32} + \frac{t_0}{8}\,, \quad p_2 = \frac{s_4}{16}. \tag{13.3.3}$$

As long as the initial spins are aligned (or anti-aligned) with the orbital angular momentum, expression (13.3.2) can be extended to *unequal-spin, unequal-mass* binaries through the substitution

$$a \;\to\; \tilde{a} \equiv \frac{a_1 + a_2 q^2}{1 + q^2}\,. \tag{13.3.4}$$

To obtain this result, it is sufficient to consider (13.3.1) and (13.3.2) as polynomial expressions of the generic quantity

$$\tilde{a} \equiv a_{\rm tot} \frac{(1 + q)^2}{1 + q^2}\,. \tag{13.3.5}$$

where $a_{\rm tot} \equiv (a_1 + a_2 q^2)/(1 + q)^2$ is the total dimensionless spin for generic aligned binaries. In this way, expressions (13.3.1) and (13.3.2) are naturally compatible, since $\tilde{a} = (a_1 + a_2)/2$ for equal-mass unequal-spin binaries, and $\tilde{a} = a$ for unequal-mass equal-spin binaries. Furthermore, the extreme mass-ratio limit (EMRL) of expression (13.3.2) with the substitution (13.3.4) yields the expected result: $a_{\rm fin}(a_1, a_2, \nu = 0) = a_1$.

As already commented above, the predictions of expressions (13.3.2) and (13.3.4) cover 3 of the 7 dimensions of the space of parameters for binaries in quasi-circular orbits; we next show how to to cover the remaining 4 dimensions and derive an analytic expression for the dimensionless spin *vector* $\boldsymbol{a}_{\rm fin}$ of the BH produced by the coalescence of two generic BHs in terms of the mass ratio q and of the initial dimensionless spin vectors $\boldsymbol{a}_{1,2}$. To make the problem tractable analytically, 4 assumptions are needed. While some of these are very natural, others can be relaxed if additional accuracy in the estimate of $\boldsymbol{a}_{\rm fin}$ is necessary. It should be noted, however, that removing any of these assumptions inevitably complicates the picture, introducing additional dimensions, such as the initial separation in the binary or the radiated mass, in the space of parameters.

Assumptions

In the simplest and yet accurate description the required assumptions are as follows:

(i) The mass radiated to gravitational waves $M_{\rm rad}$ can be neglected i.e., $M_{\rm fin} = M \equiv M_1 + M_2$. We note that $M_{\rm rad}/M = 1 - M_{\rm fin}/M \approx 5 - 7 \times 10^{-2}$ for most of the binaries evolved numerically. The same assumption was applied in the analyses of [57, 58], as well as in [450]. Relaxing this assumption would introduce a dependence on $M_{\rm fin}$ which can only be measured through a numerical simulation.

(ii) At a sufficiently large but finite initial separation the final spin vector $\boldsymbol{S}_{\rm fin}$ can be well approximated as the sum of the two initial spin vectors and of a third vector $\tilde{\boldsymbol{\ell}}$

$$\boldsymbol{S}_{\rm fin} = \boldsymbol{S}_1 + \boldsymbol{S}_2 + \tilde{\boldsymbol{\ell}}\,, \tag{13.3.6}$$

Differently from [444] and [450], where a definition similar to (13.3.6) was also introduced, here we will constrain $\tilde{\boldsymbol{\ell}}$ by exploiting the results of numerical relativity calculations rather than by relating it to the orbital angular momentum of a test particle at the innermost stable circular orbit (ISCO). When viewed as expressing the conservation of the total angular momentum, (13.3.6) also defines the vector $\tilde{\boldsymbol{\ell}}$ as the difference between the orbital angular momentum $\boldsymbol{L}$ when the binary is widely separated, and the angular momentum radiated until the merger $\boldsymbol{J}_{\rm rad}$, *i.e.*, $\tilde{\boldsymbol{\ell}} = \boldsymbol{L} - \boldsymbol{J}_{\rm rad}$.

(iii) The vector $\tilde{\boldsymbol{\ell}}$ is parallel to $\boldsymbol{L}$. This assumption is correct when $\boldsymbol{S}_1 = -\boldsymbol{S}_2$ and $q = 1$ [this can be seen from the PN equations at 2.5 order], or by equatorial symmetry when the spins are aligned with $\boldsymbol{L}$ or when $\boldsymbol{S}_1 = \boldsymbol{S}_2 = 0$ (also these cases can be seen from the PN equations). For more general configurations one expects that $\tilde{\boldsymbol{\ell}}$ will also have a component orthogonal to $\boldsymbol{L}$ as a result, for instance, of spin-orbit or spin-spin couplings, which will produce in general a precession of $\tilde{\boldsymbol{\ell}}$. In practice, the component of $\tilde{\boldsymbol{\ell}}$ orthogonal to $\boldsymbol{L}$ will correspond to the angular momentum $\boldsymbol{J}^{\perp}_{\rm rad}$ radiated in a plane orthogonal to $\boldsymbol{L}$, with a resulting error in the estimate of $|\tilde{\boldsymbol{\ell}}|$ which is[1] $\sim |\boldsymbol{J}^{\perp}_{\rm rad}|^2/|\tilde{\boldsymbol{\ell}}|^2 \sim |\boldsymbol{J}^{\perp}_{\rm rad}|^2/(2\sqrt{3}M_1M_2)^2$. Although these errors are small in all the configurations that we have analyzed, they may be larger in general configurations. Measuring $\boldsymbol{J}^{\perp}_{\rm rad}$ via numerical relativity simulations, or estimating it via high-order PN equations, is an obvious way to improve our approach. A similar assumption was also made in [450].

(iv) When the initial spin vectors are equal and opposite ($\boldsymbol{S}_1 = -\boldsymbol{S}_2$) and the masses are equal ($q = 1$), the spin of the final BH is the same as for the non-spinning binaries. Stated differently, equal-mass binaries with equal and opposite-spins behave as non-spinning binaries, at least when it comes down to the properties of the final BH. While this result cannot be derived from first principles, it reflects the expectation that if the spins are the same and opposite, their contributions to the final spin cancel for equal-mass binaries. Besides being physically reasonable, this expectation is met by all of the simulations performed to date, both for spins aligned with $\boldsymbol{L}$ [57, 58] and orthogonal to $\boldsymbol{L}$ [439]. In addition, this expectation is met by the leading-order contributions to the spin-orbit and spin-spin point-particle Hamiltonians and spin-induced radiation flux [244, 455]. A similar assumption is also made, although not explicitly, in [450] which, for $\boldsymbol{S}_{\rm tot} = 0$, predicts $\iota = 0$ and $|\boldsymbol{a}_{\rm fin}| = L_{\rm orb}(\iota = 0, |\boldsymbol{a}_{\rm fin}|)/M =$const. [*cf.* eqs. (12)–(13) in [450]].

Analytic expression

Using the assumptions from the previous subsection, we can now derive the analytic expression for the final spin. We start by expressing the vector relation (13.3.6) as

$$\boldsymbol{a}_{\rm fin} = \frac{1}{(1+q)^2}\left(\boldsymbol{a}_1 + \boldsymbol{a}_2 q^2 + \boldsymbol{\ell} q\right)\,, \tag{13.3.7}$$

where $\boldsymbol{a}_{\rm fin} = \boldsymbol{S}_{\rm fin}/M^2$ [*cf.* assumption *(i)*], $\boldsymbol{\ell} \equiv \tilde{\boldsymbol{\ell}}/(M_1M_2)$, $\boldsymbol{a}_{1,2} \equiv \boldsymbol{S}_{1,2}/M^2_{1,2}$, and its norm is then given by

$$\begin{aligned}|\boldsymbol{a}_{\rm fin}| = \frac{1}{(1+q)^2}\Big[&|\boldsymbol{a}_1|^2 + |\boldsymbol{a}_2|^2 q^4 + 2|\boldsymbol{a}_2||\boldsymbol{a}_1| q^2 \cos\alpha + \\ &2\left(|\boldsymbol{a}_1|\cos\beta + |\boldsymbol{a}_2| q^2 \cos\gamma\right)|\boldsymbol{\ell}| q + |\boldsymbol{\ell}|^2 q^2\Big]^{1/2}\,,\end{aligned} \tag{13.3.8}$$

---

[1] Assumption *(iii)* can be equivalently interpreted as enforcing that the component of the final spin $\boldsymbol{S}_{\rm fin}$ in the orbital plane equals the one of the total initial spin $\boldsymbol{S}_1 + \boldsymbol{S}_2$ in that plane.

where the three (cosine) angles α, β and γ are defined by

$$\cos\alpha \equiv \hat{\boldsymbol{a}}_1 \cdot \hat{\boldsymbol{a}}_2\,, \quad \cos\beta \equiv \hat{\boldsymbol{a}}_1 \cdot \hat{\boldsymbol{\ell}}\,, \quad \cos\gamma \equiv \hat{\boldsymbol{a}}_2 \cdot \hat{\boldsymbol{\ell}}\,. \tag{13.3.9}$$

Because $\boldsymbol{a}_{1,2} \parallel \boldsymbol{S}_{1,2}$ and $\boldsymbol{\ell} \parallel \boldsymbol{L}$ [*cf.* assumption *(iii)*], the angles α, β and γ are also those between the initial spin vectors and the initial orbital angular momentum, so that it is possible to replace $\hat{\boldsymbol{a}}_{1,2}$ with $\hat{\boldsymbol{S}}_{1,2}$ and $\hat{\boldsymbol{\ell}}$ with $\hat{\boldsymbol{L}}$ in (13.3.9). Note that α, β and γ are well-defined if the initial separation of the two BHs is sufficiently large [*cf.* assumption *(ii)*] and that the error introduced by assumption *(iii)* in the measure of $\cos\alpha, \cos\beta$ and $\cos\gamma$ is also of the order of $|\boldsymbol{J}^{\perp}_{\rm rad}|/|\tilde{\boldsymbol{\ell}}|$.

The angle $\theta_{\rm fin}$ between the final spin vector and the initial orbital angular momentum can be easily calculated from $|\boldsymbol{a}_{\rm fin}|$. Because of assumption *(iii)*, the component of the final spin in the direction of $\boldsymbol{L}$ is [*cf.* (13.3.7)]

$$a^{\parallel}_{\rm fin} \equiv \boldsymbol{a}_{\rm fin} \cdot \hat{\boldsymbol{\ell}} = \frac{|\boldsymbol{a}_1|\cos\beta + |\boldsymbol{a}_2| q^2 \cos\gamma + |\boldsymbol{\ell}| q}{(1+q)^2}\,, \tag{13.3.10}$$

so that $\cos\theta_{\rm fin} = a^{\parallel}_{\rm fin}/|\boldsymbol{a}_{\rm fin}|$, and the component orthogonal to the initial orbital angular momentum is $a^{\perp}_{\rm fin} = |\boldsymbol{a}_{\rm fin}|\sin\theta_{\rm fin}$.

In essence, therefore, our approach consists of considering the dimensionless spin vector of the final BH as the sum of the two initial spins and of a third vector parallel to the initial orbital angular momentum when the binaries are widely separated. Implicit in the assumptions made, and in the logic of mapping an initial-state of the binary into a final one, is the expectation that the length of this vector is an intrinsic "property" of the binary, depending on the initial spin vectors and mass ratio, but not on the initial separation. This is indeed a consequence of assumption *(ii)*: because the vector $\tilde{\boldsymbol{\ell}}$ measures the orbital angular momentum that cannot be radiated, it can be thought of as the angular momentum of the binary at the "effective" ISCO and, as such, it cannot be dependent on the initial separation.

A very important consequence of our assumptions is that $\boldsymbol{a}_{\rm fin}$ for a BH binary is already fully determined by the set of coefficients s_4, s_5, t_0, t_2, t_3 computed to derive expression (13.3.2). The latter, in fact, is simply the final spin for a special set of values for the cosine angles; since the fitting coefficients are constant, they must hold also for generic binaries.

In view of this, all that is needed is to measure $|\boldsymbol{\ell}|$ in terms of the fitting coefficients computed in Sections 13.1 and 13.2 [57, 58]. This can be done by matching expression (13.3.10) with (13.3.2) [with the condition (13.3.4)] for parallel and aligned spins ($\alpha = \beta = \gamma = 0$), for parallel and antialigned spins ($\alpha = 0$, $\beta = \gamma = \pi$), and for antiparallel spins which are aligned or anti-aligned ($\alpha = \beta = \pi$, $\gamma = 0$ or $\alpha = \gamma = \pi$, $\beta = 0$). This matching is not unique, but the degeneracy can be broken by exploiting assumption *(iv)* and by requiring that $|\boldsymbol{\ell}|$ depends linearly on $\cos\alpha$, $\cos\beta$ and $\cos\gamma$. We therefore obtain

$$\begin{aligned} |\boldsymbol{\ell}| = \frac{s_4}{(1+q^2)^2}\left(|\boldsymbol{a}_1|^2 + |\boldsymbol{a}_2|^2 q^4 + 2|\boldsymbol{a}_1||\boldsymbol{a}_2| q^2 \cos\alpha\right) + \\ \left(\frac{s_5\nu + t_0 + 2}{1+q^2}\right)\left(|\boldsymbol{a}_1|\cos\beta + |\boldsymbol{a}_2| q^2 \cos\gamma\right) + \\ 2\sqrt{3} + t_2\nu + t_3\nu^2\,. \end{aligned} \tag{13.3.11}$$

Results

We now consider some limits of expressions (13.3.8) and (13.3.11). First of all, when $q \to 0$, (13.3.8) and (13.3.11) yield the correct EMRL, *i.e.*, $|\boldsymbol{a}_{\rm fin}| = |\boldsymbol{a}_1|$. Secondly, for equal-mass binaries having spins that are equal and antiparallel, (13.3.8) and (13.3.11) reduce to

$$|\boldsymbol{a}_{\rm fin}| = \frac{|\boldsymbol{\ell}|}{4} = \frac{\sqrt{3}}{2} + \frac{t_2}{16} + \frac{t_3}{64} = p_0 \simeq 0.687\,. \tag{13.3.12}$$

This result allows us now to qualify more precisely a comment made before: because for equal-mass BHs which are either non-spinning or have equal and opposite spins, the vector $|\boldsymbol{\ell}|$ does not

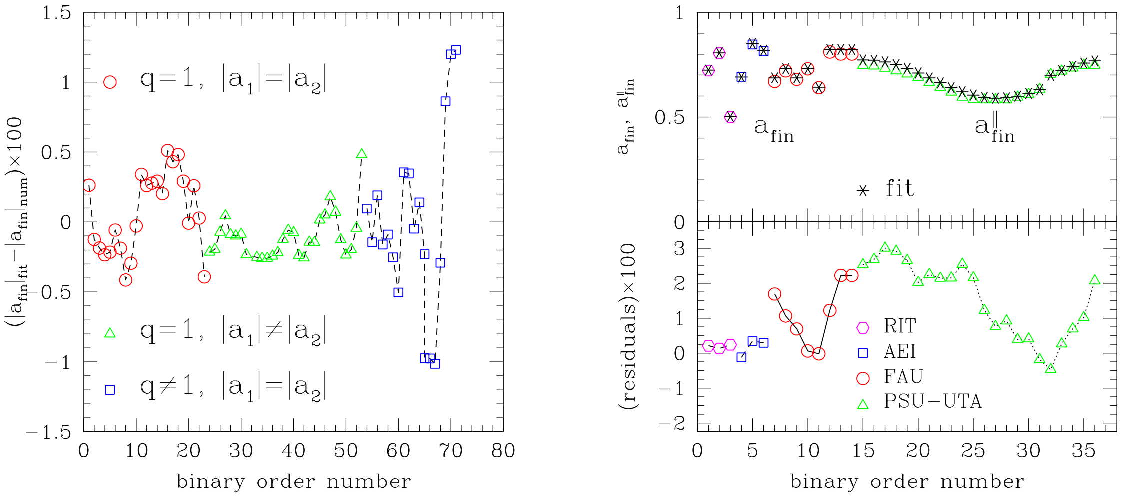

Figure 13.7: *Left panel:* Rescaled residual for aligned binaries. The circles refer to equal-mass, equal-spin binaries presented in [57, 58, 419, 453, 456, 457], triangles to equal-mass, unequal-spin binaries presented in [57, 456], and squares to unequal-mass, equal-spin binaries presented in [58, 453, 456, 457]. Here and in the right panel the "binary order number" is just a dummy index labeling the different configurations. *Right panel:* The top part reports with asterisks the final spin computed for misaligned binaries. Hexagons refer to data from [458] (labeled "RIT"), squares to the data Table 13.2 (labeled "AEI"), circles to data from [459] (labeled "FAU"), and triangles to data from [409] (labeled "PSU-UTA"). Note that these latter data points refer to the aligned component $a_{\rm fin}^{\parallel}$ since this is the only component available from [409]. The bottom part of this panel shows instead the rescaled residuals for these misaligned binaries.

a_1^x	a_1^y	a_1^z	a_2^x	a_2^y	a_2^z	ν	$\lvert\boldsymbol{a}_{\rm fin}\rvert$	$\theta_{\rm fin}(^\circ)$
0.151	0.000	-0.563	0.000	0.000	0.583	0.250	0.692	2.29
0.151	0.000	0.564	0.000	0.151	0.564	0.250	0.846	3.97
0.413	0.000	0.413	0.000	0.413	0.413	0.250	0.815	7.86

Table 13.2: Initial parameters of the new misaligned AEI binaries.

depend on the initial spins, expression (13.3.12) states that $|\boldsymbol{\ell}|M_{\rm fin}^2/4 = |\boldsymbol{\ell}|M^2/4 = |\boldsymbol{\ell}|M_1M_2$ is, for such systems, the orbital angular momentum at the effective ISCO. We can take this a step further and conjecture that $|\boldsymbol{\ell}|M_1M_2 = |\tilde{\boldsymbol{\ell}}|$ is the series expansion of the dimensionless orbital angular momentum at the ISCO also for *unequal-mass* binaries which are either non-spinning or with equal and opposite spins. The zeroth-order term of this series (namely, the term $2\sqrt{3}M_1M_2$) is exactly the one predicted from the EMRL. We note that although numerical simulations do not reveal the presence of an ISCO, the concept of an effective ISCO can nevertheless be useful for the construction of gravitational-wave templates [34, 460].

Finally, we consider the case of equal, parallel and aligned/anti-aligned spins ($|\boldsymbol{a}_2| = |\boldsymbol{a}_1|$, $\alpha = 0$, $\beta = \gamma = 0,\ \pi$), for which expressions (13.3.10) and (13.3.11) become

$$\begin{aligned} a_{\rm fin} \quad &= \quad |\boldsymbol{a}_1|\cos\beta\,[1+\nu(s_4|\boldsymbol{a}_1|\cos\beta + t_0 + s_5\nu)] + \\ &\qquad\qquad \nu(2\sqrt{3} + t_2\nu + t_3\nu^2)\,, \end{aligned} \tag{13.3.13}$$

where $\cos\beta = \pm 1$ for aligned/anti-aligned spins. As expected, expression (13.3.13) coincides with (13.3.2) when $|\boldsymbol{a}_1|\cos\beta = a$ and with (13.3.1) [through the coefficients (13.3.3)] when $q = 1$ and $2|\boldsymbol{a}_1|\cos\beta = a_1 + a_2$. Similarly, (13.3.10) and (13.3.11) reduce to (13.3.2) for equal, antiparallel and aligned/anti-aligned spins ($|\boldsymbol{a}_2| = |\boldsymbol{a}_1|$, $\alpha = 0$, $\beta = 0, \gamma = \pi$, or $\beta = \pi, \gamma = 0$).

The only way to assess the validity of expressions (13.3.8) and (13.3.11) is to compare their predictions with the numerical relativity data. This is done in Figures 13.7 and 13.8, which collect all of the published data, together with the three additional binaries computed with the `CCATIE` code [56] and reported in Table 13.2. In these plots, the "binary order number" is just a dummy index labeling the different configurations. The left panel of Figure 13.7, in particular, shows the rescaled residual, *i.e.*, $(|\boldsymbol{a}_{\rm fin}|_{\rm fit} - |\boldsymbol{a}_{\rm fin}|_{\rm num.}) \times 100$, for aligned binaries. The plot shows the numerical relativity data with circles referring to equal-mass, equal-spin binaries from [57, 58, 419, 453, 456, 457], triangles to equal-mass, unequal-spin binaries from [57, 456], and squares to unequal-mass, equal-spin binaries from [58, 453, 456, 457]. Although the data is from simulations with different truncation errors, the residuals are all very small and with a scatter of $\sim 1\%$.

A more stringent test is shown in the right panel of Figure 13.7, which refers to misaligned binaries. In the top part, hexagons indicate the numerical values for $|\boldsymbol{a}_{\rm fin}|$ from [458], squares the ones in Table 13.2, circles those from [459] and triangles those from [409]; note that these latter data points refer to the aligned component $a_{\rm fin}^{\|}$ since this is the only component available from [409]. The agreement is again very good, with errors of a couple of percent (see bottom part of the same panel), even if the binaries are generic and for some the initial and final spins differ by almost 180° [458].

Finally, Figure 13.8 reports the angle between the final spin vector and the initial orbital angular momentum $\theta_{\rm fin}$ using the same data (and convention for the symbols) as in the right panel of Figure 13.7. Measuring the final angle accurately is not trivial, particularly due to the fact that the numerical evolutions start at a finite separation which does not account for earlier evolution of the orbital angular momentum vector. The values reported in [458] (and the relative error-bars) are shown with hexagons, while the squares refer to the binaries in Table 13.2. Shown with asterisks and circles are instead the values predicted for the numerical data (as taken from [409, 458, 459] and from Table 13.2) by our analytic fit (asterisks) and by the point-particle approach suggested in [450] (circles).

Clearly, when a comparison with numerical data is possible, the estimates of our fit are in reasonable agreement with the data and yield residuals in the final angle (*i.e.*, $(\theta_{\rm fin})_{\rm fit} - (\theta_{\rm fin})_{\rm num.}$) which

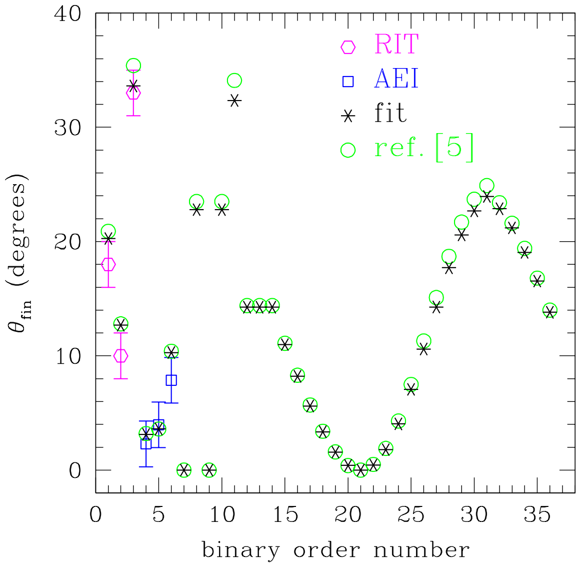

Figure 13.8: Using the same data (and convention for the symbols) as in the right panel of Figure 13.7, we here report the angle between the final spin vector and the initial orbital angular momentum $\theta_{\rm fin}$. Shown instead with asterisks and circles are the values predicted for the numerical data (as taken from [409, 458, 459] and from Table 13.2) by our analytic fit (asterisks) and by the point-particle approach suggested in [450] (circles).

are generally smaller than those obtained with the point-particle approach of [450]. However, for two of the three binaries from [458] the estimates are slightly outside the error-bars. Note that the reported angles are relative to the orbital plane at a small initial binary-separation, and thus are likely to be underestimates as they do not take into account the evolution from asymptotic distances; work is in progress to clarify this. When the comparison with the numerical data is not possible because $\theta_{\rm fin}$ is not reported (as for the data in [409]), our approach and the one in [450] yield very similar estimates.

In summary: we have considered the spin vector of the BH produced by a BH binary merger as the sum of the two initial spins and of a third vector, parallel to the initial orbital angular momentum, whose norm depends only on the initial spin vectors and mass ratio, and measures the orbital angular momentum not radiated. Without additional fits than those already available to model aligned/anti-aligned binaries, we have measured the unknown vector and derived a formula that accounts therefore for all of the 7 parameters describing a BH binary inspiralling in quasi-circular orbits. The equations (13.3.8) and (13.3.11), encapsulate the near-zone physics to provide a convenient, but also robust and accurate over a wide range of parameters, determination of the merger product of rather generic BH binaries.

Testing the formula against all of the available numerical data has revealed differences between the predicted and the simulated values of a few percent at most. Our approach is intrinsically approximate and it has been validated on a small set of configurations, but it can be improved, for instance: by reducing the χ^2 of the fitting coefficients as new simulations are carried out; by using fitting functions that are of higher-order than those in expressions (13.3.1) and (13.3.2); by estimating $\boldsymbol{J}^{\perp}_{\rm rad}$ through PN expressions or by measuring it via numerical simulations.

Chapter 14

Gravitational-wave detectability of black-hole binaries

In this chapter, we report on results that we have obtained in [51]. Particularly, we have focused on equal-mass BH binaries with spins aligned or anti-aligned with the orbital angular momentum, and which therefore do not exhibit precession effects. They provide the natural ground to start detailed studies of the influence of strong-field spin effects on gravitational wave observations of coalescing binaries. Furthermore, such systems may be the preferred end-state of the inspiral of generic supermassive BBH systems. In view of this, we have computed the inspiral and merger of a large set of binary systems of equal-mass BHs with spins parallel to the orbital angular momentum but otherwise arbitrary. Our attention is particularly focused on the gravitational-wave emission so as to quantify how much spin effects contribute to the signal-to-noise ratio, to the horizon distances, and to the relative event rates for the representative ranges in masses and detectors. Previous studies on equal-mass non-spinning BH binaries indicate that the signal-to-noise ratio for LISA can be as high as $\approx 5 \times 10^3$ for non-spinning equal-mass BHs with mass $M = 5 \times 10^6 M_\odot$ [365] at $z = 2$, and one can expect one event per year [461, 462] at that distance.

As expected, the signal-to-noise ratio increases with the projection of the total BH spin in the direction of the orbital momentum. We find that equal-spin binaries with maximum spin aligned with the orbital angular momentum are more than "three times as loud" as the corresponding binaries with anti-aligned spins, thus corresponding to event rates up to 30 times larger. We also consider the waveform mismatch between the different spinning configurations and find that, within our numerical accuracy, binaries with opposite spins $\boldsymbol{S}_1 = -\boldsymbol{S}_2$ cannot be distinguished whereas binaries with spin $\boldsymbol{S}_1 = \boldsymbol{S}_2$ have clearly distinct gravitational-wave emissions. Finally, we derive a simple expression for the energy radiated in gravitational waves and find that the binaries always have efficiencies $E_{\rm rad}/M \gtrsim 3.6\%$, which can become as large as $E_{\rm rad}/M \simeq 10\%$ for maximally spinning binaries with spins aligned with the orbital angular momentum. These binaries are therefore among the most efficient sources of energy in the Universe.

The plan in this chapter is is as follows: Section 14.2 is dedicated to the discussion of the gravitational-wave observables used for the subsequent analysis, while Section 14.3 presents the results in terms of the SNR and how this is influenced by higher-order modes. This Section also contains a discussion of the match between the waveforms from different binaries and an assessment of the accuracy of our results. Section 14.4, on the other hand, provides a brief discussion of the analytic expressions we have found representing either the SNR or the energy radiated in gravitational waves. Finally, conclusions are summarized in Section 14.5.

The simulations performed for the work in this chapter have already been discussed in Section 11.1, where we have recalled the numerical set up and illustrated the properties of the initial data used in the simulations.

14.1 Introduction

It has been a long-standing goal of the field of numerical relativity to provide results for gravitational-wave data analysis and thus enhance the capabilities of current and future gravitational wave detectors, in particular regarding the observation of compact binary coalescence. With a series of breakthroughs in 2005 [47–49], this long-term goal has suddenly become reality. However, much further work is required to actually understand the practical implications of numerical solutions of the full Einstein equations for gravitational-wave data analysis. Indeed, first studies suggest that template banks that use numerical information can increase the reach of detectors [33–35], aid the calibration of search pipelines [64, 463, 464], and improve the estimation of parameters, such as *e.g.* sky location [465].

In this chapter, we use gravitational waveforms from numerical relativity calculations of a number of sequences of equal-mass spinning BH binaries whose spins are aligned (anti-aligned) with the orbital angular momentum, and consider the detectability of these binaries for the ground-based gravitational wave-detectors as well as for the planned space-based LISA interferometer.

Across a set of different masses, we calculate the signal-to-noise ratio (SNR) for the LIGO [147, 148], enhanced LIGO (eLIGO) [466], advanced LIGO (AdLIGO) [34, 467], Virgo [149], advanced Virgo (AdVirgo) [468], and LISA [469, 470] detectors.

In this way, we attempt to address the following questions:

> *(i)* Which among the aligned-spin configurations is the "loudest" and which one is the "quietest"?
>
> *(ii)* How large is the difference in signal-to-noise ratio between the loudest and the quietest?
>
> *(iii)* How do these considerations depend on the detector used, the mass of the binary, and the number of harmonics?
>
> *(iv)* Are there configurations whose waveforms are difficult to distinguish and are hence degenerate in the space of templates?

Overall, and as expected, we find that equal-spinning, maximally anti-aligned binaries generally produce the lowest SNR while equal-spinning, maximally aligned binaries produce the highest SNR. For any mass, the SNR can be well described with a low-order polynomial of the initial spins $\rho = \rho(a_1, a_2)$ and generally it increases with the total dimensionless spin along the angular momentum direction, $a \equiv \frac{1}{2}(\boldsymbol{a}_1 + \boldsymbol{a}_2) \cdot \hat{\boldsymbol{L}}$. The possibility of describing the whole behavior of the waveforms from equal-mass, aligned/anti-aligned binaries in terms of a single scalar quantity, namely a, provides a certain amount of optimism that also more complex spin configurations can, ultimately, be described in terms of a few parameters only.

We also analyze the impact that higher-order contributions with $\ell \leq 4$ have on the maximum SNR and show that for low masses $M \in [20, 100]$ they contribute, say for the LIGO detector, $\approx 2.5\%$, whereas for intermediate masses $M > 100\ M_\odot$ they contribute $\approx 8\%$ [1]. In addition, we determine the ratio between maximum and averaged SNR for $\ell > 2$ which is known to be $\sqrt{5}$ when considering only the $\ell = 2, m = 2$ mode. We also calculate the mismatch between the waveforms from different binaries across our spin-diagram and find that binaries along the diagonal $a_1 = -a_2$ cannot be distinguished within our given numerical accuracy, whereas configurations along the diagonal $a_1 = a_2$ are clearly different (*c.f.* Figure 14.6 and 14.7, as well as Table 14.3). Finally, we derive a simple expression for the energy radiated in gravitational waves and find that this is bounded between $\simeq 3.6\%$ and $\simeq 10\%$ for maximally spinning binaries with spins anti-aligned or aligned with the orbital angular momentum, respectively.

14.2 Gravitational-wave observables

In this Section we discuss the gravitational-wave observables that have been studied from the sample reported in Table 11.2 and how these have been used to compute the radiated energy, the SNR, the horizon distances and the event rates.

---

[1] Note that for some specific angles at which the SNR is not maximum, the contribution of the higher modes can be much more significant

Table 14.1: Initial instantaneous frequencies $M\omega_{\mathrm{ini}}$ and associated minimum masses M_{min} of the numerical relativity waveforms for the different models and for each detector according to the corresponding lower cut-off frequency (*i.e.* at 30 Hz for Virgo, at 40 Hz for eLIGO, at 10 Hz for AdLIGO/AdVirgo, and at 10^{-4} Hz for LISA). All the values for the masses are in units of solar masses.

	$M\omega_{\mathrm{ini}}$	M_{min} Virgo	M_{min} eLIGO	M_{min} AdLIGO/AdVirgo	M_{min} LISA
r_0	0.080	86.2	64.6	258.5	2.58×10^7
r_2	0.078	84.0	63.0	252.0	2.52×10^7
r_4	0.077	82.9	62.2	248.8	2.49×10^7
r_6	0.076	81.8	61.4	245.5	2.46×10^7
s_{-8}	0.060	64.6	48.4	193.8	1.93×10^7
s_0	0.080	86.2	64.6	258.5	2.58×10^7
s_2	0.078	84.0	63.0	252.0	2.52×10^7
s_4	0.076	81.8	61.4	245.5	2.46×10^7
s_6	0.075	80.8	60.6	242.3	2.42×10^7
s_8	0.073	78.6	59.0	235.8	2.36×10^7
t_0	0.084	90.5	67.8	271.4	2.71×10^7
t_1	0.083	89.4	67.0	268.2	2.68×10^7
t_2	0.082	88.3	66.2	264.9	2.65×10^7
t_3	0.081	87.2	65.4	261.7	2.62×10^7
u_2	0.080	86.2	64.6	258.5	2.58×10^7
u_4	0.080	86.2	64.6	258.5	2.58×10^7
u_8	0.080	86.2	64.6	258.5	2.58×10^7

Numerical relativity waveforms

Although the `CCATIE` code computes the gravitational waveforms either via the Newman-Penrose curvature scalar Ψ_4 or via gauge-invariant metric perturbations on a Schwarzschild background (see Section 5.1, 5.2), the analysis carried hereafter will be made in terms of the latter. While the two prescriptions yield, in fact, estimates which are in very good agreement with each other and with differences below 2% (see discussion in [56]), we have found that the results obtained using gauge-invariant quantities have a smaller numerical error, and are thus preferable.

More specifically, we compute the gravitational-wave amplitudes $h^{+}_{\ell m}$ and $h^{\times}_{\ell m}$ in terms of the even and odd master functions $Q^{+}_{\ell m}$ and $Q^{\times}_{\ell m}$ via the relations (see Section 5.4)

$$h_{\ell m}(t) = h^{+}_{\ell m}(t) - \mathrm{i} h^{\times}_{\ell m}(t) = Q^{+}_{\ell m}(t) - \mathrm{i} \int_{-\infty}^{t} dt' Q^{\times}_{\ell m}(t') \,, \tag{14.2.1}$$

where the gauge-invariant perturbations are typically extracted at a radius of $r_{\mathrm{E}} = 160M$ (see Sec. 14.3 for a discussion of the accuracy of our measurements and [56] for a comparison among different extraction radii).

As discussed in Section 11.1, all our binaries [but s_{-8}] have initial separations of $d = 8.0M$ [$d = 10.0M$], which, in the parameter space that we have considered, leads to a maximum initial frequency of the numerical waveforms, that is $\omega_{\mathrm{ini}} = 0.084/M$. Depending therefore on the mass M, such an initial frequency can be greater than the lower cut-off frequency of the detector for a given source at an arbitrary distance. Because for most masses, a "real" waveform will be "longer" than the one computed here, we need to account for the missing frequency band between the lower cut-off and the initial frequency of the wave. This can be accomplished by attaching to the numerical relativity wave the PN part of the wave and will be discussed in the next section.

The values of the initial frequencies and of the associated minimum masses M_{min} for each of the detectors considered are reported in Table 14.1.

Matching PN and NR waveform amplitudes

The existence of a cut-off mass set by the initial frequency of the numerical relativity simulations would clearly restrict the validity of our considerations to large masses only. To counter this and thus include also binaries with smaller masses, we account for the early inspiral phase by describing it via PN approximations. To produce the PN waveforms, and the PN energy that we are using directly in Sec. 14.4, we have used the spinning TaylorT1 approximant used in Hannam et al. [367], and which is based on the PN expressions described in [246, 252, 441, 471–475]. The choice of TaylorT1 is motivated by that fact, that in [367] it is found to be more robust in the spinning case than the TaylorT4 approximant, which was previously found to yield excellent results in the non-spinning case [257] (see *e.g.* [257] for a comparison of different techniques to obtain the gravitational-wave phase information for quasi-circular inspiral). These waveforms are 3.5 PN accurate in the non-spinning phase, and 2.5 PN accurate in the spin-dependent terms entering the phasing. The gravitational-wave amplitudes, on the other hand, have been computed according to [476] (see also [477]) to the highest PN order that is currently known for each of the spherical harmonic modes that we use.

A phase-coherent construction of hybrid PN-NR waveforms is rather delicate, and has not yet been achieved for the higher spherical harmonic modes we use here (see [33, 34] for some recent work in the case of non-spinning binaries). However, for the present purpose of computing the SNR and the radiated energies, such a construction in the time domain is not necessary and all of the relevant work can be done much more simply in the frequency domain. In practice, we Fourier transform the PN and NR waveforms and "glue" them together at a suitable "glueing" frequency $\omega_{\rm glue}$. Since the SNR depends only on the amplitude of the waveform, [*c.f.* eq. (14.2.5)], it is not necessary to match the PN-waveform in the phase. This greatly simplifies the process of waveform matching and basically reduces to a simple check of the amplitude matching to address the error of the mismatch. Indeed, we have found that without any parameter adjustment, the PN-waveform amplitudes match rather well with the inspiral part of the NR-waveforms, and result in an error which is usually $\approx 1.5\%$ and in the worst case $\approx 4.0\%$ for the binary configuration t_0. The only care which is important to pay in the time-domain analysis, and in order to limit the noise artifacts in the Fourier-transformed amplitudes, is the use of a windowing function (*e.g.* a hyperbolic tangent) to smoothly blend the waveform to zero before the initial burst of spurious radiation and after the ring-down, in order to limit spurious oscillations in the Fourier-transformed waveform. A representative example is shown in Figure 14.1, where we report the noise strain for the Virgo and Advanced LIGO detectors, together with the Fourier-transformed amplitude of the PN and NR waveform for the maximally spinning model s_8. The waveform is assumed to be observed at $\theta = 0, \phi = 0$ for a total mass $M = 200\,M_\odot$ and from a distance $d = 100\,{\rm Mpc}$. The glueing frequency in this case is at $f_{\rm glue} = \omega_{\rm glue}/(2\pi) = 27.14$ Hz.

Since each ℓ, m mode of the gravitational-wave field will have a different initial frequency, we need to make sure that they are all properly taken into account when determining the glueing frequency, so that, at least in principle

$$\omega_{\rm glue} \geq \max_{\ell,m} (\omega_{\rm ini})_{\ell m} \,. \tag{14.2.2}$$

In practice, the initial frequency of our highest mode, $\ell = 4, m = 4$, has an initial frequency $(\omega_{\rm ini})_{44} = 2(\omega_{\rm ini})_{22}$. As a result, we select the glueing frequency according to the binary configuration with the largest initial frequency, *i.e.* the binary t_0, and take $\omega_{\rm glue} = 2(\omega_{\rm ini})_{22} = 0.168/M$. We also measure how sensitive this choice is, by considering how the results are affected when choosing instead $\omega_{\rm glue} \pm \Delta\omega$, with $\Delta\omega \ll \omega_{\rm glue}$. More specifically, for $\Delta\omega = 0.01/M$ we find a maximal difference in the computed SNR of $\sim 2.0\%$ over all configurations and all masses. Note that such a difference affects equally the maximum and averaged SNRs (see Section 14.2 for a discussion on these two different measures of the SNR). Furthermore, a change of $\Delta\omega$ in $\omega_{\rm glue}$ affects only marginally the relative difference between SNRs computed by including modes up to $\ell = 2$ and $\ell = 4$, and also in this case the differences are $\sim 2.0\%$. Overall, therefore, the uncertainties introduced by the choice of $\omega_{\rm glue}$ are much smaller than the typical error at which we report the SNRs.

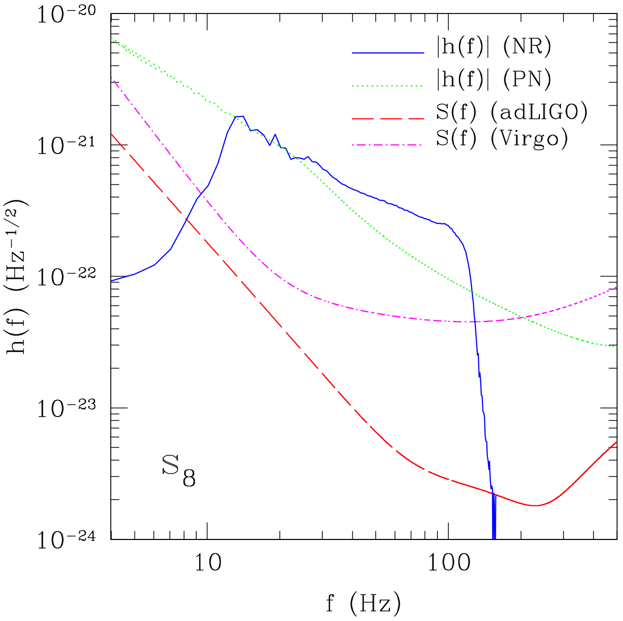

Figure 14.1: Noise strain for the Advanced LIGO and Virgo detectors and the Fourier-transformed amplitude of the PN and NR waveform at $\theta = 0, \phi = 0$ for a total mass $M = 200\,M_\odot$ at a distance $d = 100\,\mathrm{Mpc}$ for the maximally spinning model s_8. The glueing frequency is at $f_{\rm glue} = 27.14$ Hz.

Radiated energy

Since the total energy must be conserved, we can use the radiated energy as an important tool to verify the accuracy of the gravitational-wave amplitude and thus the overall precision of our calculations. More specifically, because it is straightforward to determine the initial and the final total mass, it is also straightforward to compare the difference in the two with the radiated energy. In practice, we compute the initial mass of the system as $M_{\rm ini} = \widetilde{M}_{\rm ADM}$, while the final mass of the merger remnant $M_{\rm fin}$ is deduced from the properties of the apparent horizon within the isolated-horizon formalism as first discussed in [298] and then extensively investigated in [478] (also see Chapter 4). The radiated energy is then simply given by the difference

$$E^{\rm NR}_{\rm rad} = M_{\rm ADM} - M_{\rm fin}\,, \tag{14.2.3}$$

and should be equal to the energy that has been radiated through gravitational waves during the simulation [312] (see Section 5.5)

$$E^{Q^{\times,+}}_{\rm rad} = \frac{1}{32\pi}\sum_{\ell,m}\int_0^t dt'\left(\left|\frac{dQ^{+}_{\ell m}}{dt}\right|^2 + \left|Q^{\times}_{\ell m}\right|^2\right)\,. \tag{14.2.4}$$

Overall, we have found that for all binaries the difference between $E_{\rm rad}$ and $E^{Q^{\times,+}}_{\rm rad}$ is between $\sim 0.5\%$ and $\sim 4.0\%$ and a detailed comparison of the numerical values is reported in Table 11.2. In Section 14.4 we will discuss an analytic fit to the computed data that provides a simple-to-use measure of the amount of mass radiated during the inspiral, merger and ring-down as a function of the initial spins.

SNR, horizon distances and event rates

Following [479], we define the SNR, ρ, for matched-filtering searches as

$$\rho^2 \equiv \left(\frac{S}{N}\right)^2_{\text{matched}} = 4\int_0^\infty \frac{|\tilde{h}(f)|^2}{S_h(f)}df \tag{14.2.5}$$

where $\tilde{h}(f)$ is the Fourier transform of the time domain gravitational-wave signal $h(t)$, defined in the continuum as

$$\tilde{h}(f) = \int_{-\infty}^{\infty} h(t)e^{-2\pi i f t}dt\,, \tag{14.2.6}$$

and $S_h(f)$ is the noise power spectral density for a given detector. Hereafter we will consider the $S_h(f)$ for the ground-based detectors LIGO, enhanced LIGO, advanced LIGO and Virgo, as well as the space-bound LISA interferometer. [The associated noise power spectral densities are reported in Appendix A.2.]

Note that since the SNR (14.2.5) depends on the angle from the source to the detector, it is useful to introduce the angle-averaged SNR $\langle\rho^2\rangle$, which can be computed straightforwardly after decomposing the gravitational-wave signal in terms of spherical harmonic modes. More specifically, using the orthonormality of the spin-weighted spherical harmonic basis ${}_sY_{\ell m}$, the *"angle-averaged"* SNR

$$\rho_{\text{avg}} \equiv \langle\rho^2\rangle \equiv \frac{1}{\pi}\int d\Omega \int df \frac{\left|\sum_{\ell m}\tilde{h}_{\ell m}(f)\,{}_{-2}Y_{\ell m}(\Omega)\right|^2}{S_h(f)}\,, \tag{14.2.7}$$

can be written as a simple sum of integrals of the absolute squares of the Fourier-transformed modes $\tilde{h}_{\ell m}(f)$

$$\rho_{\text{avg}} = \frac{1}{\pi}\sum_{\ell m}\int df \frac{|\tilde{h}_{\ell m}(f)|^2}{S_h(f)}\,, \tag{14.2.8}$$

and hence it can be evaluated straightforwardly. For each binary, distance and mass, we have calculated both the *"maximum"* SNR ρ_{max} for an optimally oriented detector, *i.e.* the SNR for a detector oriented such that it measures only the + polarization of the gravitational-wave signal, and the averaged SNR. Here the mass is always meant to be the *redshifted* total mass, *i.e.* $(1+z)M_{\text{source}}$, where z is the redshift and M_{source} is the mass at the source. For sources at small distances, *i.e.* less than 100 Mpc, then $z \lesssim 0.024$ and hence $M \simeq M_{\text{source}}$ to within a few percent. Identical results would have been obtained if we had considered the × polarization.

It is worth noting that if the gravitational-wave signal is modeled simply through the dominant $\ell = 2 = m$ mode (or in our case via a superposition $\ell = 2 = \pm m$)[2], the maximum SNR can be deduced from the average SNR after exploiting the properties of the spin-weighted spherical harmonic ${}_{-2}Y_{22}$ and ${}_{-2}Y_{2-2}$, namely

$$\begin{aligned}\rho_{\text{max}} &= \sqrt{5\rho^2_{\text{avg}}(\ell=2, m=2)} && (14.2.9)\\ &= \sqrt{\frac{5}{2}\rho^2_{\text{avg}}(\ell=2, m=\pm2)}\,. && (14.2.10)\end{aligned}$$

However, such a relation is no longer true when including modes with $\ell > 2$, and the relation between the maximum and the averaged value of the SNR can only be determined numerically.

When computing the SNR, a reference distance needs to be fixed and we have set such a distance to be $d_\rho = 100\,\text{Mpc}$. The results of the SNR at d_ρ across the spin diagram can then be recast in terms of an *"horizon distance"*, namely the distance at which a given binary system with redshifted mass M has an SNR equal to a threshold for detectability and which we chose to be $\rho = 8$, as customary for ground-based detectors. The horizon distance is then simply defined as

$$d_H = d_\rho\left(\frac{\rho(d=d_\rho)}{8}\right)\,\text{Mpc}\,. \tag{14.2.11}$$

---

[2] Note that in our binary configurations due to symmetry, we always have $h_{\ell m} = h_{\ell -m}$

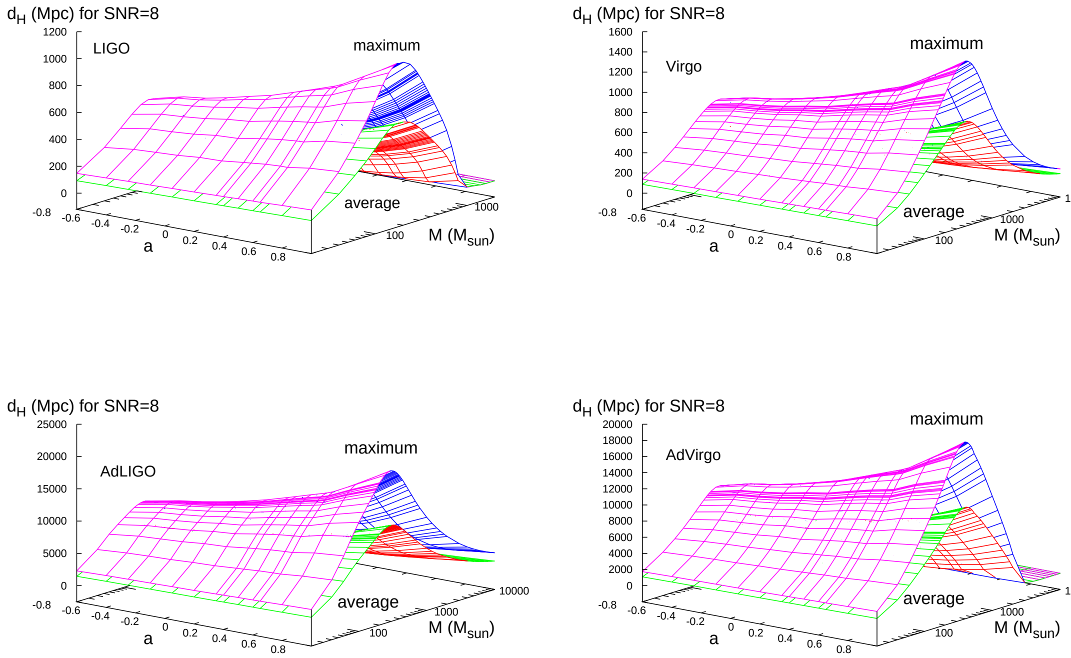

Figure 14.2: Averaged and maximum horizon distance $d_H = d_H(a, M)$ for the LIGO detector (top left panel), for the Virgo detector (top right panel), and for the advanced versions of both detectors (bottom left and right panels, respectively). The horizon distance has been computed at a reference SNR $\rho = 8.0$.

The quantity d_H is clearly equivalent to the SNR but has the advantage to provide, at least for detectors not operating at large SNRs, a simple estimate of the increase in the relative event rate R as

$$R \sim \left(\frac{d_H}{d_{H,a=-1}} \right)^3 , \tag{14.2.12}$$

where $d_{H,a=-1}$ is the horizon distance of the configuration with lowest SNR, *i.e.* which belongs to the extrapolated case $a = -1$. Although simple, this formula requires a caveat. Expression (14.2.12) is valid as an equality only for small horizon distances, namely those for which the redshift is negligible. This is because at large redshifts the observed masses would differ considerably from the masses at the source. In other words, at large redshifts the horizon distances would be different not only because of the spin, but also because the masses at the sources would be intrinsically different. This clearly impacts the deduced event rate as defined in (14.2.12), which considers only the contributions coming from the spin. Hence, for large redshifts the event rate R defined here serves only as a lower limit for masses larger than the optimal one and, vice versa, as an upper bound for masses smaller than the optimal.

To fix the ideas, let us consider a concrete example. Let us assume that we have calculated the horizon distance for a binary with $a = -1$ which, as can be deduced from Figure 14.3 and will be discussed in the next section, will lead to the smallest SNR for a given detector. We also assume that this binary has a mass at the detector which is smaller than the optimal one. Let us now consider a binary with the same mass at the detector but with $a > -1$; this binary will clearly lead to a larger SNR but because the masses at the detector are the same, the mass of the binary with $a > -1$ will be (because of the redshift) smaller at the source. As a result, its horizon distance will be overestimated, and hence the event rate coming from (14.2.12) only an upper bound. A similar argument for masses larger than the optimal one would instead lead to the conclusion that the event rate R is only a lower bound.

14.3 Results

In what follows we discuss the results obtained in terms of the SNR and how this is influenced by higher-order modes. We also discuss the match between the waveforms from different binaries and an assessment of the accuracy of our results.

Horizon distances and SNRs

The results of the analysis discussed above are nicely summarized in Figure 14.2, which shows the averaged and maximum horizon distance $d_H = d_H(a, M)$ for some of the detectors considered. As mentioned above, the horizon distance has been computed at a reference SNR $\rho = 8.0$, and is parametrized in terms of the total mass of the system (in solar masses) and of the average dimensionless spin "a" as projected along the orbital angular momentum $\boldsymbol{L}$

$$a \equiv \frac{1}{2}(\boldsymbol{a}_1 + \boldsymbol{a}_2) \cdot \hat{\boldsymbol{L}} = \frac{1}{2}(\boldsymbol{a}_1 + \boldsymbol{a}_2) \cdot \boldsymbol{e}_z \,, \tag{14.3.1}$$

where $\hat{\boldsymbol{L}} \equiv \boldsymbol{L}/|\boldsymbol{L}|$, and the orbital plane has been chosen to coincide with the $(x,\, y)$ plane of our Cartesian coordinate system. More specifically, the top left panel of Figure 14.2 refers to the LIGO detector, the top right panel to the Virgo detector, while the lower left and right panels refer to the advanced versions of both detectors, respectively.

While quite self-explanatory, these panels deserve some comments. First, as expected, the maximum SNR is always larger than the average one but the difference between the two is not constant, changing both with the total dimensionless spin a and with the total mass M. Second, for any fixed value of a, the horizon distance (and hence the SNR) grows steeply to a maximum mass and then rapidly decreases to very small values of $\sim \mathcal{O}(1)$. Clearly, this reflects the existence of a sweet-spot in the sensitivity curve of all detectors. Third, for any value of a, the maximum horizon distance/SNR also marks the "optimal mass" for the binary $M_{\rm opt}$, namely the mass of the binary whose inspiral and merger is optimally tuned with the given detector and hence can be seen from further away. Note that the differences between the maximum and average SNR are largest in the neighborhood of the optimal mass. Fourth, the configuration with spins parallel and aligned to the orbital angular momentum are generically "louder" than those with spins parallel but anti-aligned with the orbital angular momentum, with the binaries having $a = \pm 1$ being the "loudest" and "quietest", respectively; this is essentially the answer to question *(i)* in the Introduction. [3]. Fifth, in the cases of the LIGO and advanced Virgo detectors the horizon distance is essentially zero at cut-off masses which are $\sim 900\, M_\odot$ and $\sim 3000\, M_\odot$, respectively. Sixth, for any fixed value of the total mass, the SNR grows with a and, as we will discuss later on, this growth is very well described with a polynomial of 4th order (*c.f.* discussion in Section 14.4). This is shown more clearly in Figure 14.3, which reports the maximum SNR $\rho_{\rm max}$ for the LIGO detector and for a given set of masses at a distance $d = 100\,{\rm Mpc}$. Note that the growth of $\rho_{\rm max}$ with a becomes steeper for masses $M > 200\, M_\odot$, for which the NR-part of the waveform and hence the plunge and ring-down phase dominates. In these cases, the SNR is more then doubled between $a = -1$ and $a = +1$. Finally, when going from the present LIGO/Virgo detectors to their advanced versions, the average horizon distances go from $\sim 600/800\,{\rm Mpc}$ to $\sim 10^4/1.2 \times 10^4\,{\rm Mpc}$, thus with an observational *volume* of the Universe that is increased by a factor of $\sim 5000/3000$, respectively. Note that if we assume an Hubble radius of $\sim 4.1\,{\rm Gpc}$, both detectors would effectively detect binaries within a large range of masses (*e.g.* $60 \lesssim M/M_\odot \lesssim 500$ for advanced LIGO) across the whole Universe.

---

[3] This behavior can be easily understood in terms of the orbital dynamics: the binaries with larger total angular momentum will have a larger number of cycles and hence a larger SNR

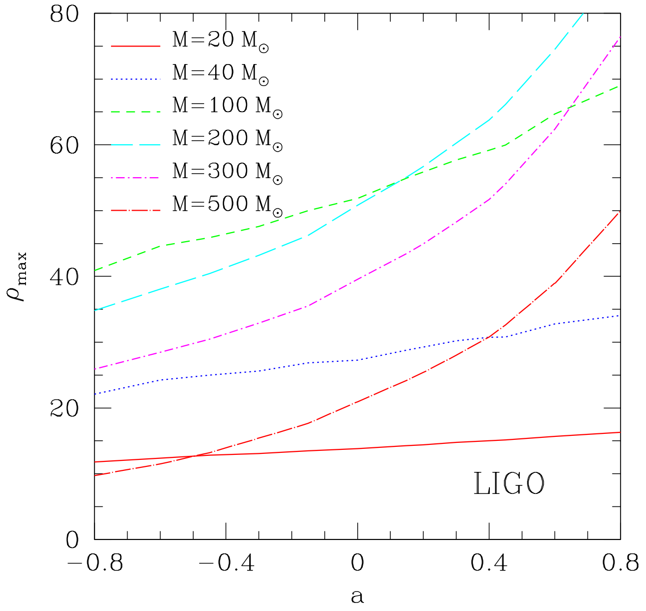

Figure 14.3: Maximum SNR $\rho_{\max} = \rho(a,\, M)$ for the LIGO detector for a given set of masses at a distance $d = 100\,\mathrm{Mpc}$. Note that the growth of $\rho_{\max}$ with a is very well described with a low-order polynomial which is of 4th order for the optimal mass (*c.f.* discussion in Section 14.4). Note also that the dependence on a becomes stronger for masses $M > 200\,M_\odot$, for which the NR-part of the waveform and hence the plunge and ring-down phase dominate. In these cases, the SNR is more then doubled between $a = -1$ and $a = +1$.

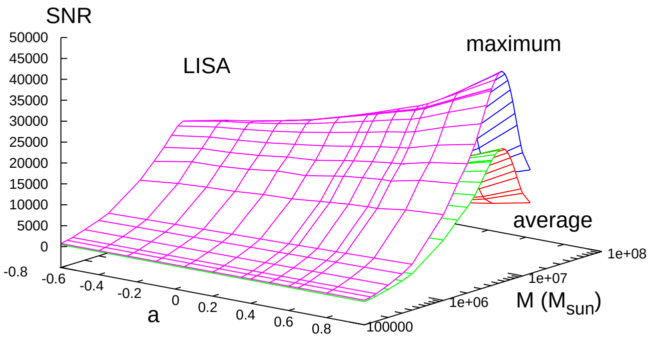

Figure 14.4: Averaged and maximum SNR $\rho = \rho(a, M)$ for the planned LISA mission and for sources at $d = 6.4\,\mathrm{Gpc}$ $(z = 1)$.

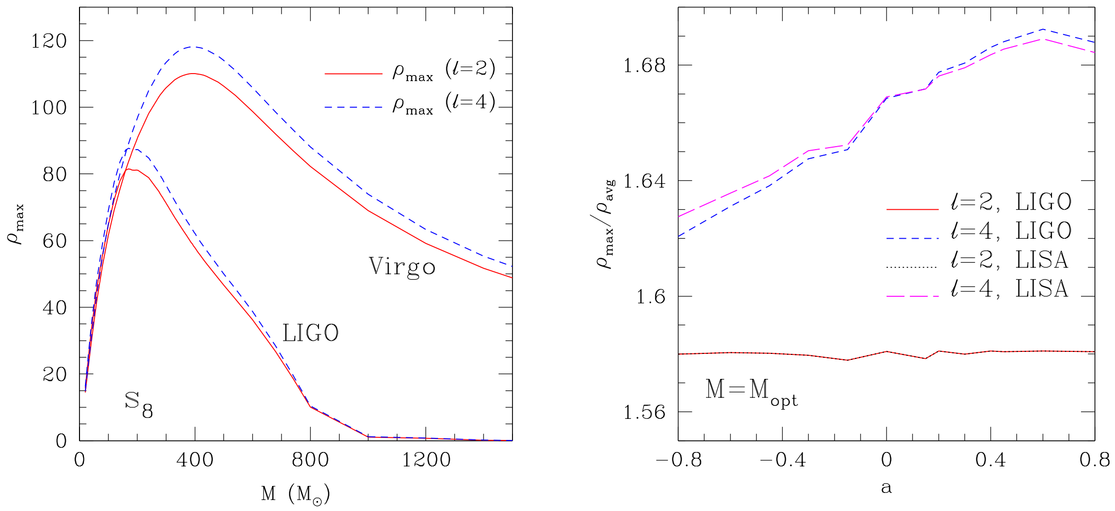

Figure 14.5: *Left panel:* maximum SNR $\rho_{\rm max}$ as a function of the mass for the highly spinning model s_8 and for the present detectors LIGO and Virgo. Different lines refer to the SNRs computed using only the $\ell = 2$ multipoles (continuous line), or up to the $\ell = 4$ multipoles (dashed line). *Right panel:* ratio between maximum and averaged SNR ρ as a function of the spins $a_1 = a_2$ for $M = 200\,M_\odot$ ($M = 3.53 \times 10^6\,M_\odot$) by including modes up to $\ell = 2$ and $\ell = 4$ for LIGO (LISA). In contrast to the case $\ell = 2$, the $\ell = 4$-curve is not constant but depends on the initial spins a_1, a_2

Figure 14.4 shows similar information but for the planned LISA mission. Since the horizon distance can well exceed the whole Hubble horizon, the figure reports the averaged and maximum SNR $\rho = \rho(a, M)$ for sources at $d = 6.4\,{\rm Gpc}$ ($z = 1$). Many of the considerations made above hold also for the LISA detector, and it is interesting to note that for sufficiently high and aligned spins (*i.e.* $a \gtrsim 0.8$), the SNR is $\gtrsim \mathcal{O}(10)$ already with binaries having masses $\gtrsim$ few $\times\, 10^3\,M_\odot$.

Finally, the most salient information of Figures 14.2 and 14.4 is collected in Table 14.2 which reports the properties of the "optimal" aligned binaries for the different detectors. More specifically, the Table reports in its different rows the optimal total aligned spin a, the optimal total mass in solar masses, the optimal maximum ρ and average $\rho_{\rm avg}$ SNRs, the optimal horizon distance d_H (expressed in Mpc and with H^{-1} being the Hubble radius), the optimal relative event rate R, and the glueing frequency $f_{\rm glue}$ for the optimal binary. The masses have been sampled with an accuracy of $2.5\,M_\odot$ for the ground-based detectors and of $2.5 \times 10^4\,M_\odot$ for LISA.

Influence of higher ℓ-modes

As discussed in Section 14.2, it is interesting to consider the impact that higher-order modes have on the SNR of equal-mass aligned binaries and some representative examples of this impact is shown in Figure 14.5. The left panel of this figure, in particular shows the maximum SNR $\rho_{\rm max}$ as a function of the mass for the highly spinning model s_8 and for the present detectors LIGO and Virgo. Different lines refer to the SNRs computed using only the $\ell = 2$ multipoles (continuous line), or up to the $\ell = 4$ multipoles (dashed line). Clearly, the contribution of the higher modes is most important near the optimal mass (*i.e.* $M \sim 200\,M_\odot$ for LIGO and $M \sim 400\,M_\odot$ for Virgo) but this is also non-negligible for larger masses, where it can produce an increase of $\sim 8\%$ in SNR in a detector such as Virgo.

The right panel of Figure 14.5, on the other hand, shows the ratio between maximum and averaged SNR as a function of the total projected spin a for a binary of $M = 200\,M_\odot$ ($5.35 \times 10^6\,M_\odot$) and the LIGO (LISA) detector. As mentioned in Section 14.2, this ratio is not expressed by

Table 14.2: Properties of the "optimal" aligned binaries for the different detectors. Shown in the different rows are the optimal total aligned spin a, the optimal total mass in solar masses, the optimal maximum $\rho_{\rm max}$ and average $\rho_{\rm avg}$ SNRs, the optimal horizon distance d_H (expressed in Mpc and where cH^{-1} is the Hubble radius), the lower bound for the optimal relative event rate R, and the glueing frequency $f_{\rm glue}$ for the optimal binary. The masses have been sampled with an accuracy of $2.5\,M_\odot$ for the ground-based detectors and of $2.5 \times 10^4\,M_\odot$ for LISA.

	LIGO	eLIGO	AdLIGO	Virgo	AdVirgo	LISA
a	0.8	0.8	0.8	0.8	0.8	0.8
$M_{\rm opt}$ $(M_\odot)$	197	180	290	395	390	5.35×10^6
$\rho_{\rm max}$	87	175	1667	118	1591	2.91×10^6
$\rho_{\rm avg}$	52	104	991	70	944	1.77×10^6
d_H (Mpc)	1091	2190	$> cH^{-1}$	1476	$> cH^{-1}$	$> cH^{-1}$
R	18	17	16	16	17	26
$f_{\rm glue}$ (Hz)	27.48	30.51	18.71	13.74	13.91	1.0×10^{-3}

a simple algebraic expression [*c.f.* equation (14.2.9)], but needs to be determined numerically. Interestingly, this ratio is not constant but increases by $\sim$ 10% for larger total projected spins, underlining the importance of higher-order contributions as the initial spins increase. Overall, therefore, Figure 14.5 provides the answer to question *(iii)* in the Introduction.

Match between different models

A quantity providing a wealth of information is the match between the amplitudes of the waveforms from two different binaries, so as to quantify the differences in the gravitational-wave signal relative to some reference models. The match between two waveforms $h_1(t)$ and $h_2(t)$ (or a template and a waveform) can be calculated via the weighted scalar product in frequency space between two given waveforms

$$\langle h_1 | h_2 \rangle = 4 \mathrm{Re} \int_0^\infty df \frac{\tilde{h}_1(f) \tilde{h}_2^*(f)}{S_h(f)} \,, \tag{14.3.2}$$

where $\tilde{h}_1(f)$ is the power spectral density of $h_1(t)$, the asterisk indicates a complex conjugate, and $S_h(f)$ is the noise power spectral density of a given detector. The overlap is then simply given by the normalized scalar product

$$\mathcal{O}[h_1, h_2] = \frac{\langle h_1 | h_2 \rangle}{\sqrt{\langle h_1 | h_1 \rangle \langle h_2 | h_2 \rangle}} . \tag{14.3.3}$$

Two parameters need to be taken into account when computing the overlap. The first one is the "time of arrival" $t_{\rm A}$ corresponding to an offset in the Fourier-transform of the signal $\exp\,[\mathrm{i}\omega(t - t_{\rm A})]$. The second one is the "initial phase" Φ of the orbital motion when it enters the detector band.

For both of these parameters the overlap should be maximized. We have considered two possible ways of doing this. The first approach involves the *best* match, which gives an upper bound by maximizing over both of the phases of each waveform

$$\mathcal{M}_{\rm best} \equiv \max_{t_{\rm A}} \max_{\Phi_1} \max_{\Phi_2} \{ \mathcal{O}[h_1, h_2] \} . \tag{14.3.4}$$

The second way, instead, involves the *minimax* match, and is obtained by maximizing over the phase of one waveform but minimizing over the phase of the other

$$\mathcal{M}_{\rm minimax} \equiv \max_{t_{\rm A}} \min_{\Phi_2} \max_{\Phi_1} \{ \mathcal{O}[h_1, h_2] \} , \tag{14.3.5}$$

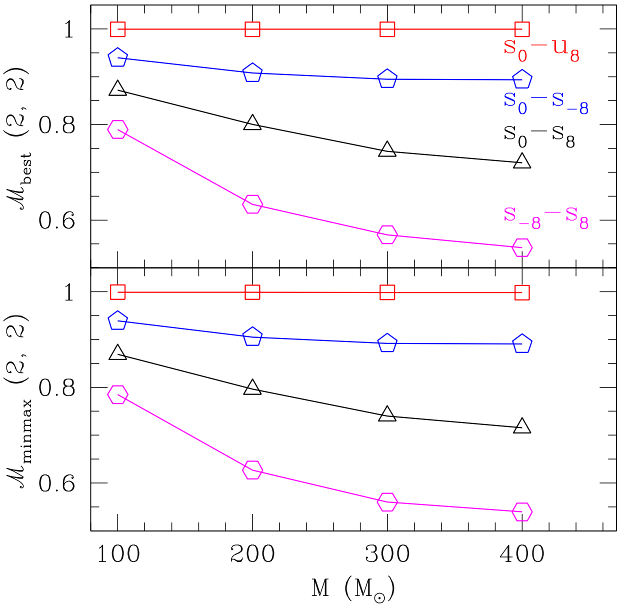

Figure 14.6: Best and minmax match as a function of mass for a waveform containing only the $\ell = 2, m = 2$ contribution and referring to the LIGO detector. Very similar behaviors can be shown also for the other detectors.

and thus represents a "worst-case" scenario since it gives lower matches although one is maximizing over the template phase. More details on the maximization procedure can be found in [424, 480]. Note that all the matches computed hereafter refer to the NR part of the waveform only.

A sensible way, if not the most sensible way, of evaluating expressions (14.3.4) and (14.3.5) is to use the binary s_0, the non-spinning binary, as a reference and to compute the overlap with the binaries at representative locations in the spin diagram, *e.g.* at the corners for $s_0 - s_8$, $s_0 - u_8$, $s_0 - s_{-8}$, or along the main diagonal, *e.g.* $s_{-8} - s_8$. In this way we can assess whether the waveform produced by a non-spinning binary can be used to detect also spinning binaries and how much the overlap is decreased in this case.

This is shown in Figure 14.6, which reports the best and minmax matches as a function of mass for a waveform containing only the $\ell = 2, m = 2$ contribution and refers to the LIGO detector. Different lines show the match computed between s_0 and other representative binaries, and show the remarkable similarity between the waveforms of binaries having a zero total spin. This is shown by the $s_0 - u_8$ match, which is essentially very close to 1 for all the masses considered (*c.f.* also Table 14.3). This result extends to all the other measured quantities, such as the radiated energy or angular momentum, and is not particularly surprising. Indeed, it was already discussed by [424], although the investigation in that case was restricted to what is here the u-sequence. In addition, the equivalence between non-spinning binaries and binaries with equal and opposite spins has been exploited in the derivation of expressions for the final spin presented in a series of works [57–59, 481]. The results of Figure 14.6 and Table 14.3 are therefore a simple example, although probably not the only possible one, of a well defined region of the space of initial configurations (*i.e.* those of binaries with equal masses and opposite spins) which can be mapped to an almost degenerate region (*i.e.* essentially to a single point) in the space of templates. This is the answer to question *(iv)* in the Introduction and clearly represents a serious obstacle towards a proper estimate of physical parameters of the binaries that may be removed, at least in part, only if the waveform is measured with a sufficiently high SNR. A proper discussion of this problem, as well as the determination of other degenerate patches in the space of templates, will be the subject of future work.

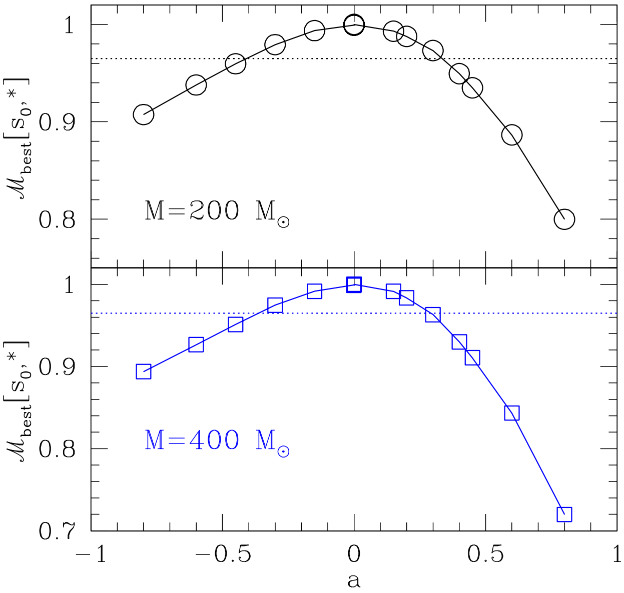

Figure 14.7: Best match as a function of the total projected spin a for a waveform containing only the $\ell = 2, m = 2$ contribution. The top/lower panels refers to binary with a total mass (200/400 $M_\odot$) which are close to the optimal ones for the LIGO/Virgo or advanced detectors, respectively. In both panels the dotted line shows the minimum best match (0.965) needed for a detection. While the data have been computed for the LIGO detector, very similar behaviors can be shown also for the other detectors.

An equally remarkable result, presented in Figure 14.6, is that the overlap is also very high between the non-spinning binary and the binary with equal and anti-aligned spins, $s_0 - s_{-8}$; also in this case, in fact, the best match is $\mathcal{M}_{\rm best} \gtrsim 0.9$ for the range of masses that is relevant here. Slightly smaller and decreasing with increasing masses are the best matches computed when comparing the non-spinning binary with the binary of parallel and aligned spins, so that $\mathcal{M}_{\rm best} \sim 0.8$, but only for very large masses. The waveforms appear clearly different (*i.e.* with $\mathcal{M}_{\rm best} \lesssim 0.6$) only when comparing the binaries along the main diagonal of the spin diagram, for $s_8 - s_{-8}$, although even in this rather extreme case the differences tend to become smaller for smaller masses. Overall, this result underlines that even simple waveforms, such as those relative to non-spinning binaries, will be effective enough to provide a detection for most configurations of equal-mass and aligned/anti-aligned binaries.

A different way to assess "how different" the waveforms are across all of the equal-mass aligned / anti-aligned spins configurations considered here is nicely summarized in Figure 14.7, which shows the best match as a function of the total projected spin a for waveforms containing only the $\ell = 2, m = 2$ contribution and referring to the LIGO detector. The top panel, in particular, refers to binary with a total mass of 200 $M_\odot$ that is close to the optimal one for the LIGO/Virgo detectors, while the bottom panel refers to a binary with mass 400 $M_\odot$ and close to the optimal one for the advanced LIGO/Virgo detectors (*c.f.* Table 14.3). Besides the remarkably smooth behavior of $\mathcal{M}_{\rm best}$ across all the values of a considered, it is clear that the waveform from a non-spinning binary can be extremely useful across the *whole* spin diagram and yield very large overlaps even for binaries with very high spins. In both panels, in fact, the dotted line shows the minimum best match ($\mathcal{M}_{\rm best} = 0.965$) needed for a detection [482]. This result is reassuring in light of the fact that most of the searches in the detector data are made using phenomenological waveforms based on non-spinning binaries.

For completeness, the results presented in Figure 14.6 (as well as those in Figure 14.8) are also reported in Table 14.3, where the different columns show $\mathcal{M}_{\rm best}$ and $\mathcal{M}_{\rm minmax}$ and for waveforms computed either using only the $\ell = 2, m = 2$ contribution (third and fourth columns), only the $\ell = 3, m = 2$ contribution (fifth and sixth columns), or all contributions up to $\ell = 4$ (last two columns). Interestingly, the matches among the high-order modes, *e.g.* $(s_0)_{\ell=3,m=2} - (u_8)_{\ell=3,m=2}$, is systematically higher than those of the lower ones and remains true even for higher modes beyond $\ell = 3, m = 2$, which however, we do not report here. This indicates that in order to do high-precision parameter estimation by including higher modes it is also important that these modes are accurately resolved, so that they can be clearly distinguished from one another.

We generally expect the match to degrade when the waveforms are computed by including higher-order modes (*e.g.* up to $\ell = 4$) and that this degradation will become larger with increasing inclination θ. The most notable example is for the degeneracy along the diagonal $a_1 = -a_2$, which should be broken by the inclusion of higher-order modes (We recall that these configurations lead to different recoil velocities [57] which can only be produced by gravitational-wave contributions other than the leading order $\ell = m = 2$ mode). For this reason we have computed the sky-averaged match of waveforms including modes up to $\ell = 4$ (*i.e.* the “complete” waveforms) and the corresponding matches are reported in the last two columns of Table 14.3. Similarly to what found in [424], we measure a marked decreased in the minmax match, but a much smaller decrease in the best match (the latter was not considered in [424]). Although our resolution should be marginally enough for us to detect such a difference in the best match, we also believe that a much higher accuracy is required to determine this with certainty. Note also that the matches with complete waveforms along other directions, *e.g.* $s_0 - s_8$ or $s_0 - s_{-8}$ do not decrease and this is simply due to the very large mismatch we already have with the $\ell = 2 = m$-waveforms (in these cases, in fact, the final BHs are considerably different and hence the associated ring-downs are expected to be different).

Finally, we note that although Figs 14.6 and 14.7 show data computed for the LIGO detector, very similar behaviors can be shown also for the other detectors.

Accuracy of NR waveform amplitudes

A reasonable concern that can be raised when looking the very high matches between the waveforms in the u-sequence is that these are simply the result of insufficient resolution. In other words, the waveforms may appear similar simply because our resolution is not sufficient to pick-up the differences. To address this concern we have computed the overlap among the waveforms obtained at three different resolutions and for a representative binary with nonzero spins, *i.e.* r_0. Clearly, a low match in this case would be an indication that our results are very sensitive to the numerical resolution and hence the conclusions drawn on the degeneracy of the space of templates would be incorrect.

The results of this validation are presented in Figure 14.8 and are reported in the last eight rows of Table 14.3. More specifically, shown with different lines in Figure 14.8 are the matches obtained when comparing the numerical waveforms of the binary r_0 computed at low resolution ($\Delta x/M = 0.024$) and medium resolution ($\Delta x/M = 0.020$, which is also the standard one), as well as at a medium and high resolution ($\Delta x/M = 0.018$). The matches are computed considering only the $\ell = 2, m = 2$ mode and for the LIGO detector, but very similar behaviors can be shown also for higher modes or for the other detectors.

Overall, the results reported in Figure 14.8 and in Table 14.3 show that $\mathcal{M}_{\rm best,minmax}[\Delta x_1, \Delta x_2] > \mathcal{M}_{\rm best,minmax}[h_1, h_2]$, *i.e.* that the differences we measure in the overlaps among two different waveforms h_1 and h_2 are always larger than the differences we are able to measure at two different resolutions Δx_1 and Δx_2. In other words, the differences in the waveforms across the spin diagram are always larger than our numerical errors, even along the degenerate u-sequence (of course, as we have a convergent numerical code, the match between medium and low resolution is worse than the match between medium and high resolution). It is also worth mentioning that as long as the dominant $\ell = 2, m = 2$ mode is considered, the differences in the matches are well within the margin of error for numerical relativity simulations of BH binaries. A recent work has in fact estimated that the differences in the waveforms produced by distinct codes is $\mathcal{M}_{\rm mismatch} = 1-\mathcal{M} \approx$

Table 14.3: Best and minmax matches as computed for the LIGO detector for binaries with different spins in the spin diagram. Different columns show $\mathcal{M}_{\rm best}$ and $\mathcal{M}_{\rm minmax}$ for waveforms computed either using only the $\ell = 2, m = 2$ contribution (third and fourth columns), only the $\ell = 3, m = 2$ contribution (fifth and sixth columns), or the sky-averaged contributions of all modes up to $\ell = 4$ (last two columns). Finally the last eight rows show the matches at different resolutions (*i.e.* $\Delta x/M = 0.024, 0.020, 0.018$) for the binary r_0.

	$M/M_\odot$	$\mathcal{M}_{\rm best}$ only $\ell = 2, m = 2$	$\mathcal{M}_{\rm minmax}$ only $\ell = 2, m = 2$	$\mathcal{M}_{\rm best}$ only $\ell = 3, m = 2$	$\mathcal{M}_{\rm minmax}$ only $\ell = 3, m = 2$	$\mathcal{M}_{\rm best}$ avg. up to $\ell = 4$	$\mathcal{M}_{\rm minmax}$ avg. up to $\ell = 4$
$s_0 - s_8$	100	0.87182	0.86914	0.87802	0.85061	0.86337	0.83272
	200	0.79987	0.79642	0.82533	0.80236	0.80070	0.75679
	300	0.74394	0.74026	0.82570	0.78819	0.74785	0.71139
	400	0.71981	0.71568	0.84074	0.81285	0.72345	0.69019
$s_0 - u_8$	100	0.99926	0.99914	0.99497	0.97411	0.99673	0.95443
	200	0.99928	0.99906	0.99372	0.95193	0.99483	0.95919
	300	0.99923	0.99870	0.99189	0.93888	0.99251	0.96105
	400	0.99919	0.99822	0.99147	0.93493	0.99110	0.96054
$s_0 - s_{-8}$	100	0.93942	0.93907	0.95717	0.94843	0.93695	0.92143
	200	0.90746	0.90536	0.95647	0.94521	0.89646	0.88041
	300	0.89491	0.89197	0.95015	0.93814	0.87303	0.84960
	400	0.89369	0.89065	0.94806	0.93550	0.85492	0.82103
$s_{-8} - s_8$	100	0.78948	0.78493	0.87041	0.85222	0.78310	0.74895
	200	0.63309	0.62703	0.90722	0.88543	0.63456	0.59426
	300	0.56934	0.56008	0.90322	0.88869	0.56941	0.52170
	400	0.54235	0.53960	0.91199	0.89848	0.55470	0.49338
$s_{-8} - u_8$	100	0.94250	0.94187	0.96299	0.94669	0.93897	0.89017
	200	0.91444	0.91229	0.96316	0.93068	0.90315	0.85958
	300	0.90188	0.89885	0.95486	0.91256	0.87846	0.83428
	400	0.89772	0.89492	0.95132	0.90583	0.85870	0.80907
$s_8 - u_8$	100	0.87127	0.86817	0.87656	0.84229	0.85866	0.80969
	200	0.79750	0.79477	0.83582	0.81476	0.79074	0.73526
	300	0.74063	0.73884	0.83897	0.80378	0.73616	0.68774
	400	0.71798	0.71343	0.84955	0.81925	0.71203	0.66611
r_0 $(0.024, 0.020)$	100	0.99979	0.99970	0.99495	0.98812	0.99855	0.99463
	200	0.99963	0.99929	0.99133	0.97100	0.99633	0.98800
	300	0.99943	0.99894	0.98752	0.95775	0.99379	0.98152
	400	0.99924	0.99868	0.98630	0.95317	0.99209	0.97683
r_0 $(0.020, 0.018)$	100	0.99990	0.99989	0.99873	0.99299	0.99881	0.99639
	200	0.99980	0.99970	0.99806	0.98074	0.99705	0.98952
	300	0.99956	0.99924	0.99707	0.97238	0.99497	0.98070
	400	0.99935	0.99866	0.99666	0.97017	0.99320	0.97429

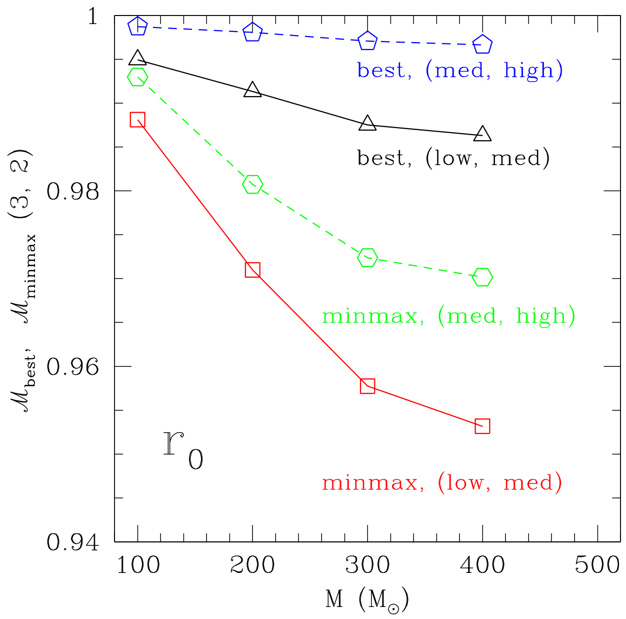

Figure 14.8: As in Figure 14.7 but now different lines represent the matches obtained when comparing the numerical waveforms of the binary r_0 computed at different resolutions. The matches are computed for the LIGO detector, but very similar behaviors can be shown also for the other detectors.

10^{-4} for the last $\approx 1000M$ of the dominant mode of non-spinning equal mass coalescence [61]. Since the next higher mode $\ell = 3, m = 2$ starts to suffer from numerical noise, it does not yield the same high agreement, and the differences between best and minimax match show a larger deviation.

A systematic source of error in the results given in this work is the finite radius $r_{\rm E} = 160\,M$ at which our waveforms are computed. In order to determine its influence on the accuracy of the values reported here, we have exploited the recent possibility of computing waveforms unambiguously at future null infinity $\mathcal{J}^+$ [50]. In this approach, which makes use of the Cauchy-characteristic extraction technique [272, 275, 277, 328, 330], the gravitational-wave information Ψ_4 is computed at $\mathcal{J}^+$ in a gauge invariant way and with no causal influence from the outer boundary (see Section 15.2).

In practice, we have computed the match between the waveforms extracted at $r_{\rm E}$ and at $\mathcal{J}^+$ for the non-spinning configuration s_0, and found that $\mathcal{M}_{\rm best} = 0.999$, which is thus within the error given by the match between different numerical resolutions (*c.f.* discussion in Section 14.3 and see also Table 14.3). Note that the initial separation of the two BHs as reported in [50], $d = 11\,M$, is larger than the one reported here, thus resulting in a much smaller initial frequency $\omega_{\rm ini}$. Nevertheless, we have considered the same glueing frequency $\omega_{\rm glue} = 0.168/M$ so as to have a fair comparison between the two waveforms.

In addition, we have also compared SNRs obtained in the two cases, when the Fourier-transform of $h(t)$ as given in terms of Ψ_4 is easily obtained as

$$\tilde{h}(f) = -\frac{\widetilde{\Psi}_4}{4\pi^2 f^2} \tag{14.3.6}$$

where $\widetilde{\Psi}_4$ is the Fourier-transform of Ψ_4. For any of the total masses considered here and for all of the detectors, we find that the differences in the SNRs is less than 1.0%. Overall, both results show that the error introduced by the use of a finite radius calculation is within our numerical error-bars of $\sim 2.0\%$ and thus does not modify significantly the results obtained in this work.

14.4 Fitting formulas

In what follows, we provide some simple analytic representation of most of the results presented in the previous sections and, in particular, We give a brief discussion of fitting expressions that can be derived to express the SNR for an optimal mass and the energy radiated in gravitational waves.

SNR

As discussed in Section 14.2, the maximum SNR depends on several factors, most notably on the two initial spins, the total mass of the system and, although more weakly, on the number of multipoles included in the waveforms. The resulting functional dependencies when one degree of freedom is suppressed and the SNRs are presented in terms of the total projected spin are shown in Figures 14.2, 14.4 and are clearly too cumbersome to be described analytically (although still possible).

However, most of the complex functional dependence can still be captured when concentrating on the best case scenario, and hence on the SNRs relative to the optimal mass $M_{\rm opt}$. The behavior of the SNR in this case is shown in Figure 14.9, where the different symbols show the numerically computed values of $\rho_{\rm max}(a, M_{\rm opt})$ for the different detectors. Stated differently, Figure 14.9 represents the cross section along the optimal mass of Figures 14.2 and 14.4 (note that the SNR for the advanced detectors have been divided by 7 to make them fit onto the same scale).

Clearly, the behavior of the SNR in this case is sufficiently simple that it can be represented with a simple quartic polynomial of the type

$$\rho_{\rm max}(a;\, \ell \leq 4, M = M_{\rm opt}) = \sum_{n=0}^{4} k_n a^n \,, \tag{14.4.1}$$

whose coefficients k_n are reported in Table 14.4 for the five detectors considered.

These results address therefore question *(ii)* formulated in the Introduction. More specifically, when considering the optimal mass, the ratio of the SNRs for maximally anti-aligned spinning binaries to maximally and aligned spinning binaries, *i.e.* $\rho_{\rm max}(a = 1)/\rho_{\rm max}(a = -1)$ is ~ 3 for both the LIGO and Virgo detectors. This ratio is also preserved when considering the advanced LIGO and Virgo detectors. Because the event rate scales like the cube of the SNR [*c.f.* expressions (14.2.9)-(14.2.12)], an increase of a factor ~ 3 in the SNR of binaries with $a = -1$ and $a = 1$ will translate into an increase of a factor ~ 27 in the event rate. It is therefore likely that many of the binaries observed will have high spins and aligned with the orbital angular momentum. This will be particularly true in the case of LISA if the prediction that the spins of SMBHs are aligned with the orbital angular momentum will hold [407].

Radiated energy

While the SNR is effectively a measure of the amount of energy released during the inspiral, it also incorporates information on the properties of the detectors and is not therefore an absolute measure of the efficiency of the gravitational-wave emission process. This information can have a number of important astrophysical applications, and in particular it can be used to study the effect the merger has on the dynamics of the circumbinary disk accreting onto the binary when this is massive (see [29] for the first suggestion and [30] for a recent nonlinear study).

In this section we present a simple formula to compute the amount of energy released and express it only in terms of the initial spins. Our formula is restricted to aligned binaries and is therefore not as generic as the one recently presented in [483], which however also requires the determination of a larger set of coefficients, some of which have uncertainties of $\sim 100\%$. As we will show below, the two expressions yield results in reasonably good agreement, at least in the part of the parameter space we investigate.

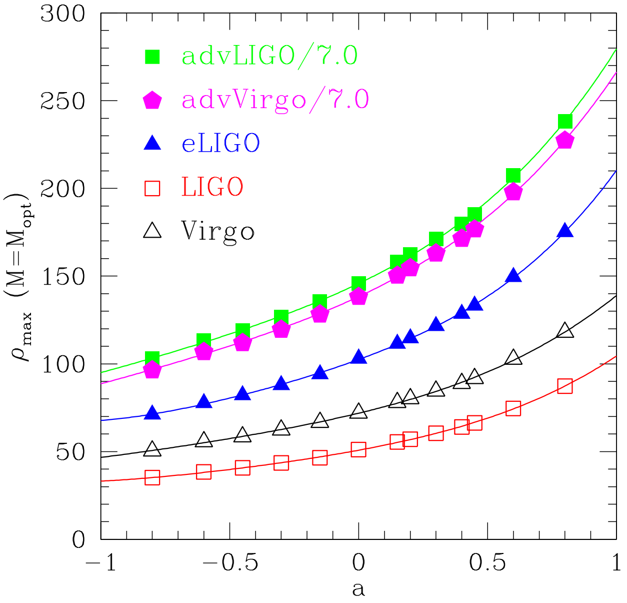

Figure 14.9: Different symbols show the numerically computed values of $\rho_{\rm max}(a, M_{\rm opt})$ for the different detectors and represent therefore the cross section along the optimal mass of Figures 14.2 and 14.4. Note that the SNR for the advanced detectors have been divided by 7 to make them fit onto the same scale.

Table 14.4: Fitting coefficients for the maximum SNR computed for the optimal mass [*c.f.* eq. (14.4.1)]. The different rows refer to the various detectors and have been computed including all modes up to $\ell = 4$.

detector	k_0	k_1	k_2	k_3	k_4
LIGO	50.76	27.11	13.43	8.58	4.63
eLIGO	102.45	53.63	25.33	17.67	11.26
AdLIGO	1020.42	492.25	243.60	153.84	46.99
Virgo	71.86	35.23	17.140	10.92	3.789
AdVirgo	968.08	481.52	236.45	140.69	37.91

In practice, the expression for the radiated energy $E_{\rm rad}$ is derived by combining a fit to the numerical data for the binaries at an initial and finite separation $d = 8\,M$ [4] (we refer to this energy as to $E^{\rm NR}_{\rm rad}$), with the estimate of the energy released from the binary when it goes from an infinite separation down to d (we refer to this energy as $E^{\rm PN}_{\rm rad}$), *i.e.*

$$E_{\rm rad} = E^{\rm NR}_{\rm rad} + E^{\rm PN}_{\rm rad} = M_{\rm ADM} - M_{\rm fin} + E^{\rm PN}_{\rm rad} \tag{14.4.2}$$

where $M_{\rm ADM}$ is the initial ADM mass as measured at spatial infinity of the binary with separation d, and $M_{\rm fin}$ the Christodoulou mass of the final BH [5]. For the fit of the radiated energy during the numerical evolution, $E^{\rm NR}_{\rm rad}$, we use the same symmetry arguments first made in [57] and then successfully used in [58, 59, 481] to write a simple expression which is a Taylor expansion in terms of the initial spins

$$\frac{E^{\rm NR}_{\rm rad}(q=1,a_1,a_2)}{M} = p_0 + p_1(a_1+a_2) + p_2(a_1+a_2)^2\,. \tag{14.4.3}$$

Fitting then the numerical data we obtain the following values for the coefficients

$$\begin{aligned} p_0 &= \frac{3.606 \pm 0.0271}{100}\,, \qquad p_1 = \frac{1.493 \pm 0.0260}{100}\,,\\ p_2 &= \frac{0.489 \pm 0.0254}{100}\,. \end{aligned} \tag{14.4.4}$$

where the reduced chi-squared is $\chi^2_{\rm red} = 0.008$, and where the largest error is in the 2nd-order coefficient but this is only $\sim 5\%$. Expressed in this way, the different coefficients (14.4.4) can then be interpreted as the non-spinning orbital contribution to the energy loss (p_0, which is the largest and of $\sim 3.6\%$), the spin-orbit contribution (p_1, which is $\lesssim 3.0\%$), and the spin-spin contribution (p_2, which is $\lesssim 2.0\%$). The relative error between the numerically computed value of $E^{\rm NR}_{\rm rad}$ and the fitted one is reported in the last column of Table 11.2.

The PN expression for the energy radiated by the binary when going from an infinite separation down to a finite one $r = d$, depends on the total mass of the binary, the mass ratio and the spin components, *i.e.* $E^{\rm PN}_{\rm rad} = E^{\rm PN}_{\rm rad}(r, M, \nu, a_1, a_2)$, which is the generalization to unequal masses of the energy expression used in the definition of the TaylorT1 approximant in [367]. However, following the spirit of deriving a simple expression that is as compact as possible and exploiting the fact that, for equal-mass binaries, the PN radiated energy $E^{\rm PN}_{\rm rad}$ follows the same series expansion used for $E^{\rm NR}_{\rm rad}$, namely a polynomial of the total spin, in this case, setting $M = 1 = q$ we obtain

$$\begin{aligned} \frac{E^{\rm PN}_{\rm rad}(a_1,a_2)}{M} &= E^{\rm PN}_{\rm rad,0}\\ &\quad + E^{\rm PN}_{\rm rad,1}(a_1+a_2) + E^{\rm PN}_{\rm rad,2}(a_1+a_2)^2\,, \end{aligned} \tag{14.4.5}$$

where the coefficients for $d = 8\,M$ are given by

$$\begin{aligned} E^{\rm PN}_{\rm rad,0} &= \frac{6401}{524288} \simeq \frac{1.220}{100}\,,\\ E^{\rm PN}_{\rm rad,1} &= \frac{985}{1048576\sqrt{2}} \simeq \frac{0.0664}{100}\,,\\ E^{\rm PN}_{\rm rad,2} &= -\frac{1}{32768} \simeq -\frac{0.00305}{100}\,. \end{aligned} \tag{14.4.6}$$

A rapid inspection of the coefficients (14.4.6) is sufficient to appreciate that the PN orbital contribution is only $\sim 33\%$, the one of the strong-field regime, but also that the spin-related PN contributions are mostly negligible, being at most of $\sim 4\%$ as produced in the last orbits.

---

[4] Note that for the binary s_0, we use an initial separation of $d = 10M$. In order to obtain the radiated energy obtained during a simulation starting from an initial separation of $d = 8M$, we only need to recalculate the initial ADM mass of the spacetime for this initial separation. The final mass of the remnant is in fact the same.

[5] Note that $M_{\rm ADM} + E^{\rm PN}_{\rm rad}$ is effectively the mass of the system when it has an infinite separation. This is approximately set to 1 in most simulations but with a precision which is smaller than the one needed here.

We can now combine expressions (14.4.3)-(14.4.4) with expressions (14.4.5)-(14.4.6) and estimate that for equal-mass binaries with aligned spins the energy radiated via gravitational waves from infinity is

$$\frac{E_{\rm rad}(a_1,a_2)}{M} = \tilde{p}_0 + \tilde{p}_1(a_1+a_2) + \tilde{p}_2(a_1+a_2)^2\,, \tag{14.4.7}$$

where

$$\tilde{p}_0 = \frac{4.826}{100}\,, \qquad \tilde{p}_1 = \frac{1.559}{100}\,, \qquad \tilde{p}_2 = \frac{0.485}{100}\,. \tag{14.4.8}$$

Of course these numbers are specific to equal-mass binaries and refer to a situation in which the match between the PN evolution and the one in the strong-field regime is made at a specific separation of $d = 8\,M$. However, we expect the results to depend only weakly on this matching separation (as long as it is within a PN regime) and hence that expressions (14.4.7) and (14.4.8) are generically valid at the precision we are considering them here, namely $\sim 5\%$.

Using expression (14.4.7) a number of quantitative considerations are possible. Firstly, the largest energy is clearly emitted by equal-mass, maximally spinning binaries with spins parallel and aligned with the orbital angular momentum at is $E_{\rm rad}(a=1)/M = 9.9\%$. With the exclusion of the astrophysically unlikely head-on collision of two BHs moving near the speed of light (in which case $E_{\rm rad} < 14 \pm 3\%$ [484]), these binaries are therefore among the most efficient sources of energy in the Universe. Secondly, equal-mass non-spinning binaries lose a considerable fraction of their mass via radiation, with $E_{\rm rad}(a=0)/M = 4.8\%$, while maximally spinning binaries with spins parallel and anti-aligned with the orbital angular momentum have $E_{\rm rad}(a=-1)/M = 3.7\%$.

Note that expression (14.4.7) is not a strictly monotonic function of the total spin and has a local minimum at $a_1 = a_2 = -\tilde{p}_1/(4\tilde{p}_2) \simeq -0.8$ rather than at $a_1 = a_2 = -1$, and yields $E_{\rm rad}(a=-0.79)/M = 3.6\%$ (*c.f.* Figure 14.10). Although rather shallow, we do not expect such a local minimum. We therefore interpret it as an artifact of the numerical error of our calculations (the difference between the energy radiated at $a_1 = a_2 = -1$ and that at $a_1 = a_2 = -0.8$ is $\sim 2\%$ and hence compatible with our overall error). Such a local minimum can be removed by adding higher-order terms in expression (14.4.3) (*e.g.* up to 4th order in $a_1 + a_2$) but these improvements are so small that they do not justify the use of a more cumbersome expression. A comparison between the numerical values and the fitting expression 14.4.7 is shown in Figure 14.10, where crosses and squares represent the $E^{\rm NR}_{\rm rad}$ and $E_{\rm rad}$ respectively, along the diagonal of the spin-diagram (*i.e.* for $a_1 = a_2$), while the continuous line refers to our fitting expression. Note that such a line is a 1-dimensional cut of a 2-dimensional surface and hence it is not expected to exactly fit all points.

As mentioned above, Lousto and collaborators have recently proposed a more general formula that should account for the radiated energy in all of the relevant space of parameters, namely for binaries with arbitrary mass ratio, spin orientation and size [483]. Restricting their expression to the specific subset of binaries considered here corresponds to setting in their expression (2): $E_B = E_E = 0$, $\nu = 1/4$ and $q = 1$. The resulting expression is then

$$\begin{aligned} \frac{E^{\rm RIT}_{\rm rad}}{M} &= \frac{1}{4}E_{\rm ISCO} + \frac{1}{16}E_2 + \frac{1}{64}E_3 \\ &+ \frac{1}{64}\left[E_S(a_1+a_2) + E_A(a_1+a_2)^2\right. \\ &+ \left. E_D(a_1-a_2)^2\right]\,, \end{aligned} \tag{14.4.9}$$

where the fitting coefficients have been determined to be $E_2 = 0.341 \pm 0.014$, $E_3 = 0.522 \pm 0.062$, $E_S = 0.673 \pm 0.035$, $E_A = -0.014 \pm 0.021$, $E_D = -0.26 \pm 0.44$ [483], and where

$$\begin{aligned} E_{\rm ISCO} = &\left(1 - \frac{\sqrt{8}}{3}\right) + \frac{0.103803}{4} \\ &+ \frac{1}{48\sqrt{3}}(a_1+a_2) + \frac{5}{648\sqrt{2}}(a_1-a_2)^2\,. \end{aligned} \tag{14.4.10}$$

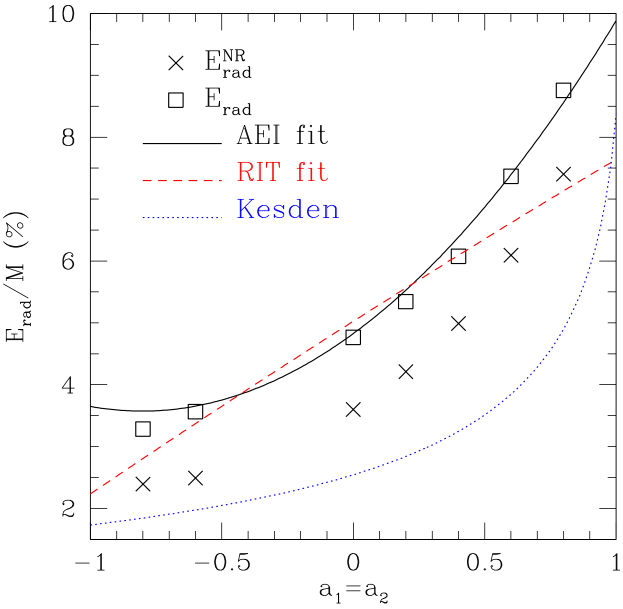

Figure 14.10: Energy radiated during the numerical calculation $E_{\text{rad}}^{\text{NR}}$ (crosses), the total radiated energy $E_{\text{rad}} = E_{\text{rad}}^{\text{NR}} + E_{\text{rad}}^{\text{PN}}$ (squares) along the diagonal of the spin diagram, *i.e.* for $a_1 = a_2$. Shown as a continuous line is the analytic expressions given here (AEI fit), while the dashed line is the one suggested in [483] (RIT fit). Note that the lines represent 1-dimensional cuts of 2-dimensional surfaces and hence are not expected to fit well all points. Finally, indicated with a dotted line is the prediction for the radiated energy coming from the point-particle approach of [450] and refined in [485].

After a bit of algebra we can rewrite (14.4.10) as

$$\frac{E^{\rm RIT}_{\rm rad}(a_1,a_2)}{M} = \tilde{q}_0 + \tilde{q}_1(a_1+a_2) + \tilde{q}_2(a_1+a_2)^2 + \tilde{q}_3(a_1-a_2)^2\,, \qquad (14.4.11)$$

where now

$$\begin{aligned}
\tilde{q}_0 &= \frac{1}{4}\left(1-\frac{\sqrt{8}}{3}+\frac{0.103803}{4}\right)+\frac{E_2}{16}+\frac{E_3}{64} \simeq \frac{5.025}{100}\,,\\
\tilde{q}_1 &= \frac{1}{192\sqrt{3}}+\frac{E_S}{64} \simeq \frac{1.352}{100}\,,\\
\tilde{q}_2 &= \frac{E_A}{64} \simeq -\frac{0.0219}{100}\,,\\
\tilde{q}_3 &= \frac{5}{2592\sqrt{2}}+\frac{E_D}{64} \simeq -\frac{0.270}{100}\,. \qquad (14.4.12)
\end{aligned}$$

Comparing (14.4.7)-(14.4.8) with (14.4.11)-(14.4.12) is now straightforward and shows that: the reduced expression from [483] has a second order contribution $\sim (a_1-a_2)^2$, which is absent in our expression. The remaining coefficients are rather similar but not identical. This comparison is summarized in Figure 14.10, where the dashed line corresponds to the fitting proposed in [483]. Note that the maximum efficiency for maximally spinning BHs predicted by expression (14.4.11) is $\sim 8\%$, but our estimate is larger and $\sim 10\%$. Not reported in Figure 14.10 is the prediction made in [486], which is linear in the total spin and very close to that coming from (14.4.11).

While the two expressions provide very similar estimates for $-0.5 \lesssim a_1 = a_2 \lesssim 0.4$, they also have predictions differing by more than $\sim 20\%$ for highly spinning binaries. Because both expressions come as a result of a number of simplifications and assumptions, it is not easy to judge which one is the most accurate one, if any. It is useful to bear in mind, however, that expressions (14.4.7)-(14.4.8) have been obtained from a "controlled" set of simulations with small truncation errors and therefore have coefficients with error-bars of the order of 5%. Expressions (14.4.11)-(14.4.12), on the other hand, because coming from more extended formulas and thus fitting a wider set of different simulations across many groups, have error-bars that are intrinsically larger, as high as 100%. In view of this, and of the fact that the coefficients are constant, the simulations carried out here could be used for a new estimate of the free coefficients E_2, E_3, E_S, and E_A in (14.4.11) [6]. Finally, indicated with a dotted line in Figure 14.10 is the prediction for the radiated energy coming from the point-particle approach of [450] and refined in [485].

Simulations involving aligned binaries with unequal masses will help to settle this issue and provide an extension to our expression (14.4.7). This will be the subject of future work.

14.5 Conclusions

We have considered in detail the issue of the detectability of binary system of BHs having equal masses and spins that are aligned with the orbital angular momentum. Because these configurations do not exhibit precession effects, they represent a natural ground to start detailed studies of the influence of strong-field spin effects on gravitational wave observations of coalescing binaries. Furthermore, such systems are far from being unrealistic and may be the preferred end-state of the inspiral of generic supermassive BBH systems. In view of this, we have computed the inspiral and merger of a large set of binary systems of equal-mass BHs with spins parallel to the orbital angular momentum but otherwise arbitrary. Our attention is particularly focused on the gravitational-wave emission so as to provide simple answers to basic questions such as what are the "loudest" and "quietest" configurations and what is the difference in SNR between the two.

Overall we find that the SNR ratio increases with the projection of the total BH spin in the direction of the orbital momentum. In addition, equal-spin binaries with maximum spin aligned with the orbital angular momentum are more than “three times as loud” as the corresponding binaries with anti-aligned spins, thus corresponding to event rates up to 30 times larger. On average these considerations are only weakly dependent on the detectors, or on the number of harmonics considered in constructing the signal.

---

[6] Because in expression for the radiated energy $\tilde{p}_3 = 0$, setting $\tilde{q}_3 = 0$ would also provide a numerical constraint for the presently inaccurate coefficient E_D

We have also investigated whether these binaries can lead to a degenerate patch in the space of templates. We do this by computing the mismatch between the different spinning configurations. Within our numerical accuracy we have found that binaries with opposite spins $\boldsymbol{S}_1 = -\boldsymbol{S}_2$ cannot be distinguished, whereas binaries with spin $\boldsymbol{S}_1 = \boldsymbol{S}_2$ have clearly distinct gravitational-wave emissions. This result, which was already partly discussed in the past [424], may represent a serious obstacle towards a proper estimate of the physical parameters of binaries and will probably be removed only if the SNR is sufficiently high.

Finally, we have derived a simple expression for the energy radiated in gravitational waves, and find that the binaries always have efficiencies $E_{\rm rad}/M \gtrsim 3.6\%$. This can become as large as $E_{\rm rad}/M \simeq 10\%$ for maximally spinning binaries with spins aligned to the orbital angular momentum. These binaries are, therefore, among the most efficient sources of energy in the Universe.

Chapter 15

Gravitational wave extraction: Results

In this chapter, we report on results obtained in [50, 53]. In the first of these two papers [53], we analyze the asymptotic behavior of the Weyl scalars for BBH spacetimes at large distances to the source. With large, we mean radii $r \approx 1000M$. To date, no other numerical relativity group is able to extract waves at that distance, and the extraction is usually carried out $r < 100M$. We therefore extend the wave-zone by more than a factor of 10! This is made possible by the application of our newly developed multiblock code (see Section 7.3), which enables us to not only have a much larger wave-zone, but also superior spatial and temporal resolution. We use extrapolation to obtain waveforms of the Weyl scalars at infinity and assess the fall-off and peeling behavior of them (see Section 1.3 for an introduction to the asymptotic fall-off behavior). Although we observe gauge ambiguities which complicate the interpretation of the Weyl scalars, we can show that Ψ_4 is the dominant component with the slowest fall-off behavior and can clearly be identified with outgoing gravitational radiation.

In the second of the two papers [50], we compute the first unambiguous BBH merger waveform at future null infinity $\mathcal{J}^+$. This is made possible by the application of the newly developed CCE code (see Section 5.3, 9.1). As current Cauchy codes usually rely on waveform extrapolation from finite radii to infinity, we compare the waveform at $\mathcal{J}^+$ to an extrapolated waveform and show that the differences can be observationally significant. We also demonstrate the gauge invariance and consistency of CCE by verifying the convergence of a signal from a single Schwarzschild BH with oscillating gauge and by verifying the invariance with respect to the world-tube location for a BBH merger simulation.

The next two sections are fully devoted to the asymptotic fall-off behavior of the Weyl scalars for BBH spacetimes and to BBH merger waveforms computed at $\mathcal{J}^+$.

15.1 The asymptotic fall-off of local waveform measurements

Numerical relativity has made great strides in recent years in the solution of the BBH problem. Since the original breakthroughs by Pretorius [47] and the moving puncture approach [48, 49] (see Section 2.5), the calculation of long, accurate gravitational waveforms has become an almost routine procedure. It is particularly satisfying that a variety of methods (numerical methods, formulations of the Einstein equations, wave extraction techniques) are in use and have been shown to produce consistent results (eg. [61], see Section 11.4).

Certain systematic errors, however, are difficult to estimate. In particular, and despite the new CCE method developed in this thesis to calculate gravitational radiation at $\mathcal{J}^+$, current methods measure gravitational waveforms at finite radii and extrapolate the results to infinity. This extrapolation has been identified as one of the largest remaining sources of systematic error within current extraction techniques, particularly during the merger and ring-down [156, 487]. Potential ambiguities arise particularly at small radii where gauge as well as nonlinear near-zone effects may dominate the expected polynomial falloff of the amplitude.

In this section, we report on work that we have achieved [53] in order to verify the extrapolation procedure for gravitational waveforms by performing accurate wave extractions at large radii, out to $r = 1000M$ from the source. The waveforms have been calculated using a new hybrid multi-patch/mesh-refinement algorithm "Llama" (see Section 7.3), which allows for an efficient discretization of the wave zone so that high accuracy can be obtained to large radii. We find that the measured waves between $r = 100M$ and $r = 1000M$ are convergent (see Section 11.2) and of good enough quality to extrapolate the phase and amplitude accurately by low-order polynomial expansions. The measurements at $r = 1000M$ can be estimated to within 0.04% in amplitude and 0.001rad in phase, if the measurements out to $r = 600M$ are used in the extrapolation. This is true over the course of the evolution, including 8 orbits of inspiral, the merger, and ring-down. If only measurements within $r = 220M$ are used, as is common, then the errors increase by an order of magnitude.

Finally, we note that the gravitational radiation is normally associated with the leading order term in the falloff of the spacetime curvature. By the peeling theorem, we expect this to be a polynomial in $1/r$ whose leading coefficient is the Weyl component Ψ_4 (see Section 1.3). By measuring all of the Weyl curvature components, we have been able to establish their respective falloff rates, and verify that Ψ_4 is indeed the leading order coefficient with the expected $1/r$ falloff rate. The exponents for the Ψ_1 and Ψ_0 components are less clear, however, and suggest that local gauge effects influence their computation.

Taking advantage of multiblock schemes

A key feature of the calculations performed for this Section is the accuracy which we are able to achieve at large radii from the source through the use of a newly implemented numerical scheme. The code makes use of finite differences and standard mesh-refinement techniques, but incorporates the use of multiple grid patches to cover the spacetime with flexible adapted local coordinates (see Section 7.3). For the BBH inspiral considered here, we consider two regions, depicted in Figure 7.11. In the near-zone region where the BHs orbit, we discretize the spacetime using standard Cartesian grids, applying 2:1 Berger-Oliger mesh refinement in order to increase the resolution around each body [357] (see Section 7.2). In the wave-zone, however, the dynamical fields are essentially radially propagating waves. We cover this zone with six overlapping patches, each of which incorporate a local radial coordinate r and transverse angular coordinates (ρ, σ). The use of six patches avoids the problem of a coordinate singularity on the axis of a single spherical polar coordinate system, as well as providing a more uniform angular resolution over the sphere. The particular coordinates which we have implemented are the "inflated cube" coordinates, given explicitly in [262] (see Section 7.3).

Derivatives on each grid are locally computed using standard finite differences at 8th-order. As described in Section 7.3, data is passed between patches by interpolation, typically via centered 5th-order Lagrange polynomials. Each patch is surrounded by a boundary zone which is populated with data mapped from the neighboring patch, so that derivatives can be calculated up to the patch edge without the need for off-centered stencils. A 4th-order Runge-Kutta integrator is used to evolve the solution. Table 11.3 summarizes all appearing convergence orders.

We write the Einstein equations in the commonly used BSSNOK form (see Section 2.2), adopting the particular variation proposed by [419], whereby the usual variable $\phi = \ln\det\gamma_{ij}/12$ is replaced by $W = \gamma^{-2}$ (with γ the 3-metric determinant, see Section 2.2). Gauges are the commonly used $1 + \log$ and $\tilde{\Gamma}$-driver conditions with advection terms (see Section 2.3).

The gravitational waveforms are measured by evaluating the Weyl curvature tensor components, $C_{\alpha\beta\gamma\delta}$, in a null frame $(\mathbf{l}, \mathbf{n}, \mathbf{m}, \bar{\mathbf{m}})$, oriented so that the outgoing vector, $\mathbf{l}$, points along the coordinate $\hat{\mathbf{r}}$ direction while the other vectors determine an orthonormal null frame in the local metric. The independent curvature components $\Psi_0 \ldots \Psi_4$ are determined by the standard projections [114] (see Section 5.1). The Weyl components are evaluated on spheres of fixed coordinate radius and projected onto a basis of spin $s = -2$ spherical harmonics, ${}_{-2}Y_{lm}$ (see Section 7.4, 9.2). For the BBH situation considered here, the dominant mode is $l = 2$, $m = 2$, which is used for the results presented here.

To establish the numerical accuracy, we have performed evolutions at three different resolutions, and find that the results converge at 4th-order during the merger, and close to 8th-order during the inspiral, in both amplitude and phase (see Section 11.2). Here we present results based on the highest resolution evolved, for which the spatial resolution for all of the gravitational waveform measurements is uniformly $h_r = 0.64M$ in the radial direction, and $h_\perp \simeq 3°$ in the angular directions. gravitational waveform measurements are taken every $0.144M$.

We have evolved an equal-mass, non-spinning binary from separation $d/M = 11.0$ through approximately 8 orbits (a physical time of around $1360M$), merger and ring-down (details on the initial parameters are given in Section 11.1).

Extrapolation to infinity

We measure the Weyl components $\Psi_0 \ldots \Psi_4$ every $20M$ from $r = 100M$ to $300M$, then at $400M$, $500M$, $600M$ and $1000M$. The radial grid structure in the wave zone allows us to extend the outer boundary of the grid at relatively little cost compared to Cartesian codes. For the runs presented here, it is placed at $r = 3600M$ with a resolution of $dr = 2.56M$ at the outer boundary so that the $l = 2$, $m = 2$ mode is reasonably well resolved throughout the grid. This allows for $2600M$ of evolution time before a physical or constraint violating mode traveling at the speed of light can reach the outermost detector at $r = 1000M$ (see Figure 7.7 for an illustration). That is, the outer boundary is effectively causally disconnected from the wave measurements presented in this section.

The Weyl components $\psi_j = A_j e^{i\phi_j}$ are assumed to fall-off as a function of radius according to

$$A_j(r,t) = \sum_{i=0}^{n_A} \frac{A_j^{(i)}(t)}{r^i}, \qquad \phi_j(r,t) = \sum_{i=0}^{n_\phi} \frac{\phi_j^{(i)}(t)}{r^i}. \tag{15.1.1}$$

The r coordinate is that of the simulation coordinates, which we find to differ by at most 0.1% from the areal radius. The gravitational waveforms are expressed in terms of the retarded time $t^* = t - r^*$ where t is the coordinate time and $r^* = r + 2M\ln[r/(2M) - 1]$ is the tortoise coordinate [156]. We do not offset the retarded time to align the peaks of the waveforms.

It is generally difficult to estimate the error incurred when extrapolating. Given the data at $r = 1000M$, we can attempt to gauge an optimal choice of extrapolation parameters by attempting to estimate this data from the measurements at smaller radii. As test cases, we construct extrapolations using four different sets of radii, $e_1 \in \{100M, 200M\}$, $e_2 \in \{160M, 280M\}$, $e_3 \in \{200M, 300M\}$ and $e_4 \in \{260M, 600M\}$. Each of these incorporates 6 data points, which over-determines low-order polynomials. We evaluate the extrapolation coefficients by a least-squares fit to these points, which can be important in removing spurious oscillations that may arise fitting high-order polynomials to noisy data.

Fitting the amplitude using various polynomial orders, n_A, suggests that in all cases $n_A = 3$ is optimal in predicting the amplitude of the measured wave at $r = 1000M$, with an error of approximately 0.02% for e_4 and 0.2% for e_1. For the phase, we find that $n_\phi = 3$ minimizes the error, at 6×10^{-4}rad and 5×10^{-3}rad for e_4 and e_1, respectively. In both amplitude and phase, we note that the error is reduced significantly if the outermost data e_4 is used. In Figure 15.1 we display the error in estimating the $r = 1000M$ data using each of the extrapolations at the optimal order. The maximum errors in both amplitude and phase tend to occur during the late inspiral ($t^* = -200M$ to $t^* = 0M$) and ring-down, although there is no sign of a rapid growth of error during this phase.

The corresponding extrapolations to $r \to \infty$ shows very similar behavior. In Figure 15.2, we have compared each of the extrapolations with an extrapolation obtained by including the $r = 1000M$ data ($e_5 \in \{280M, 1000M\}$), evaluated at $r \to \infty$. The outermost extrapolations differ by at most $\Delta A = 0.03\%$ and $\delta\phi = 0.003$rad over the course of the evolution.

Peeling properties

The interpretation of Ψ_4 as the radiated gravitational energy is a consequence of the "peeling" property (see Section 1.3), which states that for asymptotically flat spacetimes at large radii, the Weyl curvature tensor can be represented schematically as

$$C_{\alpha\beta\gamma\delta} \simeq \frac{\Psi_4}{r} + \frac{\Psi_3}{r^2} + \frac{\Psi_2}{r^3} + \frac{\Psi_1}{r^4} + \frac{\Psi_0}{r^5} + O(1/r^6). \tag{15.1.2}$$

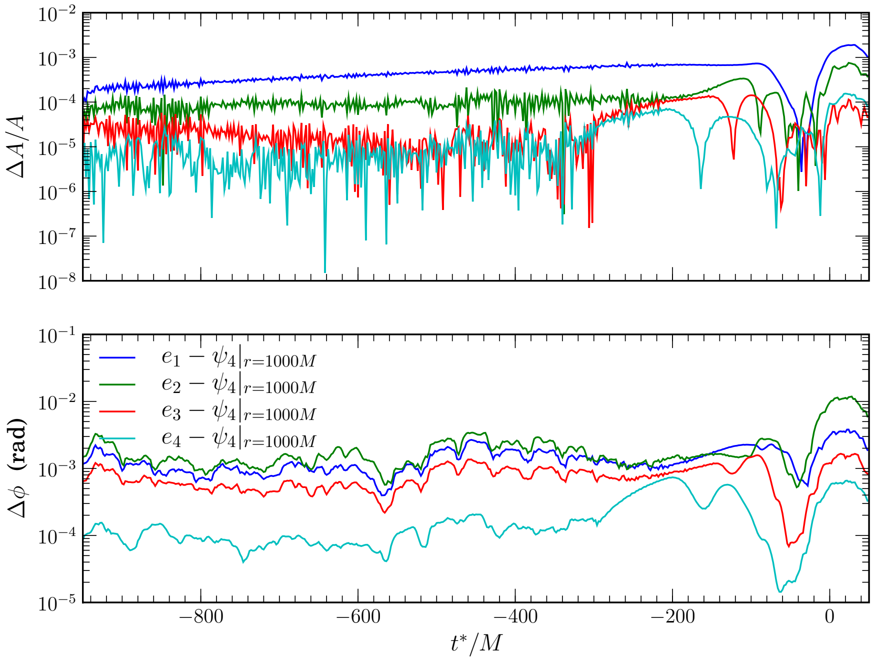

Figure 15.1: Error in the extrapolated amplitude (top panel) and phase (bottom panel) of the $\ell = 2, m = 2$ component of Ψ_4 at $r = 1000M$ as computed by extrapolations $e_1 \ldots e_4$ (defined in the text).

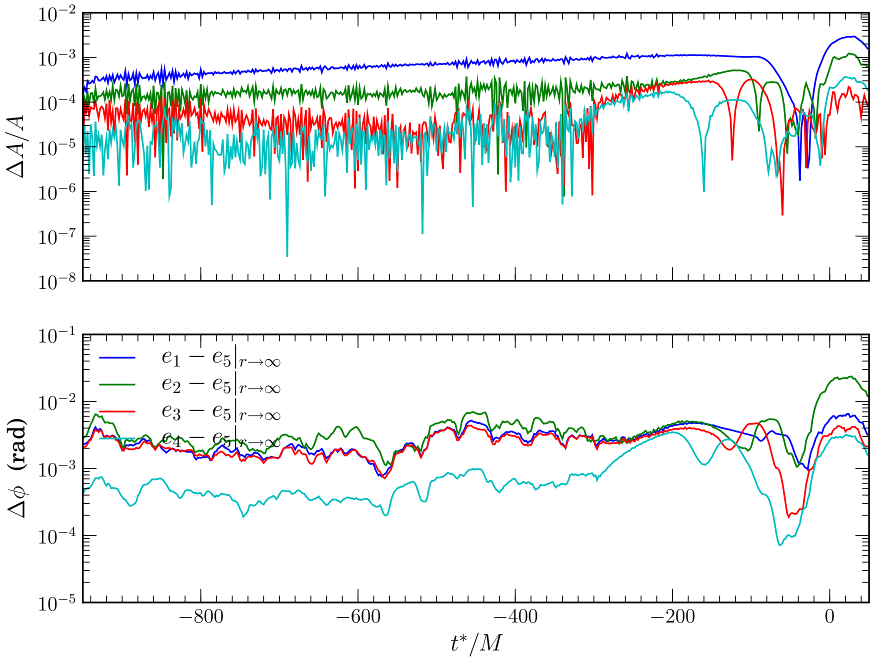

Figure 15.2: Differences between the $r \leq 600M$ extrapolations with an extrapolation including $r = 1000M$ data (e_5) evaluated in the limit $r \to \infty$.

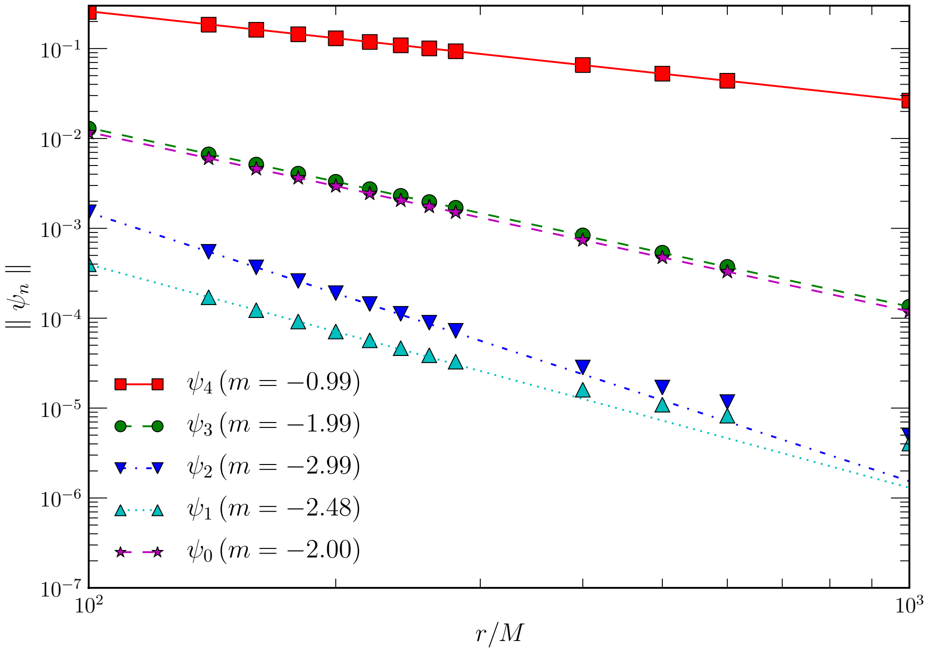

Figure 15.3: The radial falloff of the Weyl components. Lines are linear least-squares fits to all of the points of Ψ_0, Ψ_3, and Ψ_4, and the $r \leq 200M$ points for Ψ_1 and Ψ_2. Measured slopes are listed in the legend.

That is, each component of the Weyl tensor falls off at a known fixed rate, and at large radii, Ψ_4 is the dominant component. At future null infinity, $\mathscr{J}^+$, it can be related to $\dot{M}$, the change in energy of the spacetime. We note, however, that the peeling theorem involves a number of restrictions on the asymptotic form of the spacetime, and the coordinates which are used there. A rigorous connection between finite radius measurements and the asymptotic properties of the spacetime at $\mathscr{J}^+$ is difficult to make.

Given the importance of the falloff of the curvature in the identification of Ψ_4 with the gravitational waveform, it is useful to examine the behavior of the other Weyl components measured by the simulation. In Figure 15.3, we have plotted their falloff as a function of coordinate radius. The time series data for each component is mapped to a scalar by integrating the amplitude over the interval $t \in [-800M, 50M]$. (Alternatively, one could obtain a scalar by taking the measurements at a point such as the waveform peak. A similar plot results, but the averaging effect of the integral reduces local noise slightly.)

For the cases of Ψ_4 and Ψ_3, we find that a straight line can be fitted to each of the components, indicating a consistent exponent, with measured values of -0.99 and -1.99 respectively, and a rather good agreement with (15.1.2). Due to its small amplitude, the Ψ_2 measurement is dominated by numerical noise beyond a certain radius (clear from examination of the time-series data), and as a result, the curve veers from a straight line. However, if we fit a straight line to the five data points from $r \leq 200M$, we find an exponent, -2.99, again agreeing well with the expectation.

The Ψ_1 and Ψ_0 components present an interesting situation. Particularly in the case of Ψ_0, the amplitude is large enough that a clear signal is present (of almost of the same amplitude as Ψ_3). The falloff, however, is of order -2.00, rather than the -5 which the peeling theorem requires. Further, we note that the mode propagates outwards with a peak coincident with that of Ψ_4, in contrast to the interpretation of Ψ_0 as an "ingoing" component of radiation.

A possible explanation is that metric perturbations cause oscillations in the frame in which the components are measured. As described above, we define the null frame only with reference to the local space and time coordinates. Attempts to modify the falloff of Ψ_0 via frame rotations (spin-boosts and null rotations, see Section 1.3) did not preserve the falloff of the other components. However, other gauge effects are likely present. We note that measurements are taken on spheres defined by the grid coordinates. The areal radius of these spheres exhibits small (on the order of 0.1%) oscillations in the $\ell = 2$, $m = 2$ mode. The finite-radius Ψ_4 measurement is known to be susceptible to pure gauge effects such as the presence of a non-zero shift vector, which can produce spurious gravitational waveform signals in static spacetimes (see Section 15.2). Though these effects are small, so are the values of Ψ_1 and Ψ_0 and thus correspondingly sensitive compared to that of the dominant component.

Discussion

We have demonstrated a number of features related to the measurement of gravitational waveforms at finite radius. Our results suggest that polynomial extrapolation of the Ψ_4 component from small radii can provide an accurate model for estimating the measurements at larger radii. Data measured within $r = 200M$ of the source have an error in amplitude and phase of $\Delta A \simeq 0.2\%$ and $\Delta\phi \simeq 5 \times 10^{-3}$rad throughout the evolution (including merger and ring-down) compared to the measurement at $r = 1000M$. This provides an important check on numerical relativity measurements, which typically extrapolate from $r < 200M$. Larger radius measurements do, however, improve the extrapolation, and errors can be reduced by a further order of magnitude if data to $r = 600M$ is included. We also note that while Ψ_4 is dominated by the $1/r$ term beyond $r = 300M$, at smaller radii the higher order terms have a much larger contribution.

While the falloff of Ψ_4 is the leading order contribution to the curvature as expected, the results of Figure 15.3 suggest that the picture may be more complicated for the other Weyl components, and that care should be taken in interpreting local variables according to their expected asymptotic properties. With respect to the peeling property, we note that the asymptotic evolution of generic initial data sets are likely to include polyhomogenous terms, and even the situation for Bowen-York data with linear momentum is not clear [128, 131]. While it seems most likely that the effect we have observed in Ψ_0 and Ψ_1 is related to gauge, this provides a strong caution regarding physical predictions based on these quantities. Alternative gauge conditions may alleviate (or exaggerate) the issues we have noted.

The mapping of finite radius results to asymptotic values at $\mathscr{J}^+$ needs to be considered with some care. While our results suggest that the procedure of extrapolation is self-consistent and can be used to estimate the results that would be obtained by direct measurement at large radii, they do not establish the identification of the extrapolated quantities with quantities that would be measured at $\mathscr{J}^+$. In a related paper [50] (see Section 15.2), we have demonstrated that the extrapolation procedure does in fact reproduce results obtained at $\mathscr{J}^+$ to high accuracy, though a small systematic error does remain. A number of local corrections have been proposed to improve the rigor of Ψ_4 measurements at finite radius (cf. [307, 488, 489]).

Finally, we note that our accurate measurements at $r = 1000M$ are a result of a new computational infrastructure making use of adapted coordinate grids in conjunction with a finite difference, moving-puncture scheme. This is the first demonstration that such methods can produce stable evolutions for dynamical spacetimes. The efficiency gains allow the wave zone to be covered with sufficient resolution to very large radii ($3600M$ in this case), which has been crucial in reducing boundary errors.

15.2 Unambiguous determination of gravitational waveforms

The computation of gravitational radiation from BH merger events has attracted considerable attention, since the pioneering work by Smarr and collaborators [37, 38, 41]. With the advent of ground-based laser interferometric gravitational wave detectors, as well as the prospect of the Laser Interferometer Space Antenna (LISA), interest in the problem has considerably increased. The measurement of gravitational waves will soon provide an important probe of strong-field nonlinear gravity, the domain of many fundamental questions in astrophysics. The sensitivity of LISA, and of the upcoming advanced ground-based detectors AdLIGO and AdVirgo, is so high that even an error in the waveform calculation of 0.1% (in a sense made precise later) could lead to an incorrect interpretation of the astrophysical properties of a source, or of a test of GR. Nowadays, there are several codes that can produce a stable and convergent simulation of a BH spacetime. However, a particular difficulty with measuring gravitational radiation arises from the fact that, in GR, it cannot be defined locally but is defined only at $\mathscr{J}^+$ (see Section 1.3). Since numerical evolutions are normally carried out on finite domains, there is a systematic error caused by estimating the gravitational radiation from fields on a world-tube at finite radius and the uncertainty in how it relates to measurement at $\mathscr{J}^+$ [490]. Even if this error is small, the expected sensitivity of AdLIGO, AdVirgo and LISA implies that it is important to obtain an accurate result.

A rigorous formalism for the global measurement of gravitational energy at null infinity has been in place since the pioneering work of Bondi, Penrose and collaborators in the 1960s [113, 135] (see Section 1.3); and subsequently, techniques for calculating gravitational radiation at $\mathscr{J}^+$ have been developed. The idea which we pursue here is to combine a Cauchy or "3 + 1" numerical relativity code with a characteristic code [328]. Given astrophysical initial data, such a method has only discretization error [272], and a complete mathematical specification has been developed [330]. There have been efforts to implement this method, often called Cauchy characteristic extraction (CCE), or characteristic extraction [275, 277]. Previous work has considered test problems rather than that of the inspiral and merger of two black holes or neutron stars. Also, earlier efforts have combined the Cauchy and characteristic algorithms within the same code.

Here, we describe the results obtained from the newly implemented CCE code (see Section 9.1) for the inspiral and merger waveform of two equal mass, non-spinning, BHs. The waveforms are calculated at $\mathscr{J}^+$, and are thus the first unambiguous waveforms which have been obtained for this problem, in the sense of being free of gauge or finite-radius effects. Further, the code is general purpose, in that it is independent of the details of the Cauchy code, requiring only that it prescribes the required geometrical data on a world-tube (see Section 9.1). Thus its application to other astrophysical problems will be straightforward.

We give results on the gauge invariance of waveforms obtained for the test problem of a single Schwarzschild BH with oscillating gauge. In this case, the wave-signal must be zero and we show that the modes are indeed converging to zero.

For the specific problem of a BBH merger, we show that the waveform obtained at $\mathscr{J}^+$ contains only numerical error and is gauge-invariant. We demonstrate second-order convergence to zero in the amplitude and phase differences between two CCE runs using boundary data at different radii. We compare the waveform obtained at $\mathscr{J}^+$ with a finite-radius extrapolated waveform, and find that the corrections introduced by CCE are visible in the ground-based detectors AdLIGO and AdVirgo, as well as the space-based LISA detector.

Cauchy evolution

The scenario we envision is an isolated system (perturbed single body, or gravitationally bound binary), in a region on which the Einstein (and possibly hydrodynamic) equations must be solved. A standard procedure for doing this is to formulate the equations as an initial-boundary-value, or Cauchy, problem, in which data for the 3-metric and its embedding is prescribed at a given time on a closed region of the spacetime, Σ_t. These are evolved according to the Einstein equations on the interior of the domain, and artificial conditions on the timelike boundary, $\partial\Sigma_t$ (see Chapter 2). The first stable evolutions of a binary BH system were carried out by Pretorius [47]. Two approaches to the evolution of the interior equations are in use: (a) the harmonic formulation of the Einstein equations with excised BH interiors [47, 156]; (b) the BSSNOK evolution system with the BHs specified as moving "punctures" [48, 49].

For the Cauchy evolutions used here, we have followed the latter approach using the formulation outlined in [56] (see Chapter 2). The spacetime is discretized using finite differences on Cartesian grids and Berger-Oliger mesh refinement in the neighborhood of the black holes [357] (see Section 7.2 and Section 8.1). The wave zone is discretized by six overlapping coordinate patches with spherical topology. Interior boundary data between adjacent patches are communicated by interpolation [53] (see Section 7.3).

The outer boundary condition on the exterior of the domain is given by a linear outgoing wave condition on each of the evolved tensor components. Importantly, through the use of spherical grids in the wave zone, a sufficient resolution can be maintained even to a distant outer boundary, reducing the effect of grid reflections common in mesh-refinement codes. The size of the evolution domain is chosen according to the amount of time required, T, and the location of the outermost measurement sphere, r_i. Since physical as well as constraint violating modes propagate with the speed of light, an outer boundary located at $r_{\partial\Sigma_t} > T + r_i$ ensures that measurements are causally disconnected from the influence of the outer boundary (see Figure 7.7).

Cauchy characteristic extraction

The implementation of CCE is based on the mathematical prescription given in [330] (see Section 5.3), and the implementation has been described in Section 9.1. Here, we provide an outline of the procedure. The process is illustrated schematically in Figure 5.1. Within a Cauchy simulation that uses Minkowski-like coordinates (t, x, y, z), we define a world-tube Γ by $x^2 + y^2 + z^2 = r_\Gamma^2$, and compute the lapse α, the shift β^i and the 3-metric γ_{ij} on Γ, as well as their first time and radial derivatives. This data is then decomposed into spherical harmonics. The Cauchy code writes this spherical harmonic coefficient data to file, and later the CCE code post-processes the data to reconstruct the 4-metric on the inner world tube. In this way, the CCE code is general purpose, as it runs independently of whatever Cauchy code was used to generate the world-tube data.

The CCE code defines angular coordinates ϕ^A as well as a time coordinate u $(=t)$ on Γ, and constructs outgoing null geodesics with affine parameter λ. It then transforms the Cauchy 4-metric to (u, λ, ϕ^A) coordinates, and calculates a surface area radial coordinate r_S, making the coordinate transformation to (u, r_S, ϕ^A) coordinates, in order to obtain the Bondi-Sachs metric data in a neighborhood of Γ. This provides the inner boundary data for the characteristic evolution, using a Cactus [354–356] (see Section 7.1) implementation of the PITT null evolution code with square stereographic coordinate patches [273] (see Section 8.2). The characteristic code uses coordinates based on outgoing null cones, and so the equations remain regular when the radial coordinate is compactified (by $r_S \to z = r_S/(r_S + r_{S\Gamma})$), and in this way $\mathscr{J}^+$ is included on the computational grid. The code computes the gravitational radiation at $\mathscr{J}^+$ as the Weyl component Ψ_4.

Test with a Schwarzschild black hole and gauge invariance

An important test that CCE as a wave extraction method has to pass is gauge invariance with respect to changes in coordinates. As a simple test problem, we place a single static Schwarzschild BH at the origin of our spacetime, and artificially drive the shift according to

$$\beta^x = A\omega\cos(\omega t)\,, \qquad \beta^y = \beta^z = 0\,, \tag{15.2.1}$$

so that the x-coordinate oscillates with

$$x = A\sin(\omega t)\,, \tag{15.2.2}$$

where the amplitude is set to $A = 1.0$ and the frequency is set to $\omega = 0.1$. Since the spacetime is spherically symmetric and static, the resulting radiation content must be zero, and hence, in numerical simulations the residual in Ψ_4 and the news N must converge to zero. This is indeed what we find. Figure 15.4 shows the $\ell = 2, m = 0$ mode of Ψ_4 and N at two resolutions $h = 0.4M$ and $h = 0.2M$ scaled for second-order convergence. All other modes converge at the same order, too.

In contrast to this, finite radius extraction methods based on gauge-invariant perturbations of Schwarzschild fail to be convergent. This is shown in Figure 15.5, where we plot $Q^+_{\ell=2,m=0}$ for the two resolutions $h = 0.4M$ and $h = 0.2M$ without any rescaling. The two waves are on top of each other indicating no convergence.

This demonstrates the superiority of CCE over the standard methods based on finite radius computations.

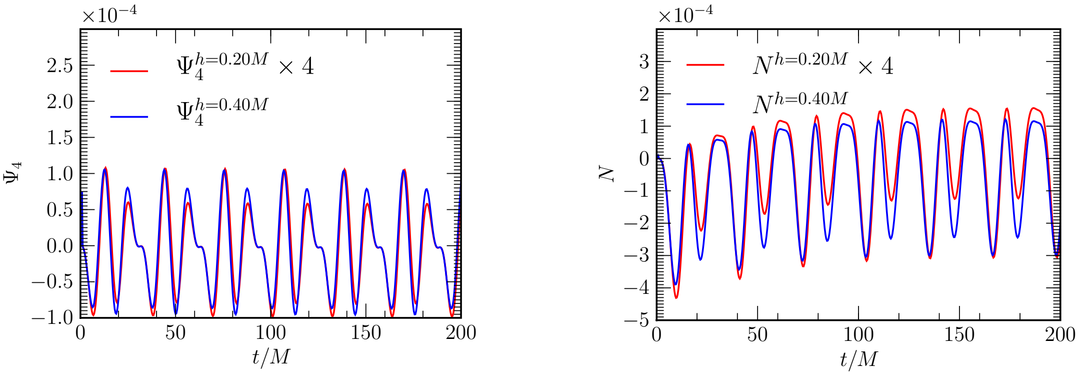

Figure 15.4: These two figures demonstrate convergence of the wave-signal to zero at second-order accuracy as expected. The *left panel* shows the $\ell = 2, m = 0$ mode of the Weyl scalar Ψ_4 for the two resolutions $h = 0.40M$ and $h = 0.20M$ where the latter is scaled for second-order convergence. The *right panel* shows the $\ell = 2, m = 0$ mode of the news N for the same resolutions and the same rescaling. Similar plots for all other modes exhibit the same order of convergence.

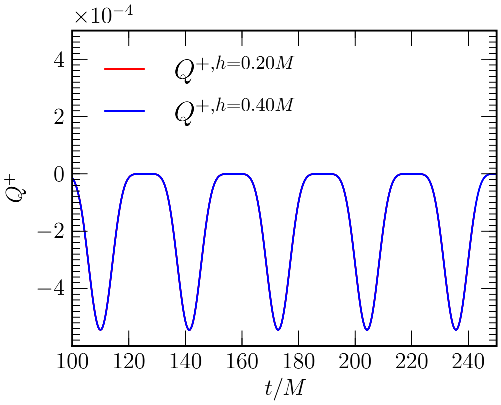

Figure 15.5: This figure demonstrates the non-convergent behavior of the even gauge-invariant master-function Q^{+} extracted at $R = 100M$. Shown are the two resolutions $h = 0.20M$ and $h = 0.40M$ of the $\ell = 2, m = 0$ mode without any rescaling. Clearly, both waveforms are on top of each other thus indicating non-convergent behavior.

Binary black hole merger waveform

We have carried out fully relativistic evolutions of an equal-mass non-spinning binary black hole inspiral and merger. The initial data parameters for the closely bound BH are determined by performing a post-Newtonian evolution from large separation in order to determine the momenta for low-eccentricity (quasi-circular) trajectories [231] (see Section 2.4). The subsequent full nonlinear numerical relativity evolution proceeds for approximately 8 orbits ($1350M$), followed by the merger and ring-down lasting another $100M$ (see Section 11.1 for the initial data of this configuration).

The evolutions have been carried out at two different grid resolutions in order to verify the convergence of the numerical scheme. The grid settings for the Cauchy code are: The central Cartesian grid consists of 6 levels of 2:1 mesh-refinement, with coarse grid spacings of $h = 0.96M$ and $h = 0.64M$, respectively. A grid of spherical topology covers the far field, $r \in [35M, 3600M]$; so that, during the time period of interest, the outer boundary is causally disconnected from any extraction sphere (see Figure 5.1). The radial spacing is commensurate with the coarse Cartesian grid at the interface, and (for reasons of efficiency) is gradually scaled to $h = 3.84M$ and $h = 2.56M$ at the outer boundary for the two runs. We use a corresponding $N_{\text{ang}} = 21$ and $N_{\text{ang}} = 31$ points in each of the angular directions per patch.

Characteristic boundary data were interpolated onto world-tubes located at $r = 100M$ and $r = 200M$, and stored in the form of spherical harmonic coefficients, up to $\ell = 8$, which was found to be the highest resolved mode. The resolutions of the characteristic evolutions are set up according to the respective resolutions of the Cauchy run. We use $N_r = 321$ and $N_r = 481$ radial points, with $N_{\text{ang}} = 51$ and $N_{\text{ang}} = 76$ angular points per angular patch. The dominant $\ell = 2$, $m = 2$ mode of the gravitational waveform resulting from the numerical evolution is plotted in Figure 15.6, to be described in more detail below.

The CCE waves can be used to evaluate the quality of standard finite radius measurements, extrapolated to $r \to \infty$. We do so by finding the Weyl component Ψ_4 relative to a radially oriented null tetrad [56] (we prefer Ψ_4 to gauge-invariant perturbative methods [309, 310, 312], see Sections 5.1, 5.2). We have evaluated Ψ_4 at six radii ($r = 280, 300, 400, 500, 600, 1000M$) and extrapolated. Details are given in [53] (see Section 15.1), and the error is estimated as 0.03% in amplitude and 0.003 radians in phase.

In Figure 15.6, we compare the extrapolated waveform with that calculated at $\mathscr{J}^+$ via CCE. The differences between the two waveforms have maximum and mean values of 1.08% and 0.166% in amplitude, and -0.019 and -0.004 radians in phase, respectively. That is, for the resolutions used, the numerical error in the characteristic evolution (see Figure 15.7) is smaller by one order of magnitude than the error between the extrapolated and characteristic waveforms in both amplitude and phase. Further, we note that the estimated error in the extrapolation is itself much smaller than the actual error between characteristic waveform and extrapolated waveform. The correction is towards slightly larger amplitudes and frequencies. Also, we note that the error between extrapolated waveform and the one calculated at $\mathscr{J}^+$ is of the same order of magnitude as the error in the Cauchy evolution itself (see Section 11.2, convergence and accuracy of the Llama code).

The close agreement between the CCE and extrapolated wave provide strong confirmation that existing computations can provide excellent approximations to the gravitational radiation at $\mathscr{J}^+$.

Observational significance

Will the small correction to waveforms introduced by CCE be relevant to interpreting observational data? The answer will depend on the signal-to-noise ratio (SNR) of the event. At low SNR, whether CCE or extrapolated waveforms are used as a template will not affect physical interpretation. This is particularly relevant, as numerical waveforms are being constructed with the intention of evaluating and parametrizing detector templates and search algorithms [64], and to constrain analytic models [34, 63, 371, 491]. Our results indicate that extrapolations from a finite

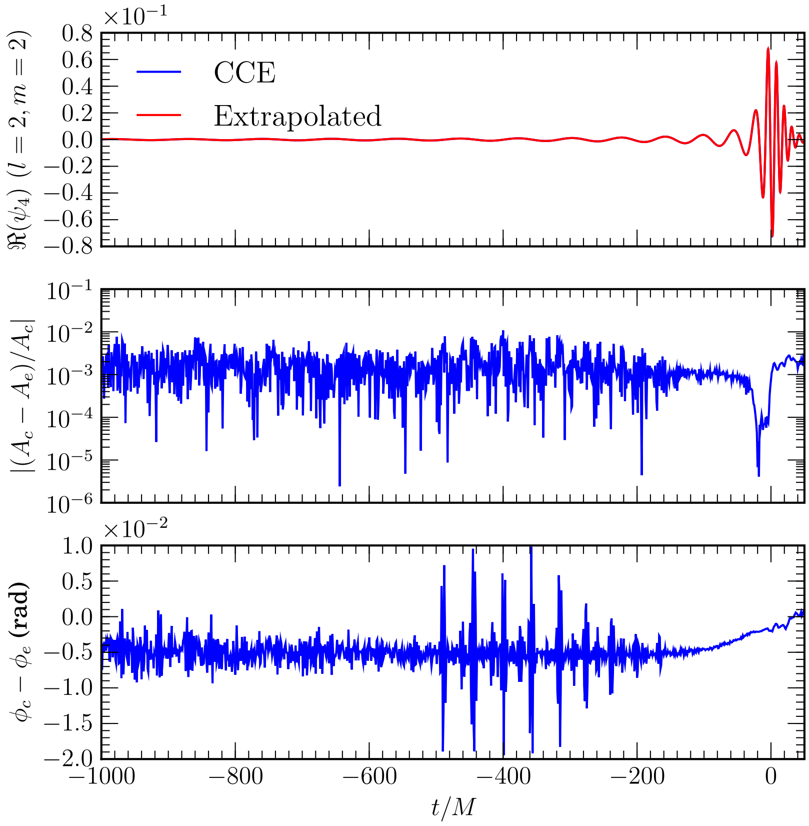

Figure 15.6: Inspiral, merger and ring-down phase of $\Psi_4(\ell = 2, m = 2)$ as obtained from finite radius extrapolation (red) and at $\mathscr{J}^+$ (blue). There is a maximum difference of 1.08% in the amplitude and a dephasing of 0.019 radians between the two waves.

radius can be used to construct detector templates well within the accuracy standards required by matched filtering algorithms.

However, at large SNR, the differences are significant to the determination of the physical parameters of a model measured in detector data. To demonstrate this, we follow methods described in [61, 492] to determine the minimum SNR needed for a detected signal from a merger event to lead to different parameter estimates depending on which waveform is used as a template.

Consider two waveforms, h_1 and h_2. As detailed in [492], these waveforms are indistinguishable to a given gravitational-wave detector with respect to parameter estimation if the difference $\delta h(t) = h_1(t) - h_2(t)$ obeys

$$\langle \delta\tilde{h} | \delta\tilde{h} \rangle < 1 \,, \tag{15.2.3}$$

where $\langle , | , \rangle$ is the detector inner-product defined by

$$\langle \tilde{h} | \tilde{h} \rangle \equiv 4 \int_0^\infty \frac{|\tilde{h}(f)|^2}{S_h(f)} df \,, \tag{15.2.4}$$

and where $S_h(f)$ is the noise power spectral density for a given detector and $\tilde{h}$ denotes the Fourier-transform of the waveform h.

In practice [61], we select a binary mass, the detector, and a distance of the source to the detector. We then calculate the match (see Section 14.3) between extrapolated waveform $h_{\rm extr}$ and waveform obtained at infinity $h_{\mathcal{J}^+}$ and determine the phase and time shift of the waves such that the match is maximized. In order to calculate the match, we have to determine the Fourier-transform of the waveforms h given in terms of Ψ_4 by

$$\tilde{h} = -\frac{\tilde{\Psi}_4}{4\pi^2 f^2} \,, \tag{15.2.5}$$

where $\tilde{\Psi}_4$ is the Fourier-transform of Ψ_4.

Given the phase and time shift that maximizes the match, we construct the difference with those two aligned waveforms in the time domain, $\delta h(t) = h_{\rm extr} - h_{\mathcal{J}^+}$, and transform to the frequency domain to produce $\delta\tilde{h}(f)$. Plugging this into (15.2.3) determines whether the two waveforms can be distinguished for the selected mass, detector and distance.

As (15.2.3) can be rescaled by choosing a different distance, we can easily determine a distance such that the product (15.2.3) becomes exactly 1, *i.e.* we set

$$\frac{d}{d_{\rm max}} \sqrt{\langle \delta\tilde{h} | \delta\tilde{h} \rangle} = 1 \,, \tag{15.2.6}$$

where d is the distance that had been selected initially, and $d_{\rm max}$ is the maximal distance so that the two waveforms are distinguishable, *i.e.* $\langle \delta\tilde{h} | \delta\tilde{h} \rangle \geqslant 1$.

Table 15.1 displays the results for selected masses, indicating the maximum distance $d_{\rm max}$ at which the difference between the waveforms will be relevant for the given merger event.

The difference between the waveforms is unlikely to be relevant for LIGO, (e)LIGO and Virgo. Reasonable stellar mass BH merger rates are expected only for a volume encompassing sources up to a distance of at least 100Mpc. Thus, there may well be events detected by AdLIGO and AdVirgo for which the difference is important. Finally, the differences will certainly be relevant for LISA as they will be applicable to any SMBH merger event throughout the visible Universe (cH^{-1} is the Hubble radius).

Invariance with respect to world-tube location

Invariance with respect to the world tube location is demonstrated in Figure 15.7. We have considered the differences between waveforms at $\mathcal{J}^+$ resulting from two independent characteristic evolutions using boundary data at $r_\Gamma = 100M$ and $r_\Gamma = 200M$, respectively, and for two resolutions, $h = 0.96M$ and $h = 0.64M$. The difference between the results should be entirely due to the discretization error, and indeed this is what we find. The differences converge to zero with

Detector	Masses	Maximum distance
LIGO	$50M_\odot + 50M_\odot$	5Mpc
(e)LIGO	$50M_\odot + 50M_\odot$	8Mpc
Virgo	$50M_\odot + 50M_\odot$	14Mpc
AdLIGO	$50M_\odot + 50M_\odot$	197Mpc
AdVirgo	$50M_\odot + 50M_\odot$	177Mpc
LISA	$10^7 M_\odot + 10^7 M_\odot$	$> cH^{-1}$

Table 15.1: Maximum distance at which the difference between the extrapolated waveform and that at $\mathscr{J}^+$ would be significant for a BH merger event.

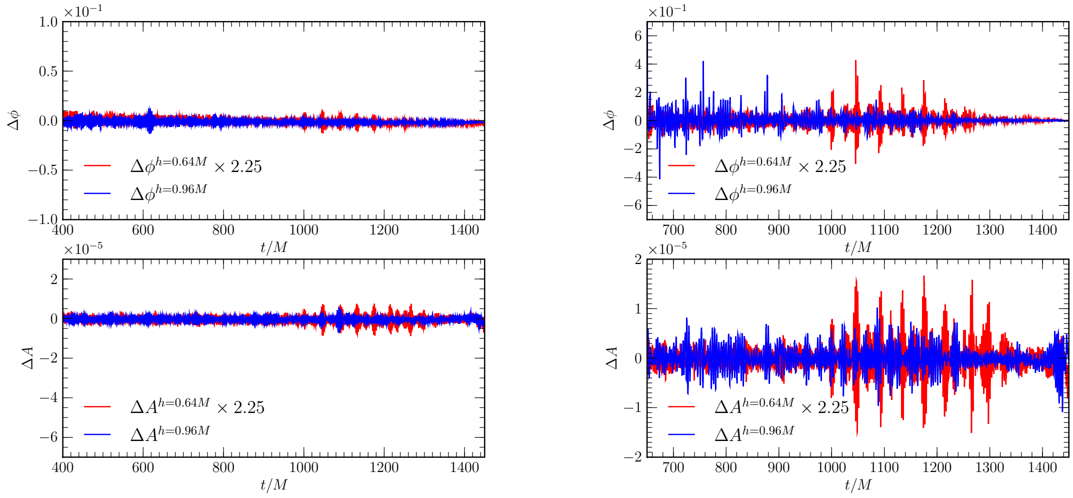

Figure 15.7: Differences in the amplitude A and phase ϕ of $\Psi_4(\ell = 2, m = 2)$ (*left panel*) and $\Psi_4(\ell = 4, m = 4)$ (*right panel*) between two characteristic runs using boundary data from $R_\Gamma = 100M$ and $R_\Gamma = 200M$. The red curve shows the difference at resolution $h = 0.96M$ while the blue curve shows the difference for $h = 0.64M$, scaled so as to line up for second-order convergence.

approximately second-order accuracy, as expected for the null evolution code. The figure displays the differences in the amplitude and phase of the wave mode $\Psi_4(\ell = 2, m = 2)$ for resolution $h = 0.96M$ and $h = 0.64M$ scaled for second-order convergence. The same order of convergence is also obtained for higher order modes such as $\Psi_4(\ell = 4, m = 4)$. The differences between the waveforms at $\mathscr{J}^+$ for resolution $h = 0.64M$ are of order of 0.03% in amplitude with a dephasing of 0.002 radians.

It should be noted that the error in the waves between different world-tube locations is by one order of magnitude smaller than the errors in amplitude and phase inherent in the Cauchy evolution (see Section 11.2, convergence and accuracy of the Llama code). We therefore expect that the dominant error in the waveforms is due to the discretization error during Cauchy evolution. Indeed, we find a very similar convergence order for a fixed world-tube location using the three resolutions $h = 0.96M$, $h = 0.80M$ and $h = 0.64M$ as for the waveforms computed during Cauchy evolution (compare Figures 11.7, 11.8 and 11.9).

Notes on characteristic code settings

There are some subtleties regarding the choice of some code and grid parameters that have been found empirically during tests of the extraction method.

Here, we collect some of the findings for future reference.

- We use conformally flat initial data on the initial null hypersurface, *i.e.* $J(u=0)=0$. This assumption is in principle incompatible with the proper radiation content of a BBH spacetime, and it is subject to the same error as on the Cauchy side, where we also use conformally flat initial data. In practice, the spurious burst of junk radiation at the beginning of the simulation quickly leaves the system and does not affect the radiation at the accuracy given by the numerics.
- The radial resolution of the physical coordinate on the characteristic grid should be at least as high at the world-tube as the radial resolution on the Cauchy side. We can estimate the compactified radial resolution in terms of the physical resolution via

  $$\frac{dr}{dx} = r_{\mathrm{wt}} \left(\frac{1}{1-x} + \frac{x}{(1-x)^2} \right) , \tag{15.2.7}$$

  which asymptotes to r_{wt} for $x \to 0$ at the world-tube, *i.e.*

  $$x \to 0, \qquad \frac{dr}{dx} \to r_{\mathrm{wt}} \, . \tag{15.2.8}$$

  It follows that

  $$\Delta r|_\Gamma \sim r_{\mathrm{wt}} \Delta x \tag{15.2.9}$$

  at the world-tube. We can then select an appropriate Δx, so that $\Delta r|_\Gamma$ at the world-tube is at least as high as the radial resolution Δr on the Cauchy side.
- The linearized approximation for the conformal factor ω as described in Section 9.1 is used for the computation of the news N. The full non-linear computation results in spurious drifts and does not converge when considering the Schwarzschild test. This is probably a bug in the existing implementation and affects only the news. Ψ_4 is only affected at higher-order which does not play a role in practice.

  However, the code operates in the linear regime because we measure $\beta(r) = \text{const.}$ during evolution for world-tube radii $r \geq 100M$. If $\beta(r) = \text{const.}$, this indicates that β is completely determined by the boundary value at the world-tube, which is only the case in the quasi-spherical appriximation (compare (8.2.6)). Accordingly, the fields at $\mathscr{J}^+$ are in the linear regime, and the linear approximation for ω is a valid simplification.
- We use the first-order evolution system, *i.e.* we use only first eth-derivatives. The implementation with second eth-derivatives does not converge and gives inconsistent results for the binary waveform when considering different world-tube locations. This might also be related to the problem formulated in [274, 493]. In pricipal, both methods should be equivalent and the non-convergence of the second-order system can be attributed to a bug in the code. However, analytically, first-order formulations offer some advantages [494]. Numerically, taking one second derivative instead of two successive first derivatives is much more accurate [495].
- The news and Ψ_4 are computed by using the second-order implementation of the extraction module, *i.e.* we use second eth-derivatives.
- All quantities are decomposed in terms of the complex-valued spin-weighted spherical harmonics ${}_sY_{\ell m}$. The real-valued harmonics ${}_sZ_{\ell m}$ are only used for code tests involving the linearized solutions.

Chapter 16

Summary and outlook

BBH mergers are the strongest source of gravitational-wave emission in the Universe. These binaries are therefore expected to be the prime candidates for gravitational-wave detection and in the process of finding their gravitational-wave signature, theoretical models of gravitational-wave templates have to be constructed.

The accurate modeling of BBH merger systems requires the numerical computation of the Einstein field equations using supercomputers on the tera and peta scale. Although initial studies have used resources on the giga scale, the determination of accurate wave templates, also in view of parameter estimation, necessitate the tapping of much larger computational resources.

Despite the construction of gravitational-wave templates, these computations also help in our understanding of the properties of the merger remnant. Particularly, they help in the construction of phenomenological expressions that can be used in other studies such as N-body simulations of galactic mergers, or hierarchical models of BH formation, where it is unfeasible to perform full non-linear spacetime evolutions.

In this thesis, and in view of accurate determination of gravitational-wave templates, we have enhanced current spacetime simulations by the following:

- **AMR coupled to multiblock schemes.** Adaptive mesh-refinement is used in almost all current numerical relativity codes, particularly in BBH merger simulations. Its application enables to place resolution where necessary and results in a computational accuracy that would have otherwise not been possible on today's supercomputers.

  However, there is a certain drawback. The grids that are typically employed in Cauchy evolutions are of Cartesian topology. As this works well for the strong field regions around the BHs, it represents a serious obstacle for the accurate modeling of a large wave-zone. By using Cartesian grids, the computational effort scales with r^3, where r is the radius to the outer boundary. The wave-zone, on the other hand, has spherical topology, and by employing spherical grids, one can exploit the fact that the angular resolution can remain constant. This has the effect that the computational effort simply scales as r, which results in tremendous savings of computational resources.

  In this thesis, we have coupled AMR Cartesian grids to a multiblock infrastructure, which allows for accurate strong field evolution with established AMR techniques while at the same time allowing for a highly accurate and efficient representation of the wave-zone all the way to the outer boundary. Furthermore, it becomes possible to causally disconnect the interior spacetime from the outer boundary over the course of the evolution, including extraction world-tubes at $r = 1000M$. This allows to limit finite-radius effects while at the same time causally disconnecting constraint violating modes that propagate from the artificial outer boundary to the interior of the domain.

  We have demonstrated convergence of wave-modes up to $(\ell, m) = (6, 6)$, which has not yet been shown before by other numerical relativity groups. In addition, we have shown that the mode frequencies of modes up to $(\ell, m) = (6, 6)$ of the excited merger remnant resemble the prograde quasi-normal modes of a Kerr BH to an accuracy of less than 0.01%.

- **Cauchy characteristic extraction.** A systematic error inherent in all current numerical wave-extraction methods is the computation of the gravitational radiation at a finite distance to the source. This is a result of the necessarily finite computational domain in current numerical relativity simulations, which forces one to set up extraction world-tubes with a finite radius. However, gravitational radiation is unambiguously defined only at future null infinity. Since this requires the full non-linear evolution of the Einstein equations out to null infinity, finite-radius extraction introduces a cut-off that results in a indeterminable loss of accuracy, especially in the highly non-linear merger phase. In addition to near-zone effects, gauge effects at the extraction sphere are another substantial source of error.

These problems can be circumvented by the application of Cauchy characteristic extraction. This technique couples characteristic evolutions to Cauchy evolutions thus combining the strengths of two independent formulations of the Einstein equations. While Cauchy evolutions can accurately model the strong field regions, characteristic evolutions have been successful in the evolution of the wave-zone. On the characteristic grid, the compactification of the radial coordinate along the outgoing null geodesics allows to place future null infinity on the finite computational domain.

In this thesis, we have successfully applied this method to BBH merger simulations and have obtained the first unambiguous gravitational waveforms for this problem. We have shown that the obtained waveforms are free of gauge-effects and possess only numerical error. Furthermore, we have been able to show that current finite-radius extraction techniques are valid to a precision of about 0.01%, but corrections have to be taken into account for the advanced gravitational-wave detectors, and when parameters estimation is crucial. Particularly, the differences will become important for the advanced detectors, and especially for LISA (see Section 15.2).

In addition, the presented code is general purpose, and can be applied to any spacetime simulation such as core-collapse supernovae or binary neutron star simulations, given metric data on a fixed coordinate sphere.

Furthermore, we have used numerical simulations to address the following questions:

- **Gravitational-wave detectability of BBH mergers.** In the 2D parameter subspace of equal-mass spin-aligned binaries, we have considered the gravitational-wave detectability for ground-based gravitational-wave detectors as well as for the planned space-based LISA interferometer.

  Across a set of different masses, we have calculated the SNR for LIGO, as well as enhanced and advanced LIGO, Virgo, as well as advanced Virgo, and LISA. We have addressed the following questions:

  (i) Which among the aligned-spin configurations is the "loudest" and which one is the "quietest"?

  (ii) How large is the difference in signal-to-noise ratio between the loudest and the quietest?

  (iii) How do these considerations depend on the detector used, the mass of the binary, and the number of harmonics?

  (iv) Are there configurations whose waveforms are difficult to distinguish and are hence degenerate in the space of templates?

  We have found the following answers, respectively:

  (i) Equal-spinning and maximally anti-aligned binaries generally produce the lowest SNR while equal-spinning aligned binaries produce the highest SNR. For any mass, the SNR can be well described with a low-order polynomial of the initial spins and generally increases with the total dimensionless spin along the angular momentum direction, $a \equiv \frac{1}{2}(\mathbf{a}_1+\mathbf{a}_2)\cdot\hat{\mathbf{L}}$. The possibility of describing the whole behavior of the waveforms from equal-mass, aligned/anti-aligned binaries in terms of a single scalar quantity, namely a, provides a certain amount of optimism that also more complex spin configurations can, ultimately, be described in terms of a few parameters only.

  (ii) The differences in the SNR between models with scalar spin parameters $a = -1$ and $a = +1$ are significant, leading to an increase in the event rate of about ~ 27 for binaries with $a = +1$ compared to binaries with $a = -1$. This indicates that the chances

for detecting a spin-aligned binary system are much larger than for spin anti-aligned configurations.

(iii) Higher harmonics can increase the SNR by about $\sim 8\%$. Furthermore, higher harmonics have a larger contribution for spin-aligned configurations than for spin anti-aligned binaries.

The average horizon distances go from $\sim 600/800$Mpc for the Virgo/LIGO detectors to $\sim 10^4/1.2\times10^4$Mpc for the advanced Virgo/LIGO detectors, thus resulting in an observational volume of the Universe that is increased by a factor of $\sim 5000/3000$, respectively. All binaries considered for LISA are visible throughout the entire Universe.

(iv) Binaries along the diagonal $a_1 = -a_2$ cannot be distinguished within the given numerical accuracy, whereas configurations along the diagonal $a_1 = a_2$ are clearly different.

This indicates that gravitational-wave template banks can be modeled in terms of the single scalar spin parameter a, at least at lowest order.

It furthermore turns out that even simple waveforms, such as those relative to non-spinning binaries, will be effective enough to provide a detection for most configurations of equal-mass and aligned/anti-aligned binaries.

Finally, we provide a phenomenological expression for the energies radiated through gravitational-wave emission. We find that configurations with a scalar spin parameter $a = -1$ loose $\sim 3.6\%$ of their total mass whereas binaries with $a = +1$ loose $\sim 10\%$ of their total mass.

- **The asymptotic fall-off behavior of local waveform measurements.** The application of the newly developed multiblock AMR code allows for an accurate analysis of the fall-off behavior of the Weyl curvature scalars at large distances to the source. We have demonstrated that current finite-radius wave-extrapolation techniques can accurately represent the radiation obtained at much larger radii, and particularly at $\mathscr{J}^+$. We have found that the leading order contribution to the curvature is contained in Ψ_4, even at rather small radii $r < 100M$. This validates that Ψ_4 can indeed be seen as the outgoing radiation component, even at small radii, and marks an important check on numerical relativity measurements. However, in order to obtain an accurate measure, results indicate that wave extraction should be carried out at least at $r = 200M$.
- **Recoil velocities of the merger remnant.** A gravitational recoil emerges if the BBH system emits gravitational radiation asymmetrically. This effect may be so large that the merger remnant is eventually "kicked out" of its host object. Clearly, this can have dramatic consequences on the further evolution of the host.

  A substantial amount of radiation is emitted during the merger process itself and is therefore inaccessible by approximate methods, such as post-Newtonian predictions. An accurate description of this effect requires full non-linear numerical computations. Consequently, various numerical relativity groups have tried to quantify this effect across the whole 7D parameter space.

  We have focused on the 2D subspace of equal-mass spin-aligned binaries. We have found that the recoil velocity can be modeled in terms of a quadratic polynomial depending on the differences between the two initial spins of the binary. We have extrapolated to a maximal recoil of $|v_{\rm recoil}| = 441.94 \pm 1.56$km/s. This is unlikely to be sufficient to kick the remnant out of its host environment. Particularly, as it is believed that the spins will generally align during the inspiral, especially in the case of SMBHs and galaxy mergers, the central BH is very likely to evolve together with the host galaxy.
- **Final spin of the merger remnant.** The merger of two orbiting BHs generally produces a remnant with non-vanishing final spin. Determining the spin dependence of the remnant in terms of the parameters of the initial BHs is one of the key aspects of BBH astrophysics.

  We have addressed the issue through a large set of numerical simulations. We have constructed phenomenological expressions which model the final spin in terms of the full 7D parameter space. We find that the remnant is typically spun-up by the merger, but it is possible to find configurations which lead to a Schwarzschild BH. Remnants below that limit will receive a spin which is “flipped” with respect to the total initial angular momentum. Remnants above that limit will have a spin which is positive with respect to the total initial angular momentum.

Conclusive remarks and outlook

It is remarkable how the accuracy of the numerical simulations has increased over the past four years. For example, at the time while finishing off this thesis, our group at the AEI and the Caltech/Cornell group were able to determine the final mass and spin of a merged BH with a confidence of more than 10^{-4}. In addition, the phase and amplitude errors in the waveforms could be reduced significantly. While some early waveforms reported by the various numerical relativity groups had errors of the order of 10%, there is now an uncertainty of less than 0.1%! In addition, and which is among the achievements of this thesis, two significant systematic errors inherent in the gravitational waveforms could be removed: contamination by constraint violations from the outer boundary and finite radius wave-extraction. The latter has been successfully removed by applying CCE as described in Sections 5.3, 9.1 and 15.2, and the former has been circumvented by pushing the outer boundary to very large radii, so that it is causally disconnected from the extraction world-tubes. This became possible by the application of multiblock techniques as described in Section 7.3.

However, there are still some remaining problems in the numerical modeling of BBH systems. One of the largest remaining source of error is the generation of proper initial data. Here, one of the problems is the determination of the “correct” linear momenta that places the two BHs on orbits with vanishing residual eccentricity. Despite post-Newtonian methods, which have significantly reduced the amount of initial eccentricity as compared to methods such as the effective potential method, the choice of conformally flat Bowen-York initial data results in an uncontrollable amount of “junk” radiation which alters the initial linear momenta sufficiently, so that the orbits can never be pushed below a certain residual eccentricity by means of conventional methods. In addition, conformally flat initial data constructions using Bowen-York extrinsic curvature do not model the proper radiation content of BBH spacetimes that have inspiralled from infinite initial separation. For example, the kick-velocity as discussed in Chapter 12 depends on the past radiation history of the BBH inspiral. Fortunately, the resulting integration constant could be estimated by methods described in Section 12.1.

However, initial conformal flatness has another severe drawback. It is not possible to construct Bowen-York BHs with maximal spin $a = 1$. This is due to the fact that the initial junk radiation generally carries away an uncontrollable amount of angular momentum, and since the violation of cosmic censorship has not been observed for Bowen-York BH initial data, the resulting spin of the BHs once the junk radiation has left the system must generally satisfy $a < 1$ as the total spin of a stationary and axisymmetric spacetime does not exceed $a = 1$ (also see Section 2.4, particularly subsection on “Bowen-York extrinsic curvature” for a discussion).

Another outstanding problem is the question of how to impose constraint-preserving outer boundary conditions. Currently, such boundary conditions are only known for the Friedrich-Nagy system, but this system is not used in current numerical relativity codes.

Other work tries to achieve approximative constraint-preserving boundary conditions, but these are limited to the harmonic evolution system only. The main problem here is that the spacetime is infinite and any boundary condition placed at the outer computational domain is necessarily an artificial one. One way of circumventing this situation is the application of Cauchy-characteristic matching. This method is an extension to CCE, but also couples the characteristic system back to the Cauchy system such that the world-tube becomes a two-way boundary. In this way, one consistently evolves the entire spacetime out to future null infinity without placing any boundary conditions ($\mathscr{J}^+$ is a purely outflowing boundary) and with the advantage of wave-extraction at future null infinity. The author of this thesis has already started work in that direction.

Finally, there are many unanswered questions and holes in the full 7D parameter space of BBH mergers regarding the properties of the remnant and the construction of a family of template waveforms to be used for gravitational-wave detection and parameter estimation. For example, the construction of a complete template bank of BBH merger waveforms covering the full 7D space of parameters is desirable, but yet has only be achieved in the equal-mass non-spinning case and its extension to equal-mass spin-aligned binaries. Here, the achievement of higher mass-ratios is especially difficult. The reason for this is the enormous computational power that is necessary to accurately evolve unequal mass BHs that have large mass ratios.

Furthermore, results obtained in this thesis indicate that there are degenerate direction in the parameter space of spin-aligned binaries, at least in the leading $(\ell, m) = (2, 2)$ harmonic mode of the gravitational-wave signal. It is further indicated that higher modes will break this degeneracy, but the differences are subtle. This, however, puts high demands on the ability of correct parameter estimation of the binaries based on gravitational-wave observations. A more refined study with higher accuracy is necessary to be able to assess the influence of higher modes.

Also, the properties of the merger remnant in terms of the full 7D space of parameters are not completely understood. Although some of the (initial) holes have been filled by work achieved in this thesis, there is still much work that needs to be done in order to validate and enhance the various phenomenological expressions for kick-velocities, final spin and mass to the full space of parameters and to a high precision. The latter, however, can only be achieved as soon as all systematic errors inherent in all current numerical relativity simulations have been completely removed.

In the very end, the author believes that complete and strict mathematical rigor is necessary in order to construct high accuracy waveform template banks that might one day be used as an ultimate test of GR, and that might eventually give clues on how to construct a unified theory of quantum fields and gravitation.

Appendix A

Reference formulae

A.1 Geometrized units

In numerical relativity computations, the Einstein equations are usually solved by using *geometrized units*. This means setting the gravitational constant G and the speed of light c to 1, *i.e.*

$$G = 1 = c. \tag{A.1.1}$$

It follows that mass, time and space are all measured in units of meters m. For example, every time interval is interpreted as the distance the light has traveled during that time interval.

In order to convert between geometrized units and physical units we can introduce the following conversion factors as listed in Table A.1.

For example, the solar mass corresponds to $\sim 1.5\,km$ or to $\sim 5\,\mu s$:

$$1M_{\odot} = 1.9891 \cdot 10^{30}\,kg = 1476.63\,m = 4.92549 \cdot 10^{-6} s\,. \tag{A.1.2}$$

In vacuum numerical relativity, the total mass M of a spacetime is therefore a free parameter, *i.e.* everything is calculated in units of M. Table A.1 shows various quantities and their relationship to M.

Table A.1: Conversion factors.

quantity	**factor**	**numerical value**
time	c	$299,792,458\,m/s$
mass	G/c^2	$7.4247 \cdot 10^{28}\,m/kg$

Table A.2: Quantities and their units in M.

quantity	**symbol**	**unit [M]**	**unit [SI]**
time	T	M	s
space	x, y, z	M	m
mass	M	M	kg
energy	E	M	J
frequency	f	$1/M$	Hz
angular momentum	J	M^2	Js
spin parameter	a	–	–
gravitational strain	$h(t)$	–	–

A.2 Sensitivity curves

For convenience, we report below the sensitivity curves used to compute the SNRs that are often difficult to collect from the literature. For LISA, we use the same noise curve as for the LISA Mock Data Challenge 3 [496] as implemented by Trias and Sintes, and made available by the LISA Parameter Estimation Task Force [497]. The noise curve for advanced Virgo can be found in tabulated form in Ref. [468].

LIGO

$$S_h(f) = S_0 \left\{ \left(\tfrac{4.49f}{f_0}\right)^{-56} + 0.16 \left(\tfrac{f}{f_0}\right)^{-4.52} + 0.52 + 0.32 \left(\tfrac{f}{f_0}\right)^2 \right\} , \qquad S_0 = 9 \times 10^{-46}, \quad f_0 = 150 \text{ Hz} , \tag{A.2.1}$$

AdLIGO

$$S_h(f) = S_0 \left\{ \left(\tfrac{f}{f_0}\right)^{-4.14} - 5 \left(\tfrac{f_0}{f}\right)^2 + 111 \left(1 - \left(\tfrac{f}{f_0}\right)^2 + \tfrac{1}{2} \left(\tfrac{f}{f_0}\right)^4\right) \left(1 + \tfrac{1}{2} \left(\tfrac{f}{f_0}\right)^2\right)^{-1} \right\} , \qquad S_0 = 10^{-49}, \quad f_0 = 215 \text{ Hz} , \tag{A.2.2}$$

Virgo

$$S_h(f) = S_0 \left\{ \left(\tfrac{7.87f}{f_0}\right)^{-4.8} + \tfrac{6}{17} \left(\tfrac{f_0}{f}\right) + \left[1 + \left(\tfrac{f}{f_0}\right)^2\right] \right\} , \qquad S_0 = 10.2 \times 10^{-46}, \quad f_0 = 500 \text{ Hz} . \tag{A.2.3}$$

Table A.3: Coefficients for centered finite difference operators. The first column denotes the order n of the derivative, while the second column denotes the order of accuracy p in terms of the spacing h. The remaining columns denote the coefficients at the nodes relative to the node x_i, where the derivative is approximated. The nodes, *i.e.* the gridpoints are assumed to be uniformly spaced with spacing h. A finite difference operator is obtained by summing all coefficients and dividing by the spacing h, *e.g.* $\partial f_i = (1/2 f_{i+1} - 1/2 f_{i-1})/h$.

n	$\mathcal{O}(h^p)$	Approximation at x_i; Nodes at x_{i+k}:								
		$k =$	-4	-3	-2	-1	0	$+1$	$+2$	$+3$	$+4$
0	∞						1				
1	2					$-\frac{1}{2}$	0	$\frac{1}{2}$			
	4				$\frac{1}{12}$	$-\frac{2}{3}$	0	$\frac{2}{3}$	$-\frac{1}{12}$		
	6			$-\frac{1}{60}$	$\frac{3}{20}$	$-\frac{3}{4}$	0	$\frac{3}{4}$	$-\frac{3}{20}$	$\frac{1}{60}$	
	8		$\frac{1}{280}$	$-\frac{4}{105}$	$\frac{1}{5}$	$-\frac{4}{5}$	0	$\frac{4}{5}$	$-\frac{1}{5}$	$\frac{4}{105}$	$-\frac{1}{280}$
2	2					1	-2	1			
	4				$-\frac{1}{12}$	$\frac{4}{3}$	$-\frac{5}{2}$	$\frac{4}{3}$	$-\frac{1}{12}$		
	6			$\frac{1}{90}$	$-\frac{3}{20}$	$\frac{3}{2}$	$-\frac{49}{18}$	$\frac{3}{2}$	$-\frac{3}{20}$	$\frac{1}{90}$	
	8		$-\frac{1}{560}$	$\frac{8}{315}$	$-\frac{1}{5}$	$\frac{8}{5}$	$-\frac{205}{72}$	$\frac{8}{5}$	$-\frac{1}{5}$	$\frac{8}{315}$	$-\frac{1}{560}$

A.3 Finite difference and dissipation operators

In this Section, we give the finite difference operators that were used for discretizing the evolution equations, as well as the associated dissipation operators.

A procedure for generating finite difference operators is given in [343, 498]. Table A.3 lists the coefficients for centered finite difference operator while Table A.4 lists the coefficients for side-winded finite difference operators. Given the coefficients at nodes $i \pm k$, we can approximate the derivative at node i according to

$$\frac{\partial f(x_i)}{\partial x} = \frac{1}{h} \sum_k C_{i+k} f_{i+k} \tag{A.3.1}$$

so that we have *e.g.*

$$\frac{\partial f(x_i)}{\partial x} = \frac{1}{h} (1/2 f_{i+1} - 1/2 f_{i-1}) \tag{A.3.2}$$

for a second-order accurate centered approximation to a first derivative.

In addition, the characteristic code uses derivatives at points between gridpoints. Particularly, we use a second-order accurate first derivative of the form

$$\frac{\partial f(x_{i+1/2})}{\partial x} = \frac{1}{h} (f_i - f_{i-1}) \, . \tag{A.3.3}$$

It should be noted that the upwind discretization of the advection terms in the BSSNOK evolution system relies on first derivatives whose difference operators use side-winded stencils that are off-centered by *one* gridpoint only. However the coefficients were generated numerically as described in [498], so that a representation in terms of fractional coefficients is not possible in all cases. The coefficients for the fourth-order off-centered stencil of the first derivative read

$$\begin{aligned} C_{-2} &= \frac{1}{6} \\ C_{-1} &= -1 \\ C_0 &= \frac{1}{2} \\ C_1 &= \frac{1}{3} \\ C_2 &= 0 \end{aligned} \tag{A.3.4}$$

Table A.4: Coefficients for completely side-winded finite difference operators. The first column denotes the order n of the derivative, while the second column denotes the order of accuracy p in terms of the spacing h. The remaining columns denote the coefficients at the nodes relative to the node x_i, where the derivative is approximated. The nodes, *i.e.* the gridpoints are assumed to be uniformly spaced with spacing h. A finite difference operator is obtained by summing all coefficients and dividing by the spacing h, *e.g.* $\partial f_i = (f_{i+1} - f_i)/h$ (forward difference). Note that there is a symmetry $i+k \rightarrow i-k$ with the coefficient changing sign so that we can also write $\partial f_i = (f_i - f_{i-1})/h$ (backward difference).

n	$\mathcal{O}(h^p)$	Approximation at x_i; Nodes at x_{i+k}:								
		$k =$	0	1	2	3	4	5	6	7	8
0	∞		1								
1	1		-1	1							
	2		$-\frac{3}{2}$	2	$-\frac{1}{2}$						
	4		$-\frac{25}{12}$	4	-3	$\frac{4}{3}$	$-\frac{1}{4}$				
	6		$-\frac{49}{20}$	6	$-\frac{15}{2}$	$\frac{20}{3}$	$-\frac{15}{4}$	$\frac{6}{5}$	$-\frac{1}{6}$		
	8		$-\frac{761}{280}$	8	-14	$\frac{56}{3}$	$-\frac{35}{2}$	$\frac{56}{5}$	$-\frac{14}{3}$	$\frac{8}{7}$	$-\frac{1}{8}$
2	1		1	-2	1						
	2		2	-5	4	-1					
	4		$\frac{15}{4}$	$-\frac{77}{6}$	$\frac{107}{6}$	-13	$\frac{61}{12}$	$-\frac{5}{6}$			
	6		$\frac{469}{90}$	$-\frac{223}{10}$	$\frac{879}{20}$	$-\frac{949}{18}$	41	$-\frac{201}{10}$	$\frac{1019}{180}$	$-\frac{7}{10}$	

The corresponding coefficients for the sixth-order off-centered stencil read

$$\begin{aligned}
C_{-4} &= \frac{1}{60} \\
C_{-3} &= -\frac{4}{3} \\
C_{-2} &= \frac{1}{2} \\
C_{-1} &= -\frac{4}{3} \\
C_{0} &= 0.5833333333333333333333333333333333333333 \\
C_{1} &= \frac{2}{5} \\
C_{2} &= -\frac{1}{30} \\
C_{3} &= 0 \\
C_{4} &= 0
\end{aligned} \tag{A.3.5}$$

Table A.5: Coefficients for Kreiss-Oliger type dissipation operators. The first column denotes the order of accuracy p in terms of the spacing h. The remaining columns denote the coefficients at the nodes relative to the node x_i, where the dissipation operator is applied. The nodes, *i.e.* the gridpoints are assumed to be uniformly spaced with spacing h. An artificial dissipation operator is obtained by summing all coefficients and dividing by the spacing h.

$\mathcal{O}(h^p)$	Dissipation at x_i; Nodes at x_{i+k}:									
	$k =$	-4	-3	-2	-1	0	$+1$	$+2$	$+3$	$+4$
2					$\frac{1}{4}$	$-\frac{2}{4}$	$\frac{1}{4}$			
4				$-\frac{1}{16}$	$\frac{4}{16}$	$-\frac{6}{16}$	$\frac{4}{16}$	$-\frac{1}{16}$		
6			$\frac{1}{256}$	$-\frac{6}{256}$	$\frac{15}{256}$	$-\frac{20}{256}$	$\frac{15}{256}$	$-\frac{6}{256}$	$\frac{1}{256}$	
8		$-\frac{1}{4096}$	$\frac{8}{4096}$	$-\frac{28}{4096}$	$\frac{56}{4096}$	$-\frac{70}{4096}$	$\frac{56}{4096}$	$-\frac{28}{4096}$	$\frac{8}{4096}$	$-\frac{1}{4096}$

The corresponding coefficients for the eighth-order off-centered stencil read

$$\begin{aligned}
C_{-5} &= -0.003571428571428571428571428571428571428571 \\
C_{-4} &= 0.03571428571428571428571428571428571428571 \\
C_{-3} &= -\frac{5}{30} \\
C_{-2} &= \frac{1}{2} \\
C_{-1} &= -\frac{10}{8} \\
C_{0} &= \frac{9}{20} \\
C_{1} &= \frac{1}{2} \\
C_{2} &= -0.07142857142857142857142857142857142857143 \\
C_{3} &= 0.005952380952380952380952380952380952380952 \\
C_{4} &= 0 \\
C_{5} &= 0
\end{aligned} \tag{A.3.6}$$

A prescription for generating Kreiss-Oliger type artificial dissipation operators is given in [344], and can also be found in [498] and in the Appendix of [381]. Table A.5 lists the dissipation operators that are applied for all orders of accuracy that are used in the codes.

A.4 Six-patch local coordinates and Jacobians

The spherical patches as described in Section 7.3 have the following relation to Cartesian coordinates [262].

- ±X patch :

$$
\begin{aligned}
(\rho,\sigma,r) &\equiv (\nu,\phi,r) \\
\nu = \text{rotation about local y} &= \arctan(z/x) && \text{(A.4.1)} \\
\phi = \text{rotation about local z} &= \arctan(y/x) && \text{(A.4.2)} \\
r = \text{radius} &= \pm x\sqrt{1+\tan^2(\phi)+\tan^2(\nu)} && \text{(A.4.3)}
\end{aligned}
$$

The Jacobians evaluate as

$$\frac{\partial a^i}{\partial x^j} = \begin{pmatrix} -\frac{z}{x^2+z^2} & 0 & \frac{x}{x^2+z^2} \\ -\frac{y}{x^2+y^2} & \frac{x}{x^2+y^2} & 0 \\ 0 & 0 & 0 \end{pmatrix} \tag{A.4.4}$$

$$\frac{\partial^2 a^i}{\partial x^j \partial x^k} = \begin{pmatrix} \left\{\frac{2xz}{(x^2+z^2)^2}, 0, \frac{z^2-x^2}{(x^2+z^2)^2}\right\} & \{0,0,0\} & \left\{\frac{z^2-x^2}{(x^2+z^2)^2}, 0, -\frac{2xz}{(x^2+z^2)^2}\right\} \\ \left\{\frac{2xy}{(x^2+y^2)^2}, \frac{y^2-x^2}{(x^2+y^2)^2}, 0\right\} & \left\{\frac{y^2-x^2}{(x^2+y^2)^2}, -\frac{2xy}{(x^2+y^2)^2}, 0\right\} & \{0,0,0\} \\ \{0,0,0\} & \{0,0,0\} & \{0,0,0\} \end{pmatrix} \tag{A.4.5}$$

- ±Y patch :

$$
\begin{aligned}
(\rho,\sigma,r) &\equiv (\mu,\phi,r) \\
\mu = \text{rotation about local x} &= \arctan(z/y) && \text{(A.4.6)} \\
\phi = \text{rotation about local z} &= \arctan(x/y) && \text{(A.4.7)} \\
r = \text{radius} &= \pm y\sqrt{1+\tan^2(\phi)+\tan^2(\nu)} && \text{(A.4.8)}
\end{aligned}
$$

$$\frac{\partial a^i}{\partial x^j} = \begin{pmatrix} 0 & -\frac{z}{y^2+z^2} & \frac{y}{y^2+z^2} \\ \frac{y}{x^2+y^2} & -\frac{x}{x^2+y^2} & 0 \\ 0 & 0 & 0 \end{pmatrix} \tag{A.4.9}$$

$$\frac{\partial^2 a^i}{\partial x^j \partial x^k} = \begin{pmatrix} \{0,0,0\} & \left\{0, \frac{2yz}{(y^2+z^2)^2}, \frac{z^2-y^2}{(y^2+z^2)^2}\right\} & \left\{0, \frac{z^2-y^2}{(y^2+z^2)^2}, -\frac{2yz}{(y^2+z^2)^2}\right\} \\ \left\{-\frac{2xy}{(x^2+y^2)^2}, \frac{x^2-y^2}{(x^2+y^2)^2}, 0\right\} & \left\{\frac{x^2-y^2}{(x^2+y^2)^2}, \frac{2xy}{(x^2+y^2)^2}, 0\right\} & \{0,0,0\} \\ \{0,0,0\} & \{0,0,0\} & \{0,0,0\} \end{pmatrix} \tag{A.4.10}$$

- ±Z patch :

$$
\begin{aligned}
(\rho,\sigma,r) &\equiv (\mu,\nu,r) \\
\mu = \text{rotation about local x} &= \arctan(y/z) && \text{(A.4.11)} \\
\nu = \text{rotation about local y} &= \arctan(x/z) && \text{(A.4.12)} \\
r = \text{radius} &= \pm z\sqrt{1+\tan^2(\mu)+\tan^2(\nu)} && \text{(A.4.13)}
\end{aligned}
$$

$$\frac{\partial a^i}{\partial x^j} = \begin{pmatrix} 0 & \frac{z}{y^2+z^2} & -\frac{y}{y^2+z^2} \\ \frac{z}{x^2+z^2} & 0 & -\frac{x}{x^2+z^2} \\ 0 & 0 & 0 \end{pmatrix} \tag{A.4.14}$$

$$\frac{\partial^2 a^i}{\partial x^j \partial x^k} = \begin{pmatrix} \{0,0,0\} & \left\{0, -\frac{2yz}{(y^2+z^2)^2}, \frac{y^2-z^2}{(y^2+z^2)^2}\right\} & \left\{0, \frac{y^2-z^2}{(y^2+z^2)^2}, \frac{2yz}{(y^2+z^2)^2}\right\} \\ \left\{-\frac{2xz}{(x^2+z^2)^2}, 0, \frac{x^2-z^2}{(x^2+z^2)^2}\right\} & \{0,0,0\} & \left\{\frac{x^2-z^2}{(x^2+z^2)^2}, 0, \frac{2xz}{(x^2+z^2)^2}\right\} \\ \{0,0,0\} & \{0,0,0\} & \{0,0,0\} \end{pmatrix} \tag{A.4.15}$$

The local angular coordinates on the nominal grid take values in $\rho, \sigma \in [-\pi/4; +\pi/4]$, and the local and global radial coordinate ranges from r_{min} to r_{max}.

Note that the coordinates above do not take into account radial stretching. The resulting expressions are too long to be reported here.

A.5 Spin-weighted spheroidal harmonics

In this section, we streamline the procedure of calculating the spin-weighted spheroidal harmonics numerically. The description is very closely following [420].

Generalized (four-dimensional) *spin-weighted spheroidal harmonics* (SWSHs) were first defined by Teukolsky [332] in the context of black hole physics. They result from the separation of angular variables in the equations describing the propagation of a spin-s field in a rotating (Kerr) black hole background.

An important application concerns quasinormal modes of Kerr black holes [108]. The damped oscillation frequencies of Kerr black holes, ω, are uniquely determined by the black hole's mass M and specific angular momentum a. The calculation of quasinormal frequencies reduces to the solution of a coupled system of differential equations. One equation belongs to the class of generalized spheroidal wave equations, and describes the radial dependence of the perturbations; the other is a SWSH with $c = a\omega$, describing the angular dependence [111, 499–503].

Using the Kinnersley tetrad [504] and Boyer-Lindquist coordinates, the angular equation definining SWSHs results from the separation of the equations describing propagation of a spin-s field in the Kerr background [332]:

$$\left[(1-x^2)\,{}_sS_{lm,x}\right]_{,x} + \left[(cx)^2 - 2csx + s + {}_sA_{lm} - \frac{(m+sx)^2}{1-x^2}\right]{}_sS_{lm} = 0\,, \tag{A.5.1}$$

where $x \equiv \cos\theta$ and θ is the Boyer-Lindquist polar angle.

The angular separation constant ${}_sA_{lm}$ and the SWSHs ${}_sS_{lm}$ are, in general, complex. They take on real values only in the oblate case ($c \in \mathbb{R}$) or, alternatively, in the prolate case ($c = ic_I$ pure-imaginary) with $s = 0$. In the limit $c \to 0$ the angular separation constant can be determined analytically:

$${}_sA_{lm} = l(l+1) - s(s+1)\,. \tag{A.5.2}$$

Leaver found the following series solution for the angular eigenfunctions [111]:

$${}_sS_{lm}(x) = e^{cx}\,(1+x)^{k_-}\,(1-x)^{k_+}\sum_{p=0}^{\infty} a_p(1+x)^p\,, \tag{A.5.3}$$

where $k_\pm \equiv |m \pm s|/2$. The expansion coefficients a_p are obtained from the three term recursion relation

$$\alpha_0 a_1 + \beta_0 a_0 = 0\,, \tag{A.5.4}$$

$$\alpha_p a_{p+1} + \beta_p a_p + \gamma_p a_{p-1} = 0\,, \qquad p = 1, 2\ldots \tag{A.5.5}$$

with

$$\begin{aligned}
\alpha_p &= -2(p+1)(p+2k_-+1)\,, \\
\beta_p &= p(p-1) + 2p(k_- + k_+ + 1 - 2c) \\
&\quad - \left[2c\,(2k_- + s + 1) - (k_- + k_+)\,(k_- + k_+ + 1)\right] - \left[c^2 + s(s+1) + {}_sA_{lm}\right]\,, \\
\gamma_p &= 2c\,(p + k_- + k_+ + s)\,.
\end{aligned} \tag{A.5.6}$$

Given a (generally complex) argument c, the separation constant ${}_sA_{lm}$ can be obtained solving numerically the continued fraction equation

$$\beta_0 - \frac{\alpha_0\gamma_1}{\beta_1 -}\frac{\alpha_1\gamma_2}{\beta_2 -}\frac{\alpha_2\gamma_3}{\beta_3 -}\ldots = 0\,, \tag{A.5.7}$$

or any of its inversions [111].

Leaver's solution gives a simple and practical algorithm for the numerical calculation of eigenvalues and eigenfunctions. Start from the known analytic eigenvalue for $c = 0$, (A.5.2). Use this as an initial guess, increase the value of c and solve numerically (A.5.7) to get the eigenvalue for $c \neq 0$. In our case, this is done by using a secant root-finding algorithm which uses an initial intervall of $[-1/2 + {}_sA_{lm}, +1/2 + {}_sA_{lm}]$, where ${}_sA_{lm}$ is the initial eigenvalue for $c = 0$. The recursion depth of the continued fraction equation (A.5.7) is chosen to be 50. Once the eigenvalue is known, compute any number of series coefficients a_p, using the recursion relation, and plug them into the series solution (A.5.3) to get the corresponding eigenfunction to any required precision. In our case, we truncate the series at $p = p_{\text{max}} = 15$.

This algorithm only determines the eigenfunction up to a normalization constant, which can easily be fixed by imposing the normalization condition

$$\int_{-1}^{1} |{}_sS_{lm}(x)|^2 dx = 1\,. \tag{A.5.8}$$

Various tests have been performed to check for the correct implementation of the SWHSs in the Mathematica notebook.

First, we have checked for orthonormality for all possible combinations of modes up to $\ell \leq \ell_{\text{max}}$, where $\ell_{\text{max}} = 8$.

Second, we have compared the overlap integrals

$$\int \; {}_{-2}\bar{S}_{lm}(a\omega_{lmN}) \; {}_{-2}S_{l'm'}(a\omega_{l'm'N'}) d\Omega = \alpha_{mll'NN'}(a)\delta_{m,m'}\,. \tag{A.5.9}$$

for spin $a = 0.8$ as given in [420].

Both tests yielded the expected results.

Acknowledgements

I would like to thank a number of people who have greatly contributed to my current understanding of numerical and general relativity.

Here at the AEI, I found excellent teachers as well as a vivid exchange of ideas and fruitful collaborations.

First, I thank Luciano Rezzolla for giving me the chance of contributing to many of the interesting black hole projects. He has been a very supportive advisor and has always been available for discussions as well as being involved in seeking solutions for all kinds of problems. Especially at the beginning, his guidance was of great help and he was able to provide me with insight into the many aspects of black hole physics. With the same gratitude, I thank Nils Dorband, Michael Koppitz, Sascha Husa, Denis Pollney and Erik Schnetter. They have been close collaborators and teachers, and I have learned a lot about black hole binaries, their numerical treatment, implementational details and beyond. Most importantly, my numerous questions have always found an open ear.

I thank Nigel T. Bishop and Béla Szilágyi for getting me into characteristic work. Their input and deep knowledge has been a great source of help during this thesis.

Furthermore, I am grateful for valuable discussions with Marcus Ansorg, Stanislav Babak, Werner Benger, Nico Budewitz, Peter Diener, Filippo Galeazzi, Bruno Giaccomazo, Mark Hannam, Jörg Hennig, Ian Hinder, Michael Jasiulek, Thorsten Kellermann, Badri Krishnan, Philipp Mösta, Christian D. Ott, Thomas Radke, Lucia Santamaria, Bernard Schutz, Jennifer Seiler, Pau Amaro-Seoane, Nikodem Szpak, Jonathan Thornburg, Aaryn Tonita, Tilman Vogel, Steve White, and Anil Zenginoglu.

I hope we stay in contact and continue with many exciting discoveries!

I would also like to thank my friends and co-fighters through university Nils Bornemann, Carsten Grabow, Michael Köhn, Jan Roden, Guybrush Threepwood (mainly first part), as well as my long-standing band-mate Johannes Bähr for releasing the punk *et al.* Hey, hey, my, my, rock'n'roll can never die [505] (except maybe at future timelike infinity).

Finally, I would like to thank my parents Barbara and Georg and my brother Philipp for making my life as comfortable as possible, as well as Katja for her love, kindness and support. Without you, I am nothing.

This research has made use of NASA's Astrophysics Data System. Computations were performed at the AEI[1], at LSU, on LONI[2] (numrel02, numrel03, numrel04), on the TeraGrid[3] (TG-MCA02N014), the Leibniz Rechenzentrum München (h0152), and on the Titan cluster at Unisa. I furthermore thank the University of South Africa, the Louisiana State University and the Universidad de les Illes Balear for hospitality. I thank the developers of Cactus and Carpet for providing an open and optimized computational infrastructure on which I have based many of my codes. I thank the MPG/AEI for financial support to the numerous travel experiences including conferences, workshops, schools, meetings and research collaborations.

Finally, it can be said that the author of this thesis favours (at this stage) level IV multiverses [506, 507] and believes that if "His Great Programmer" exists then he must have been aware of thoughts presented in [508–513] and [514].

You all contributed to a very happy and productive doctoral time here on this little spot somewhere on the outer edges of one of the trillions of sparkling island universes in a place that I and others call our universe. What a coincidence that we have met!

.

---

[1] The Peyote, Belladonna and Damiana cluster.

[2] The Queenbee and Tezpur cluster.

[3] The Ranger and Kraken cluster.

Curriculum vitae

Name:	Christian Reisswig
Citizenship:	German
Date of Birth:	1981/01/26
Marital Status:	not married
Academic Degrees:	Diploma in Physics, 2006, Overall grade: excellent, Leibniz Univ. Hannover and Max Planck Institute for Gravitational Physics, Albert Einstein Institute (AEI)
Current Position:	PhD Student, Max Planck Institue for Gravitational Physics and Leibniz Univ. Hannover. Supervisor: Prof. B. Schutz, Prof. L. Rezzolla
Professional Education:	
Oct. 2006 –	Graduate Student, AEI and Leibniz Univ. Hannover. Supervisors: Prof. B. Schutz, Prof. L. Rezzolla.
Oct. 2001 – Apr. 2006	Studies of Physics, Leibniz Univ. Hannover. Diploma thesis supervisor: Prof. B. Schutz, Prof. N. Dragon.
Feb. 2008 – Feb. 2009	Entrepreneurial Post-Graduate Education Programme (EPE), Univ. Potsdam.
Fellowships:	
Oct. 2006 – Oct. 2009	International Max Planck Research School Fellow.
School Education:	
1993 – 2000	Gymnasium Groß Ilsede.
1991 – 1993	Orienting School Hohenhameln.
1987 – 1991	Elementary School Rosenthal/Schwicheldt.
Community Service:	
2000 – 2001	Hospital for mentally handicapped people, Ilten/Köthenwald.

List of related publications

[1] C. Reisswig, N. T. Bishop, D. Pollney, and B. Szilagyi. Unambiguous determination of gravitational waveforms from binary black hole mergers. *Phys. Rev. Lett.*, 103:221101, 2009.

[2] C. Reisswig, N. T. Bishop, D. Pollney, and B. Szilagyi. Characteristic extraction in numerical relativity: binary black hole merger waveforms at null infinity. *ArXiv e-prints*, 2009. submitted to Class. and Quant. Grav.

[3] C. Reisswig, S. Husa, L. Rezzolla, E. N. Dorband, D. Pollney, and J. Seiler. Gravitational-wave detectability of equal-mass black-hole binaries with aligned spins. *Phys. Rev. D*, 80:124026, 2009.

[4] D. Pollney, C. Reisswig, E. Schnetter, E. D. Dorband, and P. Diener. High accuracy black hole simulations with an extended wave zone. *ArXiv e-prints*, 2009. submitted to Phys. Rev. D.

[5] D. Pollney, C. Reisswig, E. Schnetter, E. D. Dorband, and P. Diener. The asymptotic falloff of local waveform measurements in numerical relativity. *Phys. Rev. D*, 80:121502, 2009.

[6] E. Schnetter, C. D. Ott, P. Diener, and C. Reisswig. Astrophysical applications of numerical relativity - from teragrid to petascale. *Teragrid Conference*, 2008.

[7] M. Koppitz, D. Pollney, C. Reisswig, L. Rezzolla, J. Thornburg, P. Diener, and E. Schnetter. Recoil Velocities from Equal-Mass Binary-Black-Hole Mergers. *Phys. Rev. Lett.*, 99(4):041102–+, July 2007. doi: 10.1103/PhysRevLett.99.041102.

[8] C. Reisswig, N. T. Bishop, C. W. Lai, J. Thornburg, and B. Szilagyi. Characteristic evolutions in numerical relativity using six angular patches. *Class. and Quant. Grav.*, 24:327–+, June 2007. doi: 10.1088/0264-9381/24/12/S21.

[9] B. Aylott, J. G. Baker, W. D. Boggs, M. Boyle, P. R. Brady, D. A. Brown, B. Brügmann, L. T. Buchman, A. Buonanno, L. Cadonati, J. Camp, M. Campanelli, J. Centrella, S. Chatterji, N. Christensen, T. Chu, P. Diener, N. Dorband, Z. B. Etienne, J. Faber, S. Fairhurst, B. Farr, S. Fischetti, G. Guidi, L. M. Goggin, M. Hannam, F. Herrmann, I. Hinder, S. Husa, V. Kalogera, D. Keppel, L. E. Kidder, B. J. Kelly, B. Krishnan, P. Laguna, C. O. Lousto, I. Mandel, P. Marronetti, R. Matzner, S. T. McWilliams, K. D. Matthews, R. A. Mercer, S. R. P. Mohapatra, A. H. Mroué, H. Nakano, E. Ochsner, Y. Pan, L. Pekowsky, H. P. Pfeiffer, D. Pollney, F. Pretorius, V. Raymond, C. Reisswig, L. Rezzolla, O. Rinne, C. Robinson, C. Röver, L. Santamaría, B. Sathyaprakash, M. A. Scheel, E. Schnetter, J. Seiler, S. L. Shapiro, D. Shoemaker, U. Sperhake, A. Stroeer, R. Sturani, W. Tichy, Y. T. Liu, M. van der Sluys, J. R. van Meter, R. Vaulin, A. Vecchio, J. Veitch, A. Viceré, J. T. Whelan, and Y. Zlochower. Testing gravitational-wave searches with numerical relativity waveforms: Results from the first Numerical INJection Analysis (NINJA) project. *Class. Quant. Grav.*, 26:165008, 2009. doi: 10.1088/0264-9381/26/16/165008.

[10] D. Pollney, C. Reisswig, L. Rezzolla, B. Szilágyi, M. Ansorg, B. Deris, P. Diener, E. N. Dorband, M. Koppitz, A. Nagar, and E. Schnetter. Recoil velocities from equal-mass binary black-hole mergers: A systematic investigation of spin-orbit aligned configurations. *Phys. Rev. D.*, 76(12):124002–+, December 2007. doi: 10.1103/PhysRevD.76.124002.

[11] L. Rezzolla, E. N. Dorband, C. Reisswig, P. Diener, D. Pollney, E. Schnetter, and B. Szilágyi. Spin Diagrams for Equal-Mass Black Hole Binaries with Aligned Spins. *Astrophys. J.*, 679:1422–1426, June 2008. doi: 10.1086/587679.

[12] L. Rezzolla, P. Diener, E. N. Dorband, D. Pollney, C. Reisswig, E. Schnetter, and J. Seiler. The Final Spin from the Coalescence of Aligned-Spin Black Hole Binaries. *Astrophys. J. Lett.*, 674:L29–L32, February 2008. doi: 10.1086/528935.

[13] L. Rezzolla, E. Barausse, E. N. Dorband, D. Pollney, C. Reisswig, J. Seiler, and S. Husa. Final spin from the coalescence of two black holes. *Phys. Rev. D.*, 78(4):044002–+, August 2008. doi: 10.1103/PhysRevD.78.044002.

[14] L. Cadonati, B. Aylott, J. G. Baker, W. D. Boggs, M. Boyle, P. R. Brady, D. A. Brown, B. Brügmann, L. T. Buchman, A. Buonanno, J. Camp, M. Campanelli, J. Centrella, S. Chatterji, N. Christensen, T. Chu, P. Diener, N. Dorband, Z. B. Etienne, J. Faber, S. Fairhurst, B. Farr, S. Fischetti, G. Guidi, L. M. Goggin, M. Hannam, F. Herrmann, I. Hinder, S. Husa, V. Kalogera, D. Keppel, L. E. Kidder, B. J. Kelly, B. Krishnan, P. Laguna, C. O. Lousto, I. Mandel, P. Marronetti, R. Matzner, S. T. McWilliams, K. D. Matthews, R. A. Mercer, S. R. P. Mohapatra, A. H. Mroué, H. Nakano, E. Ochsner, Y. Pan, L. Pekowsky, H. P. Pfeiffer, D. Pollney, F. Pretorius, V. Raymond, C. Reisswig, L. Rezzolla, O. Rinne, C. Robinson, C. Röver, L. Santamaría, B. Sathyaprakash, M. A. Scheel, E. Schnetter, J. Seiler, S. L. Shapiro, D. Shoemaker, U. Sperhake, A. Stroeer, R. Sturani, W. Tichy, Y. T. Liu, M. van der Sluys, J. R. van Meter, R. Vaulin, A. Vecchio, J. Veitch, A. Viceré, J. T. Whelan, and Y. Zlochower. Status of NINJA: the Numerical INJection Analysis project. *Classical and Quantum Gravity*, 26(11):114008–+, June 2009. doi: 10.1088/0264-9381/26/11/114008.

[15] M. Hannam, S. Husa, J. G. Baker, M. Boyle, B. Brügmann, T. Chu, N. Dorband, F. Herrmann, I. Hinder, B. J. Kelly, L. E. Kidder, P. Laguna, K. D. Matthews, J. R. van Meter, H. P. Pfeiffer, D. Pollney, C. Reisswig, M. A. Scheel, and D. Shoemaker. Samurai project: Verifying the consistency of black-hole-binary waveforms for gravitational-wave detection. *Phys. Rev. D.*, 79(8):084025–+, April 2009. doi: 10.1103/PhysRevD.79.084025.

[16] P. Ajith, M. Hannam, S. Husa, Y. Chen, B. Brügmann, N. Dorband, D. Müller, F. Ohme, D. Pollney, C. Reisswig, L. Santamaría, and J. Seiler. “complete” gravitational waveforms for black-hole binaries with non-precessing spins. *ArXiv e-prints*, 2009. submitted to Phys. Rev. Lett.

Bibliography

[1] D. Richstone, E. A. Ajhar, R. Bender, G. Bower, A. Dressler, S. M. Faber, A. V. Filippenko, K. Gebhardt, R. Green, L. C. Ho, J. Kormendy, T. R. Lauer, J. Magorrian, and S. Tremaine. Supermassive black holes and the evolution of galaxies. *Nature*, 395:A14+, October 1998.

[2] L. Ferrarese and D. Merritt. A fundamental relation between supermassive black holes and their host galaxies. *Astrophys. J. Lett.*, 539:L9–L12, 2000. doi: 10.1086/312838.

[3] A. King. Black Holes, Galaxy Formation, and the M_{BH}-σ Relation. *Astrophys. J. Lett.*, 596:L27–L29, October 2003. doi: 10.1086/379143.

[4] A. Eckart and R. Genzel. Observations of stellar proper motions near the Galactic Centre. *Nature*, 383:415–417, October 1996. doi: 10.1038/383415a0.

[5] A. M. Ghez, S. Salim, S. D. Hornstein, A. Tanner, J. R. Lu, M. Morris, E. E. Becklin, and G. Duchêne. Stellar Orbits around the Galactic Center Black Hole. *Astrophys. J.*, 620:744–757, February 2005. doi: 10.1086/427175.

[6] D. Lynden-Bell. Galactic Nuclei as Collapsed Old Quasars. *Nature*, 223:690–694, August 1969. doi: 10.1038/223690a0.

[7] M. J. Valtonen. Black Holes in Active Galactic Nuclei. *American Astronomical Society, IAU Symposium #261. Relativity in Fundamental Astronomy: Dynamics, Reference Frames, and Data Analysis 27 April - 1 May 2009 Virginia Beach, VA, USA, #13.02; Bulletin of the American Astronomical Society, Vol. 41, p.888*, 261:1302–+, May 2009.

[8] M. C. Begelman, R. D. Blandford, and M. J. Rees. Massive black hole binaries in active galactic nuclei. *Nature*, 287:307–309, September 1980. doi: 10.1038/287307a0.

[9] N. Roos. Galaxy mergers and active galactic nuclei. *Astron. Astrophys.*, 104:218–228, December 1981.

[10] M. G. Haehnelt and G. Kauffmann. Multiple supermassive black holes in galactic bulges. *Mon.Not.Roy.Astr.Soc.*, 336:L61–L64, November 2002. doi: 10.1046/j.1365-8711.2002.06056.x.

[11] D. Merritt, M. Milosavljević, M. Favata, S. A. Hughes, and D. E. Holz. Consequences of Gravitational Radiation Recoil. *Astrophys. J. Lett.*, 607:L9–L12, May 2004. doi: 10.1086/421551.

[12] M. Boylan-Kolchin, C.-P. Ma, and E. Quataert. Core Formation in Galactic Nuclei due to Recoiling Black Holes. *Astrophys. J. Lett.*, 613:L37–L40, September 2004. doi: 10.1086/425073.

[13] Z. Haiman. Constraints from Gravitational Recoil on the Growth of Supermassive Black Holes at High Redshift. *Astrophys. J.*, 613:36–40, September 2004. doi: 10.1086/422910.

[14] P. Madau and E. Quataert. The Effect of Gravitational-Wave Recoil on the Demography of Massive Black Holes. *Astrophys. J. Lett.*, 606:L17–L20, May 2004. doi: 10.1086/421017.

[15] J. Yoo and J. Miralda-Escudé. Formation of the Black Holes in the Highest Redshift Quasars. *Astrophys. J. Lett.*, 614:L25–L28, October 2004. doi: 10.1086/425416.

[16] M. Volonteri and R. Perna. Dynamical evolution of intermediate-mass black holes and their observable signatures in the nearby Universe. *Mon.Not.Roy.Astr.Soc.*, 358:913–922, April 2005. doi: 10.1111/j.1365-2966.2005.08832.x.

[17] N. I. Libeskind, C. S. Frenk, S. Cole, J. C. Helly, A. Jenkins, J. F. Navarro, and C. Power. The distribution of satellite galaxies: the great pancake. *Mon.Not.Roy.Astr.Soc.*, 363:146–152, October 2005. doi: 10.1111/j.1365-2966.2005.09425.x.

[18] M. Micic, T. Abel, and S. Sigurdsson. The role of primordial kicks on black hole merger rates. *Mon.Not.Roy.Astr.Soc.*, 372:1540–1548, November 2006. doi: 10.1111/j.1365-2966.2006.11013.x.

[19] L. Blecha and A. Loeb. Effects of gravitational-wave recoil on the dynamics and growth of supermassive black holes. *Mon.Not.Roy.Astr.Soc.*, 390:1311–1325, November 2008. doi: 10.1111/j.1365-2966.2008.13790.x.

[20] A. R. King, J. E. Pringle, and J. A. Hofmann. The evolution of black hole mass and spin in active galactic nuclei. *Mon.Not.Roy.Astr.Soc.*, 385:1621–1627, April 2008. doi: 10.1111/j.1365-2966.2008.12943.x.

[21] D. Sijacki, V. Springel, and M. G. Haehnelt. Growing the first bright quasars in cosmological simulations of structure formation. *ArXiv e-prints*, May 2009.

[22] T. Tanaka and Z. Haiman. The Assembly of Supermassive Black Holes at High Redshifts. *Astrophys. J.*, 696: 1798–1822, May 2009. doi: 10.1088/0004-637X/696/2/1798.

[23] M. J. Benacquista. Relativistic Binaries in Globular Clusters. *Living Reviews in Relativity*, 9:2–+, February 2006.

[24] M. C. Miller and D. P. Hamilton. Four-Body Effects in Globular Cluster Black Hole Coalescence. *Astrophys. J.*, 576:894–898, September 2002. doi: 10.1086/341788.

[25] R. M. O'Leary, F. A. Rasio, J. M. Fregeau, N. Ivanova, and R. O'Shaughnessy. Binary Mergers and Growth of Black Holes in Dense Star Clusters. *Astrophys. J.*, 637:937–951, February 2006. doi: 10.1086/498446.

[26] J. Casares. Observational evidence for stellar-mass black holes. In V. Karas and G. Matt, editors, *IAU Symposium*, volume 238 of *IAU Symposium*, pages 3–12, April 2007. doi: 10.1017/S1743921307004590.

[27] C. F. Gammie, S. L. Shapiro, and J. C. McKinney. Black Hole Spin Evolution. *Astrophys. J.*, 602:312–319, February 2004. doi: 10.1086/380996.

[28] S. L. Shapiro. Spin, Accretion, and the Cosmological Growth of Supermassive Black Holes. *Astrophys. J.*, 620: 59–68, February 2005. doi: 10.1086/427065.

[29] N. Bode and S. Phinney. Variability in Circumbinary Disks Following Massive Black Hole Mergers. *APS Meeting Abstracts*, pages 1010–+, April 2007.

[30] Miguel Megevand et al. Perturbed disks get shocked. Binary black hole merger effects on accretion disks. 2009.

[31] C. F. Sopuerta, N. Yunes, and P. Laguna. Gravitational recoil from binary black hole mergers: The close-limit approximation. *Phys. Rev. D.*, 74(12):124010–+, December 2006. doi: 10.1103/PhysRevD.74.124010.

[32] A. Buonanno, Y. Pan, J. G. Baker, J. Centrella, B. J. Kelly, S. T. McWilliams, and J. R. van Meter. Approaching faithful templates for nonspinning binary black holes using the effective-one-body approach. *Phys. Rev. D.*, 76(10): 104049–+, November 2007. doi: 10.1103/PhysRevD.76.104049.

[33] P. Ajith, S. Babak, Y. Chen, M. Hewitson, B. Krishnan, J. T. Whelan, B. Brügman, J. Gonzalez, M. Hannam, S. Husa, M. Koppitz, D. Pollney, L. Rezzolla, L. Santamaría, A. M. Sintes, U. Sperhake, and J. Thornburg. Phenomenological template family for black-hole coalescence waveforms. *Class. Quant. Grav.*, 24:S689–S700, 2007.

[34] P. Ajith, S. Babak, Y. Chen, M. Hewitson, B. Krishnan, J. T. Whelan, B. Brügman, J. Gonzalez, M. Hannam, S. Husa, M. Koppitz, D. Pollney, L. Rezzolla, L. Santamaría, A. M. Sintes, U. Sperhake, and J. Thornburg. A template bank for gravitational waveforms from coalescing binary black holes: I. non-spinning binaries. *Phys. Re. D*, 77:104017, 2008.

[35] P. Ajith. Gravitational-wave data analysis using binary black-hole waveforms. *Class. Quant. Grav.*, 25:114033, 2008. doi: 10.1088/0264-9381/25/11/114033.

[36] S. G. Hahn and R. W. Lindquist. The two-body problem in geometrodynamics. *Ann. Phys.*, 29:304–331, 1964.

[37] L. L. Smarr. *The Structure of General Relativity with a Numerical Illustration: the Collision of Two Black Holes.* PhD thesis, THE UNIVERSITY OF TEXAS AT AUSTIN., 1975.

[38] Larry Smarr, Andrej Čadež, Bryce DeWitt, and Kenneth R. Eppley. Collision of two black holes: Theoretical framework. *Phys. Rev. D*, 14(10):2443–2452, 1976.

[39] L. Smarr. Space-Time Generated by Computers: Black Holes with Gravitational Radiation. In M. D. Papagiannis, editor, *Eighth Texas Symposium on Relativistic Astrophysics*, volume 302 of *New York Academy Sciences Annals*, pages 569–+, December 1977. doi: 10.1111/j.1749-6632.1977.tb37076.x.

[40] L. Smarr and J. W. York, Jr. Radiation gauge in general relativity. *Phys. Rev. D.*, 17:1945–1956, April 1978. doi: 10.1103/PhysRevD.17.1945.

[41] L. Smarr and J. W. York, Jr. Kinematical conditions in the construction of spacetime. *Phys. Rev. D.*, 17:2529–2551, May 1978. doi: 10.1103/PhysRevD.17.2529.

[42] D. M. Eardley and L. Smarr. Time functions in numerical relativity: Marginally bound dust collapse. *Phys. Rev. D.*, 19:2239–2259, April 1979. doi: 10.1103/PhysRevD.19.2239.

[43] P. Anninos, D. Hobill, E. Seidel, L. Smarr, and W.-M. Suen. Collision of two black holes. *Physical Review Letters*, 71:2851–2854, November 1993. doi: 10.1103/PhysRevLett.71.2851.

[44] P. Anninos, J. Massó, E. Seidel, W.-M. Suen, and J. Towns. Three-dimensional numerical relativity: The evolution of black holes. *Phys. Rev. D.*, 52:2059–2082, August 1995. doi: 10.1103/PhysRevD.52.2059.

[45] P. Anninos, D. Hobill, E. Seidel, L. Smarr, and W.-M. Suen. Head-on collision of two equal mass black holes. *Phys. Rev. D.*, 52:2044–2058, August 1995. doi: 10.1103/PhysRevD.52.2044.

[46] B. Brügmann. Binary black hole mergers in 3D numerical relativity. *International Journal of Modern Physics D*, 8:85–100, February 1999. doi: 10.1142/S0218271899000080.

[47] F. Pretorius. Evolution of binary black-hole spacetimes. *Phys. Rev. Lett.*, 95, 2005.

[48] M. Campanelli, C. O. Lousto, P. Marronetti, and Y. Zlochower. Accurate Evolutions of Orbiting Black-Hole Binaries without Excision. *Physical Review Letters*, 96(11):111101–+, March 2006. doi: 10.1103/PhysRevLett.96.111101.

[49] J. G. Baker, J. Centrella, D.-I. Choi, M. Koppitz, and J. van Meter. Gravitational-Wave Extraction from an Inspiraling Configuration of Merging Black Holes. *Physical Review Letters*, 96(11):111102–+, March 2006. doi: 10.1103/PhysRevLett.96.111102.

[50] C. Reisswig, N. T. Bishop, D. Pollney, and B. Szilagyi. Unambiguous determination of gravitational waveforms from binary black hole mergers. *Phys. Rev. Lett.*, 103:221101, 2009.

[51] C. Reisswig, S. Husa, L. Rezzolla, E. N. Dorband, D. Pollney, and J. Seiler. Gravitational-wave detectability of equal-mass black-hole binaries with aligned spins. *ArXiv e-prints*, 2009. accepted by Phys. Rev. D.

[52] C. Reisswig, N. T. Bishop, D. Pollney, and B. Szilagyi. Characteristic extraction in numerical relativity: binary black hole merger waveforms at null infinity. 2009. submitted to Class. Quant. Grav.

[53] D. Pollney, C. Reisswig, E. Schnetter, E. D. Dorband, and P. Diener. The asymptotic falloff of local waveform measurements in numerical relativity. *Phys. Rev. D*, 80:121502, 2009.

[54] D. Pollney, C. Reisswig, E. Schnetter, E. D. Dorband, and P. Diener. High accuracy black hole simulations with an extended wave zone. 2009. submitted to Phys. Rev. D.

[55] M. Koppitz, D. Pollney, C. Reisswig, L. Rezzolla, J. Thornburg, P. Diener, and E. Schnetter. Recoil Velocities from Equal-Mass Binary-Black-Hole Mergers. *Physical Review Letters*, 99(4):041102–+, July 2007. doi: 10.1103/PhysRevLett.99.041102.

[56] D. Pollney, C. Reisswig, L. Rezzolla, B. Szilágyi, M. Ansorg, B. Deris, P. Diener, E. N. Dorband, M. Koppitz, A. Nagar, and E. Schnetter. Recoil velocities from equal-mass binary black-hole mergers: A systematic investigation of spin-orbit aligned configurations. *Phys. Rev. D.*, 76(12):124002–+, December 2007. doi: 10.1103/PhysRevD.76.124002.

[57] L. Rezzolla, E. N. Dorband, C. Reisswig, P. Diener, D. Pollney, E. Schnetter, and B. Szilágyi. Spin Diagrams for Equal-Mass Black Hole Binaries with Aligned Spins. *Astrophys. J.*, 679:1422–1426, June 2008. doi: 10.1086/587679.

[58] L. Rezzolla, P. Diener, E. N. Dorband, D. Pollney, C. Reisswig, E. Schnetter, and J. Seiler. The Final Spin from the Coalescence of Aligned-Spin Black Hole Binaries. *Astrophys. J. Lett.*, 674:L29–L32, February 2008. doi: 10.1086/528935.

[59] L. Rezzolla, E. Barausse, E. N. Dorband, D. Pollney, C. Reisswig, J. Seiler, and S. Husa. Final spin from the coalescence of two black holes. *Phys. Rev. D.*, 78(4):044002–+, August 2008. doi: 10.1103/PhysRevD.78.044002.

[60] C. Reisswig, N. T. Bishop, C. W. Lai, J. Thornburg, and B. Szilagyi. Characteristic evolutions in numerical relativity using six angular patches. *Classical and Quantum Gravity*, 24:327–+, June 2007. doi: 10.1088/0264-9381/24/12/S21.

[61] M. Hannam, S. Husa, J. G. Baker, M. Boyle, B. Brügmann, T. Chu, N. Dorband, F. Herrmann, I. Hinder, B. J. Kelly, L. E. Kidder, P. Laguna, K. D. Matthews, J. R. van Meter, H. P. Pfeiffer, D. Pollney, C. Reisswig, M. A. Scheel, and D. Shoemaker. Samurai project: Verifying the consistency of black-hole-binary waveforms for gravitational-wave detection. *Phys. Rev. D.*, 79(8):084025–+, April 2009. doi: 10.1103/PhysRevD.79.084025.

[62] E. Schnetter, C. D. Ott, P. Diener, and C. Reisswig. Astrophysical applications of numerical relativity - from teragrid to petascale. *Teragrid Conference*, 2008.

[63] P. Ajith et al. 'Complete' gravitational waveforms for black-hole binaries with non-precessing spins. 2009.

[64] B. Aylott, J. G. Baker, W. D. Boggs, M. Boyle, P. R. Brady, D. A. Brown, B. Brügmann, L. T. Buchman, A. Buonanno, L. Cadonati, J. Camp, M. Campanelli, J. Centrella, S. Chatterji, N. Christensen, T. Chu, P. Diener, N. Dorband, Z. B. Etienne, J. Faber, S. Fairhurst, B. Farr, S. Fischetti, G. Guidi, L. M. Goggin, M. Hannam, F. Herrmann, I. Hinder, S. Husa, V. Kalogera, D. Keppel, L. E. Kidder, B. J. Kelly, B. Krishnan, P. Laguna, C. O. Lousto, I. Mandel, P. Marronetti, R. Matzner, S. T. McWilliams, K. D. Matthews, R. A. Mercer, S. R. P. Mohapatra, A. H. Mroué, H. Nakano, E. Ochsner, Y. Pan, L. Pekowsky, H. P. Pfeiffer, D. Pollney, F. Pretorius, V. Raymond, C. Reisswig, L. Rezzolla, O. Rinne, C. Robinson, C. Röver, L. Santamaría, B. Sathyaprakash, M. A. Scheel, E. Schnetter, J. Seiler, S. L. Shapiro, D. Shoemaker, U. Sperhake, A. Stroeer, R. Sturani, W. Tichy, Y. T. Liu, M. van der Sluys, J. R. van Meter, R. Vaulin, A. Vecchio, J. Veitch, A. Viceré, J. T. Whelan, and Y. Zlochower. Testing gravitational-wave searches with numerical relativity waveforms: Results from the first Numerical INJection Analysis (NINJA) project. *ArXiv e-prints*, January 2009.

[65] L. Cadonati, B. Aylott, J. G. Baker, W. D. Boggs, M. Boyle, P. R. Brady, D. A. Brown, B. Brügmann, L. T. Buchman, A. Buonanno, J. Camp, M. Campanelli, J. Centrella, S. Chatterji, N. Christensen, T. Chu, P. Diener, N. Dorband, Z. B. Etienne, J. Faber, S. Fairhurst, B. Farr, S. Fischetti, G. Guidi, L. M. Goggin, M. Hannam, F. Herrmann, I. Hinder, S. Husa, V. Kalogera, D. Keppel, L. E. Kidder, B. J. Kelly, B. Krishnan, P. Laguna, C. O. Lousto, I. Mandel, P. Marronetti, R. Matzner, S. T. McWilliams, K. D. Matthews, R. A. Mercer, S. R. P. Mohapatra, A. H. Mroué, H. Nakano, E. Ochsner, Y. Pan, L. Pekowsky, H. P. Pfeiffer, D. Pollney, F. Pretorius, V. Raymond, C. Reisswig, L. Rezzolla, O. Rinne, C. Robinson, C. Röver, L. Santamaría, B. Sathyaprakash, M. A. Scheel, E. Schnetter, J. Seiler, S. L. Shapiro, D. Shoemaker, U. Sperhake, A. Stroeer, R. Sturani, W. Tichy, Y. T. Liu, M. van der Sluys, J. R. van Meter, R. Vaulin, A. Vecchio, J. Veitch, A. Viceré, J. T. Whelan, and Y. Zlochower. Status of NINJA: the Numerical INJection Analysis project. *Classical and Quantum Gravity*, 26(11):114008–+, June 2009. doi: 10.1088/0264-9381/26/11/114008.

[66] VisIt Carpet Database Plugin. `http://www.cactuscode.org/Visualization/VisIt`.

[67] C. W. Misner, K. S. Thorne, and J. A. Wheeler. *Gravitation.* 1973.

[68] V. Kalogera, K. Belczynski, C. Kim, R. O'Shaughnessy, and B. Willems. Formation of double compact objects. *Phys. Reports*, 442:75–108, April 2007. doi: 10.1016/j.physrep.2007.02.008.

[69] K. A. Postnov and L. R. Yungelson. The Evolution of Compact Binary Star Systems. *Living Reviews in Relativity*, 9:6–+, December 2006.

[70] C. M. Will. Testing the General Relativistic "No-Hair" Theorems Using the Galactic Center Black Hole Sagittarius A*. *Astrophys. J. Lett.*, 674:L25–L28, February 2008. doi: 10.1086/528847.

[71] S. J. Bush, Z. Wang, M. Karovska, and G. G. Fazio. The Structure of Active Merger Remnant NGC 6240 from IRAC Observations. *Astrophys. J.*, 688:875–884, December 2008. doi: 10.1086/592180.

[72] S. Komossa, V. Burwitz, G. Hasinger, P. Predehl, J. S. Kaastra, and Y. Ikebe. Discovery of a Binary Active Galactic Nucleus in the Ultraluminous Infrared Galaxy NGC 6240 Using Chandra. *Astrophys. J. Lett.*, 582:L15–L19, January 2003. doi: 10.1086/346145.

[73] T. Thiemann. Loop Quantum Gravity: An Inside View. In I.-O. Stamatescu and E. Seiler, editors, *Lecture Notes in Physics, Berlin Springer Verlag*, volume 721 of *Lecture Notes in Physics, Berlin Springer Verlag*, pages 185–+, 2007.

[74] K. J. Foley, R. S. Jones, S. J. Lindenbaum, W. A. Love, S. Ozaki, E. D. Platner, C. A. Quarles, and E. H. Willen. Experimental Test of the Pion-Nucleon Forward Dispersion Relations at High Energies. *Physical Review Letters*, 19:193–198, July 1967. doi: 10.1103/PhysRevLett.19.193.

[75] S. W. Hawking and G. F. Ellis. *The large scale structure of space-time.* Cambridge Monographs on Mathematical Physics, 1973.

[76] B. F. Schutz, J. Centrella, C. Cutler, and S. A. Hughes. Will einstein have the last word on gravity? 2009. preprint: arXiv:0903.0100v1.

[77] B. G. Schmidt. A new definition of singular points in general relativity. *General Relativity and Gravitation*, 1: 269–280, September 1971. doi: 10.1007/BF00759538.

[78] R. Penrose. The cosmic censorship hypothesis. *The Observatory*, 96:138–+, August 1976.

[79] A. B. Nielsen. Black Holes without Event Horizons. *ArXiv e-prints*, February 2008.

[80] K. Schwarzschild. On the Gravitational Field of a Mass Point According to Einstein's Theory. *Abh. Konigl. Preuss. Akad. Wissenschaften Jahre 1906,92, Berlin,1907*, pages 189–196, 1916.

[81] W. Israel. Event Horizons in Static Vacuum Space-Times. *Physical Review*, 164:1776–1779, December 1967. doi: 10.1103/PhysRev.164.1776.

[82] P. O. Mazur. Black Uniqueness Theorems. *ArXiv High Energy Physics - Theory e-prints*, December 2001.

[83] D. C. Robinson. Uniqueness of the Kerr black hole. *Physical Review Letters*, 34:905–+, April 1975. doi: 10.1103/PhysRevLett.34.905.

[84] R. P. Kerr. Gravitational Field of a Spinning Mass as an Example of Algebraically Special Metrics. *Physical Review Letters*, 11:237–238, September 1963. doi: 10.1103/PhysRevLett.11.237.

[85] E. T. Newman, E. Couch, K. Chinnapared, A. Exton, A. Prakash, and R. Torrence. Metric of a Rotating, Charged Mass. *Journal of Mathematical Physics*, 6:918–919, June 1965. doi: 10.1063/1.1704351.

[86] S. W. Hawking. Black holes in general relativity. *Communications in Mathematical Physics*, 25:152–166, June 1972. doi: 10.1007/BF01877517.

[87] B. Carter. Axisymmetric Black Hole Has Only Two Degrees of Freedom. *Physical Review Letters*, 26:331–333, February 1971. doi: 10.1103/PhysRevLett.26.331.

[88] D. C. Robinson. Classification of black holes with electromagnetic fields. *Phys. Rev. D.*, 10:458–460, July 1974. doi: 10.1103/PhysRevD.10.458.

[89] M. C. Miller and E. J. M. Colbert. Intermediate-Mass Black Holes. *International Journal of Modern Physics D*, 13:1–64, January 2004. doi: 10.1142/S0218271804004426.

[90] P. Amaro-Seoane, C. Eichhorn, E. Porter, and R. Spurzem. Binaries of massive black holes in rotating clusters: Dynamics, gravitational waves, detection and the role of eccentricity. *ArXiv e-prints*, August 2009.

[91] I. Mandel, D. A. Brown, J. R. Gair, and M. C. Miller. Rates and Characteristics of Intermediate Mass Ratio Inspirals Detectable by Advanced LIGO. *Astrophys. J.*, 681:1431–1447, July 2008. doi: 10.1086/588246.

[92] J. M. Fregeau, S. L. Larson, M. C. Miller, R. O'Shaughnessy, and F. A. Rasio. Observing IMBH-IMBH Binary Coalescences via Gravitational Radiation. *Astrophys. J. Lett.*, 646:L135–L138, August 2006. doi: 10.1086/507106.

[93] P. Amaro-Seoane and M. Freitag. Intermediate-Mass Black Holes in Colliding Clusters: Implications for Lower Frequency Gravitational-Wave Astronomy. *Astrophys. J. Lett.*, 653:L53–L56, December 2006. doi: 10.1086/510405.

[94] C. Reisswig, S. Husa, L. Rezzolla, E. N. Dorband, D. Pollney, and J. Seiler. Gravitational-wave detectability of equal-mass black-hole binaries with aligned spins. *Phys. Rev. D*, 80:124026, July 2009.

[95] K. Gebhardt and J. Thomas. The Black Hole Mass, Stellar Mass-to-Light Ratio, and Dark Halo in M87. *Astrophys. J.*, 700:1690–1701, August 2009. doi: 10.1088/0004-637X/700/2/1690.

[96] T. Regge and J. A. Wheeler. Stability of a Schwarzschild singularity. *Physical Review*, 108(4):1063–1069, 1957.

[97] R. Bartnik and J. McKinnon. Particlelike solutions of the Einstein-Yang-Mills equations. *Physical Review Letters*, 61:141–144, July 1988. doi: 10.1103/PhysRevLett.61.141.

[98] P. Bizon. Colored black holes. *Physical Review Letters*, 64:2844–2847, June 1990. doi: 10.1103/PhysRevLett.64.2844.

[99] R. H. Price. Nonspherical perturbations of relativistic gravitational collapse. i. Scalar and gravitational perturbations. *Phys. Rev. D.*, 5:2419–2438, 1972.

[100] R. H. Price. Nonspherical perturbations of relativistic gravitational collapse. ii. Integer-spin, zero-rest-mass fields. *Phys. Rev. D.*, 5:2439–2454, 1972.

[101] C. W. Misner, K. S. Thorne, and J. A. Wheeler. *Gravitation*. Freeman, New York, 1973.

[102] E. Berti, V. Cardoso, and C. M. Will. Gravitational-wave spectroscopy of massive black holes with the space interferometer LISA. *Phys. Rev. D.*, 73(6):064030–+, March 2006. doi: 10.1103/PhysRevD.73.064030.

[103] C. V. Vishveshwara. Stability of the Schwarzschild metric. *Phys. Rev. D.*, 1:2870–2879, 1970.

[104] C. V. Vishveshwara. Scattering of gravitational radiation by a Schwarzschild black-hole. *Nature*, 227:936–938, 1970.

[105] W. H. Press. Long wave trains of gravitational waves from a vibrating black hole. *Astrophys. J.*, 170:L105–L108, 1971.

[106] M. Davis, R. Ruffini, W. H. Press, and R. H. Price. Gravitational radiation from a particle falling radially into a schwarzschild black hole. *Phys. Rev. Lett.*, 27:1466–1469, 1971.

[107] S. Chandrasekhar and S. Detweiler. The quasi-normal modes of the Schwarzschild black hole. *Proc. R. Soc. Lond. A.*, 344:441–452, 1975.

[108] K. D. Kokkotas and B. G. Schmidt. Quasi-normal modes of stars and black holes. *Living Reviews in Relativity*, 2, 1999.

[109] S. Detweiler. On resonant oscillations of a rapidly rotating black hole. *Proc. R. Soc. Lond. A.*, 352:381–395, 1977.

[110] S. Detweiler. Black holes and gravitational waves. ii - Trajectories plunging into a nonrotating hole. *Astrophys. J.*, 231:211–218, 1979.

[111] E. W. Leaver. An analytic representation for the quasi-normal modes of kerr black holes. *Proc. R. Soc. Lond. A.*, 402:285–298, 1985.

[112] S. W. Hawking. The event horizon. *Black Holes, Les Houches Lectures*, 1972.

[113] R. Penrose. Asymptotic properties of fields and space-times. *Phys. Rev. Lett.*, 10(2):66–68, 1963.

[114] E. Newman and R. Penrose. An approach to gravitational radiation by a method of spin coefficients. *J. of Math. Phys.*, 3(3), 1962.

[115] R. Penrose. Zero Rest-Mass Fields Including Gravitation: Asymptotic Behaviour. *Royal Society of London Proceedings Series A*, 284:159–203, February 1965.

[116] H. Friedrich. Smoothness at Null Infinity and the Structure of Initial Data. In P. T. Chruściel and H. Friedrich, editors, *The Einstein Equations and the Large Scale Behavior of Gravitational Fields*, pages 121–+, 2004.

[117] John Stewart. *Advanced general relativity.* Cambridge Monographs on Mathematical Physics, 1991.

[118] H. Friedrich. 1. Conformal Einstein Evolution. In J. Frauendiener and H. Friedrich, editors, *The Conformal Structure of Space-Time*, volume 604 of *Lecture Notes in Physics, Berlin Springer Verlag*, pages 1–50, 2002.

[119] R. Penrose and W. Rindler. *Spinors and space-time Vol. 2: Spinor and twistor methods in space-time geometry.* Cambridge Monographs on Mathematical Physics, 1986.

[120] R. Geroch, A. Held, and R. Penrose. A space-time calculus based on pairs of null directions. *Journal of Mathematical Physics*, 14:874–881, July 1973. doi: 10.1063/1.1666410.

[121] R. Penrose and W. Rindler. *Spinors and space-time Vol. 1: Two-spinor calculus and relativistic fields.* Cambridge Monographs on Mathematical Physics, 1984.

[122] A. Z. Petrov. *Einstein spaces.* 1969.

[123] Miguel Alcubierre. *Introduction to 3+1 Numerical Relativity.* Oxford University Press, 2008.

[124] R. Sachs. Gravitational waves in general relativity. VI. The outgoing radiation condition. *Proc. R. Soc. Lond. A.*, 264:309–338, 1961.

[125] R. K. Sachs. Gravitational waves in general relativity. VIII. Waves in asymptotically flat space-time. *Proc. R. Soc. Lond. A.*, 270(1340):103–126, 1962.

[126] R. A. Bartnik and A. H. Norton. 16. Numerical Experiments at Null Infinity. In J. Frauendiener and H. Friedrich, editors, *The Conformal Structure of Space-Time*, volume 604 of *Lecture Notes in Physics, Berlin Springer Verlag*, pages 313–326, 2002.

[127] D. Christodoulou. The global initial value problem in general relativity. In V. G. Gurzadyan, R. T. Jantzen, and R. Ruffini, editors, *The Ninth Marcel Grossmann Meeting*, pages 44–54, 2002.

[128] Piotr T. Chrusciel, Malcolm A. H. MacCallum, and David B. Singleton. Gravitational waves in general relativity: 14. Bondi expansions and the polyhomogeneity of Scri. *Proc. Roy. Soc. Lond.*, A436:299–316, 1992.

[129] J. A. Valiente Kroon. Can one detect a non-smooth null infinity? *Classical and Quantum Gravity*, 18:4311–4316, October 2001. doi: 10.1088/0264-9381/18/20/310.

[130] J. Winicour. Logarithmic asymptotic flatness. *Foundations of Physics*, 15:605–616, May 1985. doi: 10.1007/BF01882485.

[131] Juan Antonio Valiente Kroon. Asymptotic properties of the development of conformally flat data near spatial infinity. *Class. Quant. Grav.*, 24:3037–3054, 2007. doi: 10.1088/0264-9381/24/11/016.

[132] R. Arnowitt, S. Deser, and C. Misner. *Dynamics of General Relativity, in "Gravitation: An Introduction to Current Research"*. Wiley, New York, 1962.

[133] N. Ó Murchadha and J. W. York. Gravitational energy. *Phys. Rev. D.*, 10:2345–2357, October 1974. doi: 10.1103/PhysRevD.10.2345.

[134] H. Bondi. Gravitational waves in general relativity. *Nature*, 186:535, 1960.

[135] H. Bondi, M. G. J. van der Burg, and A. W. K. Metzner. Gravitational waves in general relativity. VII. Waves from axi-symmetric isolated systems. *Proc. R. Soc. London. Series A*, 269(1336):21–52, 1962.

[136] R. A. Hulse and J. H. Taylor. Discovery of a pulsar in a binary system. *Astrophys. J.*, 159:L51–L53, 1975.

[137] I. H. Stairs, S. E. Thorsett, J. H. Taylor, and A. Wolszczan. Studies of the relativistic binary pulsar psr b1534+12. I. Timing analysis. *Astrophys. J.*, 581:501–508, 2002.

[138] W. T. Deich and S. R. Kulkarni. The masses of the neutron stars in m15c. 1996. Compact stars in binaries, proceedings from IAU symposium 165 held 15 through 19 August 1994, as part of the 22nd General Assembly of the IAU in The Hague, the Netherlands.

[139] M. Burgay et al. An increased estimate of the merger rate of double neutron stars from observations of a highly relativistic system. *Nature*, 426:531–533, 2003.

[140] B. F. Schutz B. S. Sathyaprakash. Physics, astrophysics and cosmology with gravitational waves. *Living Rev. Relativity*, 12, 2009. preprint: arXiv:0903.0338v1.

[141] É. É. Flanagan and S. A. Hughes. The basics of gravitational wave theory. *New J.Phys.*, 7:204, 2005.

[142] A. Abramovici, W. E. Althouse, R. W.P. Drever, Y. Gursel, S. Kawamura, F. J. Raab, D. Shoemaker, L. Sievers, R. E. Spero, and K. S. Thorne. LIGO - The laser interferometer gravitational-wave observatory. *Science*, 256: 325–333, 1992.

[143] R. Isaacson. Gravitational radiation in the limit of high frequency. I. The linear approximation and geometrical optics. *Phys. Rev. D.*, 166:1263–1271, 1968.

[144] R. Isaacson. Gravitational radiation in the limit of high frequency. II. Nonlinear terms and the effective stress tensor. *Phys. Rev. D.*, 166:1272–1279, 1968.

[145] K. S. Thorne. Multipole expansions of gravitational radiation. *Rev. Mod. Phys.*, 52:299–340, 1980.

[146] D. R. Brill and J. B. Hartle. Method of the Self-Consistent Field in General Relativity and its Application to the Gravitational Geon. *Physical Review*, 135:271–278, July 1964. doi: 10.1103/PhysRev.135.B271.

[147] B. Abbott et al. LIGO: The Laser Interferometer Gravitational-Wave Observatory. 2007.

[148] S. Waldman and (for the LIGO Science Collaboration). Status of ligo at the start of the fifth science run. *Class. Quantum Grav. 23 (2006) S653 – S660*, 2006.

[149] F. Acernese et al. The virgo status. *Classical Quantum Gravity*, 23:S635–S642, 2006.

[150] S. A. Hughes, S. Marka, P. L. Bender, and C. J. Hogan. New physics and astronomy with the new gravitational-wave observatories. *ArXiv Astrophysics e-prints*, October 2001.

[151] P. C. Peters. Gravitational radiation and the motion of two point masses. *Phys. Rev.*, 136:B1224–B1232, 1964.

[152] A. Buonanno and T. Damour. Effective one-body approach to general relativistic two-body dynamics. *Phys. Rev. D*, 59(8):084006, Mar 1999. doi: 10.1103/PhysRevD.59.084006.

[153] J. Lewandowski, T. Pawlowski, and A. Ashtekar. Geometric Characterizations of the Kerr Isolated Horizon. *International Journal of Modern Physics D*, 11:739–746, 2002. doi: 10.1142/S0218271802001986.

[154] A. Ashtekar, C. Beetle, and J. Lewandowski. Geometry of generic isolated horizons. *Classical and Quantum Gravity*, 19:1195–1225, March 2002. doi: 10.1088/0264-9381/19/6/311.

[155] M. Campanelli, C. O. Lousto, and Y. Zlochower. Algebraic classification of numerical spacetimes and black-hole-binary remnants. *Phys. Rev. D.*, 79(8):084012–+, April 2009. doi: 10.1103/PhysRevD.79.084012.

[156] Mark A. Scheel et al. High-accuracy waveforms for binary black hole inspiral, merger, and ringdown. *Phys. Rev.*, D79:024003, 2009. doi: 10.1103/PhysRevD.79.024003.

[157] M. Favata. Nonlinear Gravitational-Wave Memory from Binary Black Hole Mergers. *Astrophys. J. Lett.*, 696: L159–L162, May 2009. doi: 10.1088/0004-637X/696/2/L159.

[158] M. Favata. Gravitational-wave memory revisited: Memory from the merger and recoil of binary black holes. *Journal of Physics Conference Series*, 154(1):012043–+, March 2009. doi: 10.1088/1742-6596/154/1/012043.

[159] M. Favata. Post-Newtonian corrections to the gravitational-wave memory for quasicircular, inspiralling compact binaries. *Phys. Rev. D.*, 80(2):024002–+, July 2009. doi: 10.1103/PhysRevD.80.024002.

[160] Luciano Rezzolla. Private communication.

[161] F. Markopoulou. Space does not exist, so time can. *ArXiv e-prints*, September 2009.

[162] L. Mersini-Houghton. Notes on Time's Enigma. *ArXiv e-prints*, September 2009.

[163] Courant and Hilbert. *Methods of Mathematical Physics*, volume 2. Wiley Classics Library, 1989.

[164] R. Arnowitt, S. Deser, and C. W. Misner. Republication of: The dynamics of general relativity. *General Relativity and Gravitation*, 40:1997–2027, September 2008. doi: 10.1007/s10714-008-0661-1.

[165] J. W. York, Jr. Kinematics and dynamics of general relativity. In L. L. Smarr, editor, *Sources of Gravitational Radiation*, pages 83–126, 1979.

[166] T. W. Baumgarte and S. L. Shapiro. Numerical relativity and compact binaries. *Phys. Reports*, 376:41–131, March 2003. doi: 10.1016/S0370-1573(02)00537-9.

[167] O. Sarbach, G. Calabrese, J. Pullin, and M. Tiglio. Hyperbolicity of the Baumgarte-Shapiro-Shibata-Nakamura system of Einstein evolution equations. *Phys. Rev. D.*, 66(6):064002–+, September 2002. doi: 10.1103/PhysRevD.66.064002.

[168] T. Nakamura, K. Oohara, and Y. Kojima. General Relativistic Collapse to Black Holes and Gravitational Waves from Black Holes. *Progress of Theoretical Physics Supplement*, 90:1–218, 1987. doi: 10.1143/PTPS.90.1.

[169] M. Shibata and T. Nakamura. Evolution of three-dimensional gravitational waves: Harmonic slicing case. *Phys. Rev. D.*, 52:5428–5444, November 1995. doi: 10.1103/PhysRevD.52.5428.

[170] T. W. Baumgarte and S. L. Shapiro. Numerical integration of Einstein's field equations. *Phys. Rev. D.*, 59(2): 024007–+, January 1999. doi: 10.1103/PhysRevD.59.024007.

[171] M. Alcubierre, B. Brügmann, M. Miller, and W.-M. Suen. Conformal hyperbolic formulation of the Einstein equations. *Phys. Rev. D.*, 60(6):064017–+, September 1999. doi: 10.1103/PhysRevD.60.064017.

[172] H. Friedrich. On the hyperbolicity of Einstein's and other gauge field equations. *Communications in Mathematical Physics*, 100:525–543, December 1985. doi: 10.1007/BF01217728.

[173] H. Friedrich and A. Rendall. The Cauchy Problem for the Einstein Equations. In B. G. Schmidt, editor, *Einstein's Field Equations and Their Physical Implications*, volume 540 of *Lecture Notes in Physics, Berlin Springer Verlag*, pages 127–+, 2000.

[174] F. Pretorius. Numerical relativity using a generalized harmonic decomposition. *Classical and Quantum Gravity*, 22:425–451, January 2005. doi: 10.1088/0264-9381/22/2/014.

[175] L. Lindblom, M. A. Scheel, L. E. Kidder, R. Owen, and O. Rinne. A new generalized harmonic evolution system. *Classical and Quantum Gravity*, 23:447–+, August 2006. doi: 10.1088/0264-9381/23/16/S09.

[176] H. Friedrich. Hyperbolic reductions for Einstein's equations. *Classical and Quantum Gravity*, 13:1451–1469, June 1996. doi: 10.1088/0264-9381/13/6/014.

[177] P. Marronetti, W. Tichy, B. Brügmann, J. González, M. Hannam, S. Husa, and U. Sperhake. Binary black holes on a budget: simulations using workstations. *Classical and Quantum Gravity*, 24:43–+, June 2007. doi: 10.1088/0264-9381/24/12/S05.

[178] S. Frittelli and O. A. Reula. Well-posed forms of the 3+1 conformally-decomposed Einstein equations. *Journal of Mathematical Physics*, 40:5143–5156, October 1999. doi: 10.1063/1.533022.

[179] M. Alcubierre, B. Brügmann, T. Dramlitsch, J. A. Font, P. Papadopoulos, E. Seidel, N. Stergioulas, and R. Takahashi. Towards a stable numerical evolution of strongly gravitating systems in general relativity: The conformal treatments. *Phys. Rev. D.*, 62(4):044034–+, August 2000. doi: 10.1103/PhysRevD.62.044034.

[180] M. Alcubierre, G. Allen, B. Brügmann, E. Seidel, and W.-M. Suen. Towards an understanding of the stability properties of the 3+1 evolution equations in general relativity. *Phys. Rev. D.*, 62(12):124011–+, December 2000. doi: 10.1103/PhysRevD.62.124011.

[181] S. Frittelli and R. Gomez. Ill-posedness in the Einstein equations. *Journal of Mathematical Physics*, 41:5535–5549, August 2000. doi: 10.1063/1.533423.

[182] H. Friedrich and G. Nagy. The Initial Boundary Value Problem for Einstein's Vacuum Field Equation. *Communications in Mathematical Physics*, 201:619–655, 1999. doi: 10.1007/s002200050571.

[183] O. Reula. Hyperbolic Methods for Einstein's Equations. *Living Reviews in Relativity*, 1:3–+, January 1998.

[184] M. Alcubierre, B. Brügmann, P. Diener, M. Koppitz, D. Pollney, E. Seidel, and R. Takahashi. Gauge conditions for long-term numerical black hole evolutions without excision. *Phys. Rev. D.*, 67(8):084023–+, April 2003. doi: 10.1103/PhysRevD.67.084023.

[185] M. Alcubierre, B. Brügmann, P. Diener, F. S. Guzmán, I. Hawke, S. Hawley, F. Herrmann, M. Koppitz, D. Pollney, E. Seidel, and J. Thornburg. Dynamical evolution of quasicircular binary black hole data. *Phys. Rev. D.*, 72(4): 044004–+, August 2005. doi: 10.1103/PhysRevD.72.044004.

[186] L. T. Buchman and O. C. A. Sarbach. Towards absorbing outer boundaries in general relativity. *Classical and Quantum Gravity*, 23:6709–6744, December 2006. doi: 10.1088/0264-9381/23/23/007.

[187] M. C. Babiuc, H.-O. Kreiss, and J. Winicour. Constraint-preserving Sommerfeld conditions for the harmonic Einstein equations. *Phys. Rev. D.*, 75(4):044002–+, February 2007. doi: 10.1103/PhysRevD.75.044002.

[188] J. Seiler, B. Szilágyi, D. Pollney, and L. Rezzolla. Constraint-preserving boundary treatment for a harmonic formulation of the Einstein equations. *Classical and Quantum Gravity*, 25(17):175020–+, September 2008. doi: 10.1088/0264-9381/25/17/175020.

[189] F. Estabrook, H. Wahlquist, S. Christensen, B. Dewitt, L. Smarr, and E. Tsiang. Maximally slicing a black hole. *Phys. Rev. D.*, 7:2814–2817, 1973. doi: 10.1103/PhysRevD.7.2814.

[190] M. Alcubierre, W. Benger, B. Brügmann, G. Lanfermann, L. Nerger, E. Seidel, and R. Takahashi. 3D Grazing Collision of Two Black Holes. *Physical Review Letters*, 87(26):A261103+, December 2001. doi: 10.1103/PhysRevLett.87.271103.

[191] M. Alcubierre, B. Brügmann, D. Pollney, E. Seidel, and R. Takahashi. Black hole excision for dynamic black holes. *Phys. Rev. D.*, 64(6):061501–+, September 2001. doi: 10.1103/PhysRevD.64.061501.

[192] P. Anninos, G. Daues, J. Massó, E. Seidel, and W.-M. Suen. Horizon boundary condition for black hole spacetimes. *Phys. Rev. D.*, 51:5562–5578, May 1995. doi: 10.1103/PhysRevD.51.5562.

[193] C. Bona, J. Massó, E. Seidel, and J. Stela. New Formalism for Numerical Relativity. *Physical Review Letters*, 75: 600–603, July 1995. doi: 10.1103/PhysRevLett.75.600.

[194] J. Balakrishna, G. Daues, E. Seidel, W.-M. Suen, M. Tobias, and E. Wang. Coordinate conditions in three-dimensional numerical relativity. *Classical and Quantum Gravity*, 13:L135–L142, December 1996. doi: 10.1088/0264-9381/13/12/001.

[195] M. Alcubierre. Hyperbolic slicings of spacetime: singularity avoidance and gauge shocks . *Classical and Quantum Gravity*, 20:607–623, February 2003.

[196] C. Bona, J. Massó, E. Seidel, and J. Stela. First order hyperbolic formalism for numerical relativity. *Phys. Rev. D.*, 56:3405–3415, September 1997. doi: 10.1103/PhysRevD.56.3405.

[197] J. R. van Meter, J. G. Baker, M. Koppitz, and D.-I. Choi. How to move a black hole without excision: Gauge conditions for the numerical evolution of a moving puncture. *Phys. Rev. D.*, 73(12):124011–+, June 2006. doi: 10.1103/PhysRevD.73.124011.

[198] A. Einstein and N. Rosen. The Particle Problem in the General Theory of Relativity. *Physical Review*, 48:73–77, July 1935. doi: 10.1103/PhysRev.48.73.

[199] J. A. Wheeler. Geons. *Physical Review*, 97:511–536, January 1955. doi: 10.1103/PhysRev.97.511.

[200] C. W. Misner and J. A. Wheeler. Classical physics as geometry. *Annals of Physics*, 2:525–603, December 1957. doi: 10.1016/0003-4916(57)90049-0.

[201] C. W. Misner. Wormhole Initial Conditions. *Physical Review*, 118:1110–1111, May 1960. doi: 10.1103/PhysRev.118.1110.

[202] C. W. Misner. The method of images in geometrostatics. *Annals of Physics*, 24:102–117, October 1963. doi: 10.1016/0003-4916(63)90067-8.

[203] D. R. Brill and R. W. Lindquist. Interaction Energy in Geometrostatics. *Physical Review*, 131:471–476, July 1963. doi: 10.1103/PhysRev.131.471.

[204] G. B. Cook, M. W. Choptuik, M. R. Dubal, S. Klasky, R. A. Matzner, and S. R. Oliveira. Three-dimensional initial data for the collision of two black holes. *Phys. Rev. D.*, 47:1471–1490, February 1993. doi: 10.1103/PhysRevD.47.1471.

[205] E. Gourgoulhon, P. Grandclément, and S. Bonazzola. Binary black holes in circular orbits. I. A global spacetime approach. *Phys. Rev. D.*, 65(4):044020–+, February 2002. doi: 10.1103/PhysRevD.65.044020.

[206] J. M. Bowen. General form for the longitudinal momentum of a spherically symmetric source. *General Relativity and Gravitation*, 11:227–231, October 1979. doi: 10.1007/BF00762132.

[207] J. M. Bowen and J. W. York, Jr. Time-asymmetric initial data for black holes and black-hole collisions. *Phys. Rev. D.*, 21:2047–2056, 1980. doi: 10.1103/PhysRevD.21.2047.

[208] J. M. Bowen. General solution for flat-space longitudinal momentum. *General Relativity and Gravitation*, 14: 1183–1191, December 1982. doi: 10.1007/BF00762642.

[209] A. D. Kulkarni, L. C. Shepley, and J. W. York, Jr. Initial data for N black holes. *Physics Letters A*, 96:228–230, July 1983. doi: 10.1016/0375-9601(83)90338-9.

[210] J. Bowen, J. Rauber, and J. W. York, Jr. Two black holes with axisymmetric parallel spins - Initial data. *Classical and Quantum Gravity*, 1:591–610, September 1984. doi: 10.1088/0264-9381/1/5/012.

[211] A. D. Kulkarni. Time-asymmetric initial data for the N black hole problem in general relativity. *Journal of Mathematical Physics*, 25:1028–1034, April 1984. doi: 10.1063/1.526270.

[212] J. W. York, Jr. Initial data for N black holes. *Physica A Statistical Mechanics and its Applications*, 124:629–637, 1984. doi: 10.1016/0378-4371(84)90279-6.

[213] J. W. York, Jr. *Initial data for collisions of black holes and other gravitational miscellany.*, pages 89–109. 1989.

[214] G. B. Cook. Initial data for axisymmetric black-hole collisions. *Phys. Rev. D.*, 44:2983–3000, November 1991. doi: 10.1103/PhysRevD.44.2983.

[215] J. Thornburg. Coordinates and boundary conditions for the general relativistic initial data problem. *Classical and Quantum Gravity*, 4:1119–1131, September 1987. doi: 10.1088/0264-9381/4/5/013.

[216] S. Brandt and B. Brügmann. A Simple Construction of Initial Data for Multiple Black Holes. *Physical Review Letters*, 78:3606–3609, May 1997. doi: 10.1103/PhysRevLett.78.3606.

[217] R. Beig and N. Ó Murchadha. Trapped surfaces in vacuum spacetimes. *Classical and Quantum Gravity*, 11:419–430, February 1994. doi: 10.1088/0264-9381/11/2/013.

[218] R. Beig and N. Ó Murchadha. Vacuum spacetimes with future trapped surfaces. *Classical and Quantum Gravity*, 13:739–751, April 1996. doi: 10.1088/0264-9381/13/4/014.

[219] R. Beig. Generalized Bowen-York Initial Data. In S. Cotsakis and G. W. Gibbons, editors, *Mathematical and Quantum Aspects of Relativity and Cosmology*, volume 537 of *Lecture Notes in Physics, Berlin Springer Verlag*, pages 55–+, 2000.

[220] S. Dain. Initial Data for Two Kerr-like Black Holes. *Physical Review Letters*, 87(12):121102–+, September 2001. doi: 10.1103/PhysRevLett.87.121102.

[221] Andre Lichnerowicz. L'intégration des équations de la gravitation relativiste et la problème des n corps. *J. Math. Pures et Appl.*, 23:37, 1944.

[222] J. W. York. Gravitational Degrees of Freedom and the Initial-Value Problem. *Physical Review Letters*, 26:1656–1658, June 1971. doi: 10.1103/PhysRevLett.26.1656.

[223] J. W. York. Role of Conformal Three-Geometry in the Dynamics of Gravitation. *Physical Review Letters*, 28: 1082–1085, April 1972. doi: 10.1103/PhysRevLett.28.1082.

[224] J. W. York, Jr. Conformally invariant orthogonal decomposition of symmetric tensors on Riemannian manifolds and the initial-value problem of general relativity. *Journal of Mathematical Physics*, 14:456–464, April 1973. doi: 10.1063/1.1666338.

[225] G. Cook. Initial Data for Numerical Relativity. *Living Reviews in Relativity*, 3:5–+, December 2000.

[226] J. W. York, Jr. Conformal "Thin-Sandwich" Data for the Initial-Value Problem of General Relativity. *Physical Review Letters*, 82:1350–1353, February 1999. doi: 10.1103/PhysRevLett.82.1350.

[227] H. P. Pfeiffer and J. W. York. Extrinsic curvature and the Einstein constraints. *Phys. Rev. D.*, 67(4):044022–+, February 2003. doi: 10.1103/PhysRevD.67.044022.

[228] M. Ansorg, B. Brügmann, and W. Tichy. Single-domain spectral method for black hole puncture data. *Phys. Rev. D.*, 70(6):064011–+, September 2004. doi: 10.1103/PhysRevD.70.064011.

[229] G. B. Cook. Three-dimensional initial data for the collision of two black holes. II. Quasicircular orbits for equal-mass black holes. *Phys. Rev. D.*, 50:5025–5032, October 1994. doi: 10.1103/PhysRevD.50.5025.

[230] H. P. Pfeiffer, S. A. Teukolsky, and G. B. Cook. Quasicircular orbits for spinning binary black holes. *Phys. Rev. D.*, 62(10):104018–+, November 2000. doi: 10.1103/PhysRevD.62.104018.

[231] S. Husa, M. Hannam, J. A. González, U. Sperhake, and B. Brügmann. Reducing eccentricity in black-hole binary evolutions with initial parameters from post-Newtonian inspiral. *Phys. Rev. D.*, 77(4):044037–+, February 2008. doi: 10.1103/PhysRevD.77.044037.

[232] A. Garat and R. H. Price. Nonexistence of conformally flat slices of the Kerr spacetime. *Phys. Rev. D.*, 61(12): 124011–+, June 2000. doi: 10.1103/PhysRevD.61.124011.

[233] S. Dain, C. O. Lousto, and R. Takahashi. New conformally flat initial data for spinning black holes. *Phys. Rev. D.*, 65(10):104038–+, May 2002. doi: 10.1103/PhysRevD.65.104038.

[234] R. A. Matzner, M. F. Huq, and D. Shoemaker. Initial data and coordinates for multiple black hole systems. *Phys. Rev. D.*, 59(2):024015–+, January 1999. doi: 10.1103/PhysRevD.59.024015.

[235] Wolfgang Tichy, Bernd Brügmann, and Pablo Laguna. Gauge conditions for binary black hole puncture data based on an approximate helical killing vector. *Phys. Rev. D*, 68(6):064008, Sep 2003. doi: 10.1103/PhysRevD.68.064008.

[236] M. Hannam, S. Husa, D. Pollney, B. Brügmann, and N. Ó. Murchadha. Geometry and Regularity of Moving Punctures. *Physical Review Letters*, 99(24):241102–+, December 2007. doi: 10.1103/PhysRevLett.99.241102.

[237] M. Hannam, S. Husa, B. Brügmann, J. A. González, U. Sperhake, and N. Ó. Murchadha. Where do moving punctures go? *Journal of Physics Conference Series*, 66(1):012047–+, May 2007. doi: 10.1088/1742-6596/66/1/012047.

[238] J. D. Brown. Puncture evolution of Schwarzschild black holes. *Phys. Rev. D.*, 77(4):044018–+, February 2008. doi: 10.1103/PhysRevD.77.044018.

[239] D. Garfinkle, C. Gundlach, and D. Hilditch. Comments on Bona Massó-type slicing conditions in long-term black hole evolutions. *Classical and Quantum Gravity*, 25(7):075007–+, April 2008. doi: 10.1088/0264-9381/25/7/075007.

[240] M. Hannam, S. Husa, F. Ohme, B. Brügmann, and N. Ó Murchadha. Wormholes and trumpets: Schwarzschild spacetime for the moving-puncture generation. *Phys. Rev. D.*, 78(6):064020–+, September 2008. doi: 10.1103/PhysRevD.78.064020.

[241] J. Thornburg. Finding apparent horizons in numerical relativity. *Phys. Rev. D.*, 54:4899–4918, October 1996. doi: 10.1103/PhysRevD.54.4899.

[242] J. Thornburg. A fast apparent horizon finder for three-dimensional Cartesian grids in numerical relativity. *Classical and Quantum Gravity*, 21:743–766, January 2004. doi: 10.1088/0264-9381/21/2/026.

[243] M. Miller. Circular orbit approximation for binary compact objects in general relativity. *Phys. Rev. D.*, 69(12): 124013–+, June 2004. doi: 10.1103/PhysRevD.69.124013.

[244] A. Buonanno, Y. Chen, and T. Damour. Transition from inspiral to plunge in precessing binaries of spinning black holes. *Phys. Rev. D.*, 74(10):104005–+, November 2006. doi: 10.1103/PhysRevD.74.104005.

[245] P. Jaranowski and G. Schäfer. Third post-Newtonian higher order ADM Hamilton dynamics for two-body point-mass systems. *Phys. Rev. D.*, 57:7274–7291, June 1998. doi: 10.1103/PhysRevD.57.7274.

[246] T. Damour, P. Jaranowski, and G. Schäfer. Dimensional regularization of the gravitational interaction of point masses. *Physics Letters B*, 513:147–155, July 2001. doi: 10.1016/S0370-2693(01)00642-6.

[247] L. Blanchet and G. Faye. General relativistic dynamics of compact binaries at the third post-Newtonian order. *Phys. Rev. D.*, 63(6):062005–+, March 2001. doi: 10.1103/PhysRevD.63.062005.

[248] V. C. de Andrade, L. Blanchet, and G. Faye. Third post-Newtonian dynamics of compact binaries: Noetherian conserved quantities and equivalence between the harmonic-coordinate and ADM-Hamiltonian formalisms. *Classical and Quantum Gravity*, 18:753–778, March 2001. doi: 10.1088/0264-9381/18/5/301.

[249] L. Blanchet and B. R. Iyer. Third post-Newtonian dynamics of compact binaries: equations of motion in the centre-of-mass frame . *Classical and Quantum Gravity*, 20:755–776, February 2003.

[250] L. Blanchet. Gravitational-wave tails of tails. *Classical and Quantum Gravity*, 15:113–141, January 1998. doi: 10.1088/0264-9381/15/1/009.

[251] L. Blanchet, B. R. Iyer, and B. Joguet. Gravitational waves from inspiraling compact binaries: Energy flux to third post-Newtonian order. *Phys. Rev. D.*, 65(6):064005–+, March 2002. doi: 10.1103/PhysRevD.65.064005.

[252] L. Blanchet, T. Damour, G. Esposito-Farèse, and B. R. Iyer. Gravitational Radiation from Inspiralling Compact Binaries Completed at the Third Post-Newtonian Order. *Physical Review Letters*, 93(9):091101–+, August 2004. doi: 10.1103/PhysRevLett.93.091101.

[253] B. M. Barker and R. F. O'Connell. Derivation of the equation of motion of a gyroscope from the quantum theory of gravitation. *Phys. Rev. D.*, 2:1428–1435, 1970. doi: 10.1103/PhysRevD.2.1428.

[254] B. M. Barker and R. F. O'Connell. Nongeodesic motion in general relativity. *General Relativity and Gravitation*, 5:539–554, October 1974. doi: 10.1007/BF02451397.

[255] B. M. Barker and R. F. O'Connell. The gravitational interaction: spin, rotation, and quantum effects - a review. *General Relativity and Gravitation*, 11:149–175, October 1979. doi: 10.1007/BF00756587.

[256] B. Brügmann, J. A. González, M. Hannam, S. Husa, U. Sperhake, and W. Tichy. Calibration of moving puncture simulations. *Phys. Rev. D.*, 77(2):024027–+, January 2008. doi: 10.1103/PhysRevD.77.024027.

[257] Michael Boyle et al. High-accuracy comparison of numerical relativity simulations with post-Newtonian expansions. *Phys. Rev.*, D76:124038, 2007. doi: 10.1103/PhysRevD.76.124038.

[258] H. P. Pfeiffer, D. A. Brown, L. E. Kidder, L. Lindblom, G. Lovelace, and M. A. Scheel. Reducing orbital eccentricity in binary black hole simulations. *Classical and Quantum Gravity*, 24:59–+, June 2007. doi: 10.1088/0264-9381/24/12/S06.

[259] E. Seidel and W.-M. Suen. Towards a singularity-proof scheme in numerical relativity. *Physical Review Letters*, 69: 1845–1848, September 1992. doi: 10.1103/PhysRevLett.69.1845.

[260] P. Diener, N. Jansen, A. Khokhlov, and I. Novikov. Adaptive mesh refinement approach to the construction of initial data for black hole collisions. *Classical and Quantum Gravity*, 17:435–451, January 2000. doi: 10.1088/0264-9381/17/2/312.

[261] S. H. Hawley and R. A. Matzner. Tips for implementing multigrid methods on domains containing holes. *Classical and Quantum Gravity*, 21:805–821, February 2004. doi: 10.1088/0264-9381/21/4/004.

[262] J. Thornburg. Black-hole excision with multiple grid patches. *Classical and Quantum Gravity*, 21:3665–3691, August 2004. doi: 10.1088/0264-9381/21/15/004.

[263] B. Szilágyi, D. Pollney, L. Rezzolla, J. Thornburg, and J. Winicour. An explicit harmonic code for black-hole evolution using excision. *Classical and Quantum Gravity*, 24:275–+, June 2007. doi: 10.1088/0264-9381/24/12/S18.

[264] B. Brügmann, W. Tichy, and N. Jansen. Numerical Simulation of Orbiting Black Holes. *Physical Review Letters*, 92(21):211101–+, May 2004. doi: 10.1103/PhysRevLett.92.211101.

[265] P. Diener, F. Herrmann, D. Pollney, E. Schnetter, E. Seidel, R. Takahashi, J. Thornburg, and J. Ventrella. Accurate Evolution of Orbiting Binary Black Holes. *Physical Review Letters*, 96(12):121101–+, March 2006. doi: 10.1103/PhysRevLett.96.121101.

[266] M. Hannam, S. Husa, and N. Ó Murchadha. Bowen-York trumpet data and black-hole simulations. *ArXiv e-prints*, August 2009.

[267] J. Thornburg, P. Diener, D. Pollney, L. Rezzolla, E. Schnetter, E. Seidel, and R. Takahashi. Are moving punctures equivalent to moving black holes? *ArXiv General Relativity and Quantum Cosmology e-prints*, January 2007.

[268] Y. Zlochower, R. Gómez, S. Husa, L. Lehner, and J. Winicour. Mode coupling in the nonlinear response of black holes. *Phys. Rev. D.*, 68(8):084014–+, October 2003. doi: 10.1103/PhysRevD.68.084014.

[269] R. Gómez, L. Lehner, R. L. Marsa, and J. Winicour. Moving black holes in 3D. *Phys. Rev. D.*, 57:4778–4788, April 1998. doi: 10.1103/PhysRevD.57.4778.

[270] R. W. Corkill and J. M. Stewart. Numerical Relativity. II. Numerical Methods for the Characteristic Initial Value Problem and the Evolution of the Vacuum Field Equations for Space- Times with Two Killing Vectors. *Royal Society of London Proceedings Series A*, 386:373–391, April 1983.

[271] J. M. Stewart. The Characteristic Initial Value Problem in General Relativity. In K.-H. A. Winkler and M. L. Norman, editors, *Astrophysical Radiation Hydrodynamics*, pages 531–+, 1986.

[272] N. T. Bishop, R. Gómez, L. Lehner, and J. Winicour. Cauchy-characteristic extraction in numerical relativity. *Phys. Rev. D.*, 54:6153–6165, November 1996. doi: 10.1103/PhysRevD.54.6153.

[273] N. T. Bishop, R. Gómez, L. Lehner, M. Maharaj, and J. Winicour. High-powered gravitational news. *Phys. Rev. D.*, 56:6298–6309, November 1997. doi: 10.1103/PhysRevD.56.6298.

[274] R. Gómez, S. Husa, and J. Winicour. Complete null data for a black hole collision. *Phys. Rev. D.*, 64(2):024010–+, July 2001. doi: 10.1103/PhysRevD.64.024010.

[275] M. Babiuc, B. Szilágyi, I. Hawke, and Y. Zlochower. Gravitational wave extraction based on Cauchy characteristic extraction and characteristic evolution. *Classical and Quantum Gravity*, 22:5089–5107, December 2005. doi: 10.1088/0264-9381/22/23/011.

[276] J. Winicour. Characteristic evolution and matching. *Living Rev. Relativity*, 8, 2008. preprint: arXiv:0810.1903v2.

[277] M. C. Babiuc, N. T. Bishop, B. Szilágyi, and J. Winicour. Strategies for the characteristic extraction of gravitational waveforms. *Phys. Rev. D.*, 79(8):084011–+, April 2009. doi: 10.1103/PhysRevD.79.084011.

[278] R. Gómez, W. Barreto, and S. Frittelli. Framework for large-scale relativistic simulations in the characteristic approach. *Phys. Rev. D.*, 76(12):124029–+, December 2007. doi: 10.1103/PhysRevD.76.124029.

[279] R. Gomez, W. Barreto, and S. Frittelli. Large-scale relativistic simulations in the characteristic approach. *APS Meeting Abstracts*, pages 10004–+, April 2008.

[280] R. Gomez, L. Lehner, P. Papadopoulos, and J. Winicour. The eth formalism in numerical relativity. *Classical and Quantum Gravity*, 14:977–990, April 1997. doi: 10.1088/0264-9381/14/4/013.

[281] J.N. Goldberg, A.J. MacFarlane, E.T. Newman, F. Rohrlich, and E.C.G. Sudarshan. Spin-s spherical harmonics and ð. *Journal of Mathematical Physics*, 8(11), 1967.

[282] S. W. Hawking and R. Penrose. The Singularities of Gravitational Collapse and Cosmology. *Royal Society of London Proceedings Series A*, 314:529–548, January 1970.

[283] R. Penrose. Gravitational Collapse and Space-Time Singularities. *Physical Review Letters*, 14:57–59, January 1965. doi: 10.1103/PhysRevLett.14.57.

[284] T. W. Baumgarte, G. B. Cook, M. A. Scheel, S. L. Shapiro, and S. A. Teukolsky. Implementing an apparent-horizon finder in three dimensions. *Phys. Rev. D.*, 54:4849–4857, October 1996. doi: 10.1103/PhysRevD.54.4849.

[285] P. Anninos, K. Camarda, J. Libson, J. Massó, E. Seidel, and W.-M. Suen. Finding apparent horizons in dynamic 3D numerical spacetimes. *Phys. Rev. D.*, 58(2):024003–+, July 1998. doi: 10.1103/PhysRevD.58.024003.

[286] M. F. Huq, M. W. Choptuik, and R. A. Matzner. Locating boosted Kerr and Schwarzschild apparent horizons. *Phys. Rev. D.*, 66(8):084024–+, October 2002. doi: 10.1103/PhysRevD.66.084024.

[287] M. Alcubierre, S. Brandt, B. Brügmann, C. Gundlach, J. Massó, E. Seidel, and P. Walker. Test-beds and applications for apparent horizon finders in numerical relativity. *Classical and Quantum Gravity*, 17:2159–2190, June 2000. doi: 10.1088/0264-9381/17/11/301.

[288] D. M. Shoemaker, M. F. Huq, and R. A. Matzner. Generic tracking of multiple apparent horizons with level flow. *Phys. Rev. D.*, 62(12):124005–+, December 2000. doi: 10.1103/PhysRevD.62.124005.

[289] E. Schnetter. A fast apparent horizon algorithm. *ArXiv General Relativity and Quantum Cosmology e-prints*, June 2002.

[290] E. Schnetter. Finding apparent horizons and other 2-surfaces of constant expansion. *Classical and Quantum Gravity*, 20:4719–4737, November 2003. doi: 10.1088/0264-9381/20/22/001.

[291] A. Ashtekar, C. Beetle, O. Dreyer, S. Fairhurst, B. Krishnan, J. Lewandowski, and J. Wiśniewski. Generic Isolated Horizons and Their Applications. *Physical Review Letters*, 85:3564–3567, October 2000. doi: 10.1103/PhysRevLett.85.3564.

[292] A. Ashtekar and B. Krishnan. Dynamical Horizons: Energy, Angular Momentum, Fluxes, and Balance Laws. *Physical Review Letters*, 89(26):261101–+, December 2002. doi: 10.1103/PhysRevLett.89.261101.

[293] Erik Schnetter, Badri Krishnan, and Florian Beyer. Introduction to Dynamical Horizons in numerical relativity. *Phys. Rev. D*, 74:024028, 2006.

[294] P. T. Chruściel and G. J. Galloway. Horizons Non-Differentiable on a Dense Set. *Communications in Mathematical Physics*, 193:449–470, 1998. doi: 10.1007/s002200050336.

[295] J. Thornburg. Event and Apparent Horizon Finders for 3+1 Numerical Relativity. *Living Reviews in Relativity*, 10:3–+, June 2007.

[296] P. Diener. A new general purpose event horizon finder for 3D numerical spacetimes. *Classical and Quantum Gravity*, 20:4901–4917, November 2003. doi: 10.1088/0264-9381/20/22/014.

[297] M. Kriele and S. A. Hayward. Outer trapped surfaces and their apparent horizon. *Journal of Mathematical Physics*, 38:1593–1604, March 1997. doi: 10.1063/1.532010.

[298] Olaf Dreyer, Badri Krishnan, Deirdre Shoemaker, and Erik Schnetter. Introduction to Isolated Horizons in Numerical Relativity. *Phys. Rev. D*, 67:024018, 2003.

[299] A. Ashtekar and B. Krishnan. Dynamical horizons and their properties. *Phys. Rev. D.*, 68(10):104030–+, November 2003. doi: 10.1103/PhysRevD.68.104030.

[300] J. L. Friedman, K. Schleich, and D. M. Witt. Topological censorship. *Physical Review Letters*, 71:1486–1489, September 1993. doi: 10.1103/PhysRevLett.71.1486.

[301] A. Ashtekar, S. Fairhurst, and B. Krishnan. Isolated horizons: Hamiltonian evolution and the first law. *Phys. Rev. D.*, 62(10):104025–+, November 2000. doi: 10.1103/PhysRevD.62.104025.

[302] A. Ashtekar, C. Beetle, and J. Lewandowski. Mechanics of rotating isolated horizons. *Phys. Rev. D.*, 64(4):044016–+, August 2001. doi: 10.1103/PhysRevD.64.044016.

[303] D. Christodoulou. Reversible and Irreversible Transformations in Black-Hole Physics. *Physical Review Letters*, 25: 1596–1597, November 1970. doi: 10.1103/PhysRevLett.25.1596.

[304] L. Smarr. Mass Formula for Kerr Black Holes. *Physical Review Letters*, 30:71–73, January 1973. doi: 10.1103/PhysRevLett.30.71.

[305] L. Blanchet. Gravitational Radiation from Post-Newtonian Sources and Inspiralling Compact Binaries. *Living Reviews in Relativity*, 5:3–+, April 2002.

[306] L. Gunnarsen, H. Shinkai, and K. Maeda. A '3+1' method for finding principal null directions. *Class. Quant. Grav.*, 12:133–140, 1995.

[307] L. Lehner and O. M. Moreschi. Dealing with delicate issues in waveform calculations. *Phys. Rev. D.*, 76:124040, 2007.

[308] F. J. Zerilli. Gravitational field of a particle falling in a Schwarzschild geometry analyzed in tensor harmonics. *Phys. Rev. D.*, 2:2141–2160, 1970.

[309] F. J. Zerilli. Effective potential for even-parity Regge-Wheeler gravitational perturbation equations. *Phys. Rev. Lett.*, 24:737–738, 1970.

[310] V. Moncrief. Gravitational perturbations of spherically symmetric systems. i. The exterior problem. *Ann. Phys.*, 88:323–342, 1974.

[311] S. Chandrasekhar. *The Mathematical Theory of Black Holes*. Oxford University Press, 1983.

[312] A. Nagar and L. Rezzolla. Gauge-invariant non-spherical metric perturbations of Schwarzschild black-hole spacetimes. *Class. Quant. Grav.*, 22, 2005.

[313] K. Tomita. On the non-linear behavior of nonspherical perturbations in relativistic gravitational collapse. *Prog. Theor. Phys.*, 52:1188–1204, 1974.

[314] K. Tomita and N. Tajima. Nonlinear behavior of nonspherical perturbations of the Schwarzschild metric. *Prog. Theor. Phys.*, 56:551–560, 1976.

[315] C. O. Lousto and H. Nakano. Regular second-order perturbations of binary black holes in the extreme mass ratio regime. *Class. Quant. Grav.*, 26:015007, 2009.

[316] D. Brizuela, J. M. Martín-García, and M. Tiglio. A complete gauge-invariant formalism for arbitrary second-order perturbations of a Schwarzschild black hole. 2009. preprint arXiv:0903.1134v1.

[317] A. M. Abrahams and R. H. Price. Applying black hole perturbation theory to numerically generated spacetimes. *Phys. Rev. D.*, 53:1963–1971, 1996.

[318] K. Camarda and E. Seidel. Three-dimensional simulations of distorted black holes. i. Comparison with axisymmetric results. *Phys. Rev. D.*, 59, 1999.

[319] U. H. Gerlach and U. K. Sengupta. Gauge-invariant perturbations on most general spherically symmetric space-times. *Phys. Rev. D.*, 19:2268–2272, 1979.

[320] E. Seidel G. Allen, K. Camarda. Evolution of distorted black holes: A perturbative approach. *arXiv:gr-qc/9806014v2*, 1998.

[321] J. Frauendiener. Numerical treatment of the hyperboloidal initial value problem for the vacuum Einstein equations. I. The conformal field equations. *Phys. Rev. D.*, 58(6):064002–+, September 1998. doi: 10.1103/PhysRevD.58.064002.

[322] J. Frauendiener. Numerical treatment of the hyperboloidal initial value problem for the vacuum Einstein equations. II. The evolution equations. *Phys. Rev. D.*, 58(6):064003–+, September 1998. doi: 10.1103/PhysRevD.58.064003.

[323] J. Frauendiener. Numerical treatment of the hyperboloidal initial value problem for the vacuum Einstein equations. III. On the determination of radiation. *Class. Quant. Grav.*, 17:373–387, January 2000. doi: 10.1088/0264-9381/17/2/308.

[324] A. Zenginoğlu. Hyperboloidal foliations and scri-fixing. *Class. Quant. Grav.*, 25(14):145002–+, July 2008. doi: 10.1088/0264-9381/25/14/145002.

[325] A. Zenginoğlu. Hyperboloidal evolution with the Einstein equations. *Class. Quant. Grav.*, 25(19):195025–+, October 2008. doi: 10.1088/0264-9381/25/19/195025.

[326] A. Zenginoğlu. A hyperboloidal study of tail decay rates for scalar and Yang Mills fields. *Class. Quant. Grav.*, 25 (17):175013–+, September 2008. doi: 10.1088/0264-9381/25/17/175013.

[327] F. Ohme, M. Hannam, S. Husa, and N. Ó. Murchadha. Stationary hyperboloidal slicings with evolved gauge conditions. 2009.

[328] N. T. Bishop. Numerical relativity: combining the Cauchy and characteristic initial value problems. *Class. Quant. Grav.*, 10:333–341, February 1993. doi: 10.1088/0264-9381/10/2/015.

[329] N. T. Bishop. Cauchy Characteristic Evolution and Waveforms. *Journal of Computational Physics*, 136:140–167, September 1997. doi: 10.1006/jcph.1997.5754.

[330] N. T. Bishop, R. Gomez, L. Lehner, B. Szilagyi, J. Winicour, and R. A. Isaacson. Cauchy-Characteristic Matching. In B. R. Iyer and B. Bhawal, editors, *Black Holes, Gravitational Radiation, and the Universe: Essays in Honor of C.V. Vishveshwara*, pages 383–+, 1999.

[331] N. Bishop and S. Deshingkar. New approach to calculating the news. *Phys. Rev. D.*, 68(2):024031–+, July 2003. doi: 10.1103/PhysRevD.68.024031.

[332] S. A. Teukolsky. Perturbations of a rotating black hole. I. Fundamental equations for gravitational, electromagnetic, and neutrino-field perturbations. *Astrophys. J.*, 185:635–648, 1973.

[333] C. T. Cunningham, R. H. Price, and V. Moncrief. Radiation from collapsing relativistic stars. I - Linearized odd-parity radiation. *Astrophys. J.*, 224:643–667, 1978.

[334] C. T. Cunningham, R. H. Price, and V. Moncrief. Radiation from collapsing relativistic stars. II - Linearized even-parity radiation. *Astrophys. J.*, 230:870–892, 1979.

[335] M. Campanelli and C. O. Lousto. Second order gauge invariant gravitational perturbations of a kerr black hole. *Phys. Rev. D.*, 59:124022, 1999.

[336] M. Ruiz, M. Alcubierre, D. Núnez, and R. Takahashi. Multipole expansions for energy and momenta carried by gravitational waves. *Gen. Relativ. Gravit.*, 40:2467–2467, 2008.

[337] M. Favata, S. A. Hughes, and D. E. Holz. How black holes get their kicks: Gravitational radiation recoil revisited. *Astrophys. J.*, 607:L5–L8, 2004.

[338] T. Damour and A. Gopakumar. Gravitational recoil during binary black hole coalescence using the effective one body approach. *Phys. Rev. D.*, 73:124006, 2006.

[339] E. F. Toro. *Riemann Solvers and Numerical Methods for Fluid Dynamics - A practical introduction.* Springer, 2nd edition edition, 1999.

[340] J.S. Hesthaven and T. Warburton. *Nodal Discontinuous Galerkin Methods: Algorithms, Analysis, and Applications.* Springer, 2008.

[341] B. Szilágyi, L. Lindblom, and M. A. Scheel. Simulations of Binary Black Hole Mergers Using Spectral Methods. *ArXiv e-prints*, September 2009.

[342] G. Zumbusch. Finite Element, Discontinuous Galerkin, and Finite Difference evolution schemes in spacetime. *ArXiv e-prints*, January 2009.

[343] Bengt Fornberg. Generation of finite difference formulas on arbitrarily spaced grids. *Mathematics of Computation*, 51(184):699–706, 1988. ISSN 00255718. URL `http://www.jstor.org/stable/2008770`.

[344] H. O. Kreiss and J. Oliger. *Methods for the approximate solution of time dependent problems.* GARP publication series No. 10, Geneva, 1973.

[345] Bertil Gustafsson, Heinz-Otto Kreiss, and Joseph Oliger. *Time Dependent Problems And Difference Methods.* Pure And Applied Mathematics: A Wiley-Interscience Series of Texts, Monographs, and Tracts, 1995.

[346] J. Crank, P. Nicolson, and D. R. Hartree. A practical method for numerical evaluation of solutions of partial differential equations of the heat-conduction type. *Mathematical Proceedings of the Cambridge Philosophical Society*, 43:50–+, 1947. doi: 10.1017/S0305004100023197.

[347] J. G. Charney, R. Fjrtoft, and J. von Neumann. Numerical Integration of the Barotropic Vorticity Equation. *Tellus*, 2:237–254, 1950.

[348] R. Courant, K. Friedrichs, and H. Lewy. Über die partiellen Differenzengleichungen der mathematischen Physik. *Mathematische Annalen*, 100(1), 1928.

[349] J. Heine. *Topologie und Funktionalanalysis.* Oldenbourg Verlag, 2002.

[350] C. Reisswig. A characteristic einstein evolution code in adapted coordinates. Master's thesis, Leibniz University Hannover, May 2006.

[351] C. Bona and C. Palenzuela-Luque. *Elements of Numerical Relativity.* Springer, 2005.

[352] M. W. Choptuik. Consistency of finite-difference solutions of Einstein's equations. *Phys. Rev. D.*, 44:3124–3135, November 1991. doi: 10.1103/PhysRevD.44.3124.

[353] L. F. Richardson. On the Approximate Arithmetical Solution by Finite Differences of Physical Problems Involving Differential Equations, with an Application to the Stresses in a Masonry Dam. *Royal Society of London Proceedings Series A*, 83:335–336, March 1910.

[354] T. Goodale, G. Allen, G. Lanfermann, J. Massó, T. Radke, E. Seidel, and J. Shalf. The Cactus framework and toolkit: Design and applications. In *Vector and Parallel Processing – VECPAR'2002, 5th International Conference, Lecture Notes in Computer Science*, Berlin, 2003. Springer.

[355] G. Allen, W. Benger, T. Goodale, H. Hege, G. Lanfermann, A. Merzky, T. Radke, E. Seidel, and J. Shalf. The cactus code: A problem solving environment for the grid. In *Proceedings of First Egrid Meeting at ISTHMUS, Poznan, April 2000*, 2000.

[356] Cactus Computational Toolkit. `http://www.cactuscode.org`.

[357] E. Schnetter, S. H. Hawley, and I. Hawke. Evolutions in 3D numerical relativity using fixed mesh refinement. *Classical and Quantum Gravity*, 21:1465–1488, March 2004. doi: 10.1088/0264-9381/21/6/014.

[358] URL `http://www.carpetcode.org/`. Mesh refinement with Carpet.

[359] Message passing interface (mpi) standard. www-unix.mcs.anl.gov/mpi/index.htm.

[360] URL `http://www.openmp.org/`. The OpenMP API specification for parallel programming.

[361] Marsha J. Berger and Joseph Oliger. Adaptive mesh refinement for hyperbolic partial differential equations. *J. Comput. Phys.*, 53:484–512, 1984.

[362] M. J. Berger and P. Colella. Local adaptive mesh refinement for shock hydrodynamics. *Journal of Computational Physics*, 82:64–84, May 1989. doi: 10.1016/0021-9991(89)90035-1.

[363] T. Plewa and E. Müller. AMRA: An Adaptive Mesh Refinement hydrodynamic code for astrophysics. *Computer Physics Communications*, 138:101–127, August 2001. doi: 10.1016/S0010-4655(01)00199-0.

[364] John G. Baker, James R. van Meter, Sean T. McWilliams, Joan Centrella, and Bernard J. Kelly. Consistency of post-Newtonian waveforms with numerical relativity. 2006.

[365] A. Buonanno, G. B. Cook, and F. Pretorius. Inspiral, merger, and ring-down of equal-mass black-hole binaries. *Phys. Rev. D.*, 75(12):124018–+, June 2007. doi: 10.1103/PhysRevD.75.124018.

[366] Mark Hannam, Sascha Husa, Ulrich Sperhake, Bernd Bruegmann, and Jose A. Gonzalez. Where post-Newtonian and numerical-relativity waveforms meet. *Phys. Rev.*, D77:044020, 2008. doi: 10.1103/PhysRevD.77.044020.

[367] Mark Hannam, Sascha Husa, Bernd Bruegmann, and Achamveedu Gopakumar. Comparison between numerical-relativity and post-Newtonian waveforms from spinning binaries: the orbital hang-up case. *Phys. Rev.*, D78:104007, 2008. doi: 10.1103/PhysRevD.78.104007.

[368] T. Damour, A. Nagar, E. N. Dorband, D. Pollney, and L. Rezzolla. Faithful effective-one-body waveforms of equal-mass coalescing black-hole binaries. *Phys. Rev. D.*, 77(8):084017–+, April 2008. doi: 10.1103/PhysRevD.77.084017.

[369] Alessandra Buonanno et al. Toward faithful templates for non-spinning binary black holes using the effective-one-body approach. *Phys. Rev.*, D76:104049, 2007. doi: 10.1103/PhysRevD.76.104049.

[370] Thibault Damour, Alessandro Nagar, Mark Hannam, Sascha Husa, and Bernd Bruegmann. Accurate Effective-One-Body waveforms of inspiralling and coalescing black-hole binaries. *Phys. Rev.*, D78:044039, 2008. doi: 10.1103/PhysRevD.78.044039.

[371] Alessandra Buonanno et al. Effective-one-body waveforms calibrated to numerical relativity simulations: coalescence of non-spinning, equal- mass black holes. 2009.

[372] M. A. Scheel, H. P. Pfeiffer, L. Lindblom, L. E. Kidder, O. Rinne, and S. A. Teukolsky. Solving Einstein's equations with dual coordinate frames. *Phys. Rev. D.*, 74(10):104006–+, November 2006. doi: 10.1103/PhysRevD.74.104006.

[373] Eric Gourgoulhon, Philippe Grandclement, Keisuke Taniguchi, Jean-Alain Marck, and Silvano Bonazzola. Quasiequilibrium sequences of synchronized and irrotational binary neutron stars in general relativity. I. Method and tests. *Phys. Rev.*, D63:064029, 2001. doi: 10.1103/PhysRevD.63.064029.

[374] Philippe Grandclement, Eric Gourgoulhon, and Silvano Bonazzola. Binary black holes in circular orbits. II. Numerical methods and first results. *Phys. Rev.*, D65:044021, 2002. doi: 10.1103/PhysRevD.65.044021.

[375] Erik Schnetter, Peter Diener, Ernst Nils Dorband, and Manuel Tiglio. A multi-block infrastructure for three-dimensional time- dependent numerical relativity. *Class. Quant. Grav.*, 23:S553–S578, 2006. doi: 10.1088/0264-9381/23/16/S14.

[376] Ernst Nils Dorband, Emanuele Berti, Peter Diener, Erik Schnetter, and Manuel Tiglio. A numerical study of the quasinormal mode excitation of Kerr black holes. *Phys. Rev.*, D74:084028, 2006. doi: 10.1103/PhysRevD.74.084028.

[377] E. Pazos, M. Tiglio, M. D. Duez, L. E. Kidder, and S. A. Teukolsky. Orbiting binary black hole evolutions with a multipatch high order finite-difference approach. *Phys. Rev. D.*, 80(2):024027–+, July 2009. doi: 10.1103/PhysRevD.80.024027.

[378] Mark H. Carpenter, David Gottlieb, and Saul Abarbanel. The stability of numerical boundary treatments for compact high-order finite-difference schemes. *Journal of Computational Physics*, 108(2), 1993.

[379] Mark H. Carpenter, David Gottlieb, and Saul Abarbanel. Time-stable boundary conditions for finite-difference schemes solving hyperbolic systems: Methodology and application to high-order compact schemes. *Journal of Computational Physics*, 111:220–236, 1994.

[380] Mark H. Carpenter, Jan Nordström, and David Gottlieb. A stable and conservative interface treatment of arbitrary spatial accuracy. *Journal of Computational Physics*, 148:341–365, 1999.

[381] L. Lehner, O. Reula, and M. Tiglio. Multi-block simulations in general relativity: high-order discretizations, numerical stability and applications. *Classical and Quantum Gravity*, 22:5283–5321, December 2005. doi: 10.1088/0264-9381/22/24/006.

[382] James R. Driscoll and Dennis M. Healy, Jr. Computing fourier transforms and convolutions on the 2-sphere. *Adv. Appl. Math.*, 15(2):202–250, 1994. ISSN 0196-8858. doi: http://dx.doi.org/10.1006/aama.1994.1008.

[383] H. Bateman. *Higher transcendental functions*. 1955.

[384] William H. Press, Saul A. Teukolsky, William T. Vetterling, and Brian P. Flannery. *Numerical Recipes in C*. Cambridge University Press, 1992.

[385] A. Lewis, A. Challinor, and N. Turok. Analysis of CMB polarization on an incomplete sky. *Phys. Rev. D.*, 65(2): 023505–+, January 2002. doi: 10.1103/PhysRevD.65.023505.

[386] D. A. Varshalovich, A. N. Moskalev, and V. K. Khersonsky. QUANTUM THEORY OF ANGULAR MOMENTUM: IRREDUCIBLE TENSORS, SPHERICAL HARMONICS, VECTOR COUPLING COEFFICIENTS, 3NJ SYMBOLS. SINGAPORE, SINGAPORE: WORLD SCIENTIFIC (1988) 514p.

[387] Matias Zaldarriaga and Uros Seljak. An All-Sky Analysis of Polarization in the Microwave Background. *Phys. Rev.*, D55:1830–1840, 1997. doi: 10.1103/PhysRevD.55.1830.

[388] Marc Kamionkowski, Arthur Kosowsky, and Albert Stebbins. Statistics of Cosmic Microwave Background Polarization. *Phys. Rev.*, D55:7368–7388, 1997. doi: 10.1103/PhysRevD.55.7368.

[389] R. Barrett, M. Berry, T. Chan, J. Dongarra, V. Eijkhout, C. Romine, and H. van der Vorst. *Templates for the Solution of Linear Systems: Building Blocks for Iterative Methods*. SIAM, `http://www.netlib.org/templates/`, 1993.

[390] E. Schnetter. Finding apparent horizons and other 2-surfaces of constant expansion. *Classical and Quantum Gravity*, 20:4719–4737, November 2003. doi: 10.1088/0264-9381/20/22/001.

[391] E. Schnetter, F. Herrmann, and D. Pollney. Horizon pretracking. *Phys. Rev. D.*, 71(4):044033–+, February 2005. doi: 10.1103/PhysRevD.71.044033.

[392] Luis Lehner. *Gravitational Radiation From Black Hole Spacetimes*. PhD thesis, University of Pittsburgh, 1998.

[393] Béla Szilágyi. *Cauchy-Characteristic Matching In General Relativity*. PhD thesis, University of Pittsburgh, 2000.

[394] R. Gómez, P. Papadopoulos, and J. Winicour. Null cone evolution of axisymmetric vacuum space-times. *Journal of Mathematical Physics*, 35:4184–4204, August 1994. doi: 10.1063/1.530848.

[395] R. A. Isaacson, J. S. Welling, and J. Winicour. Null cone computation of gravitational radiation. *Journal of Mathematical Physics*, 24:1824–1834, 1983.

[396] Michael Pürrer. Critical collapse in compactified spacetime. Master's thesis, Universität Wien, 2003.

[397] Luis Lehner. A dissipative algorithm for wave-like equations in the characteristic formulation. *Journal of Computational Physics*, 149(1):59–74, 1999.

[398] Nigel Bishop. Private communication.

[399] VisIt. `https://wci.llnl.gov/codes/visit/`.

[400] VTK. `http://www.vtk.org/`.

[401] OpenDX. `http://www.opendx.org/`.

[402] HDF5. `http://www.hdfgroup.org/HDF5/`.

[403] VisIt Manuals. `https://wci.llnl.gov/codes/visit/manuals.html`.

[404] L. Baiotti, B. Giacomazzo, and L. Rezzolla. Accurate evolutions of inspiralling neutron-star binaries: Prompt and delayed collapse to a black hole. *Phys. Rev. D.*, 78(8):084033–+, October 2008. doi: 10.1103/PhysRevD.78.084033.

[405] Bruno Giacomazzo. Private communication.

[406] Jeremy D. Schnittman. Spin-orbit resonance and the evolution of compact binary systems. *Phys. Rev.*, D70:124020, 2004.

[407] T. Bogdanović, C. S. Reynolds, and M. C. Miller. Alignment of the Spins of Supermassive Black Holes Prior to Coalescence. *ApJ*, 661:L147–L150, June 2007.

[408] QNM frequencies. `http://www.astro.auth.gr/ berti/qnms.html`.

[409] F. Herrmann, I. Hinder, D. M. Shoemaker, P. Laguna, and R. A. Matzner. Binary black holes: Spin dynamics and gravitational recoil. *Phys. Rev. D.*, 76(8):084032, October 2007. doi: 10.1103/PhysRevD.76.084032.

[410] F. Herrmann, I. Hinder, D. Shoemaker, P. Laguna, and R. A. Matzner. Gravitational Recoil from Spinning Binary Black Hole Mergers. *Astrophys. J.*, 661:430–436, May 2007. doi: 10.1086/513603.

[411] A. Loeb. Observable Signatures of a Black Hole Ejected by Gravitational-Radiation Recoil in a Galaxy Merger. *Physical Review Letters*, 99(4):041103–+, July 2007. doi: 10.1103/PhysRevLett.99.041103.

[412] E. W. Bonning, G. A. Shields, and S. Salviander. Recoiling Black Holes in Quasars. *Astrophys. J. Lett.*, 666: L13–L16, September 2007. doi: 10.1086/521674.

[413] N. T. Bishop. Linearized solutions of the Einstein equations within a Bondi Sachs framework, and implications for boundary conditions in numerical simulations. *Classical and Quantum Gravity*, 22:2393–2406, June 2005. doi: 10.1088/0264-9381/22/12/006.

[414] Edward Seidel. Black Hole Coalescence and Mergers: Review, Status, and “Where are We Heading?”. *Prog. Theor. Phys. Suppl.*, 136:87–106, 1999. URL `http://ptp.ipap.jp/link?PTPS/136/87/`.

[415] S. Brandt and E. Seidel. Evolution of distorted rotating black holes II: Dynamics and analysis. *Phys. Rev. D*, 52 (2):870–886, 1995. URL `http://link.aps.org/abstract/PRD/v52/p870`.

[416] G. Kupi, P. Amaro-Seoane, and R. Spurzem. Dynamics of compact object clusters: a post-Newtonian study. *Mon. Not. R. Astron. Soc.*, 371:L45–L49, September 2006. doi: 10.1111/j.1745-3933.2006.00205.x.

[417] C. Lousto, M. Campanelli, and Y. Zlochower. Modeling gravitational recoil from precessing highly-spinning unequal-mass black-hole binaries. *APS Meeting Abstracts*, pages 11001–+, May 2009.

[418] Manuela Campanelli, Carlos O. Lousto, Hiroyuki Nakano, and Yosef Zlochower. Comparison of Numerical and Post-Newtonian Waveforms for Generic Precessing Black-Hole Binaries. *Phys. Rev.*, D79:084010, 2009.

[419] P. Marronetti, W. Tichy, B. Brügmann, J. González, and U. Sperhake. High-spin binary black hole mergers. *Phys. Rev. D.*, 77(6):064010–+, March 2008. doi: 10.1103/PhysRevD.77.064010.

[420] Emanuele Berti, Vitor Cardoso, and Marc Casals. Eigenvalues and eigenfunctions of spin-weighted spheroidal harmonics in four and higher dimensions. *Phys. Rev. D*, 73:024013, 2006.

[421] Emanuele Berti, Vitor Cardoso, and Andrei O. Starinets. Quasinormal modes of black holes and black branes. *Class. Quant. Grav.*, 26:163001, 2009. doi: 10.1088/0264-9381/26/16/163001.

[422] S. Husa, J. A. González, M. Hannam, B. Brügmann, and U. Sperhake. Reducing phase error in long numerical binary black hole evolutions with sixth-order finite differencing. *Classical and Quantum Gravity*, 25(10):105006–+, May 2008. doi: 10.1088/0264-9381/25/10/105006.

[423] B. Imbiriba, J. Baker, D.-I. Choi, J. Centrella, D. R. Fiske, J. D. Brown, J. R. van Meter, and K. Olson. Evolving a puncture black hole with fixed mesh refinement. *Phys. Rev. D.*, 70(12):124025–+, December 2004. doi: 10.1103/PhysRevD.70.124025.

[424] B. Vaishnav, I. Hinder, F. Herrmann, and D. Shoemaker. Matched filtering of numerical relativity templates of spinning binary black holes. *Phys. Rev. D.*, 76(8):084020–+, October 2007. doi: 10.1103/PhysRevD.76.084020.

[425] A. Peres. Classical radiation recoil. *Phys. Rev.*, 128:2471–2475, 1962.

[426] J. D. Bekenstein. Extraction of energy and charge from a black hole. *Phys. Rev.*, D7:949–953, 1973.

[427] M. J. Fitchett. The influence of gravitational wave momentum losses on the centre of mass motion of a Newtonian binary system. *Mon.Not.Roy.Astr.Soc.*, 203:1049–1062, June 1983.

[428] M. J. Fitchett and S. Detweiler. Linear momentum and gravitational waves – Circular orbits around a Schwarzschild black hole. *Mon. Not. R. astr. Soc.*, 211:933–942, December 1984.

[429] Marc Favata, Scott A. Hughes, and Daniel E. Holz. How black holes get their kicks: Gravitational radiation recoil revisited. *Astrophys. J.*, 607:L5–L8, 2004.

[430] Thibault Damour and Achamveedu Gopakumar. Gravitational recoil during binary black hole coalescence using the effective one body approach. *Phys. Rev.*, D73:124006, 2006. doi: 10.1103/PhysRevD.73.124006.

[431] John G. Baker, Joan Centrella, Dae-Il Choi, Michael Koppitz, James van Meter, and M. Coleman Miller. Getting a kick out of numerical relativity. *Astrophys. J.*, 653:L93–L96, 2006.

[432] J. A. González, M. Hannam, U. Sperhake, B. Brügmann, and S. Husa. Supermassive Recoil Velocities for Binary Black-Hole Mergers with Antialigned Spins. *Physical Review Letters*, 98(23):231101–+, June 2007. doi: 10.1103/PhysRevLett.98.231101.

[433] David Merritt and R. D. Ekers. Tracing black hole mergers through radio lobe morphology. *Science*, 297:1310–1313, 2002.

[434] F. Herrmann, I. Hinder, D. Shoemaker, and P. Laguna. Unequal mass binary black hole plunges and gravitational recoil. *Classical and Quantum Gravity*, 24:33, June 2007. doi: 10.1088/0264-9381/24/12/S04.

[435] Jose A. Gonzalez, Ulrich Sperhake, Bernd Bruegmann, Mark Hannam, and Sascha Husa. Total recoil: the maximum kick from nonspinning black-hole binary inspiral. *Phys. Rev. Lett.*, 98:091101, 2007.

[436] J. A. Gonzalez, M. D. Hannam, U. Sperhake, Bernd Bruegmann, and S. Husa. Supermassive kicks for spinning black holes. *Phys. Rev. Lett.*, 98:231101, 2007. doi: 10.1103/PhysRevLett.98.231101.

[437] Manuela Campanelli, Carlos O. Lousto, Yosef Zlochower, and David Merritt. Large merger recoils and spin flips from generic black-hole binaries. *Astrophys. J.*, 659:L5–L8, 2007.

[438] Manuela Campanelli, Carlos O. Lousto, Yosef Zlochower, and David Merritt. Maximum gravitational recoil. *Phys. Rev. Lett.*, 98:231102, 2007.

[439] B. Brügmann, J. A. González, M. Hannam, S. Husa, and U. Sperhake. Exploring black hole superkicks. *Phys. Rev. D.*, 77(12):124047–+, June 2008. doi: 10.1103/PhysRevD.77.124047.

[440] J. Healy, F. Herrmann, I. Hinder, D. M. Shoemaker, P. Laguna, and R. A. Matzner. Superkicks in Hyperbolic Encounters of Binary Black Holes. *Physical Review Letters*, 102(4):041101–+, January 2009. doi: 10.1103/PhysRevLett.102.041101.

[441] Lawrence E. Kidder. Coalescing binary systems of compact objects to post$^{5/2}$-Newtonian order. V. Spin effects. *Phys. Rev. D*, 52:821–847, 1995.

[442] J. G. Baker, W. D. Boggs, J. Centrella, B. J. Kelly, S. T. McWilliams, M. C. Miller, and J. R. van Meter. Modeling Kicks from the Merger of Generic Black Hole Binaries. *Astrophys. J. Lett.*, 682:L29–L32, July 2008. doi: 10.1086/590927.

[443] E. Berti and M. Volonteri. Cosmological Black Hole Spin Evolution by Mergers and Accretion. *Astrophys. J.*, 684: 822–828, September 2008. doi: 10.1086/590379.

[444] S. A. Hughes and R. D. Blandford. Black Hole Mass and Spin Coevolution by Mergers. *Astrophys. J. Lett.*, 585: L101–L104, March 2003. doi: 10.1086/375495.

[445] M. Campanelli, C. O. Lousto, Y. Zlochower, B. Krishnan, and D. Merritt. Spin flips and precession in black-hole-binary mergers. *Phys. Rev. D.*, 75(6):064030–+, March 2007. doi: 10.1103/PhysRevD.75.064030.

[446] Thibault Damour. Coalescence of two spinning black holes: An effective one- body approach. *Phys. Rev. D*, 64: 124013, 2001.

[447] A. Buonanno and T. Damour. Transition from inspiral to plunge in binary black hole coalescences. *Phys. Rev. D.*, 62(6):064015–+, September 2000. doi: 10.1103/PhysRevD.62.064015.

[448] T. Damour and A. Nagar. Final spin of a coalescing black-hole binary: An effective-one-body approach. *Phys. Rev. D.*, 76(4):044003–+, August 2007. doi: 10.1103/PhysRevD.76.044003.

[449] Latham Boyle, Michael Kesden, and Samaya Nissanke. Binary black hole merger: symmetry and the spin expansion. *Phys. Rev. Lett.*, 100:151101, 2008. doi: 10.1103/PhysRevLett.100.151101.

[450] A. Buonanno, L. E. Kidder, and L. Lehner. Estimating the final spin of a binary black hole coalescence. *Phys. Rev. D.*, 77(2):026004, January 2008.

[451] Ian Hinder, Birjoo Vaishnav, Frank Herrmann, Deirdre Shoemaker, and Pablo Laguna. Universality and Final Spin in Eccentric Binary Black Hole Inspirals. *Phys. Rev.*, D77:081502, 2008. doi: 10.1103/PhysRevD.77.081502.

[452] Latham Boyle and Michael Kesden. The spin expansion for binary black hole merger: new predictions and future directions. *Phys. Rev.*, D78:024017, 2008. doi: 10.1103/PhysRevD.78.024017.

[453] E. Berti, V. Cardoso, J. A. Gonzalez, U. Sperhake, M. Hannam, S. Husa, and B. Brügmann. Inspiral, merger, and ringdown of unequal mass black hole binaries: A multipolar analysis. *Phys. Rev. D.*, 76(6):064034–+, September 2007. doi: 10.1103/PhysRevD.76.064034.

[454] Manuela Campanelli, C. O. Lousto, and Y. Zlochower. The last orbit of binary black holes. *Phys. Rev.*, D73:061501, 2006. doi: 10.1103/PhysRevD.73.061501.

[455] B.M. Barker and R.F. O'Connell. *Phys. Rev. D*, 2:1428, 1970.

[456] E. Berti, V. Cardoso, J. A. González, U. Sperhake, and B. Brügmann. Multipolar analysis of spinning binaries. *Classical and Quantum Gravity*, 25(11):114035–+, June 2008. doi: 10.1088/0264-9381/25/11/114035.

[457] A. Buonanno, Y. Pan, J. G. Baker, J. Centrella, B. J. Kelly, S. T. McWilliams, and J. R. van Meter. Approaching faithful templates for nonspinning binary black holes using the effective-one-body approach. *Phys. Rev. D.*, 76(10): 104049–+, November 2007. doi: 10.1103/PhysRevD.76.104049.

[458] Manuela Campanelli, Carlos O. Lousto, and Yosef Zlochower. Spin-orbit interactions in black-hole binaries. *Phys. Rev. D*, 74:084023, 2006.

[459] W. Tichy and P. Marronetti. Binary black hole mergers: Large kicks for generic spin orientations. *Phys. Rev. D.*, 76(6):061502, September 2007. doi: 10.1103/PhysRevD.76.061502.

[460] C. Hanna, M. Megevand, E. Ochsner, and C. Palenzuela. Method to estimate ISCO and ring-down frequencies in binary systems and consequences for gravitational wave data analysis. *arXiv:0801.4297*, January 2008.

[461] A. Sesana, F. Haardt, P. Madau, and M. Volonteri. The Gravitational Wave Signal from Massive Black Hole Binaries and Its Contribution to the LISA Data Stream. *Astrophys. J.*, 623:23–30, April 2005. doi: 10.1086/428492.

[462] A. Sesana, F. Haardt, P. Madau, and M. Volonteri. Low-frequency gravitational radiation from coalescing massive black holes. *Classical and Quantum Gravity*, 22:363–+, May 2005. doi: 10.1088/0264-9381/22/10/030.

[463] Benjamin Farr, Stephen Fairhurst, and B. S. Sathyaprakash. Searching for binary coalescences with inspiral templates: Detection and parameter estimation. 2009.

[464] Lucia Santamaria, Badri Krishnan, and John T. Whelan. Searching for numerically-simulated signals of black hole binaries with a phenomenological template family. 2009.

[465] Stanislav Babak, Mark Hannam, Sascha Husa, and Bernard F. Schutz. Resolving Super Massive Black Holes with LISA. 2008.

[466] R. Adhikari, P. Fritschel, and S. Waldman. Enhanced ligo. Technical Report LIGO-T060156-01-I, LIGO Scientific Collaboration, 2006.

[467] Advanced LIGO. `http://www.ligo.caltech.edu/advLIGO/`.

[468] Virgo Collaboration. Advanced Virgo Preliminary Design, Virgo internal report VIR-089A-08 (2008).

[469] K. Danzmann, P. Bender, A. Brillet, I. Ciufolini A.M. Cruise, C. Cutler, F. Fidecaro, W.M. Folkner, J. Hough, P. McNamara, M. Peterseim, D. Robertson, M. Rodrigues, A. Rüdiger, M. Sandford, G. Schäfer, R. Schilling, B. Schutz, C. Speake, R.T. Stebbins, T. Sumner, P. Touboul, J.-Y. Vinet, S. Vitale, H. Ward, and W. Winkler. Lisa pre-phase a report. *Max-Planck-Inistitut für Quantenoptik, Report MPQ*, 233:184–209, 1998.

[470] Karsten Danzmann and Albrecth Rüdiger. LISA technology – Concept, status, prospects. *Class. Quantum Grav.*, 20:S1–S9, 2003. URL `stacks.iop.org/CQG/20/S2`.

[471] Luc Blanchet, Guillaume Faye, Bala R. Iyer, and Benoit Joguet. Gravitational-wave inspiral of compact binary systems to 7/2 post-Newtonian order. *Phys. Rev. D*, 65:061501, 2002.

[472] Eric Poisson. Gravitational waves from inspiraling compact binaries: The quadrupole-moment term. *Phys. Rev.*, D57:5287–5290, 1998. doi: 10.1103/PhysRevD.57.5287.

[473] Kashif Alvi. Energy and angular momentum flow into a black hole in a binary. *Phys. Rev.*, D64:104020, 2001. doi: 10.1103/PhysRevD.64.104020.

[474] Luc Blanchet, Alessandra Buonanno, and Guillaume Faye. Higher-order spin effects in the dynamics of compact binaries II. Radiation field. *Phys. Rev.*, D74:104034, 2006. doi: 10.1103/PhysRevD.74.104034.

[475] Guillaume Faye, Luc Blanchet, and Alessandra Buonanno. Higher-order spin effects in the dynamics of compact binaries. I: Equations of motion. *Phys. Rev.*, D74:104033, 2006. doi: 10.1103/PhysRevD.74.104033.

[476] Luc Blanchet, Guillaume Faye, Bala R. Iyer, and Siddhartha Sinha. The third post-Newtonian gravitational wave polarisations and associated spherical harmonic modes for inspiralling compact binaries in quasi-circular orbits. 2008.

[477] Lawrence E. Kidder. Using Full Information When Computing Modes of Post- Newtonian Waveforms From Inspiralling Compact Binaries in Circular Orbit. *Phys. Rev. D*, 77:044016, 2007.

[478] Luca Baiotti, Ian Hawke, Pedro J. Montero, Frank Löffler, Luciano Rezzolla, Nikolaos Stergioulas, José A. Font, and Ed Seidel. Three-dimensional relativistic simulations of rotating neutron star collapse to a Kerr black hole. *Phys. Rev. D*, 71:024035, 2005.

[479] É. É. Flanagan and S. A. Hughes. Measuring gravitational waves from binary black hole coalescences. i. Signal to noise ratios for inspiral, merger, and ringdown. *Phys. Rev. D.*, 57(8):4535–4565, 1998.

[480] T. Damour, B. R. Iyer, and B. S. Sathyaprakash. Improved filters for gravitational waves from inspiraling compact binaries. *Phys. Rev. D.*, 57:885–907, January 1998. doi: 10.1103/PhysRevD.57.885.

[481] Enrico Barausse and Luciano Rezzolla. Predicting the direction of the final spin from the coalescence of two black holes. 2009.

[482] B. Abbott et al. Joint ligo and tama300 search for gravitational waves from inspiralling neutron star binaries. *Phys. Rev. D*, 73:102002, 2006.

[483] Carlos O. Lousto, Manuela Campanelli, and Yosef Zlochower. Remnant Masses, Spins and Recoils from the Merger of Generic Black-Hole Binaries. 2009.

[484] Ulrich Sperhake, Vitor Cardoso, Frans Pretorius, Emanuele Berti, and Jose A. Gonzalez. The high-energy collision of two black holes. *Phys. Rev. Lett.*, 101:161101, 2008. doi: 10.1103/PhysRevLett.101.161101.

[485] M. Kesden. Can binary mergers produce maximally spinning black holes? *Phys. Rev. D.*, 78(8):084030, October 2008. doi: 10.1103/PhysRevD.78.084030.

[486] W. Tichy and P. Marronetti. The final mass and spin of black hole mergers. *Phys. Rev. D.*, 78:081501, July 2007.

[487] Michael Boyle and Abdul H. Mroue. Extrapolating gravitational-wave data from numerical simulations. 2009.

[488] Andrea Nerozzi. Scalar functions for wave extraction in numerical relativity. *Phys. Rev.*, D75:104002, 2007. doi: 10.1103/PhysRevD.75.104002.

[489] E. Deadman and J. M. Stewart. Numerical Relativity and Asymptotic Flatness. *Class. Quant. Grav.*, 26:065008, 2009. doi: 10.1088/0264-9381/26/6/065008.

[490] B. Kocsis and A. Loeb. Distortion of gravitational-wave packets due to their self-gravity. *Phys. Rev. D.*, 76(8): 084022–+, October 2007. doi: 10.1103/PhysRevD.76.084022.

[491] Thibault Damour and Alessandro Nagar. An improved analytical description of inspiralling and coalescing black-hole binaries. 2009.

[492] L. Lindblom, B. J. Owen, and D. A. Brown. Model waveform accuracy standards for gravitational wave data analysis. *Phys. Rev. D.*, 78(12):124020–+, December 2008. doi: 10.1103/PhysRevD.78.124020.

[493] Roberto Gómez, Sascha Husa, Luis Lehner, and Jeffrey Winicour. Gravitational waves from a fissioning white hole. *Phys. Rev. D*, 66(6):064019, Sep 2002. doi: 10.1103/PhysRevD.66.064019.

[494] Roberto Gómez and Simonetta Frittelli. First-order quasilinear canonical representation of the characteristic formulation of the einstein equations. *Phys. Rev. D*, 68(8):084013, Oct 2003. doi: 10.1103/PhysRevD.68.084013.

[495] H.-O. Kreiss and O.E. Ortiz. Some mathematical and numerical questions connected with first and second order time-dependent systems of partial differential equations. In J. Frauendiener and H. Friedrich, editors, *The Conformal Structure of Space-Time: Geometry, Analysis, Numerics*, volume 604 of *Lecture Notes in Physics*, pages 359–370, Berlin; New York, 2002. Springer. doi: 10.1007/3-540-45818-2.

[496] Stanislav Babak et al. The Mock LISA Data Challenges: from Challenge 1B to Challenge 3. *Class. Quant. Grav.*, 25:184026, 2008. doi: 10.1088/0264-9381/25/18/184026.

[497] LISA parameter estimation wiki. `http://www.tapir.caltech.edu/dokuwiki/lisape:home`.

[498] P. Diener, E. N. Dorband, E. Schnetter, and M. Tiglio. New, efficient, and accurate high order derivative and dissipation operators satisfying summation by parts, and applications in three-dimensional multi-block evolutions. *ArXiv General Relativity and Quantum Cosmology e-prints*, November 2005.

[499] E. W. Leaver. Solutions to a generalized spheroidal wave equation: Teukolsky's equations in general relativity, and the two-center problem in molecular quantum mechanics. *Journal Math. Phys.*, 27(5):1238–1265, 1986.

[500] E. W. Leaver. Spectral decomposition of the perturbation response of the Schwarzschild geometry. *Phys. Rev. D*, 34(2):384–408, 1986.

[501] H. Onozawa. Detailed study of quasinormal frequencies of the Kerr black hole. *Phys. Rev. D.*, 55:3593–3602, March 1997. doi: 10.1103/PhysRevD.55.3593.

[502] E. Berti, V. Cardoso, K. D. Kokkotas, and H. Onozawa. Highly damped quasinormal modes of Kerr black holes. *Phys. Rev. D.*, 68(12):124018–+, December 2003. doi: 10.1103/PhysRevD.68.124018.

[503] E. Berti, V. Cardoso, and S. Yoshida. Highly damped quasinormal modes of Kerr black holes: A complete numerical investigation. *Phys. Rev. D.*, 69(12):124018–+, June 2004. doi: 10.1103/PhysRevD.69.124018.

[504] W. Kinnersley. Type D Vacuum Metrics. *Journal of Mathematical Physics*, 10:1195–1203, July 1969. doi: 10.1063/1.1664958.

[505] Neil Young and Crazy Horse. Hey, hey, my, my (into the black), rust never sleeps, 1979.

[506] M. Tegmark. Many lives in many worlds. *Nature*, 448:23–24, July 2007. doi: 10.1038/448023a.

[507] M. Tegmark. The Mathematical Universe. *Foundations of Physics*, 38:101–150, February 2008. doi: 10.1007/s10701-007-9186-9.

[508] S. Lloyd. Universe as quantum computer. *Complexity*, 3:32–35, 1997.

[509] J. Schmidhuber. Algorithmic Theories of Everything. *ArXiv Quantum Physics e-prints*, November 2000.

[510] M. Tegmark. Is "the Theory of Everything" Merely the Ultimate Ensemble Theory? *Annals of Physics*, 270:1–51, November 1998. doi: 10.1006/aphy.1998.5855.

[511] M. Tegmark. Does the universe in fact contain almost no information? *Foundations of Physics Letters*, 9:25–41, February 1996. doi: 10.1007/BF02186207.

[512] Reiner Hedrich. Quantum Gravity: Motivations and Alternatives. 2009.

[513] Reiner Hedrich. Quantum Gravity: Has Spacetime Quantum Properties? 2009.

[514] Douglas Adams. *Hitchikers guide to the galaxy.* Pan Books, 1979.